3-D TRANSPORT PHENOMENA IN VERTICAL DIRECT CHILL CASTING PROCESSES

LATIFA BEGUM

Department of Mining and Materials Engineering
McGill University
Montreal, Quebec, Canada

A thesis submitted to the Faculty of Graduate and Postdoctoral Studies
in partial fulfillment of the requirements for the
Doctor of Philosophy

December, 2013

ABSTRACT

Maintaining the uniformity of the temperature distribution of the liquid metal before it enters the mold of Direct Chill (DC) casting processes is critical from the standpoint of defect formation. The temperature of the liquid phase depends on the flow pattern of the molten metal which is strongly inter-connected to the design characteristics of the metal distributor and the process parameters used for a particular alloy such as, casting speed, melt superheat, mold water flow rate, etc. If the melt distribution system is improperly designed and can't sufficiently reduce the turbulence of the incoming melt in the liquid pool, then it will act as a continuous source of oxide formation and contamination during the whole casting process. This will impact adversely on the cast quality and enhance the scrap rate. In order to minimize the impurities in the cast, the present research study suggests and models various new designs of melt distribution systems where the melt is filtered before entering the mold.

As part of this effort, a comprehensive 3-D mathematical model of the coupled turbulent fluid flow, heat transfer with mushy region solidification was developed for the vertical DC casting process during steady state phase for an industrial scale rolling ingot. The model was specifically used for understanding the complex interactions between the melt flow and temperature evolution in the solidifying Al-1050 ingot under different melt feeding arrangements for various casting speeds and melt superheats. The model is based on the control volume finite difference technique. The SIMLPE algorithm was used to couple the velocity and pressure fields such that the velocities satisfy the continuity equation. A single phase formulation was adopted to solve the three regions, namely, liquid, mushy, and solid, by a single set of governing equations. The low-Reynolds number k- ε model of Launder and Sharma was used in the melt region to account for the increase in the effective viscosity and effective thermal conductivity to accommodate the effects of turbulence there. The popular 'enthalpy-porosity' approach was used in order to couple the energy equation with the momentum equations. Darcy law of porous media was employed in the momentum equations to model the melt flow in the mushy region. The convective terms of the governing equations were discretized using the hybrid

difference scheme. The effects of the natural convection in the liquid metal were included through the Boussinesq approximation. To model the filter, which was placed in the liquid pool at the hot-top, the Brinkman-Forchheimer extended Darcy equations for porous medium was used. To model the turbulent flow and heat transfer in porous medium, the approach proposed by Pedras and de Lemos was used. Using their approach, the volume-averaged operator was applied to the local time-averaged turbulent equations. The primary and the secondary cooling zones of the caster were simulated by changing the effective heat transfer coefficient on the slab surface. The heat transfer coefficient values were taken from the relevant DC casting literature.

The 3-D CFD model was validated against steady state solidification front measurements obtained from real casting experiments of others for a 1320 mm × 660 mm AA3104 rolling ingot casted with a standard combo bag delivery system. Comparison of the predicted solidification front with the measured data, which was collected by using embedded sacrificial thermocouples, indicates that the model gives reliable results.

The CFD model was then modified to develop a simple thermal model to investigate the solidification heat transfer process in the rolling ingot, by considering only the advection heat transfer in the axial direction. To get a preliminary understanding of the casting process, this simplified 3-D heat transfer model was used to predict the temperature profiles, as well as the sump depth and the solid-shell thickness of the ingot for various casting parameters. A detail quantitative comparison of the results was made between the thermal and the CFD models for identical operating conditions. The differences obtained in the predicted results between these two models are presented and discussed.

Using the CFD model, six distinct metal distribution systems, namely, the open-top, open-top with a full filter, open-top with a half filter, channel bag, two types of combo bags, and nozzle with a full filter, were simulated for various process parameters. The predicted results are presented in the form of temperature and velocity fields. In addition, the quantitative values of the sump depth, the mushy zone thickness, the shell thickness, and the local surface heat flux are given in both graphical and tabular forms.

The results show that the temperature distributions and the velocity fields in the melt and in the mushy region are significantly different under different melt feeding schemes. The predictions of the various aspects of the ingot have provided a clear insight about the thermal variations in the entire cross-sections of the ingot. The fundamental models which have been developed in this research can be used as a powerful tool for process optimization and quality control.

Résumé

Maintenir l'uniformité de la distribution de température d'un métal liquide avant qu'il soit mis dans un moule de traitement thermique Direct Chill (DC) est critique pour réduire la formation de défauts. La température de la phase liquide d'un métal en fusion dépend sur sa configuration d'écoulement, et ce dernier est fortement liée aux particularités du distributeur de métal utilisé, ainsi qu'aux paramètres choisis pour l'alliage en question, tel que la vitesse de moulage, la fusion en surchauffe, la vitesse d'écoulement de l'eau de moule, etc. Si le système de distribution de température a des défauts de conception et ne peut pas réduire suffisamment la turbulence du métal en fusion qui arrive dans le réservoir, il agira comme source continuel de formation d'oxyde et de contamination durant le processus de moulage. Ceci aura des effets négatifs sur la qualité du moulage et augmentera le taux de rebuts. Pour minimiser les impuretés durant le moulage, notre projet de recherche vise à développer plusieurs conceptions de systèmes de distributions de température où le métal en fusion est filtré avant d'arriver dans la moule.

Dans ce but, un modèle mathématique 3-D représentant l'écoulement de fluide turbulent couplé, ainsi que le transfert de chaleur avec solidification de région molle, a été développé pour le processus de moulage DC durant la phase stable pour un lingot roulé de taille industrielle. Plus précisément, ce modèle a été utilisé pour comprendre les interactions complexes qui se produisent entre l'écoulement de métal en fusion et l'évolution de température du lingot solidifié Al-1050 sous différentes paramètres de fusion, pour plusieurs vitesses de moulage et de fusion en surchauffe. Ce modèle est basé sur le la méthode des volumes finis. Cet algorithme simple a été utilisé pour couplé la vélocité et les champs de pression pour que les vélocités répondent à l'équation de conservation. Une formulation de phase simple a été adoptée pour résoudre les trois régions, dont liquide, molle et solide, grâce à un ensemble d'équations gouverneurs. Le modèle 'low-Reynolds number k- ε' de Launder et Sharma a été utilisé dans la région en fusion pour justifier l'augmentation de viscosité effective et la conductivité thermique effective, et donc balancer les effets de turbulence qui se présentaient. La méthode

populaire ‘enthalpy-porosity’ a été adopté pour couplé l’équation d’énergie avec l’équation de quantité de mouvement. La loi de Darcy a été utilisée dans les équations de quantité de mouvement pour modeler l’écoulement de fusion dans la région molle. Les termes de convections des équations ont été discrétisées en utilisant la méthode de la différence hybride. Les effets de convection naturelle dans le métal liquide ont été ajoutés grâce à l’approximation Boussinesq. Le filtre, qui a été placé sur le sommet du réservoir, a été modelé grâce à l’équation ‘Brinkman-Forchheimer extended Darcy’ pour matières poreuses. L’approche proposé par Pedras et de Lemos a été utilisé pour modeler le courant turbulent et le transfert de chaleur dans les matières poreuses. Avec cette approche, l’opérateur de la moyenne des volumes a été appliqué à l’équation des heures de turbulence locales. Les zones de refroidissement primaires et secondaires ont été simulées en changeant le coefficient de transfert de chaleur sur la surface du lingot. Les données de coefficient de transfert de chaleur ont été prises de la littérature sur le moulage DC.

Le modèle 3-D CFD a été validé contre les résultats de phases de solidification stable obtenus par d’autres études sur le moulage, pour un lingot roulé 1320 mm x 660 mm AA3104, moulé avec un système de délivrance combo ‘standard bag’. La comparaison du front de solidification prévu avec les données mesurées, récupérées avec des thermocouples sacrificiels intégrés, indiquent que le modèle donne des résultats fiables.

Par la suite, le modèle CFD a été modifié pour développer un modèle thermique simple dans le but d’examiner les processus de solidifications et transferts de chaleur dans le lingot roulé, en tenir compte seulement du transfert de chaleur en advection, direction axial. Pour avoir une compréhension de base du processus de moulage, ce modèle de transfert de chaleur 3-D a été utilisé pour prédire les profiles thermiques, ainsi que la profondeur du puisard et l’épaisseur de la carapace dure du lingot, pour plusieurs paramètres de moulage. Une comparaison quantitative des résultats a été faite entre le modèle thermique et le modèle CFD avec des conditions d’opérations identiques. Les différences obtenus entre les deux modèles dans les résultats prévus sont présentées et discutées.

En utilisant le modèle CFD, six systèmes de distribution de métal différentes, dont le couvercle ouvert, le couvercle ouvert avec filtre plein, le couvercle ouvert avec demi filtre, le channel bag, deux types de combo bag, et le bec avec filtre plein, ont été simulés pour plusieurs paramètres. Les résultats prédits sont présentés sous forme de champs de température et de vélocité. De plus, les données quantitatives de la profondeur du puisard, de l'épaisseur des zones molles, de l'épaisseur de la carapace dure, et le flux de chaleur sur la surface locale sont présentées en tableaux et sous forme de graphiques. Les résultats démontrent que la distribution de température et les champs de vélocité dans le métal en fusion, ainsi que dans les régions molles, sont significativement différentes sous différentes méthodes de fusion. Les prédictions de plusieurs aspects du lingot nous offrent un aperçu clair sur la variation thermale dans les sections transversales du lingot. Les modèles fondamentales qui ont été développé dans ce projet de recherche peuvent devenir des outils essentiels pour optimiser le processus et assurer la qualité de production.

ACKNOWLEDGMENTS

I would like to express my sincere and deep appreciation to my thesis supervisor, Prof. Mainul Hasan for recommending this practical topic of research of industrial importance. The financial support he has provided me during the course of my research program is highly appreciated. His constant encouragements, guidance, constructive suggestions and insights are highly valued and I have often sought. I am especially thankful to Prof. Mainul Hasan, who taught me how to write the complex FORTRAN CFD code, and for his excellent teaching of courses related to transport phenomena and advanced computational methods in fluid flow, heat and mass transfer. I have not met yet any professor who can teach many difficult concepts so clearly. He has been my true mentor, and has greatly contributed to my professional and personal development at McGill. I also gratefully acknowledge the enormous amount of time he has spent in reviewing and correcting my thesis.

Thanks are also due to Prof. Mihriban Pekguleryuz and Prof. Laurent B. Mydlarski for allowing me to audit their informative courses related to aluminum alloys and turbulent flow, respectively.

This work could not have been even attempted and completed without the deep understanding, patience, and continuous encouragement of my only daughter, Tasnim Tabassum. She has spent countless hours alone at home while I was working towards my Ph.D. at McGill. Over the years, the sacrifices she has made to see me complete my Ph.D. work, I will never be able to repay.

I would like to express my heartfelt appreciations to my parents, Abdur Razzak and Hamida Razzak, and to my three younger brothers and two younger sisters for their sincere love, moral support and constant inspiration to achieve my academic dream.

I dedicate this thesis to my daughter as a token of my eternal indebtedness.

TABLE OF CONTENTS

	Page
ABSTRACT …….....	i
RESUME …….....	iv
ACKNOWLEDGEMENTS ……	vii
TABLE OF CONTENTS …….....	viii
LIST OF FIGURES …….....	xv
LIST OF TABLES ……..	xxxvi
NOMENCLATURE……	xli

CHAPTER 1: INTRODUCTION

1.1 Introduction …….	1-1
1.2 Direct Chill (DC) Casting Process – A Brief Introduction……..	1-2
1.3 Probable Defects in DC Cast……	1-6
1.4 Optimization of the D.C. Casting Process……	1-13
1.5 Complexities of Numerical Modeling……..	1-15
1.6 Objectives of the Present Study ……..	1-17
1.7 Overview of the Present Work …….....	1-22

CHAPTER 2: LITERATURE REVIEW

2.1 Introduction ……..	2-1
2.2 Thermal models for the phase change problems……..	2-2
2.3 CFD models …….	2-8
2.4 Closure …….....	2-31

CHAPTER 3: MATHEMATICAL MODEL AND NUMERICAL APPROACH

3.1 Introduction ……..... 3-1

3.2 Mathematical Formulation …… 3-3

a. Model Geometry…… 3-4

b. Test Material…….. 3-5

3.2.1 Assumptions and Simplification of the Mathematical Model……... 3-5

3.2.2 Modeling of Turbulence Parameters……..... 3-8

3.2.2.1 Launder and Sharma Low Reynolds Number Two-Equation k-ε Model……..... 3-11

3.2.2.2 Modeling of Reynolds Stress Terms…….. 3-11

3.2.2.3 Modeling of Turbulence Heat Fluxes……. 3-12

3.2.2.4 Governing Equations for k and ε …….. 3-12

3.2.3 Solidification Modeling …… 3-13

3.2.4 Modeling of Fluid Flow in the Mushy Region ……. 3-16

3.2.5 Modeling of Buoyancy Term in the X-Momentum Equation…..... 3-17

3.2.6 Boundary Conditions …… 3-20

3.2.7 Calculation of the Local Heat flux at the Surface ……. 3-26

3.2.8 Non-Dimensionalization of the Governing Equations and Boundary Conditions…….. 3-28

3.3 Numerical Approach ……. 3-31

3.3.1 Discretization Procedures ……. 3-31

3.3.2 Solution Procedure and Convergence Criteria …….. 3-31

3.3.3 Under-relaxation factor…….. 3-33

3.3.4 Post Processing of the Results…….. 3-34

CHAPTER 4: QUANTITATIVE VERIFICATION OF THE MODEL AND GRID INDEPENDENCY TESTS

4.1 Code Verification…….. 4-1
4.1.1 Introduction…… 4-1
4.1.2 Description of the DC Casting Experimental Set-up and Procedures… 4-1
4.1.3 Numerical Modeling Set-up…….. 4-2
4.1.4 Difficulties in Validating the Code…… 4-5
4.1.5 Numerical Results…….. 4-7
4.1.6 Quantitative Verification of Results and Related Discussion…… 4-9
4.1.7 Closure……... 4-11
4.2 Grid Independency Test……. 4-11

CHAPTER 5: THREE-DIMENSIONAL THERMAL MODEL

5.1 Introduction ……..... 5-1
5.2 Governing Equations…….. 5-5
5.3 Boundary Conditions……. 5-7
5.4 Results and Discussion…….. 5-8
a. Effect of Casting Speed for a Fixed Inlet Superheat of 32^{o}C……. 5-10
i. Temperature Field…….. 5-10
ii. Quantitative Analysis for $\Delta T = 32^{o}C$……. 5-12
1. Sump Depth and Mushy Layer Thickness…… 5-12
2. Formation of Solidified Shell…… 5-13
3. Local Surface Heat Flux……... 5-13
b. Effect of Casting Speed for a Fixed Inlet Superheat of 64^{o}C……. 5-16
i. Temperature Field…….. 5-16
ii. Quantitative Analysis for $\Delta T = 64^{o}C$……. 5-16
1. Sump Depth and Mushy Layer Thickness…… 5-16
2. Formation of Solidified Shell…… 5-18
3. Local Surface Heat Flux……... 5-19
5.5 Concluding Remarks…….. 5-20

CHAPTER 6: OPEN-TOP MELT FEEDING SYSTEM

6.1 Introduction ……... 6-1

6.2 Results and Discussion…….. 6-2

6.2.1 Velocity Fields for $\Delta T = 32^{o}C$……... 6-3

6.2.2 Temperature Fields for $\Delta T = 32^{o}C$……. 6-4

6.2.3 Quantitative Analysis for $\Delta T = 32^{o}C$…… 6-6

i. Sump Depth and Mushy Layer Thickness……. 6-6

ii. Formation of Solidified Shell…… 6-7

iii. Local Surface Heat Flux…… 6-7

6.2.4 Velocity and Temperature Fields for $\Delta T = 64^{o}C$…….. 6-9

6.2.5 Quantitative Analysis for $\Delta T = 64^{o}C$ …… 6-10

i. Sump Depth and Mushy Layer Thickness……. 6-10

ii. Formation of Solidified Shell……. 6-12

iii. Local Surface Heat Flux…… 6-13

6.3 Comparison Between the Thermal and CFD Models…… 6-13

A. Predicted Shell Thickness……. 6-14

B. Sump Depth Predictions…….. 6-15

6.4 Effect of Primary Coolant Heat Transfer Coefficient…… 6-16

i Solid-shell Thickness…….. 6-17

ii Surface Temperature…….. 6-18

6.5 Concluding Remarks……..... 6-18

CHAPTER 7: OPEN TOP WITH FULL AND HALF POROUS FILTER

7.1 Introduction ……..... 7-1

7.2 Assumptions and Governing Equations……. 7-7

7.3 Fluid/Porous Interface Boundary Condition…….. 7-10

7.4 Results and Discussion…….. 7-11
7.4.1 Full-Filtered Case…….. 7-12
a. Velocity and Temperature Fields for $\Delta T = 32^oC$…….. 7-12
b. Quantitative Analysis for $\Delta T = 32^oC$…… 7-15
i. Sump Depth and Mushy Layer Thickness…… 7-15
ii. Formation of Solidified Shell…… 7-16
iii. Local Surface Heat Flux…… 7-17
c. Velocity and Temperature Fields for $\Delta T = 64^oC$…….. 7-19
d. Quantitative Analysis for $\Delta T = 64^oC$ …….. 7-20
i. Sump Depth and Mushy Layer Thickness……. 7-20
ii. Formation of Solidified Shell……. 7-22
iii. Local Surface Heat Flux……. 7-23
7.4.2 Half-Filtered Case…….. 7-23
a. Velocity and Temperature Fields for $\Delta T = 32^oC$, and $\Delta T = 64^oC$… 7-24
b. Quantitative Analysis for $\Delta T = 32^oC$ and $\Delta T = 64^oC$…….. 7-26
i. Sump Depth and Mushy Layer Thickness……. 7-26
ii. Formation of Solidified Shell……. 7-28
iii. Local Surface Heat Flux…… 7-29
7.5 Conclusions……..... 7-31

CHAPTER 8: SUBMERGED NOZZLE WITH CHANNEL AND COMBO-BAG

8.1 Introduction ……..... 8-1
8.2 Results and Discussion…….. 8-7
8.2.1 Geometry-1…… 8-7
a. Velocity and Temperature Fields …….. 8-7
b. Quantitative Analysis…… 8-11
i. Sump Depth and Mushy Layer Thickness……. 8-11
ii. Formation of Solidified Shell……. 8-12

iii. Local Surface Heat Flux…… 8-13
8.2.2 Geometry-2…… 8-15
a. Velocity and Temperature Fields…….. 8-15
b. Quantitative Analysis…….. 8-19
i. Sump Depth and Mushy Layer Thickness……. 8-19
ii. Formation of Solidified Shell……. 8-20
iii. Local Surface Heat Flux…… 8-21
8.2.3 Geometry-3…… 8-22
a. Velocity and Temperature Fields…….. 8-22
b. Quantitative Analysis……... 8-24
i. Sump Depth and Mushy Layer Thickness……. 8-24
ii. Formation of Solidified Shell……. 8-25
iii. Local Surface Heat Flux…… 8-27
8.3 Concluding Remarks……..... 8-28

CHAPTER 9: DELIVERY SYSTEM WITH A SUBMERGED NOZZLE AND A POROUS FILTER

9.1 Introduction ……..... 9-1
9.2 Results and Discussion…….. 9-3
a. Velocity and Temperature Fields …….. 9-4
b. Quantitative Analysis……. 9-7
i. Predicted Sump Depth and Mushy Layer Thickness……. 9-7
ii. Formation of Solidified Shell…… 9-8
iii. Local Surface Heat Flux…… 9-9
9.3 Conclusions……..... 9-10

CHAPTER 10: SUMMERY

10.1 Overall Concluding Remarks…….. 10-1

10.2 Statement of Originality…….. 10-8
10.3 Suggestions for Future Work…… 10-10

REFERENCES…….. 1-16

LIST OF FIGURES

Figure

1.1 Summary of Direct Chill (DC) casting and downstream processes for manufacturing aluminum rolled sheet……. 1-1

1.2 Schematic of the D.C. casting process for rolling ingots…… 1-4

1.3 Schematic of the horizontal D.C. casting process…….. 1-5

1.4 A rolling ingot is removed from casting pit at the end of the D.C. casting process…….. 1-5

1.5 Interaction between process parameters and the structure and defect formation upon DC casting of Al ingots……. 1-6

1.6 Schematic of cold crack defects related to secondary cooling during DC casting of aluminum…… 1-9

1.7 The schematic diagram shows the cooling of the ingot base in the presence of the bottom block during the start-up phase and also showing the probable heat transfer processes occurring near the centre of the ingot (Region A), and the outer edges (Region B)…….. 1-9

1.8 Proposed melt feeding distributors for VDC casting processes. (a) Open-top melt feeding scheme (b) Open top with a full porous filter melt feeding scheme (c) Open-top with a half porous filter melt feeding scheme (d) Submerged nozzle and a porous filter melt feeding scheme (e) Submerged nozzle with a distributor bag having a bottom solid plate melt feeding scheme and (f) Submerged nozzle with a distributor bag having a fine (filter) and coarse (foam) bottom porous plate melt feeding scheme……. 1-21

2.1 Schematic representation of (a) Equivalent specific heat, and (b) Enthalpy method……. 2-4

3.1 Schematic of the DC caster with the yellow part representing the computational domain……. 3-4

3.2 Calculation domain showing the boundary surfaces…….. 3-22

3.3 The schematic diagram shows the two regions where the local surface heat fluxes were calculated: (a) A-A' and (b) B-B'…… 3-27

3.4 Staggered grid……. 3-34

3.5 Flow chart of the 3-D turbulent fluid flow and solidification code…… 3-35

4.1 Schematic of a combo-distribution bag……. 4-15

4.2 3-D surface plot using the combo bag, casting speed = 50.8 mm/min, inlet melt superheat = 45°C, Gr = 10^9……. ……. 4-16

4.3 Computed results parallel to the slab rolling face using the combo bag at the casting speed of 50.8 mm/min, inlet melt superheat of 45°C and Gr = 10^9: (a,c,e) vector and streamlines plot, (b,d,f) temperature contours in Kelvin……..... 4-17

4.4 Top view of the real casting experiment showing thermocouples distribution……. 4-18

4.5 Sump profiles at the wide symmetry plane determined through experiments and the corresponding numerical predictions……. 4-19

4.6 Non-uniform distribution of the grid in the x, y, z directions, respectively, inside the calculation domain, for: (i) coarse sized grid of $60\times42\times24$ grid points (ii) medium sized grid of $70\times52\times34$ grid points, and (iii) fine sized grid of $80\times62\times44$ grid points……. 4-20

4.7 Variations of local surface heat flux at a casting speed of 100 mm/min and a melt superheat of 32°C along the axial distance of the strand on the wide slab face at y = 430.5 mm from the ingot center for an open top melt delivery system for a coarse, medium and fine grid distribution…… 4-21

4.8 Variations of local surface heat flux at a casting speed of 100 mm/min for a melt superheat of 32°C along the axial distance of the strand on the narrow slab face at z = 322.5 mm from the ingot center for an open top melt delivery system for a coarse, medium and fine grid distribution…… 4-21

5.1 Schematic of the DC caster with the yellow part representing the computational domain for an open-top melt feeding scheme…… 5-4

5.2 Schematic illustrations of the configuration with the boundary conditions… 5-8

5.3 Schematic explanation of the sump depth ($\bar{x}$) and shell thickness (y_b)……. 5-9

5.4 3-D surface plots of the temperature distributions in the complete solution domain for an inlet superheat of 32^0C using thermal model at:(a) 60 mm min^{-1} (b) 100 mm.min^{-1} (c) 140 mm min^{-1} (d) 180 mm min^{-1}……. 5-22

5.5 Enlarged 2-D view of temperature contours of the top domain using thermal model for an inlet superheat of 32°C and at a casting speed of: 60 mm/min (a, e, i at z = 0, z = 62.5 mm, and z = 312.5 mm, respectively); 100 mm/min (b, f, j at z = 0, z = 62.5 mm, and z = 312.5 mm, respectively): 140 mm/min (c, g, k at z = 0, z = 62.5 mm, and z = 312.5 mm, respectively): 180 mm/min (d, h, l at z = 0, z = 62.5 mm, and z = 312.5 mm, respectively)…….. 5-23

5.6 Contours of solidus and liquidus temperatures at various transverse cross-sectional planes (y-z planes) of the top part of the ingot using thermal model for a superheat of 32°C and casting speeds of (a) 60 mm min^{-1} (b) 100 mm min^{-1} (c) 140 mm min^{-1} (d) 180 mm min^{-1}……. 5-24

5.7 3-D surface plots of the temperature distributions in the complete solution domain for an inlet superheat of 64^0C using thermal model at:(a) 60 mm min^{-1} (b) 100 mm.min^{-1} (c) 140 mm min^{-1} (d) 180 mm min^{-1}……. 5-25

5.8 Enlarged 2-D view of temperature contours of the top domain using thermal model for an superheat of 64°C and at a casting speed of: 60 mm/min (a, e, i at z = 0, z = 62.5 mm, and z = 312.5 mm, respectively); 100 mm/min (b, f, j at z = 0, z = 62.5 mm, and z = 312.5 mm, respectively): 140 mm/min (c, g, k at z = 0, z = 62.5 mm, and z = 312.5 mm, respectively): 180 mm/min (d, h, l at z = 0, z = 62.5 mm, and z = 312.5 mm, respectively)…….. 5-26

5.9 Contours of solidus and liquidus temperatures at various transverse cross-sectional planes (y-z planes) of the top part of the ingot using thermal model for a superheat of 64°C and casting speeds of (a) 60 mm min^{-1} (b) 100 mm min^{-1} (c) 140 mm min^{-1} (d) 180 mm min^{-1}…….. 5-27

5.10 Solidified layer thickness from the narrow slab face at an axial distance of x = 160 mm from the top surface at the wide symmetry plane versus casting speed using the thermal model for: (a) inlet superheat of 32^{o}C, (b) inlet superheat of 64^{o}C…… 5-28

5.11 Variations of local surface heat fluxes for various casting speeds during solidification at 32°C superheat along the axial direction of the strand wall at: (a) z = 185 mm (b) y = 857.5 mm, using the thermal model……. 5-29

5.12 Variations of local surface heat fluxes for various casting speeds during solidification at 64°C superheat along the axial direction of the strand wall at: (a) z = 185 mm (b) y = 857.5 mm, using the thermal model……. 5-29

6.1 3-D surface plots for the complete solution domain at four casting speeds and 32^{0}C superheat using the open top delivery system: (i) temperature contours (a) and velocity field (b) for casting speed of 60 mm/min; (ii) temperature contours (c) and velocity field (d) for casting speed of 100 mm/min; (iii) temperature contours (e) and velocity field (f) for casting speed of 140 mm/min; (iv) temperature contours (g) and velocity field (h) for casting speed of 180 mm/min…… 6-20

6.2 Enlarged 2-D view of temperature contours and velocity vectors of the top domain using the open top delivery system for a casting speed of 60 mm/min and 32°C superheat at: (a) wide symmetry plane at z = 0 mm, (b) vertical plane parallel to the wide face at z = 62.5 mm, (c) vertical plane parallel to the wide face at z = 312.5 mm……... 6-21

6.3 Enlarged 2-D view of temperature contours and velocity vectors of the top domain using the open top delivery system for a casting speed of 100 mm/min and 32°C superheat at: (a) wide symmetry plane at z = 0 mm, (b) vertical plane parallel to the wide face at z = 62.5 mm, (c) vertical plane parallel to the wide face at z = 312.5 mm…….. 6-22

6.4 Enlarged 2-D view of temperature contours and velocity vectors of the top domain using the open top delivery system for a casting speed of 140 mm/min and 32°C superheat at: (a) wide symmetry plane at z = 0 mm, (b) vertical plane parallel to the wide face at z = 62.5 mm, (c) vertical plane parallel to the wide face at z = 312.5 mm…….. 6-23

6.5 Enlarged 2-D view of temperature contours and velocity vectors of the top domain using the open top delivery system for a casting speed of 180 mm/min and 32°C superheat at: (a) wide symmetry plane at z = 0 mm, (b) vertical plane parallel to the wide face at z = 62.5 mm, (c) vertical plane parallel to the wide face at z = 312.5 mm…….. 6-24

6.6 Contours of solidus and liquidus temperatures at various transverse cross-sectional planes (y-z planes) of the top part of the ingot using the open top delivery system for a superheat of 32°C and a casting speed of 60 mm min^{-1}…… 6-25

6.7 Contours of solidus and liquidus temperatures at various transverse cross-sectional planes (y-z planes) of the top part of the ingot using the open top delivery system for a superheat of 32°C and a casting speed of 100 mm min^{-1}…… 6-26

6.8 Contours of solidus and liquidus temperatures at various transverse cross-sectional planes (y-z planes) of the top part of the ingot using the open top delivery system for a superheat of 32°C and a casting speed of 140 mm min^{-1}…… 6-27

6.9 Contours of solidus and liquidus temperatures at various transverse cross-sectional planes (y-z planes) of the top part of the ingot using the open top delivery system for a superheat of 32°C and a casting speed of 180 mm min^{-1}…… 6-28

6.10 3-D surface plots for the complete solution domain for four casting speeds and 64^0C superheat using the open top delivery system: (i) temperature contours (a) and velocity field (b) for casting speed of 60 mm/min; (ii) temperature contours (c) and velocity field (d) for casting speed of 100 mm/min; (iii) temperature contours (e) and velocity field (f) for casting speed of 140 mm/min; (iv) temperature contours (g) and velocity field (h) for casting speed of 180 mm/min…….. 6-29

6.11 Enlarged 2-D view of temperature contours and velocity vectors of the top domain using the open top delivery system for a casting speed of 60 mm/min and 64°C superheat at: (a) wide symmetry plane at z = 0 mm, (b) vertical plane parallel to the wide face at z = 62.5 mm, (c) vertical plane parallel to the wide face at z = 312.5 mm…….. 6-30

6.12 Enlarged 2-D view of temperature contours and velocity vectors of the top domain using the open top delivery system for a casting speed of 100 mm/min and 64°C superheat at: (a) wide symmetry plane at z = 0 mm, (b) vertical plane parallel to the wide face at z = 62.5 mm, (c) vertical plane parallel to the wide face at z = 312.5 mm…….. 6-31

6.13 Enlarged 2-D view of temperature contours and velocity vectors of the top domain using the open top delivery system for a casting speed of 140 mm/min and 64°C superheat at: (a) wide symmetry plane at z = 0 mm, (b) vertical plane parallel to the wide face at z = 62.5 mm, (c) vertical plane parallel to the wide face at z = 312.5 mm…….. 6-32

6.14 Enlarged 2-D view of temperature contours and velocity vectors of the top domain using the open top delivery system for a casting speed of 180 mm/min and 64°C superheat at: (a) wide symmetry plane at z = 0 mm, (b) vertical plane parallel to the wide face at z = 62.5 mm, (c) vertical plane parallel to the wide face at z = 312.5 mm…….. 6-33

6.15 Contours of solidus and liquidus temperatures at various transverse cross-sectional planes (y-z planes) of the top part of the ingot using the open top delivery system for a superheat of 64°C and casting speeds of (a) 60 mm min^{-1} (b) 100 mm min^{-1} (c) 140 mm min^{-1} (d) 180 mm min^{-1}…… 6-34

6.16 Solidified layer thickness from the narrow slab face at an axial distance of x = 160 mm from the top surface at the wide symmetry plane versus casting speed using the open top delivery system for: (a) inlet superheat of 32°C, (b) inlet superheat of 64°C…… 6-35

6.17 Variations of local surface heat fluxes for various casting speeds during solidification at 32°C superheat along the axial direction of the strand wall at: (a) z = 185 mm (b) y = 857.5 mm, using the open top delivery system… 6-36

6.18 Variations of local surface heat fluxes for various casting speeds during solidification at 64°C superheat along the axial direction of the strand wall at: (a) z = 185 mm (b) y = 857.5 mm, using the open top delivery system… 6-36

6.19 Comparison between thermal and CFD models on shell thickness predicted from the narrow slab face at an axial distance of x = 160 mm from the top surface at the wide symmetry plane versus casting speed using the open top melt feeding system, for: (a) inlet superheat of 32°C, (b) inlet superheat of 64°C……. 6-37

6.20 Comparison between thermal and CFD models on sump depth versus casting speed using an open top melt delivery system, for: (a) inlet superheat of 32°C, (b) inlet superheat of 64°C…… 6-37

6.21 Effect of primary heat transfer coefficient on (a) solidified layer thickness (b) surface temperature, for an open top melt feeding system at a casting speed of 100 mm/min and an inlet superheat of 32^{o}C at the axial end of the mold (x = 205 mm) from the narrow face at the wide symmetry plane…… 6-38

7.1 Schematic of a vertical DC caster with the calculation domain represented by yellow color for an open top melt delivery system with a full filter……. 7-4

7.2 2-D schematic view of the computational domain for an open top delivery system; (a) full-filtered case, and (b) half-filtered case…….. 7-6

7.3 3-D surface plots for the complete solution domain for four casting speeds and 32^{0}C superheat using the open top delivery system with a porous filter having a width of 865 mm for porosity, ϕ = 0.4 and Darcy value 0f 1.0 x 10^{-4}: (i) temperature contours (a) and velocity field (b) for a casting speed of 60 mm/min; (ii) temperature contours (c) and velocity field (d) for a casting speed of 100 mm/min; (iii) temperature contours (e) and velocity field (f) for a casting speed of 140 mm/min; (iv) temperature contours (g) and velocity field (h) for a casting speed of 180 mm/min…….. 7-32

7.4 Enlarged 2-D view of temperature contours and velocity vectors of the top domain using the open top delivery system with a porous filter having a width of 865 mm for porosity, ϕ = 0.4 and Darcy value 0f 1.0 $\times$ 10^{-4} for a casting speed of 60 mm/min and 32°C superheat at: (a) wide symmetry plane at z = 0 mm, (b) vertical plane parallel to the wide face at z = 62.5 mm, (c) vertical plane parallel to the wide face at z = 312.5 mm…….. 7-33

7.5 Enlarged 2-D view of temperature contours and velocity vectors of the top domain using the open top delivery system with a porous filter having a width of 865 mm for porosity, ϕ = 0.4 and Darcy value 0f 1.0 $\times$ 10^{-4} for a casting speed of 100 mm/min and 32°C superheat at: (a) wide symmetry plane at z = 0 mm, (b) vertical plane parallel to the wide face at z = 62.5 mm, (c) vertical plane parallel to the wide face at z = 312.5 mm…….. 7-34

7.6 Enlarged 2-D view of temperature contours and velocity vectors of the top domain using the open top delivery system with a porous filter having a width of 865 mm for porosity, ϕ = 0.4 and Darcy value 0f 1.0×10^{-4} for a casting speed of 140 mm/min and 32°C superheat at: (a) wide symmetry plane at z = 0 mm, (b) vertical plane parallel to the wide face at z = 62.5 mm, (c) vertical plane parallel to the wide face at z = 312.5 mm…….. 7-35

7.7 Enlarged 2-D view of temperature contours and velocity vectors of the top domain using the open top delivery system with a porous filter having a width of 865 mm for porosity, ϕ = 0.4 and Darcy value 0f 1.0×10^{-4} for a casting speed of 180 mm/min and 32°C superheat at: (a) (a) wide symmetry plane at z = 0 mm, (b) vertical plane parallel to the wide face at z = 62.5 mm, (c) vertical plane parallel to the wide face at z = 312.5 mm… 7-36

7.8 Contours of solidus and liquidus temperatures at various transverse cross-sectional planes (y-z planes) of the top part of the ingot using the open top delivery system with a porous filter having a width of 865 mm for porosity, ϕ = 0.4 and Darcy value 0f 1.0×10^{-4} for a superheat of 32°C and casting speeds of (a) 60 mm min^{-1} (b) 100 mm min^{-1} (c) 140 mm min^{-1} (d) 180 mm min^{-1}…… 7-37

7.9 3-D surface plots for the complete solution domain for four casting speeds and 64^0C temperature superheat using the open top delivery system with a porous filter having a width of 865 mm for porosity, ϕ = 0.4 and Darcy value 0f 1.0×10^{-4}: (i) temperature contours (a) and velocity field (b) for a casting speed of 60 mm/min; (ii) temperature contours (c) and velocity field (d) for a casting speed of 100 mm/min; (iii) temperature contours (e) and velocity field (f) for a casting speed of 140 mm/min; (iv) temperature contours (g) and velocity field (h) for a casting speed of 180 mm/min…….. 7-38

7.10 Enlarged 2-D view of temperature contours and velocity vectors of the top domain using the open top delivery system with a porous filter having a width of 865 mm for porosity, ϕ = 0.4 and Darcy value 0f 1.0×10^{-4} for a casting speed of 60 mm/min and 64°C superheat at: (a) wide symmetry plane at z = 0 mm, (b) vertical plane parallel to the wide face at z = 62.5 mm, (c) vertical plane parallel to the wide face at z = 312.5 mm…….. 7-39

7.11 Enlarged 2-D view of temperature contours and velocity vectors of the top domain using the open top delivery system with a porous filter having a width of 865 mm for porosity, ϕ = 0.4 and Darcy value 0f 1.0×10^{-4} for a casting speed of 100 mm/min and 64°C superheat at: (a) wide symmetry plane at z = 0 mm, (b) vertical plane parallel to the wide face at z = 62.5 mm, (c) vertical plane parallel to the wide face at z = 312.5 mm…….. 7-40

7.12 Enlarged 2-D view of temperature contours and velocity vectors of the top domain using the open top delivery system with a porous filter having a width of 865 mm for porosity, ϕ = 0.4 and Darcy value 0f 1.0×10^{-4} for a casting speed of 140 mm/min and 64°C superheat at: (a) wide symmetry plane at z = 0 mm, (b) vertical plane parallel to the wide face at z = 62.5 mm, (c) vertical plane parallel to the wide face at z = 312.5 mm…….. 7-41

7.13 Enlarged 2-D view of temperature contours and velocity vectors of the top domain using the open top delivery system with a porous filter having a width of 865 mm for porosity, ϕ = 0.4 and Darcy value 0f 1.0×10^{-4} for a casting speed of 180 mm/min and 64°C superheat at: (a) wide symmetry plane at z = 0 mm, (b) vertical plane parallel to the wide face at z = 62.5 mm, (c) vertical plane parallel to the wide face at z = 312.5 mm…….. 7-42

7.14 Contours of solidus and liquidus temperatures at various transverse cross-sectional planes (y-z planes) of the top part of the ingot using the open top delivery system with a porous filter having a width of 865 mm for porosity, ϕ = 0.4 and Darcy value 0f 1.0×10^{-4} for a superheat of 64°C and casting speeds of (a) 60 mm min^{-1} (b) 100 mm min^{-1} (c) 140 mm min^{-1} (d) 180 mm min^{-1}…… 7-43

7.15 Solidified layer thickness from the narrow slab face at an axial distance of x = 160 mm from the top free surface at the wide symmetry plane versus casting speed using the open top delivery system with a porous filter having a width of 865 mm for porosity, ϕ = 0.4 and Darcy value 0f 1.0 $\times$ 10^{-4} for: (a) inlet superheat of 32^{o}C, (b) inlet superheat of 64^{o}C…… 7-44

7.16 Variations of local surface heat fluxes for various casting speeds during solidification at 32°C superheat along the axial direction of the strand wall at: (a) z = 185 mm (b) y = 857.5 mm, using the open top delivery system with a porous filter having a width of 865 mm for porosity, ϕ = 0.4 and Darcy value 0f 1.0 $\times$ 10^{-4}…… 7-45

7.17 Variations of local surface heat fluxes for various casting speeds during solidification at 64°C superheat along the axial direction of the strand wall at: (a) z = 185 mm (b) y = 857.5 mm, using the open top delivery system with a porous filter having a width of 865 mm for porosity, ϕ = 0.4 and Darcy value 0f 1.0 $\times$ 10^{-4}…… 7-45

7.18 3-D surface plots for the complete solution domain for four casting speeds and 32^{0}C superheat using the open top delivery system with a porous filter having a width of 433 mm for porosity, ϕ = 0.4 and Darcy value 0f 1.0 $\times$ 10^{-4}: (i) temperature contours (a) and velocity field (b) for a casting speed of 60 mm/min; (ii) temperature contours (c) and velocity field (d) for a casting speed of 100 mm/min; (iii) temperature contours (e) and velocity field (f) for a casting speed of 140 mm/min; (iv) temperature contours (g) and velocity field (h) for a casting speed of 180 mm/min…….. 7-46

7.19 Enlarged 2-D view of temperature contours and velocity vectors of the top domain using the open top delivery system with a porous filter having a width of 433 mm for porosity, ϕ = 0.4 and Darcy value 0f 1.0 $\times$ 10^{-4} for a casting speed of 60 mm/min and 32°C superheat at: (a) wide symmetry plane at z = 0 mm, (b) vertical plane parallel to the wide face at z = 62.5 mm, (c) vertical plane parallel to the wide face at z = 312.5 mm…….. 7-47

7.20 Enlarged 2-D view of temperature contours and velocity vectors of the top domain using the open top delivery system with a porous filter having a width of 433 mm for porosity, ϕ = 0.4 and Darcy value 0f 1.0×10^{-4} for a casting speed of 100 mm/min and 32°C superheat at: (a) wide symmetry plane at z = 0 mm, (b) vertical plane parallel to the wide face at z = 62.5 mm, (c) vertical plane parallel to the wide face at z = 312.5 mm…….. 7-48

7.21 Enlarged 2-D view of temperature contours and velocity vectors of the top domain using the open top delivery system with a porous filter having a width of 433 mm for porosity, ϕ = 0.4 and Darcy value 0f 1.0×10^{-4} for a casting speed of 140 mm/min and 32°C superheat at: (a) wide symmetry plane at z = 0 mm, (b) vertical plane parallel to the wide face at z = 62.5 mm, (c) vertical plane parallel to the wide face at z = 312.5 mm…….. 7-49

7.22 Enlarged 2-D view of temperature contours and velocity vectors of the top domain using the open top delivery system with a porous filter having a width of 433 mm for porosity, ϕ = 0.4 and Darcy value 0f 1.0×10^{-4} for a casting speed of 180 mm/min and 32°C superheat at: (a) wide symmetry plane at z = 0 mm, (b) vertical plane parallel to the wide face at z = 62.5 mm, (c) vertical plane parallel to the wide face at z = 312.5 mm……... 7-50

7.23 Contours of solidus and liquidus temperatures at various transverse cross-sectional planes (y-z planes) of the top part of the ingot using the open top delivery system with a porous filter having a width of 433 mm for porosity, ϕ = 0.4 and Darcy value 0f 1.0×10^{-4} for a superheat of 32°C and casting speeds of (a) 60 mm min^{-1} (b) 100 mm min^{-1} (c) 140 mm min^{-1} (d) 180 mm min^{-1}…… 7-51

7.24 3-D surface plots for the complete solution domain fort four casting speeds and 64^0C superheat using the open top delivery system with a porous filter having a width of 433 mm for porosity, ϕ = 0.4 and Darcy value 0f 1.0 $\times$ 10^{-4}: (i) temperature contours (a) and velocity field (b) for a casting speed of 60 mm/min; (ii) temperature contours (c) and velocity field (d) for a casting speed of 100 mm/min; (iii) temperature contours (e) and velocity field (f) for a casting speed of 140 mm/min; (iv) temperature contours (g) and velocity field (h) for a casting speed of 180 mm/min…….. 7-52

7.25 Enlarged 2-D view of temperature contours and velocity vectors of the top domain using the open top delivery system with a porous filter having a width of 433 mm for porosity, ϕ = 0.4 and Darcy value 0f 1.0 $\times$ 10^{-4} for a casting speed of 60 mm/min and 64°C superheat at: (a) wide symmetry plane at z = 0 mm, (b) vertical plane parallel to the wide face at z = 62.5 mm, (c) vertical plane parallel to the wide face at z = 312.5 mm…….. 7-53

7.26 Enlarged 2-D view of temperature contours and velocity vectors of the top domain using the open top delivery system with a porous filter having a width of 433 mm for porosity, ϕ = 0.4 and Darcy value 0f 1.0 $\times$ 10^{-4} for a casting speed of 100 mm/min and 64°C superheat at: (a) wide symmetry plane at z = 0 mm, (b) vertical plane parallel to the wide face at z = 62.5 mm, (c) vertical plane parallel to the wide face at z = 312.5 mm…….. 7-54

7.27 Enlarged 2-D view of temperature contours and velocity vectors of the top domain using the open top delivery system with a porous filter having a width of 433 mm for porosity, ϕ = 0.4 and Darcy value 0f 1.0 $\times$ 10^{-4} for a casting speed of 140 mm/min and 64°C superheat at: (a) wide symmetry plane at z = 0 mm, (b) vertical plane parallel to the wide face at z = 62.5 mm, (c) vertical plane parallel to the wide face at z = 312.5 mm…….. 7-55

7.28 Enlarged 2-D view of temperature contours and velocity vectors of the top domain using the open top delivery system with a porous filter having a width of 433 mm for porosity, ϕ = 0.4 and Darcy value 0f 1.0 $\times$ 10^{-4} for a casting speed of 180 mm/min and 64°C superheat at: (a) wide symmetry plane at z = 0 mm, (b) vertical plane parallel to the wide face at z = 62.5 mm, (c) vertical plane parallel to the wide face at z = 312.5 mm…….. 7-56

7.29 Contours of solidus and liquidus temperatures at various transverse cross-sectional planes (y-z planes) of the top part of the ingot using the open top delivery system with a porous filter having a width of 433 mm for porosity, ϕ = 0.4 and Darcy value 0f 1.0 $\times$ 10^{-4} for a superheat of 64°C and casting speeds of (a) 60 mm min^{-1} (b) 100 mm min^{-1} (c) 140 mm min^{-1} (d) 180 mm min^{-1}…… 7-57

7.30 Solidified layer thickness from the narrow slab face at an axial distance of x = 160 mm from the top free surface at the wide symmetry plane versus casting speed using the open top delivery system with a porous filter having a width of 433 mm for porosity, ϕ = 0.4 and Darcy value 0f 1.0 $\times$ 10^{-4} for: (a) inlet superheat of 32°C, (b) inlet superheat of 64°C…… 7-58

7.31 Variations of local surface heat fluxes for various casting speeds during solidification at 32°C superheat along the axial direction of the strand wall at: (a) z = 185 mm (b) y = 857.5 mm, using the open top delivery system with a porous filter having a width of 433 mm for porosity, ϕ = 0.4 and Darcy value 0f 1.0 $\times 10^{-4}$……. 7-59

7.32 Variations of local surface heat fluxes for various casting speeds during solidification at 64°C superheat along the axial direction of the strand wall at: (a) z = 185 mm (b) y = 857.5 mm, using the open top delivery system with a porous filter having a width of 433 mm for porosity, ϕ = 0.4 and Darcy value 0f 1.0 $\times 10^{-4}$……. 7-59

8.1 Schematic of a vertical DC caster with the calculation domain represented by ash color for a submerged nozzle with a distributor plate……. 8-4

8.2 Schematic of a channel bag……. 8-5

8.3 Schematic of a combo bag having a bottom porous plate…….. 8-6

8.4 3-D surface plots for the complete solution domain for four casting speeds and 32^0C superheat using the submerged nozzle with a distributor plate melt feeding scheme: (i) temperature contours (a) and velocity field (b) for a casting speed of 40 mm/min; (ii) temperature contours (c) and velocity field (d) for a casting speed of 60 mm/min; (iii) temperature contours (e) and velocity field (f) for a casting speed of 80 mm/min; (iv) temperature contours (g) and velocity field (h) for a casting speed of 100 mm/min…….. 8-29

8.5 Enlarged 2-D view of temperature contours and velocity vectors of the top domain using the submerged nozzle with a distributor plate melt feeding scheme for a casting speed of 40 mm/min and 32°C superheat at: (a) wide symmetry plane at z = 0 mm, (b) vertical plane parallel to the wide face at z = 62.5 mm, (c) vertical plane parallel to the wide face at z = 312.5 mm…….. 8-30

8.6 Enlarged 2-D view of temperature contours and velocity vectors of the top domain using the submerged nozzle with a distributor plate melt feeding scheme for a casting speed of 60 mm/min and 32°C superheat at: (a) wide symmetry plane at z = 0 mm, (b) vertical plane parallel to the wide face at z = 62.5 mm, (c) vertical plane parallel to the wide face at z = 312.5 mm…….. 8-31

8.7 Enlarged 2-D view of temperature contours and velocity vectors of the top domain using the submerged nozzle with a distributor plate melt feeding scheme for a casting speed of 80 mm/min and 32°C superheat at: (a) wide symmetry plane at z = 0 mm, (b) vertical plane parallel to the wide face at z = 62.5 mm, (c) vertical plane parallel to the wide face at z = 312.5 mm…. 8-32

8.8 Enlarged 2-D view of temperature contours and velocity vectors of the top domain using the submerged nozzle with a distributor plate melt feeding scheme for a casting speed of 100 mm/min and 32°C superheat at: (a) wide symmetry plane at z = 0 mm, (b) vertical plane parallel to the wide face at z = 62.5 mm, (c) vertical plane parallel to the wide face at z = 312.5 mm…. 8-33

8.9 Contours of solidus and liquidus temperatures and velocity fields at various transverse cross-sectional planes (y-z planes) of the top part of the ingot using the submerged nozzle with a distributor plate melt feeding scheme for a superheat of 32°C and casting speeds of: (i) 40 mm min^{-1} (ii) 60 mm min^{-1} (iii) 80 mm min^{-1} (iv) 100 mm min^{-1}……. 8-35

8.10 Solid shell thickness from the narrow slab face at an axial distance of x = 160 mm from the top free surface at the wide symmetry plane versus casting speed at an inlet superheat of 32^{o}C using the submerged nozzle with a distributor plate melt feeding scheme…….. 8-36

8.11 Variations of local surface heat fluxes for various casting speeds during solidification at 32°C superheat along the axial direction of the strand wall at: (a) z = 185 mm (b) y = 857.5 mm, using the submerged nozzle with a distributor plate melt feeding scheme……..... 8-36

8.12 3-D surface plots for the complete solution domain for four casting speeds and 32^{0}C superheat using the submerged nozzle with a porous bottom plate distributor bag melt feeding scheme for porosity, ϕ = 0.4 and Darcy value 0f 1.0 x 10^{-4}: (i) temperature contours (a) and velocity field (b) for a casting speed of 40 mm/min; (ii) temperature contours (c) and velocity field (d) for a casting speed of 60 mm/min; (iii) temperature contours (e) and velocity field (f) for a casting speed of 80 mm/min; (iv) temperature contours (g) and velocity field (h) for a casting speed of 100 mm/min…….. 8-37

8.13 Enlarged 2-D view of temperature contours and velocity vectors of the top domain using the submerged nozzle with a porous bottom plate distributor bag melt feeding scheme at porosity, ϕ = 0.4 and Darcy value 0f 1.0 x 10^{-4} for a casting speed of 40 mm/min and 32°C superheat at: (a) wide symmetry plane at z = 0 mm, (b) vertical plane parallel to the wide face at z = 62.5 mm, (c) vertical plane parallel to the wide face at z = 312.5 mm…….. 8-38

8.14 Enlarged 2-D view of temperature contours and velocity vectors of the top domain using the submerged nozzle with a porous bottom plate distributor bag melt feeding scheme at porosity, $\phi = 0.4$ and Darcy value 0f 1.0×10^{-4} for a casting speed of 60 mm/min and 32°C superheat at: (a) wide symmetry plane at z = 0 mm, (b) vertical plane parallel to the wide face at z = 62.5 mm, (c) vertical plane parallel to the wide face at z = 312.5 mm…….. 8-39

8.15 Enlarged 2-D view of temperature contours and velocity vectors of the top domain using the submerged nozzle with a porous bottom plate distributor bag melt feeding scheme at porosity, $\phi = 0.4$ and Darcy value 0f 1.0×10^{-4} for a casting speed of 80 mm/min and 32°C superheat at: (a) wide symmetry plane at z = 0 mm, (b) vertical plane parallel to the wide face at z = 62.5 mm, (c) vertical plane parallel to the wide face at z = 312.5 mm…….. 8-40

8.16 Enlarged 2-D view of temperature contours and velocity vectors of the top domain using the submerged nozzle with a porous bottom plate distributor bag melt feeding scheme at porosity, $\phi = 0.4$ and Darcy value 0f 1.0×10^{-4} for a casting speed of 100 mm/min and 32°C superheat at: (a) wide symmetry plane at z = 0 mm, (b) vertical plane parallel to the wide face at z = 62.5 mm, (c) vertical plane parallel to the wide face at z = 312.5 mm…….. 8-41

8.17 Contours of solidus and liquidus temperatures and velocity fields at various transverse cross-sectional planes (y-z planes) of the top part of the ingot using the submerged nozzle with a porous bottom plate distributor bag melt feeding scheme at porosity, $\phi = 0.4$ and a Darcy value 0f 1.0×10^{-4} for a superheat of 32°C and casting speeds of: (i) 40 mm min^{-1} (ii) 60 mm min^{-1} (iii) 80 mm min^{-1} (iv) 100 mm min^{-1}…….. 8-43

8.18 Solid shell thickness from the narrow slab face at an axial distance of x = 160 mm from the top free surface at the wide symmetry plane versus casting speed at an inlet superheat of 32^{o}C using the submerged nozzle with a porous bottom plate distributor bag melt feeding scheme at porosity, ϕ = 0.4 and Darcy value 0f 1.0 x 10^{-4}…… 8-44

8.19 Variations of local surface heat fluxes with various casting speeds during solidification at 32°C superheat along the axial direction of the strand wall at: (a) z = 185 mm (b) y = 857.5 mm, using the submerged nozzle with a porous bottom plate distributor bag melt feeding scheme at porosity, ϕ = 0.4 and Darcy value 0f 1.0 x 10^{-4}…… 8-44

8.20 3-D surface plots for the complete solution domain fort four casting speeds and 32^{0}C superheat using the submerged nozzle with a porous bottom plate distributor bag melt feeding scheme for porosity, ϕ = 0.9 and Darcy value 0f 1.0 x 10^{-4}: (i) temperature contours (a) and velocity field (b) for a casting speed of 40 mm/min; (ii) temperature contours (c) and velocity field (d) for a casting speed of 60 mm/min; (iii) temperature contours (e) and velocity field (f) for a casting speed of 80 mm/min; (iv) temperature contours (g) and velocity field (h) for a casting speed of 100 mm/min…….. 8-45

8.21 Enlarged 2-D view of temperature contours and velocity vectors of the top domain using the submerged nozzle with a porous bottom plate distributor bag melt feeding scheme at porosity, ϕ = 0.9 and Darcy value 0f 1.0 x 10^{-4} for a casting speed of 40 mm/min and 32°C superheat at: (a) wide symmetry plane at z = 0 mm, (b) vertical plane parallel to the wide face at z = 62.5 mm, (c) vertical plane parallel to the wide face at z = 312.5 mm…. 8-46

8.22 Enlarged 2-D view of temperature contours and velocity vectors of the top domain using the submerged nozzle with a porous bottom plate distributor bag melt feeding scheme at porosity, ϕ = 0.9 and Darcy value 0f 1.0 x 10^{-4} for a casting speed of 60 mm/min and 32°C superheat at: (a) wide symmetry plane at z = 0 mm, (b) vertical plane parallel to the wide face at z = 62.5 mm, (c) vertical plane parallel to the wide face at z = 312.5 mm…. 8-47

8.23 Enlarged 2-D view of temperature contours and velocity vectors of the top domain using the submerged nozzle with a porous bottom plate distributor bag melt feeding scheme at porosity, ϕ = 0.9 and Darcy value 0f 1.0 x 10^{-4} for a casting speed of 80 mm/min and 32°C superheat at: (a) wide symmetry plane at z = 0 mm, (b) vertical plane parallel to the wide face at z = 62.5 mm, (c) vertical plane parallel to the wide face at z = 312.5 mm…. 8-48

8.24 Enlarged 2-D view of temperature contours and velocity vectors of the top domain using the submerged nozzle with a porous bottom plate distributor bag melt feeding scheme at porosity, ϕ = 0.9 and Darcy value 0f 1.0 x 10^{-4} for a casting speed of 100 mm/min and 32°C superheat at: (a) wide symmetry plane at z = 0 mm, (b) vertical plane parallel to the wide face at z = 62.5 mm, (c) vertical plane parallel to the wide face at z = 312.5 mm…. 8-49

8.25 Contours of solidus and liquidus temperatures and velocity fields at various transverse cross-sectional planes (y-z planes) of the top part of the ingot using the submerged nozzle with a porous bottom plate distributor bag melt feeding scheme at porosity, ϕ = 0.9 and a Darcy value 0f 1.0 x 10^{-4} for a superheat of 32°C and casting speeds of: (i) 40 mm min^{-1} (ii) 60 mm min^{-1} (iii) 80 mm min^{-1} (iv) 100 mm min^{-1}…….. 8-51

8.26 Solid shell thickness from the narrow slab face at an axial distance of x = 160 mm from the top free surface at the wide symmetry plane versus casting speed at an inlet superheat of 32°C using the submerged nozzle with a porous bottom plate distributor bag melt feeding scheme at porosity, ϕ = 0.9 and Darcy value 0f 1.0 x 10^{-4}……. 8-52

8.27 Variations of local surface heat fluxes for various casting speeds during solidification at 32°C superheat along the axial direction of the strand wall at: (a) z = 185 mm (b) y = 857.5 mm, using the submerged nozzle with a porous bottom plate distributor bag melt feeding scheme at porosity, ϕ = 0.9 and Darcy value 0f 1.0 x 10^{-4}…..... 8-52

9.1 Schematic of a vertical DC caster with the calculation domain represented by yellow color for a submerged nozzle and a filter…….. 9-2

9.2 3-D surface plots for the complete solution domain for four casting speeds and 32^0C superheat using the submerged nozzle and a porous filter feeding scheme for porosity, ϕ = 0.4 and Darcy value 0f 1.0 x 10^{-4}: (i) temperature contours (a) and velocity field (b) for a casting speed of 40 mm/min; (ii) temperature contours (c) and velocity field (d) for a casting speed of 60 mm/min; (iii) temperature contours (e) and velocity field (f) for a casting speed of 80 mm/min; (iv) temperature contours (g) and velocity field (h) for a casting speed of 100 mm/min…….. 9-12

9.3 Enlarged 2-D view of temperature contours and velocity vectors field using the submerged nozzle and a porous filter feeding scheme for porosity, ϕ = 0.4 and Darcy value 0f 1.0 x 10^{-4} for a casting speed of 40 mm/min and 32°C superheat at: (a) wide symmetry plane at z = 0 mm, (b) vertical plane parallel to the wide face at z = 62.5 mm, (c) vertical plane parallel to the wide face at z = 312.5 mm……..... 9-13

9.4 Enlarged 2-D view of temperature contours and velocity vectors field using the submerged nozzle and a porous filter feeding scheme for porosity, ϕ = 0.4 and Darcy value 0f 1.0 x 10^{-4} for a casting speed of 60 mm/min and 32°C superheat at: (a) wide symmetry plane at z = 0 mm, (b) vertical plane parallel to the wide face at z = 62.5 mm, (c) vertical plane parallel to the wide face at z = 312.5 mm……..... 9-14

9.5 Enlarged 2-D view of temperature contours and velocity vectors field using the submerged nozzle and a porous filter feeding scheme for porosity, ϕ = 0.4 and Darcy value 0f 1.0 x 10^{-4} for a casting speed of 80 mm/min and 32°C superheat at: (a) wide symmetry plane at z = 0 mm, (b) vertical plane parallel to the wide face at z = 62.5 mm, (c) vertical plane parallel to the wide face at z = 312.5 mm……..... 9-15

9.6 Enlarged 2-D view of temperature contours and velocity vectors field using the submerged nozzle and a porous filter feeding scheme for porosity, ϕ = 0.4 and Darcy value 0f 1.0 x 10^{-4} for a casting speed of 100 mm/min and 32°C superheat at: (a) wide symmetry plane at z = 0 mm, (b) vertical plane parallel to the wide face at z = 62.5 mm, (c) vertical plane parallel to the wide face at z = 312.5 mm……..... 9-16

9.7 Contours of solidus and liquidus temperatures and velocity fields at various transverse cross-sectional planes (y-z planes) of the top part of the ingot using the submerged nozzle and a porous filter feeding scheme for porosity, ϕ = 0.4 and Darcy value 0f 1.0 x 10^{-4} melt feeding scheme for a superheat of 32°C and casting speeds of: (i) 40 mm min^{-1} (ii) 60 mm min^{-1} (iii) 80 mm min^{-1} (iv) 100 mm min^{-1}…….. 9-18

9.8 Solidified layer thickness from the narrow slab face at an axial distance of x = 160 mm from the top free surface at the wide symmetry plane versus casting speed at an inlet superheat of 32°C using the submerged nozzle and a porous filter feeding scheme for porosity, ϕ = 0.4 and Darcy value 0f 1.0 x 10^{-4}…….. 9-19

9.9 Variations of local surface heat fluxes for various casting speeds during solidification at 32°C superheat along the axial direction of the strand wall at: (a) z = 185 mm (b) y = 857.5 mm, using the submerged nozzle and a porous filter feeding scheme for porosity, ϕ = 0.4 and Darcy value 0f 1.0 x 10^{-4}…….. 9-19

LIST OF TABLES

Table

3.1	Physical properties of Al-1050 and DC caster geometrical parameters…….	3-5
3.2	Summary of the Non-Dimensional Governing Equations……..	3-30
4.1	Thermo-physical properties of aluminum Al-3104 for the quantitative verification of the code……..	4-3
4.2	Boundary conditions used for the quantitative verification……..	4-4
4.3	Comparison of experimentally measured and numerically predicted vertical distance of the solidification front from the top of the mold at the wide symmetry plane (z = 0) for aluminum (Al-3104) alloy…….....	4-10
4.4	Numerical values of local surface heat flux at a casting speed of 100 mm/min and at a superheat of 32°C along the axial distance of the strand on the wide slab face at y = 430.5 mm from the ingot center ……	4-13
4.5	Numerical values of local surface heat fluxes at a casting speed of 100 mm/min for a melt superheat of 32°C along the axial distance of the strand on the narrow slab face at z = 322.5 mm from the ingot center …….....	4-14
5.1	Values of the parameter used in thermal model……..	5-7
5.2	Sump depth and mushy thickness in mm at the center of the ingot using thermal model for four casting speeds and melt superheat of 32^{o}C……	5-12
5.3	The thickness of the solidified shell (mm) at wide symmetry plane from the narrow slab face at an axial distance of 160 mm inside the mold for four casting speeds and inlet superheat of 32°C using thermal model……..	5-13
5.4	The local heat flux (kW/m^2) at z = 185 mm at an axial distance of 215 mm from the top surface for four casting speeds and for an inlet superheats of 32°C using thermal model……..	5-15
5.5	Sump depth and mushy thickness (mm) at the ingot center for four casting speeds and for a superheat of 64^{o}C predicted by the thermal model…….	5-17

5.6 The thickness of the solidified shell (mm) at wide symmetry plane from the narrow slab face at an axial distance of 160 mm inside the mold for four casting speeds and superheat of 64°C using thermal model…….. 5-19

5.7 The local heat flux (kW/m^2) at z = 185 mm at an axial distance of 215 mm from the top surface for four casting speeds and for an inlet superheats of 64°C using thermal model…….. 5-20

6.1 Values of the parameter used in open-top melt delivery arrangements…….. 6-2

6.2 Sump depth and mushy thickness in mm at the center of the ingot for an open-top delivery system for four casting speeds and superheat of 32^oC….. 6-6

6.3 The thickness of the solidifying shell (mm) at wide symmetry plane from the narrow slab face at an axial distance of 160 mm inside the mold for four casting speeds and inlet superheat of 32°C for an open-top delivery…. 6-7

6.4 The local heat flux (kW/m^2) at z = 185 mm at an axial distance of 215 mm from the top surface for four casting speeds and for an inlet superheats of 32°C for an open-top delivery system……. 6-9

6.5 Maximum values of the resultant velocity in m/sec……... 6-10

6.6 Sump depth and mushy thickness (mm) at the center of the ingot for an open-top delivery system for four casting speeds and for superheat of 64^oC……. 6-11

6.7 The thickness of the solidifying shell (mm) at wide symmetry plane from the narrow slab face at an axial distance of 160 mm inside the mold for four casting speeds and superheat of 64°C for an open-top delivery system…….. 6-12

6.8 The local heat flux in kW/m^2 at z = 185 mm at an axial distance of 215 mm from the top surface for four casting speeds and for an inlet superheats of 64°C, an open-top delivery system……. 6-13

7.1 Physical properties of stainless steel for the filter and nozzle…… 7-6

7.2 Description of the parameters used for open top delivery system with a filter……. 7-6

7.3 Sump depth and mushy thickness in mm at the center of the ingot for an open-top delivery system with a full filter having a width of 865 mm for four casting speeds and at a superheat of 32^{o}C…….. 7-16

7.4 The thickness of the solidifying shell (mm) at wide symmetry plane from the narrow slab face at an axial distance of 160 mm from the top surface inside the mold for four casting speeds and inlet superheat of 32°C for an open-top delivery system with a filter having a width of 865 mm……. 7-17

7.5 The local heat flux (kW/m^2) at z = 185 mm at an axial distance of 215 mm from the top surface for four casting speeds and for an inlet superheats of 32°C, an open-top delivery system with a filter having a width of 865 mm.. 7-18

7.6 Sump depth and mushy thickness in mm at the center of the ingot for an open-top delivery system with a filter having a width of 865 mm at four casting speeds and a superheat of 64^{o}C…….. 7-21

7.7 The thickness of the solidifying shell (mm) at wide symmetry plane from the narrow slab face at an axial distance of 160 mm from the top surface inside the mold for four casting speeds and inlet superheat of 64°C for an open-top delivery system with a filter having a width of 865 mm……. 7-22

7.8 The local heat flux in kW/m^2 at z = 185 mm at an axial distance of 215 mm from the top surface for four casting speeds and for an inlet superheats of 64°C, an open-top delivery system with a filter having a width of 865 mm.. 7-23

7.9 Comparison of maximum resultant velocities (m/sec) between the full-filtered and half-filtered case…….. 7-25

7.10 Sump depth and mushy thickness in mm at the center of the ingot for an open-top delivery system with a filter having a width of 433 mm at four casting speeds and a superheat of 32^{o}C…….. 7-27

7.11 Sump depth and mushy thickness in mm at the center of the ingot for an open-top delivery system with a filter having a width of 433 mm at four casting speeds and a superheat of 64^{o}C…….. 7-28

7.12 The thickness of the solidifying shell (mm) at wide symmetry plane from the narrow slab face at an axial distance of 160 mm from the top surface inside the mold for four casting speeds and inlet superheats of 32°C, and 64°C for an open-top delivery system with a filter having a width of 433 mm…….. 7-29

7.13 The local heat flux (kW/m^2) at z = 185 mm at an axial distance of 215 mm from the top surface for four casting speeds and for two inlet superheats of 32°C and 64°C, for an open-top delivery system with a filter having a width of 433 mm……. 7-30

8.1 Values of the parameter used in three melt delivery arrangements…… 8-7

8.2 Sump depth and mushy thickness in mm at the center of the ingot for geometry-1 for four casting speeds and a superheat of 32^oC……. 8-12

8.3 The thickness of the solidifying shell (mm) at wide symmetry plane from the narrow slab face at an axial distance of 160 mm from the top free surface inside the mold for four casting speeds and inlet superheat of 32°C for geometry-1……. 8-13

8.4 The local heat flux in kW/m^2 at z = 185 mm at an axial distance of 215 mm from the top free surface for four casting speeds and inlet superheats of 32°C for geometry-1…….. 8-15

8.5 Sump depth and mushy thickness in mm at the ingot center for geometry-2 for four casting speeds and a temperature superheat of 32^oC……. 8-19

8.6 The thickness of the solidifying shell (mm) at wide symmetry plane from the narrow slab face at an axial distance of 160 mm from the top free surface inside the mold for four casting speeds and inlet superheat of 32°C for geometry-2……..... 8-20

8.7 The local heat flux in kW/m^2 at z = 185 mm at an axial distance of 215 mm from the top free surface for four casting speeds and inlet superheats of 32°C for geometry-2……... 8-22

8.8 Sump depth and mushy thickness in mm at wide symmetry plane (z = 0) for geometry-3 for four casting speeds and a superheat of 32^oC…… 8-25

8.9 The thickness of the solidifying shell in mm at wide symmetry plane from the narrow slab face at an axial distance of 160 mm from the top free surface inside the mold for four casting speeds and inlet superheat of 32°C for geometry-3……. 8-26

8.10 The local heat flux in kW/m^2 at z = 185 mm at an axial distance of 215 mm from the top free surface for four casting speeds and inlet superheats of 32°C for geometry-3…….. 8-27

9.1 Description of the parameters used for melt delivered through a nozzle and a porous filter…….. 9-3

9.2 Maximum values of the resultant velocity in mm/min at inlet superheat of 32^{o}C……. 9-6

9.3 Sump depth and mushy thickness (mm) at wide symmetry plane (z = 0) for melt delivered through a nozzle and a filter for four casting speeds and a superheat of 32^{o}C……..... 9-7

9.4 The thickness of the solidifying shell (mm) at wide symmetry plane from the narrow slab face at an axial distance of 160 mm from the top free surface inside the mold for four casting speeds and inlet superheat of 32°C for a submerged nozzle and a filter…… 9-8

9.5 The local heat flux (kW/m^2) at z = 185 mm at an axial distance of 215 mm from the top free surface for four casting speeds and inlet superheats of 32°C, for a submerged nozzle and a filter……. 9-10

NOMENCLATURE

A	Darcy coefficient
a_p, a_{nb}, b	coefficients in the discretized governing equations
c_1, c_2, c_μ	empirical constants for low Reynolds number model
c_p	specific heat
C	morphology constant
D	open-top/nozzle hydraulic diameter
D_k	extra dissipation term in k-equation
Da	Darcy number
E_ε	extra generation term in ε-equation
f_1, f_2, f_μ	empirical constants used in low-Re version of k-ϵ models
f_l	liquid fraction
G	production term in turbulent kinetic energy equation
Gr	Grashof number
g	gravitational acceleration
h	sensible heat
H	total heat (sensible and latent)
K'	permeability of porous media
k	turbulent kinetic energy
k_l	thermal conductivity of the liquid
k_s	thermal conductivity of the solid
k_{ps}	thermal conductivity of the porous structure
P	hydrodynamic pressure
Pe	Peclet number
Pr	laminar Prandtl number
Re	Reynolds number
Re_P	pore Reynolds number = Re/ϕ
Re_t	turbulent Reynolds number based on the turbulent quantities

S	source term
S_Φ	source term associated with Φ
Sc	Schmidt number
Sc_t	turbulent Schmidt number
T	temperature
T'	fluctuation of temperature
T_{in}	inlet temperature
T_l	liquidus temperature
T_s	solidus temperature
T_{surf}	slab surface temperature
u_i	velocity component in the *i-th* direction; corresponding to u
$\overline{u}_i$	time-average velocity component in the *i-th* direction
u_i'	fluctuation of velocity in the *i-th* direction
u_{in}	inlet velocity
u_s	casting speed

Greek Symbols

ΔH	nodal latent heat
ΔH_f	latent heat of fusion
Γ_Φ	diffusion coefficient associated with Φ
ρ	alloy density
φ	generalized dependent variable
μ_e	effective viscosity equal to $\mu_t + \mu$
μ	laminar viscosity
μ_t	turbulent viscosity or eddy diffusivity
Φ	generalized dependent variable

β_T	thermal expansion coefficient
Γ_{eff}	effective diffusivity
ϵ	rate of energy dissipation
ϵ_{in}	inlet rate of energy dissipation
γ	convective heat transfer coefficient
σ_k, σ_ϵ	turbulence model constants
σ_t	turbulent Prandtl number
ϕ	porosity of filter

CHAPTER 1

INTRODUCTION

1.1 Introduction

Direct-chill (DC) casting of aluminum was invented during 1936-1938 almost simultaneously in Germany (W. Roth, VAW) and the USA (W.T. Ennor, ALCOA). The semi-continuous DC casting technique has been used exclusively to produce rolling ingots and extrusion billets owing to its robust nature and relative simplicity. Many non-ferrous alloys such as aluminum, magnesium and copper are now-a-days cast through this technology [88]. Among non-ferrous metal sheets, aluminum is widely preferred for its light weight, strength and corrosion resistance. It is used in numerous applications such as automotive, transport, packaging, construction and printing industry to name but a few. At present, the world production of aluminum using DC casting technology is approximately 25 million tons per annum [Prasad and Bainbridge, 2013]. Figure 1.1 shows several manufacturing steps for the commercial production of aluminum sheet after the DC slab casting process. This include casting and homogenization of aluminum ingots, hot and cold rolling of the ingots to obtain sheets of required thickness, and finally heat treating the sheets to achieve desired mechanical properties. One of the challenges in producing these sheets is the ability to cast high strength aluminum slab ingots economically as well as defects free.

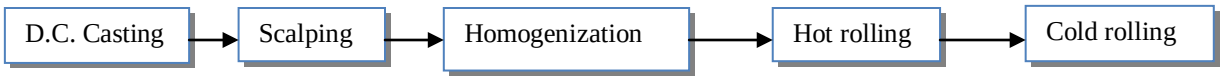

Figure 1.1. Summary of Direct Chill (DC) casting and downstream processes for manufacturing aluminum rolled sheet.

1.2 Direct Chill (DC) Casting Process – A Brief Introduction

A number of excellent reviews are available concerning the technological developments together with the insights into the process [9,24,31,39,44,45,79,110,112, 121]. Depending on the mold orientation, DC casters can be classified into two main types, namely, horizontal and vertical (predominant). Typical DC cast products include large rectangular sections known as ingots where the size can vary from approximately 400-800 mm in thickness, 1000 – 2000 mm in width and 5000-10000 mm in length. The ingots are further rolled into plate, sheet and foil. The cylindrical sections known as billets are cast up to a maximum of 1100 mm in diameter, which are then further forged or extruded to form rods, bars, tubes and wires. Dimensions of the rolling ingots/round billets vary depending on the casting technology used in each cast house and the requirements of downstream processing. A schematic of the vertical DC casting process for the production of rolled ingot is presented in Figure 1.2.

In a Vertical Direct Chill (VDC) casting process, the liquid metal is poured into a bottomless static water-cooled mould, which is initially enclosed partially at the bottom with a metallic block. At the beginning of this casting process, the bottom block is placed such that the top edge is about 20 to 35 mm inside the mould [116]. A metal feeding system feeds the superheated liquid aluminum into the cavity formed by the mold and the bottom block. The metal level on the bottom block is allowed to increase slowly as specified by the casting house practice, until the liquid metal comes in contact with the four mold faces. Once the liquid metal freezes on the metallic block and a solid shell is formed close to the mould walls, the metallic block is lowered slowly by means of a hydraulic ram towards the casting pit until a constant casting speed is reached. During this process the metal level in the mould is kept at a certain height by controlling the metal flow through a distributor system. At the beginning, the solid shell forms due to the heat extraction through the water-cooled mould (referred to as primary cooling) as well as through the bottom block. Now the outer part of the ingot is solid, but the inner core is still semi-solid/liquid. As the partially solidified ingot is lowered under the mould, further cooling of the ingot bulk is achieved by spraying chilled water from a series of holes at the mold base to get the temperature of the cast below the alloy solidus. This

quenching of the strand is referred to as secondary cooling. During the steady state operation of a VDC casting process, typically around 80% ~ 95 % of the total heat content in the metal is removed by secondary cooling [Etienne et. al., 2012] while about 5 to 20% is extracted through the primary cooling zone. The VDC casting process is actually semi-continuous because of the fact that after achieving a desired cast length, the process is stopped and the cast is lifted away from the casting pit as illustrated in Figure 1.4. The casting is restarted when the metal and machinery are ready for the next new cast. A horizontal variant of the process known as Horizontal Direct Chill (HDC) casting can be truly continuous with flying saws separating completely solid part throughout the casting duration as depicted in Fig. 1.3. Unlike the continuous steel casting processes, because of the short sump depth in a VDC process, it is not practical to bend the semi-solidified metal so that it moves horizontally, and this prevents to achieve a continuous cast. A HDC casting is used less often, but does provide the opportunity to cast continuously compared to a VDC process.

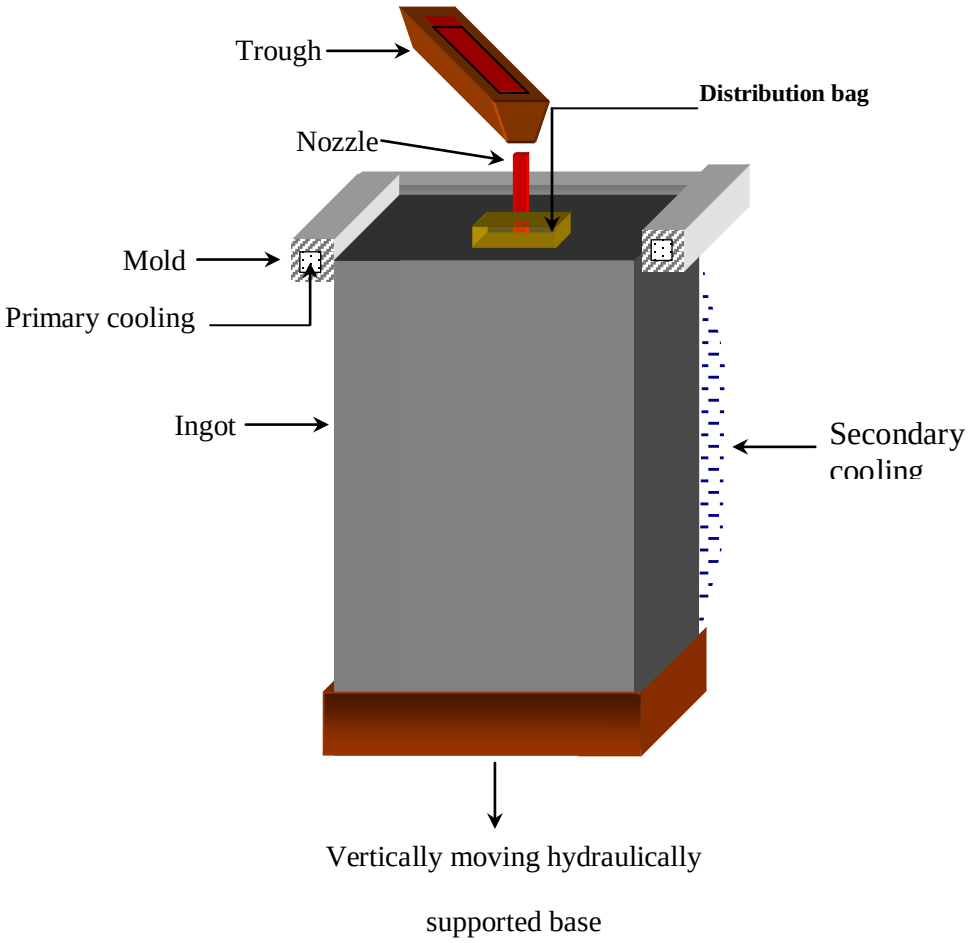

Figure 1.2: Schematic of the DC casting process for rolling ingots.

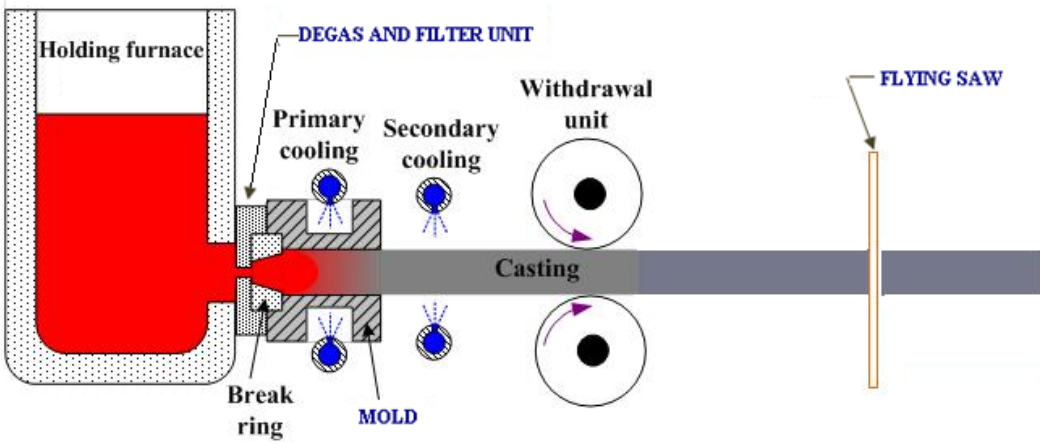

Figure 1.3: Schematic of the horizontal DC casting process.

[source: http.//www.substech.com/dokuwiki/lib/exe/fetch/php.]

Figure 1.4: A rolling ingot is removed from casting pit at the end of the DC casting process [1].

1.3 Probable Defects in DC Cast

Though the basic process of DC casting is, in principle, straightforward, but the interaction of various process parameters with heat extraction, micro structure evolution, development of solidification stresses, etc makes the process too complex. Due to these complexities a lot of defects may develop in the cast, which are internal and surface cracks (starting cracks, edge/face cracks, stress/midway cracks, etc.), macro and micro segregation, micro-voids, hot tears and cold cracks, and distortions in the ingot [18,46,65,67]. Among these defects, hot tear and macro-segregation are considered as two major defects in the industry which are thought to be connected through solidification phenomena. In the literature, there exists a number of studies which were dedicated to delineate the effects of inter-linked parameters on the formation of the above two defects during solidification, as shown by the flow chart in Fig. 1.5.

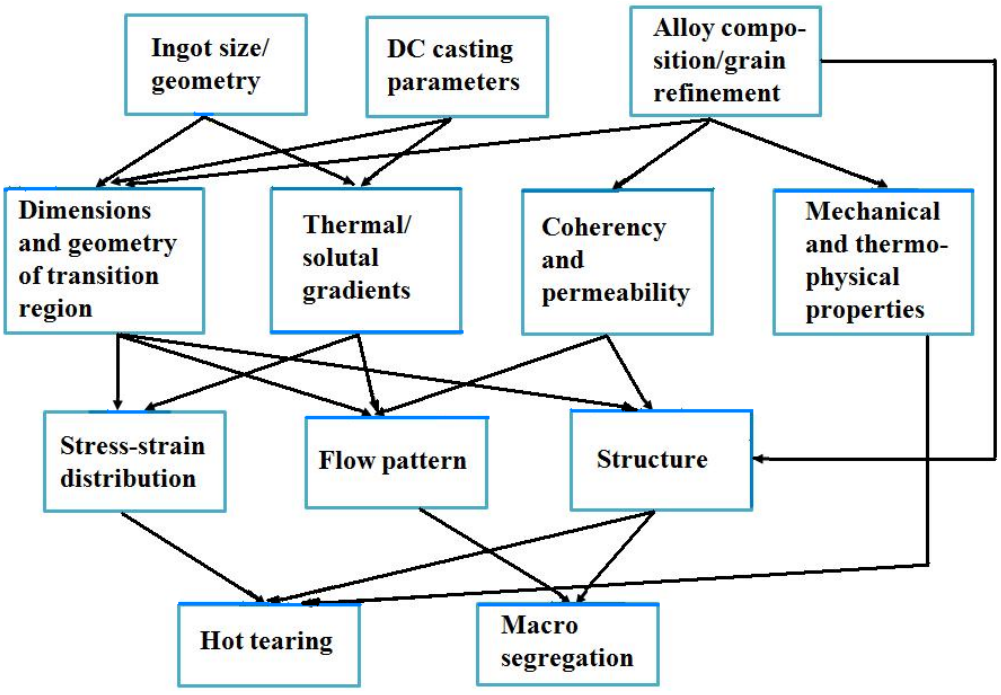

Fig. 1.5: Interaction between process parameters and the structure and defect formation upon DC casting of Al ingots [Nadella et. al., 2008].

The research performed by various investigators over the past 80 years deserves much credit for the establishment of the fundamental understanding of interconnected phenomena for the defect formations. Despite 80 years of extensive research and practice in this field, there is not yet any uniform consensus in terms of process design and operating conditions which are necessary to consistently and repeatedly produce premium quality products with low scrap rates (<5%) [18]. It should be mentioned here, due to the surface defects on the as-cast products, a significant amount of scrap is generated in the DC casting process.

It is believed that majority of the surface defects are initiated at the start-up phase of the DC casting process [137-139]. During the start-up stage, the ingot is simultaneously cooled by the mold (primary cooling), the chill water (secondary cooling), and the bottom block (base cooling). These three heat transfer mechanisms are complex and inter related. The rate of heat extraction from the surface of the ingot to the chill water is quite high while the inner core is relatively hot. Because of this, the ingot experiences large differential thermal stresses due to inhomogeneous thermal contractions which are thought to be responsible to initiate a number of surface defects like hot tears, cold shuts, butt curl, butt swell and cracks, and in extreme cases breakouts [111]. The steady state regime is usually achieved after about 0.5 m of the casting for a fully developed sump [113].

Various types of crack defects and distortion in the ingot that often occur in the DC cast aluminum ingots are shown schematically in Figures 1.6 [27] and 1.7 [115], respectively. It is practically seen in industry that hot tears generally form near the bottom part and between the quarter points of a rectangular ingot beneath the ingot surface. As shown in Figure 1.6, cold cracks originate at the ingot base and are seen in the center half of the ingot width. These defects are primarily attributed to tensile/mechanical and thermal stresses/strains generated during the casting process. Inadequate mold lubrication can introduce mechanically generated tensile strains and thermal strains as well as expansion and contraction of the ingot can be generated due to rapid cooling which lead to steep temperature gradients in the solidifying shell. Sudden localized cooling can create tensile strains at the surface, whereas reheating can produce tensile strains at the solidification front [114]. Upon first solidification in contact with the

mold walls, due to the increase in density of the metal, shrinkage is generated, which will cause the cast to form an air gap between the cast surfaces and mold walls. This leads to a rapid decrease in the local heat fluxes by reducing the cooling rate (which depends on the mold design). This reduced cooling rate can lead to a partial re-melting of the shell. Thus, the subsurface is formed under decreased heat extraction. As a consequence, the ingot needs to be 'scalped' by removing the defected surface layer prior to further processing.

After extensive experimental and theoretical studies by various researchers on hot tear, now there is a uniform consensus that hot tears or pre-solidification cracks form in the mushy zone, when a tensile stress is imposed across partially solidified grains, and the surrounding liquid cannot fill the gap between the dendrites. Hence, these cracks are seen to be always inter-dendritic and inter-granular. The cold cracks are seen to be trans-granular in nature and these cracks are believed to originate at a temperature below the alloy's solidus due to the development of high thermal stresses during the secondary cooling at the start-up phase. Among the practitioners of the VDC process, it is recognized that low casting speeds increase the risk of cold cracks while the high casting speeds favor hot tears [35]. Various researchers have also linked the formation of hot tears with the frictional forces between the ingot and mold (related to mold cleanliness) [95], and the differences in cooling conditions during transient phase [137,138].

In addition to the various macro-cracks, macro-deformation of the ingot base or butt curl also occurs, especially during start-up, which is the manifestation of non-uniform heat transfer rates between the base of the ingot and 'dummy' bottom block [113]. Due to the butt curl an air gap is formed, and two major heat transfer effects appear in this region as presented in Figure 1.7. One of the effects is the reduction of the rate of heat extraction from the ingot to the bottom metallic block due to reduced thermal contact. This might cause re-melting of the ingot base. The second effect is the enhancement of heat transfer in the air gap region for the incursion of water which comes from the secondary cooling. Formation of butt curl leads to the following associated problems, and they are: run outs of the melt, cold shuts, reduced rigid standing (instability) of the ingot on the bottom block [Droste and Schneider (26)]. Ultimately, if the magnitude of butt curl is excessive, the ingot bottom may have to be sawed off which

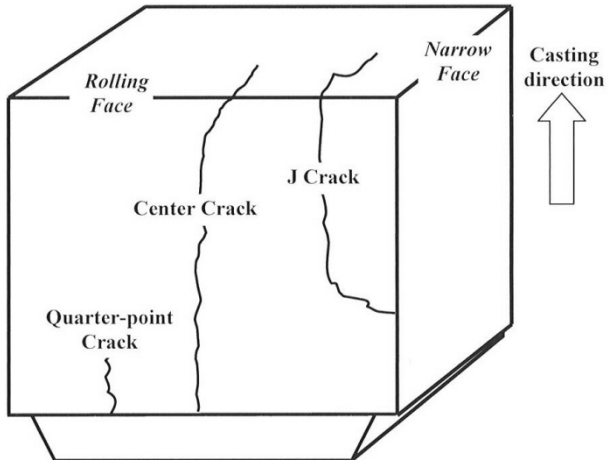

Fig. 1.6: Schematic of cold crack defects related to secondary cooling during DC casting of aluminum [27].

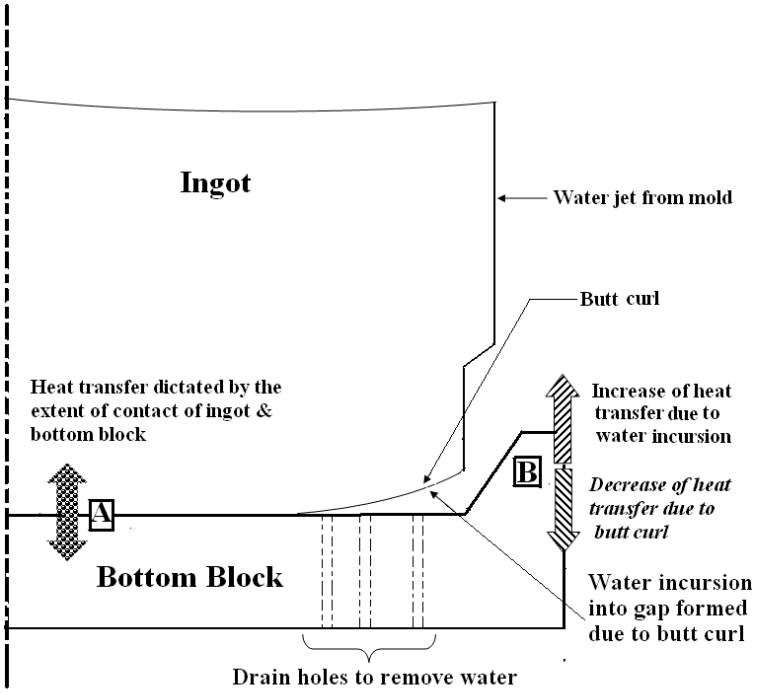

Figure 1.7: The schematic diagram shows the cooling of the ingot base in the presence of the bottom block during the start-up phase and also showing the probable heat transfer processes occurring near the centre of the ingot (Region A), and the outer edges (Region B) [115].

will lead in the loss of productivity. Various attempts have been made in the industry to control the start-up phase in order to reduce/eliminate the evolution of butt curl. For example, experiments conducted by Droste and Schneider suggest` that for some alloys the base deformation can be reduced by decreasing the volumetric rate of cooling water in the secondary cooling region with simultaneously increasing the casting speed. However, in practice the above mentioned suggestion is seemed to cause extreme butt shrinkage and leads to dangerous casting situations. The formation of a thick bottom shell can reduce the butt curl due to the lesser shrinkage upon direct impingement of water. A longer filling rate in the mold cavity or a change in design of the top of the bottom block can reduce the butt curl [113]. During start-up, one needs to quantitatively predict the temperature fields, cooling rates, thermal stresses, strains, and strain rates generated in the ingot to control the formation of cold cracks, distortions in the ingot, and hot tears in the mushy zone.

The cracks are seen to form in the vicinity of the bottom block lip, along the base of ingot, and along the surface of rolling face [116]. Among the various cracks the face crack is the most serious problem; since this crack can propagate through the entire length of the casting, and thereby can make the cast unsuitable for further downward processing steps. In VDC casting process the metal level needs to be controlled in order to reduce depth of scalp on rolling faces. There is a continuous effort by the industry to control the metal level for improving the quality of the cast. Wagstaff et al [132] carried out experimental investigation on DC casting for Wagstaff Inc., and proposed to use the Low Head Casting (LHC) technology which could permit faster casting speeds and minimal lubrication requirements. Caron et al. [14] reported that the LHC technique proposed by Wagstaff et al. is not good enough for the formation of shell of sufficient thickness in order to achieve the desired goal of casting. In addition, it is often seen in production plants that the use of the LHC technique leads water to go onto the top of the metal head. As a result, the ingot needs to be rejected due to severe cold folding at ingot corners or overlapping of melt during steady state conditions. Starvation of lubricant causing ingot surface tearing is another problem. If the meniscus level inside the mold is too high, due to the large metallostatic pressure and re-circulation of the melt, and the corresponding longer wider air gap, the shell tends to remelt, leading to liquation and

intense macrosegregation [36,89]. Optimum melt level (metal head) is essential for the formation of a stable and strong solid shell as the liquid metal starts to freeze onto the mould surface. To cast an ingot economically would require less scalping and edge trimming. To achieve these objectives, several mould technologies have been introduced such as low-head casting, hot top casting, lubrication through the mould, air pressurized moulds, electromagnetic casting (EMC), etc. with the aim to control the mould (primary) cooling. Nowadays in the DC casting process the most widely used technology to control the metal level is the hot top mold. The hot top is designed by placing a refractory reservoir at the top of the mold which is made with ceramic insert in the inner top surfaces of the mould.

Productivity is linked with quality and less scrap rates. Besides the latter factor, the quality is dependent on many other factors, such as, macro-segregation, microstructure, and ingot shape. Control of surface microstructure and the minimization of surface defects in VDC casting process have been improved by continual process development.

From the standpoint of quality issues, one of the most prevalent defects in DC cast of aluminum alloy sheet ingots is the formation of macro-segregation. Macro-segregation can be defined as the spatial chemical non-homogeneity in the alloy composition on the scale of a solidified casting. The size of the ingot, alloy composition and the allowable speed (as a consequence, the productivity) at which direct chill (DC) cast billets/ingots can be produced are restricted due to the occurrence of this defect [89]. The control on macro-segregation during solidification is difficult due to the large number of casting parameters involved, as shown in Figure 1.5. In order to control this defect, it is essential to optimize these parameters mentioned in Fig. 1.5. Unfortunately, macro-segregation constitutes an irreversible defect and is bound to occur in large castings. Since it is not possible to eliminate macro-segregation completely, the question then remains: how far we can exert a control over this phenomenon. Unlike the necessity of controlling the factors responsible for hot tearing where it needs to be completely prevented; else the ingot will be rejected for further processing, the approach of handling macro-segregated is not that drastic.

The solidification characteristic of an alloy depends on a multiple of factors, namely, freezing range, solidification time, feeding conditions, and casting speed. It is critical for the formation of macrosegregation in DC cast Al alloys [32,43,83,87]. Although macrosegregation is the result of global effects of all the mechanisms presented in the flow chart in Fig. 1.5, but technologically, it is possible to control macrosegregation by controlling the melt flow using an optimized melt distribution system [89]. Several studies on metal feeding systems have concluded that, the direction of melt flow as it enters the mould has a great influence on the severity of segregation. For example, experiments conducted by Chu and Jacoby [16] with an Al-Zn-Mg-Cu ingot, show that the ingot cast by the bi-level transfer method had 15% more negative centerline segregation as compared to the same ingot cast by the level pour method due to the stronger convection in the former one. These results indicate that the degree of negative centerline segregation is influenced by the convective flow in the liquid pool. Strong and irregular turbulent flow which is caused by direct or oblique entry of liquid aluminum during DC casting can create unfavorable (columnar) grain structures and uneven distribution of the alloying elements [115]. To overcome these problems, Grun et al. [52] proposed a melt distribution system where the nozzle is surrounded by a distributor bag. The latter diffuses some of the jet momentum created by the nozzle and encourages a slower and more stable flow patterns that is also influenced by natural convection.

The above studies reflect that the melt distribution system at the top part of the ingot exerts a great control on the flow patterns and turbulence in the liquid pool. The turbulence at the top surface affects the meniscus solidification and has a significant impact on the oxide contaminations. The latter causes a rough cast surface and internal defects in the final product. An optimum design of the metal distribution scheme can reduce segregation and significantly control the entrapment of inclusions by the solidified shell through a stable and turbulent free filling. Over the last 80 years a lot of studies have been carried mainly by industrial researchers to get a better understanding about different metal inlets and melt distribution designs to ensure a stable and turbulent-free filling. Besides the various metal feeding systems, presently there are many available technologies for this process, such as, selective forced convection, electromagnetic

stirring, ultrasonic cavitation, mechanical stirring, dirrected fluid flow, etc. which can control the macrosegregation by managing the convective flow which induces a complex relative movement between the solid and liquid phase. Some laboratory experimental results have shown that macrosegregation pattern in laboratory-scale DC caster of aluminum alloy can be changed from inverse to normal through mechanically or electromagnetically stirring effect [89].

It is well known from the practical research in this field, that the quality of the final as-cast product is dependent on the solidification phenomena. One needs to understand the fundamentals of solidification processing which is intricately related to the process parameters, structure formation and occurrence of defects. Until now, not enough effort has been put in terms of fundamental understanding of the relationship of the process parameters for DC casting processes with regards to controlling the final ingot quality. To minimize defects, various DC casting industries develop their own proprietary casting conditions through trial-and-error to obtain an acceptable quality cast. These industries do not publish their proprietary casting parameters in the open literature [116].

1.4 Optimization of the DC Casting Process

The following are the open questions with regard to the VDC casting and cast quality:

1. Would it be possible to cast safely the rolling ingots for various low and high freezing range aluminum alloys with high aspect ratios relatively crack free?
2. If one is successful in the first step then the question arises what amount of ingot deformation such as butt curl, butt swell, etc. is acceptable?
3. How one can distribute the melt at the top of the mold such that the melt enters the whole cross –section of the mold at a relatively uniform temperature?
4. If Step three is successful, will the melt distributor generate excessive turbulence to create unacceptable levels of oxide scales and inclusions [12,41]?
5. Would it be possible to permit a faster casting speed for large aspect ratio ingots for a specified alloy by the selected metal distributor which could produce a

smooth ingot surface without sub-surface segregation and form a stable solid shell that could prevent the break-out of the liquid metal at the exit of the mold?

6. If Step five is successfully accomplished, would it be possible to produce a good quality cast with acceptable macro-segregation at a faster casting speed for the required aluminum alloy ingot.

Furthermore, among the crucial solidification defects, the inclusions distributions in an ingot/billet are also one of the critical defects [Guthrie and Nilmani, 1993; Prillhofer et al., 2010]. After the last melt refinement step in the launder, it is of paramount importance to avoid re-entry of impurities, since all such impurities will end-up in the solidified shell. On the basis of the large number of investigations in the literature, one can identify the re-entry of oxides occur mainly from two sources:

1. The way the launder is filled and the way the melt is distributed to the mold can have a major impact on the re-entry of impurities.
2. A faulty-design of the melt distribution scheme can lead to a constant oxide input into the cast during the whole casting process.

For the production of a high quality rolling ingot, it is required to take the above factors into consideration. Overall, the following areas of the process are of main concern:

1. Heat transfer, and the role that it plays during the development of the cracks, butt curl and subsequent ingot distortion.
2. Metal distribution inside the ingot head which induces severe convection currents and carry broken oxide films from the top surface and upstream generated inclusions to the mold.

For a particular aluminum alloy, an ideal DC cast slab should have a fine, equiaxed and uniform grain structure distribution across the ingot (billet) cross-section for improved yield strength, fracture toughness, ductility, and other required properties with acceptable limits of inclusions contents, shrinkage, hot tear, and segregation

[49,90,107]. The above desired quality of the cast is partially related to the metal feeding scheme, since it determines the convection in the liquid pool and oxide and/or inclusion contaminations at the top surface of the ingot which causes the inhomogeneity and deteriorated properties during downstream processing. In reality, the convection in the liquid pool determines the profile of a sump (sump depth and shape), the temperature distributions and the flow patterns in liquid and mushy regions [69,108,109], which are difficult to observe directly during the DC casting processing operations. Because of opacity of the liquid metal it is not possible to visualize directly the velocity patterns in the melt. Indirect experimental measurements are also difficult due to appreciably high melt temperature as well as the unavailability of suitable velocity measurement techniques. Isothermal water models with particle-velocity tracking measurements are normally used in industries and in laboratories to predict the actual flow fields in liquid metal. This approach has a number of limitations besides the fact that the DC casting operation is a non-isothermal phenomenon.

To overcome the above restrictions in liquid metal flow measurements, nowadays, various numerical and analytical modeling techniques are used to simulate the actual caster operation which allows one to visualize and analyze the solidification patterns, temperature and velocity fields during casting. Ideally, both experimental and numerical analysis are essential to fully understand and to analyze the physical processes involved in the formation of complex real-life flow patterns and to evaluate the individual effects of all factors mentioned in the flow chart. Before doing the casting experiments one should do the numerical simulation first which could complement the experimental study and hence the numerical study can be used a tool of research.

1.5 Complexities of Numerical Modeling

The numerical solution of the DC casting problem involves solving of coupled system of complex partial differential equations, namely, continuity, momentum, energy and mass transfer equations along with macroscopic solidification. The geometrical complexities and nonlinearities of equations practically do not support any analytical

solutions. Numerical technique is a better and a justifiable option to get the solution of these kinds of problems. Although the assumption of two dimensional modeling is applicable for a round billet caster, it limits the applicability of the model for a slab caster. In real slab DC casting systems, the transport processes are essentially three-dimensional in nature and a two dimensional model will therefore predict grossly unsatisfactory results. The development of a comprehensive model for the prediction of coupled three-dimensional turbulent flow, heat transfer, and macroscopic solidification in a strand during DC casting is a very challenging task. Once such a mathematical model is developed, it can then play a major role to optimize the parameters as well as capture most of the complexities of the physical phenomena active during the industrial process. In reality, the production of new castings requires an expensive, time-consuming trial-and-error experimental diagnostic approach. As a result, the present trend in the industry is to use the available commercial CFD codes. However, at present the commercial codes and their numerical solutions generated by the codes are not adequate for the comprehensive answer of such a complex multi-dimensional process. For example, Gruen et al. [50] reported that for a 3-D simulation of a rolling aluminum ingot, the predicted turbulent flow patterns and temperature distributions in the liquid pool at high temperature regimes varied significantly for the use of four different CFD codes namely, ALSIM, FIDAP, PHOENICS, CFX.

This point is seen to be crucial for the commercial codes, as there are some serious doubts as to whether it is possible to generate correct results using such codes for complex 3-D turbulent flow with coupled solidification problems. So, a comprehensive 3-D CFD code should be developed to observe both the start-up and steady state phase of the casting operations. The code can be then used to identify an optimum metal feeding system with associated process parameters so that a uniform heat transfer takes place particularly within the mold region.

A lot of studies, both experimental and numerical, exist in the literature on the surface quality and microstructure for various cooling conditions, mold designs and filling systems. Numerous studies also exist on thermally induced ingot shape distortion which occurs during the start-up phase of a DC casting process. A very few experiments/numerical models exist in the literature on the metal feeding system in the

mold which has identified its impact on the formation of various defects on the cast. To the best of the author's knowledge, no previous numerical work exist in the literature which has combined turbulent fluid flow, heat transfer and solidification for various melt feeding schemes for a rolling ingot. This may be due to the factors such as, the complexity of the problem, the lack of material properties and proper data on boundary conditions, as well as the limitations of the concerned turbulence and mushy region solidification models.

1.6 Objectives of the Present Study

The primary objective of this study is to develop a comprehensive 3-D numerical model. The model should incorporate the turbulent fluid flow, heat transfer and solidification in a coupled manner for the simulation of industrial scale vertical Direct Chill (DC) casting of aluminum-alloy slabs during the steady state phase. In accomplishing this primary objective, the following sub-objectives are formulated:

1. Validate the model quantitatively by comparing the predicted solidification front with the experimentally measured solidification front of the real casting experiment of Jones et al. [70] for Al 3104 rolling ingot having a 0.66 m mold thickness and a 1.32 m mold width. It should be noted that unlike the present delivery system, Jones et al. used a combo bag melt delivery system in their experiments.
2. Develop a 3-D thermal model for the prediction of heat transfer processes from the ingot surfaces during the solidification at steady state.

It should be pointed out that over the last few decades several numerical studies have been conducted to quantify the rate of heat transfer from the cast by thermal models. Most thermal models have used smaller (laboratory scale) ingot geometry compared to the industrial scale size and hence do not accurately represent the solidification front which develops in a real geometry. The uniqueness of the present study concerning the thermal model lies on the following facts:

1. In this study, a thermal model has been developed to gain fundamental understanding of the thermal behavior during solidification of a high aspect ratio industrial-scaled rolling ingot.
2. The developed thermal model should be able to predict the temperature distributions for an industrial-scaled rolling ingot operating at any casting speed. To increase the productivity, now-a-days high casting speeds are usually practiced in industry, such as 180 mm/min or more. It should be noted here that most of the thermal models available in the literature deal with much lower casting speeds.

It is well known that the flow conditions (laminar and/or turbulent) affect the heat extraction rate from the ingot. In order to take this into consideration, a number of simulations will be performed for the identical slab ingot to evaluate the influence of the flow field on the heat extraction rates. The present author has not come across any work for a DC casting process which compares the heat transfer predictions by considering the 3-D flow field and without considering the flow field. Such predictions are necessary to ascertain the quantitative effect of the flow field on heat transfer rates. In the industry, the thermal models are widely used to develop and optimize the automatic control systems for such casting processes without correctly recognizing the effects of flow on heat transfer.

The prime objective of this study is to evaluate the effects of different melt feeding designs (melt distributor) as presented in Fig. 1.8, for various casting parameters, such as casting speeds, melt superheats, etc during DC casting of an Al-1050 ingot. The casting speed directly influences convection in a proportional way [89]. The inlet melt temperature has a strong effect on the temperature gradients in the liquid pool [32]. Increasing casting speed and/or ingot size normally deteriorates the quality in terms of macro-segregation and hot cracking tendency and as a result it is necessary to come-up with a suitable balance between the stated factors. The present model also includes the hot top to control the metal level in the mold as is normally practiced in the industry. Furthermore, to prevent the oxide scales and inclusions re-entry into the mold, a special

melt distributor is necessary to capture the above harmful impurities. In this study, a special design of the melt distribution system will be proposed. Specifically a fine porous distributor plate will be modeled. The model will predict turbulent melt flow patterns, temperature distributions, local surface heat flux, thickness of the mushy region, extent of the solidified shell as well as sump depth for different melt feeding configurations. The model will specifically deal with the following melt feeding schemes:

1. Open-top with metallostatic head (hot top);
2. Open top with a full porous filter inside the hot-top;
3. Open-top with a half porous filter inside the hot-top;
4. Submerged nozzle and a porous filter inside the hot-top;
5. Submerged nozzle with a distributor bag having a bottom solid plate;
6. Submerged nozzle with a distributor bag having a fine (filter) and coarse (foam) bottom porous plate.

If we compare Cases 1 and 2, it is expected that the melt turbulences due to high flow velocities of the liquid metal will be reduced by the presence of the filter. In Case 3, more melt is expected to enter through the narrow side of the hot-top in the upper-part of the ingot. In Case 4, one expects that the melt from the submersed nozzle will fall near the ingot center with high momentum, and then it will spread out on the filter which is placed across the total cross-section in the hot-top. In Case 5, the metal entry is directed towards the end face of the hot-top, whereas in Case 6, less metal is expected to exit towards the narrow side of the hot-top in the upper-part of the ingot.

Specific aims of this study include the following:

1. Identify which features of the distribution schemes should be used to achieve the desired result, and how the basic design features influence the fluid flow.
2. Ascertain the ability to feed metal into a “standard” ingot format (approximately 1730 mm wide and 660 mm thick) with respect to temperature distribution and temperature uniformity.

3. Determine the effect of various heat transfer coefficients imposed on the mold surface as suggested in the literature to predict the impact of chill water on shell formation inside the mold.

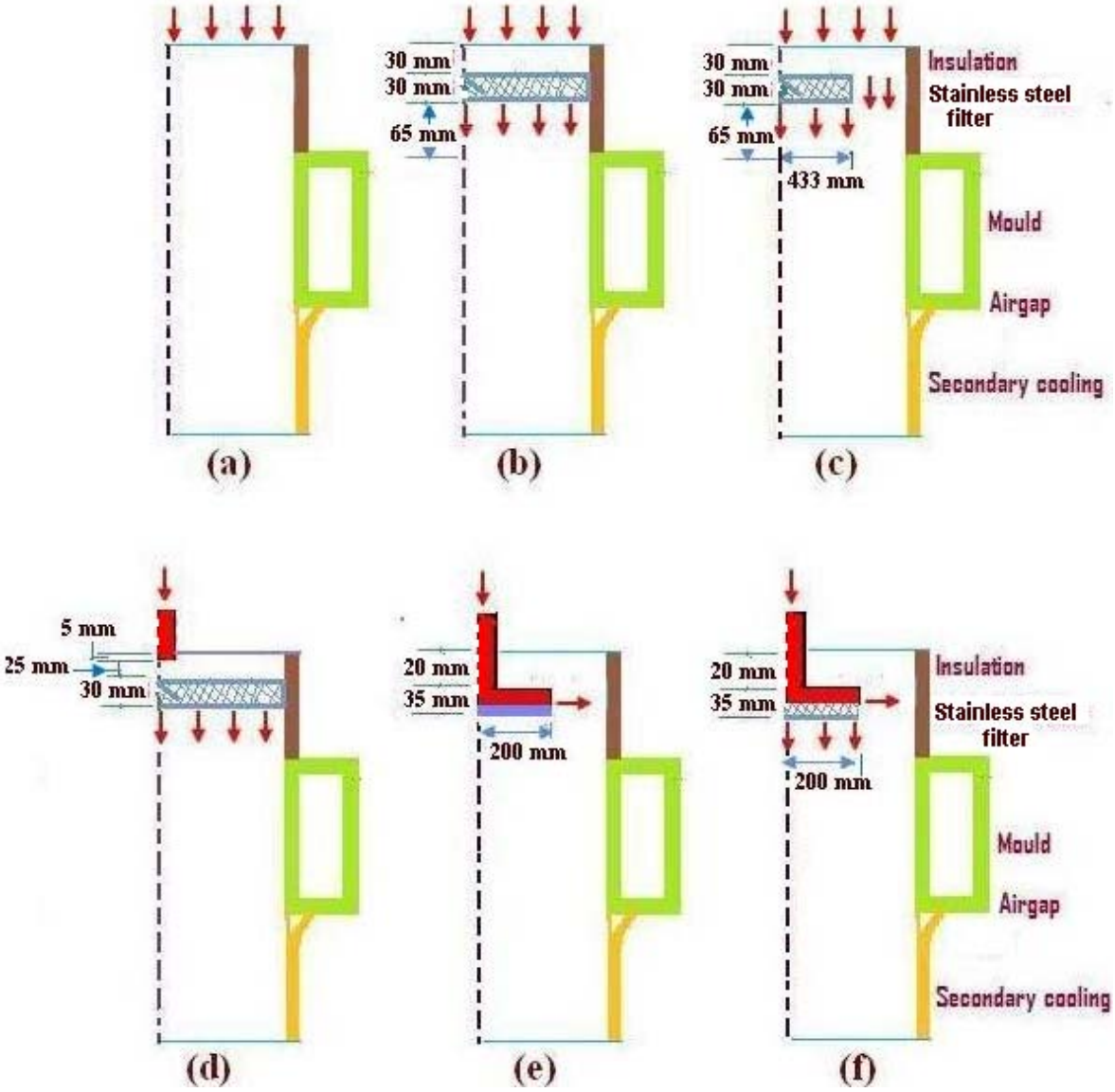

Fig. 1.8 Proposed melt feeding distributors for VDC casting processes. (a) Open-top melt feeding scheme. (b) Open top with a full porous filter melt feeding scheme. (c) Open-top with a half porous filter melt feeding scheme. (d) Submerged nozzle and a pouous filter melt feeding scheme. (e) Submerged nozzle with a distributor bag having a bottom solid plate melt feeding scheme. (f) Submerged nozzle with a distributor bag having a fine (filter) and coarse (foam) bottom porous plate melt feeding scheme.

1.7 Overview of the Present Work

The results of the numerical simulations obtained in the present study are structured and documented in the form of following ten Chapters:

Chapter-1 gives the introduction, the background and objectives of the study.

Chapter-2 discusses the relevant literature, both experimental and numerical, for the VDC casting process that has been published mainly over the past two decades.

Chapter-3 illustrates the mathematical formulation and the numerical approach to be used to solve the governing equations with associated boundary conditions. The necessary assumptions, turbulence model used, the mushy region solidification approach implemented are also discussed in this chapter.

Chapter-4 provides the quantitative verification of the developed mathematical model and grid independency tests.

Chapter-5 is devoted to the development of thermal modeling of VDC casting for open top melt feeding scheme with relevant parametric study.

Chapter-6 reports the results for an open top melt feeding scheme in its first section. A comparative study between the thermal model and the CFD model is also discussed here. The second section of this chapter covers the study of various thermal boundary conditions (TBC) in the primary cooling region.

Chapter-7 provides the simulation results for open top with a full and a half-filtered feeding geometry. This chapter also explains the role of porous filter inside the domain.

Chapter-8 repots the simulated results for submerged nozzle with a distributor bag having a solid/porous (fine and coarse) bottom plate. The role of porosity of the bottom plate of

the distributor bag with regard to melt flow and solidification patterns are explained in this chapter.

Chapter-9 presents the simulation results for flow and temperature distributions for a submerged nozzle and a full porous filter feeding scheme.

Chapter-10 states the major conclusions of the present work. It also documents the statements of originality, and offers a few suggestions for possible future work.

CHAPTER 2

LITERATURE REVIEW

2.1 Introduction

Research into the mathematical modeling of the DC casting process has been usually separated into two distinct, but inter-related tasks: (i) computation of the thermal fields in phase change problems, and (ii) computation of convection-diffusion phase change problems during the casting process.

The heat transfer analysis can be advantageous in two ways: (1) the thermal model results are the vital first rapid step to understand the effects of the casting practices on the final physical properties of the cast, such as, micro structure, segregation and strength; (2) in order to get quick results about the stress field, the thermal model results can be used. But if more accurate and detail analysis are required, then the effect of melt flow should be incorporated into the model. For example, to include the effects of inclusions and to minimize the severe defects such as hot tear and macro-segregation during solidification, the CFD model should be developed.

In the following sections, detailed descriptions of the previous work related to thermal model and CFD models of DC casting process currently available in the published literature have been critically reviewed. Previous experimental work that has a direct relevance with the subject matter of the current research is also reviewed.

To justify the present work, an attempt is made here to shed some light on points where there is a gap in the surveyed work. The survey is organized in a way that follows a chronological order of the developments of the modeling of DC casting process. Since some good reviews are already available, hence to conserve space this review will only concentrate on the published work after 1990. This review will be helpful in

understanding the modern developments in terms of modeling of the DC casting process and will also set the stage for the need of the current research work.

2.2 Thermal Models for the Phase Change Problems

In the 1970s and 1980s, thermal models first became available and typically these were simple 2-D models for steady state regime of the process. An extensive review on the development of the thermal models for the DC casting process was performed by Weckman and Niessen [135] for the period ranging from 1947 to 1983. The above authors discussed both the analytical and numerical models concerning this process. In is apparent from their review that the one dimensional analytical models could not correctly predict the solidification profiles. Although, three-dimensional thermal models were available before 1983, unfortunately due to the lack of appropriate experimental thermal boundary conditions the predicted results showed serious discrepancy compared to the experimentally measured solidification profile. Another drawback was that only pure or eutectic alloys with a fixed solidus temperature were modeled. In their review paper the authors concluded that experimental boundary conditions, considering the heat transfer mechanisms over the external boundary of the DC cast ingot in both the primary-cooling zone within the mold and the secondary-cooling zone below the mold, are required for accurate predictions of the thermal field.

Tarapore in 1989 [120] used a series of DC casting experimental trial runs to produce 394 mm diameter billets for an aluminum alloy 2024 and to validate and further to improve a simplified finite element code (TEMPERI) previously developed by Weckman [133] at the University of Waterloo, Ontario, for the simulation of semi-continuous casting of aluminum. His developed 2-D thermal model was then used to study the effects of three casting variables – drop rate, water flow rate, and metal superheat – on the solidification characteristics of AA2024 billets at steady state condition. The solid-liquid interface was modeled by using effective specific heat method where an average freezing temperature between the solidus and liquidus temperature was taken instead of considering the actual solidus and liquidus temperatures for an alloy. The

effect of thermal convection in the liquid pool was considered by increasing the melt thermal conductivity as a function of melt superheat in the sump in an iterative manner. One of the important findings of this study is that the predicted temperature gradients in the sump and the sump depth were found to be in excellent agreement with experimentally measured values, despite the simplification made by decoupling the thermal problem from the equations of continuity and momentum. On the basis of his experimental and thermal modeling results, the author reported three observations; (i) increasing of drop rate markedly increased the depth of the sump; (ii) higher casting temperature increased the sump depth slightly, especially at the lower drop rate; (iii) increased mold water flow lowered the thermal gradients as well the temperature in the sump. Besides not solving the momentum equations for the thermal convection terms in the energy equation, one major drawback of this model is that it could not take into account the solidification range of the alloy and as a result the mushy zone could not be predicted using his code. His work, however, gives an insight into the importance of various casting parameters like water flow rate, casting speed, and metal inlet temperature on the development of the temperature field and sump profile.

One of the most active research groups concerning DC casting is Katgerman and his co-workers [71] in the Netherlands. In 1991, Katgerman reviewed the major developments concerning semi-continuous DC casting process for non-ferrous metals that took place prior to 1991. He described in details the DC casting process and explained the metallurgical characteristics of the cast obtained through this process. The author critically reviewed the work that appeared during the period from 1970-1991, and summarized the technical constraints that existed then. He strongly suggested that advanced mathematical modeling techniques should be used to gain clear understanding of heat flow that takes place during the casting/solidification process in order to improve the quality of the as-cast product.

Devadas and Grandfield in 1991 [22] used the code TEMPERI (developed by Weckman at the University of Waterloo, Ontario) to model the DC casting of aluminum billets. The simulated results of the model were later compared with the results obtained from the commercial heat transfer and fluid flow package, FIDAP (developed by FDI,

Chicago). The authors forwarded two significant observations. First, they correctly divided the primary mold cooling into three district regions; namely, meniscus, mould contact, and air gap cooling. For each of these regions, they prescribed three different effective heat transfer coefficients which varied from 10-8000 $Wm^{-2}K^{-1}$, with the highest value at the meniscus and the lowest value at the air gap region. Secondly, while modeling the phase change problem, they handled the release of the latent heat during solid-liquid phase change in two ways as shown in Fig. 2.1. In the first approach, they used an equivalent (average) specific heat method and noticed that this method suffered from numerical instability near the phase change temperature and resulted in jig-jag temperature profiles, particularly near the phase change region. In their second approach, they implemented the well-known enthalpy method and found that this method predicted stable solutions and could track the phase change interfaces in a more stable manner.

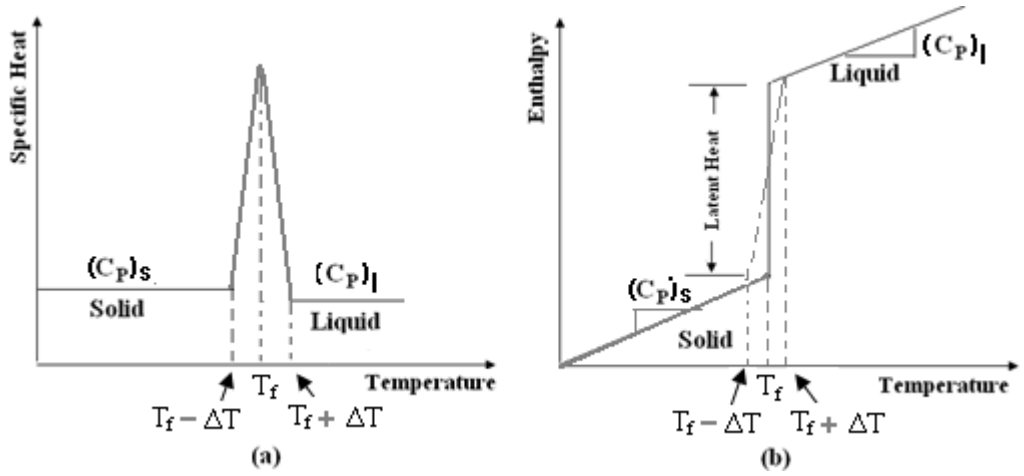

Fig. 2.1: Schematic representation of (a) Equivalent specific heat, and (b) Enthalpy method.

El-Demerdash in 1993 [29] developed a simple 2-D finite difference thermal model in cylindrical coordinates to study the effects of two casting variables- metal inlet temperature, and casting speed – on the solidification characteristics of a AA6063 round billet for a constant metallostatic head during the steady state. To handle the mushy zone

they used the effective heat capacity method which depended on the liquid fraction. Using an approximate expression for the liquid fraction with regard to the temperature in the mushy region they obtained the contribution of solidification on the heat capacity. A variable heat transfer coefficient was used to extract heat from the surface of the ingot in both the primary and secondary cooling zones. Their findings indicated that for a fixed inlet superheat of 39°C, the increase in casting speed ranging from 90 to 105 mm/min had a remarkable effect on the temperature contours of the billets having a diameter of 203 mm. An increase in the casting speed caused the solidification front to go deeper and resulted in the expanded mushy zone. On the other hand, for a fixed casting speed of 100 mm/min, the increase in superheat ranging from 29°C to 49°C had a minimal effect on the temperature distribution of the said billet. A further refinement of the model was recommended through fine-tuning of the heat transfer coefficient values at different axial surface zones. The major drawback of this model is that the temperature fields were not verified with either experimentally measured or numerically predicted data.

El-Raghy et al. in 1995 [30] developed a finite difference, simple 2-D thermal model for a cylindrical DC cast billet for AA6063 alloy. Both transient and steady state conditions were modeled for open-top delivery system. The cooling condition on the outer surface of the billet was assumed to be purely convective (HTC = 10,000 W/m^2K), and was not discussed in detail. Since the authors claimed that only about 0.6% of the total heat is lost (extracted) due to radiation and convection from the top surface of the billet, as a result, this heat loss was neglected in their model. They used the solid fraction dependent equivalent heat capacity method to account for the latent heat release during solidification. The equivalent heat capacity was only prescribed and applied over the liquidus-to-solidus temperature range. In modeling the solidification phase change of the above alloy, the authors did not report any numerical instability in their model, which was experienced by Devadas and Grandfield [22] for pure materials for using the similar method. The authors experimentally also measured the sump profile for the said alloy for a casting speed of 95 mm/min and for a pouring temperature of 675^oC by using a calibrated-rod technique. The water flow rate was kept fixed at 130 m^3/hr during their experiment. The cast length was 600 mm. They claimed that the error between the measured and predicted sump profiles at steady state from the center to the surface for the

same horizontal plane of the 203 mm diameter billet varied between 4-12%. Their numerical studies revealed that at a fixed melt temperature of 680^{o}C, increasing the casting speed from 90 mm/min to 105 mm/min decreased the time spent by the melt inside the mold and in the chilling zone and resulted in a lesser heat extraction from the system at a same location. Increasing the casting speed caused the temperature contours to shift downwards. At the start-up phase the predicted mushy zone was almost linear in shape but at the steady state the shape changed from linear to parabolic. They also found that the cooling rate at the surface was higher than at the center. The bottom block was treated as a surface with a constant temperature boundary condition. Only conduction heat transfer was considered at the metal-stationary block interface. The cross-sectional geometry of the extrusion billet is more realistic but the billet base geometry has been simplified. The evolution of the temperature field with time at the start-up phase will depend on the heat transfer from the ingot base to the bottom block. Though they modeled the start-up phase but the model failed to predict accurately the evolution of temperature field during this stage.

Das in 1999 [19] developed a thermal model of DC casting of 152.4 diameter AA6063 Al-Mg alloy for cylindrical billets for the steady state condition. He used an orthogonal coordinate transformation technique for tracking the solidification front assuming the alloy to be pure with a freezing temperature of 650^{o}C. For the external boundary conditions in the post mold region, particularly for secondary cooling region, he developed effective heat transfer coefficients by using the theories of nucleate boiling with forced convection and film cooling by a free-falling film of water. Numerical simulations were carried out for a fixed pouring temperature of the liquid metal of 689^{o}C and for three casting speeds of 97.8, 152.4 and 240.06 mm/min. A very good agreement was obtained in terms of the temperature field with published experimental data for a similar system. In order to take into account thermal convection, although, the author considered a slag flow in the liquid sump, but failed to consider explicitly the thermo-fluid dynamics aspect of the problem. Furthermore, he considered an alloy for modeling but assumed it to be a pure material having a fixed solidification temperature. His front tracking method of solution can’t be extended easily for an alloy which solidifies over a temperature range.

Nallathambi et al. in 2009 [92] developed a temperature-based finite element technique for modeling the phase-change heat conduction problems. After verifying the solution method with the analytical solution of the phase-change of a semi-infinite 1-D slab, they modeled the start-up thermal problem of a 2-D Al-1050 billet by applying the relevant thermal boundary conditions at appropriate sections of the billet caster. The simulated billet was of 200 mm diameter with a length of 600 mm. The authors noticed that, the size of the time step played a key rolled on the results because of adding the grids required to accommodate the expanding region which was necessary to solve the start-up phase. They predicted the sump depth at the center of the billet for four different time steps, which ranged from 0.7 – 10 sec. Both during the start-up and steady state periods, they predicted a higher sump depth for a smaller time step. By using a reduced time step size of 1 sec, their predicted sump depth at steady state showed a good agreement with the predicted sump depth of another researchers. One of the major drawbacks of their finite element scheme which was developed for solving transient phase-change heat conduction problems is that it is time step dependent and can't be relied upon.

Shuyan et al. in 2009 [117] developed a pseudo transient 3-D mathematical model for a DC slab caster having a cross-section of 400 x 200 mm and predicted the thermal fields for two commercial magnesium alloys, LA141 and AZ31. They used effective interfacial heat transfer coefficients for the primary and secondary cooling zones which were taken from the relevant literature. In their model they also took into account the dummy block and the related thermal boundary conditions. They concluded that the pouring temperature of the melt and cooling water flow rate in the mold impacted the temperature profile of the cast rather slightly compared to the effect of the casting speed. Of the two alloys model, LA141 showed higher solidification rate and lower sump depth compared to AZ31.

Hu et al. in 2013 [60] modeled the 3-D temperature field for a DC cast slab of 800 mm x 300 mm cross-section of AZ31 alloy for casting speeds ranging from 20 to 70 mm/min for a fixed pouring temperature of 600^0C. They have reported the sold shell thickness, and the temperature contours and temperature gradients at the wide symmetry

plane for various mentioned casting speeds. They concluded that the temperature gradient was larger in the length direction then that in the width direction. They also reported the maximum value of temperature gradient appeared when the slab first came in contact with the cooling water. The optimum casting speed for the above caster was found to be between 30-35 mm/min to avoid the crack. Although the paper stated that a thermo-fluid analysis was carried out but no supporting results were reported, nor provided any explanation on how the melt flow analysis was carried out.

2.3 CFD Models

In 1989, Flood et al. [40] described a 3-D thermal and fluid flow model using PHOENICS (a commercial control volume based finite difference CFD package), and then the predicted thermal fields were used to compute the stress distribution using ANSYS (another commercial finite element package). The predicted solidification front profiles for a rolling ingot were validated against measured solidification front profiles. In their experiments, the solidification front was obtained by adding copper as a tracer during casting. To model a 550 mm diameter cylindrical billet, a 2-D version of the PHOENICS code was used invoking axis-symmetry condition. Two melt feeding schemes were modeled. In one case, the melt was assumed to have been delivered over entire top surface. In another case, the melt was delivered at the center by restricting the flow to 10% of the billet diameter. The modeled alloy was the binary aluminum-copper alloy (Al-4 wt% Cu). Two casting speeds, viz., 45 and 50 mm/min, and a fixed inlet temperature of 695^{o}C were selected for the simulations. The fluid flow in the mushy zone was modeled in two ways. In one case, the velocity field in the mushy region was fixed to the casting speed by using a fixed but very high Darcy source term which was implemented for $f_S \geq 0.1$. In another case, enthalpy-porosity scheme was used where the Darcy source term depended on the solid fraction in the mushy region. To account for the turbulent effect of the flow, in one case the authors solved the laminar flow equations by enhancing the kinematic viscosity of the melt by a fixed value of 5 x 10^{-5} m^2/sec, and in another case, the full $k-\varepsilon$ turbulent model equations were solved. Two different

concepts of modeling the flow field in the mushy region were implemented both in the laminar and turbulent flow cases. The authors found a shallower sump profile when the melt was delivered over the entire top surface because of buoyancy dominated flow. For the restricted entry flow condition, a deeper sump profile was obtained due to predominantly forced filling condition. From their plotted results, it appears that a significant difference in temperature contours in the liquid pool occurred for modified laminar flow compared to turbulent flow modeling. In their two approaches of handling the mushy zone, they obtained remarkable differences in the sump depth and in the isotherms for using modified laminar flow equations. Unfortunately, the authors did not provide the details of the boundary conditions used in their models. From their work, it is also not clear how they have implemented the Scheil equation for calculating the solid fraction in the mushy region without solving the concentration equation for copper.

Chu and Jacoby in 1990 [16] experimentally observed the composition and microstructure from the surface to the center of a 1270 x 406 mm Al-Zn-Mg-Cu alloy rectangular ingot cast by different metal entry systems such as bi-level transfer and level pour method. In the bi-level method, liquid metal was transferred from the pouring trough (high level) to the mold (low level) and in the level pour method, the metal was passed from the trough to the mold without a change in elevation. They showed that Al-Zn-Mg-Cu ingot cast by the level pour method registered about 15% decrease in the negative centerline segregation (particularly for Cu) compared to the same ingot cast by bi-level transfer method due to the more uniform distribution of molten metal entering the basin area during casting. A simplified analysis was proposed by these researchers to estimate macro-segregation. Their analysis showed that the level of centerline negative segregation is strongly affected by the volume fraction of detached cellular dendrites and the partition coefficient of each major alloying element. Results of this work indicate that the filling condition in the liquid pool imparts a serious effect on macro-segregation, which resulted from strong convective current produced by the bi-level transfer method.

Dorward and Beerntsen in 1990 [25] undertook an experimental program to evaluate the effects of metal temperature, casting speed and mold water flow rate on thermal profiles, microstructures, and macro-segregation in a 400 mm diameter 2024

alloy billet. Two pairs of ingots were cast with a cooling water flow rate of 550 l/min, and 230 l/min in the mold. The casting speed was decreased from 63.5 mm/min to 38 mm/min. A trough metal temperature difference of about 55^0C (715^0C vs. 660^0C) between the two casting speeds was achieved. They found that a lower water-flow rate (230 l/min) and a lower melt temperature (660^0C), increased the macro-segregation, whereas an opposite trend was observed at higher water flow rates, which means the macro-segregation may be dependent on the water flow rate. They observed that the largest and the most isothermal dendrites were formed in billets for casting speed of 63.5 mm/min compared to the lower casting speed of 38 mm/min. They concluded that at a high casting speed, a deep liquid metal sump was produced which led to the collection of coarse solute-depleted isothermal dendrites in the center of the billet. Although, the high melt superheat increased the sump depth slightly, but overall it caused a beneficial effect in terms of the severity of macro-segregation compared to a low melt superheat which was more conductive to the growth of floating isothermal primaries.

In 1994, Grun et al. [52] reported the use of a 3-D coupled turbulent fluid flow, heat transfer and solidification model at steady state to investigate the influence of nozzle-distributor systems on temperature and sump profiles for DC casting of AA1050 rolling ingot using finite element commercial CFD code FIDAP. The effect of natural convection inside the liquid phase was ignored due to the forced convection dominated flow. Two ingot cross-sections, a larger 1730 x 660 mm and a smaller 1200 x 600 mm, were simulated. The hot top height and the mold length were taken as 65 mm, and 80 mm, respectively. A 34 mm diameter nozzle was considered with a submerged depth of 20 mm from the liquid metal level. Two rectangular bags having a dimension of 300 x 100 x 50 and 150 x 100 x 50 were investigated. Two casting speeds, namely, 40 and 60 mm/min, and a melt inlet temperature of 720^oC, were chosen for the simulations. To model the turbulence quantities, the k- ε model was used. Their predicted results indicated that the flow pattern in the sump, and the extent of the mushy zone were governed by the aspect ratio (length to width ratio) of the distributor bag. Changing the ingot size and the casting speed had only a small effect on the characteristics of the flow field and temperature distributions. In addition to the CFD calculations, the authors also did a simple thermal model analysis for the same caster and compared the thermal field

with the predicted one from the CFD model. They showed that the solidification profiles from the two models are almost similar but other temperature contours above and below the solidus varied significantly. The predicted velocity profiles from the CFD model were compared qualitatively with the results of the water model which was performed by the R & D department of VAW aluminum AG and found to be satisfactory. However, temperature profiles were not verified with experimentally measured data.

Amin and co-workers published three papers [2, 3, 4] on 2-D modeling of slab casting process for pure aluminum. The authors used the finite element code NACHOS II, which was originally developed by Gartling (1987) at Sandia National Laboratory, Albaquerque, NM. This code is a general purpose code designed to solve the two-dimensional continuity, momentum, and energy equations for both steady state and transient problems. The authors modified the code to solve their phase change problems. In all the three papers, an effective heat capacity method was used to tackle the solid-liquid phase change aspect of the process. In order to allow for the solid layer to take the withdrawal speed, a very high value of fluid viscosity (of the order of 10^{20}) was specified when the nodal temperature reached at or was below the solidification temperature. In their first paper [2], the authors took into account the mold-metal interface radiation heat transfer effects and in addition, the conduction heat transfer effects in the mold and solidified metal were considered. Their second paper [3] is similar to the first one, except that the conjugate heat transfer between the mold and solidified metal was not considered. In both the papers, heat transfer coefficients in the form of Biot number for pre-mold, mold and post mold regions were pre-assigned and varied and model results were provided for various combinations of casting speed, inlet superheat and pre mold, mold and post mold cooling conditions. In both papers, the liquid metal flow in the sump was assumed to be laminar and except for the heat transfer results, no fluid flow results were provided in the two papers. The predicted temperature fields and progress of solid/liquid interface for various casting speeds, cooling conditions and inlet superheats showed expected trends. In their third paper [4], the authors modeled the same problem as in their earlier two papers, but took into account the turbulent aspect of the melt flow by implementing Prandtl mixing length theory (also called zero equation model of turbulence). In addition to the effects of the parameters studied in their earlier two papers,

in their third paper the authors studied the effect of the mold length on various predicted quantities and suggested remedies of breakout for higher casting speeds and inlet superheats. The shell thickness, the local heat flux, the temperature contours and the location and slope of the solidification front were reported for various combinations of the studied parameters. And in addition, they provided turbulent viscosity contours, axial velocity profiles and velocity vectors. One major weakness of their work is that, in addition to the limitation of the model being 2-D instead of 3-D, the results are only applicable for pure aluminum and hence cannot be applied for aluminum alloys where mushy zone develops during solidification. Further, the turbulence aspect of the melt flow was considered in a cursory manner without invoking any standard turbulence model equations. Also, the implemented thermal boundary conditions in the form of Biot numbers do not correspond to the experimental boundary conditions suggested by others for similar casting problems.

Mortensen in 1999 [84] predicted fluid flow and thermal fields for the start-up period for a rolling sheet ingot of dimensions 600 mm x 200 mm for Al-1050 alloy. He used the ALSIM finite element code to model the transient aspect of the 3-D turbulent flow, heat transfer and solidification process of the start-up problem. The turbulence in the melt was incorporated in the model by using the low Reynolds number (LRN) model of Launder and Sharma and natural convection was taken into account by invoking Boussinesq approximation. The enthalpy porosity scheme of Voller and Prakash (1987) was used to model mushy zone solidification in the presence of a flow. Since the objectives of the author was to understand the basic mechanisms of the DC casting process during start-up and to interpret casting experiments, hence modeling results were obtained only for a single casting speed of 60 mm/min. The mold used was a hot-top type with a height of 120 mm, with its 75 mm of the upper part was assumed to be insulated by a solid insulating material. The hot top was fitted with a standard combo bag distributor at the center. The effective heat transfer coefficients used in the mold and post mold regions were prescribed on the basis of the experimental thermal boundary conditions suggested in the literature. Specifically, in the mold contact zone a value of 3000 W/m^2K was used while in the air gap region the value was varied from 250 to 350 W/m^2K. The model took into account the heat transfer between the ingot and the moving

bottom block and also allowed for the intrusion of water between the two from the secondary cooling zone. The author reported that it took about 400 sec in real time (not the computational time) to get steady state velocity and temperature fields and further stated that fluid flow had a significant effect on how the solid shell solidified against the bottom block and the mold. The predicted temperatures showed a reasonable agreement with the temperatures obtained through measurements in the bottom block. It is to be stressed here that prior to this study, there was no modeling study concerning DC casting which modeled the start-up period in 3-D while taking into account the turbulence effect of the melt on the mushy zone solidification process.

Gruen et al. in 2000 [50] described 3-D thermal and fluid flow models using a proprietary code named ALSIM and three commercial codes, namely FIDAP, PHOENICS, and CFX. The first two codes are based on finite element approach while the latter two are based on control-volume finite-difference approach. On the basis of the predicted velocity fields and temperature profiles for laminar and turbulent flows, a comparison was made among the above mentioned models. For the comparison purpose, a rectangular ingot was chosen where the melt was delivered through a nozzle with a rectangular distributor bag which was assumed to be impervious both on the bottom side as well as on the side walls. The distributor had openings at the front faces. The selected casting speed and pouring temperature were 60 mm/min and 680^{o}C, respectively. The ALSIM model for turbulent flow was validated against measured time-averaged temperature in the liquid pool obtained from the laboratory scale casting experiment for a combo-bag melt distribution system of an AA3004 rolling ingot. The authors did not show or discuss anything about the validation of the other three CFD models. They showed that the flow fields and temperature distributions predicted by the four different CFD codes for turbulent flow, differed significantly in the liquid region. Also, the extent of the mushy region predicted by the four codes varied widely. They also got remarkable differences in the thermal fields, especially above the liquidus temperature for using the laminar flow models. In their paper, the variations of the temperature field with respect to positions are not shown and only qualitatively the predicted temperature contours are compared. If the authors would have given the scale used in their figures, one could have estimated the magnitude of the relative errors in the obtained results. However, this work

is a good attempt wherein the impact of the commercial codes in predicting the velocity and temperature fields along with the solidification profile, are reported. In the DC casting literature this type of comparison has never been explored earlier. It is to be noted here that the PHOENICS and FIDAP codes are not available commercially any longer. In addition, ALSIM is a proprietary CFD code applicable for modeling a DC casting process only, and is developed by IFE on a contract from Elkem Aluminum, Hydro Aluminum, Raufoss-Hydro Automotive Research Center, and the Research Council of Norway.

After extensive reviews of the production facilities around the world concerning DC casting processes, Grealy et al. in 2001 [47, 48] identified that a vertical DC caster of size 3000 x 600 mm was never been commissioned. In order to produce such a caster, the authors did some exploratory studies which consisted of full scale physical water modeling, mathematical modeling and experimental casting trials on AA5083 ingot of dimensions 600x1685 mm, 610 x 2400 mm, and 610x2700 mm. To provide a more in-depth understanding of the influence of a number of operational parameters for a large ingot in the start and steady state phases during the vertical DC casting process, the authors first studied the effect of metal distribution system which was published in the first part of their two-part paper [47] and the follow-up study on heat transfer and solidification was presented in the second part of the paper [48]. While doing the water modeling, they injected ink through the wall of the downspout and used Ultrasonic Doppler Velocity Measurements (UVDM) to study qualitatively the flow characteristics. Similar to Xu et al. [141], the authors also tried to use the PIV technique during the early part of their water modeling campaign. Because of the difficulty in obtaining accurate flow measurements, particularly in the areas of low velocities, and for time consuming nature of gathering and analyzing data, the authors stopped using PIV technique. The basic premise of doing water modeling experiments was to develop a distributor system which could give desired flow characteristics for the conceived caster. They tested two distribution bags, one was a standard-distribution bag and the other one was a modified-distribution bag. They used these two bags on each of the two different sizes water models. Their main motivation was to identify the number of dead zones or eddies that develop in the simulated sump, and how to prevent such eddies where low fluid refreshments prevail. Although the authors did not explain the design of their modified

distributor bag, they found that the modified distributor performed better for the ingot with large aspect ratio compared to the standard distributor used in the standard ingot. To complement the water modeling exercise of the metal delivery system, the authors developed a mathematical model for the AA5083 ingots having cross-sections of 600x1685 mm and 610x2700 mm and for the said two different combo bags melt distribution systems. They used a proprietary software ALSIM/ALSPEN. They claimed that the predicted fluid flow results were qualitatively similar to the physical water modeling results. While implementing the ALSIM code the authors allowed the flow to occur in the mushy zone up to a liquid fraction of 0.8. Below the liquid fraction of 0.8, a rapid convective damping was implemented. During their real casting experimental campaign, they reported a skewed temperature profile which they attributed to the misalignment of the distributor bag. When the distributor bag was placed symmetrically in a balanced position, they found a symmetrical temperature distribution. A 5°C difference in temperature was recorded between the two rolling faces of the slab in the case of the perfectly aligned distribution bag, whereas a 17°C difference in temperature was found when the distribution bag was misaligned. The circumferential temperature distribution measured from the experiment and predicted by numerical simulation was found to be satisfactory. In order to obtain the final cast of the desired cross-section with flat rolling faces, the authors used an empirical formula to calculate mold opening and by using that measurement the slabs were cast. Although, the desired cross-section was 2700 x 610 mm, the experimental cast was 2 mm thicker at the central regions of the rolling face. Despite serious attempts by the authors to attain sufficient knowledge and experience for their conceived high aspect ratio caster, a number of discrepancies are seen in their reported work. They are the following: (a) The predicted melt flow at the wide symmetry plane for 610 x 2700 mm cross-section ingot shows completely opposite trend from that what is expected. The authors showed that the melt is flowing from the narrow side towards the ingot center at that plane which is grossly in error. It appears that the fluid part of the code was not working correctly. It should be emphasized here that accurate fluid flow modeling is very important in order to reasonably predict the flow fields and corresponding temperature distributions in the ingot. (b) Whether the laminar or turbulent melt flow problem was solved is not mentioned in the paper. (c) Though the

water modeling results were presented in the first part of their two papers, where they have studied the flow behavior for using two different distributor bags but these results were not used for qualitative verification. Also, the predicted results were not compared to any experimental measurements performed by themselves or others. (d) The boundary conditions at the ingot surface, and ingot base/bottom block interface were not discussed in the paper. In the modeling, whether the effect of the air gap in the mold was included or not was not reported. (e) Also, neither the casting speed nor the pouring temperature of the melt was mentioned. (f) The geometrical dimensions of the distributor bag used were not provided. Despite the above deficiencies in reporting their results, the authors should be appreciated for their combined effort of water modeling, mathematical modeling and experimental campaign and for providing some good insights for controlling the complexities in vertical DC slab casters.

Evans and Jones in 2002 [38] briefly reviewed the CFD models for DC casting of molten aluminum that appeared until 2002. Although, they reviewed many of the relevant papers which appeared in Light Metals Proceedings, unfortunately, a good many relevant papers published before year 2000 were missed. Despite the minor weakness of the review, the authors have correctly credited the useful work pertinent to the coupled turbulent flow, heat transfer and solidification model concerning DC casting. In their paper, the authors also reviewed the work on molten aluminum treatment and discussed its importance. In a cursory manner the electromagnetic casting process for aluminum casting was also reviewed. Unfortunately, nothing has been mentioned about the weaknesses of the various papers reviewed and no comparisons of the stated results were made. From this review, it is not clear in order to undertake the complex 3-D CFD modeling study for this system which approach one should follow. It is the opinion of this author that barely stating the results without critically analyzing them does not serve much useful purpose. Nonetheless, the number of papers cited in the review is a useful source for future studies.

Tremblay and Lapointe in 2002 [123] engineered a new reusable rigid distributor for DC sheet ingot casting and named it as Reusable Molten Aluminum Distributor (ReMAD) with a view to replacing the standard combo bag which is made of fiberglass

fabrics. ReMAD consisted of a refractory frame wherein a fiberglass bag was snugly fitted. To avoid wetting of the frame by molten aluminum, the frame was coated with a semi-permanent proprietary boron nitride (BN) refractory material. Full-scaled water modeling experiments were used to design the shape and dimensions of the frame. In order to reduce the turbulence of the inlet flow, they placed a dome just under the spout exit. Their water modeling results showed that the flow was slower and less concentrated at the surface than the standard combo bag. Also, a calmer flow within the ReMAD resulted due to the presence of the dome. The authors also showed the real casting experimental test results for AA-1045, AA-3003 and AA-5052 alloys by using the ReMAD and standard combo bag at ABI (Aluminerie de Becancour, Quebec, Canada). With the use of the ReMAD, they claimed to have obtained a thinner oxide layer at the ingot surface particularly for AA-3003 compared to the standard combo bag. After analyzing the ingot slices from the head of the ingot for AA-3003, they observed that fewer oxides and inclusions were generated and the temperature difference between the maximum and the lowest temperature around the mold was lower by $2^{o}C$ for using the ReMAD compared to the standard combo bag. For the other two alloys casted, they did not find any change in metal quality for using new ReMAD technology.

Flexible combo bags are now extensively used in delivering liquid metal in DC casting of non-ferrous metals. Kieft et al. in 2003 [73] developed a new strategy to incorporate the influence of the distortion of the flexible combo bag in the modeling of DC slab casting. The reported work was divided into two parts. In the first part, full-scale water modeling experiments were performed to investigate the flow behavior for a distorted combo bag. At the flexible distribution bag outlets (side and bottom openings), the flow was measured quantitatively by using the image analysis technique PIV (Particle Image Velocimetry). Their research work mainly focused on studying the 3-D metal flow behavior inside the liquid sump at steady state for a combo bag melt distribution system where one bag was surrounded by the flexible walls and another one had stiff walls. To model these two cases they used commercial CFD software package CFX version 4.4. For the first case, to account the flexibility in shape of the distribution bag on flow patterns, the velocity measurements at the outflow of the distribution bag from the water model were used as input instead of modeling the flexible combo bag. Their predicted

results indicated that the flow pattern in the liquid pool which was produced by the combo bag with stiff walls differed significantly from the flow patterns obtained by the model in which the velocity measurements were used as input. They claimed that the modeling strategy, which simply included the measured velocity as an input, is correct since it represents the dynamic interaction of the flow with the distributor bag more accurately. A major drawback of these models is that it does not include the heat transfer analysis which has significant effect on the flow fields. Thus, in the model where they used the measured velocities from the water model as an input cannot address the correct input because they did not match the Richardson number (also called Tundish number in process metallurgical studies), for thermal similarity, between the water model and aluminum caster. The computed and measured velocities were not compared with any published results for the purpose of model validation. In addition, they did not directly incorporate the deformation of the bag which is due for the heat transfer of the incoming melt.

In order to study the interactions of the thermal, flow, and solid mechanics behavior and to assess their mutual impact on the start-up phase of a DC slab casting process, Williams et al. in 2003 [136] developed a 3-D model for an AA1201 alloy. This work is one of the most comprehensive modeling studies in the DC casting literature. The authors have used multi-physics modeling software PHYSICA to predict the liquid metal flow from a combo bag melt distribution system. They predicted the thermal and solidification phase change behaviors, the development of the stress fields and distortion of the ingot as it grew. Their main objective was to determine the impact of the inlet liquid inflow condition on the developments of the stress distributions and deformation in the solidifying ingot. The in-house code PHYSICA is based on control volume finite difference approach on a collocated mesh and uses SIMPLEC pressure correction procedure. Through a series of 3-D simulations they predicted that the butt curl was not sensitive to the inlet flow conditions except for the extreme case of very high vertical inlet velocities. The butt curl, which they predicted through fully coupled analysis, was found to be less than that predicted by equivalent thermo-mechanical–only analysis by other workers. Similar to others, they found highest level of stress immediately below the mold and at the base of the centerline. They also found high effective stress level, which

they claimed not to be obviously intuitive, appeared in the body of the ingot. The authors then suggested that melt inflow distribution design should be such that it minimizes the stress levels while respecting the thermal performance constraints required by operators. Although, this study is quite comprehensive in nature, unfortunately, the fluid part of the model is based on laminar flow equations instead of turbulent flow. It is to be mentioned here that the melt flow in a DC casting process is predominantly turbulent, and this is particularly true for high casting speeds and for high aspect ratio casters. Except for the overall estimate of the stress field, the authors neither compared their predicted fluid flow, temperature and solidification results from others nor have given any estimate regarding the accuracy of their predicted results. However, the novelty of their work lies in the fact that their model incorporated coupled fluid flow, heat transfer, solidification, and visco-plastic behavior of the aluminum ingot, all in a 3-D format on a moving mesh and modeled the development of the ingot.

Korti and Khadraoui in 2004 [74] simulated DC casting of a 152.4 mm diameter round billet for steady state phase using the average heat capacity method for Al-Mg alloy (Al-6063). Using the 2-D finite control volume laminar flow code, the effect of casting speed (ranging from 97.8 – 228.6 mm/min) on fluid flow, temperature and surface heat flux evolution was investigated. The predicted temperature distribution and surface heat flux were compared with experimental measurements and numerical predictions of Weckman and Niessen, and the authors reported a reasonably good agreement. Although, the diameter of the billet and the three casting speeds the authors have simulated corresponds to an industrial scale operation, unfortunately a laminar flow code was used for modeling. For the simulated billet caster along with the casting speeds used for parametric study will result in a turbulent flow field in the liquid sump within the billet.

Eskin et al. in 2005 [34] experimentally observed that for DC casting of an Al-2.8% Cu alloy for the variations in melt temperature from 701 to 760^{o}C (48-107^{o}C melt superheat) , the centre-line macro-segregation remained unaffected but the subsurface segregation became more pronounced. They suggested that deepening of the sump and more severe currents in the vicinity of the mushy zone with increasing melt temperature and casting speed created more possibilities for ‘floating’ grains to form, grow and settle.

Their statement completely contradicts Tarapore's [120] suggestion. The latter author in 1989 suggested that with the increase of the melt temperature, the sump depth deepens and higher temperature gradients prevail in the liquid pool which might reduce the amount of floating grains.

Through the combined effort of water modeling, temperature measurements during actual DC casting and mathematical modeling, Fortier et al. in 2005 [42] obtained the effects of process parameter changes on the flow and temperature distributions in the sump and meniscus. Specifically, they studied the effects of distributor bag stiffness, presence of a spout sock, casting speed, casting temperature and presence of a skim dam on the latter quantities. The authors observed that in a water model, a rigid distributor bag directed the water downwards into the sump whereas a regular soft combo bag directed the water upward and towards the meniscus. By measuring the temperatures at the meniscus during real casting experiments they obtained lower meniscus temperatures for the rigid distributor bag than for the soft bag, which they attributed to the downward melt outflow into the liquid sump for the rigid bag. For the numerical modeling of the top part of the caster along with its distribution system, the authors used commercial ANSYS/CFX software. Their numerical simulations with and without spout sock for the combo bag used, revealed that a hot spot was generated at the meniscus without spout sock, while the spout sock rectified the flow exiting the distributor and prevented the creation of hot spot in the rolling face. In order to study the effect of the presence of a skim dam on the metal distribution, the shape of the skim dam and its depth of submergence were varied through modeling. Results of their simulations showed that the temperature at the meniscus was colder when a skim dam was implemented. This was because the skim dam redirected the flow to a colder region inside the sump, thereby cooling down the metal before it reached the meniscus region. For a change of casting speed from 50 to 100 mm/min, they experimentally obtained a temperature difference of approximately 10^{o}C in front of the distributor bag openings and near the short side, whereas they found very little difference in temperature away from the corner along the rolling face. Since the authors did not solve the solidification aspects of the problem, their predicted temperatures at the meniscus may not be necessarily accurate. Further, they did not mention whether the flow they modeled was laminar or turbulent. In addition, no

dimensions of the metal transfer and distribution systems are reported in their paper. The authors did not validate their predicted results with similar results from others.

Long with nine other co-investigators in 2005 [80] developed an integrated 3-D DC-casting model for the start-up phase using the commercial finite element code ProCAST^{TM}.for Al-3004 slab. The model included heat transfer, fluid flow, solidification and thermal stress. A temperature dependent heat transfer coefficient between the cooling water and the ingot surface was employed taking into account the cooling water flow rate and the air gap formation in the mold. In addition, the effect of air gap formation during casting on the heat transfer coefficient between the bottom block and the curled portion of the ingot was considered in the model. An elasto-viscoplastic model was developed, based on high temperature mechanical testing, to calculate the thermal stress and strain. Based on the ratio of local stress to local alloy strength, an ingot cracking index was proposed. The ingot cracking index for different casting speeds was calculated, and the results were found to be consistent with ingot cracking observations seen in industrial casting practices. The temperature measurements were performed in an industrial slab casting facility. The calculated and measured temperature profiles at location near the surface and center were compared and an excellent agreement was obtained. The authors did not report any velocity field nor the delivery system used to supply the melt to the mold.

In the same year 2005, Sengupta et al. [115] reviewed in details the cooling process of continuous casting of steel slab and semi-continuous casting of aluminum alloy ingots and drew some conclusions by comparing and contrasting the different practices used in each process. They pointed out that due to the difference in thermo-physical properties of steel and aluminum alloys, these alloys are cast through two distinctly different process designs, but the fundamental heat transfer processes characterized by the removal of superheat, latent heat, and sensible heat are similar. They mentioned that both primary and secondary cooling play significant roles in dictating the complex heat transfer phenomena under both unsteady and steady state conditions. The heat transfer coefficient during secondary cooling depends mostly on the ingot surface temperature. The change in slab surface temperature remarkably changes the heat

removal rate. Sudden change in temperature gradients within the solidifying shell will cause thermal stresses. Hot tears and several types of cracks are often seen to form for these unwanted stresses. Several technological improvements are introduced in the industrial casting design to avoid the sudden changes of the cast surface temperature. The authors stressed the fact that the hot tearing susceptibility not only depends on the ingot surface temperature but also on the values of the inlet Peclet number (*Pe*) and the Biot number (*Bi*) at the ingot surface. The thickness of the mushy zone and the hot tearing susceptibility are related with the value of the inlet Peclet (*Pe*) number. For $Bi > 10$, the liquid pool shape lengthens almost linearly with increasing *Pe* and is almost insensitive to surface heat extraction rate. However, they suggested that the goal in each process is to design the caster in such a way that it will be capable to lower the surface temperature monotonically until cooling is complete.

Coates and Argyropoulos in 2007 [17] experimentally measured heat transfer coefficients at the mold-metal interface using a unique and versatile apparatus where they used thermocouples and two linear variable differential transformers (LVDTs). The thermocouples were used to measure the temperatures and the two LVDTs were used to simultaneously measure the air-gap formation between the mold and the cast with time. Commercial purity aluminum was cast against steel and high carbon iron molds. In order to see the impact of the roughness of the mold surface on the heat transfer coefficient and on the initiation of air-gap formation, three different mold surface roughnesses were experimentally studied for two different liquid temperatures for each of the two molds. Although, their investigation is for a static mold and is more applicable for the horizontal casting configurations, nonetheless, a very useful correlation between the heat transfer coefficient and the air-gap size was provided. Similar to others, the authors found that an increase in mold surface roughness resulted in a decrease in the heat transfer coefficient in the metal-mold interface.

Argyropoulos and Carletti in 2008 [5] experimentally determined through the inverse heat transfer method and by simultaneously measuring the temperatures and the gap formation with time the heat transfer coefficient (HTC) during casting at the mold-metal interface. Using a unique experimental set-up, they injected helium and

compressed air at the metal-mold interface during horizontal casting of an aluminum alloy to determine the effect of the two gases on the HTC. The HTCs as well as the onset of the metal mold gap formation were compared under these two types of solidification. They observed a higher HTC for using helium compared to air. It was found that helium resulted in the decrease in time for the onset of the metal-mold gap formation compared to air. The impact of helium gas on heat transfer relative to air was higher and was found to be largest with higher mold roughness. The authors noticed that the rate of decrease of HTC was higher at the early stages of gap development then at the later stages and they provided a useful correlation for HTC at the metal-mold interface against the size of the gap.

In 2008, Arsenault et al. [6] used a 3-D coupled laminar fluid flow, thermal and solidification model to predict the influence of the combo bag on the temperature and velocity fields for a DC caster fitted with a submersed nozzle inside a Thermally Formed (TF) semi-rigid combo bag supplied by Pyrotec (QC, Canada) distributor system. The authors employed the continuous casting module of the commercial software named ProCAST^{TM} (v2006.1). They were interested in the steady state results but initially started with the transient condition. Unfortunately, the authors couldn't reach the steady state. The predictions were made for AA5052 rolling ingot having a cross-section of 1346 mm x 660 mm and a length of 1350 mm. The combo bag had a cross-section of 336 mm x 102 mm and had an immersion length of 76 mm from the melt top surface. A square shaped nozzle was modeled. The bottom of the bag had two holes of 48 mm diameter. The permeability of the fine filter (refractory material) was taken to be 7.0×10^{-10} m^2. The model predicted the velocity fields and temperature contours at 8.46 seconds for a casting speed of 50.8 mm/min and a pouring temperature of 700^{o}C. Their findings indicate that the flow behavior and temperature distributions they predicted are for the start-up phase. Although, the results they presented are for the start-up phase, but they obtained those results by using the steady state heat transfer condition at the bottom of the ingot. Further nothing was mentioned about the bottom block. It is well known that during the start-up phase, the bottom block plays a significant role in the heat transfer from the base of the ingot and contributes to the solidification behavior of the ingot. They didn't compare their predicted results with experimental or industrial data, but they

claimed that their predicted velocity profile inside the impervious skirt of the TF combo bag was visually similar in nature with their water model results. The authors did not report on how the solidification aspect of the process was modeled nor indicated how they handled the mushy zone.

Nadella et al. in 2008 [89] in their comprehensive review paper provided an extensive review of most of the existing work on fluid flow, heat and mass transfer with solidification for DC casting that appeared up to 2007. In their excellent review paper they pointed out the current understanding of the macro-segregation mechanisms which they concluded are due to the relative movement of liquid and solid phases during solidification in the presence of solute partitioning (macro-segregation) and due to the enrichment of the liquid phase. After reviewing a large number of papers in this field, they found that the solidification research in the past largely focused on the prediction of inter-phase stability and segregation patterns under diffusive conditions. But in reality the macro-segregation modeling requires a quantitative understanding of the convective heat and mass transfer interactions at the different length scales. Finally they concluded that more work, both experimental and theoretical, is still needed to understand fully the effects of the movement of equiaxed grains, their morphology, and the permeability of the mushy zone in its different regions on the segregation.

Eskin and Katgerman in 2009 [33] reviewed the mechanisms of structure and defect formation during solidification of DC cast billets. They demonstrated the complexity of the mechanisms involved in the formation of structure, macro-segregation and hot tearing. Finally, they concluded that a combined modeling and experimental effort is necessary to understand the contributions of all the mechanisms involved and the ratio of these contributions in order to predict the cast microstructure.

Ilinca et al. in 2009 [61] provided 3-D modeling results of the fluid flow and heat transfer for DC casting of aluminum ingots where the hot-top mold was fitted with a Thermally Formed (TF) combo-bag delivery system. A 3-D finite element commercial code was used to compute the flow and heat transfer phenomena. First the authors performed an isothermal study to quantify the effect of the combo-bag on the flow and effective viscosity field was determined for the respective flow conditions. Later, the

authors solved the coupled fluid flow and heat transfer for forced convection conditions and as well as for mixed convections. The authors have shown that the inlet flow rate near the vicinity of the combo bag was dominated by the forced convection and by natural convection outside this region. In order to accommodate the flow though the fabric cloth of the combo bag they artificially took the porous structure of the fabric by describing the pressure drop there as a non linear function of vertical velocity. It is to be noted here that the same group tried to solve the above discussed DC casting problem in 2008. Their objective was to simulate the coupling between the flow in the dip tube in the combo-bag and in the sump in order to ascertain the effects such coupling of the flow field offers on the turbulence quantities outside the combo bag. Unfortunately, the authors could not reach a steady state solution and as a result they could not verify the influence of turbulence generated by the dip tube entry of the melt. Ilinca et al. did not validate their code with measured temperatures obtained from experiments by others.

Prillhofer et al. in 2010 [106] analyzed the overall inclusion distributions by using ultra sonic inspection, metallographic analysis and the PreFil$^{@}$ Footprinter for 36 rolling ingots produced by AMAG casting GmbH, and finished by AMAG rolling GmbH. They found the turbulence during filling of the distribution launder and the melt distribution system had a strong impact on the final ingot quality in terms of inclusions, pores, segregation etc. The authors described the flow phenomena during filling of the distribution launder and the melt distribution system at the start-up phase by using CFD analysis for a 1:1 model. They predicted that the turbulences and vortices were generated when the liquid metal reached at the deflection point with high flow velocities and when the melt was reflected at the end walls of the launder, which led to a re-entry of oxides into the mold. Based on their CFD analysis, four important strategies were proposed by the authors to optimize the fluid flow in order to reduce the high kinetic energy in the melt distribution system without causing surface turbulences. The strategies they suggested were based from only isothermal fluid flow results obtained from their CFD simulations. They concluded that the risk of the re-entry of inclusions could be reduced by taking the following measures: (i) inserting a fluid flow divider to optimize the melt deflection of the distribution launder; (ii) attaching an adapter with the spout to split the melt flow and directing in both long sides of the distribution bag to avoid surface

turbulences; (iii) implementing an additional special components in the distribution bag to avoid flow eddies which was found to form due to using a spout adapter; and (iv) introducing additional filter cloth within the melt distribution bag to decrease the fluid flow velocity. In the paper, the authors did not mention anything about the CFD model set-up. In addition, they also did not consider the effect of thermal buoyancy force since nothing was mentioned about the temperature fields. However, they described in detail the difficulties of the existing technologies to evaluate the inclusion distributions in a rolling ingot.

Xu et al. in 2011 [143] developed a comprehensive 3-D turbulent fluid flow, heat transfer and solidification model for a vertical DC caster of size 360 x 180 mm of AA7050 high strength rolling ingot. The commercial CFD code FLUENT was used to study the effects of water-restricted panel on the casting process. To account the turbulent aspect of the melt flow $k-\varepsilon$ turbulent model of the code was switched on. The relevant thermal boundary conditions were taken from the literature. By taking into account the thermal conductivity and specific heat as functions of temperature, the authors predicted the temperature profiles and the sump depths at various locations of the ingot by varying the positions of the panel below the mold bottom. The temperature profiles predicted by the mathematical model at the ingot center, corner, rolling face center-line and narrow face center-line were compared with experimentally measured temperature profiles at the same respective positions along the vertical distance from the top liquid surface, and were found to be satisfactory. The ingot sump was found to be sensitive to the position of the panel. The higher the panel, the dipper was the sump and the average cooling rate as well as the temperature of the ingot increased significantly below the position where the panel was applied. It is to be noted here that, an increase in the sump depth will lead to a favorable condition for hot tearing while the decrease in heat extraction rate below the mold will favor the suppression of cold cracking. When the panel was set at above the sump bottom obtained under conventional casting process, the sump depth increased remarkably, while it increased slightly when the panel was applied below it. The authors finally suggested that to decrease the hot tearing susceptibility and to minimize cold cracking, the panel should be applied below the conventionally casted sump depth. The main drawbacks of this study are; (a) the laboratory scale model was simulated, hence for

an industrial size caster the predicted trends of the results may not be applicable, (b) nothing was mentioned about the melt feeding scheme, which is known to have a major influence on the sump depth and accompanying defects in the cast, (c) it was not discussed in their paper what form of $k-\varepsilon$ model was used, since FLUENT offers a multitude of options of using the $k-\varepsilon$ turbulence model, and (d) finally, no fluid flow results were provided and discussed.

Baserinia et al. in 2012 [8] developed a simple density-based shrinkage model of the solidifying shell coupled with a commercial computational fluid dynamics (CFD) package to predict the air-gap formation between the ingot and mold and to predict its effect on the primary cooling for a rectangular ingot DC caster. In thermo-elastic model, the elastic stress equations for small deformations were solved with the effect of thermal strain taken into account. The viscoelastic deformation and metallostatic pressure of the liquid sump were neglected in thermo-elastic model. To model the water-cooled mold a commercial computational fluid dynamics (CFD) package ANSYS CFX (ANSYS Inc., Canonsburg, PA) was used. From this CFD analysis the effective heat transfer coefficient at the mold wall was estimated by considering the water temperature of 10^{o}C at the mold outer surface. The secondary thermal boundary condition was taken from the empirical model proposed by Weckman and Niessen [1982] with slight modification in the model constants. To implement the mathematical model the above stated CFD package was used to simulate the heat transfer and fluid flow in the ingot considering the metal flow to be laminar for the steady state condition by implementing the obtained heat transfer coefficient from the above two models. The model alloys were AA3003 and AA4045 with an assumption of the coherency temperature of 649^{o}C and 588^{o}C, respectively. The results predicted by the developed density-based shrinkage model were then compared with those predicted by a more complex three-dimensional thermo-elastic model. To validate the developed model the authors performed a series of experiments using a laboratory-scaled rectangular DC caster and measured the temperature distributions and solidification profile of the DC cast ingots. The caster had water-cooled mold having a cross-section of 227 x 95.2 mm with a corner radius of 12.7 mm. The mold was 76 mm high and 9.5 mm thick, and it was made of aluminum alloy. The aluminum alloy AA3003 with an initial pouring temperature of 700^{o}C and aluminum alloy AA4045 with an initial

pouring temperature of 640^{o}C were cast using casting speeds ranging from 102 to 150 mm/min. A cooling water volumetric flow rate of 1.8 L/s was used during casting. They got a very good agreement between the experimentally observed and simulated results obtained by using the two models for the liquid sump profiles and the temperature distributions. They found that on the narrow side of the ingot, the predicted air gap size obtained from the density-based and the thermo-elastic models matched reasonably well. In contrast, on the wide side of the ingot, the density based model slightly underestimated the air gap size compared to that predicted by the thermo-elastic model. Finally, they concluded that, for an industrial shape caster a more sophisticated air-gap model that should include the effects of viscoelastic deformations and metallostatic pressure was needed to predict the air gap size and shell thickness more accurately. They suggested that an efficient predictive model may be the substitute of the experiments to determine the mold heat-transfer coefficient. One of the major drawbacks of this study is that the authors have assumed a temperature profile along the axial length of the mold without stating the origin of such a profile.

Etienne et al. in 2012 [37] studied heat transfer in the primary cooling zone in laboratory-scaled DC casting experiments, in which rectangular AA3003 and AA4045 aluminum alloy ingots were cast at speeds ranging between 94.8 and 126 mm/min and for two initial melt temperatures of 640^{o}C and 700^{o}C. The caster had water-cooled mold with a cross-section of 227 x 95.2 mm and had a corner radius of 12.7 mm. The mold was 76.2 mm high and 9.5 mm thick, and it was made of AA5052 alloy. A cooling water volumetric flow rate of 1.79 l/s was used during casting. The temperatures measured with subsurface thermocouples in the mold for the steady-state phase of the casting process were used as input into inverse heat-conduction (IHC) algorithm to calculate the heat flux and the surface temperature of the ingot. Then the global effective heat-transfer coefficients (HTCs) for the primary cooling zone were derived taking into account the convection of the cooling water at the mold surfaces and conduction through the mold wall. They found that with increased in casting speed the air gap thickness between the ingot surface and the inner wall of the mold decreased and as a result HTCs increased. The HTC was found to be higher near the mold top (up to 824 W/m^{2}K) where the melt first came in contact with the mold walls than near the bottom (as low as 242 W/m^{2}K).

These authors compared the calculated HTCs from IHC analysis of measured temperatures for the said two alloys with two 3-D CFD models, namely, density based HTC model and thermo-elastic based HTC model. They observed that the density based HTC model overestimated the HTC values while the thermo-elastic based HTC model underestimated the same values. It is to be notated that the air gap model was developed based on one-dimensional thermal contraction. Since it is known that the ingot size affects the values of HTC, hence HTC values obtained from a laboratory-scaled caster may not be truly representative of an industrial size caster.

To improve the quality of the cast, there is a need to reduce the presence of inclusions in as-cast billets and slabs. Jaradeh and Carlberg in the year 2012 [66], investigated the inclusion content and distribution in commercial aluminum DC-cast billets and slabs obtained from Kubikenborg Aluminum AB, Sweden. They developed a deep-etching method capable of analyzing the inclusions distributions. For the analysis of inclusions, they selected various transverse and longitudinal slices from AA6063 billets having a diameter of 152 and 228 mm, and AA3003 ingots having a cross-section of 1440 x 460 mm and 1440 x 500 mm. Before casting, three ceramic foam filters (CFFs) having pore size of 30-ppi (coarse), 50-ppi (fine), and 50-ppi+HF were used by the industry for metal treatment. The above authors determined the effect of CFFs on the distribution of inclusions on final ingot quality. For billet casting, 1kg/ton of A15TilB grain refiner was added, whereas for slab casting twice as much amount of A15TilB was used than billet. The authors reported that in DC cast products, inclusions were non-uniformly distributed in terms of size and numbers. In as-cast billets, more non-metallic inclusions were found at the beginning and end of the billet length. At various transverse cross-sections of the billets they obtained less but variable inclusions distributions. The largest inclusions were found at the bottom of the billet, whereas small inclusions predominated in the interior of the billets. Near the billet center more inclusions were present than near the surface. Their analysis on slabs indicated that most of the inclusions were located at the surface and in the interior on both sides of the centerline. One of the interesting conclusions of this work is that finer pore-sized CFFs reduce significantly the number of large inclusions. They also concluded that large inclusions, mostly consisting

of oxides, mainly appear at the surface and small inclusions, mostly consisting of grain refiner TiB_2, prevail in a significant pattern in the interior.

Zhang et al. in 2012 [145] experimentally examined the evolution of microstructure with two different metal feeding schemes at the casting speeds of 50, 60, and 90 mm/min for different water flow rates in a 315 mm diameter cylindrical billet for AA7050 alloy. The melt was delivered at a fixed temperature of 680^{o}C through a semi-horizontal and a vertical melt distributor in a conventional vertical DC casting mold without hot top. In the semi-horizontal feeding scheme, the melt was diverted to four branches through a cross-shaped splitter, while in vertical feeding arrangement, all melt was poured directly in the center of the mold. The authors also used ALSIM6 (a casting-simulation software developed by the Norwegian Institute for Energy Technology, Kjeller, Norway) program, to develop a 2-D axis symmetric model capable of analyzing both turbulent fluid flow and temperature distributions coupled with solidification at steady state phase. The purpose of their study was to determine the influences of the melt feeding scheme on the sump profiles and flow patterns for the above mentioned alloy. Their work, both the experimental and simulation results, gives an insight into the importance of various factors like casting speed, water flow rate, melt feeding scheme on the evolution of cast structures in DC casting of Al alloy. Their experimental studies revealed that with a semi-horizontal melt feeding scheme the grains tend to coarsen towards the center of a billet, while the minimum grain size was found in the center of the billet for the vertical melt feeding scheme. They noted that if the casting speed is increased, a deeper sump is developed in the ingot and increases the cooling requirements, which results in the refinement of grain structure. They found that the predicted solidification front and velocity distribution of the melt in the liquid bath were very different under different melt feeding system. The authors did not provide the boundary conditions used in their model nor verified the predicted results with any experimental measurements.

Very recently, Prasad and Bainbridge [105] determined the heat transfer coefficients across the metal-mold gap by carrying out heat transfer experiments on a laboratory scale simulated billet caster under a steady state condition. They showed that

the gap heat transfer coefficient (h_g) not only varied with the gap size but it also varied with the gas type within the gap. The authors provided three correlations for calculating h_g for a fixed gap size for dry-air, nitrogen, and argon. They verified their experimentally obtained correlations with analogous experimental measurements done by others. One of the drawbacks of their suggested correlations is that these correlations can only be used if the gap size between the metal and the mold is known in advance and further one also needs to know the type of the gas that exists in the prevailing gap. The given correlations for h_g are only applicable for a DC billet caster and it is really questionable if these correlations are applicable for a DC slab caster. A major drawback of their experimental set-up is that, the heat transfer experiments carried out there do not correspond to real DC casting operations. During the experiments, although the authors varied the gap size but in each experiment the gap size (vertical distance between the crucible and the cooling surface) was kept uniform which may not be true in the mold region of a real caster.

2.4 Closure

The above survey shows that numerous numerical models have appeared in the literature for simulating either thermal field or heat transfer coupled with fluid flow and solidification during vertical DC casting. Most of the numerical work that exists in the literature on DC casting of non-ferrous metals is concerned with round extrusion billets. Many of these studies have shown good agreements between measured and predicted temperature profiles. The models helped to understand the effects of various casting parameters on natural and forced convection in the liquid sump as well as the flow patterns in the liquid pool, the transients during startup, development and shape of the sump, temperature distributions in the liquid, solid and mushy regions, growth of the solid shell, etc. The above predicted results contributed greatly to ascertain the probable defects that can arise in the cast. Many of these studies advocated that numerical modeling should precede the experimental measurements in order to avoid trial-and-error campaigns.

From the above critical review of the relevant literature, it is clear that all the serious attempts made so far to numerically model the process, are either simple models or models which depended on commercial codes. The major problems of the commercial codes are, they are too general, in many cases they are not too user friendly, and are not specifically coded to model DC casting problems. The turbulent fluid dynamics part of these commercial codes is indeed very cumbersome to use and often suffers from serious convergence difficulties. In addition, arbitrarily using the various turbulent flow modeling options and discretization schemes as well as the pressure-velocity resolution methods the codes offer as choices, do not necessarily provide converged and consistent results. Further, only a few have verified the results predicted by the commercial codes with experimentally measured data. Many of these verifications were conducted using the results of other computer codes that were not verified in the first place.

On surveying the experimental studies on DC casting processes, one notices that most of the previous research works were conducted using physical water model experiments. In the water models, in order to simulate the solidification profile, a predefined and fixed geometrical construction was used to represent the solidification front. Such predefined solidification front can't truly reflect the actual solidification process that occurs for an alloy in this complex process where a lot of parameters interact. Therefore, a dedicated code which can be relied upon in designing, analyzing and answering matters which are common to the vertical DC casting industries is needed at this stage. It is well known in the industry that metal feeding systems have remarkable influence on the quality of the cast product. Unfortunately, from the above reviews, it is apparent that no one has looked seriously into the effects of metal feeding systems on the solidification process. In this research, an attempt has been made to develop a 3-D CFD model which will enable to study the effects of various existing and novel melt feeding schemes on solidification characteristics and turbulent melt flow for vertical DC casting processes.

CHAPTER 3

MATHEMATICAL MODEL AND NUMERICAL APPROACH

3.1 Introduction

Modeling and solving of a CFD problem essentially requires to consider four major aspects, namely, (a) selection of geometry and an appropriate grid generation method, (b) setting-up of relevant governing equations and boundary conditions of the physical process, (c) discretization and solving of equations, and finally (d) post-processing of the numerical data. For laminar flow problems, associated with coupled heat and mass transfer as well as solidification, there are a lot of choices in the literature to handle the above four aspects of CFD problems. Unfortunately, this is not true, particularly for complex turbulent flow problems. In modeling latter types of problems, one needs to employ an appropriate turbulence model with minimum empirical constants which will capture the essential and relevant characteristics of the process. Due to the complex nature of a turbulent flow, which is inherently nonlinear, time-dependent, and is three-dimensional, one must use turbulence closer models in employing Navier-Stokes equation (N-S equation) for such flows. At high Reynolds numbers (Re), the laminar flow usually turns into turbulent flow due to hydrodynamic instability in the flow. The instabilities are believed to originate from the interactions between non-linear inertia terms and viscous terms in N-S equations. The three-dimensional interactions and rotational motion of the fluid particles are mutually connected via vortex stretching. The vortex stretching is inherently three-dimensional in nature. Hence, a two-dimensional description of a turbulent flow is not necessarily correct.

Since turbulence is a random process with respect to time, therefore, it is not possible to describe such flows by using a deterministic approach. By employing

appropriate statistical methods, one can learn about certain properties of turbulent flows. The latter introduces specific correlation functions among various flow variables. These correlation functions depend on the flow conditions, and hence it is practically impossible to determine these functions in advance. One important feature of turbulent flow is that the vortex structures move along the flow direction and they may exist for a long time. As a consequence, certain turbulent properties can't be described as a local phenomenon. The upstream conditions in such flows impact significantly on the downstream flow behaviors. Presently, there exist various turbulence models of varying complexities to analyze such flows.

In this chapter, a comprehensive model for the prediction of three-dimensional turbulent flow, heat transfer and macroscopic solidification in a vertical direct chill slab casting process for aluminum alloys is developed. The governing transport equations are highly non-linear, and these equations consist of continuity, momentum, and energy equations. The governing partial differential equations need to be supplemented with appropriate boundary conditions. There are various low-Reynolds number k-ε turbulence models to solve turbulent flow problems. In this study, the low-Reynolds number k-ε turbulence model of Launder and Sharma [78] is used to simulate the turbulence aspect of the flow. This model is easier to implement, particularly for coupled flow and solidification problems.

This chapter is divided into two main sections: the first section describes the mathematical formulation and the second section provides detail of the numerical approach used to solve the governing equations. The first section is divided into eight sub-sections, the first of which is dedicated to listing the assumptions employed in developing the current mathematical model, while the second sub-section is devoted to the development of the equations used to model the turbulence in fluid flow and heat transfer for the DC-casting of aluminum alloys. The third sub-section describes the approach for modeling solidification, and the forth discusses the modeling of fluid flow in the mushy region. In sub-section five, the modeling of thermal buoyancy term is described to account for the natural convection effects. The boundary conditions for the

transport equations are listed in the sixth sub-section. The expression for calculating the local surface heat flux is given in sub-section seven, and the last sub-section is devoted to the non-dimensionalization of the governing equations and boundary conditions in order to generalize the obtained solutions. The numerical approach section is divided into four sub-sections: the first of which deals with the control volume finite difference discretization procedures, while the second sub-section describes the solution procedure of the discretized equations and convergence criteria used. In sub-section three, the various under-relaxation factors used in getting converged solution are presented. The post processing of the results are described in sub-section four.

3.2 Mathematical Formulation

In order to model a physical problem numerically, first the geometry has to be correctly defined. This definition also should include specifying the calculation domain, the assumptions used in developing the mathematical model, the physical properties needed, the boundary conditions, and any other constitutive relations deemed to be pertinent to the problem. In a vertical DC caster, the transport processes prevailing there are essentially three dimensional in nature. In order to take the advantage of the two-fold symmetry of the caster, a quarter of the ingot, as presented by yellow color in Figure 3.1 is considered.

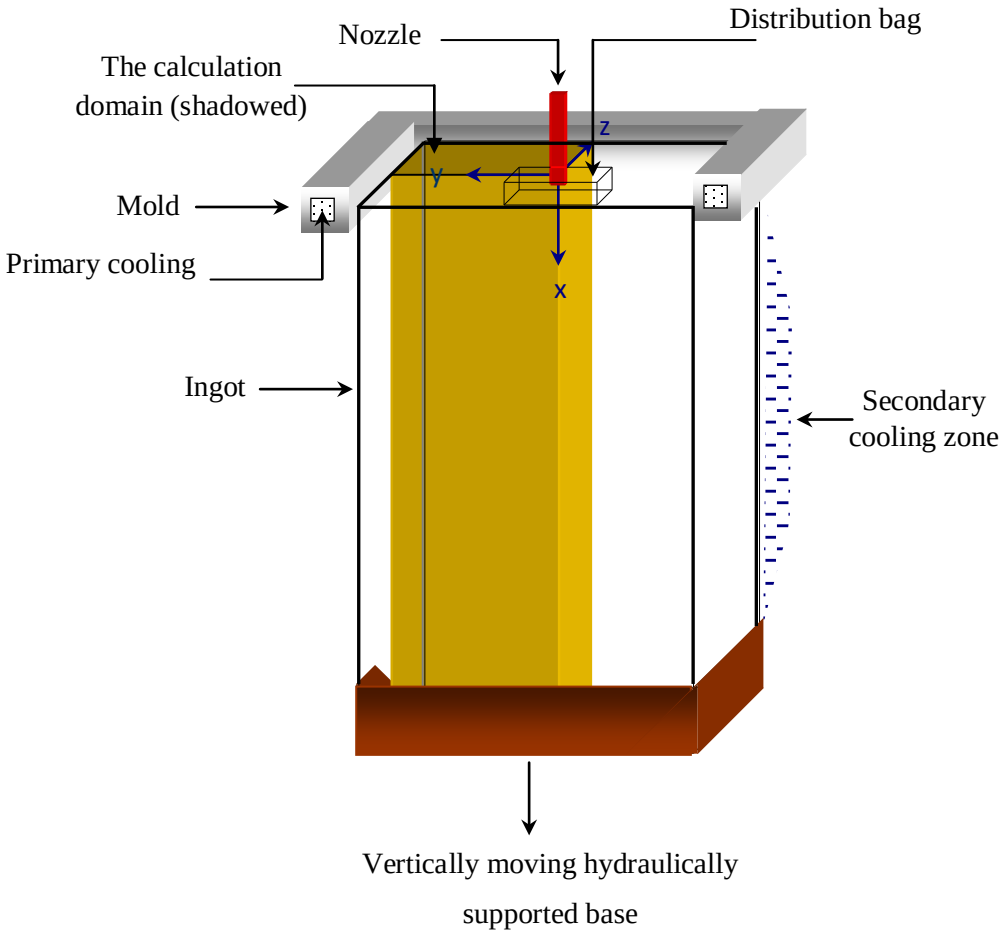

Figure 3.1: Schematic of the DC caster with the yellow part representing the computational domain.

(a) Model Geometry

The solution domain in all parametric cases is taken as presented by yellow part in Fig. 3.1. A quarter of the rectangular shaped ingot with the following dimensions, with the origin at x = 0, y = 0, z = 0 at the top surface, is simulated.

x_{ingot} = 2500 mm casting length

y_{ingot} = 865 mm half of ingot width

z_{ingot} = 330 mm half of ingot thickness

(b) Test Material

A popular grade of aluminum alloy for sheet, AA-1050 is adopted as the model alloy for comprehensive investigation. This alloy has an excellent corrosion resistance. It is highly ductile and has highly reflective finish. The physical properties of AA-1050 alloy [146] and the geometrical dimensions incorporated in the mathematical model are summarized in Table 3.1.

Table-3.1: Physical properties of AA-1050 and DC caster geometrical parameters.

Variable [unit]	Value
Thermal conductivity (liquid or solid) [kW/m-K]	0.231
Specific heat (liquid or solid) [kJ/kg-K]	0.90
Latent heat of fusion [kJ/kg]	396.4
Liquidus temperature [°C]	657.0
Solidus temperature [°C]	646.0
Viscosity at 657^{o}C [kg/m-s]	16.2×10^{-4}
Density (liquid or solid) at 646^{o}C [kg/m^{3}]	2700
Total slab width (parallel to rolling face) [mm]	1730.0
Total slab thickness [mm]	660.0
Slab length simulated [mm]	2500.0

3.2.1 Assumptions and Simplifications of the Mathematical Model

In order to realistically model the problem, the following assumptions were invoked in developing the current mathematical model:

1. A fixed-coordinate system (Eulerian approach) was employed in the simulation.
2. Local thermodynamic equilibrium during solidification was assumed to prevail. Heat flow was taken to be very fast and every point reached equilibrium with its neighboring points instantaneously.
3. A columnar dendritic solidification was assumed and pore formation was ignored.
4. Flow in the mushy region was modeled similar to a flow through a porous medium.
5. Molten aluminum was assumed to behave as an incompressible Newtonian fluid and turbulence effects were approximated using a popular version of two equations low Reynolds number $k-\varepsilon$ model of turbulence.
6. Heat released due to solid-solid transformation was not taken into consideration.
7. Evolution of latent heat in the solidification domain was not influenced by the microscale species transport.
8. Variation of liquid fraction in the mushy zone was assumed to be a linear function of temperature.
9. The thermo-physical properties of aluminum were invariant with respect to the temperature and there was no viscous dissipation effect. The thermal buoyancy term was incorporated in the momentum equations by employing the Boussinesq approximation.
10. The top free surface was assumed to be insulated for a nozzle entry of the melt.
11. Only the steady-state situation was modeled without taking into account the transient start-up condition.

In engineering applications, turbulent flows are usually modeled by modifying the Navier-Stokes equations. The modification is carried out by considering the instantaneous velocity consists of a time-averaged value and a fluctuating component. The current turbulence model is based on the time-averaged Navier-Stokes equations which are often referred to as Reynolds-averaged equations. In the present model, the three instantaneous components of velocities (*u*, *v*, *w*), pressure (*p*), and energy (*H*) are decomposed into time-averaged and fluctuating components as follows:

$$\begin{aligned} u &= \overline{u} + u' \\ v &= \overline{v} + v' \\ w &= \overline{w} + w' \\ H &= \overline{H} + H' \\ p &= \overline{p} + p' \end{aligned} \tag{3.1}$$

where the bar represents average variable quantity, and the second term on the right hand side of each equation represents the fluctuating component of the variables presented by the superscript $(''')$. Substituting equation (3.1) into the laminar form of Navier-Stokes and energy equations, the time-averaged forms of the conservation equations are obtained. These single-phase equations for an incompressible fluid can be written in Cartesian-tensor notation in the following form:

Continuity equation (conservation of mass)

$$\frac{\partial(\overline{\rho u}_i)}{\partial x_i} = 0 \tag{3.2}$$

Momentum equation (conservation of linear momentum)

$$\frac{\partial(\rho \overline{u}_i \overline{u}_j)}{\partial x_j} = -\frac{\partial \overline{P}}{\partial x_i} + \frac{\partial}{\partial x_j}\left[\mu_l\left(\frac{\partial \overline{u}_i}{\partial x_j} + \frac{\partial \overline{u}_j}{\partial x_i}\right) - \rho\,\overline{u_i' u_j'}\right] \tag{3.3}$$

Conservation of energy (Energy equation)

$$\frac{\partial(\rho \overline{u}_j \overline{H})}{\partial x_j} = \frac{\partial}{\partial x_j}\left(K\frac{\partial \overline{T}}{\partial x_j} - \rho\,\overline{u_j' H'}\right) \tag{3.4}$$

The over bars represent time-averaged quantities, while the turbulent stresses are represented by the following expression:

$$\overline{\rho u_i' u_j'} = \frac{1}{\Delta t}\int_0^{\Delta t} \rho u_i'(t) u_j'(t) dt \tag{3.5}$$

where Δt is longer than any significant period of the fluctuations themselves.

If one compares equations (3.3) and (3.4) with the corresponding laminar form of Navier-Stokes and energy equations, one can see there are additional terms in the above mentioned equations. These new terms (variables) contain the fluctuation components, and they are designated as the Reynolds stress terms $\overline{\rho u_i' u_j'}$ in the momentum equations and the turbulent heat flux terms ($\overline{\rho u_j' H'}$) in the energy equation. With the use of a suitable turbulence closure model, these new variables can be taken into consideration in the governing equations.

3.2.2 Modeling of Turbulence Parameters

At present, in engineering applications two types of models, namely, eddy viscosity models and Reynolds stress model are used extensively to account for the Reynolds stress and turbulent heat flux quantities in the time-averaged transport equations. Because of the simplicity and ease of implementation of the eddy viscosity model, it is widely used in solving practical engineering problems. In the eddy viscosity model, the Reynolds stresses or the turbulent heat fluxes are assumed to be proportional to the gradients of mean flow variables. The constant of proportionality is the eddy diffusivity, which is a scalar quantity and unlike laminar flow problem is a flow property. In this model, the eddy diffusivity is assumed to be isotropic. The eddy diffusivity can be determined by using one of the three models. Depending on the number of partial differential equations used to determine the eddy diffusivity, the models can be classified as zero, one, and two-equation models.

In the zero equation models, the turbulence viscosity (eddy diffusivity) is calculated using an empirical relationship such as:

$$\mu_t = \mathrm{C}\,\rho\,u\,l \tag{3.6}$$

where u and l are the eddy characteristic velocity and mixing length of the eddies, respectively. The mixing length and the constant C are determined based on experimental data. The characteristic eddy velocity u is taken to be proportional to the gradient of the mean flow. A major drawback of the zero equation model is the fact that it takes a zero value at the symmetry planes which is contrary to the measurements made in the laboratories where it is found that the eddy diffusivity is not zero there. In one equation model, the characteristic eddy velocity is considered to be proportional to the square root of kinetic energy of turbulence. Therefore, the eddy diffusivity can be expressed as:

$$\mu_t = \mathrm{C_k}\,\rho\;l_m\;\sqrt{k} \tag{3.7}$$

where k is found by solving a transport partial differential equation for the mean turbulent kinetic energy and it takes the following form:

$$\rho\frac{Dk}{Dt}=\frac{\partial}{\partial x_m}\left[\left(\mu+\frac{\mu_t}{\sigma_k}\right)\frac{\partial k}{\partial x_m}\right]+\mu_t\left(\frac{\partial \overline{u}_i}{\partial x_j}+\frac{\partial \overline{u}_j}{\partial x_j}\right)\frac{\partial \overline{u}_i}{\partial x_j}-\frac{C_D\,\rho\,k^{1.5}}{l} \tag{3.8}$$

where $\mathrm{C_D}$ is an empirical constant, and l is the mixing length. The ratio of momentum turbulent diffusivity to the turbulent diffusivity of kinetic energy is represented by σ_k. In this equation, the mixing length needs to be specified using empirical relations. It is difficult to calculate in advance the mixing length for complex flow situations. In order to overcome the latter difficulty, the two equation models of turbulence have been proposed. In two equation models, both the eddy viscosity and mixing eddy length are calculated from two separate transport equations representing the two variables. The most popular of the two equation models is the k-ε equation model in which k is the kinetic energy of turbulence, and ε is the rate of dissipation of the kinetic energy of turbulence. The k-ε model is based on the eddy diffusivity model in which the eddy turbulent viscosity is correlated using k and ε via the Kolmogorov-Prandtl expression as:

$$\nu_t = C_\mu \frac{k^2}{\varepsilon} \tag{3.9}$$

where C_μ is an empirical constant. There are essentially two forms of k-ε models. One is called high Reynolds number k-ε model and the other is called the low Reynolds number k-ε model. The high Reynolds number model cannot be applied in low Reynolds number regions, such as near the solid boundaries where viscous effects become predominant. To overcome such a problem, two solution schemes are proposed in the literature. The first is based on the use of special functions near the solid boundaries known as wall functions. The second approach is the use of a damping factor to cover the viscous sub-layer. The wall function approach is appropriate for solving simple single phase confined turbulent flow problems. This model requires less computational time to implement but it is difficult to apply in complex flow situations such as turbulent flows with centrifugal force, buoyancy, phase change and flow over spinning surfaces. It is also difficult to employ this model for solid-liquid phase change problems in which the solid boundaries are not known a priori, which is the case in the current model (vertical DC casting).

The above shortcomings can be resolved by the use of the low-Reynolds-number k-ε model. This model does not require the prescriptions of the wall functions since it covers the whole flow domain including the buffer and viscous sub-layer. The basis of the model is the employment of a damping function proposed by Van Driest [128] for the mixing length model. The main purpose of the damping function is to reduce the production of the eddy diffusivity μ_t and to increase the production of the dissipation of the kinetic energy of turbulence (ε) so that the turbulence effects are reduced in the viscous sub-layer. In the literature, a number of low Reynolds number k-ε models are proposed by different researchers. A comprehensive list of these models can be found in [15,76,91,98]. The low-Reynolds-number k-ε models were originally developed to predict fluid flow and heat transfer for boundary layer type of problems. The constants of these models were optimized from boundary layer experiments. One should note that these models were not developed for complex internal re-circulating flows. The low Reynolds number models developed by Lauder and Sharma, Lam and Bremhorst, and Chein have gained wide acceptance from the CFD communities because these models

perform fairly well in comparison with experimental results. Unfortunately, the latter two models require the distance from the solid boundary to be prescribed in advance to calculate the eddy diffusivity. Because of this limitation, these two models cannot be used easily for modeling DC casting problems since the distance from the solidified boundary is not known a priori. The model proposed by Launder and Sharma is much easier to use for mushy region solidification/melting problems as this model does not depend on the distance from the solid boundaries in computing the turbulent eddy viscosity (μ_t). In this work, the model proposed by Lauder and Sharma [78] is implemented. A brief summary of the model is given below.

3.2.2.1 Launder and Sharma Low Reynolds Number Two-Equation k-ε Model

3.2.2.2 Modeling of Reynolds Stress Terms $\left(-\rho\overline{u_i'u_j'}\right)$

The low Reynolds number two equation k-ε turbulence model of Launder and Sharma is based on the assumption of linear isotropic formulation of the eddy viscosity in presenting Reynolds stress terms. The eddy viscosity concept is based upon the observation that the main effect of turbulence is to increase the transport of the conserved properties and dissipation effects with respect to the laminar state. Since for laminar flows, the laminar viscosity of the fluid controls these processes, it is natural to represent turbulence in a similar way in terms of apparent viscosity (turbulent viscosity) in the form:

$$\overline{\rho u_i' u_j'} = -\mu_t\left(\frac{\partial \overline{u}_i}{\partial x_j} + \frac{\partial \overline{u}_j}{\partial x_i}\right) + \frac{2}{3}\delta_{ij}k \tag{3.10}$$

where k is the turbulent kinetic energy defined as:

$$k = \frac{1}{2}\overline{u_i' u_j'}$$

the Kronecker delta (δ) is defined as:

$$\delta = \begin{cases} 0 & when \quad i \neq j \\ 1 & when \quad i = j \end{cases}$$

The second term on the right hand side in equation (3.10) is added so that the equation can be applicable to homogeneous and isotropic turbulent flows.

3.2.2.3 Modeling of Turbulence Heat Fluxes

Following the same analogy as the Reynolds stresses, the turbulent heat fluxes (Reynolds heat fluxes) is obtained using the eddy diffusivity concept to relate the turbulence heat flux to the local mean temperature gradient in what is known as the Turbulence Prandtl Number Approach (TPNA) can be written as:

$$\frac{1}{c_p}\overline{\rho u_j' H'} = -\frac{\mu_t}{\sigma_t}\frac{\partial \overline{T}}{\partial x_j} \tag{3.11}$$

where σ_t is the turbulent Prandtl number, and μ_t, the turbulent viscosity defined as:

$$\mu_t = \frac{c_\mu f_\mu k^2}{\varepsilon} \tag{3.12}$$

The function f_μ ($f_\mu = 1.0 - 0.3e^{-\mathrm{Re}_t}$) is a damping factor to account for the laminar viscosity onto the turbulent viscosity for the low turbulent Reynolds number flow near the wall (the viscous sub-layer and the buffer zone).

3.2.2.4 Governing Equations for k and ε

The variables *k* and ε, as defined earlier, are the turbulent kinetic energy and its rate of dissipation, respectively. The values of these variables are obtained from the solution of another two transport partial differential equations. The first equation is the turbulence kinetic energy, while the second is the rate of dissipation of kinetic energy. Since the detailed derivation of these two equations is given by Lam and Bremhorst [76], and Hollworth and Berry [58], only the final forms of the equations are given below.

Henceforth, the symbols *u*, *v*, and *w* without the over bars represent the average velocities:

(a) Transport equation for turbulence kinetic energy:

$$\frac{\partial(\rho u_j k)}{\partial x_j} = \frac{\partial}{\partial x_j}\left[\left(\mu_l + \frac{\mu_t}{\sigma_k}\right)\frac{\partial k}{\partial x_j}\right] + \mu_t\left(\frac{\partial u_i}{\partial x_j} + \frac{\partial u_j}{\partial x_i}\right)\frac{\partial u_i}{\partial x_j} - \rho(\varepsilon - D_k) \tag{3.13}$$

(b) Transport equation for rate of dissipation of kinetic energy:

$$\frac{\partial(\rho u_j \varepsilon)}{\partial x_j} = \frac{\partial}{\partial x_j}[(\mu_l + \frac{\mu_t}{\sigma_\varepsilon})\frac{\partial \varepsilon}{\partial x_j}] + c_1 \rho f_1 \frac{\varepsilon}{k} G - c_2 \rho f_2 \frac{\varepsilon^2}{k} + \rho E_\varepsilon \tag{3.14}$$

In equation (3.14), the coefficient f_1 is a function that increases the magnitude of the destruction of the kinetic energy of turbulence (ε) near the wall. In Launder and Sharma model the value of f_1 is set to 1, and f_2 is a function that corrects the destruction term of ε in low turbulent Reynolds number flows.

3.2.3 Solidification Modeling

In mathematical modeling a DC casting process both fluid flow that prevail in the molten sump and mushy zone as well as the associated heat transfer and solidification due to external cooling should be taken into consideration. In case of alloys, because of the freezing range it will release latent heat over the liquidus and solidus temperatures. As a result, the release of the latent heat would be a function of the fraction solidified. The major barrier in analyzing phase change problems for alloys (impure materials) is that two interfaces appear, namely, solid-mushy and mushy-liquid interfaces whose locations are unknown a priori, and across which the latent heat is released. At the phase boundaries, continuity of velocity and shear stresses do prevail. Also, the continuity of temperature is to be respected at each interface. In addition, an account has to be made in the jump of the heat fluxes across each interface, which is proportional to the latent heat.

There are two main approaches for modeling the solidification of pure metals and alloys, namely, the multiple and single domain approaches. The multiple domain technique is based on dividing the whole domain into discrete regions according to their phases. The transport equations are then solved separately for each region. The

conservation equations at the different regions are coupled through a proper interface boundary condition. This makes the technique too difficult to implement particularly for two and three dimensional problems. The complexity in the modeling using the multiple domain approach stems from the fact that the interface between various regions needs to be traced continuously. Hence, the single domain approach is followed in the present simulation since it does not require the tracking of the unknown interface (solidification front). Among the various fixed domain techniques that take into account the release of latent heat, are apparent or effective heat capacity method and enthalpy based method. In the current work, the enthalpy based method is implemented [130]. The most popular among the enthalpy based methods is the enthalpy-porosity approach. One advantage of this method is that, a single set of transport equation is appropriately applied for the liquid, mushy, and solid regions. In this method the total enthalpy is decomposed into sensible and nodal latent heat in the energy equation:

$$H=h+\Delta H \tag{3.15}$$

where h is the sensible heat defined as:

$$\int_{h_{ref}}^{h} dh = \int_{T_{ref}}^{T} c_p \, dT \tag{3.16}$$

For constant $c_{p,}$ and taking $h_{ref} = 0$ at T_{ref}, the above equation can be integrated to obtain the sensible heat as:

$$h= c_p (T-T_{ref}) \tag{3.17}$$

In order to establish the region of phase change, the latent heat contribution is specified as a dependent variable with respect to the local temperature, i.e. $\Delta H= f(T)$.

The energy equation is applied for the entire calculation domain including solid, liquid, and mushy regions, by changing the nodal latent heat as a specific function of liquid fraction. It is prescribed in such a way that it takes a value of zero in the solid phase and becomes equal to the latent heat of fusion (ΔH_f) in the liquid phase. In the mushy region, any functional form of the latent heat with respect to the liquid fraction

can be implemented provided the end conditions of the mushy region are respected. In the present model, the latent heat release is assumed to be a linear function of the liquid fraction, that is

$$\Delta H=\Delta H_f f_l \tag{3.18}$$

where f_l is the liquid fraction. It is assumed in the present model that $f_s=(1-f_l)$ increases linearly from zero at the liquidus temperature to one at the solidus temperature. Mathematically the above statement can be represented by the following expression in terms of equivalent liquid fraction f_l:

$$f_l = \begin{cases} 1 & when \quad T \geq T_l, \\ \dfrac{T-T_s}{T_l-T_s} & when \quad T_l \geq T \geq T_s, \\ 0 & when \quad T \leq T_s. \end{cases} \tag{3.19}$$

where T_l and T_s are the liquidus and solidus temperatures, respectively. It is to be noted here T_l and T_s are constant in the present model. Ideally for an alloy one needs to solve the micro-segregation problem in order to allow changes of T_l and T_s as solidification progresses. This would have enormously complicated the modeling effort, particularly for three-dimensional modeling of mushy zone solidification in the presence of turbulent melt flow. Hence, the above simplification was adopted.

The final form of the energy equation is obtained by substituting Equations (3.11) and (3.15) into the energy equation (3.4):

$$\frac{\partial(\rho\overline{u}_j\overline{H})}{\partial x_j}=\frac{\partial}{\partial x_j}\left[\left(\frac{\mu_l}{\mathrm{Pr}}+\frac{\mu_t}{\sigma_t}\right)\frac{\partial\overline{h}}{\partial x_j}\right]-\frac{\partial(\rho\overline{u}_j\overline{\Delta H})}{\partial x_j} \tag{3.20}$$

The last term in Equation (3.20) represents the latent heat exchange rate due to solid-liquid phase change resulting from the turbulent convective flow.

At present, there is no uniform consensus as how to model the turbulent transport phenomena in case of turbulent flow alloy solidification problems. Many authors arbitrarily dampened the value of the eddy viscosity there by multiplying it with a

damping function which is dependent on the liquid fraction in that region. It was Masuoka and Takatsu [1996] who made the first attempt to model turbulent flow through a porous media. Netto and Guthrie [2000a, 2000b] contradicted the use of the above model for solving the mushy region solidification problems, since they believed that the turbulent is totally dampened in the solid-liquid coherent structures. Based on the physical considerations, the above authors used laminar formulation in the mushy region which has also been assumed in the present model.

3.2.4 Modeling of Fluid Flow in the Mushy Region

In solidification of casting alloys, a region develops between the solid and liquid phases where there is a coexistence of solid and liquid. This region is called mushy region. In this study, it is assumed that the solidification is predominantly columnar (dendritic). In columnar solidification the convection of inter-dendritic liquid occurs through the solid network. This hindered liquid convection is believed to be the major cause of hot tear and macro segregation in cast products. The flow of melts through the solid porous matrix is quite complicated because of the complex inter connected networks that the dendrits form in the mushy region. Most modelers in this area either use empirical measurements of a system parameter known as permeability, or measurements of friction factors to model the fluid flow in the mushy region. Because of the simplicity of the Darcy law for porous media, in the current model this law is adopted. This law is based on the empirical measurement of the permeability. Darcy's law for a porous media can be written as:

$$\overline{u}_i = -\frac{K'}{\mu}\left(\frac{\partial P}{\partial x_i} - \rho g_{xi}\right) \tag{3.21}$$

where K' is the permeability, which is a function of porosity, or in the case of a mushy region of a binary alloy, a function of liquid fraction. The permeability decreases with decreasing liquid fraction and ultimately forces all the velocities to become zero in the case of a stationary solid or in the case of vertical DC casting it forces the solid to take the casting speed. In this study, a simplified assumption is made about the movement of

the solid dentritic network structure along with the intervening melt there. The solid and the liquid in the mushy region move downward at the specified casting speed. Incorporating the diffusive and convective momentum flux terms, one can write the modified Darcy equation in the following form:

$$\frac{\partial(\rho\overline{u}_i\overline{u}_j)}{\partial x_j} = \frac{\partial}{\partial x_j}\left[(\mu_l + \mu_t)\frac{\partial \overline{u}}{\partial x_j}\right] - S_{\overline{U}_i} - \frac{\mu}{K'}(\overline{u}_i - u_{i_s}) \tag{3.22}$$

where the coefficient $\frac{\mu}{K'}$ decreases from a large value in the solid phase to zero in the liquid phase. Consequently, the Darcy term vanishes as the liquid fraction becomes one. It is to be noted that the third term in the right hand side of Eqn. (3.22) (Darcy term) is an adhoc sink term. The Carman-Koseny equation is adopted for the relation between the permeability and the liquid fraction.

$$\frac{\mu}{K'} = \frac{C(1-f_l)^2}{f_l^3 + q} \tag{3.23}$$

where q is a small positive number introduced to avoid division by zero during the numerical calculations. C is a constant that depends on the morphology of the porous media. The value of C has been estimated from the expression given by Minakawa et al. (1987) as:

$$C=180/d^2 \tag{3.24}$$

where d is assumed to be constant and is equal to the secondary dendrite arm spacing (DAS). The value of d is of the order of 1×10^{-4} m. A large C value would force the velocity to be equal to the casting speed.

3.2.5 Modeling of Buoyancy Term in the X-Momentum Equation

Although DC casting is predominantly a forced convection problem, natural convection does play some role in modifying the flow within the caster [21]. The effect

of natural convection is incorporated in this study through the use of Boussinesq approximation. The essence of this approximation is that liquid density is assumed constant in all the terms except the thermal buoyancy term in the momentum equations, which is given by:

$$\rho = \rho_{\infty}[1-\beta\ (T-T_{\infty})] \tag{3.25}$$

where β is the thermal volumetric expansion coefficient defined as:

$$\beta = -\frac{1}{\rho}\left(\frac{\partial\rho}{\partial T}\right)_{P} \tag{3.26}$$

In a vertical DC casting process, the thermal buoyancy term appears only in the vertical momentum equation (x-momentum equation). For the sake of simplicity, the x-momentum equation is written in the following short from as:

$$\rho_{\infty}(u\frac{\partial u}{\partial x}+v\frac{\partial u}{\partial y}+.....) = -\frac{\partial p}{\partial x}+\rho\, g+\mu\frac{\partial^2 u}{\partial x^2}+..... \tag{3.27}$$

where the second term on the R.H.S. represents the body force term. In this problem, the flow of the molten aluminum is gravity driven. Note that the vertical coordinate in the calculation domain is the x-axis, which is increasing in the downward direction and is in-line with the gravitational field. Therefore, the pressure gradient can be written in the following form:

$$\frac{\partial p}{\partial x} = \rho_{\infty}\, g \tag{3.28}$$

Substituting Equation (3.28) in to Equation (3.27), one gets the following equation:

$$\rho_{\infty}(u\frac{\partial u}{\partial x}+v\frac{\partial u}{\partial y}+.....) = g(\rho-\rho_{\infty})+\mu\frac{\partial^2 u}{\partial x^2}+..... \tag{3.29}$$

If Equation (3.25) is substituted into Equation (3.29) and after simplification one gets:

$$\rho_{\infty}(u\frac{\partial u}{\partial x}+v\frac{\partial u}{\partial y}+.....) = -\rho_{\infty} g\,\beta(T-T_{\infty})+\mu\frac{\partial^2 u}{\partial x^2}+..... \ ..... \tag{3.30}$$

The above equation can be written in a non-dimensional form using the non-dimensional parameters stated in the subsequent section (3.2.8). From Equation (3.30), noting that $T = \frac{h}{c_p}$, the following equation can be obtained:

$$U\frac{\partial U}{\partial X} + V\frac{\partial U}{\partial Y} + ... = -\frac{\Delta H_f \, g \, \beta \, D}{c_p \, u_{in}^2}(h^* - h_\infty^*) + \frac{\mu}{\rho_\infty \, D u_{in}}(\frac{\partial^2 U}{\partial X^2} + ... \tag{3.31}$$

Multiplying and dividing the first coefficient on the R.H.S. by $D^2.\nu^2$ and rearranging, the above equation can be written in the following form:

$$U\frac{\partial U}{\partial X} + V\frac{\partial U}{\partial Y} + ... = -\frac{Gr_{Modified}}{\mathrm{Re}^2}(h^* - h_\infty^*) + \frac{1}{\mathrm{Re}}(\frac{\partial^2 U}{\partial X^2} + ... \tag{3.32}$$

where, $Gr_{Modified}$ is the modified Grashof number, which is the ratio of Grashof number (*Gr*) to Stefan number (*Ste*)

$$Gr_{Modified} = \frac{Gr}{Ste} = \frac{g \, \beta \, \Delta H_f \, D^3}{c_p \, \nu^2} \tag{3.33}$$

Here, *Gr* is the ratio of buoyancy force to viscous force, and Ste is the ratio of sensible heat to latent heat.

Re is the Reynolds number which is the ratio of inertial force to viscous force and is given by: $\mathrm{Re} = \frac{u_{in} D}{\nu}$,

The parameter Gr/Re^2 in the first term on the R.H.S. of Equation (3.32) is known as the Richardson number (*Ri*) and it represents the strength of natural convection relative to forced convection. It is noted that natural convection is negligible when $Ri < 0.1$, forced convection is negligible when $Ri > 10$, and neither is negligible when $0.1 < Ri < 10$. In a typical casting scenario *Ri* values varies from 1.5 to 10. It was found that the effect of buoyancy force does not change the solidification profile and the sump depth. Near the bottom of the sump the vertical temperature gradients decrease significantly, and as a result the buoyancy forces will decease accordingly [75]. This first term is

implemented in the solution scheme as a linear source term (S) in the x-momentum equation. This source term is written in the following linear form:

$$S = S_c + S_p \Phi_p \tag{3.34}$$

where S_c stands for the constant part of the source (S), while S_p is the coefficient of Φ_p (the dependent variable). Since in this case, the source term is not a function of the dependent variable (u), therefore it can be linearized in the following way:

$$S_c = -\frac{Gr_{Modified}}{\mathrm{Re}^2}(h_\infty^* - h^*), \tag{3.35}$$

and $$S_p = 0.$$

It is to be noted that h^* *and* h_∞^* represent the non-dimensional enthalpies of each scalar cell in the calculation domain (variable) and the solidus enthalpy, respectively. The buoyancy term in the discretized form can give rise to serious instabilities in the solution procedure [129]. Severe under-relaxation factor is often required to handle the buoyancy term. During actual simulations of the current mathematical model, the buoyancy term was heavily under relaxed with respect to iteration such that after certain number of iterations the full effect of the buoyancy term appeared in the x-momentum equation.

3.2.6 Boundary Conditions

In order to produce satisfactory results from numerical simulations of the developed model, one needs accurate input of boundary conditions and reliable material data. One can get the thermal boundary conditions at the cast surfaces through the measurements of inside temperatures in the cast using thermocouples and then by adopting the measured temperatures along with the inverse heat conduction modeling techniques. This technique is usually used by the DC casting industries to ascertain the realistic thermal boundary conditions on the slab surfaces.

In a DC casting process, an ingot undergoes two different cooling regions, namely, direct contact with the mold, followed by an air gap in the mold, and finally it is cooled by the chilled water jet. The first region is called the primary cooling, and the second region is called the secondary cooling region. In the water cooling region the effective convective heat transfer coefficient can vary widely depending on the ingot surface temperature and the way the water cools the surface. It has been experimentally seen in the industry that the water jets in a DC caster result in a high heat flux of the order of 2-10 MW/m^2. The magnitude of the local heat flux depends on the water boiling mode on the surface of the ingot. The water cooling process could be either due to forced convection or nucleate boiling or film boiling. Below the ingot surface temperature of about 100^0C forced convection cooling occurs. The nucleate boiling process offers the maximum removal of heat from the ingot due to the transformation of the water into its vapor by gaining latent heat. In the film boiling region, a layer of vapor film covers the surface and as a result the water can't come in contact with the solid surface, and this causes a lower heat transfer rate. The effective heat transfer coefficient in the water cooling region depends on a multitude of factors, viz., aspect ratio of the ingot, casting speed, casting alloy composition, surface temperature, water temperature, quality of water, the physical characteristics of the water jet and falling film (flow rate per perimeter, angle of the jet), etc. It is therefore difficult to theoretically predict the heat transfer coefficient in such a complex heat transfer process. From industry to industry the heat transfer surface boundary conditions will therefore vary. As a result, general thermal boundary conditions will not necessarily be appropriate for numerical simulations. Ideally, experimental measurements should provide the actual boundary conditions for a specific caster and alloy. Since no such experiments have been carried out in the present study, therefore the heat transfer coefficients suggested by Vreeman and Incropera for primary and secondary cooling zones were used in the developed model [131].

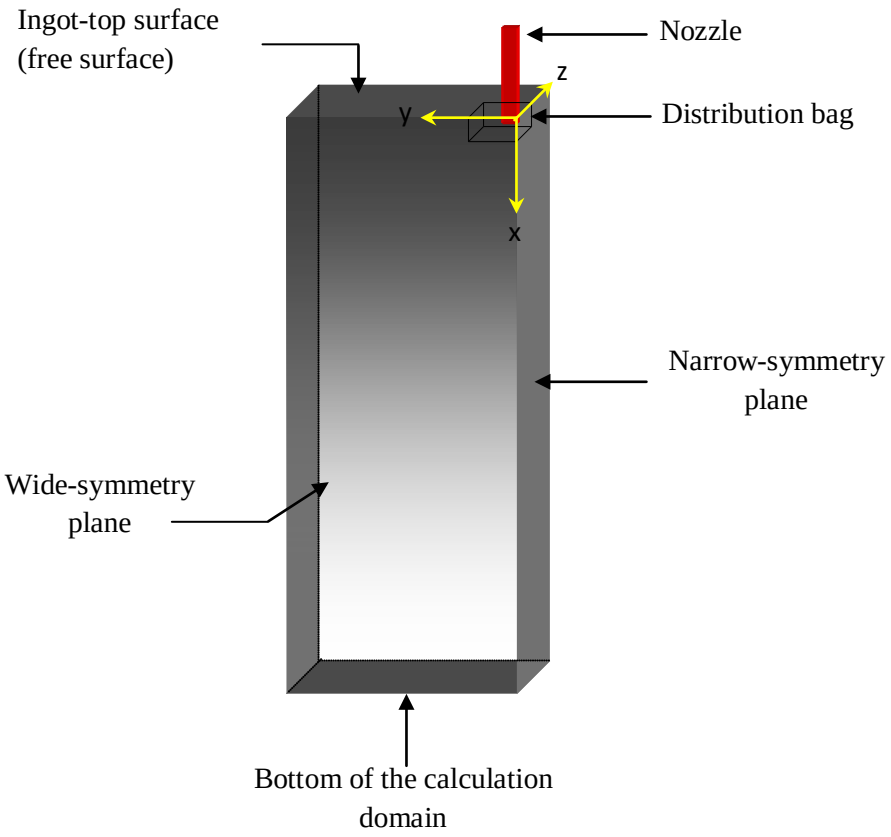

Figure 3.2: Calculation domain showing the boundary surfaces.

To reduce the computational cost and by taking advantage of the two-fold symmetry of the problem, only a quarter of the slab was considered as the calculation domain. The employed boundary conditions, referring to Figure 3.2, are given below:

Nozzle inlet

In order to satisfy the overall mass balance, for a pre-specified casting speed, the melt inlet velocity was adjusted.

$$u = u_{in}, \quad v = w = 0, \quad h = h_{in}, \quad k = 0.01 \times u_{in}^2, \quad \varepsilon = c_\mu k_{in}^{3/2} / 0.05D$$

Free surface

The normal gradient of all variables were set to zero but the velocity component normal to the surface was assumed to be zero.

$$\frac{\partial v}{\partial x} = \frac{\partial w}{\partial x} = \frac{\partial k}{\partial x} = \frac{\partial \varepsilon}{\partial x} = \frac{\partial h}{\partial x} = 0, \qquad u = 0 \tag{3.36}$$

Symmetry planes

At the x-y plane: $$\frac{\partial u}{\partial z} = \frac{\partial v}{\partial z} = \frac{\partial k}{\partial z} = \frac{\partial \varepsilon}{\partial z} = \frac{\partial h}{\partial z} = 0, \qquad w = 0 \tag{3.37}$$

At the x-z plane: $$\frac{\partial u}{\partial y} = \frac{\partial w}{\partial y} = \frac{\partial k}{\partial y} = \frac{\partial \varepsilon}{\partial y} = \frac{\partial h}{\partial y} = 0, \qquad v = 0 \tag{3.38}$$

It is to be noted that zero sensible heat gradients at the symmetry planes imply that these planes can be treated as adiabatic surfaces.

Outlet

At outlet, the fully developed boundary condition was imposed, i.e., all gradients normal to the outlet plane were specified to be zero, except for the velocity components parallel to the outlet-plane which were specified to be zero:

$$\frac{\partial u}{\partial x} = \frac{\partial k}{\partial x} = \frac{\partial \varepsilon}{\partial x} = \frac{\partial h}{\partial x} = 0 \tag{3.39}$$

$$v = w = 0 \tag{3.40}$$

Moving Walls

At the ingot surface, a no slip boundary condition ($u=0$) was applied in the liquid region, and an axially translating boundary with the casting speed ($u=u_{cs}$) was imposed on the solid and mushy regions, with the assumption that no liquid escaped the computational domain.

$$v = w = k = \varepsilon = 0 \tag{3.41}$$

The energy boundary conditions at the slab surfaces were applied through the use of variable heat transfer coefficients. The governing equation for the heat transfer at the slab surface is given by:

$$\frac{\partial h}{\partial y} = \frac{\partial h}{\partial z} = -\frac{\gamma}{K}(h_s - h_a) \tag{3.42}$$

where γ is the effective heat transfer coefficient between the solid surface and the surrounding. h_s represents the enthalpy at the surface and h_a represents the product of ambient temperature and the specific heat of the aluminum.

It is well known that in vertical DC casting process the heat transfer coefficient varies significantly in two cooling regions, namely, primary and secondary cooling sections. It should be noted here at steady state, that only 10-20 % of the total heat content of the melt is removed in the primary cooling zone through the circulation of the chilled water in the mold, whereas the rest (80-90 %) of the total heat content is extracted in the secondary cooling zone. The Alcan aluminum industry developed the concept of a hot top mold for VDC casting processes. The hot top mold provides improved surface characteristics, and reduces sub-surface macro-segregation, hot tears and cold cracks. When this technique was first developed by Alcan they named the process as Alcan Sheet Mold (ASM) technique. The original concept of the ASM technique involved insulating the top part of the mold using insulation rings. This modification of the mold allowed the melt to remain at the inlet temperature up to a certain depth, and it also dampened the turbulence that originated from the inlet delivery system.

In the model, the hot-top or adiabatic section was considered to be 125 mm in length, which was followed by the mold of 80 mm length. The air gap region was assumed to be an axial length of 10 mm within the mold. In the mold section, a higher but constant heat transfer coefficient was imposed which corresponded to the heat extraction from the melt through direct mold contact, and in the air gap region a much lower but constant heat transfer coefficient (γ_{gap}) was used representing heat removal through conduction and radiation across the air gap [85]. The cooling of the mold is referred to as

primary cooling and the post mold cooling which is done by the water jet coming from the base of the mold is called the secondary cooling region. The heat transfer coefficient in the secondary cooling zone was allowed to vary on the basis of the measurements made on a DC cast billets. After emerging from the mold the shell was subjected to a progressively higher heat transfer coefficient due to upward movement of the injected water jets coming from the impingement region which was considered to be 10 mm in length. In this region, the heat transfer coefficient varied linearly but very sharply with the axial distance and achieved a maximum value (referred as γ_{max}). This value corresponded to the heat transfer at the water impingement point. For the following axial length of 40 mm, the heat transfer coefficient was considered to decrease linearly, and it reached a uniform value referred to as γ_{film}. This uniform value of the heat transfer coefficient was assumed to prevail along the remaining length of the slab. Unless mentioned otherwise, the above prescription of the heat transfer coefficient along the length of the slab can be mathematically expressed by the following equations:

Adiabatic section: $\gamma(x) = 0.$ kW/m^2 K $(0 \le x < 125 \text{ mm})$ ----(3.43)

Mold region: $\gamma(x) = 1.5$ kW/m^2 K $(125 \le x < 195 \text{ mm})$ ----(3.44)

Air gap in mold: $\gamma(x) = 0.15$ kW/m^2 K $(195 \le x < 205 \text{ mm})$ ----(3.45)

Spray zone: $$\gamma(x) = \gamma_{gap} + \frac{x - x_1}{x_2 - x_1}(\gamma_{max} - \gamma_{gap}) \text{ kW/m}^2 \text{ K}$$

$(205 \le x < 215 \text{ mm})$ ----(3.46)

$$\gamma(x) = \gamma_{max} + \frac{x - x_2}{x_3 - x_2}(\gamma_{film} - \gamma_{max}) \text{ kW/m}^2 \text{ K}$$

$(215 \le x < 255 \text{ mm})$ -----(3.47)

$$\gamma(x) = \gamma_{film}$$ $(x \ge 255 \text{ mm})$ ----(3.48)

where x_1 = 205 mm, x_2 = 215, and x_3 = 255 mm. As mentioned in the literature review, most of the experimental measurements concerning heat transfer coefficients in the primary and cooling regions were carried out for billet casters [51,72,134]. In this study, the suggested heat transfer coefficients for the above two zones for DC billet casters were used. The mold region was considered to have two zones, a melt-mold contact zone and an air-gap zone. In the contact zone, a heat transfer coefficient of γ_{mold} =1.5 kW/m^2 K was used and in the air gap region a heat transfer coefficient of γ_{gap} = 0.15 kW/m^2 K was used with T_{water} = 30^{o}C for the convection cooling water temperature. The values of γ_{max} and γ_{flim} are available from several sources, including Tarapore [120]. For example, Tarapore reported a maximum heat transfer coefficient of approximately 22.0 kW/m^2 K and a uniform, falling film coefficient of approximately 12.0 kW/m^2 K for 40 cm diameter billet cast at 60 mm/min. For the secondary cooling region, on the contrary, Grun et al. [51] suggested that the heat transfer coefficient for a DC cast billet should vary from 7.0 to 30.0 kW/m^2 K. In the current study, the maximum heat transfer coefficient of γ_{max} = 20.0 kW/m^2 K with γ_{flim} = 10.0 kW/m^2 K was used similar to that implemented for the billet by Vreeman and Incropera [131].

3.2.7. Calculation of the Local Heat flux at the Surface

Three different regions were distinguished along the caster faces, namely the mold, the air gap and the spray zone. According to the cooling conditions, various heat transfer coefficients were specified in these various regions which were provided above in Section 3.2.6. In this study, the air gap inside the mold, which formed due to solidification shrinkage of the shell, was arbitrarily selected to be of length 10 mm. Since the surface temperature of the cast was not known before the simulation, at the surface for each control volume a one-dimensional heat balance of the conductive heat flux from the inside of the cast to the surface and the convective heat flux to the cooling water was performed which allowed to obtain the surface temperature of the cast at each grid point. To evaluate the local heat flux at every grid point on the cast surface both inside and down the mold, the model considered the corresponding heat transfer coefficient, γ, the

predicted surface temperature of the aluminum shell at the ith axial grid, T_{surf_i} and the chill water temperature, T_{water} (taken as 30^{o}C):

$\frac{q_i}{A_i} = \gamma\left(T_{surf_i} - T_{water}\right)$, where, q_i is the total heat transferred through the ith control volume surface A_i.

In Chapters 5 to 9, the predicted local surface heat flux on the narrow and wide faces of the slab will be reported for the two locations along A-A' and B-B', as shown in Fig. 3.3.

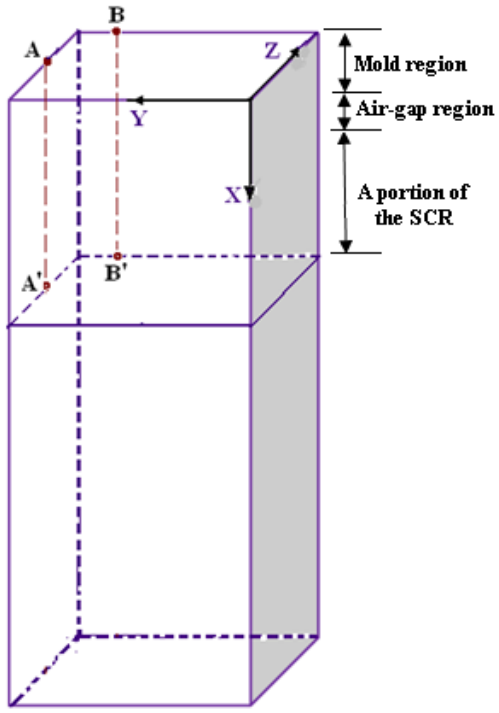

Fig.3.3: The schematic diagram shows the two regions where the local surface heat fluxes were calculated: (a) A-A' and (b) B-B'.

3.2.8 Non-Dimensionalization of the Governing Equations and Boundary Conditions

In order to obtain the relevant parameters and for the generalization of the results it is a better practice to solve the non-dimensionalized from of the governing equations and associated boundary conditions. The following dimensionless variables are used to non-dimensionalize the governing partial differential equations and boundary conditions:

$$X = \frac{x}{D},\ Y = \frac{y}{D},\ Z = \frac{z}{D},\ U = \frac{u}{u_{in}},\ V = \frac{v}{u_{in}},\ W = \frac{w}{u_{in}},$$

$$P^* = \frac{P}{\rho_o u_{in}^2},\ k^* = \frac{k}{u_{in}^2},\ \varepsilon^* = \frac{\varepsilon D}{u_{in}^3},\ h^* = \frac{h}{\Delta H_f},\ \Delta H^* = \frac{\Delta H}{\Delta H_f},\ \mu_t^* = \frac{\mu_t}{\mu} \qquad (3.49)$$

where D is the hydraulic diameter for the inlet geometry , u_{in} is the inlet velocity and ΔH_f is the latent heat of fusion. All the conservation equations presented above can be expressed in a general form of a non-dimensional partial differential equation. The Cartesian-tensor form of this equation is:

$$\frac{\partial(\rho U_i \Phi^*)}{\partial X_i} = \frac{\partial}{\partial X_i}(\Gamma_\Phi^* \frac{\partial \Phi^*}{\partial X_i}) + S_\Phi^* \qquad i=1,2,3$$

(3.50)

where, Φ^*, Γ_Φ^*, and S_Φ^* are the general dependent variable, the generalized diffusion coefficient, and the relevant source term, respectively. The values of Φ^*, and the associated definition of Γ_Φ^* and S_Φ^*, for all of the transport equations discussed earlier, are listed in Table (3.2). The development of a general-purpose program is considerably simplified because of the casting of the governing equations in a general form. The non-dimensional form of the boundary conditions becomes:

Nozzle inlet

$$U=1, \quad V=W=0, \qquad h^{*}=h_{in}^{*}, \qquad k^{*}=0.01, \qquad \varepsilon^{*}=c_{\mu}(0.01)^{3/2}/0.05 \tag{3.51}$$

Free surface

$$\frac{\partial V}{\partial X}=\frac{\partial W}{\partial X}=\frac{\partial k^{*}}{\partial X}=\frac{\partial \varepsilon^{*}}{\partial X}=\frac{\partial h^{*}}{\partial X}=0, \quad U=0 \tag{3.52}$$

Symmetry planes

At the X-Y plane: $$\frac{\partial U}{\partial Z}=\frac{\partial V}{\partial Z}=\frac{\partial k^{*}}{\partial Z}=\frac{\partial \varepsilon^{*}}{\partial Z}=\frac{\partial h^{*}}{\partial Z}=0, \quad W=0 \tag{3.53}$$

At the X-Z plane: $$\frac{\partial U}{\partial Y}=\frac{\partial W}{\partial Y}=\frac{\partial k^{*}}{\partial Y}=\frac{\partial \varepsilon^{*}}{\partial Y}=\frac{\partial h^{*}}{\partial Y}=0, \quad V=0 \tag{3.54}$$

Outlet

$$\frac{\partial U}{\partial X}=\frac{\partial k^{*}}{\partial X}=\frac{\partial \varepsilon^{*}}{\partial X}=\frac{\partial h^{*}}{\partial X}=0 \tag{3.55}$$

$$V=W=0 \tag{3.56}$$

Moving walls

$$U=U_s=u_s/u_{in}, \qquad V=W=k^{*}=\varepsilon^{*}=0, \qquad \frac{\partial h^{*}}{\partial Y}=\frac{\partial h^{*}}{\partial Z}=-\frac{\gamma D}{K}(h_s^{*}-h_a^{*}) \tag{3.57}$$

It should be noted here that in the present model the non-dimensionalized transport equations and associated boundary conditions were solved, which therefore

generated non-dimensional results. To make the results easily understandable, all predicted results in this thesis are reported and discussed in their primitive (dimensional) forms.

Table 3.2: Summary of the Non-Dimensional Governing Equations.

Equation	Φ^*	Γ^*_Φ	S^*_Φ
Continuity	**1**	**0**	**0**
U-momentum	U	$\frac{1}{\mathrm{Re}}(1+\mu_t^*)$	$-\frac{\partial P^*}{\partial X}+\frac{\partial}{\partial X_i}\left(\Gamma^*_\Phi\frac{\partial U_i}{\partial X}\right)-\frac{A^*}{\mathrm{Re}}(U-U_s)$
V-momentum	V	$\frac{1}{\mathrm{Re}}(1+\mu_t^*)$	$-\frac{\partial P^*}{\partial Y}+\frac{\partial}{\partial X_i}\left(\Gamma^*_\Phi\frac{\partial U_i}{\partial Y}\right)-\frac{A^*}{\mathrm{Re}}(V-V_s)$
W-momentum	W	$\frac{1}{\mathrm{Re}}(1+\mu_t^*)$	$-\frac{\partial P^*}{\partial Z}+\frac{\partial}{\partial X_i}\left(\Gamma^*_\Phi\frac{\partial U_i}{\partial Z}\right)-\frac{A^*}{\mathrm{Re}}(W-W_s)$
Kinetic Energy	k^*	$\frac{1}{\mathrm{Re}}(1+\frac{\mu_t^*}{\sigma_k})$	$\frac{G^*}{\mathrm{Re}}-\varepsilon^*-\frac{D_k^*}{\mathrm{Re}}$
Rate of energy dissipation	ϵ^*	$\frac{1}{\mathrm{Re}}(1+\frac{\mu_t^*}{\sigma_\varepsilon})$	$\frac{1}{\mathrm{Re}}f_1C_1G^*\frac{\varepsilon^*}{k^*}-C_2f_2\frac{\varepsilon^{*2}}{k^*}+\frac{E^*_\varepsilon}{\mathrm{Re}^2}$
Energy	h^*	$\frac{1}{\mathrm{Re}}(\frac{1}{\mathrm{Pr}}+\frac{\mu_t^*}{\sigma_t})$	$-\left(\frac{\partial U\Delta H^*}{\partial X}+\frac{\partial V\Delta H^*}{\partial Y}+\frac{\partial W\Delta H^*}{\partial Z}\right)$

where:

$$\mathrm{Re}=\frac{\rho u_{in}D}{\mu}$$

$$G^*=\mu_t^*\left(\frac{\partial U_i}{\partial X_j}+\frac{\partial U_j}{\partial X_i}\right)\frac{\partial U_i}{\partial X_j},\qquad D_k^*=2\frac{\partial\sqrt{k^*}}{\partial X_i}\frac{\partial\sqrt{k^*}}{\partial X_i},$$

$$E_\varepsilon^*=2\mu_t^*\left(\frac{\partial^2U_i}{\partial X_j\partial X_k}\right)_t\left(\frac{\partial^2U_i}{\partial X_j\partial X_k}\right),\qquad f_\mu^*=e^{\frac{-3.4}{(1+\mathrm{Re}_t^*/50)^2}},\qquad \mathrm{Re}_t=\mathrm{Re}\frac{k^{*2}}{\varepsilon^*},$$

$$\mu_t^* = \mathrm{Re} C_\mu f_\mu^* \frac{k^{*2}}{\varepsilon^*}, \qquad f_1 = 1,\ f_2 = 1 - 0.3e^{-\mathrm{Re}_t^2}, \qquad A^* = \frac{C^*(1-f_l)^2}{f_l^3 + q},$$

$C_\mu = 0.09,\ C_1 = 1.44,$ **C_2 =1.92,** $\sigma_k = 1.0,\quad \sigma_\varepsilon = 1.3,\quad \sigma_t = 0.9,\ q = 1\times10^{-30}$

3.3 Numerical Approach

3.3.1 Discretization Procedures

Once the governing equations and the associated boundary conditions are set, the next step involves the numerical solutions of the above sets of equations listed in Table 3.2. In order to implement the numerical solutions, the equations must be converted from the partial differential equations to their equivalent algebraic form by a suitable discretization method. In this study, a control volume (CV) based finite difference approach was adopted to discretize the equations. Staggered control volumes were employed in the computational domain. For a typical control volume, the governing equation was integrated to obtain a local averaged conservation equation, the terms of which were approximated from the discrete values of the variable from the surrounding nodal values. A hybrid difference scheme (Patankar [96]) was used to discretize the convection-diffusion terms. In the present study there are seven variables, namely, U, V, W, P^*, k^*, ε^*, h^* which were solved sequentially to obtain a converged solution. A detailed description of the discretization procedure can also be found in a relatively new book by Versteeg and Malalasekera [129]. To solve the discretized set of equations a suitable solution procedure or algorithm is required. In the current study, a line-by-line Tri-Diagonal Matrix Algorithm (TDMA) was used to solve the discretized equations for each of the three coordinate directions. The following section is devoted to explaining briefly the solution method.

3.3.2 Solution Procedure and Convergence Criteria

For each of the transport variable, the discretized equation was cast in the following general form:

$$a_p\phi_p = a_E\phi_E + a_W\phi_W + a_N\phi_N + a_S\phi_S + a_T\phi_T + a_B\phi_B + b_\phi \tag{3.58}$$

where a_E, a_W, a_N, a_S, a_T, and a_B are the coefficients of the six neighboring nodes of node P of a box-shaped rectangular control volume. For easy of understanding of the discretized equation, a two-dimensional control volume with associated variables are shown in Figure 3.4. The term b_Φ represents the linearized source term. The convection and diffusion terms are embedded in the coefficients, depending on the transport variable, the source term may contain various terms such as pressure gradient, buoyancy force, and Darcy terms. The developed 3-D turbulent flow computer program is an in-house code which is based on the control volume approach. Once the general discretization equation is obtained, a suitable solution procedure (algorithm) is subsequently required. To resolve the velocity-pressure coupling in the three momentum equations, the SIMPLE algorithm, which stands for Semi-Implicit Method for Pressure-Linked Equations, was used. The flowchart for the algorithm is portrayed in Figure 3.5. The SIMPLE algorithm is very well documented in many CFD literature, such as, Patankar and Spalding [99], and Caretto et al. [13], Patankar [97], etc.

In actual implementation of the SIMPLE algorithm, an iterative solution scheme was adopted using an implicit relaxation technique to solve the discretized equations. As mentioned earlier, the well known line-by-line Tri-Diagonal Matrix Algorithm (TDMA) solver was used until a converged solution was obtained. The discretized equations for each variable was declared to have converged when the sum of the residuals for that particular variable (R_Φ) was less than 0.001. The convergence criterion described above can be defined mathematically as follows:

$$R_\Phi = \sum_{all\ nodes} \left| a_p\Phi_p - \sum_{nb} a_{nb}\Phi_{nb} - b \right| \tag{3.59}$$

The CPU time per iteration was about 2.0 s. The computations were performed on a personal computer having a speed of 2.66 GHz and fitted with a RAM of 4 Gigabytes. For a typical case, to obtain a fully converged solution it took about 10 days and required 30,000 iterations. In order to decrease the computational time, for various parametric studies, the numbers of runs were restarted from the converged solutions of the variables obtained for different parametric cases.

3.3.3 Under-relaxation factor

Because of the nonlinearity and since the governing equations are inter-linked, the values of the computed variables may swing widely from one iteration to another. These rapid changes influence the magnitude of the coefficients of the tri-diagonal matrix which then loses its diagonal dominance and often leads to the divergence of the solutions. To prevent the code from divergence during the solution process, various under-relaxation parameters are introduced to arrest the rapid changes from one iteration to another for each variable such as velocities, pressure, temperature, $\mu_t^*, \mathrm{k}^*, \varepsilon^*$. Because of the implicit implementation of the under-relaxation factors, the coefficients of the algebraic equation change as follows:

$$\frac{a_{\mathrm{P}}}{\alpha_{\Phi}}\Phi_{\mathrm{P}} = \sum_{nb} a_{nb}\Phi_{nb} + b_{\Phi} + (1-\alpha_{\Phi})\frac{a_{\mathrm{P}}}{\alpha_{\Phi}}\Phi_{\mathrm{P}}^{\bullet} \text{ ---------- } (3.60)$$

where, α_{Φ} is the under relaxation factor for the general variable Φ. The suitable values of the relaxation factor are found from earlier modeling experience since they depend upon a number of factors (grid resolution, Reynolds number, Peclet number, Grashof number, etc.). In the present study, extensive trial-error runs were conducted using various combinations of under-relaxation factors to find the suitable and relevant under-relaxation factors before the production runs were carried out. Irrespective of the various parametric values, the use of the following combination of under-relaxation factors provided converged solutions:

α_{u^*}=0.1; α_{v^*}= 0.1; α_{w^*} =0.1; α_{P^*}= 0.1; α_{h^*} =0.1; α_{κ^*}=0.1; α_{ε^*}=0.1; and α_{μ^*}=0.3.

3.3.4 Post Processing of the Results

A commercial graphics software package which is particularly suitable for CFD applications named TECPLOT (Version 9.0) was used for post processing of the predicted results. It is to be noted that in this software the length of a 3-D vector was measured tangentially to the plane of the paper. Therefore, the reference vector would not give the exact magnitude of the velocity field, since to measure the exact magnitude of the velocity vectors, the vector orientation must be taken into account. The vector orientation could not be presented on a 2-D paper.

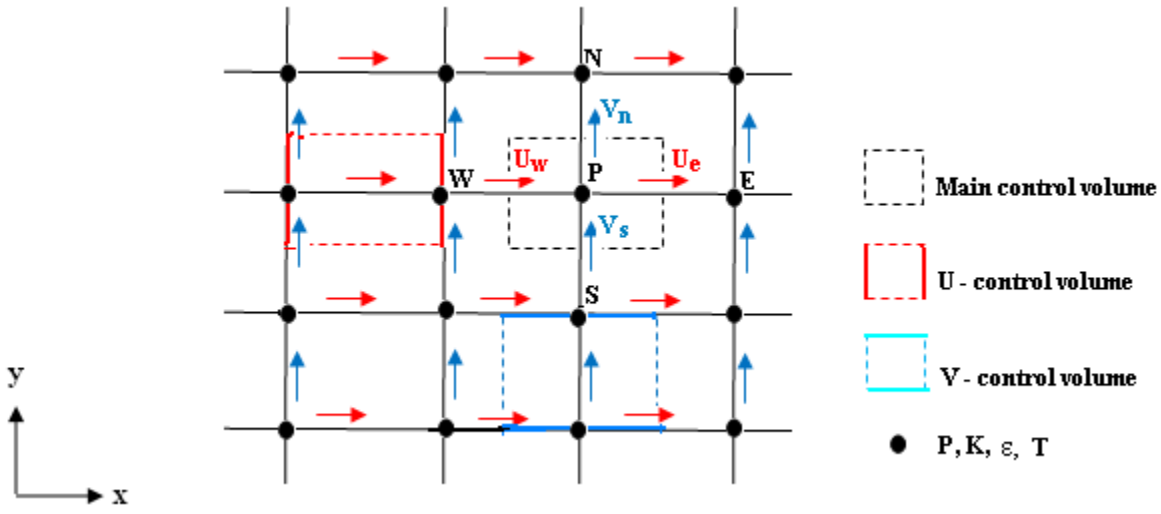

Figure 3.4: Staggered grid

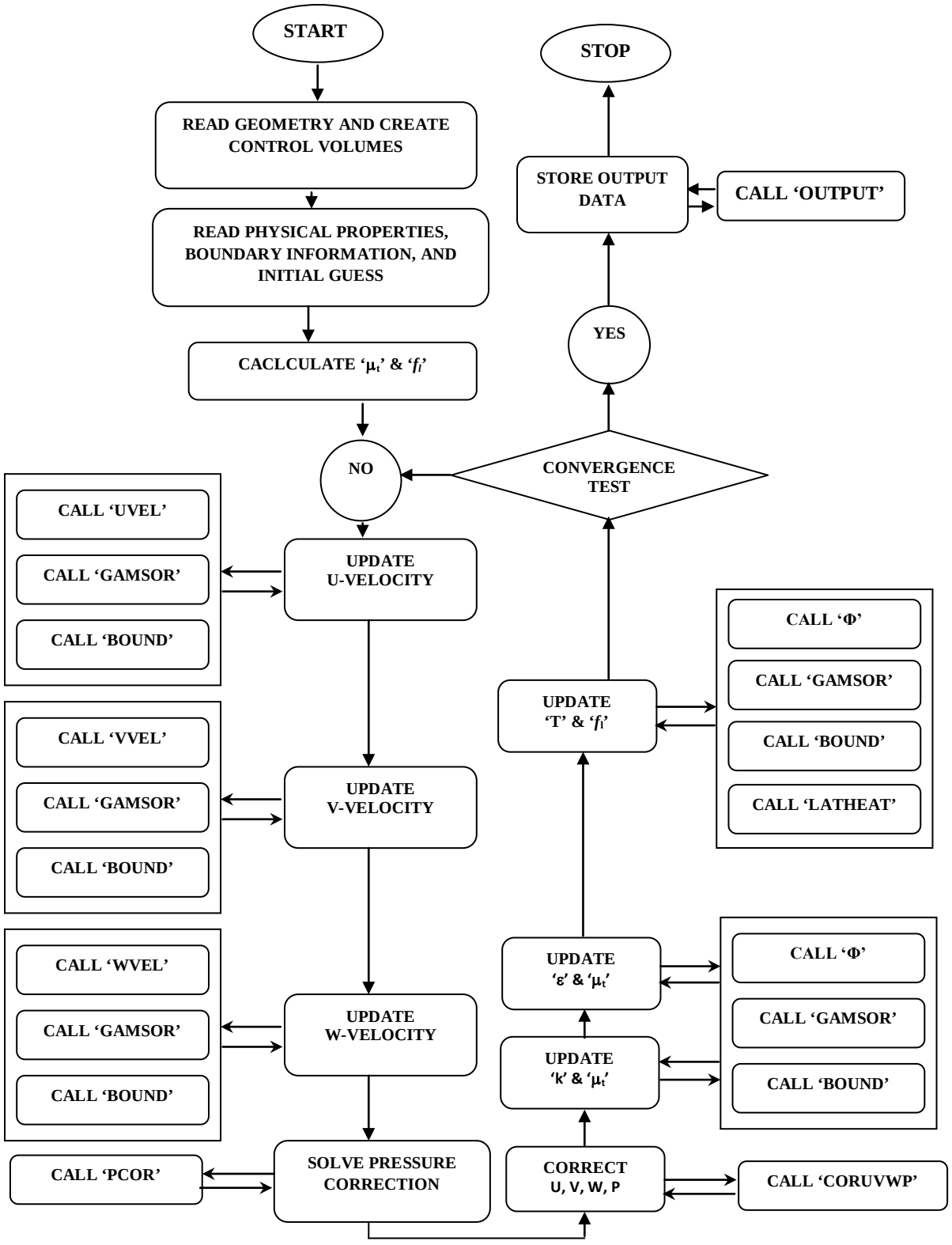

Figure 3.5: Flow chart of the 3-D turbulent fluid flow and solidification code.

CHAPTER 4

QUANTITATIVE VERIFICATION OF THE MODEL AND GRID INDEPENDENCY TESTS

4.1 Code Verification

4.1.1 Introduction

To validate the code, it is necessary to compare the predicted results with the experimental or numerical results of the same vertical DC casting problem under identical operating conditions provided by other researchers. This section is devoted to the quantitative verification of the code. This task was performed by comparing the measured and predicted solidification front distances from the top surface of the mold for the VDC casting of an aluminum alloy. Similar to the experiment, in the model a combo-bag melt feeding system was used. The predictions were for a steady state and the model took into account the thermal buoyancy effect. For the validation of the code, the experimental results were taken from the real DC casting experiments carried out at Reynolds Metal Company Casting Technology Center, Chester, VA, which were performed by Jones et al. [70].

4.1.2 Description of the DC Casting Experimental Set-up and Procedures

The DC caster experimental set-up with a typical combo bag used to acquire the solidification front distances from the top of the mold at transient and steady state is shown in Figure 4.4. A T-shaped bar was secured on the top of the mold having dimensions of 1.32 × 0.66 m to guide the sacrificial thermocouples (TC). The aluminum alloy (Al 3104) melt in the mold was delivered at an average temperature of 700°C. The metal was cast at a casting speed of 50.8 mm/min. The metal level in the trough above

the mold was kept constant at 58.4 mm and the primary cooling water within the mold was circulated at a rate of 18.3 l/s. In the experiments a 330 mm length combo bag was used. At three-second interval the temperatures were recorded by a portable data recorder. Sacrificial thermocouples were fed via stainless steel wires through the T-shaped guide into the liquid metal. During the start-up phase, the stainless steel covered thermocouples were coated with solidified metal, which were pulled down into the solid and moved with the casting speed. The length of the wires was set at 1.5 times the distance needed to reach the steady state solid profile. The shape of the solidification front was measured by setting the time equal to zero when the thermocouple first read the temperature of the liquid metal. This allowed for the positions of the thermocouples, while in the melt, to be tracked. By measuring the time interval for the thermocouples to reach the solidification front, and by multiplying the time intervals by the drop speed, the solidification front depths were calculated. Only thermocouples TC1, TC2, TC3 and TC4, shown in Fig. 4.4, which are parallel to the rolling face, were used for the verification, since thermocouple 5 failed to measure the depth of the solidification front. It was not possible to use thermocouple results in the transverse direction, i.e. (TC6, TC7, TC8), for the code verification purpose, because there was a geometrical scale-type error in reporting the results from these thermocouples.

4.1.3 Numerical Modeling Set-up

By keeping consistency with the experimental measurement, a numerical simulation of the problem was performed using a three dimensional control volume based finite difference approximation of the Navier-Strokes and energy equations. The Navier-Strokes equations were solved by considering a Darcy type source term and low Reynolds number two equation k-ε turbulence model of Launder and Sharma was chosen to solve the turbulence problem in this simulation, all of which were described in details in Chapter-3. The buoyancy term in the x-momentum equation was derived by applying the Boussinesq approximation which also can be found in Chapter-3. To simulate as closely as possible the physical experiments, in the numerical model the configuration adopted was identical to that used in the real experiment. The simulated ingot had a

dimension of 2.5 × 1.32 × 0.66 m in the x, y and z directions, respectively, as given in Figure 3.1 of Chapter-3. Invoking symmetry considerations, a quarter of the ingot was taken as the calculation domain. The yellow part in Figure 3.1 represents the section modeled. A combo type of bag, as shown in Figure 4.1, was used to distribute the molten aluminum alloy and was located at the center of the hot top as shown in Figure 3.1. The bag had dimension of 50 × 330 × 152 mm in the x, y, and z directions, respectively. The end windows extended along the whole thickness of the bag, and the bottom windows had a dimension of 20 × 40 mm in the y and z directions, respectively. The mold was of 80 mm in length. A square type of submerged nozzle was used to deliver the inlet melt which had a dimension of 20 × 30 × 30 mm in the x, y, and z directions, respectively. The numerical solutions were computed on a 60 × 42 × 24 grid system in the x, y, and z directions using non-uniform grids, where appropriated. This grid system was chosen as a compromise between accuracy and cost. Convergence was declared when the sum of the residuals for each calculated variable (R_Φ) was less than 0.01. In total, about 240 CPU hours were spent for 30,000 iterations to complete the combo bag case with a casting speed of 50.8 mm/min and inlet superheat of 45^{o}C. Thermo-physical properties for Al-3104 alloy and boundary conditions used in this simulation are given in Tables 4.1 and 4.2. For code verification purposes, the model used different axial distances of the various zones than those considered in the model geometry in Chapter-3. Specifically, the hot top was taken here as 75 mm. The mold length was the same as the model which was 80 mm. This air gap within the mold was taken as 10 mm and was followed by an impingement zone of 20 mm in length, where intense cooling of the slab took place. This region was followed by a region of 40 mm in length, where the heat transfer coefficient was allowed to vary with the axial distance. The values of the heat transfer coefficients employed in the above regions were identical to those discussed in Capter-3.

Table-4.1: Thermophysical properties of aluminum Al-3104 for the quantitative verification of the code.

Variable [unit]	Value
Thermal conductivity (liquid or solid) [kW/m-K]	0.170

Specific heat (liquid or solid) [kJ/kg-K]	0.88
Latent heat of fusion [kJ/kg]	396.4
Liquidus temperature [°C]	655.0
Solidus temperature [°C]	630.0
Viscosity at 655°C [kg/m-s]	16.2×10^{-4}
Density (liquid or solid) at 630°C [kg/m^3]	2720
Liquid thermal expansion coefficient [1/K]	1.020D-04

Table-4.2: Boundary conditions used for the quantitative verification.

		Dependent variables					
Regions		u	v	w	h	k	ε
Nozzle exit		u_{in}	0	0	h_{in}	-0.01 × u^2_{in}	$c_\mu k_{in}^{3/2} / 0.05\ D$
Free surface		0	$\frac{\partial v}{\partial x}=0$	$\frac{\partial w}{\partial x}=0$	$\frac{\partial h}{\partial x}=0$	$\frac{\partial k}{\partial x}=0$	$\frac{\partial \varepsilon}{\partial x}=0$
Symmetry planes	Narrow	$\frac{\partial u}{\partial y}=0$	0	$\frac{\partial w}{\partial y}=0$	$\frac{\partial h}{\partial y}=0$	$\frac{\partial k}{\partial y}=0$	$\frac{\partial \varepsilon}{\partial y}=0$
	Wide	$\frac{\partial u}{\partial z}=0$	$\frac{\partial v}{\partial z}=0$	0	$\frac{\partial h}{\partial z}=0$	$\frac{\partial k}{\partial z}=0$	$\frac{\partial \varepsilon}{\partial z}=0$
Outlet		$\frac{\partial u}{\partial x}=0$	0	0	$\frac{\partial h}{\partial x}=0$	$\frac{\partial k}{\partial x}=0$	$\frac{\partial \varepsilon}{\partial x}=0$
Ingot outside surface	Melt in contact with mold	0	0	0	γ(x)	0	0
	solidified	u_{cs}	0	0	γ(x)	0	0
Adiabatic section: γ (x) = 0. kW / m^2 K						$0 \le x < 75$ mm.	

Mold region :	$\gamma(x) = 1.5$ kW / m^2 K	$75 \le x < 145$ mm.
Air gap in mold:	$\gamma(x) = 0.15$ kW / m^2 K	$145 \le x < 155$ mm.
Spray zone :	$\gamma(x) = \gamma_{gap} + (x - x_1) / (x_2 - x_1)$	
	* $[\gamma_{max} - \gamma_{gap}]$ kW / m^2 K	$155 \le x < 175$ mm.
	$\gamma(x) = \gamma_{max} + (x - x_2) / (x_3 - x_2)$	
	* $[\gamma_{film} - \gamma_{max}]$ kW / m^2 K	$175 \le x < 215$ mm.
	$\gamma(x) = \gamma_{film}$ kW / m^2 K	$x \ge 215$ mm.

where $\gamma_{gap} = 0.15$ kW / m^2 K

$\gamma_{film} = 10.0$ kW / m^2 K

$\gamma_{max} = 20.0$ kW / m^2 K

$x_1 = 155$ mm, $x_2 = 175$ mm, $x_3 = 215$ mm.

4.1.4 Difficulties in Validating the Code

The difficulties in validating the code which aroused during the present investigations are discussed below.

(a) Thermal boundary conditions (TBC)

The general approach to the TBC imposed on the boundaries of a computational domain is very pragmatic. The authors in their experimental work did not measure the TBC of the physical problem. Due to the lack of detailed experimental information on thermal boundary conditions on the slab surfaces, idealizations were made in the modeling exercise. Usually, either adiabatic, isothermal, or imposed heat flux or imposed heat transfer coefficient are used in the DC casting literature as the imposed thermal boundary conditions in the developed mathematical model in order to validate the experimental heat transfer measurements. Unfortunately, no experimental work concerning the thermal boundary conditions exists in the literature for DC casting of Al 3104 rolling ingots. To validate the numerical code, in the present mathematical model, the experimental thermal boundary conditions available in the literature for a billet were taken to be applicable also for the rectangular ingots.

In the current developed mathematical model, the heat transfer coefficient at the outside surfaces of the ingot was assumed constant peripherally and was allowed to change only in the axial direction to represent the different stages of cooling rates the ingot was subjected to as it descended towards the casting pit. In a real casting situation, the surface heat transfer coefficient not only varies axially but also changes peripherally. Due to unavailability of the experimentally measured heat transfer coefficient in the transverse directions, only the axial change of the heat transfer coefficient was considered here.

(b) Inlet conditions for k and ε

In order to prescribe inlet conditions for kinetic energy and rate of dissipation equations for the k-ε model, one needs to measure the inlet melt velocity accurately. Since, this information was not available in Jones et al. [70] experiments, hence in the current model the inlet conditions for k and ε were approximated.

(c) Uncertainty analysis

For the verification of numerical results with experimental data, the experimental uncertainties that develop due to the use of various instruments should be recorded and reported. Unfortunately, Jones et al., in their paper did not describe anything about the experimental uncertainties which invariably existed in their reported experimental measurements.

(d) Geometrical measurement

The authors in their description of the experimental set-up, neither they provided the axial length of the mold (the mold-metal contact and air-gap regions) nor they reported the water jet-angle and length of the impingement region in the secondary cooling zone. The discussed three quantities are of crucial importance for the numerical modeling of the DC casting problem as the heat extraction rates depend on the above quantities.

Without acquiring the proper values mentioned in items (a)-(d), the numerical results generated for the verification of the experimental results are potentially questionable.

4.1.5 Numerical Results

In this section, the results obtained from the developed mathematical model using the material properties of Al-3104 and boundary conditions listed in Tables 4.1 and 4.2, respectively are discussed. The physical dimensions of the caster with the combo bag are provided above in the numerical modeling set-up. It is expected that the predicted results will be closed to the experimental data provided all the stated difficulties are fulfilled.

A 3-D surface plot of the calculated temperature contours, vector fields and streamlines, are portrayed in Figures 4.2 (a-c), respectively. The results in these three figures are presented for the one half of the rolling and narrow faces along with the top surface. In order to clearly visualize the flow field, in Figures 4.2 (b-c), the velocity field and streamlines for the top part of the caster are presented in a magnified format. For the purpose of code validation, the modeling results in magnified form for three longitudinal cross-sections, representing the x-y planes at z = 0 (symmetry), z = 79 mm, and z = 142 mm of the 3-D calculation domain are illustrated in Figures 4.3 (a-f). It should be noted that in each of the Figures 4.3 (a,c,e) both velocity vectors and streamlines are presented in a combined format. A close examination of Figure 4.3 (a) shows that the flow has changed from largely horizontal to exhibiting a stronger vertical component which is in opposite direction of the flow exiting from the bottom window of the combo-bag around the slab center. A large anti-clockwise vortex is seen in this figures which has been formed due to the downward convective flow along the cold solidification front and side walls and upward flow in the warm center of the pool. In the isothermal water model experiment, a similar trend in flow pattern at the symmetry plan was observed [140-142]. The flow that originated from the side opening of the combo-bag and traveled downward along the solidification front and latter moving upward, is obstructed by the downward flow coming from the bottom window of the combo-bag. This resulted in the upward flow to turn towards the wide slab wall and instead of creating a recirculation zone at the

top free surface it is directed to the narrow symmetry plane, which can be clearly seen in the 3-D surface plot (Figs. 4.2 (b-c)). Because of the thermal buoyancy force the upward flow is strengthen. In contrast to Fig. 4.3(a), Figure 4.3 (c) shows two vortices circulating anti-clock wise, the bigger one is near the center and the smaller one is near the top of the narrow wall. These vortices are much smaller compared to the singe vortex that is seen in the wide symmetry plane. These types of vortices usually develop inside a cavity because of the separation of the flow in a confined region. Figure 4.3 (e) shows that as one travels toward the rolling wall, the corner vortex is gaining strength with the increase of the horizontal distance, while the vortex that developed earlier near the center has decayed. The velocity patterns in the described three figures (Figures 4.3 (a,c,e)) show that there is a good mixing effect of the convective currents.

A 3-D surface plot of the calculated temperature contours is presented in Fig. 4.2(a). Here, the dark yellow region represents the mushy region, which is confined between the solidus (903 K) and liquidus (928 K) contours. From this figure one can see that the solidification front is almost an inclined straight line with a negative slope, and it turns to an almost horizontal straight line as one move toward the center. Because of the combo-bag delivery system, a hot stream is exiting downward with a high velocity from the bottom window of the bag which is preventing to form the solidification layer, and hence a thicker mushy layer is seen to have formed. Another region for the formation of a thicker mushy layer is the fact that a part of the main flow coming from the side window and circulating in the wide symmetry plane is cooled down as it flows down along the solidification front. If one compares the mushy layer thickness in the narrow and wide symmetry plane in the same figure, one sees that the extent of the mushy layer on the narrow plane is much thinner compared to the wider plane. This is due to the fact that the diverted hot melt from the adiabatic section at the center of the mold leads to the formation of a thinner mushy layer. It is well know that a thicker mushy zone restricts the metal feeding inside the dendritic network, and this may lead to the enhancement of stress build up and hot cracks [89]. Therefore, the melt delivery system should be designed in such a way so that a thinner mushy layer is formed. The portion of the flow which comes from the side window and travels downward along the solidification front towards the center will carry the fragments of broken dendrites which are depleted of

alloying elements, will cause negative centerline macro-segregation [89]. In designing the melt distribution system, one should also consider the way one can minimize the negative centerline macro-segregation.

It is well known that longer the length of the combo-bag the greater is the sump profile, which is not beneficial for the prevention of macro-segregation. The computed solidification front at the wide symmetry plane is deeper and more uniform and this is consistent with the observations made by Xu et al. [141,142]. The general shape of the predicted solidification profile of the present model is in good agreement with the general shape of the predefined and the design of the artificial solidification profiles which are used in most physical water models such as the one designed by Xu et al. [141,142]. From the solidification profiles measured in real vertical DC casters, the physical water models are usually designed to take in to account the resistance which is offered by the solidification front.

Figures 4.3 (b,d,f) show the temperature contours for three longitudinal planes. From these figures one can see that the solidification front moves upward as one travels toward the wider face and it becomes more horizontal which indicates the increase of the heat extraction rates.

4.1.6 Quantitative Verification of Results and Related Discussion

The positions of the solidification front from the experimental measurements and predicted from the present numerical model are compared graphically in Figure 4.5 and quantitatively in Table 4.3. Similar to the experimental results, the computed results are shown from the top of the mold, neglecting the axial length of the hot top.

Jones et al. [70] provided the measured temperatures at the ingot wide symmetry plane (Fig. 4.4). During the real casting experiment, because of the failure of the thermocouple number 5 (TC5), the authors could not record the temperature at a distance of 284 mm from the slab center. The nearest distance from the slab center they could measure the temperature was 309 mm (thermocouple four (TC4)). The relative percentage difference in the vertical distance of the solidification front measured by TC4 and the present predicted value at the same position is 10.31 %. The predicted

solidification front from the top of the mold for the same experimental location as thermocouple number 3 (TC3), which is 411 mm away from the center, matches more closely with the measured solidification front. The computed vertical distance of the solidus isotherm was 382 mm, whereas, the vertical distance of the solidus isotherm was 418.2 mm measured by TC3. A relative percentage difference of 8.7 % is therefore observed (Table 4.3). At location TC3, the predicted and measured solidification front distance from the top of the mold show a very good agreement. Near the boundary, the discrepancy between the predicted and observed solidification front is quite high. At 45 and 147 mm distance from the narrow side of the mold wall, at the wide symmetry plane, the observed relative percentage differences of the depth of the solidus isotherm are 119.4 % and 46.89 % (TC1, TC2). It is apparent from the above comparison of the depth of the solidification front that closer to the slab center, the predicted and measured distances matched quite well, while further the thermocouples were away from the center and near the side wall the match is not that satisfactory. This could be due to the fact Jones et al. did not measure the thermal boundary conditions experimentally, and as a result, the employed thermal boundary conditions used in the model might not have been appropriate.

Table-4.3: Comparison of experimentally measured and numerically predicted vertical distance of the solidification front from the top of the mold at the wide symmetry plane (z = 0) for aluminum (Al-3104) alloy.

Number of sacrificial thermocouple	Horizontal distance from the narrow face of the mold wall at the wide symmetry plane (mm)	Jones et al. exp. (1999) (mm)	Present numerical prediction (mm)	Relative percent error
1	45	63.8	140	119.4 %
2	147	191.3	281	46.89 %
3	249	418.2	382	8.66 %
4	351	568.6	510	10.31 %

4.1.7 Closure

The current mathematical model has been verified quantitatively with the real casting experiment of Jones et al. [70]. The discrepancies between experimentally measured and numerically predicted solidification profile decreased with the horizontal distance from the slab narrow face towards the center of the slab. It is believed that the discrepancies could be minimized if the following conditions were fulfilled:

1. Appropriate thermal boundary conditions of the experiment were known.
2. All of the geometrical parameters were correctly known.
3. Instrumental uncertainties, which invariably arouse in the experiments, were reported.

Closer to the ingot center, a good agreement obtained with regard to the vertical distances of the solidification front is an indication that the heat transfer, namely, conductive, convective, solidification which are at play in the caster as well as the turbulent aspects of the process are well incorporated in the mathematical model.

4.2 Grid Independency Test

The grid independency tests are presented in this section. Any numerical solution results can be taken as a realistic representation of the model only if the simulation results show that they are essentially independent of the small changes in the time step and grid structure. In order to generate grid independent results three sets of grid distributions were tested for an open-top melt delivery system for Al-1050 alloy. The properties of Al-1050 and the geometrical dimensions employed in the mathematical model are summarized in Table 3.1 of Chapter-3. The boundary conditions for the momentum, energy and turbulence variables were the same as those given in detail in Chapter-3 earlier. The casting speed and inlet melt superheat were kept at 100 mm/min, and 32^0C, respectively. To incorporate the thermal buoyancy effect, the Grashof number, Gr = 10^9

was considered in all three cases. The first run was carried out with a coarse grid having a size of $60\times42\times24$ (x, y, z directions respectively) grid points, which constituted 51,040 control volumes. The second run was implemented with a medium sized grid of $70\times52\times34$ grid points, which constituted 108,800 control volumes. In the third run, a fine grid distribution of $80\times62\times44$ grid points, which constituted 196,560 control volumes, was employed. From the coarse grid distribution, the grid was refined by adding about 63,280 nodes and 94,480 nodes at two successive steps to generate the medium and fine grid distribution, respectively. In the current developed mathematical model, the grid points were arbitrarily distributed non-uniformly with more grids at the regions of high gradients and near the expected locations of the solidification front. Figures 4.6 (i, ii, iii) show typical non-uniform distributions of the grids in the calculation domain for three cases, where, Figures 4.6(i)(a) and 4.6(i)(b) indicate grid distributions at the narrow and wide slab faces for the coarse grid, Figures 4.6(ii)(c) and 4.6(ii)(d) show grid distributions at the narrow and wide slab faces for the medium grid, and Figures 4.6(iii)(e) and 4.6(iii)(f) represent grid distributions at the narrow and wide slab faces for the fine grid. The local surface heat flux at around the middle of the wide slab face at y = 430.5 mm and at around the corner of the narrow slab face at z = 322.5 mm from the center of the ingot and along the axial distance for three different grid arrangements are compared at steady state. The results are compared in the graphical form (from x = 135 to x = 400 mm from the top free surface) in Figures 4.7, and 4.8. In Tables 4.4 and 4.5 the numerical values of the local surface heat flux (kW/m^2) along the axial direction (from near the end of the mold-metal contact inside the mold to x = 395 mm) at y = 430.5 mm and at z = 322.5 mm are listed. Convergence was declared when the sum of the residuals for each calculated variable (R_Φ) was less than 10^{-4}. It is evident from Figures 4.7, and 4.8 that at the mold-metal contact region the local heat flux reduces gradually. In the air-gap region, the local surface heat flux is decreased dramatically. Then the heat flux again is enhanced due to the intense cooling of the slab surface at the secondary cooling region. The coarse, medium, and fine grid simulations results presented in the above two figures show insignificant variations in the local surface heat flux at two different locations of the slab caster. The numerical values of the relative percentage change in the local surface heat flux with respect to the coarse grid from the bottom part of the mold and along the

vertical direction at two different locations of the slab caster (at y = 430.5 mm, and z = 322.5 mm) are summarized in Tables 4.4, and 4.5. It can be seen from the Tables that the relative percentage change in the local surface heat flux is less than 5 %. The three runs show very good agreement considering the appreciable variation in grid size or number of cells. Therefore, to optimize CPU resources with an acceptable level of accuracy and reasonable computational time, all production runs were performed with a grid distribution of $60\times42\times24$ grid points (or 60,480 nodes).

Table-4.4: Numerical values of local surface heat flux at a casting speed of 100 mm/min and at a superheat of 32°C along the axial distance of the strand on the wide slab face at y = 430.5 mm from the ingot center.

Distance from the top free surface (mm)	Local surface heat flux (kW/m^2)			Relative Difference between grid size of 70x52x34 and 60x42x24 in %	Relative Difference between grid size of 80x62x44 and 60x42x24 in %
	Grid distribution: $60\times42\times24$	Grid distribution: $70\times52\times34$	Grid distribution: $80\times62\times44$		
195	670.66	663.86	664.12	1.013927	0.975159
205	59.16	58.27	58.1	1.504395	1.791751
215	4161.93	4173.91	4153.37	-0.28785	0.205674
225	3036.67	3027.02	3005.09	0.317782	1.039955
235	2427.81	2422.05	2399.95	0.237251	1.147536
245	1999.21	1994.82	1974.21	0.219587	1.250494
255	1619.37	1613.97	1596.26	0.333463	1.427098
265	1561.9	1557.64	1540.27	0.272745	1.384852
275	1499.04	1495.29	1478.74	0.25016	1.3542
285	1438.43	1435.75	1420.2	0.186314	1.267354
295	1381.96	1380.99	1366.5	0.07019	1.118701
305	1329.96	1331.22	1317.77	-0.09474	0.916569
317.5	1268.85	1273.52	1261.34	-0.36805	0.591875
335	1193.17	1203.32	1192.74	-0.85068	0.036038
360	1098.42	1117.09	1108.48	-1.69971	-0.91586
395	990.77	1020.53	1013.95	-3.00372	-2.33959

Table-4.5: Numerical values of local surface heat fluxes at a casting speed of 100 mm/min for a melt superheat of 32°C along the axial distance of the strand on the narrow slab face at z = 322.5 mm from the ingot center.

Distance from the top free surface (mm)	Local surface heat flux (kW/m^2)			Relative Difference between grid size of 70x52x34 and 60x42x24 in %	Relative Difference between grid size of 80x62x44 and 60x42x24 in %
	Grid distribution: $60\times42\times24$	Grid distribution: $70\times52\times34$	Grid distribution: $80\times62\times44$		
195	434.16	436.88	447.92	-0.6265	-3.16934
205	35.11	35.13	36.1	-0.05696	-2.81971
215	1967.69	1945.88	2003.81	1.108406	-1.83566
225	1172.46	1135.88	1181.39	3.119936	-0.76165
235	820	794.31	841.96	3.132927	-2.67805
245	624.37	606.54	637.02	2.855679	-2.02604
255	482.68	469.6	495.23	2.70987	-2.60007
265	445.27	432.92	457.71	2.773598	-2.79381
275	409.3	397.02	427.46	3.000244	-4.43684
285	377	364.84	391.89	3.225464	-3.9496
295	348.57	336.68	361.04	3.41108	-3.57747
305	323.72	312.2	334.4	3.558631	-3.29915
317.5	295.93	284.99	304.92	3.69682	-3.03788
335	263.77	253.77	271.29	3.791182	-2.85097
360	226.65	218.13	233.07	3.7591	-2.83256
395	188.32	181.86	194.31	3.430331	-3.18076

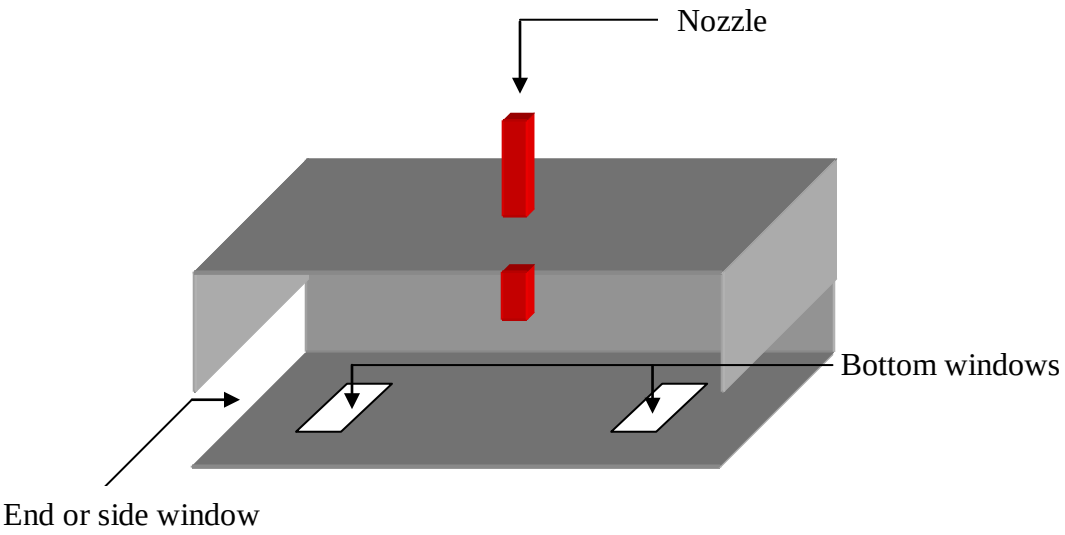

(a) Combo bag

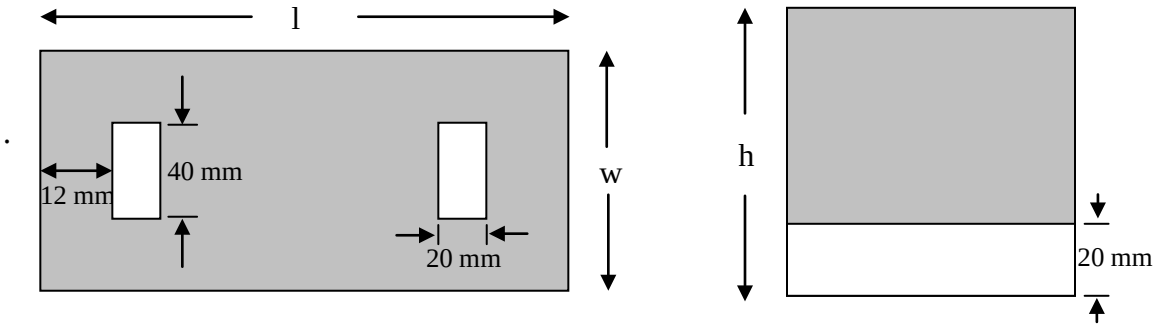

(b) Bottom view (c) Side view

Figure 4.1: Schematic of a combo-distribution bag

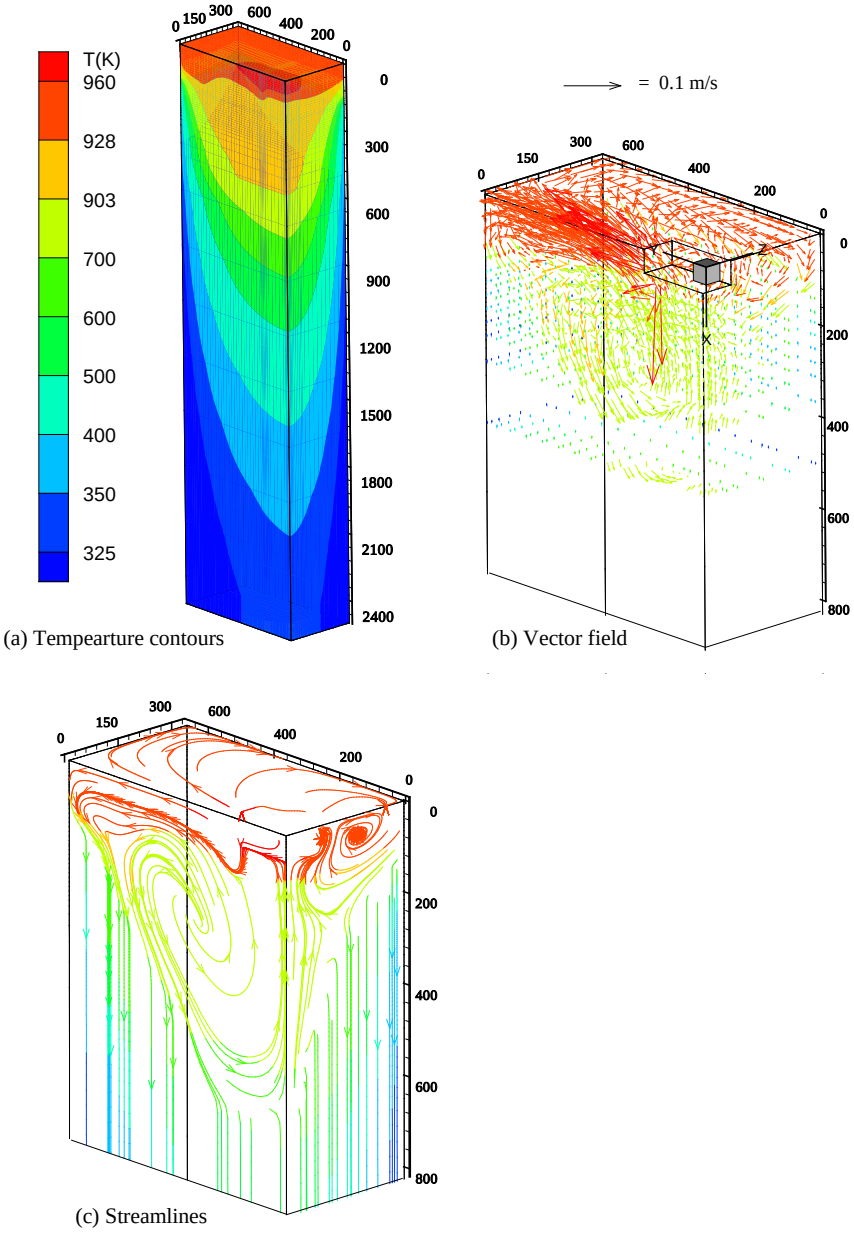

(a) Tempearture contours

(b) Vector field

(c) Streamlines

Figure 4.2: 3-D surface plot using the combo bag, casting speed = 50.8 mm/min, inlet melt superheat = 45°C, Gr = 10^9.

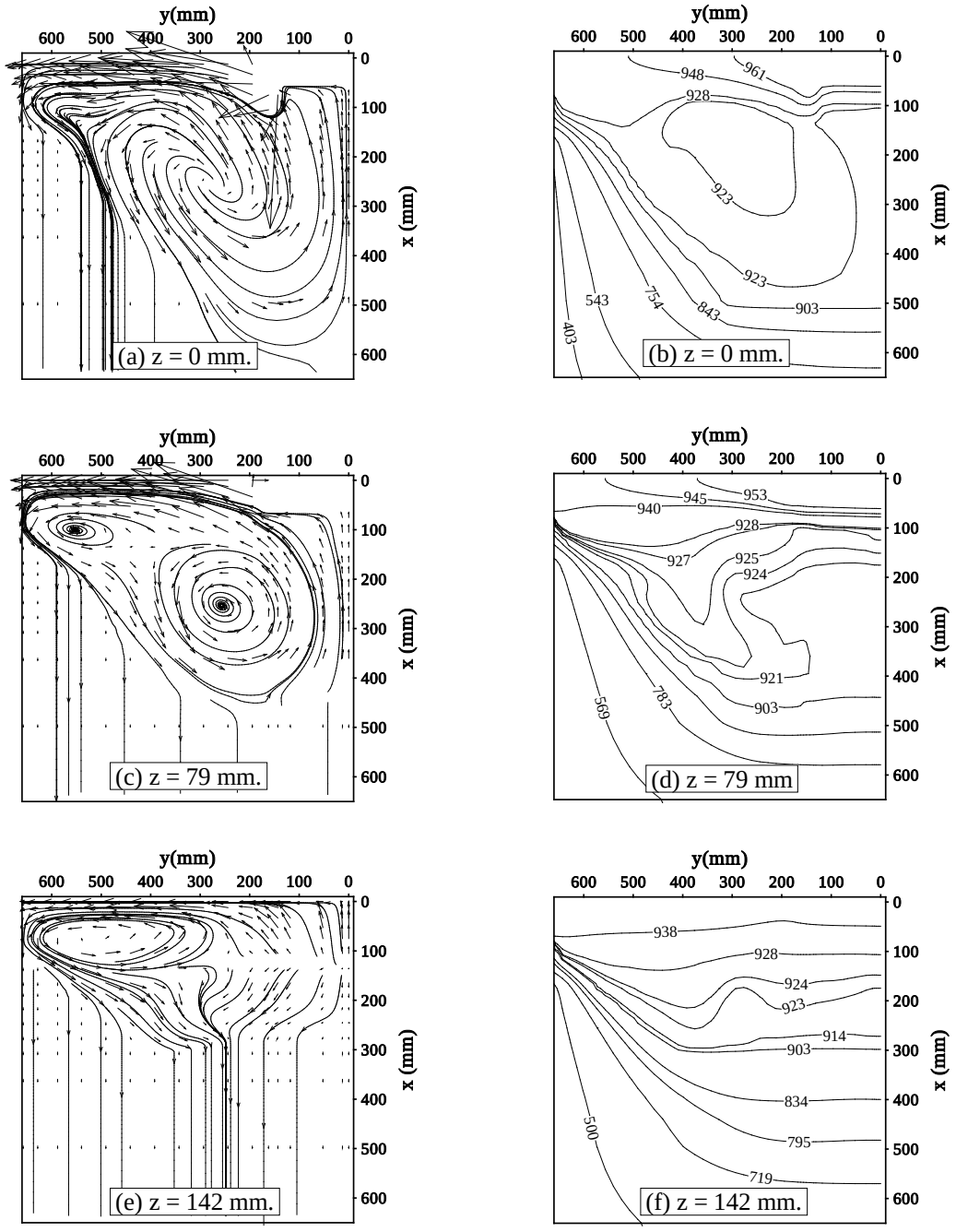

Figure 4.3: Computed results parallel to the slab rolling face using the combo bag at the casting speed of 50.8 mm/min, inlet melt superheat of 45°C and Gr = 10^9: (a,c,e) vector and streamlines plot, (b,d,f) temperature contours in Kelvin.

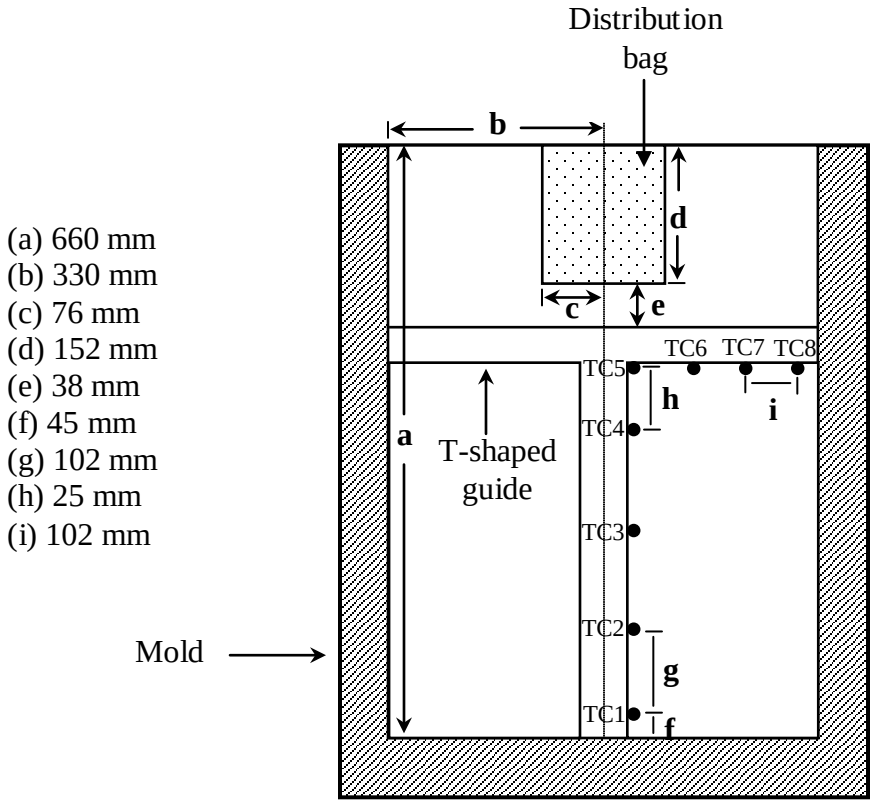

Figure 4.4: Top view of the real casting experiment showing thermocouples distribution.

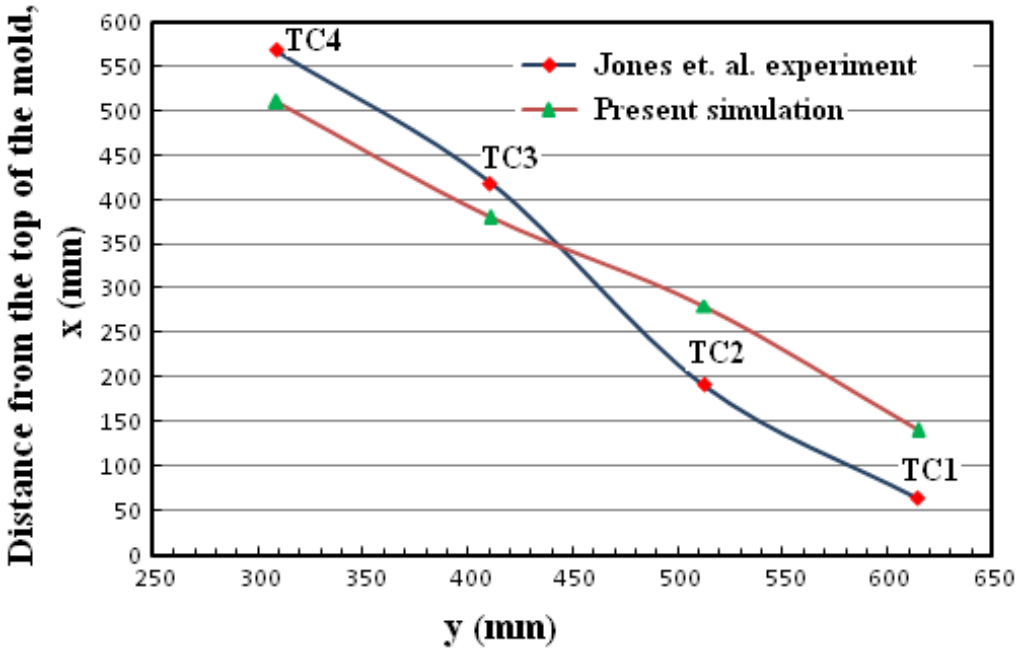

Figure 4.5: Sump profiles at the wide symmetry plane determined through experiments and the corresponding numerical predictions.

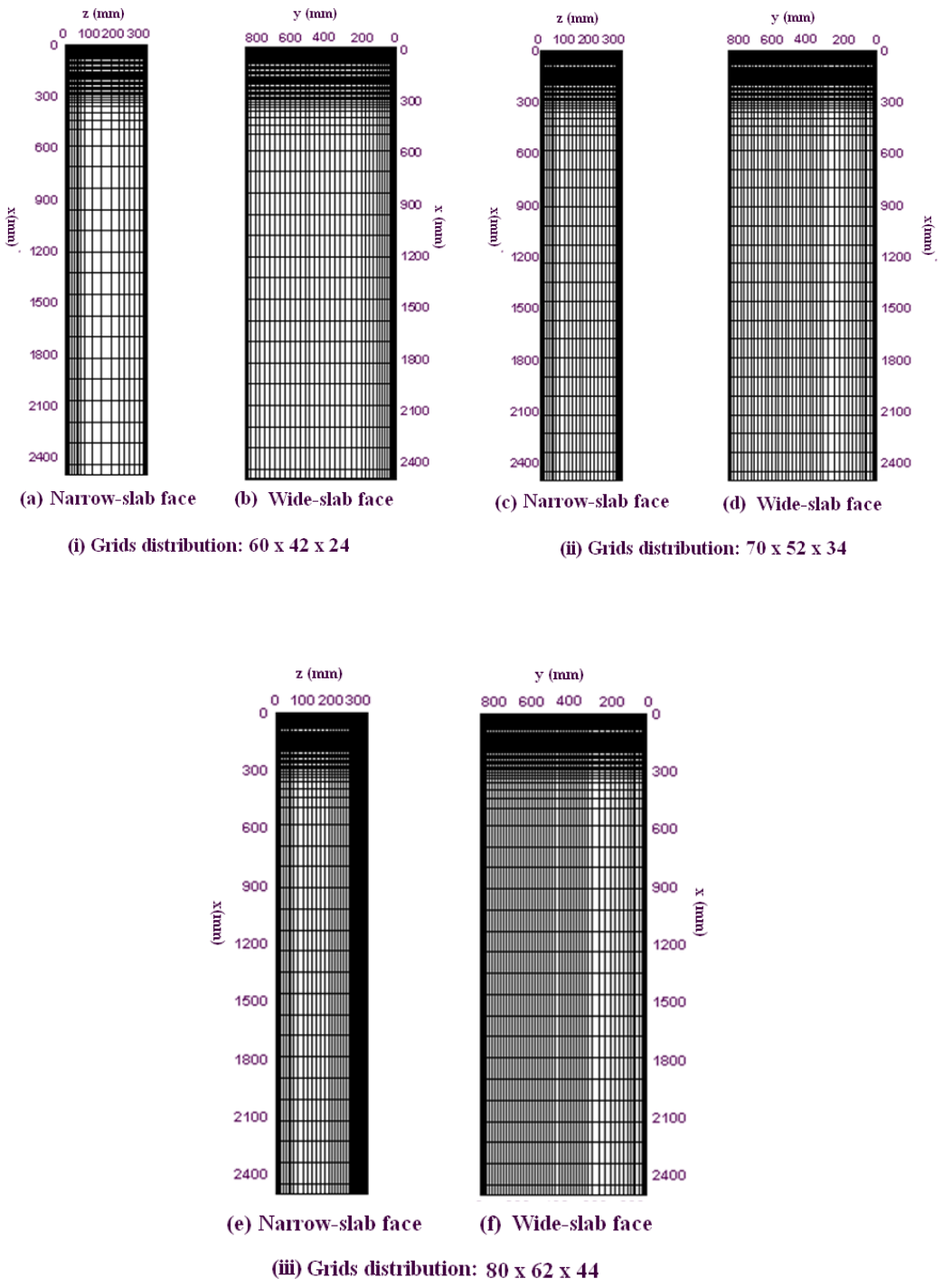

Figure 4.6: Non-uniform distribution of the grid in the x, y, z directions, respectively, inside the calculation domain, for: (i) coarse-sized grid of $60\times42\times24$ grid points (ii) medium-sized grid of $70\times52\times34$ grid points, and (iii) fine-sized grid of $80\times62\times44$ grid points.

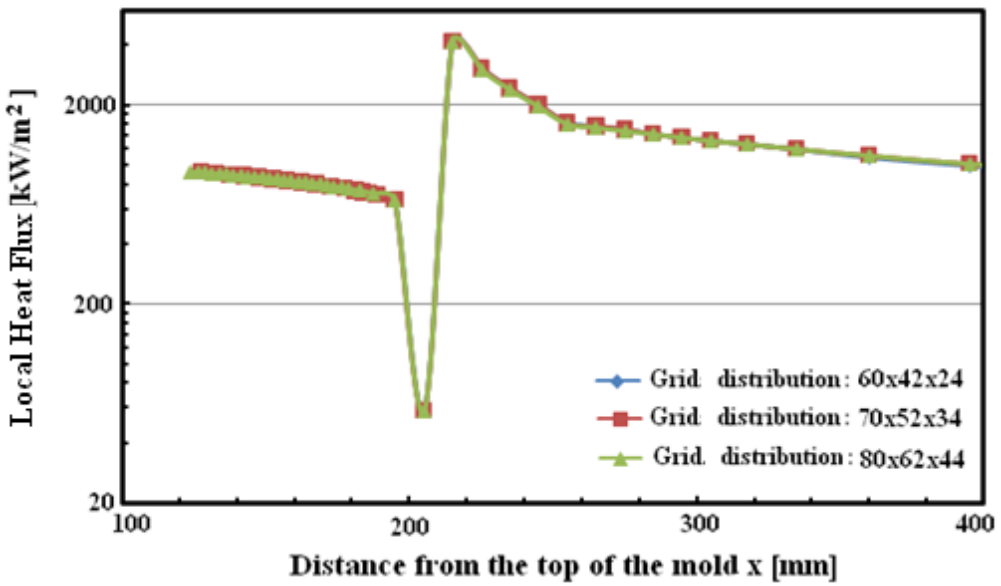

Figure 4.7: Variations of local surface heat flux at a casting speed of 100 mm/min and a melt superheat of 32°C along the axial distance of the strand on the wide slab face at y = 430.5 mm from the ingot center for an open top melt delivery system for a coarse, medium and fine grid distribution.

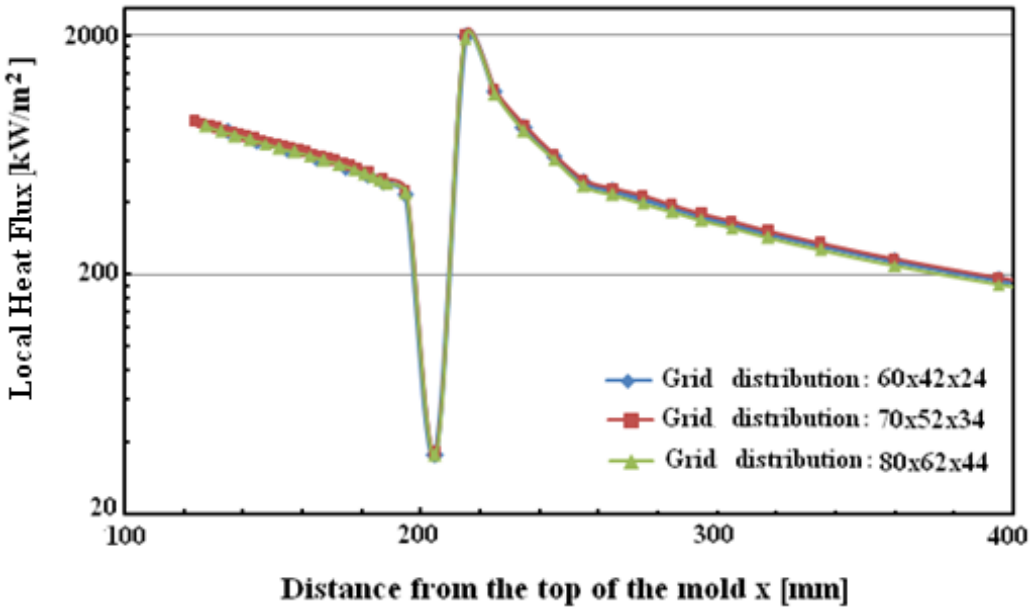

Figure 4.8: Variations of local surface heat flux at a casting speed of 100 mm/min for a melt superheat of 32°C along the axial distance of the strand on the narrow slab face at z = 322.5 mm from the ingot center for an open top melt delivery system for a coarse, medium and fine grid distribution.

CHAPTER 5

THREE-DIMENSIONAL THERMAL MODEL

5.1 Introduction

The temperature distribution in a DC cast aluminum ingot is closely related with the majority of the phenomena appearing during casting, such as surface quality, microstructure, cracks, deformation and porosity, etc [23,54,55,68,86]. The casting parameters used during a cast control the distribution of temperature. These parameters can be defined in terms of heat input and heat sink. The heat input is mostly governed by the melt inlet temperature, filling practices and casting speed, while the heat sink is controlled by the mold technology, the water flow rate, water composition, impingent angle and length, ingot surface temperature, start-up technologies such as pulsed water, heat extraction through the bottom block [57,104,116], etc.

In DC casting the duration of the mold-metal contact is quite short, ending within 70-90 mm. As a result, this process needs faster heat extraction through the shorter mold to form a thicker, and stronger solid shell. Due to solidification shrinkage of solid aluminum, the newly formed solid shell starts to contract away from the mold faces starting from very near to the meniscus. This leads to the generation of contact resistances or air gap (which depends on the mold design) around the entire perimeter, which in turn reduces the heat transfer to the mold and results in a reheating effect within the shell. In addition, the cast surface develops thicker oxide layers with different properties, which may further enhance the contact resistance of the interfacial gap. These interfacial resistances predominantly control the heat transfer in the mold region.

The heat extraction rate in the mold region during DC casting is termed primary cooling, and is one of the most prominent features since the mold cooling should be efficient enough to form a stable solid shell at the exit of the mold. Two important factors are believed to control the extent of primary cooling. The first one is the velocity of cooling water which determines the temperature of the hot face wall of the mold. If the

velocity of the cooling water becomes too low, this will lower the heat-transfer coefficient at the cold-face wall of the mold, and thereby can decrease the heat removal rates. Another factor affecting the heat transfer on the mold walls is the impurities in the water, which sometimes form deposition of scale on the mold cold-face, leading to an increase in mold temperature, especially near the meniscus where the mold temperature is too high. In the extreme cases, the increasing temperature of the mold cold-face may locally boil the water which may lead to the formation of a stable film of air bubble on the inner mold walls. This may virtually stops heat extraction and cause surface defects on the cast. In the literature, the study on the impact of mold cooling water on primary cooling has not been well explored.

In DC casting, the mold cooling water also has an important role, since the same water is used in the secondary cooling zone. The secondary heat extraction process is also critical as primary cooling [20]. In secondary cooling regions, continuous streams of water jet emerge from the series of holes located below the water-cooled mold. These holes are located at the base of the mold and they are machined to maintain a certain inter-space distance between them. In the water impingement zone, the distance between the holes prevents a direct contact of water on the vertical ingot surface, which leads to uneven heat extraction rates on the hot metal surface exiting the mold.

Because of the above mentioned complexities, it is important to understand the physical concepts of the DC casting process, and to estimate the important process parameters, the input variables and to finally calculate the effects of varying of any of the parameters on the temperature distributions. In order to reduce the associated costs and to improve product quality, a theoretical model can offer a powerful alternative to study many of the complex sequence of events which governs heat transfer in the DC casting process as compared with the experimental work. It is, however, inevitably a challenging work to develop a comprehensive mathematical model including all diverse phenomena. The present work is undertaken to develop a 3-D mathematical model by solving the energy equation, taking into account mushy-zone and solidification of an aluminum alloy. The model is capable of determining the temperature profile across a cast slab in three different regions, namely, liquid, solid, and mushy at steady state by considering the critical factors that affect the quality of a strand. The developed model only considers the

axial heat convective effect. In the later chapters, the effects of 3-D fluid flow are included in the model.

Several previous modeling attempts have been made by other researchers incorporating the turbulent fluid flows, heat transfer, and macroscopic solidification of the aluminum alloy to get the desired thermal history of the strand surface. All these modeling efforts reported excessive computational time. In order to develop an automatic control system for this process, one needs either temperature predictions within a very short time or real time temperature measurements. Only, the thermal modeling studies can provide within a short time the predicted temperature distributions in the cast which could be beneficial for the development of process control strategies for such processes. The thermal model could also be used in the initial design and process developments. Hence, in this study a 3-D heat convection-conduction model is developed which could provide a greater incentive in implementing a real-time automation system on a DC caster.

Over the years, a number of thermal models have been developed incorporating various complexities to predict the temperature profile in the ingot based on casting practice variables. Majorities of these studies were concerned with round billets where a 2-D analysis is applicable due to axis-symmetry. For a square or a rectangular cross-sectional ingot a 2-D analysis will invariably give incorrect results. There are very few studies on square and rectangular slabs where a three-dimensional analysis has been carried out. To the best of the author's knowledge the 3-D convection-conductive numerical study for the said caster (Chapter-3, Section 3.2(a)) and alloy (Chapter-3, Section 3.2(b)) is not available in the literature.

Many researchers without solving the turbulent flow field in the liquid pool have developed the thermal models by increasing arbitrarily the conductivity of the liquid metal by a factor of 7 to10 to incorporate the effects of turbulent melt convection on the growth of the solid shell and sump depth. A uniform and arbitrary increment of liquid conductivity in the liquid sump cannot give the true picture of thermal convection there. In this model such a practice is not implemented.

Figure 5.1 shows a schematic view of a vertical DC casting slab. Due to two-fold symmetry, a quarter of a slab was considered as the simulation domain which is

represented by the yellow part in Fig. 5.1. The coordinate system was fixed to the hot-top. The origin of the coordinate system was at the center of the ingot, and the axial coordinate was in the direction of gravity. The solid-shell once formed was shifted downward at the casting speed. The molten metal was supplied at the casting speed at the entire cross-section of the top surface. The thermo-physical properties of AA-1050 aluminum alloy used in the simulations are listed in Table 3.1 of Chapter-3.

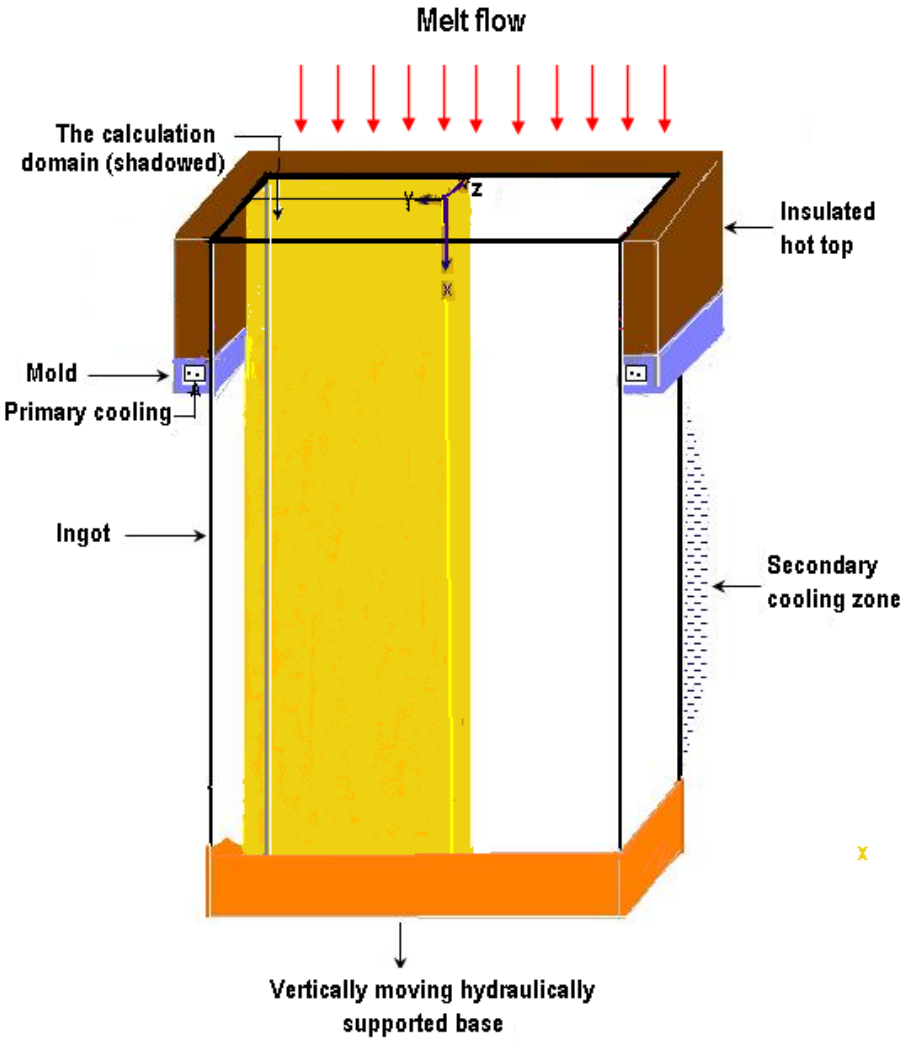

Figure 5.1: Schematic of the DC caster with the yellow part representing the computational domain for an open-top melt feeding scheme.

5.2 Governing Equations

The steady-state temperature field within the considered domain can be described by the following governing equations.

$$\frac{\partial(\rho\ C_P T)}{\partial t}+\frac{\partial(\rho C_P u_i T)}{\partial x_i}=\frac{\partial}{\partial x_i}\left[k\frac{\partial T}{\partial x_i}\right] \qquad \text{----------(5.1)}$$

The above equation is written in Cartesian tensor notation form, where 'j' represents x, y, or z direction. In the steady state model, the term $\left[\partial(\rho C_P T)\big/\partial t\right]$, as well as the two convective terms in the y and z directions are also neglected. A single domain enthalpy-porosity approach is considered in the present model, and details of this technique are presented in Section 3.2.3 of Chapter-3.

After implementing this concept, the energy equation takes the following form:

$$\frac{\partial(\rho u_i h)}{\partial x_i}=\frac{\partial}{\partial x_i}\left[\frac{k}{C_P}\frac{\partial h}{\partial x_i}\right]-\frac{\partial(\rho u_i \Delta H)}{\partial x_i} \qquad \text{----------(5.2)}$$

Because of using a single domain approach the above energy equation is applicable for the entire calculation domain including solid, liquid, and mushy regions. The control volume which contains the mushy region, where liquid and solid fractions co-exist, the liquid fraction there can be shown to represent the nodal latent heat. The nodal latent heat is zero in the solid phase and is equal to the latent heat of fusion (λ) in the liquid phase. In the mushy region, the latent heat can be any function of liquid fraction. In the current model, it is assumed to very linearly with the liquid fraction.

$$\Delta H=\lambda f_l \qquad \text{----------(5.3)}$$

Where f_l is the liquid fraction, which is related to temperature as:

$$f_l=\begin{cases} 1 & when \quad T \geq T_l, \\ \dfrac{T-T_s}{T_l-T_s} & when \quad T_l \geq T \geq T_s, \\ 0 & when \quad T \leq T_s. \end{cases} \qquad \text{----------(5.4)}$$

where T_l and T_s are the liquidus and solidus temperatures, respectively.

In order to get generalized results, the governing energy equation and associated boundary conditions were cast into its dimensionless form. The details of the primitive and dimensionless variables were presented in Section 3.2.8 of Chapter-3. Using the dimensionless parameters given in Chapter-3, the Eqn. (5.2) becomes:

$$\frac{\partial(Uh^*)}{\partial X} = \frac{1}{Pe}\frac{\partial}{\partial X_i}\left[\frac{\partial h^*}{\partial X_i}\right] - \frac{\partial(U\Delta H^*)}{\partial X} \qquad \text{----------(5.5)}$$

where, U is the slug velocity which is 1.0 (non-dimensional value) and the primitive inlet velocity u_{in} is equal to the casting speed. A governing parameter Pe which appears in the right hand side of Eqn. 5.5 is called the Peclet number. The Peclet number for heat transfer can be defined as the ratio of heat transfer due to convection and conduction, and it is a product of Prandlt number (Pr) and Reynolds number (Re_L).

$$Pe = \frac{\rho C_P U_S L}{k} = \text{Pr x Re}_\text{L}$$

where, ρ is the density, C_P is the specific heat, U_S is the casting speed, L is the characteristic length, k is the thermal conductivity. From Table-5.1, it is evident that at four casting speeds the Peclet number is relatively large, i.e., *Pe* > 10. For a high *Pe* one can neglect the effect of downstream flow on upstream which makes the computation model simpler. In the context of the present model one could have neglected the diffusive component in the axial direction. In the present model this approximation has not been invoked.

It is to be recognized here that beside *Pe* another parameter appears in the non-dimensionalization of the thermal boundary conditions, which is the Biot number ($Bi = \frac{\gamma D}{K}$) where, γ is the effective convective heat transfer coefficient, D is the characteristic length, and K is the conductivity of the solid. The parameter *Bi* represents the ratio of convective to conductive heat transfer at the surface. In the present thermal

model, at the mold *Bi* was kept fixed at about 6.2 while at the air gap region it took a value of 0.62. At the water impingement point *Bi* was about 82.73 and it decreased linearly to a value of 41.36 within a cast length of 40 mm. For the rest of the length of the caster beyond 255 mm the value of *Bi* was fixed at the latter value.

Table 5.1: Values of the parameter used in thermal model.

Case	Casting speed (mm/min)	Prandtl number (Pr)	Inlet Peclet number (Pe)
1	60	0.0063	10.07
2	100	0.0063	16.78
3	140	0.0063	23.5
4	180	0.0063	30.21

5.3 Boundary conditions

The dimensionless thermal boundary conditions imposed on the computational domain are given in Figure 5.2 for easy visualization. The details of the used effective heat transfer coefficients at various regions of the ingot surface and geometrical dimensions were presented and discussed in Sections 3.2.6, and 3.2 (a) of Chapter-3. The corresponding Biot numbers (*Bi*) are given in the earlier section.

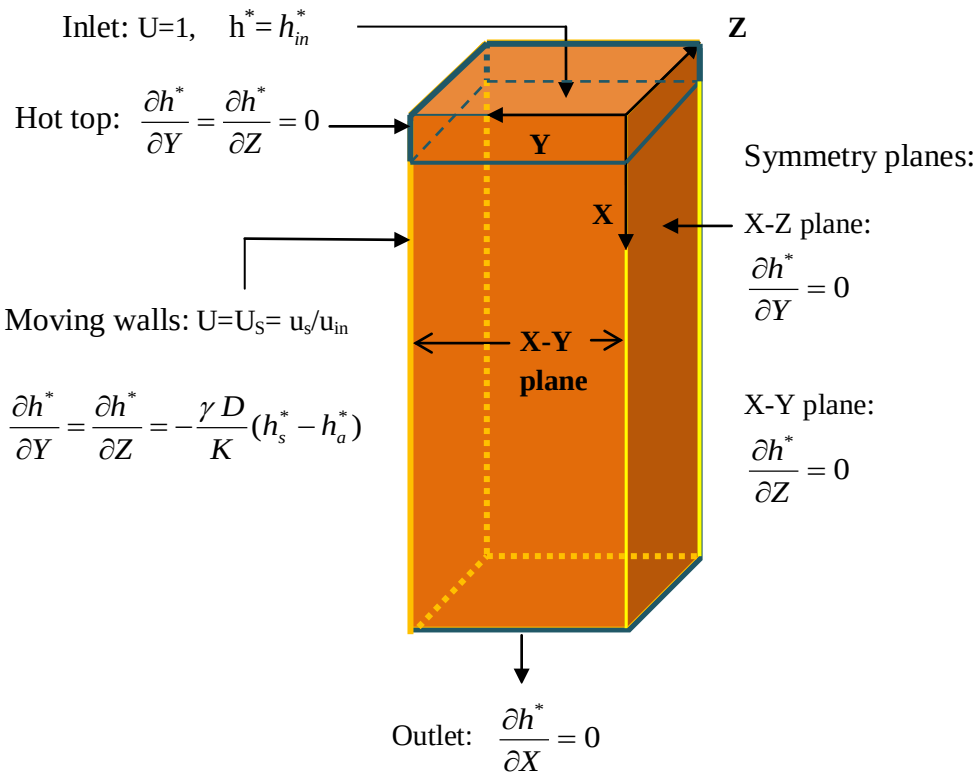

Figure 5.2: Schematic illustrations of the configuration with the boundary conditions.

5.4 Results and Discussion

In this section, the definition of related variables which will be used in the presentation of results will be discussed. These are the sump depth, thickness of the solid shell and local surface heat flux along the ingot length. Detail of the calculation of local surface heat flux is given in Section 3.2.7 of Chapter-3.

The sump depth is defined here as the vertical distance along the ingot centerline from the top of the mold to the solidus isotherm. In Figure 5.3, sump depth ($\bar{x}$) is shown. The thickness of the solid layer (y_b) is measured from the narrow face at the wide symmetry plane. Figure 5.3 shows how the above quantities are obtained from the plot of solidification front at the wide symmetry plane.

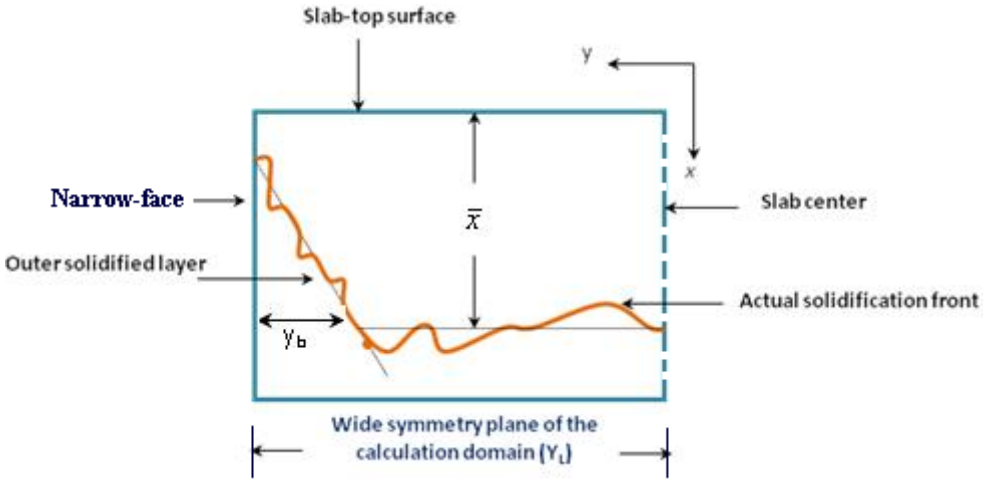

Figure 5.3: Schematic explanation of the sump depth ($\overline{x}$) and shell thickness (y_b).

In order to improve the quality of the castings and reduce production costs, it has become increasingly important to understand and control the casting process. The main parameters that influence the ingot characteristics are:

- Casting speed: This refers to the speed at which the solid is withdrawn from the mold. The casting speed directly influences convection in a proportional way.
- Melt inlet superheat: This is defined as the difference between the inlet and liquidus temperature. The inlet melt temperature has a strong effect on the temperature gradients in the liquid pool. The superheat needs to be adjusted for each alloy to accommodate for the proper growth of the solidified shell.
- Water-flow rate (the cooling rate): The cooling rate in the primary and secondary regions critically depends on the water flow rate and its temperature. Other parameters such as the quality as well as the pH of the cooling water will also have an effect on the heat extraction rates.

In this study, the first two important parameters, namely, casting speed and melt inlet superheat were varied. Instead of varying the water flow rate and its temperature, the imposed effective heat transfer coefficients for the primary and secondary cooling zones were taken as suggested in the literature. In order to ascertain the effects of the casting speed and delivered superheat on the temperature distribution, the solidification profile,

and the local surface heat flux, the simulation runs are carried out for four casting speeds viz., 60, 100, 140 and 180 mm/min and for two inlet superheats of 32^{o}C and 64^{o}C.

a. Effect of Casting Speed for a Fixed Inlet Superheat of 32^{o}C

i. Temperature Field

Figures 5.4 (a,b,c,d) show the 3-D surface plot of the numerically predicted isotherms distribution in a flooded format for four casting speeds and for a fixed melt inlet superheat of 32°C. Each 3-D surface plot corresponds to a one-quarter section of the domain which consists of two symmetry planes, a wide (x-y plane) and a narrow (x-z plane) planes as well as the top melt entry region of the rolling slab ingot. In these figures, the red color and the dark yellow color represents the liquid and the mushy region (located between liquidus (657^{o}C) and solidus (646^{o}C) temperature contours), respectively. Below the solidus isotherm, the aluminum alloy is in the solid state. A classical parabolic-shaped solidification front is obtained at each casting speed, while the solidus and liquidus isotherms remain nearly planner in shape over a significant portion in the central area. The horizontal extent of the solidus isotherm is decreasing with the increase of casting speed. The reason behind this observation is that at a lower casting speed the conduction mode of heat transfer near the solidification front is increasing. From these figures, it can be clearly seen that the volume of the liquid region inside the domain is increased with increasing in the casting speed which is visible in the increased red color region. As casting speed increases, the solidification front as well as the other isotherms are becoming steeper and are moving downward. The mushy region is also seen to be expanding with casting speed. Due to the increase in the volumetric flow rate as well as with the accompanying decrease of the residence time of the melt, with the increase of the casting speed, the ingot is not sufficiently cooled by the extraction of heat for the same effective convective heat transfer coefficients in the primary and secondary cooling regions. In all of the above figures, the solidification front is non-uniform, and this is particularly visible near the middle of the wide symmetry plane. This non-uniformity may be due to the numerical artifact from the modeling technique used in the mushy region or it could be due to the representation of the real solidification process

happening in the ingot. Experimentally, a considerably more coarse-cell structure towards the center of the ingot is observed for higher sump depth. Also, more solute depleted grains are seen to accumulate in the central part for a higher sump depth, and this is believed to be the cause of negative centerline segregation [36]. So, deepening of the sump is not desirable in a DC casting process.

Figs. 5.5 (i) to (iii) illustrate the 2-D projections of the temperature contours at three longitudinal cross-sections. Isotherms shown in Figs 5.5 (a,b,c,d) through Figs 5.5 (i,j,k,l) represent the effect of the casting speed at the wide symmetry plane (z = 0) and parallel to the wide symmetry plane at two inward locations, viz., z = 62.5 mm, and z = 312.5 mm, for four casting speeds all for an inlet superheat of 32^{o}C. As one proceeds from the wide symmetry plane along the narrow face toward the wide face, the rate of heat extraction increases, which is manifested through the shapes and locations of the isotherms at these three longitudinal planes for each casting speed. The isotherms are observed to have lifted upward compared to the symmetry plane. From these figures, one can further see that with the increase of the casting speed both the liquidus and the solidus isotherms are moved downward and there is an increase in the vertical distance between them.

Through 2-D plots, the developments of the solid shell and mushy zone at different transverse cross-sections (y-z plane) parallel to the top surface, for four casting speeds and for a delivered superheat of 32^{o}C, are illustrated in Figures 5.6(a-d). In these figures, the shape of the solidification front and the extent of the mushy zone have been depicted for an interval of 100 mm distance in the cast direction from the ingot top, at seven y-z planes. With the increase in the axial distance, as more heat is being extracted from the ingot through the mold and by the chilled water jets, the thickness of the solid layer from the wide and narrow sides, presented by the blue color, progressively increases as can be seen from these figures at each casting speed. The apparent uniformity in the thickness of the solid shell on the narrow and wide faces signifies that a uniform rate of heat extraction has taken place from both of these sides at each cross-section. Around the corner of the two faces, heat is extracted by these two sides, and as a result there is a higher rate of heat extraction which has resulted in an almost round-

shaped solid layer and mushy zone. The spectacular reduction of the solid region (represented by blue color) along the cast direction with the increase in the casting speed is clearly visible from the above figures. The reasons for which have already been explained in earlier paragraph.

(ii) Quantitative Analysis for $\Delta T = 32^{o}C$

1. Sump Depth and Mushy Layer Thickness

Table 5.2 lists the numerically predicted sump depth and the mushy layer thickness at the ingot center for four casting speeds. From this table it is observed that a deeper sump depth and a thicker mushy layer are obtained at a higher casting speed. The sump depth is found to be approximately 342 mm from the top of the mold for a withdrawal speed of 60 mm/min. Compared to the lowest simulated casting speed of 60 mm/min, the relative difference in sump depth for higher casting speeds of 100, 140, and 180 mm/min, is about 43 %, 116 %, and 189 %, respectively higher. From this table it is observed that the mushy region or the vertical distance between the liquidus and solidus isotherms at the ingot center has enlarged with casting speed.

Table-5.2: Sump depth and mushy thickness in mm at the center of the ingot using thermal model for four casting speeds and melt superheat of $32^{o}C$.

Quantity	Values of casting speed (u_s) in mm/min			
	60	100	140	180
Sump depth (mm)	342	43.3 % higher than u_s = 60 mm/min	116.4 % higher than u_s = 60 mm/min	188.9 % higher than u_s = 60 mm/min
Mushy thickness (mm)	50	44 % higher than u_s = 60 mm/min	296 % higher than u_s = 60 mm/min	586 % higher than u_s = 60 mm/min

2. Formation of Solidified Shell

The shell thickness is predicted from the narrow slab face at the wide symmetry plane at an axial distance of 160 mm from the top surface, which is plotted as a function of casting speed in Figure 5.10(a). This axial position is located at around the middle of the mold. A gradual decrease of the shell thickness is seen to occur for the increase in the casting speed from 60 to 180 mm/min. For easy comprehension, the magnitude of the relative difference of shell thickness for four casting speeds is demonstrated in Table 5.3. The table is self explanatory so far the casting speed is concerned.

Table-5.3: The thickness of the solidified shell (mm) at wide symmetry plane from the narrow slab face at an axial distance of 160 mm inside the mold for four casting speeds and inlet superheat of 32°C using thermal model.

Quantity	Values of casting speed (u_s) in mm/min			
	60	100	140	180
Thickness of the solidifying shell (mm)	55	50.9 % lower than u_s = 60 mm/min	72.7 % lower than u_s = 60 mm/min	80 % lower than u_s = 60 mm/min

3. Local Surface Heat Flux

Figures 5.11(a) and (b) illustrate the predicted profiles of the local surface heat flux along the cast at the narrow and wide faces for four casting speeds and for $\Delta T = 32^oC$. Generally, the shell is shown to experience rapid changes in the surface heat extraction rate at the mold and in the top portion of the secondary cooling region which creates sharp surface temperature variations that generate high local thermal stress near the shell surface and that usually aggravate cracking problems. In order to investigate any sudden increase or decrease in the surface heat extraction rate, the local heat flux profile is drawn from x =135 mm to x = 587 mm down from the very near of the top of the mold, which is one of the crucial regions for the formation of surface and sub-surface cracks.

Two representative locations have been selected arbitrarily at the narrow and wide face to show a complete picture of the heat extraction rate there. The two locations are:

1. At z = 185 mm (from the wide symmetry plane at z = 0) on the narrow face; this position is located at around the middle of the narrow face of the computational domain.
2. At y = 857.5 mm (from the narrow symmetry plane at y = 0) on the wide face; this position is located near the corner of the wide face of the computational domain.

Near the mold top region at x = 135 mm, a relatively high heat flux is observed due to the higher melt temperature and high effective heat transfer coefficient. The heat flux gently decreases at the surface inside the mold up to an axial length of 195 mm. A very low surface heat flux is obtained due to the application of a low heat transfer coefficient in the air gap compared to the mold region (0.15 versus 1.5 kW/m^2K), which is located at around x = 205 mm. Because of non-uniform heat transfer in the mold and air-gap regions, a significant thermal stress may be developed there which can lead to the unwanted surface and shape defects.

In the secondary cooling region, the maximum heat flux is obtained at the point where water impinges on the slab surface (water impingement point), at x = 215 mm. This is due to the implementation of a very high effective heat transfer coefficient of h = 20 kW/m^2K in that region. The impingement zone is divided into two sections, the water impingement point and the region below the water impingement point. As one moves along the ingot length from the impingement point, the heat flux decreases. There is a sharp decrease of heat flux in the impingement region. In the water impingement zone, the heat transfer coefficient is allowed to vary linearly with the axial distance. Further downstream (from x = 255 mm), the heat transfer coefficient is kept at a fixed value of h = 10 kW/m^2K, and as a result the heat flux decreases gradually with the axial distance. This trend is observed for all casting speeds at these two said locations. The predicted local surface heat fluxes in Figs. 5.11(a) and (b) are the reflection of the imposition of cooling conditions. One should, however be very careful in attributing the

cooling conditions on the strand surface since it is one of the influential factors which determines the solidification structure of the cast.

To understand clearly the role played by the casting speed during the solidification process, and to be more precise, the predicted values of the surface heat flux are listed in Table 5.4 for four casting speeds at z = 185 mm, x = 215 mm, which represents the water jet impingement region. The predicted value of the heat flux at this location is quite high and is the highest compared to the other values along the cast surface. It increases with the increase of the casting speed. From Table-5.4, it is observed that, at a casting speed of 60 mm/min, it is about 3011 kW/m^2, while it is about 30 %, 50 %, and 58 % higher for the higher casting speeds of 100, 140, and 180mm/min, respectively in comparison to the lower casting speed of 60 mm/min.

For the identical effective convective heat transfer boundary condition, at the rolling and end faces, it is evident that, there is a significant difference in the rate of heat extraction for the same axial position. For a fixed casting speed, the local heat flux at z = 185 mm is much higher compared to the value obtained at y = 857.5 mm. The reason is due to the proximity of the wide slab face from the symmetry axis compared to the narrow side.

Table-5.4: The local heat flux (kW/m^2) at z = 185 mm at an axial distance of 215 mm from the top surface for four casting speeds and for an inlet superheats of 32°C using thermal model.

Quantity	Values of casting speed (u_s) in mm/min			
	60	100	140	180
Local surface heat flux (kW/m^2)	3010.6	30.2 % more as compared with 60 mm/min	49.7 % more as compared with 60 mm/min	57.8 % more as compared with 60 mm/min

b. Effect of Casting Speed for a Fixed Inlet Superheat of 64^{o}C

i. Temperature Field

In order to ascertain the effect of a higher inlet melt superheat, simulations were carried out for a superheat of 64^{o}C. The 3-D surface plots of the predicted isotherms for four casting speeds are shown in Figures 5.7(a-d). Figs. 5.8(i) to (iii) illustrate the 2-D projections of the temperature contours at three longitudinal cross-sections. Isotherms shown in Figs 5.8(a,b,c,d) through Figs 5.8(i,j,k,l) represent the effect of the casting speed at the wide symmetry plane (z = 0) and parallel to the wide symmetry planes at two inward locations, viz., z = 62.5 mm, and z = 312.5 mm, for four casting speeds. The temperature fields, at different transverse cross-sections (y-z plane) parallel to the slab top surface, are illustrated for four casting speeds in Figs. 5.9(a-d). In Figs. 5.9(a-d), the shape of the solidification front and the extent of the mushy zone have been depicted for an interval of 100 mm distance in the cast direction from the top of the ingot, at seven y-z planes.

Temperature distributions which are depicted in Figures 5.7(a-d), Figures 5.8(i) to (iii), and Figs. 5.9(a-d) closely resemble to those observed for $\Delta T = 32^{o}$C in the corresponding Figures 5.4(a-d), Figures 5.5(i) through 5.5(iii), and 5.6(a-d). Due to the increase in melt superheat, the existence of additional heat in the liquid region has led the isotherms to move slightly downward.

From the above figures it is apparent that when the superheat is fixed, the change in casting speed has caused the isotherms to move sharply downward but when the withdrawal speed is fixed, a change in superheat has led the isotherms to move rather slightly downward.

(ii) Quantitative Analysis for $\Delta T = 64^{o}$C

1. Sump Depth and Mushy Layer Thickness

For an initial superheat of 64^{o}C, the obtained sump depth and the mushy zone thickness at the ingot center for various casting speeds are listed in Table 5.5. This table

provides a comparison of sump depth and mushy thickness for variable casting speeds. With an increase in casting speed, the above two quantities are increasing proportionately, due to the higher thermal convection caused by the additional melt and lower residence time.

For $\Delta T = 64^oC$, at a casting speed of 60 mm/min, the sump depth is 342 mm, whereas at the higher casting speeds of 100, 140, and 180 mm/min, the sump depth is about 43 %, 131 %, 219 % , respectively , higher in comparison to the lower casting speed of 60 mm/min.

The predicted sump depth at lower casting speeds (≤ 100 mm/min) show that there is virtually no effect of the change in superheat on it. But there is a reasonable difference between the predicted sump depth at two inlet superheats of 32^oC and 64^oC for higher casting speeds (≥140 mm/min). A comparison between these two inlet superheats reveals that, the sump depth at casting speeds of 140, and 180 mm/min for $\Delta T = 64^oC$, is only 7%, and 10%, respectively higher compared to those found for $\Delta T = 32^oC$ (refer to Table 5.2). The insensitivity of the sump depth at lower casting speeds (≤ 100 mm/min) may be due to the approximation made in the thermal model as opposed to the full CFD-type model. Whereas at higher casting speeds (≥ 140 mm/min) the difference in sump depth is observed, because a higher melt superheat for a fixed casting speed introduces more heat into the system, leading to more thermal convection, which justifies the deepening of the sump.

From Tables 5.2 and 5.5, the overall observation is that, for a fixed superheat, a remarkable increase in sump depth has been observed with increase in casting speed, whereas, for a fixed casting speed, the depth of the sump is comparatively insensitive for the selected change in superheat.

Table-5.5: Sump depth and mushy thickness (mm) at the ingot center for four casting speeds and for a superheat of 64^oC predicted by the thermal model.

Quantity	Values of casting speed (u_s) in mm/min			
	60	100	140	180
Sump depth	342	43.3 % higher than	131 % higher than	219 % higher than

(mm)		u_s = 60 mm/min	u_s = 60 mm/min	u_s = 60 mm/min
Mushy thickness (mm)	47	44.7 % higher than u_s = 60 mm/min	338.3 % higher than u_s = 60 mm/min	736.2 % higher than u_s = 60 mm/min

2. Formation of Solidified Shell

The solidified shell thickness, at an inlet superheat of 64^{o}C, as a function of casting speed is plotted in Fig. 5.10(b). Here, the solid-shell thickness is predicted from the narrow slab face at the wide symmetry plane (z = 0) at an axial distance of x = 160 mm from the slab top surface. These values are also quantitatively given in Table 5.6 for four casting speeds. Both, the figure and table show that, an increase in the casting speed gradually decreases the solidified-layer thickness. The same trend has been observed in Fig. 5.10(a) and Table 5.3 for $\Delta T = 32^oC$.

From Table 5.6, it is evident that, for $\Delta T = 64^oC$, at a casting speed of 60 mm/min, the shell thickness is approximately 55 mm, whereas at the higher casting speeds of 100, 140, and 180 mm/min, the thickness of the solidifying shell is about 51 %, 76 %, 94 %, respectively lower in comparison to the lower casting speed of 60 mm/min. A higher thermal convection created by the higher casting speeds is thereby resulting in a thinner shell thickness.

A comparison between the two inlet superheats reveals that, the shell thickness at casting speeds of 140, and 180 mm/min for $\Delta T = 64^oC$, is about 13 %, and 68 %, respectively lower compared to those predicted for $\Delta T = 32^oC$ (refer to Table 5.3). This lower value is obtained due to the additional heat carried by the incoming melt for higher casting speeds which is required to be removed from the liquid before solidification can take place. At lower casting speeds up to 100 mm/min, the change in superheat is found to have almost no influence on the growth rate of solid-shell. As casting speed increases from 140 to 180 mm/min the difference of the shell thickness increases progressively as inlet superheat increases. A potential explanation for this discrepancy is the simplifying

assumptions made in the thermal model, which is the slug flow acting only in the axial direction.

Table-5.6: The thickness of the solidified shell (mm) at wide symmetry plane from the narrow slab face at an axial distance of 160 mm inside the mold for four casting speeds and superheat of 64°C using thermal model.

Quantity	Values of casting speed (u_s) in mm/min			
	60	100	140	180
Solid shell thickness (mm)	55	50.9 % lower than u_s = 60 mm/min	76.4 % lower than u_s = 60 mm/min	93.6 % lower than u_s = 60 mm/min

3. Local Surface Heat Flux

The local surface heat flux on the narrow face at z = 185 mm and on the wide face at y = 857.5 mm along the cast direction for $\Delta T = 64^oC$, for four casting speeds is shown in Figs. 5.12(a) and (b), respectively. The graphs show a very much similar trend to those observed for melt superheat of 32^oC (refer to Figs 5.11(a,b)), and the reasons behind this have already been explained earlier. With the increase in the casting speed, the local surface heat flux increases, as seen previously. Quantitative values of the local surface heat flux for each casting speed at z = 185 mm, x = 215 mm are listed in Table 5.7.

From Table 5.7 one can see, for $\Delta T = 64^oC$, at a casting speed of 60 mm/min, the local surface heat flux, is about 3055 kW/m^2, whereas at the higher casting speeds of 100, 140, and 180 mm/min, the local surface heat flux is about 30 %, 48 %, 58 %, respectively higher in comparison to the lower casting speed of 60 mm/min.

A comparison between the two inlet superheats reveals that, for $\Delta T = 64^oC$, the local surface heat flux at z = 185 mm, x = 215 mm, at casting speeds of 60, 100, 140, and 180 mm/min, is only about 1.5 %, 1.4 %, 0.2 %, and 1.4 %, respectively greater compared to those predicted for $\Delta T = 32^oC$ (refer to Table 5.4).

Comparisons among the four casting speeds and between the two superheats reveal that for a fixed superheat, the predicted local surface heat flux increases

significantly with increase in casting speed, whereas for a fixed casting speed, it increases slightly with increase in superheat.

Table-5.7: The local heat flux (kW/m^2) at z = 185 mm at an axial distance of 215 mm from the top surface for four casting speeds and for an inlet superheats of 64°C using thermal model.

Quantity	Values of casting speed (u_s) in mm/min			
	60	100	140	180
Local surface heat flux (kW/m^2)	3055.34	30.1 % more as compared with 60 mm/min	47.8 % more as compared with 60 mm/min	57.6 % more as compared with 60 mm/min

5.5 Concluding Remarks

In this work, the modeling of 3-D heat transfer and solidification has been carried out by using a simple thermal model for the DC casting of a rectangular rolling slab ingot. The contributions of the studied parameters on the sump depth, the mushy thickness, the thickness of the solidified shell, and the local surface heat flux are as follows:

1. With the increase in the casting speed, the sump depth and the mushy thickness increase significantly at each inlet metal superheat.
2. The predicted sump depth remains virtually independent of the change in the inlet melt superheat at lower casting speeds up to a value of 100 mm/min. But the increase in melt superheat is deepening the sump slightly at a casting speed of 140 mm/min and above.
3. With the increase in the casting speed, the solid-shell thickness decreases gradually at each inlet metal superheat.

4. The change in inlet melt superheat has virtually no effect on the growth of solid shell at lower casting speeds (≤ 100 mm/min), but it has a considerable effect on the retardation of the shell formation at higher casting speeds (≥ 140 mm/min).
5. With the increase in the casting speed, the local surface heat flux increases remarkably for each delivered melt superheat.
6. An increase in the inlet melt superheat only slightly increases the local surface heat flux at each casting speed.

In summary, the above results show a discrepancy on the formation of solid-shell and sump depth at lower casting speeds with increasing delivered superheat. This discrepancy can be attributed to the fact that an approximation of a constant speed was made for the melt flow in the sump to develop the thermal model. This obscured the development of true sump profile especially at the bottom of the sump and registered a greater rate of growth of the solid-shell near the mold walls. Therefore, based on the computed results, it is believed that in order to get more realistic predicted results, particularly for an industrial scale DC slab caster, the model should take into account the coupled process of solidification heat transfer and fluid flow.

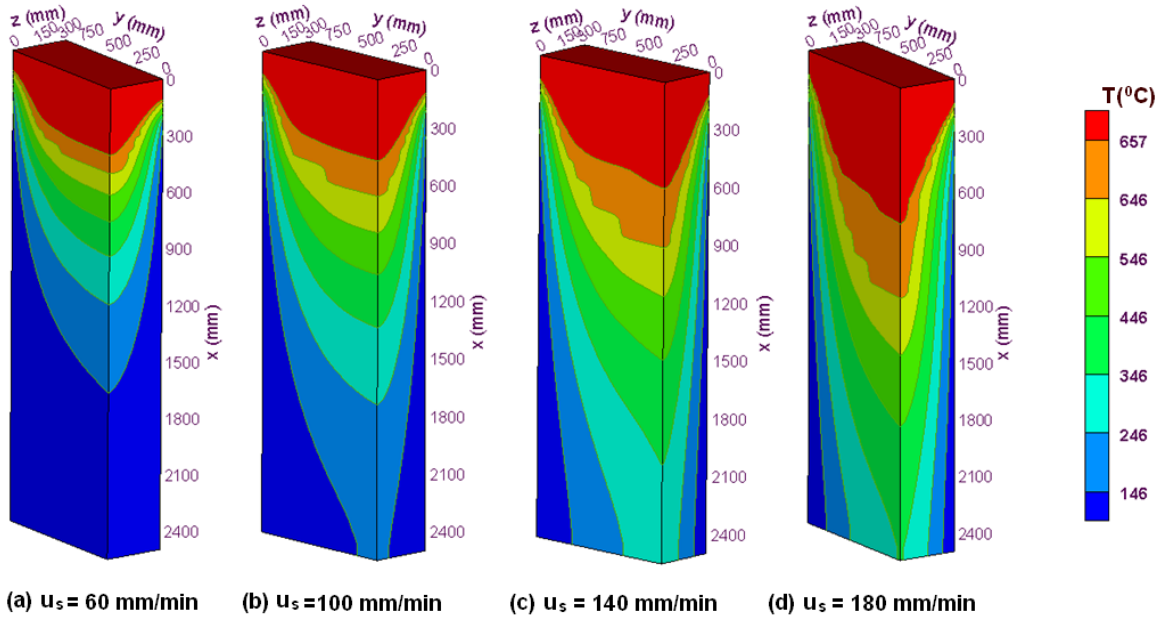

Figure 5.4: 3-D surface plots of the temperature distributions in the complete solution domain for an inlet superheat of 32^0C using thermal model at:(a) 60 mm min^{-1} (b) 100 mm.min^{-1} (c) 140 mm min^{-1} (d) 180 mm min^{-1}.

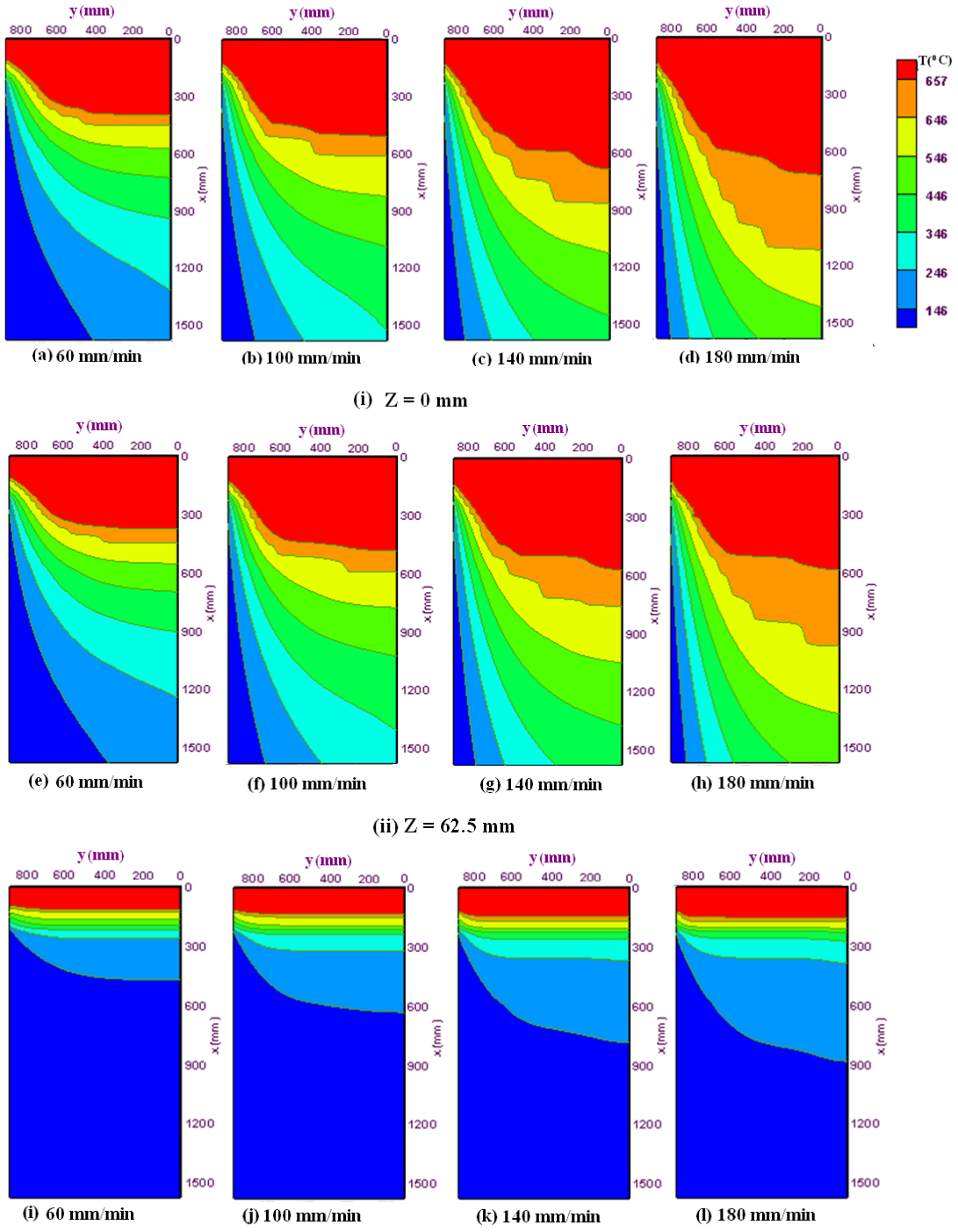

Figure 5.5: Enlarged 2-D view of temperature contours of the top domain using thermal model for an inlet superheat of 32°C and at a casting speed of: 60 mm/min (a, e, i at z = 0, z = 62.5 mm, and z = 312.5 mm, respectively); 100 mm/min (b, f, j at z = 0, z = 62.5 mm, and z = 312.5 mm, respectively): 140 mm/min (c, g, k at z = 0, z = 62.5 mm, and z = 312.5 mm, respectively): 180 mm/min (d, h, l at z = 0, z = 62.5 mm, and z = 312.5 mm, respectively).

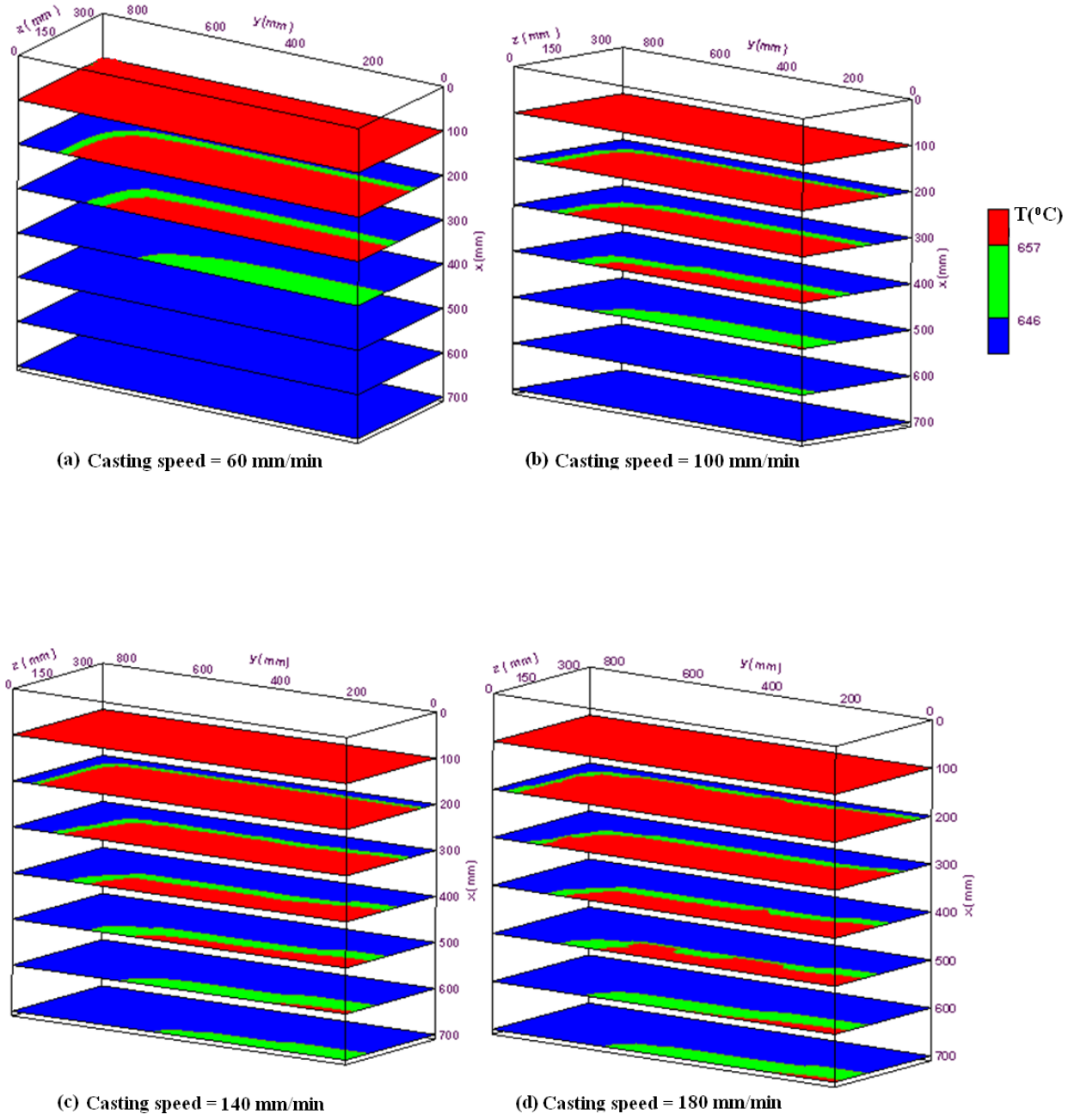

Figure 5.6: Contours of solidus and liquidus temperatures at various transverse cross-sectional planes (y-z planes) of the top part of the ingot using thermal model for a superheat of 32°C and casting speeds of (a) 60 mm min^{-1} (b) 100 mm min^{-1} (c) 140 mm min^{-1} (d) 180 mm min^{-1}.

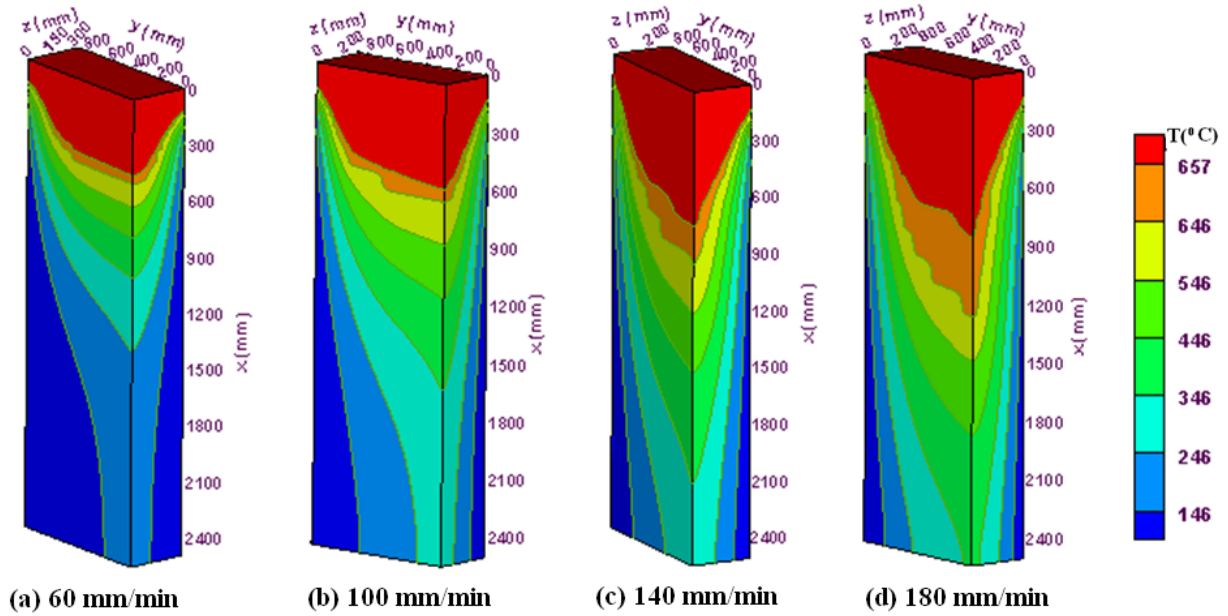

Figure 5.7: 3-D surface plots of the temperature distributions in the complete solution domain for an inlet superheat of 64^0C using thermal model at:(a) 60 mm min^{-1} (b) 100 mm.min^{-1} (c) 140 mm min^{-1} (d) 180 mm min^{-1}.

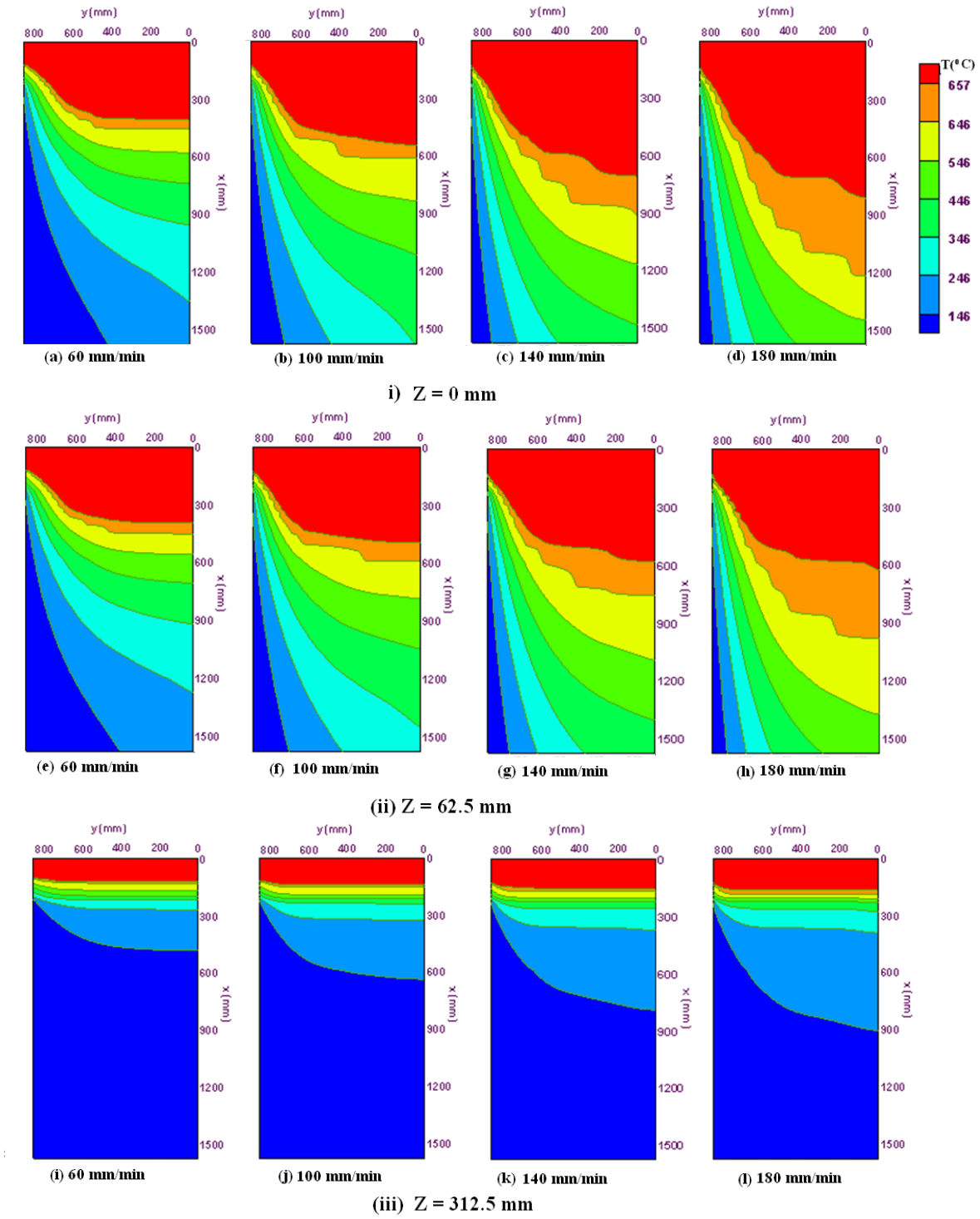

Figure 5.8: Enlarged 2-D view of temperature contours of the top domain using thermal model for an superheat of 64°C and at a casting speed of: 60 mm/min (a, e, i at z = 0, z = 62.5 mm, and z = 312.5 mm, respectively); 100 mm/min (b, f, j at z = 0, z = 62.5 mm, and z = 312.5 mm, respectively): 140 mm/min (c, g, k at z = 0, z = 62.5 mm, and z = 312.5 mm, respectively): 180 mm/min (d, h, l at z = 0, z = 62.5 mm, and z = 312.5 mm, respectively).

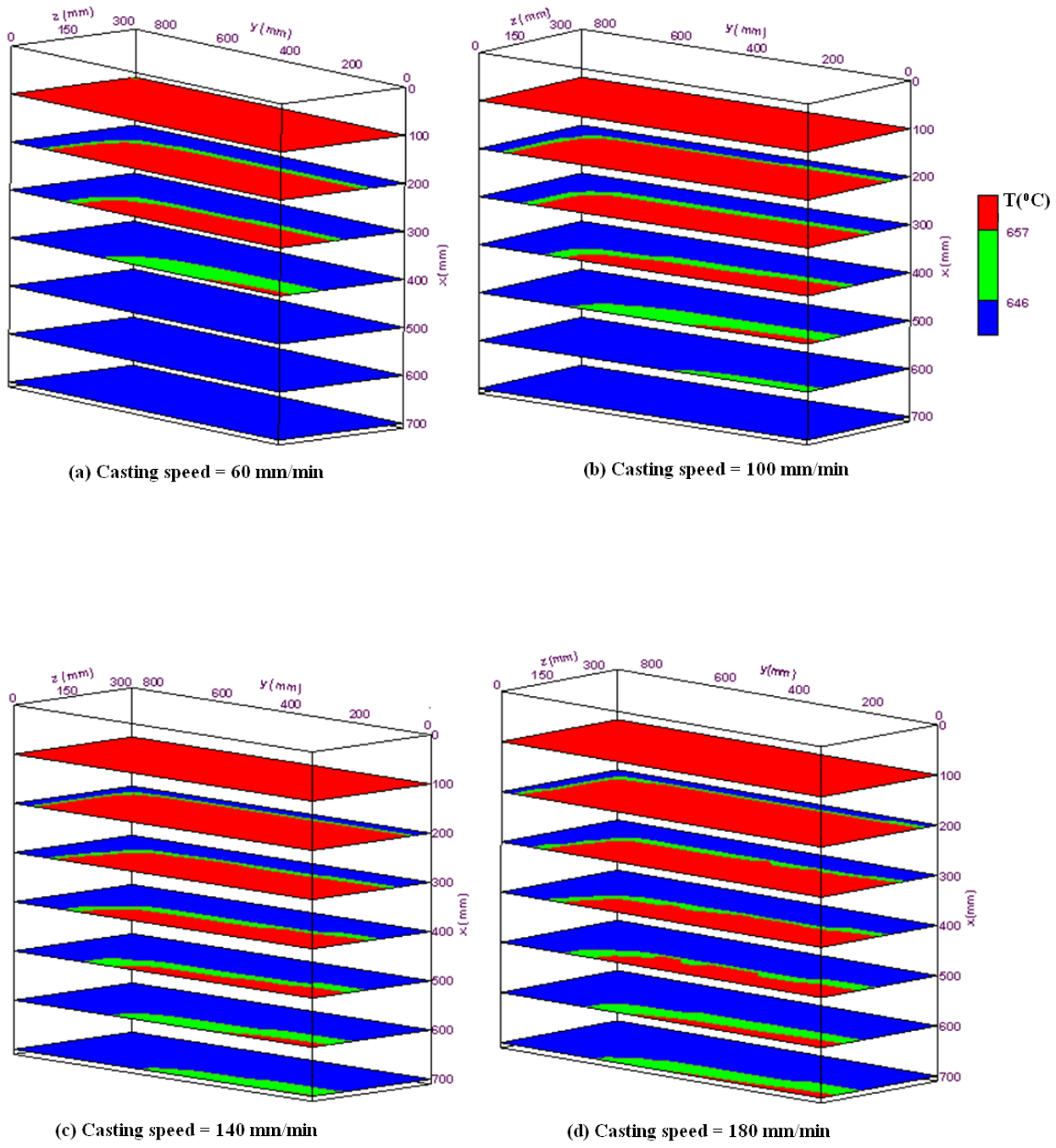

Figure 5.9: Contours of solidus and liquidus temperatures at various transverse cross-sectional planes (y-z planes) of the top part of the ingot using thermal model for a superheat of 64°C and casting speeds of (a) 60 mm min^{-1} (b) 100 mm min^{-1} (c) 140 mm min^{-1} (d) 180 mm min^{-1}.

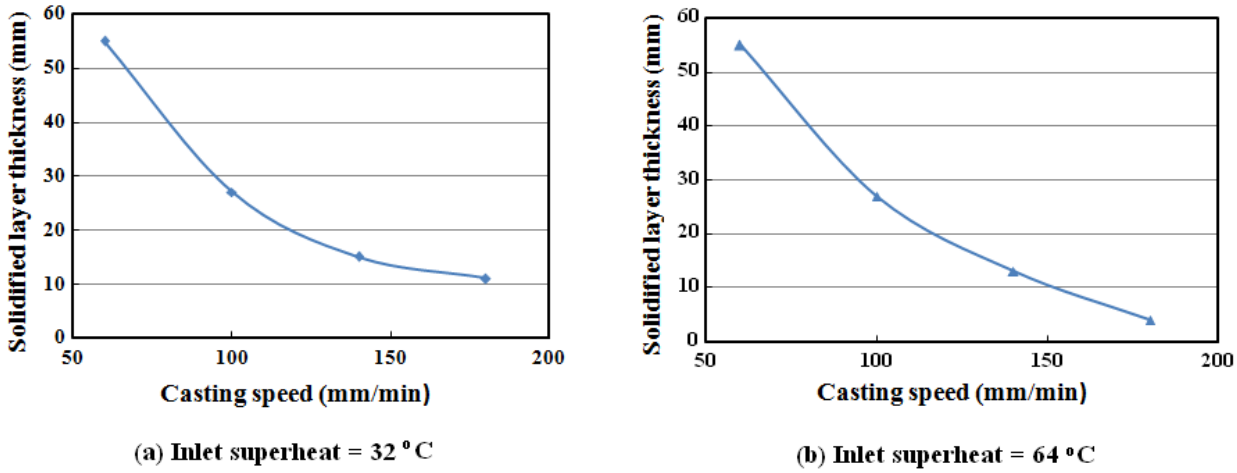

Figure 5.10: Solidified layer thickness from the narrow slab face at an axial distance of x = 160 mm from the top surface at the wide symmetry plane versus casting speed using the thermal model for: (a) inlet superheat of 32°C, (b) inlet superheat of 64°C.

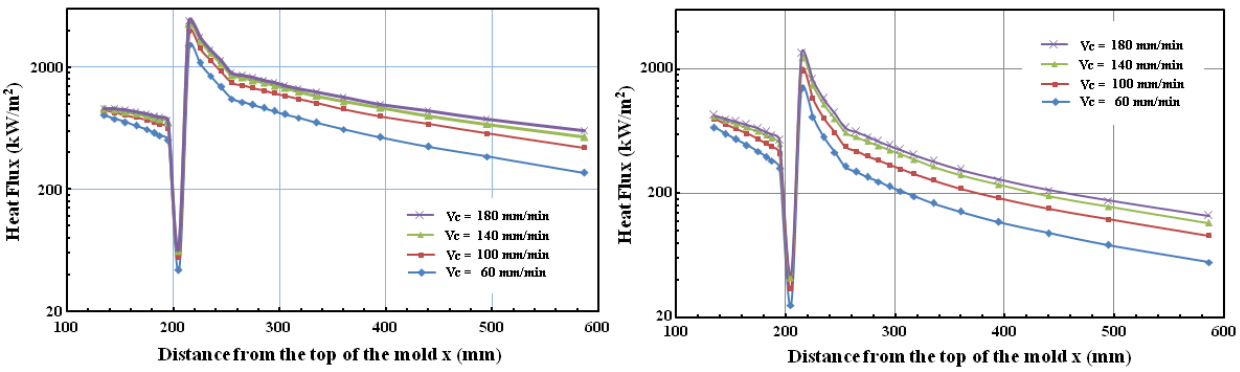

(a) Narrow slab face = 185 mm

(b) Wide slab face = 857.5 mm

(i) Inlet superheat = 32°C

Figure 5.11: Variations of local surface heat fluxes for various casting speeds during solidification at 32°C superheat along the axial direction of the strand wall at: (a) z = 185 mm (b) y = 857.5 mm using the thermal model.

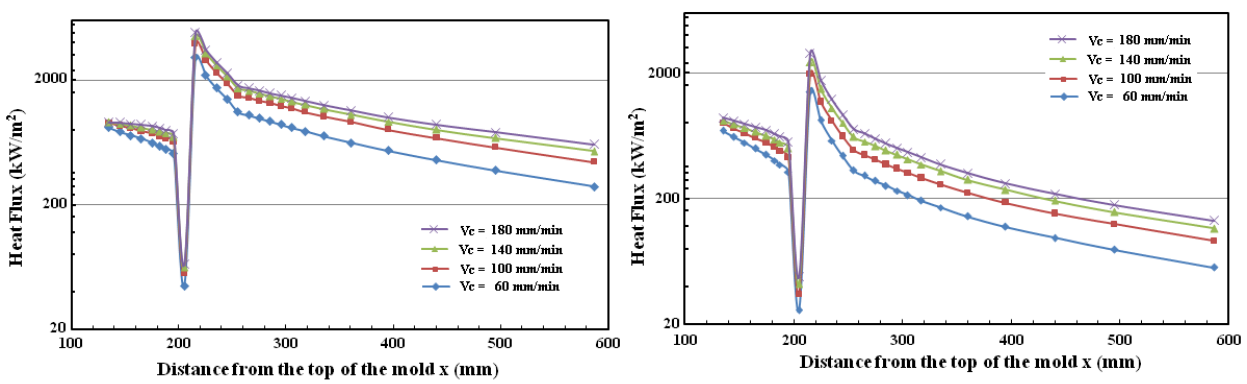

(a) Narrow slab face = 185 mm

(b) Wide slab face = 857.5 mm

(i) Inlet superheat = 64°C

Figure 5.12: Variations of local surface heat fluxes for various casting speeds during solidification at 64°C superheat along the axial direction of the strand wall at: (a) z = 185 mm (b) y = 857.5 mm using the thermal model.

CHAPTER 6

OPEN-TOP MELT FEEDING SYSTEM

6.1 Introduction

It is an experimental fact that the metal feeding system and the direction of melt flow as it enters the mould have significant influences on the severity of segregation [89]. Further, it is well established that the surface and internal defects in cast slabs are closely related to the fluid flow of the molten aluminum in the DC casting mold. In order to ensure a stable and turbulent-free filling, a lot of experimental research has been carried out both in industry and in academic institutions using physical water models for better understandings about different metal inlets and melt distribution designs. The ultimate objective of a flow distribution system for a slab caster is to ensure an even melt temperature distribution in the metal pool [51,68]. Since in such a caster, the narrow face is further away from the center compared to the wide face, and as a result some modifications of inlet distribution system at the center are necessary such that the narrow face is not supplied with a melt which is relatively too cold compared to the melt arriving at the wide face.

To optimize the melt flow in the mold, in this thesis research work six different metal feeding systems were investigated, which were discussed in Chapter-1. Out of the six melt feeding systems one is an open-top with metallostatic head. To the best of the author's knowledge such a delivery system has not been previously modeled. The present chapter reports the numerically predicted results for the open-top delivery system.

Unlike the simple conduction model discussed in Chapter-5, in the present chapter the turbulent aspect of the melt flow in conjunction with the solidification heat transfer was modeled for the above delivery system. The geometrical dimensions of the caster as well as the thermal boundary conditions employed here are identical to those studied in Chapter-5. A schematic view of the configurations of open-top melt feeding system is

given in Figure 5.1. To facilitate the discussion a summary of the relevant parameters is given in Table 6.1.

Table 6.1: Values of the parameter used in open-top melt delivery arrangements.

Case	Casting speed (mm/min)	Prandtl number (Pr)	Inlet Raynolds number (Re_L)	Inlet Peclet number (Pe)
1	60	0.0063	1595.42	10.07
2	100	0.0063	2659.08	16.78
3	140	0.0063	3722.64	23.5
4	180	0.0063	4786.25	30.21

6.2 Results and Discussion

The simulation results are generated for four casting speeds (u_s = 60, 100, 140, 180 mm/min), and two inlet superheats (ΔT = 32^{o}C, 64^{o}C). From the non-dimensionalization of the governing transport equations one can identify two important inlet parameters, namely the inlet Reynolds number, and the inlet Peclet number. Both of these numbers represent the inlet velocity of the melt. It is to be recognized here, because of the open top entry, the inlet velocity is equal to the casting speed. The inlet Reynolds, and Peclet numbers for the aforementioned casting speeds are given in Table 6.1. Although, the developed code is based on modeling of turbulent flow with coupled solidification problems, the code automatically handles the laminar flow cases as is seen to develop for the lower casting speed of 60 mm/min (refer to Table 6.1). In the present model, to incorporate the thermal buoyancy, the Grashof number (Gr) was considered to be 10^9, which was kept fixed for all cases.

First the results will be discussed for an inlet superheat of 32^{o}C for four casting speeds which will be followed by the results for an inlet superheat of 64^{o}C for the same casting speeds. A comparison of the predicted results generated by the thermal model and the present CFD model will be made. The effect of the imposed heat transfer coefficients in the primary cooling zone on the predicted results will be discussed. Finally, some concluding remarks will be provided.

6.2.1 Velocity Fields for $\Delta T = 32^{o}C$

To gain an overall understanding of the casting/solidification process, Figures 6.1(i-iv) are drawn which show a 3-D surface plot of the numerically predicted temperature and velocity fields for four casting speeds and for a melt inlet superheat of 32°C for an open top melt delivery system. Each 3-D surface plot consists of two symmetry planes, a wide (x-y plane) and a narrow (x-z plane) planes as well as the top melt entry surface of the slab caster. Figures 6.1(b,d,f,h) show the velocity vector fields in the corresponding three planner surfaces. From these figures, it is clearly visible that all of the melt flows downward along the axial direction, since the melt is delivered uniformly at the corresponding casting speed across the whole top cross-section. Parts of the vertical melt flow near the walls are diverted by the developing solidified shells, both along the narrow and wide faces, then they move along the solidification fronts. In general, an increase in the casting speed increases the volume of the melt. As a consequence, the magnitude of the velocity vector increases. This observation is in accord with the above stated fact.

The right hand panels of Figs. 6.2(a,b,c) – 6.5(a,b,c) illustrate the 2-D projections of the velocity vectors at the wide symmetry plane (z = 0) and parallel to the wide symmetry plane at two inward locations, viz., z = 62.5 mm, and z = 312.5 mm, for four casting speeds for an inlet superheat of 32^{o}C. For easy and clear understanding of the developed velocity vectors within the cast, about two-third of the axial domain is magnified and plotted. Figures 6.2(a) through 6.5(a) show the velocity vectors for wide symmetry plane (z = 0) for four casting speeds, which have already been observed in the corresponding 3-D surface plots.

The velocity fields on the longitudinal planes at a distance of z = 62.5 mm and z = 312.5 mm from the wide symmetry plane, are presented in Figures 6.2(b) through 6.5(b), and 6.2(c) through 6.5(c), respectively for four withdrawal rates. The velocity vector field in each panel at z = 62.5 mm shows that the corner stream near the narrow face is still obstructed by the developing solid shell, whereas the velocity field at z = 312.5 mm, which is close to the wide face shows an almost uniform downward flow. The magnitude of the velocity vectors at z = 312.5 mm is slightly higher than the casting speed, which signifies the melt is accelerated with respect to the casting speed in the hot-top.

6.2.2 Temperature Fields for $\Delta T = 32^{o}C$

One of the very important aspects of a DC casting process is the prevailing temperature field. The solidification front, and the liquidus isotherm along with other iso-temperature contours are presented in Figures 6.1(a,c,e,g) for the aforementioned casting speeds. The dark yellow color region in these figures represents the mushy region, which is confined by the solidus (646°C) and liquidus (657°C) temperatures. A classical parabolic-shaped solidification front is obtained at each casting speed, which signifies a weaker thermal convection effect in the mushy region. By studying the above figures, the effect of casting speed on temperature fields can be ascertained. From these figures, it can be clearly seen that the volume of the liquid region inside the domain is increased with increasing in the casting speed which is visible in the increased red color region. As casting speed increases, the solidification front as well as the other isotherms are becoming steeper and are moving downward. The mushy region is also seen to be expanding as a result of stronger thermal convection. Due to the increase in the volumetric flow rate as well as with the accompanying decrease of the residence time of the melt, with the increase of the casting speed, the ingot is not sufficiently cooled by the extraction of heat for the same effective convective heat transfer coefficients in the primary and secondary cooling regions. In all of the above figures, the solidification front is non-uniform, and this is particularly visible near the middle of the wide symmetry plane. This non-uniformity may be due to the numerical artifact from the modeling

technique used in the mushy region or it could be due to the representation of the real solidification process happening in the ingot. It is also observed from these figures that at and near the central area of the ingot, the parabolic shape of the developed solidification front has turned to almost horizontal in shape. The weak vertical melt flow at and near the central area has caused negligible thermal convection, and as a result the parabolic shape of the solidification front has altered. The horizontal extent of the solidus isotherm is decreasing with the increase of casting speed. The reason behind this observation is that at a lower casting speed the conduction mode of heat transfer near the solidification front is increased with respect to the thermal convection.

The temperature contours in the left hand panels, at z = 0, z = 62.5 mm and z = 312.5 mm, for four casting speeds are presented in Figures 6.2(a) through 6.5(a), 6.2(b) through 6.5(b), and 6.2(c) through 6.5(c), respectively. As one proceeds from the wide symmetry pane along the narrow face toward the wide face, the rate of heat extraction increases, which is manifested through the shapes and locations of the isotherms at these three longitudinal planes. The isotherms are observed to have lifted upward compared to the symmetry plane. From these figures, one can further see that with the increase of the casting speed both the liquidus and the solidus isotherms are moved downward and there is an increase in the vertical distance between them.

Through 2-D plots, the developments of the solid shell and mushy zone at different transverse cross-sections (y-z plane) parallel to the slab-top surface, for four casting speeds at a melt superheat of 32^{o}C, are illustrated in Figures 6.6(a-i), 6.7(a-i), 6.8(a-i), 6.9(a-i), respectively. In these figures, a total of nine cross-sections of the ingot are depicted at various axial distances down the cast which are located in the mold and post mold regions. With the increase in the axial distance, as more heat is being extracted from the ingot through the mold and by the chilled water jets, the thickness of the solid layer from the wide and narrow sides, presented by the blue color, progressively increases as can be seen from these figures at each casting speed. The apparent uniformity in the thickness of the solid shell on the narrow and wide faces signifies that a uniform rate of heat extraction has taken place from both of these sides at each cross-section. Around the corner of the two faces, heat is extracted by these two sides, and as a result there is a higher rate of heat extraction which has resulted in almost round-shaped

solid layer and mushy zone. The spectacular reduction of the solid region (represented by blue color) along the cast direction with the increase in the casting speed is clearly visible from the above figures. The reasons for which have already been explained in earlier paragraph.

6.2.3 Quantitative Analysis for $\Delta T = 32^{o}C$

(i) Sump Depth and Mushy Layer Thickness

Table 6.2 lists the numerically predicted sump depth and the mushy layer thickness at the ingot center for four casting speeds. From this table it is observed that a deeper sump depth and a thicker mushy layer are obtained at a higher casting speed, except that the mushy layer is the thinnest at a casting speed of 100 mm/min instead at 60 mm/min. The sump depth is found to be approximately 334 mm from the top of the mold for a withdrawal speed of 60 mm/min. Compared to the lowest simulated casting speed of 60 mm/min, the relative difference in sump depth for higher casting speeds of 100, 140, and 180 mm/min, is respectively about 46 %, 119 %, and 193 % higher. In Table 6.2, the numerical values of the thickness of the mushy layer at the center do not follow a given trend. At the center, for a casting speed of 100 mm/min the mushy thickness decreases by about 29 %, whereas, for casting speeds of 140, and 180, the thickness increases by 171 %, and 364%, respectively compared to the casting speed of 60 mm/min. The reason for this anomalous behavior is difficult to explain, since a complex interaction between the flow and thermal field prevails in that region.

Table-6.2: Sump depth and mushy thickness in mm at the center of the ingot for an open-top delivery system for four casting speeds and superheat of $32^{o}C$.

Quantity	Values of casting speed (u_s) in mm/min			
	60	100	140	180
Sump depth	334	45.5 % higher than	118.6 % higher	193.4 % higher

(mm)		u_s = 60 mm/min	than u_s = 60 mm/min	than u_s = 60 mm/min
Mushy thickness (mm)	56	28.6 % lower than u_s = 60 mm/min	171.4 % higher than u_s = 60 mm/min	364.3 % higher than u_s = 60 mm/min

(ii) Formation of Solidified Shell

Casting speed is an obvious controlling parameter that determines the magnitude of the shell thickness. The shell thickness is predicted from the narrow slab face at an axial distance of 160 mm from the top of the slab, and it is plotted as a function of casting speed in Figure 6.16 (a). This axial position is located at around the middle of the mold. A rapid decrease of the shell thickness is seen to occur for a change of casting speed from 60 to 100 mm/min, while the higher change of the casting speed from 100 to 180 mm/min shows a rather gradual decrease of shell thickness. For easy comprehension, the magnitudes of the shell thickness for four casting speeds are demonstrated in Table-6.3. The table is self explanatory so far the casting speed is concerned.

Table-6.3: The thickness of the solidifying shell (mm) at wide symmetry plane from the narrow slab face at an axial distance of 160 mm inside the mold for four casting speeds and inlet superheat of 32°C for an open-top delivery.

Quantity	Values of casting speed (u_s) in mm/min			
	60	100	140	180
Thickness of the solidifying shell (mm)	55	63.7 % lower than u_s = 60 mm/min	81.8 % lower than u_s = 60 mm/min	87.3 % lower than u_s = 60 mm/min

(iii) Local Surface Heat Flux

The general consensus in this field is that, an increase in the casting speed would increase the surface temperature of the cast, which seemingly explains the increase of the local surface heat flux. A quite persistent feature of casting speed on the local surface heat flux distributions is illustrated in Figures 6.17(a) and (b) and the magnitudes of the same quantity at the water impingement point located at z = 185 mm are listed in Table-6.4.

Figures 6.17 (a) and 6.17 (b) show the local surface heat flux distribution along the axial direction of the caster for four casting speeds at $\Delta T = 32^{o}C$ on the narrow face at z = 185 mm, and on the wide face at y = 857.5 mm. The values used for the imposed effective convective heat transfer coefficients (HTC) on the ingot surface were discussed in detail in Section 3.2.6 of Chapter-3.

For a casting speed of 60 mm/min and at z = 185 mm, based on the imposed HTC of 1.5 kW/m^2-K, a local flux of 834 kW/m^2 is obtained near the top of the mold, and then it drops gradually inside the mold and it takes a minimum value of 521 kW/m^2. In the air gap region, the imposed HTC was 0.15 kW/m^2-K which has caused a sharp reduction in the solidification rate, with a value of 45 kW/m^2. At the water impingement point, the peak HTC was 20 kW/m^2-K and that predicts the highest heat flux, which is 3074 kW/m^2. A sharp decrease of the local heat flux is found in the secondary cooling region, dropping from a value of 3074 to a value of 1112 kW/m^2, representing the nucleate boiling regime. After that, the heat flux decreases to 279 kW/m^2 in the film boiling regime. From the analysis of Figure 6.17 (a) one can see, in the air gap an oscillatory behavior of the surface temperature will arise, which may lead to the remelting of the solid shell and result in the formation of a coarse DAS (Dendritic Arm Spacing) region below the surface. The shell reheating might cause in the loss of shell strength and may lead to the collapse back against the mold. With the increase in the casting speed, the local surface heat flux increases at each axial position, as can be seen in Figs. 6.17(a,b). From Table-6.4, it is observed that, at a fixed location of z = 185 mm, x = 215 mm, the surface heat flux at a casting speed of 60 mm/min, is about 3074 kW/m^2, while it is about 32 %, 50 %, and 61 % higher for the higher casting speeds of 100, 140, and 180mm/min, respectively in comparison to the lower casting speed of 60 mm/min.

For the identical effective convective heat transfer boundary condition, at the rolling and end faces, one should note that, there is a significant difference in the local heat flux for the same axial position. The local heat flux at z = 185 mm is much higher compared to the value obtained at y = 857.5 mm (for example, 4045 kW/m^2 versus 1967 kW/m^2, at x= 215 mm and u_s = 100 mm/min). The reason is due to the proximity of the wide slab face from the symmetry axis compared to the narrow side.

Table-6.4: The local heat flux (kW/m^2) at z = 185 mm at an axial distance of 215 mm from the top surface for four casting speeds and for an inlet superheats of 32°C for an open-top delivery system.

Quantity	Values of casting speed (u_s) in mm/min			
	60	100	140	180
Local surface heat flux (kW/m^2)	3073.81	31.6 % more as compared with 60 mm/min	49.9 % more as compared with 60 mm/min	61.2 % more as compared with 60 mm/min

6.2.4 Velocity and Temperature Fields for $\Delta T = 64^oC$

In order to ascertain the effect of a higher inlet superheat, simulations were carried out for a superheat of 64°C. The 3-D surface plots of the predicted isotherms and velocity vectors for four casting speeds are shown in Figures 6.10(i-iv). The velocity field in the right hand panel and the temperature field in the left hand panel, at three longitudinal cross-sections (z = 0, z = 62.5 mm, and z = 312.5 mm), for the aforementioned casting speeds are shown in Figures 6.11(a,b,c) through 6.14(a,b,c). The temperature fields, at different transverse cross-sections (y-z plane) parallel to the slab top surface, are illustrated for four casting speeds in Figs. 6.15(a-d). In Figs. 6.15(a-d), the shape of the solidification front and the extent of the mushy zone have been depicted

for an interval of 100 mm distance in the cast direction from the top of the ingot, at seven y-z planes.

Flow patterns and temperature distributions which are depicted in Figures 6.10(i-iv), Figures 6.11(a,b,c) through 6.14(a,b,c), and temperature contours in Figs. 6.15(a-d) closely resemble to those observed for $\Delta T = 32^oC$ in the corresponding Figures 6.1(i-iv), Figures 6.2(a,b,c) through 6.5(a,b,c) and temperature contours in Figs. 6.6 - 6.9 at the same casting speeds. Due to the increase in melt superheat, the influence of thermal convection in the liquid region is enhanced, which is evident from the magnitudes of the velocity vector inside the ingot. The magnitude of the maximum resultant velocity is enhanced for each casting speed compared to the previous case of inlet superheat of 32^oC. The magnitudes of the maximum resultant velocities are listed in Table-6.5, which are obtained from 3-D surface velocity vector plots.

Table 6.5: Maximum values of the resultant velocity in mm/min.

Inlet superheat (ΔT)	Values of casting speed (u_s) in mm/min			
	60	100	140	180
32^oC	102.0	156.0	204.0	258.0
64^oC	122.4	187.2	230.4	297.6

By inspecting the above figures representing temperature contours, the delay in the local solidification process is evident and this is due to the increase in thermal convection resulting from the increase of the melt superheat from $\Delta T = 32^oC$ to $\Delta T = 64^oC$. With the increase in the casting speed from 60 to 180 mm/min, a similar trend has been found for $\Delta T = 64^oC$. This trend is due to the additional enthalpy of the incoming melt. For a fixed superheat, the change in casting speed has caused the isotherms to move sharply downward but for a fixed casting speed, a change in superheat has led the isotherms to move rather slightly downward.

6.2.5 Quantitative Analysis for $\Delta T = 64^oC$

(i) Sump Depth and Mushy Layer Thickness

For an initial superheat, $\Delta T = 64^oC$, the obtained sump depth and the mushy zone thickness at the ingot center for various casting speeds are listed in Table-6.6. From this table it is evident that with the increase of casting speed, the above mentioned quantities are enhanced sharply and this is due mainly for the increase of thermal convection in the liquid pool. One exception to the above trend is that, the mushy thickness at a casting speed of 100 mm/min shows the smallest value compared to the other three casting speeds, and this trend is similar to the lower superheat of 32^oC.

For $\Delta T = 64^oC$, at a casting speed of 60 mm/min, the sump depth is 338 mm, whereas at the higher casting speeds of 100, 140, and 180 mm/min, the sump depth is about 44 %, 117 %, 191 % , respectively , higher in comparison to the lower casting speed of 60 mm/min.

The sump depth and liquid pool depth at the ingot center at each casting speed for $\Delta T = 64^oC$ (Table 6.6) differ significantly from those predicted for $\Delta T = 32^oC$ (refer to Table 6.2). The comparison between these two inlet superheats reveals that, the sump depth at casting speeds of 60, 100, 140, and 180 mm/min for $\Delta T = 64^oC$, is only 1.2 %, 0.2 %, 0.6%, and 0.2%, respectively larger, whereas the liquid pool depth at the slab center is only 0.7 %, 0.7%, 0.3%, and 0.4%, respectively higher compared to those found for $\Delta T = 32^oC$. With regard to the locations of the liquidus and solidus isotherms at the ingot center, at each casting speed for two different melt superheats, there is relatively an insignificant difference.

Table-6.6: Sump depth and mushy thickness (mm) at the center of the ingot for an open-top delivery system for four casting speeds and for superheat of 64^oC.

Quantity	Values of casting speed (u_s) in mm/min			
	60	100	140	180
Sump depth (mm)	338	44.1 % higher than u_s = 60 mm/min	117.2 % higher than u_s = 60 mm/min	190.5 % higher than u_s = 60 mm/min
Mushy thickness (mm)	58	32.8 % lower than u_s = 60 mm/min	165.5 % higher than u_s = 60 mm/min	343.1 % higher than u_s = 60 mm/min

(ii) Formation of Solidified Shell

The solidified layer thickness at an inlet superheat of 64^{o}C is given graphically in Figs. 6.16(b) and the predicted values are also listed in Table 6.7 for four casting speeds. Here, the thickness of the solidified shell from the narrow slab face at the wide symmetry plane (z = 0) at an axial distance of x = 160 mm from the slab top surface is predicted. Both the figure and table illustrate that the increase in the casting speed leads to the decrease in the growth of the solid shell. From the above figure it is seen that unlike the lower inlet superheat, there is a monotonic decrease in shell thickness with casting speed. The magnitude of the shell thickness shown in the Fig. 6.16(b) is also given in Table 6.7.

From the above table one can see, for ΔT = 64^{o}C, at a casting speed of 60 mm/min, the shell thickness is 40 mm, whereas at the higher casting speeds of 100, 140, and 180 mm/min, the thickness of the solidifying shell is about 53 %, 83 %, 93 %, respectively lower in comparison to the lower casting speed of 60 mm/min. At higher casting speeds, the growth rate of solid shell is retarded due to the stronger thermal convective effect.

A comparison between the two inlet superheats reveals that, the shell thickness at casting speeds of 60, 100, 140, and 180 mm/min for ΔT = 64^{o}C, is about 27 %, 5 %, 30 %, and 57 %, respectively lower compared to those predicted for ΔT = 32^{o}C. This lower value is obtained due to the additional heat carried by the incoming melt for higher casting speeds which is required to be removed from the liquid before solidification can take place.

Table-6.7: The thickness of the solidifying shell (mm) at wide symmetry plane from the narrow slab face at an axial distance of 160 mm inside the mold for four casting speeds and superheat of 64°C for an open-top delivery system.

Quantity	Values of casting speed (u_s) in mm/min			
	60	100	140	180
Solid shell thickness (mm)	40	52.5 % lower than u_s = 60 mm/min	82.5 % lower than u_s = 60 mm/min	92.5 % lower than u_s = 60 mm/min

(iii) Local Surface Heat Flux

The local surface heat flux on the narrow face at z = 185 mm and on the wide face at y = 857.5 mm along the cast direction for $\Delta T = 64^oC$, for four casting speeds is shown in Figs. 6.18(a,b), respectively. The graphs show a very much similar trend to those observed for melt superheat of 32^oC (refer to Figs 6.17(a,b)). With the increase in the casting speed, the local surface heat flux increases, as seen previously.

On a quantitative basis, for $\Delta T = 64^oC$, at a casting speed of 60 mm/min, the local surface heat flux at the location z = 185 mm, x = 215 mm, is 3136.92 kW/m^2, whereas at the higher casting speeds of 100, 140, and 180 mm/min, the local surface heat flux is about 32 %, 48 %, 63 %, respectively higher in comparison to the lower casting speed of 60 mm/min, as can be seen in Table 6.8.

A comparison between the two inlet superheats reveals that, the local surface heat flux at z = 185 mm, x = 215 mm, at casting speeds of 60, 100, 140, and 180 mm/min for $\Delta T = 64^oC$, is only about 2 %, 2.5 %, 0.7 %, and 3 %, respectively greater compared to those predicted for $\Delta T = 32^oC$ (refer to Table 6.4).

Table-6.8: The local heat flux in kW/m^2 at z = 185 mm at an axial distance of 215 mm from the top surface for four casting speeds and for an inlet superheats of 64°C, an open-top delivery system.

Quantity	Values of casting speed (u_s) in mm/min			
	60	100	140	180
Local surface heat flux (kW/m^2)	3136.92	32.2 % more as compared with 60 mm/min	47.9 % more as compared with 60 mm/min	62.9 % more as compared with 60 mm/min

6.3 Comparison Between the Thermal and CFD Models

In this section, to investigate the impact on the predicted results using the 3-D CFD and simple thermal models, the shell thickness and sump depth generated for four casting speeds and two melt superheats are compared. The temperature fields, which were predicted using the thermal model were presented and discussed in Capter-5.

A. Predicted Shell Thickness

It is worth noting that the solid-shell thickness is an indicator of the primary cooling. Here, the shell thickness is predicted from the narrow face at the wide symmetry plane (z = 0) at an axial distance of x = 160 mm from the top surface. Figures 6.19 (a) and (b) provide a clear comparison between the solid-shell thickness for an inlet superheat of 32^{o}C and 64^{o}C, respectively, predicted by the CFD and thermal models, for four casting speeds.

For $\Delta T = 32^{o}$C, Fig. 6.19(a) shows, the shell thickness predicted by the two models is almost identical for a casting speed of 60 mm/min, while the CFD model predictions underestimate the shell thickness for higher casting speeds (viz., 100, 140, 180 mm/min). A comparison between the two models for $\Delta T = 32^{o}$C reveals that, the shell thickness at casting speeds of 60, 100, 140, and 180 mm/min using CFD model, is about 0 %, 26 %, 33 %, and 36 %, respectively lower compared to those predicted using thermal model (refer to Tables 6.3 and 5.3). The reason for this is that there is more convective flow in the transverse directions in the CFD model which retarded the growth of the shell on the narrow side.

For $\Delta T = 64^{o}$C, Fig. 6.19(b) shows the difference in shell thickness predicted by the two models is decreasing with increasing casting speed and for a casting speed of 180 mm/min there is only a small difference in shell thickness. A comparison between the two models for $\Delta T = 64^{o}$C reveals that, the shell thickness at casting speeds of 60, 100, 140, and 180 mm/min using CFD model, is about 27 %, 30 %, 46 %, and 14 %, respectively lower compared to those predicted using thermal model (refer to Tables 6.7 and 5.6), for the transverse convection of the flow and for the high non-linearity of the transport equations.

Depending on the melt superheat, from the above two figures and tables, one can see, the trend in the difference in shell thickness predicted by two models varies with the increase in the casting speed. This is due to the influence of velocities acting in the y and z direction in the CFD model. Due to the v and w velocities, the thermal convection opposes the growth of the shell in the horizontal plane, resulting in the decrease of the shell thickness. In the thermal model, the absence of these velocities justifies the solidification rate enhancement, despite the existence of the slug flow.

B. Sump Depth Predictions

The sump depth at the ingot center at an inlet superheat of 32^oC, and 64^oC for four casting speeds are shown in Figures 6.20(a) and (b), respectively. In these figures, the sump depths predicted by the CFD model are compared with the sump depths obtained from the thermal model. As shown, the CFD predictions match closely with the thermal model at each casting speed for a fixed melt superheat, $\Delta T = 32^oC$ (Figure 6.20(a)). A comparison between the two models for $\Delta T = 32^oC$ evidences that, the sump depth at casting speeds of 60, 100, 140, and 180 mm/min using CFD model, is only about 2.3 %, 0.8 %, 1.4 %, and 0.8 %, respectively lower compared to those predicted using the thermal model (refer to Tables 6.2 and 5.2).

Figure 6.20(b) shows a comparison between the sump depth predicted for $\Delta T = 64^oC$. From this figure, it is observed that there is negligible difference between the sump depth predicted by the CFD and thermal models at a casting speed of 60 and 100 mm/min, while there is a significant sump depth variations observed at a higher casting speed, such as, at 140 and 180 mm/min. A comparison between the two models for $\Delta T = 64^oC$ provides that, the sump depth at casting speeds of 60, 100, 140, and 180 mm/min using CFD model, is only about 1.2 %, 0.6 %, 7 %, and 10 %, respectively lower compared to those predicted using thermal model (refer to Tables 6.6 and 5.5).

In the case of CFD model, a portion of the vertical melt flow near the walls are diverted by the developing solidified shells, both along the narrow and wide faces, which then moves along the solidification front as can be seen from the velocity vector plots of

Figs. 6.1(i-iv). These flows are quite strong and are comparable to the vertically downward flow coming from the entry region, and appear in an inclined manner in the velocity vector plots of these figures. The collision between the inclined and a part of the vertical flows decelerates the motion of the fluid. This decelerated fluid then combines with the rest of the vertical flow and is diverted toward the center, resulting in lower thermal convection. In the thermal model it is assumed that the liquid, solid and mushy regions all are moving axially with a constant casting speed, hence the effect of thermal convection is enhanced, resulting in a higher sump depth.

In summary, the results show that the thermal model, due to its simplicity and approximation, provides overestimated results. Nonetheless, the simple thermal model developed in this work is especially useful in modeling the DC casting process because it can provide much faster approximate temperature and stress fields than a more complex CFD model. Because of its quick turn over of results, the thermal model will also be useful in developing a real-time control system for such a process. If more accurate results are necessary then a CFD model is more preferable.

6.4 Effect of Primary Coolant Heat Transfer Coefficient

The heat extraction rate through the mold not only depends on the imposed thermal boundary conditions during casting, it also depends on the melt temperature, the casting speed and the latent heat of solidification. In order to facilitate the investigation of the influence of the heat transfer coefficient (HTC) an open top melt feeding scheme for a fixed casting speed of 100 mm/min and an inlet superheat of 32^{o}C for AA-1050 was selected. A total of six HTCs, ranging from the lowest value of 225 W/m^{2}K to the highest value of 3000 W/m^{2}K, were implemented. In the model, two fixed HTCs were employed in the primary cooling zone. The simulation results presented earlier were based on the HTC of 1500 W/m^{2}K which was imposed in the region of direct contact between the metal and mold and comparatively a very low value of HTC (150 W/m^{2}K) was used for the air gap region. For vertical DC casting processes, in the mold region a higher value of HTC ranging from 1000 to 5000 W/m^{2}K, and a lower value ranging from 100 to 500

W/m^2K, have been reported in the literature [85]. It is to be noted that not many experimental studies concerning HTC in the mold for industrial-sized slab caster are available in the literature. In this section, a sensitivity analysis has been carried out by changing the value of HTC in the mold-metal contact region only. The reasons for examining different HTCs are as follows:

1. If the HTC is not high enough, it is well known that the shell at the exit of the mold will not be capable of holding the molten aluminum core, thereby a break-out condition can arise.
2. The heat flux oscillations discussed before in sections 6.2.3(iii) and 6.2.5(iii), can also be suppressed by using a suitable HTC.
3. In casting practices, typically the desired surface temperature in the impingement zone is in the range of 200-300^oC to achieve the nucleate boiling mode of heat transfer. The mold cooling condition is one of the important factors for obtaining the above desired surface temperatures.
4. A lower value of HTC usually delays the solidification process.

For a lower HTC, the above-mentioned problems are seen to occur, which may cause various types of crack formations and can deteriorate the quality of the cast. On the other hand, a very high HTC will increase the cost of production due to a larger amount of cooling water requirement. Therefore, an optimum value of HTC is always desirable.

i. Solid-shell Thickness

In Figure 6.21(a) the solid shell thickness, at the exit of the mold (x = 205 mm) from the narrow face at the wide symmetry plane (z = 0), for various HTCs is plotted in the form of a bar chart. In general, it is found that a higher HTC results in a thicker solid-shell. It is clear from this figure that the growth of the solidifying shell is directly affected by the imposed HTC. The quantitative values of the predicted shell thickness are also provided in mm inside each bar of Fig 6.21(a). For a low HTC of 225 W/m^2K, the predicted shell thickness is 33 mm, whereas it is 78 mm for HTC of 3000 W/m^2K, as can

be seen in this figure. The thickness for HTC of 500 W/m^{2}K is 48 mm, beyond this value and up to a value of 2000 kW/m^{2}K, a minor increase in shell thickness is observed. The predominant influence on the growth of the solid-shell is found for the lowest HTC of 225 W/m^{2}K and for the highest value of 3000 W/m^{2}K. For the other values of HTCs, ranging from 500-2000 W/m^{2}K, the influence on shell thickness is relatively small compared to the highest and the lowest values.

ii. Surface Temperature

Figure 6.21(b) demonstrates the plot of predicted ingot surface temperature (*Tsurf.*) for the corresponding location of the predicted shell thickness discussed above. This temperature is found to decrease with the increase in HTCs. As shown in this figure, the surface temperatures are approximately 497, 471, 451, 426, 397, and 357 °C for HTCs of 225, 500, 1000, 1500, 2000, and 3000 W/m^{2}K, respectively at the exit of the mold (x = 205 mm) from the narrow face at the wide symmetry plane.

From this study, it is evident that the primary cooling is mostly governed by the effective heat transfer coefficient, provided all other operating conditions are the same. A relatively high heat transfer coefficient of more than 3000 W/m^{2}K seems to be more promising to achieve the desired ingot surface temperature at the impingement zone for the nucleate boiling mode of heat transfer to prevail on the surface of the ingot for the said aluminum slab and operating conditions.

6.5 Concluding Remarks

Several conclusions can be reached from the simulated results of the CFD model, these being:

1. The numerically predicted data show that the lower casting speed produces a shallower sump and thinner mushy thickness than the higher casting speed and also causes lower turbulence fluctuations in the liquid pool.

2. With the increase of the melt superheat, the liquidus and solidus isotherms in the center of the ingot shift slightly downward but the thickness of the mushy zone changes very slightly.
3. The melt flow patterns (Figures 6.1(i-iv) and 6.10(i-iv)) show that a higher superheat produces a stronger thermal convective flow in the liquid pool compared to the lower superheat.
4. The solid shell thickness decreases with the increase in casting speed and melt inlet temperature, which in turn is reflected by the increase of the wall temperature of the strand. As a consequence, the local surface heat flux increases with the increase in casting speed and delivered superheat.
5. By doubling the inlet superheat, one sees a minimal effect on the enhancement of the surface heat flux but there is a significant effect on the growth rate of the solid shell.
6. The effect of the change in melt superheat on the predicted quantities is not as pronounced as like the change in casting speed.

It is well known that, centerline macro-segregation increases with sump depth. From this study, it would appear that the lower casting speed is preferable. Though the higher casting speed enhances the productivity, but it also increases the depth of the sump and will result in greater macro-segregation which will adversely affect the quality of the cast. Hence, a compromise has to be reached with regard to the productivity and quality when enhancing the casting speed. Since, in practice, it is difficult to deliver the melt uniformly across the entire top of the VDC caster. Hence a suitable melt delivery system is necessary in order to obtain a relatively turbulence-free flow in the liquid pool.

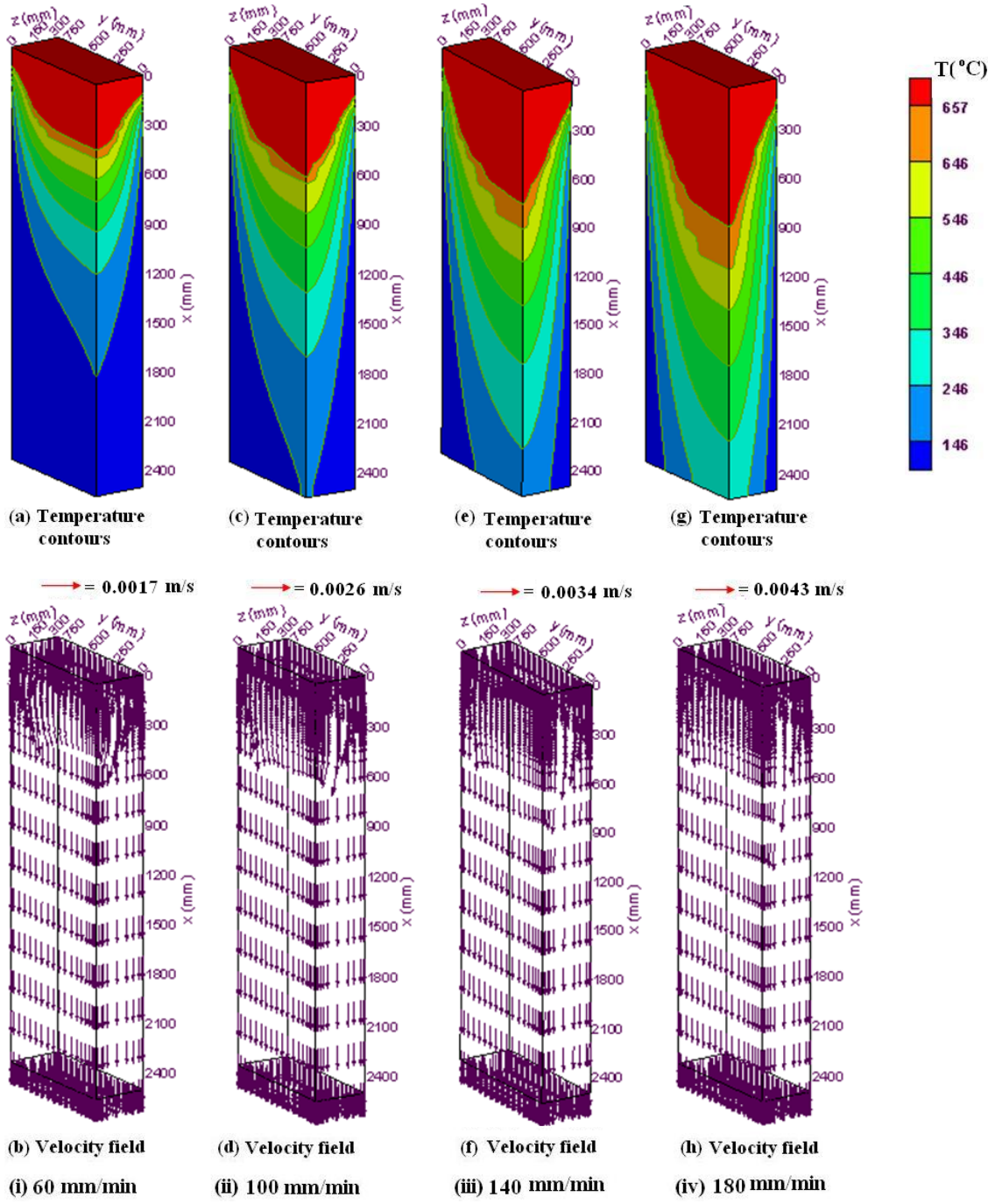

Figure 6.1: 3-D surface plots for the complete solution domain at four casting speeds and 32^0C superheat using the open top delivery system: (i) temperature contours (a) and velocity field (b) for casting speed of 60 mm/min; (ii) temperature contours (c) and velocity field (d) for casting speed of 100 mm/min; (iii) temperature contours (e) and velocity field (f) for casting speed of 140 mm/min; (iv) temperature contours (g) and velocity field (h) for casting speed of 180 mm/min.

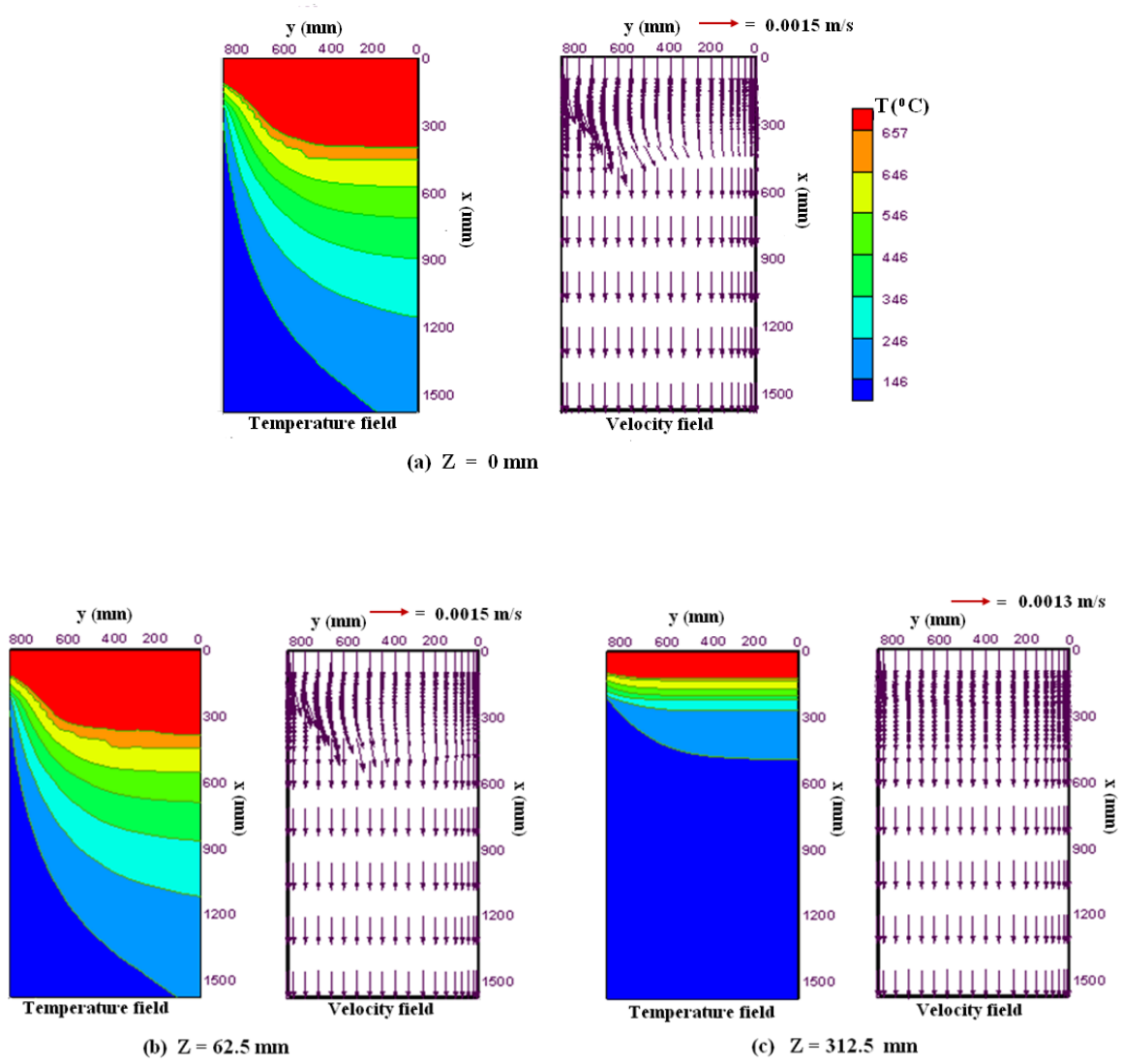

Figure 6.2: Enlarged 2-D view of temperature contours and velocity vectors of the top domain using the open top delivery system for a casting speed of 60 mm/min and 32°C superheat at: (a) wide symmetry plane at z = 0 mm, (b) vertical plane parallel to the wide face at z = 62.5 mm, (c) vertical plane parallel to the wide face at z = 312.5 mm.

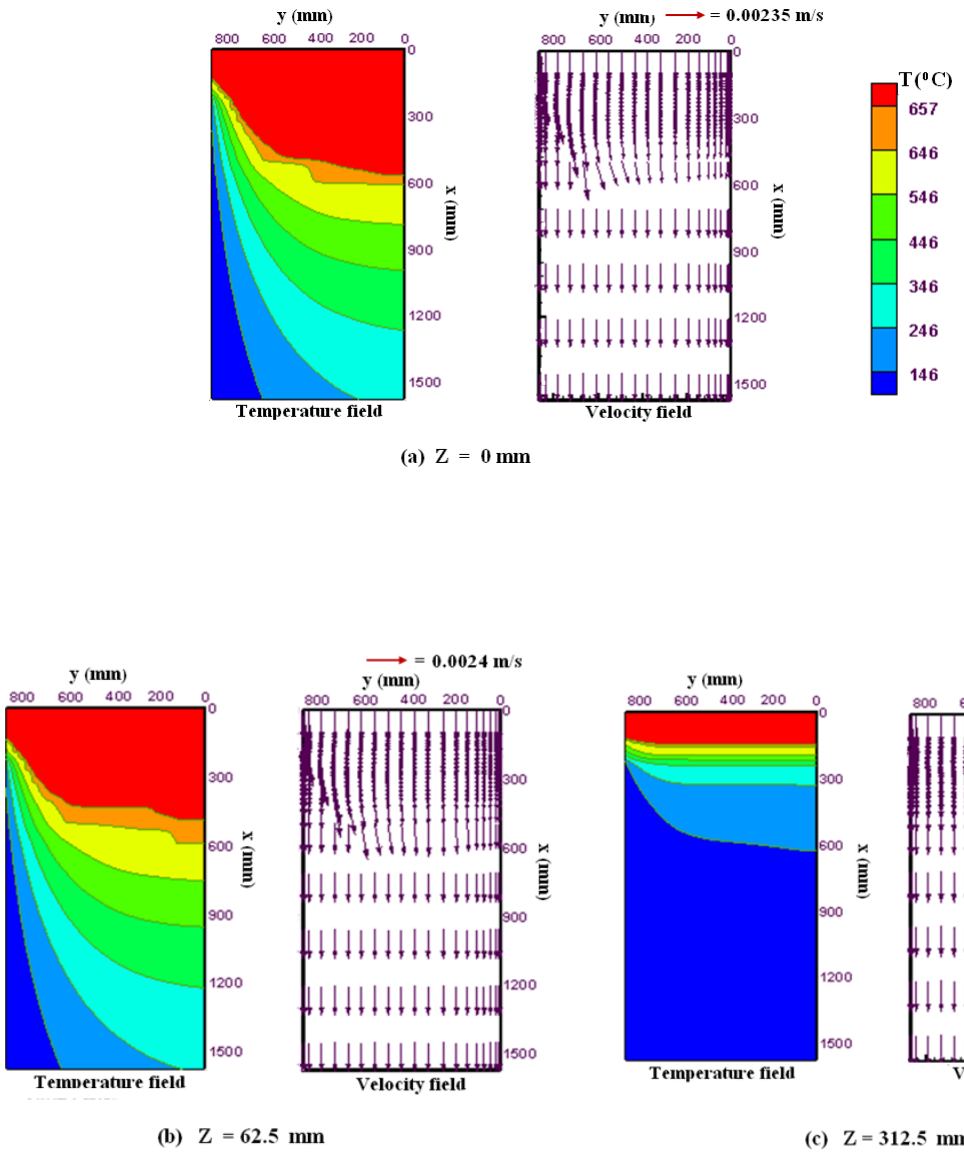

Figure 6.3: Enlarged 2-D view of temperature contours and velocity vectors of the top domain using the open top delivery system for a casting speed of 100 mm/min and 32°C superheat at: (a) wide symmetry plane at z = 0 mm, (b) vertical plane parallel to the wide face at z = 62.5 mm, (c) vertical plane parallel to the wide face at z = 312.5 mm.

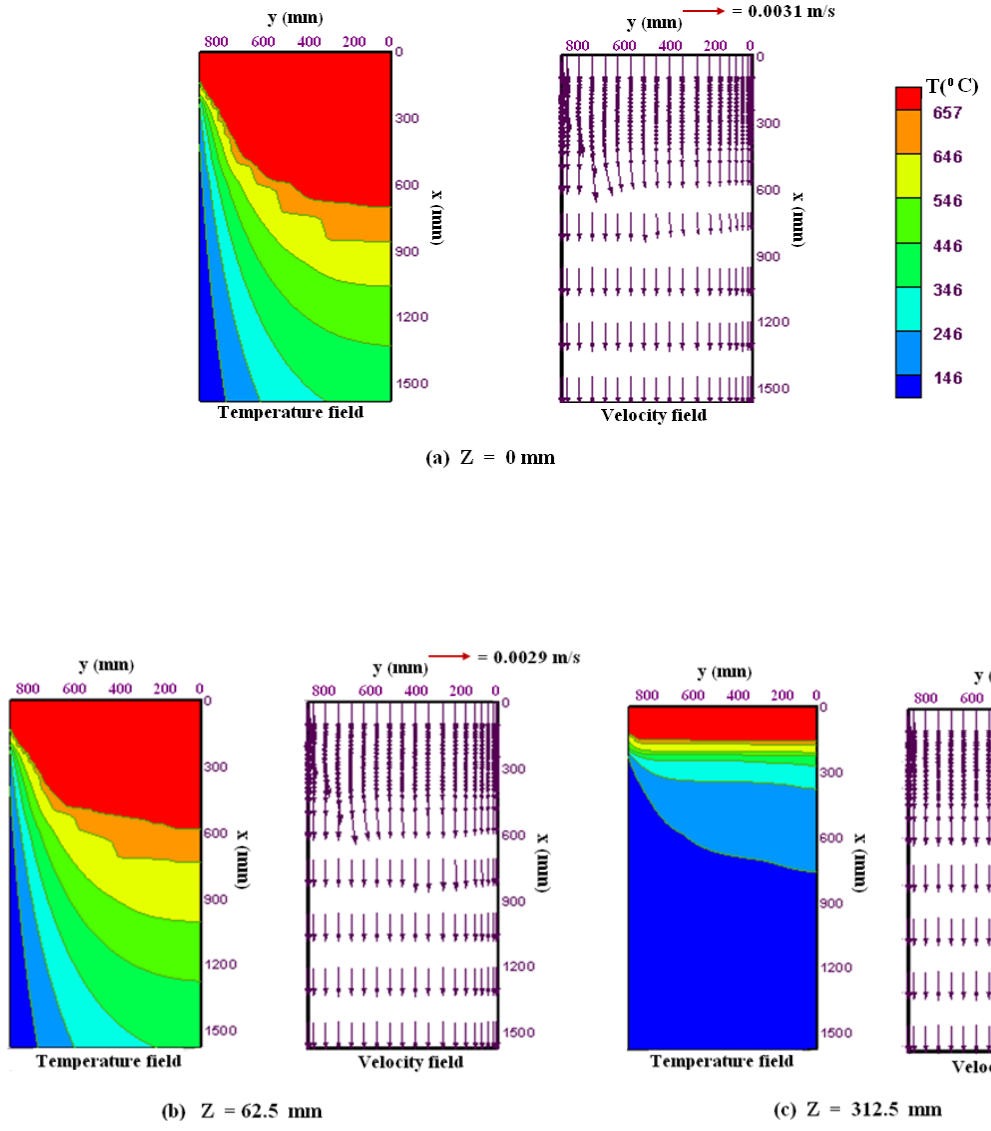

Figure 6.4: Enlarged 2-D view of temperature contours and velocity vectors of the top domain using the open top delivery system for a casting speed of 140 mm/min and 32°C superheat at: (a) wide symmetry plane at z = 0 mm, (b) vertical plane parallel to the wide face at z = 62.5 mm, (c) vertical plane parallel to the wide face at z = 312.5 mm.

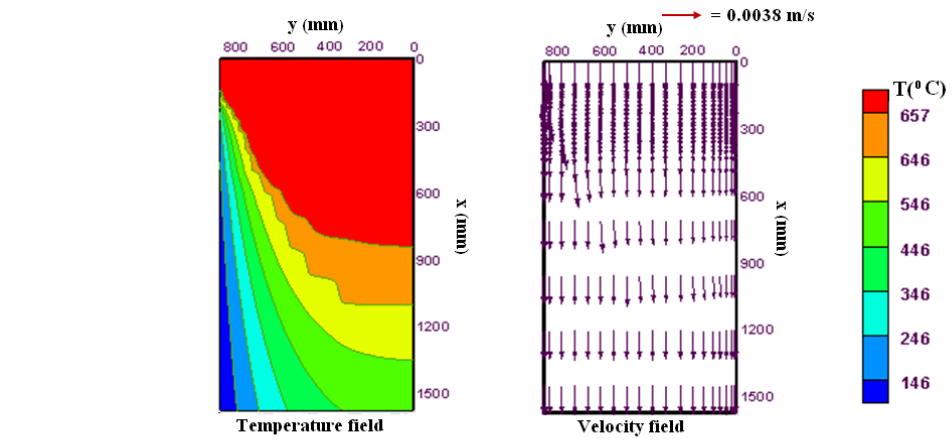

(a) Z = 0 mm

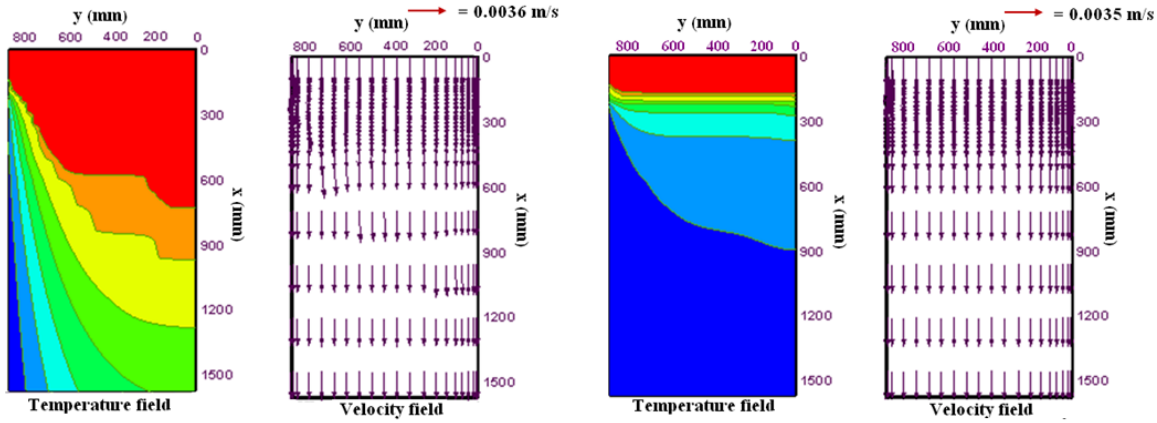

(b) Z = 62.5 mm (c) Z = 312.5 mm

Figure 6.5: Enlarged 2-D view of temperature contours and velocity vectors of the top domain using the open top delivery system for a casting speed of 180 mm/min and 32°C superheat at: (a) wide symmetry plane at z = 0 mm, (b) vertical plane parallel to the wide face at z = 62.5 mm, (c) vertical plane parallel to the wide face at z = 312.5 mm.

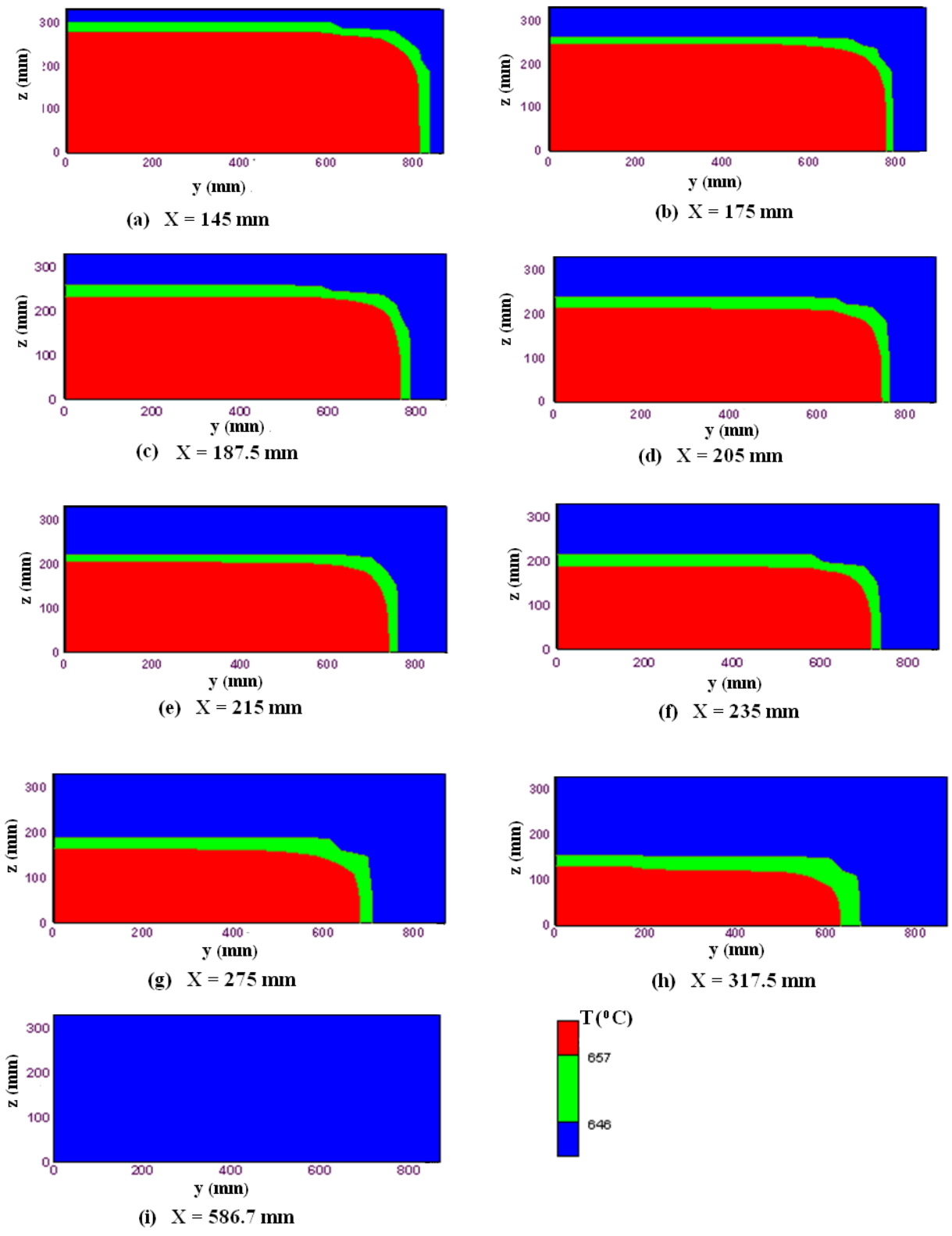

Figure 6.6: Contours of solidus and liquidus temperatures at various transverse cross-sectional planes (y-z planes) of the top part of the ingot using the open top delivery system for a superheat of 32°C and a casting speed of 60 mm min^{-1}.

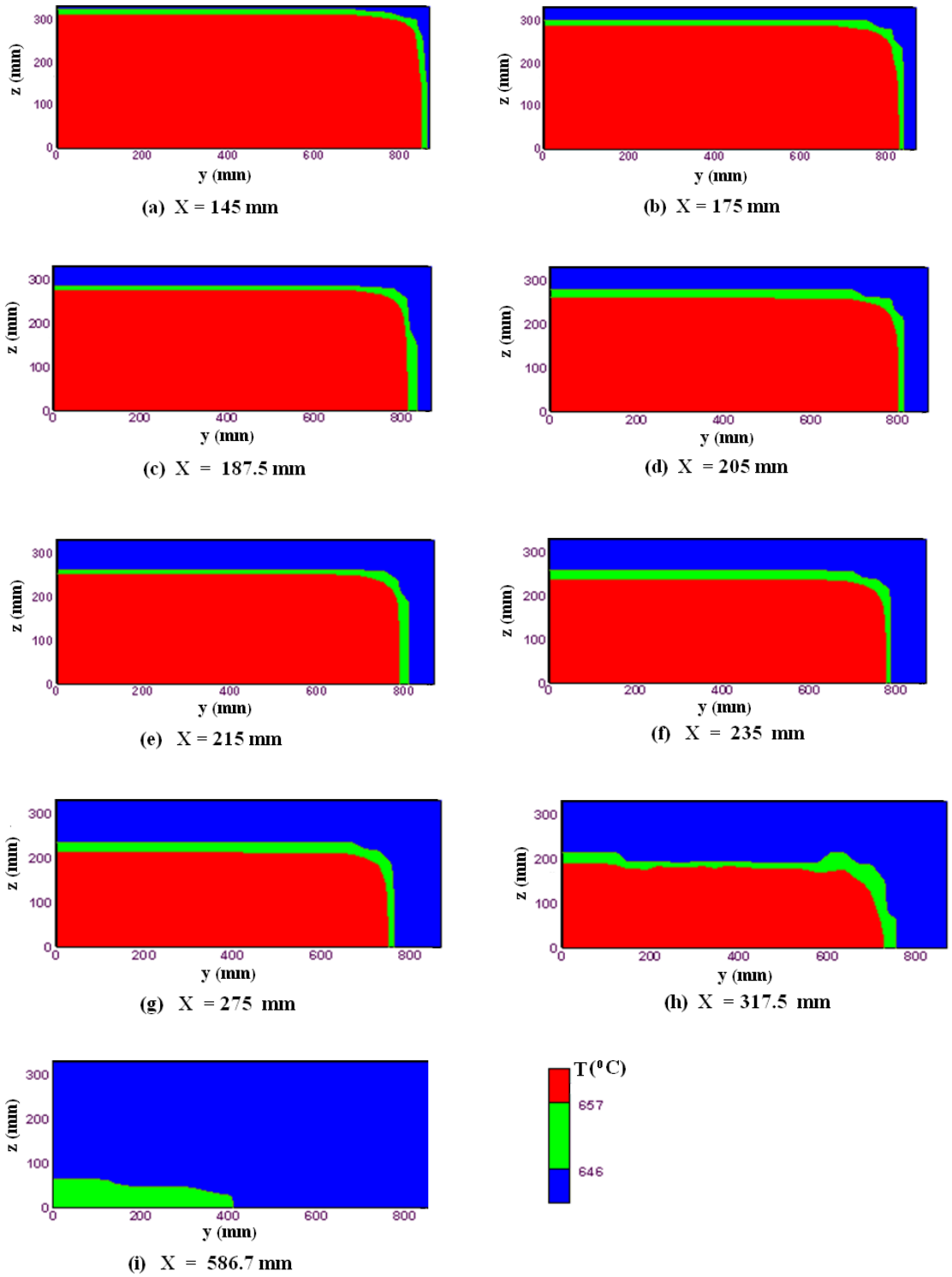

Figure 6.7: Contours of solidus and liquidus temperatures at various transverse cross-sectional planes (y-z planes) of the top part of the ingot using the open top delivery system for a superheat of 32°C and a casting speed of 100 mm min^{-1}.

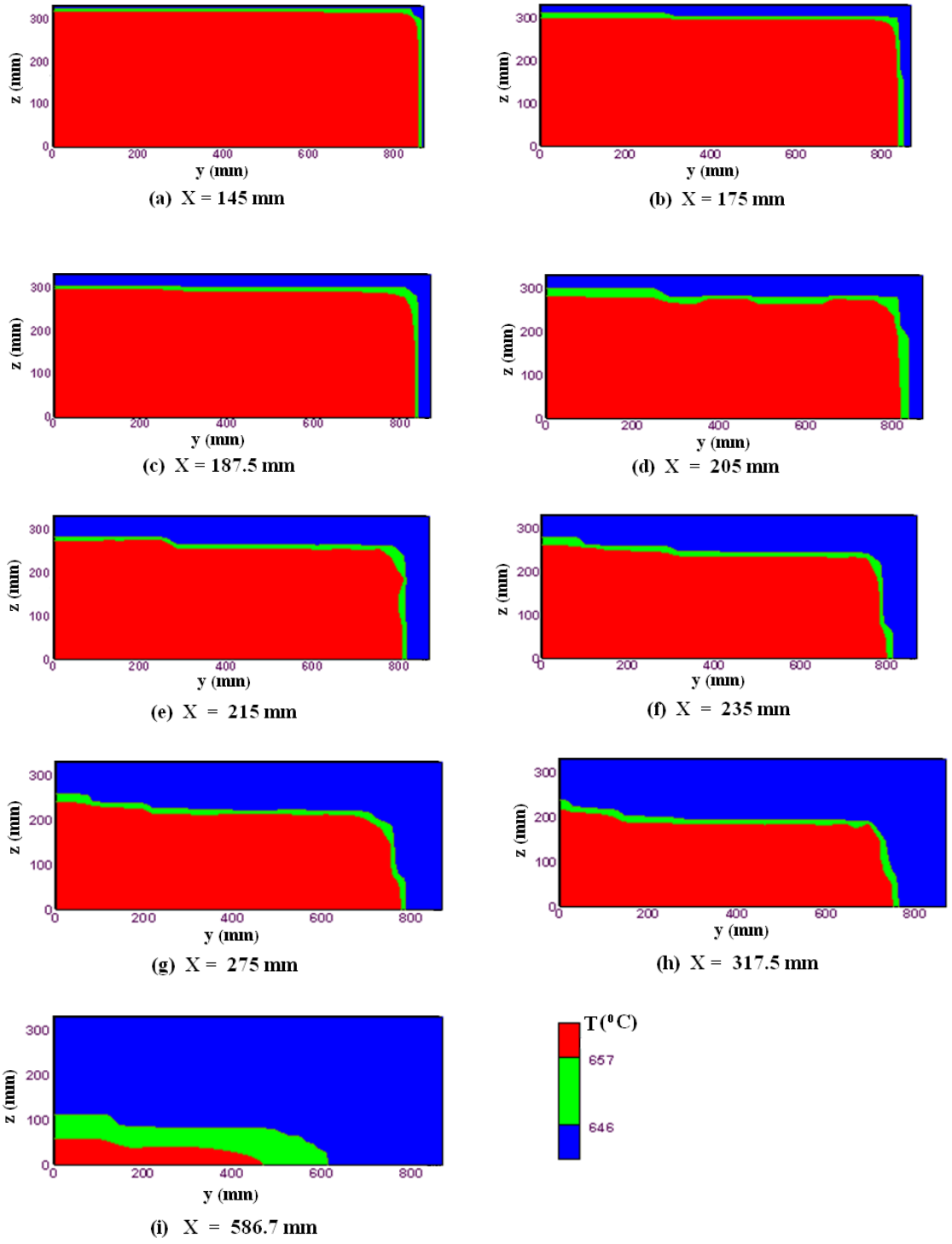

Figure 6.8: Contours of solidus and liquidus temperatures at various transverse cross-sectional planes (y-z planes) of the top part of the ingot using the open top delivery system for a superheat of 32°C and a casting speed of 140 mm min^{-1}.

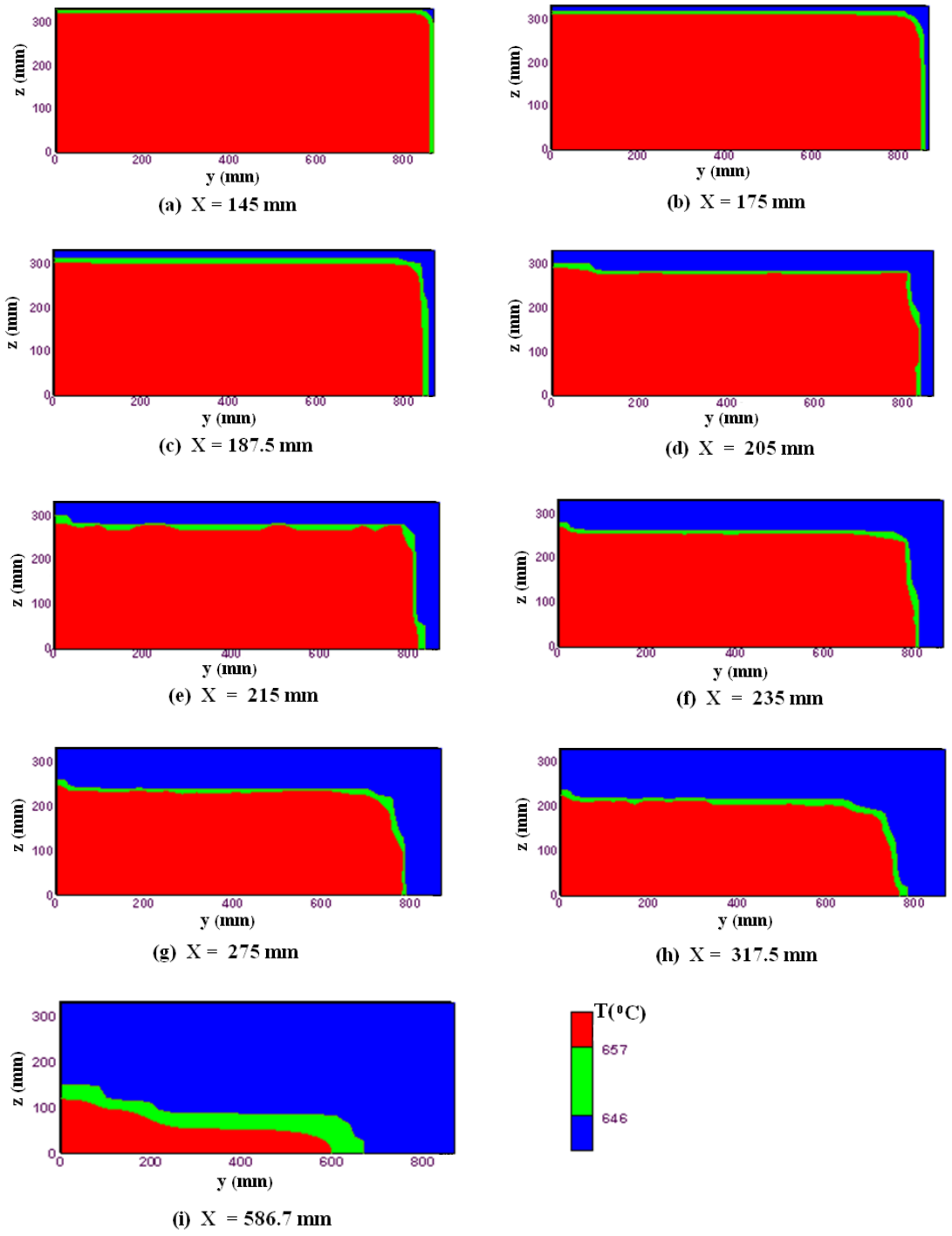

Figure 6.9: Contours of solidus and liquidus temperatures at various transverse cross-sectional planes (y-z planes) of the top part of the ingot using the open top delivery system for a superheat of 32°C and a casting speed of 180 mm min^{-1}.

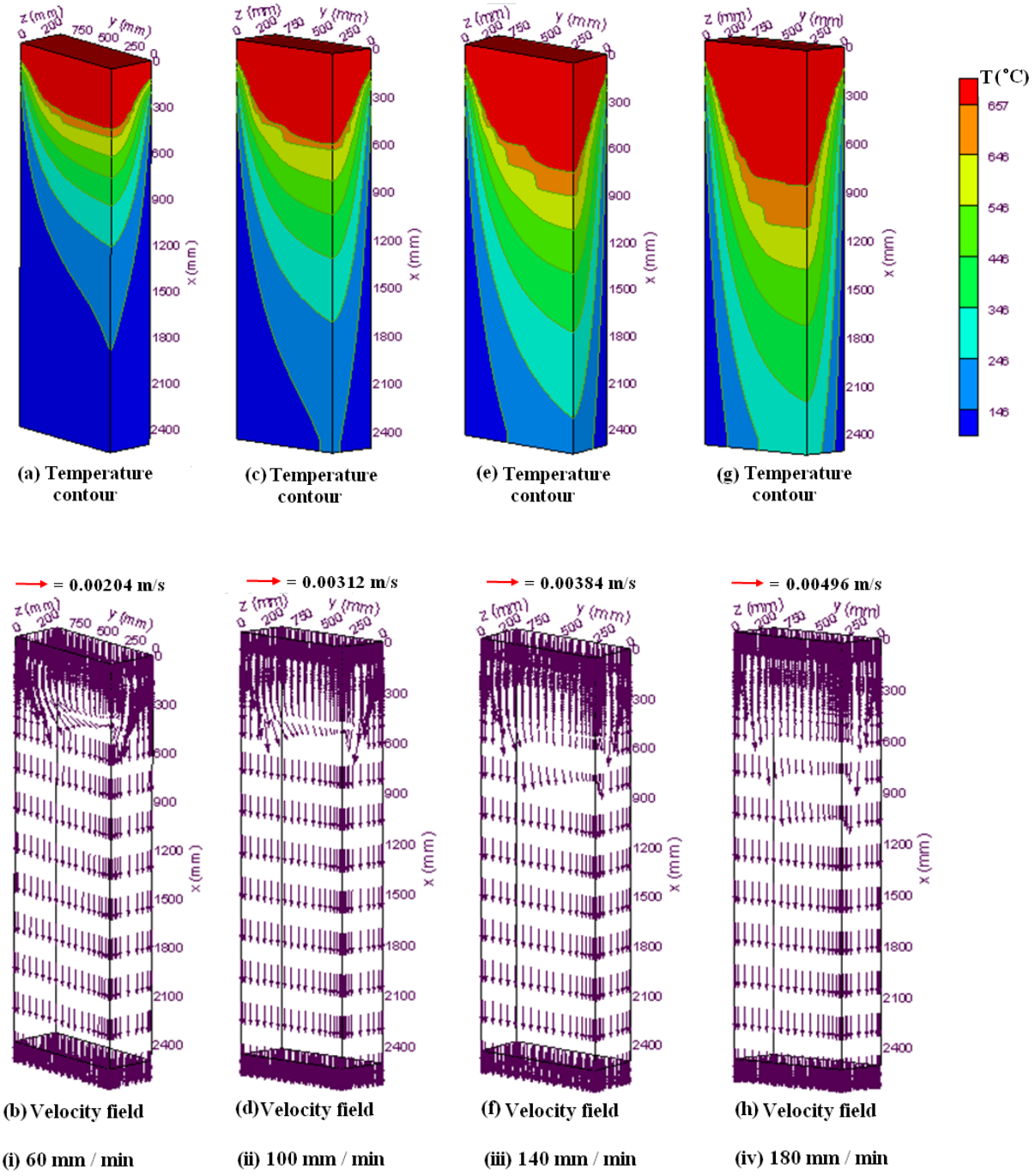

Figure 6.10: 3-D surface plots for the complete solution domain for four casting speeds and 64^0C superheat using the open top delivery system: (i) temperature contours (a) and velocity field (b) for casting speed of 60 mm/min; (ii) temperature contours (c) and velocity field (d) for casting speed of 100 mm/min; (iii) temperature contours (e) and velocity field (f) for casting speed of 140 mm/min; (iv) temperature contours (g) and velocity field (h) for casting speed of 180 mm/min.

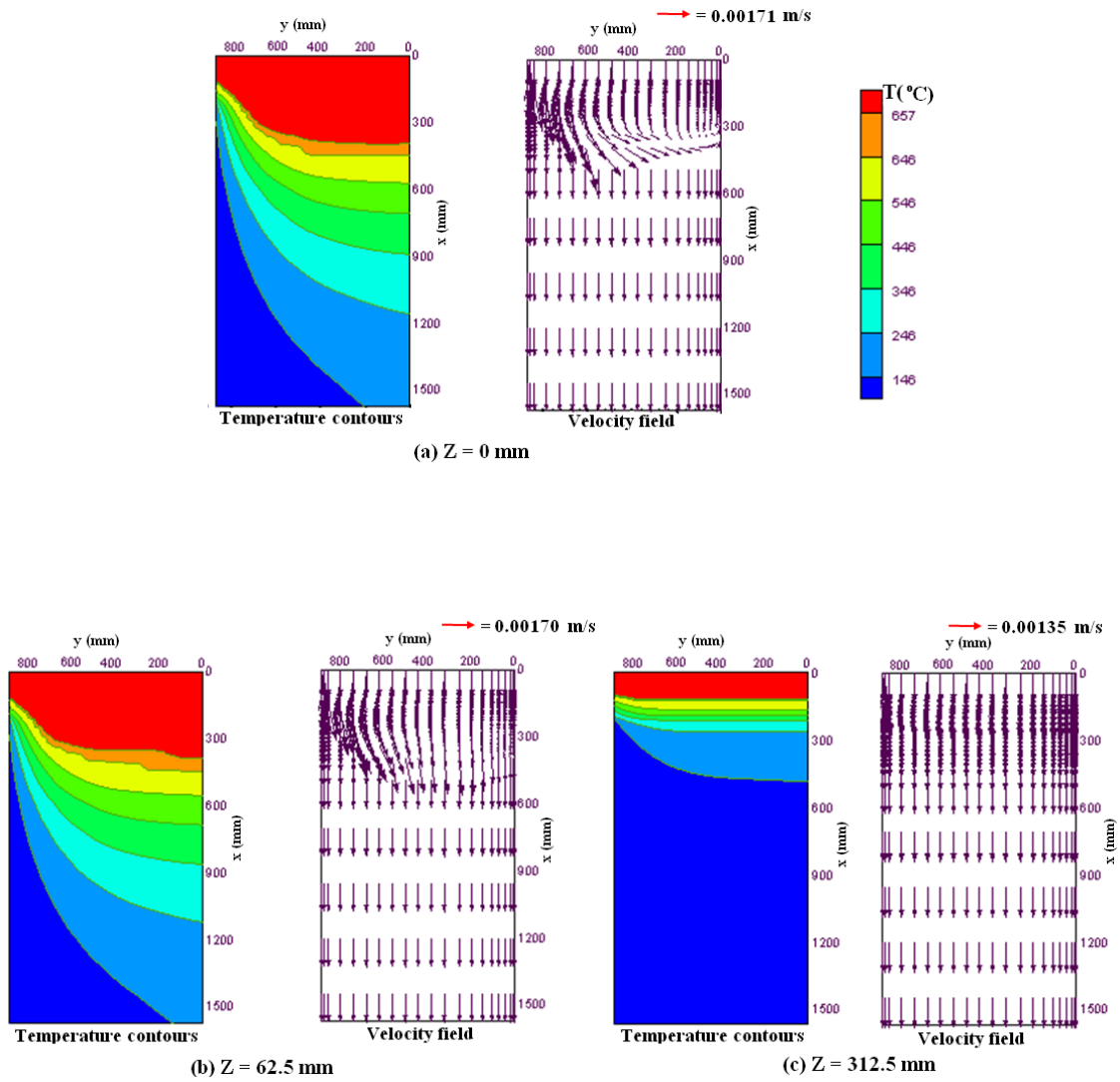

Figure 6.11: Enlarged 2-D view of temperature contours and velocity vectors of the top domain using the open top delivery system for a casting speed of 60 mm/min and 64°C superheat at: (a) wide symmetry plane at z = 0 mm, (b) vertical plane parallel to the wide face at z = 62.5 mm, (c) vertical plane parallel to the wide face at z = 312.5 mm.

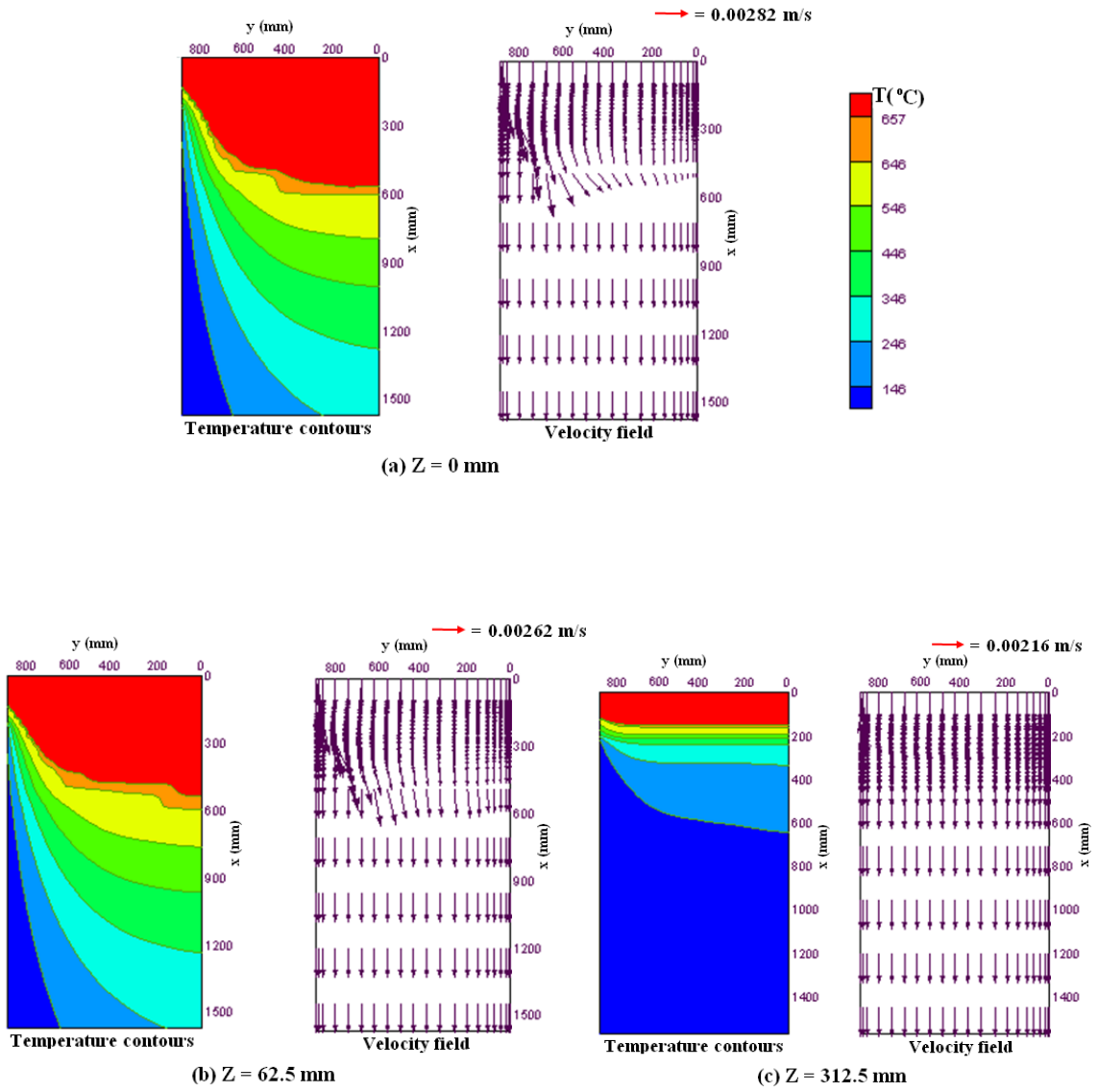

Figure 6.12: Enlarged 2-D view of temperature contours and velocity vectors of the top domain using the open top delivery system for a casting speed of 100 mm/min and 64°C superheat at: (a) wide symmetry plane at z = 0 mm, (b) vertical plane parallel to the wide face at z = 62.5 mm, (c) vertical plane parallel to the wide face at z = 312.5 mm.

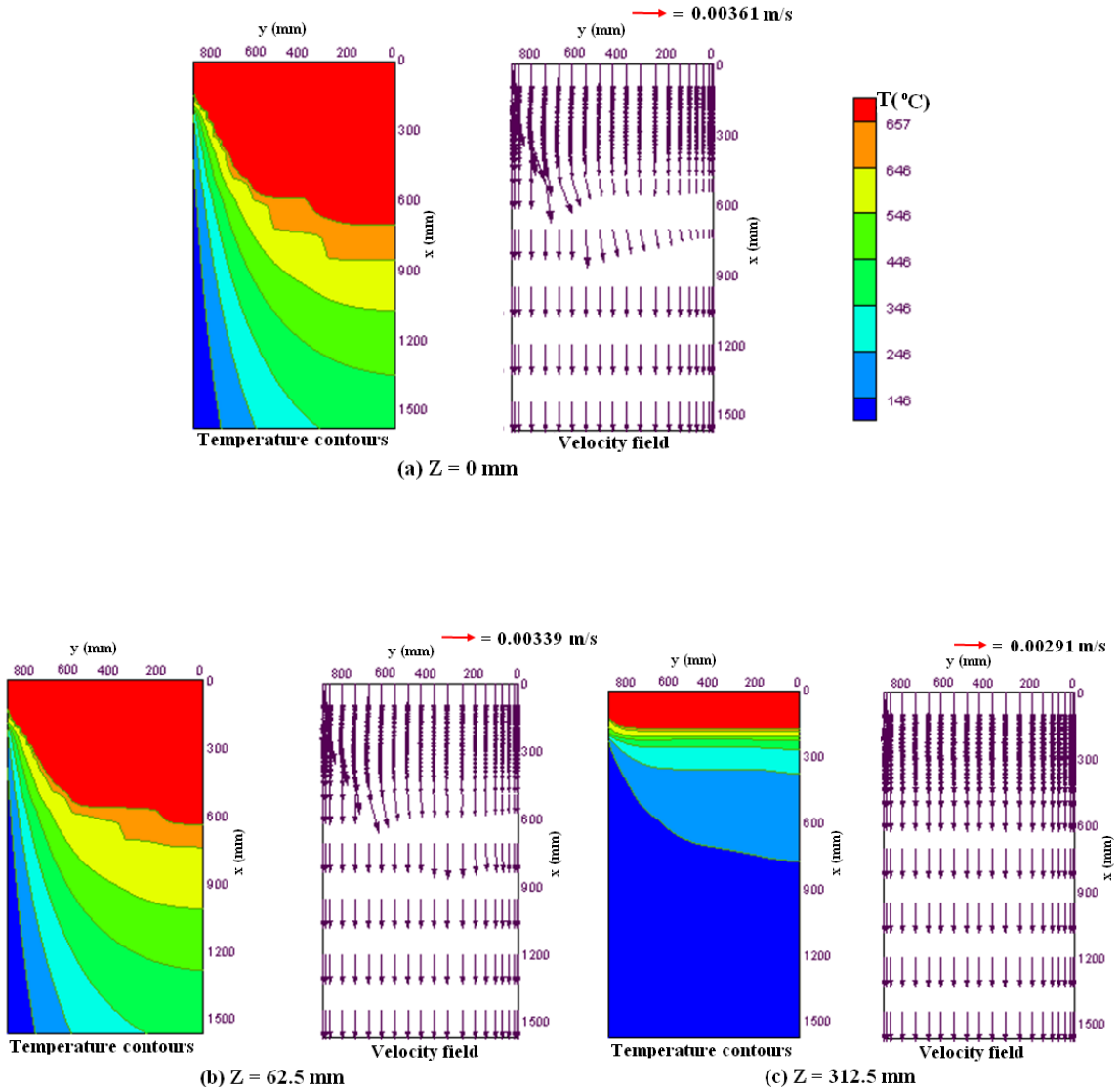

Figure 6.13: Enlarged 2-D view of temperature contours and velocity vectors of the top domain using the open top delivery system for a casting speed of 140 mm/min and 64°C superheat at: (a) wide symmetry plane at z = 0 mm, (b) vertical plane parallel to the wide face at z = 62.5 mm, (c) vertical plane parallel to the wide face at z = 312.5 mm.

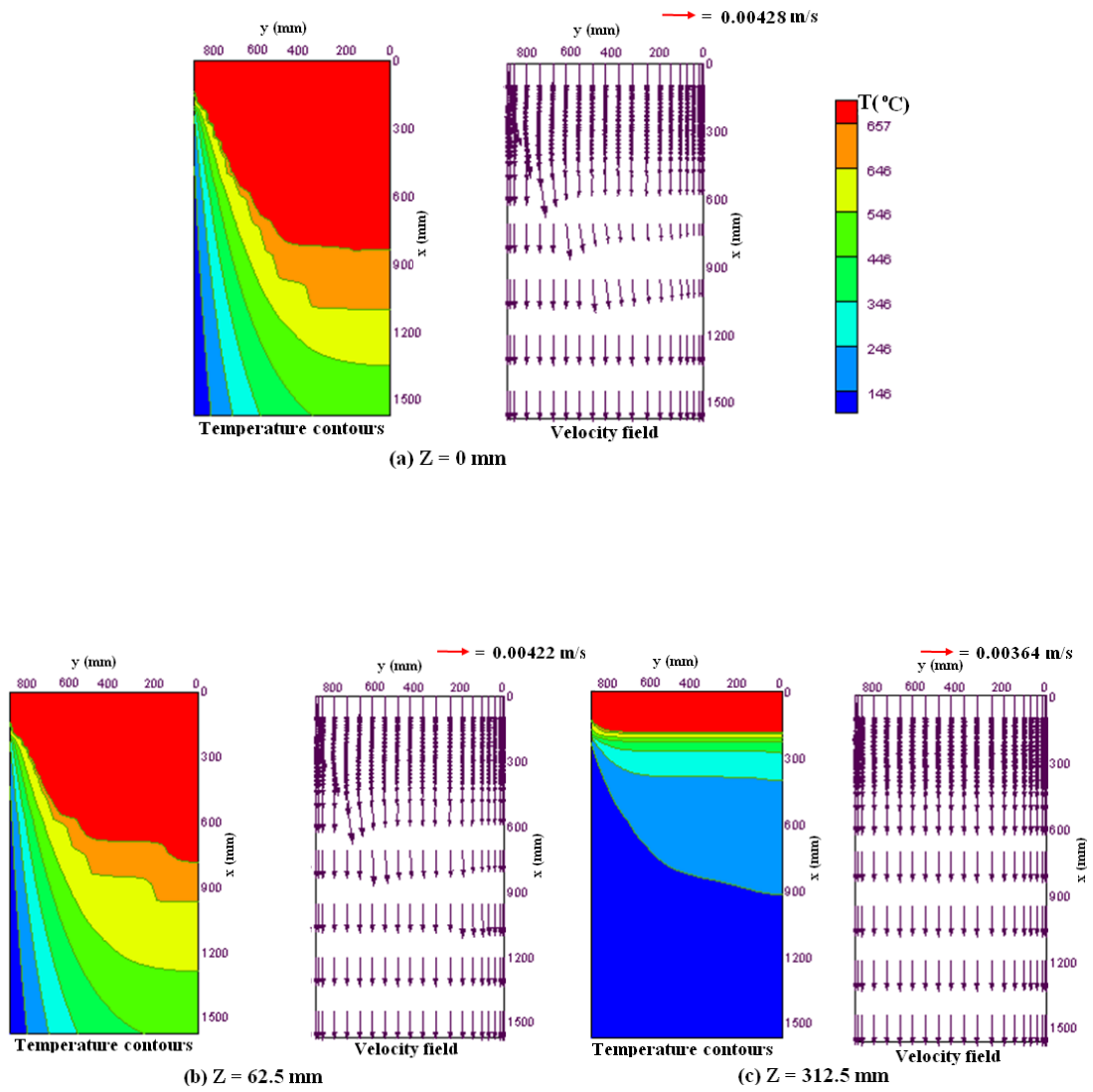

Figure 6.14: Enlarged 2-D view of temperature contours and velocity vectors of the top domain using the open top delivery system for a casting speed of 180 mm/min and 64°C superheat at: (a) wide symmetry plane at z = 0 mm, (b) vertical plane parallel to the wide face at z = 62.5 mm, (c) vertical plane parallel to the wide face at z = 312.5 mm.

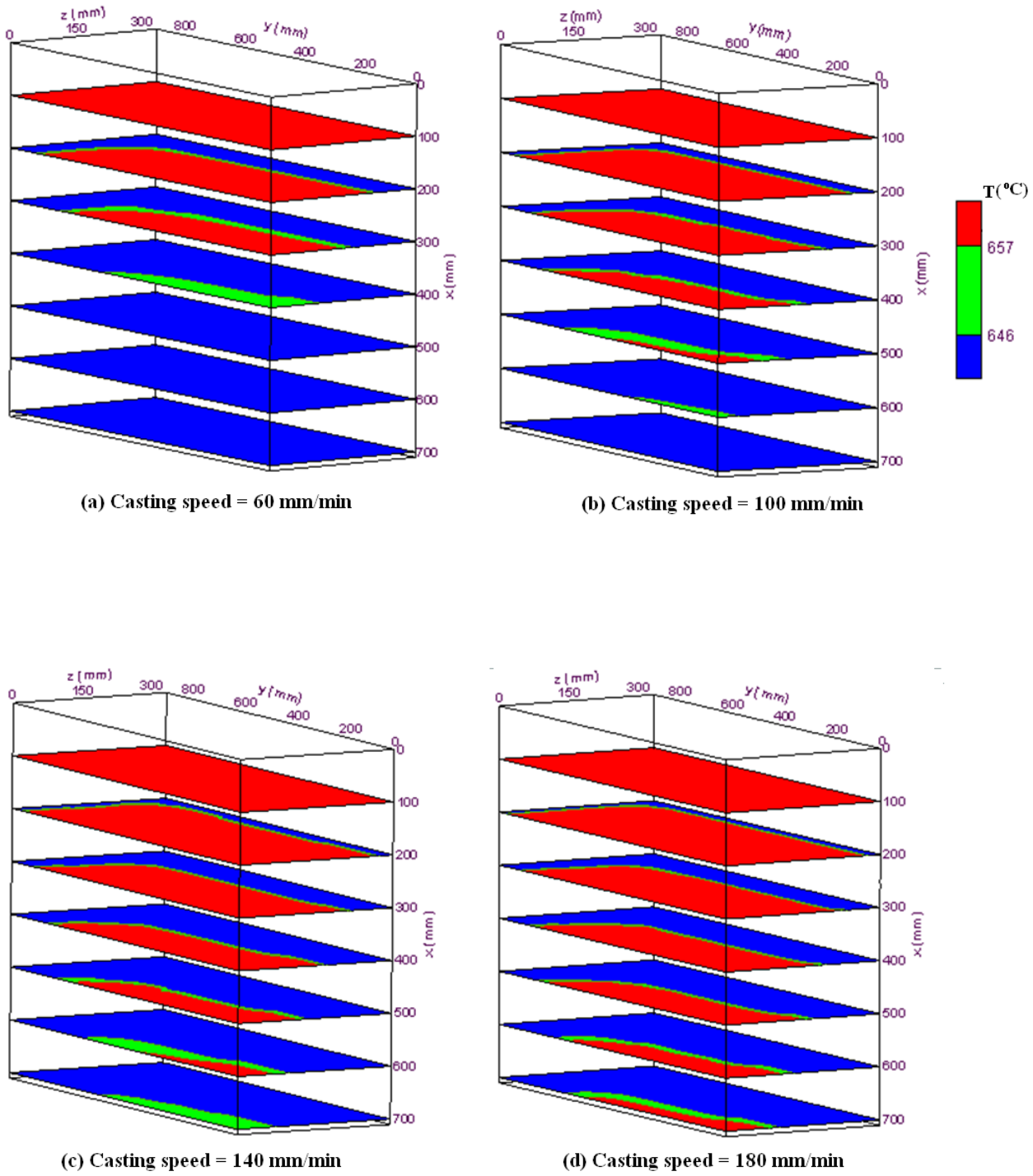

Figure 6.15: Contours of solidus and liquidus temperatures at various transverse cross-sectional planes (y-z planes) of the top part of the ingot using the open top delivery system for a superheat of 64°C and casting speeds of(a) 60 mm min^{-1} (b) 100 mm min^{-1} (c) 140 mm min^{-1} (d) 180 mm min^{-1}.

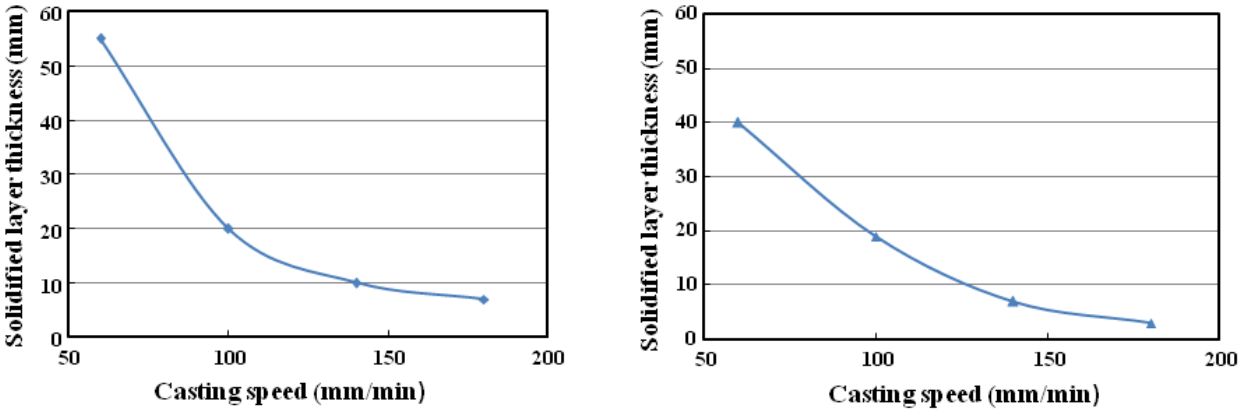

Figure 6.16: Solidified layer thickness from the narrow slab face at an axial distance of x = 160 mm from the top surface at the wide symmetry plane versus casting speed using the open top delivery system for: (a) inlet superheat of 32°C, (b) inlet superheat of 64°C.

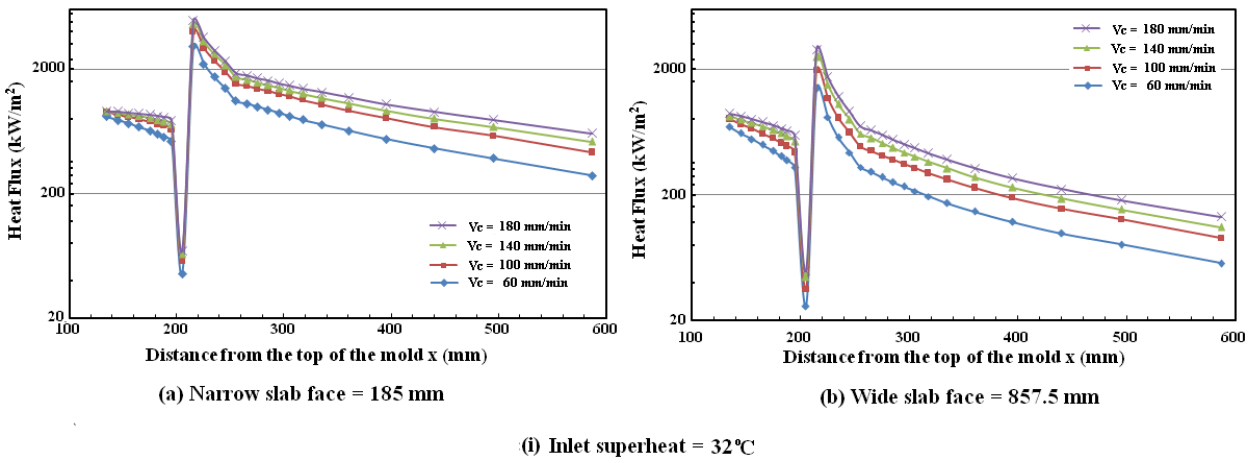

Figure 6.17: Variations of local surface heat fluxes for various casting speeds during solidification at 32°C superheat along the axial direction of the strand wall at: (a) z = 185 mm (b) y = 857.5 mm using the open top delivery system.

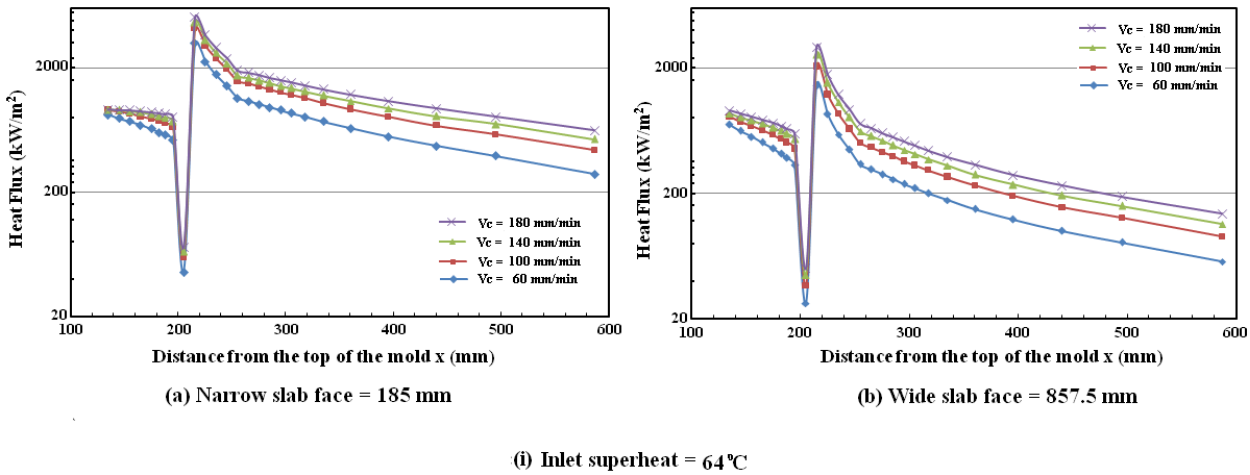

Figure 6.18: Variations of local surface heat fluxes for various casting speeds during solidification at 64°C superheat along the axial direction of the strand wall at: (a) z = 185 mm (b) y = 857.5 mm using the open top delivery system.

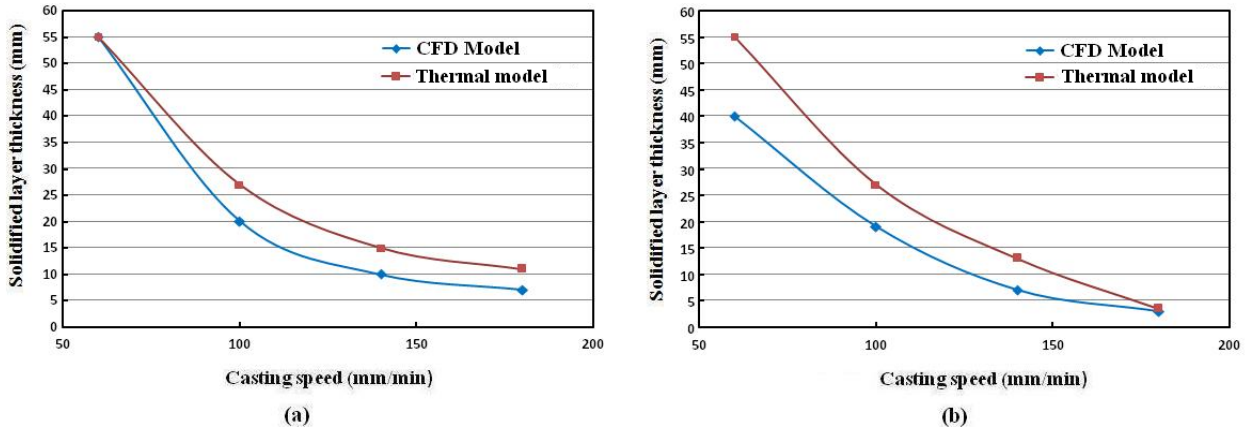

Figure 6.19: Comparison between thermal and CFD models on shell thickness predicted from the narrow slab face at an axial distance of x = 160 mm from the top surface at the wide symmetry plane versus casting speed using the open top melt feeding system, for: (a) inlet superheat of 32^{o}C, (b) inlet superheat of 64^{o}C.

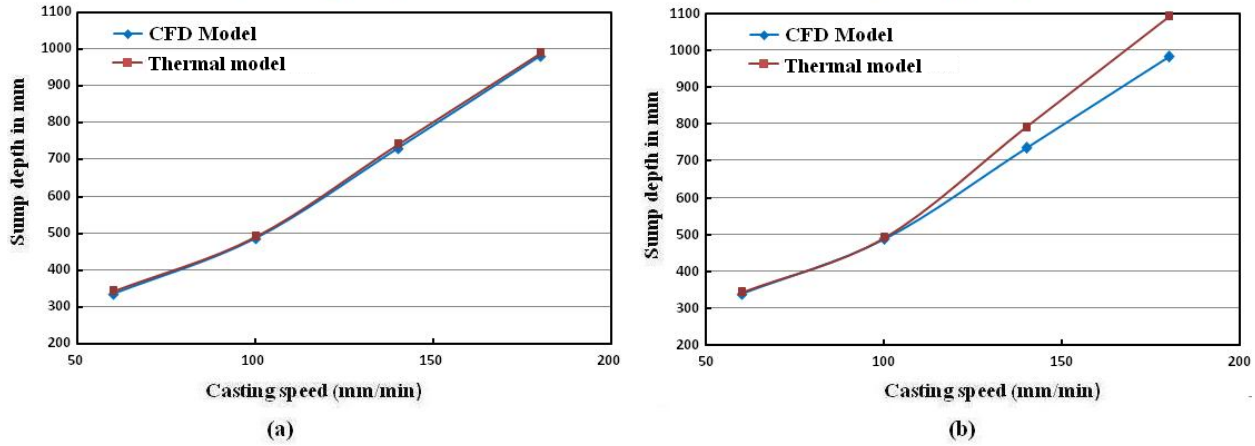

Figure 6.20: Comparison between thermal and CFD models on sump depth versus casting speed using an open top melt delivery system, for: (a) inlet superheat of 32^{o}C, (b) inlet superheat of 64^{o}C.

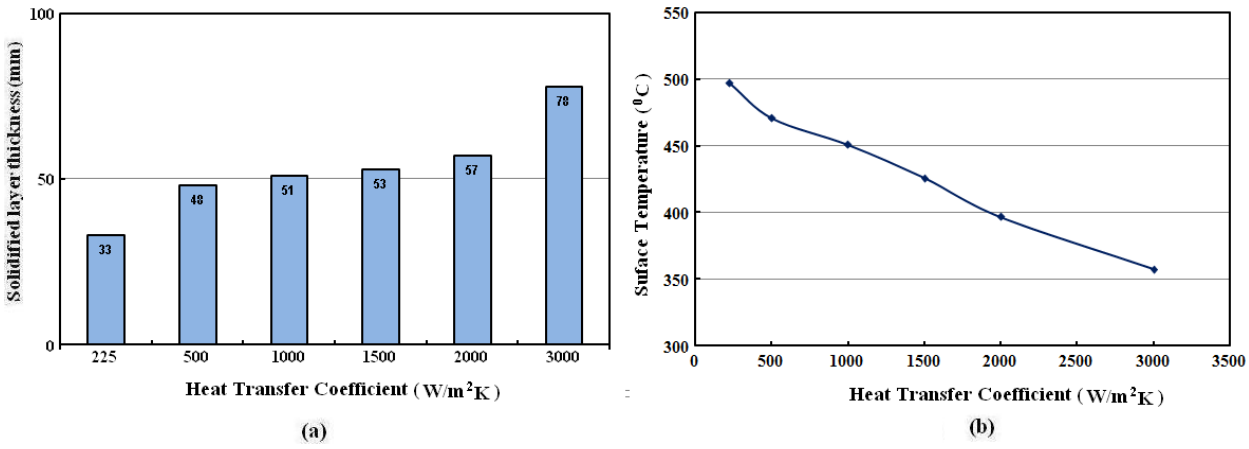

Figure 6.21: Effect of primary heat transfer coefficient on (a) solidified layer thickness (b) surface temperature, for an open top melt feeding system at a casting speed of 100 mm/min and an inlet superheat of 32^{o}C at the axial end of the mold (x = 205 mm) from the narrow face at the wide symmetry plane.

CHAPTER 7

OPEN TOP WITH FULL AND HALF POROUS FILTER

7.1 Introduction

Both plastic deformation during the extrusion of the billet and the final surface quality of the product are significantly affected by the presence of inclusions. The inclusions can also affect adversely the required mechanical properties of the cast and further they can damage the extrusion dies. The latter events could result in a long production delay [62]. In contrast to the extrusion of the round billets, the slabs are usually rolled to make the final products. During the rolling process, if a large number of inclusions are present there, they may create a number of unwanted defects, namely, edge cracking, pinholes, and foil breaks [33,63]. In a DC-casting process, the melt is filtered before it is transferred to the launder and casting table. After filtration the melt can pick-up inclusions in the latter two facilities and can end-up in the cast if an appropriate removal scheme is not implemented before the melt enters the mold. Once the melt enters the mold, the oxide inclusions and oxide scale that develop at the top free surface of the caster due to oxidation, may be picked-up by the strong turbulent flow generated by the melt delivery system. These inclusions will also invariably end-up in the cast if they are not removed. The strong turbulent flow at the free top surface of the caster will influence strongly the inclusion content and distribution in the final cast [7,64]. Recently, Jaradeh and Carlberg [66] investigated experimentally the distribution of inclusions in DC-slab casts. They have found that mostly oxide inclusions, which are larger and more harmful, appear at the slab surface, while the smaller inclusions remain in a significant pattern in the interior of the slab. They have concluded that the non uniform distribution of inclusion is mainly due to the fluid flow conditions during solidification.

The number of inclusions in the cast can probably be minimized by filtering the melt before it enters the mold using a filter of fine pore size. The major focus in this

study is to prevent the transportation of the inclusions from the hot top into the mold by employing a suitable melt delivery system, such that the inclusions remain trapped before the melt enters the mold. This can be accomplished by inserting a porous filter above the mold.

Figure 7.1 schematically shows the physical model and the computational domain (yellow color region) considered in this study. This figure also shows the origin and the directions of the coordinate axes. A reticulated stainless steel filter is placed at a vertical distance of 30 mm from the top free surface inside the hot-top. The 30 mm thick filter is introduced across the cross-section of the domain [123]. Perhaps, this is the first time that the melt distribution through a reticulated filter for a commercial-sized rolling ingot for the DC-casting of an aluminum alloy has been modeled. It is not the objective of the present analysis to determine how the inclusions are distributed in the slab, or how the flow will interact with the inclusions in the free fluid region or inside the porous filter. Further, how the inclusions are trapped on the surface and/or inside the pore of the filter is also not the objective of this study. The main purpose of this present study is to investigate the influence of the porous filter on the flow behavior, temperature distributions, and solidification characteristics in the mold and post mold regions.

Due to the presence of a filter inside the hot-top, the inlet melt in this process will follow two different regions, namely,

1. Clear fluid regions under and above the reticulated filter.
2. Porous region of the filter, where the internal fluid field of the porous region must be coupled with the over- and under-lying fluid fields.

To model the DC casting process with an internally placed filter, two different sets of transport equations (continuity, momentum and energy) for clear fluid and porous regions are needed. For clear fluid region the time-averaged turbulent form of the governing conservation equations are well known. But the mathematical description of the turbulent flow in the porous region is still a controversial issue. Based on the so-called pore Reynolds number Re_p, different classical mathematical treatments of the flow in the porous medium are reported in the literature [101], namely:

(i) Darcy or creeping flow regime ($Re_P < 1$);

(ii) Forchheimer flow regime ($1\sim10 < Re_P < 150$);

(iii) Post- Forchheimer flow regime (unsteady laminar flow, $150 < Re_P < 300$);

(iv) Fully turbulent flow ($Re_P > 300$).

For the pore Reynolds number, $Re_P > 300$, the researchers have proposed two different approaches to model turbulent flow and heat transfer through a rigid porous structure. In the first approach, the governing equations are first volume-averaged and latter they are time averaged. In the second approach, the above averaging techniques are reversed. These two approaches yield different sets of governing equations for turbulent kinetic energy and rate of dissipation and therefore, a contradictory situation arises (Pedras and de Lemos, 2000; 2001a; 2001b; and 2003). Though, many researchers believe that the flow through a porous media becomes laminar, even if the flow upstream of the medium is turbulent. This is because the flow velocities are drastically reduced by the network of the rigid structure of the porous matrix. For high Reynolds number flow through a non-deformable porous media, the non-Darcy form of the momentum equations is usually used [119]. In this study the flow of the melt inside the porous filter was considered to be turbulent and incompressible. However, the present mathematical model followed the second approach where a volume-averaged operator was applied to the local time-averaged turbulent equations, proposed by Pedras and De Lemos for turbulent flow in porous medium.

The full blown 3-D non-Darcy form of momentum equations, which incorporated both Brinkman and Forchheimer extensions to the Darcy model, were considered in this study. The Brinkman and Forchheimer terms in the momentum equations represent respectively, the viscous and inertia effects on the flow inside the porous matrix [118]. The linear additions of the above two terms in the Darcy model are based on semi-empirical models from the experimental fittings of the results. For the clear fluid and porous regions the low Reynolds number two equation k-ε turbulence model of Launder and Sharma was used. It is to be noted here the 3-D modeling of such a process is truly a challenging exercise. The model developed in this study and the control volume solution scheme implemented here offer a great advantage by the fact that the discretized governing equations are derived by integrating the partial differential equations over each

control volume of the calculation domain which can automatically handle the strong momentum exchange at the interface of the clear fluid and porous filter.

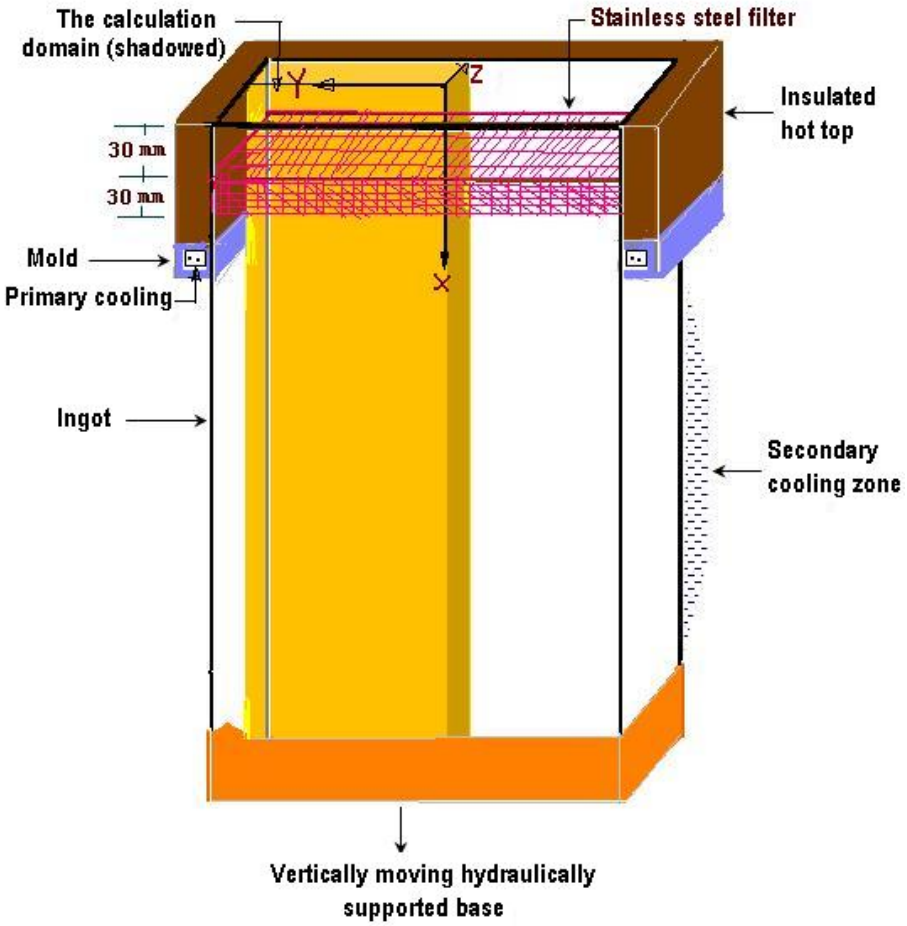

Figure 7.1: Schematic of a vertical DC caster with the calculation domain represented by yellow color for an open top melt delivery system with a full filter.

The ingot dimension details are given in Chapter-3. Here, the mold was hot top-type with a total length of 205 mm. The upper part of the mold, which forms the hot-top, was of length of 125 mm, and was designed by covering the four faces of the mold with a solid insulating material. The distance from the bottom of the mold to the water impingement point was 10 mm. The melt was delivered through the entire top cross-section of the hot top and then it passed through a filter which was placed inside the hop-

top. The melt distributor geometry used in the model is outlined in Figs 7.1. In addition, to get a clear picture about the position and size of the filter a 2-D view is presented in Figures 7.2 (a) and 7.2 (b). In this chapter two cases of the filter were simulated. In one case the filter dimensions inside the rectangular domain was arbitrarily set to 30 x 865 x 330 mm (Fig. 7.2(a)), and in another case it was taken as 30 x 433 x 330 mm (Fig. 7.2(b)), in the x, y, and z directions, respectively. For the sake of convenience during discussion, the filter width of 865 mm will be referred to as full-filtered case and the filter width of 433 mm will be referred to as half-filtered case. In the latter distributor system, the filter was placed in the center of the hot-top. The thermo-physical properties of the aluminum alloy (Al-1050) used in the simulations are shown in Table-3.1 in Chapter-3. To withstand the high inlet temperature of the aluminum melt, stainless steel was chosen for its high melting point as a material of the solid structure of the porous filter. The thermo-physical properties of the stainless steel used in reticulated filter are listed in Table-7.1. To account for the variable thermal conductivities, variable specific heats and density variations of the solid and liquid regions, the effective values of these variables were used. The porosity (ϕ) and permeability (K) of the porous media were considered to be 0.4, and 9 x 10^{-5}, respectively. The reason for choosing a value of 0.4 for porosity is the fact that, in many porous systems the porosity has been experimentally found to lie between 0.3- 0.5, and hence an average value of 0.4 was selected. The permeability of the solid porous structure has to be experimentally determined and is usually provided by the vendors who supply the filters. For steel filters the permeability usually lies between 10^{-6}-10^{-7}. In the present model Darcy number ($Da = K/D^2$) is an important parameter which appeared during the non-dimensionalization of the momentum equations for the porous media. In order to render Darcy number a convenient value of 10^{-4}, the permeability of the steel filter was considered to have a higher value of 9 x 10^{-5}.

In the present study, all the values of the relevant process parameters were kept same which were presented in Chapter-6. In these simulations, to incorporate the natural convection effect in the presence of forced convection, similar to the earlier study concerning open top delivery system, the Grashof number (Gr) was kept fixed at 10^9. The computational cases for Al-1050 (Prandtl number, Pr = 0.0063) which were studied in

this chapter are given in Table-7.2. It is to be noted that identical cases were also studied for the open top delivery system without a filter, which was discussed in Chaper-6.

Table-7.1: Physical properties of stainless steel for the filter and nozzle.

Properties (symbol)	Value [units]
Thermal conductivity (solid) (k)	0.036 [kW/(m-K)]
Density (solid) (ρ)	7850 [kg/m^3]
Specific heat (solid) (C_P)	0.69 [kJ/(kg-K)]

Table-7.2: Description of the parameters used for open top delivery system with a filter.

Case	Casting speed, u_s [mm/min]	Porosity, ϕ	Darcy number, Da = K/D^2	Inlet Reynolds number, (Re_L)	Inlet Peclet number, (Pe = Re_L x Pr)
1	60	0.4	1.0 x 10^{-4}	1595.42	10.07
2	100	0.4	1.0 x 10^{-4}	2659.08	16.78
3	140	0.4	1.0 x 10^{-4}	3722.64	23.50
4	180	0.4	1.0 x 10^{-4}	4786.25	30.21

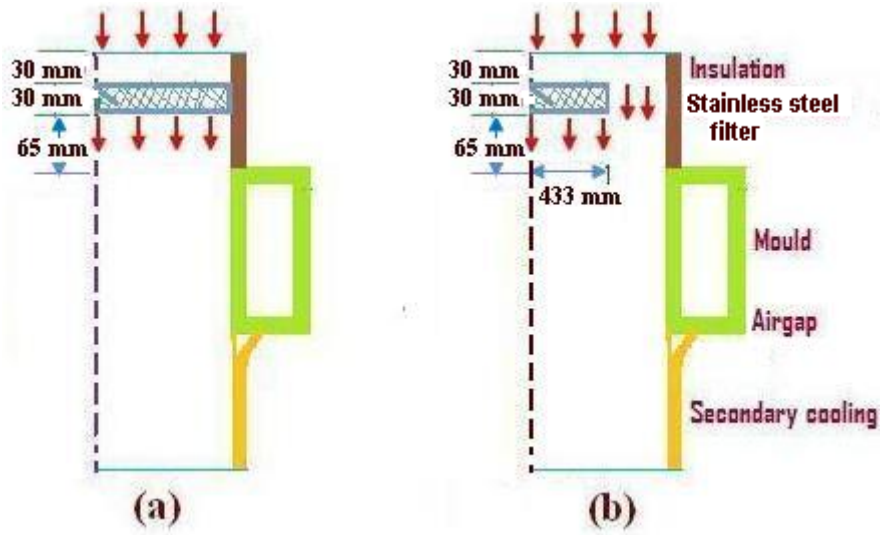

Figure 7.2: 2-D schematic view of the computational domain for an open top delivery system; (a) full-filtered case, and (b) half-filtered case.

7.2 Assumptions and Governing Equations

In addition to the assumptions listed in Chapter-3 the following assumptions were also made.

1. The filter was considered as non-deformable, homogeneous and isotropic porous media, which was saturated with the incoming melt.
2. The solid matrix of the porous media was considered to be in local thermal equilibrium with the surrounding melt.

For the clear fluid region, the 3-D turbulent Navier-Stokes and energy equations were used and a low-Reynolds number version of the popular k-ε eddy viscosity concept was adopted to account for the turbulence levels in the liquid pool, all were described in details in Capter-3. The details on the boundary conditions except for the porous region were documented in Chapter-3.

The conservation equations for the porous region, as mentioned earlier, were based on a non-Darcian model, incorporating the Brinkman and Forchheimer extensions to account for viscous and inertia effects, respectively. Beckermann et al. [1986 and 1987] have discussed the importance of the two extensions of the Darcy model. These authors have found that for modeling porous media with a high permeability (i,e,. a high Darcy number) the aforementioned two extensions are necessary. In terms of the superficial (Darcian) velocity, the volume-averaged conservative forms of the transport equations for turbulent flow in Cartesian-tensor notation for the porous layer are (Vafai, 1981; Hong et al., 1985; Large, 1998) as follows:

Continuity equation: $$\left(\frac{1}{\phi}\right) * \frac{\partial(\bar{u}_i)}{\partial x_i} = 0 \qquad \text{---------- (7.1)}$$

Momentum equation:

$$\left(\frac{1}{\phi^2}\right)*\frac{\partial(\rho\overline{u}_i\overline{u}_j)}{\partial x_j}=-\frac{\partial\overline{P}}{\partial x_i}+\left(\frac{1}{\phi^2}\right)*\frac{\partial}{\partial x_j}\left[\phi*\mu_l\left(\frac{\partial\overline{u}_i}{\partial x_j}+\frac{\partial\overline{u}_j}{\partial x_i}\right)-\rho\overline{u_i'u_j'}\right]-\frac{\mu}{K}\overline{u}_i$$

$$-\frac{C_F\rho|\overline{u}_j|\overline{u}_i}{\sqrt{K}}+\rho g_x \text{ ----------}\quad (7.2)$$

Energy equation: $$\left(\frac{1}{\phi}\right)*\frac{\partial(\rho\overline{u}_j\ \overline{H})}{\partial x_j}=\frac{\partial}{\partial x_j}\left(k_{Effective}\frac{\partial\overline{T}}{\partial x_j}-\left\{1/\phi\right\}*\rho\overline{u_j'H'}\right) \quad \text{-------}\ (7.3)$$

Transport equation for turbulence kinetic energy:

$$\left(\frac{1}{\phi}\right)*\frac{\partial(\rho\overline{u}_j k)}{\partial x_j}=\frac{\partial}{\partial x_j}\left[\left(\mu_l+\frac{\mu_t}{\sigma_k}\right)\frac{\partial k}{\partial x_j}\right]+\left(1/\phi^2\right)*\mu_t\left(\frac{\partial\overline{u}_i}{\partial x_j}+\frac{\partial\overline{u}_j}{\partial x_i}\right)\frac{\partial\overline{u}_i}{\partial x_j}+C_k\frac{\rho k|\overline{u}_j|}{\sqrt{K}}-$$

$$\rho(\varepsilon-D_k) \text{ ----------}\quad (7.4)$$

Transport equation for rate of dissipation of kinetic energy:

$$\left(1/\phi\right)*\frac{\partial\left(\rho\overline{u}_j\varepsilon\right)}{\partial x_j}=\frac{\partial}{\partial x_j}[(\mu_l+\frac{\mu_t}{\sigma_\varepsilon})\frac{\partial\varepsilon}{\partial x_j}]+c_1 f_1\frac{\varepsilon}{k}G-c_2\rho\left(C_k\varepsilon\frac{|\overline{u}_j|}{\sqrt{K}}+f_{\ 2}\frac{\varepsilon^2}{k}\right)+\rho E_\varepsilon \text{ ---}$$

(7.5)

Where, K = permeability of the porous media; ϕ is the porosity (void fraction) of the porous matrix; C_F = Forchheimer coefficient. As in Vafai et al. (1985), C_F can be represented as: $C_F=\frac{1.75}{\sqrt{150(1/\phi)^3}}$; The value 0.55 of C_F was used in this work. $k_{effective}$ = effective thermal conductivity = $\phi k_{fluid}+(1-\phi)k_{solid}$ in the energy equation. The value of C_k was taken as 0.28 as suggested by Pedras and de Lemos (2001b).

Here, $\overline{u}$ represents the time-averaged velocity vector; u' = turbulent fluctuations; k = turbulence energy = $\frac{1}{2}\overline{u_i'u_j'}$; ε = turbulence dissipation rate; $\overline{\rho u_i'u_j'}$ = Reynolds stresses in

the momentum equations; and ($\overline{\rho u_j' H'}$) = the turbulent heat flux in the energy equation. The right hand side of the momentum equation contains the pressure gradient term, the viscous diffusion term (Brinkman term), the turbulent diffusion term, the Darcy term and the Forchheimer term and gravitational term.

The macroscopic Reynolds stress $\overline{\rho u_i' u_j'}$ were also modeled by using the eddy viscosity concept and was given by: $\overline{\rho u_i' u_j'} = -\mu_t \left(\frac{\partial \overline{u}_i}{\partial x_j} + \frac{\partial \overline{u}_j}{\partial x_i}\right) + \frac{2}{3}\delta_{ij} k$; and the turbulent viscosity was given by: $\mu_t = \frac{\rho c_\mu f_\mu k^2}{\varepsilon}$.

In the above equations (4.5) and (4.6), σ_k , σ_ε , c_1 , c_2 , c_μ = dimensionless constants; and f_2 and f_μ = damping functions. The coefficient f_1 is a function that increases the magnitude of the destruction of the kinetic energy of turbulence (ε) near the wall. The Launder and Sharma (1974) low-Reynolds model was used here to take into account the low turbulent Reynolds number effects. The following damping functions f_2 and f_μ suggested by Launder and Sharma were used:

$$f_\mu = \exp\left[\frac{-3.4}{\left(1+\left\{R_T/50\right\}\right)^2}\right] \quad \text{---------- (7.6)}$$

$$f_2 = 1 - 0.3\exp\left(-R_T^2\right) \quad \text{----------(7.7)}$$

Where $R_T = \frac{k^2}{\nu\varepsilon}$ = turbulent Reynolds number; and ν is the kinematic viscosity. Following Launder and Sharma (1974), the model constants used here are given by: $C_\mu = 0.09$, $C_1 = 1.44$, $C_2 = 1.92$, $\sigma_k = 1.0$, $\sigma_\varepsilon = 1.3$, and the value of f_1 is set to 1.

Similar to the transport equations for the melt, the porous media transport equations (Eqns. 7.1-7.5) were non-dimensionalized with the same dimensional variables and were cast in the general form as Eqn (3.50) of Chaper-3 with appropriate coefficients, and

source and sink terms. It is to be noted here that the non-dimensional transport equations for the porous filter contained two additional parameters, porosity (ϕ) of the medium and Darcy number $(Da = K/D^2)$ both of which needed to be prescribed before solving the equations.

7.3 Fluid/Porous Interface Boundary Conditions

At the free fluid and porous surface, interface conditions for the mass, momentum, energy and the transport equations for k and ε are still not quite well established. The exact conditions applicable at the microscopic/macroscopic level are controversial even today. At the porous-fluid interface, the following boundary conditions were needed to be implemented. Similar boundary conditions were used by Yang and Hwang (2008) for the numerical simulation of turbulent flow and heat transfer in a rectangular porous channel.

$$\overline{u}_i\big|_f = \overline{u}_i\big|_p \;;\; \overline{p}_f = \overline{p}_p \;; \textit{and} \quad \overline{T}_f = \overline{T}_p \quad \text{----------(7.8)}$$

$$(\mu_l + \mu_t)\frac{\partial \overline{u}_i}{\partial x}\bigg|_f = (\mu_l + \mu_t)\frac{\partial \overline{u}_i}{\partial x}\bigg|_p \;; \qquad k_{f,eff}\frac{\partial \overline{T}_f}{\partial x} = k_{p,eff}\frac{\partial \overline{T}_p}{\partial x} \quad \text{----------(7.9)}$$

$$(\mu_l + \mu_t)\left(\frac{\partial \overline{u}_i}{\partial x_j} + \frac{\partial \overline{u}_j}{\partial x_i}\right)\bigg|_f = (\mu_l + \mu_t)\left(\frac{\partial \overline{u}_i}{\partial x_j} + \frac{\partial \overline{u}_j}{\partial x_i}\right)\bigg|_p \quad \text{----------(7.10)}$$

$$k\big|_f = k\big|_p \;; \quad \left(\mu_l + \frac{\mu_t}{\sigma_k}\right)\frac{\partial k}{\partial x_j}\bigg|_f = \left(\mu_l + \frac{\mu_t}{\sigma_k}\right)\frac{\partial k}{\partial x_j}\bigg|_p \quad \text{----------(7.11)}$$

$$\varepsilon\big|_f = \varepsilon\big|_p \;; \quad \left(\mu_l + \frac{\mu_t}{\sigma_\varepsilon}\right)\frac{\partial \varepsilon}{\partial x_j}\bigg|_f = \left(\mu_l + \frac{\mu_t}{\sigma_\varepsilon}\right)\frac{\partial \varepsilon}{\partial x_j}\bigg|_p \quad \text{----------(7.12)}$$

For the present calculations, the following porosity and permeability limits are applied for the clear and porous regions:

$$\phi = 1 \textit{ and } K \to \infty \quad \Rightarrow \quad \textit{clear fluid region}; \quad \textit{and}$$
$$\phi < 1 \textit{ and } K = \textit{finite} \quad \Rightarrow \quad \textit{porous region} \quad \text{----------(7-13)}$$

Where, the subscript ‘f’ and ‘p’ refer to the melt located in the clear fluid region and porous region. Here, $k_{f,eff}$ denotes effective thermal conductivity of the melt (or melt and solid) while $k_{p,eff}$ signifies the effective thermal conductivity of the porous medium. The above quantities can be expressed as

$$k_{f,eff} = f_l k_l + (1 - f_l) k_s \; ; \quad k_{p,eff} = k_{f,eff}\phi + k_{ps}(1-\phi) \text{ ---------- (7.14)}$$

Equations (7.8) – (7.10) represent the continuity of velocities, pressure, temperature, fluxes and shear stresses across the fluid/porous interface respectively. These interface conditions are used in the turbulent regime. The interface conditions in Equations (7.11) – (7.12) specify the continuity of k, ε and their fluxes across the interface for the turbulent regime, which were previously used by de Lemos and Pedras (2000).

In the control volume approach of Patanker (1980), based on an orthogonal Cartesian coordinate system, the above boundary conditions at the interface between the melt and the porous media as described in Eqs. (7.8) – (7.14) are automatically taken care off without an additional iterative procedure to match the interface conditions when the relevant thermo-physical properties of the porous medium are appropriately prescribed. In this study the porous filter was assumed to have been made of stainless steel. Furthermore, very dense grids are located near the fluid/porous interface.

7.4 Results and Discussion

In order to avoid confusion, the full-filtered case and the half-filtered case will be discussed separately. The discussion of the velocity and temperature fields will be followed by the discussion of the quantitative values of the sump depth, the mushy layer thickness, the growth of the shell, and finally, the local surface heat flux.

Under identical cooling conditions, the casting speed is one of the important parameters that govern the solidification rate, which can be measured in units of either

mm/min or m/s. The main parameters of interest in this study are the casting speed u_s, and the inlet superheat ΔT (T_{inlet} - $T_{liquidus}$). The values of the parameter considered were the four values of casting speed (u_s = 60, 100, 140, 180 mm/min), and two inlet superheats (ΔT = 32°C, 64°C). The inlet Reynolds and Peclet numbers for the aforementioned casting speeds are given in Table 7.2. A brief discussion of the results for the quantities mentioned in the above paragraph for an inlet superheat of 32°C is provided first and then it is followed by the discussion for inlet superheat of 64°C for full-filtered case. For half-filtered case, the results for the two inlet superheats on above the quantities are discussed simultaneously.

7.4.1 Full-Filtered Case

(a) Velocity and Temperature Fields for $\Delta T = 32^oC$

Figures 7.3(i-iv) show a 3-D surface plot of the computed temperature and velocity fields for four casting speeds and for a melt inlet superheat of 32°C for a filter having a width of 865 mm. Each figure shows the calculation domain, which consists of two symmetry planes [wide (x-y plane) and narrow (x-z plane)] as well as the top melt entry surface of the ingot. Figures 7.3(b,d,f,h) illustrate the 3-D velocity vector fields in the corresponding planner surfaces. From the plots of velocity vector, it can be noticed that all of the melt flows downward along the axial direction. This is because the melt in this feeding scheme is delivered at the top of the hot-top region along the entire top cross-section. As the melt reaches the porous filter it is directed downward through the pores of the filter. The resistance force created by the pore structure reduces the momentum of the downward flow inside the filter. At the exit of the filter, the momentum and buoyancy forces direct the flow downward. The weak downward jet is believed to be desirable, as it would reduce the turbulence in the mold region remarkably, that would lead to the minimization of macro-segregation. At the narrow and wide sides, the melt is bent and flows downward and towards the center in an inclined way. This is due to the fact that, as the melt contacts the solid shell that forms along the narrow and wide faces it is redirected along the solidification front.

In general, an increase in the casting speed results in an increased volume of the melt, which is accompanied by a relatively large amount of heat content. A comparison of Figs. 7.3(b,d,f,h), clearly show that in the liquid pool the magnitude of the velocities are increased with the increase of the casting speed. For example, at a casting speed of 60 mm/min, the maximum resultant velocity is found approximately 101.4 mm/min, whereas with the increase in casting speed of V_C = 180 mm/min, the resultant maximum velocity increases to 257.4 mm/min. With the increase of the casting speed, the gradient of velocity is also increased there, which in effect is causing the turbulence to enhance. Because of the presence of the filter, the fluctuations of velocities are diminished, and hence the turbulence is also decreased significantly. For a DC caster, a decrease in turbulence is beneficial for the uniformity of temperature across the cross-section of the cast.

Figures 7.3(a,c,e,g) show the temperature contours along with the solidification front and the liquidus isotherm. The effect of casting speed on temperature fields can be seen by studying the above figures. The dark yellow color region in these figures represents the mushy region. This region is confined by the solidus (646°C) and liquidus (657°C) temperature contours. A classical parabolic shaped solidification front is obtained at each casting speed due to the uniformity of the flow by the porous filter. Isotherm plots in these figures indicate that increasing the casting speed increases liquid melt region inside the domain which is represented by the red color. With the increase of the casting speed, the solidification front is becoming steeper and moving downward, and the mushy region is expanding due to the stronger thermal convection. In all of the above figures, the non-uniformity of the solidus isotherm is visible particularly near the middle of the wide symmetry plane. This non-uniformity is seen to increase with increase of the casting speed. One possible reason behind this unexpected characteristic of the solid profile could be due to the implementation of the enthalpy-porosity technique adopted here for the modeling of mushy region solidification problem in the presence of turbulence. Since with the increase of the casting speed the residence time of the melt decreases and as a result there is not enough time for the extraction of the heat from the melt. This is the reason for the downward movement of the solidification profile and thickening of the mushy layer for higher casting speeds. At and near the central area, the

parabola shape of the solidus isotherm is altered to the horizontal shape. The weak vertical flow into this limited area, locally alters the parabolic shape of the solid front. Due to predominantly conduction mode of heat transfer near the central area the extent of the horizontal length of the solidus isotherm is found to increase at lower casting speeds.

Figs. 7.4(a,b,c) – 7.7(a,b,c) illustrate explicitly a 2-D temperature contours and vector field at the wide symmetry plane (z = 0) and parallel to the wide symmetry plane at z = 62.5 mm, and z = 312.5 mm for various casting speeds for an inlet superheat of 32^{o}C. The left hand panels of these figures show the temperature contours while the right hand panels depict the velocity vectors at these three longitudinal cross-sections. The right hand panels of Figures 7.4(a), 7.5(a), 7.6(a), 7.7(a) show the velocity vectors for wide symmetry plane (z = 0) for four casting speeds. The velocity vector plot of each of these figures illustrates the strong vertical stream of hot melt is coming from the top of the domain. The corner stream is impacting on the solid front near the narrow face and is diverted and it moves along the solidification front, while the rest of the streams in the other part of the ingot are flowing vertically downward, as seen in these figures. The velocity fields in the right hand panels, at z = 62.5 mm and z = 312.5 mm, for four casting speeds are presented in Figures 7.4(b) through 7.7(b), and 7.4(c) through 7.7(c), respectively. A close look of the velocity vector field in each panel at z = 62.5 mm shows the corner stream near the narrow face is still obstructed by the developing solidification front, whereas the velocity field at z = 312.5 mm, which is close to the rolling face show an uniform downward flow. The magnitude of the velocity vectors at z = 312.5 mm is almost equal to the casting speed.

The temperature contours in the left hand panels, at z = 0, z = 62.5 mm and z = 312.5 mm, for four casting speeds are presented in Figures 7.4(a) through 7.7(a), 7.4(b) through 7.7(b), and 7.4(c) through 7.7(c), respectively. As one moves toward the rolling face from the slab center, the heat extraction rate increases, which is reflected on the shapes and locations of the isotherms at these three longitudinal cross-sections and the isotherms are seen to have lifted upward. These figures further show with the increase of the casting speed both liquidus and solidus isotherms are shifted downward and the vertical distance between them increases.

The temperature contours for four casting speeds for a melt superheat of 32^{o}C, at different transverse cross-sections (y-z plane) parallel to the top free surface, are illustrated in Figs. 7.8(a-d). These figures show how the growth of the solid shell and mushy region are progressing along the ingot axial direction. Below the sump profile, the melt is completely solidified and the solid moves with the casting speed where only conduction mode of heat transfer prevails. Only the part where liquid exist and convective heat transfer takes place, that part has been magnified here for better explaining the results. Seven cross-sections of the ingot are taken, which are at an axial distance of 100, 200, 300, 400, 500, 600, and 700 mm from the top ingot surface. As more heat is extracted from the melt along the axial distance through the solidified shell, the thickness of the solid layer presented by the blue color progressively increases for each casting speed. The growth rate and shell thickness on the rolling face are both higher compared to the narrow face because of higher heat extraction rate from the former face. Because of the closer proximity of the wide face from the symmetry axis there is less heat transfer resistance and hence the rate of growth of the solid shell is greater there compared to the narrow face. Almost round-shaped solidification front and mushy zone are seen around the corner formed by the wide and narrow faces, because of higher heat extraction rate through the two sides of the ingot. The remarkable decrease of the solidified region (represented by blue color) along the axial distance is clearly seen with increase in casting speed by inspecting the above figures, the reasons for which have already been explained earlier.

(b) Quantitative Analysis for $\Delta T = 32^{o}C$

(i) Sump Depth and Mushy Layer Thickness

The predicted sump depth and the mushy zone thickness at the ingot center for various casting speeds are listed in Table 7.3. The results clearly show that a higher sump depth is obtained at a higher casting speed, which is consistent with the experimentally observed fact reported in other studies [89]. At a given casting speed of 60 mm/min, the sump depth is approximately 329 mm from the top of the mold. The relative difference of

sump depth at casting speeds of 100, 140, and 180 mm/min, is about respectively 46 %, 116 %, and 196 % higher, in comparison to the lowest casting speed of 60 mm/min, which can be seen in Table 7.3. In the same table, the results show that the thickness of the mushy layer at the center do not follow a specific trend. At the center, for a casting speed of 100 mm/min the mushy thickness decreases by about 25 %, whereas, for casting speeds of 140, and 180, the thickness increases by 164 %, and 400%, respectively compared to the casting speed of 60 mm/min. The reason for this anomalous behavior in the formation of mushy layer zone at the center could be due to the complex interaction of the flow and buoyancy effected thermal fields.

Table-7.3: Sump depth and mushy thickness in mm at the center of the ingot for an open-top delivery system with a full filter having a width of 865 mm for four casting speeds and at a superheat of 32^{o}C.

Quantity	Values of casting speed (u_s) in mm/min			
	60	100	140	180
Sump depth (mm)	329	45.9 % higher than u_s = 60 mm/min	115.8 % higher than u_s = 60 mm/min	196.4 % higher than u_s = 60 mm/min
Mushy thickness (mm)	53	24.5 % lower than u_s = 60 mm/min	164.2 % higher than u_s = 60 mm/min	400.0 % higher than u_s = 60 mm/min

(ii) Formation of Solidified Shell

Figure 7.15 (a) shows the shell thickness versus casting speed profile at the wide symmetry plane. This shell thickness is measured from the narrow slab face at an axial distance of 160 mm below the slab top surface. This axial position is located at around the middle of the mold. In Table 7.4, the predicted values of the shell thickness for the same location are listed for four specified casting speeds. From both, Fig. 7.15 (a) and Table 7.4, it is observed that with the increase in the casting speed the shell thickness

decreases rapidly up to a casting speed of about 100 mm/min, and then there is a gradual decrease until the casting speed reaches to a value of 180 mm/min.

Table-7.4: The thickness of the solidifying shell (mm) at wide symmetry plane from the narrow slab face at an axial distance of 160 mm from the top surface inside the mold for four casting speeds and inlet superheat of 32°C for an open-top delivery system with a filter having a width of 865 mm.

Quantity	Values of casting speed (u_s) in mm/min			
	60	100	140	180
Thickness of the solidifying shell (mm)	55	56.4 % lower than u_s = 60 mm/min	76.4 % lower than u_s = 60 mm/min	83.6 % lower than u_s = 60 mm/min

(iii) Local Surface Heat Flux

For four casting speeds the predicted profiles of the local surface heat flux along the cast at the narrow and wide faces are illustrated in Figures 7.16(a, b). In order to capture the sudden decrease and increase in the surface heat extraction rate, the local heat flux profile is drawn from x =135 mm to x = 587 mm below from the top surface. For the simulated slab the stated axial distance is one of the crucial regions for the formation of surface and sub-surface cracks. For the comparison purposes two locations have been selected arbitrarily at the narrow and wide faces, at z = 185 mm, and y = 857.5 mm, respectively.

Figs. 7.16(a) and 7.16(b) show how the local heat flux varies axially at z = 185 mm, and y = 857.5 mm. In each figure, there are four graphs representing the results for four casting speeds. The general trend of these graphs is quite similar in nature except their quantitative values. It is to be noted that the surface temperature is numerically predicted from the model from which the local surface heat flux is calculated. Therefore, the trend of the surface temperature and the local heat flux is similar. The local surface

heat flux is therefore a reflection of the surface temperature. An examination of any of the four graphs shows that, within the mold there is an almost linear decrease of heat flux (heat extraction rate) with the axial distance. In the air- gap region (10 mm) within the mold, a low value of the heat transfer coefficient was imposed to remain consistent with the experimental observation reported by various researchers. The rapid decrease of the local heat flux at that region is a reflection of the above fact. Between the exit of the mold and the impingement point (from x = 205 mm to x = 215 mm), the heat transfer coefficient was assumed to increase linearly, and as a result the local heat flux increases very sharply there. At the water jet impingement point, the imposed heat transfer coefficient was the highest. This resulted in the highest heat flux at that point. From the impingement point (x = 215 mm) to a distance of about 40 mm (x = 255 mm), the heat transfer coefficient was assumed to decrease linearly, and as a result there is a steep decrease of the local heat flux in that region. For rest of the cast, a fixed value of the heat transfer coefficient was imposed in conformity with the observed experimental fact. The monotonic decrease of the local heat flux for the rest of the cast bears this testimony. The region from x = 205 mm to the end of the cast was called the secondary cooling region.

The higher casting speed shows the higher local heat flux at each grid point. The quantitative values of the local heat flux at a fixed location (z = 185 mm and x = 215 mm) show the same trend (Table 7.5). The reason for this has been explained earlier.

It should be mentioned that, for the same convective heat transfer boundary condition at the wide and narrow slab faces, there is a distinct difference in the axial distributions of the local heat flux. For each casting speed, a higher value of the local heat flux is achieved along the cast at z = 185 mm compared to the value obtained for the same axial location but at y = 857.5 mm, the reason is due to the proximity of the wide slab face from the symmetry axis compared to the narrow side.

Table-7.5: The local heat flux (kW/m^2) at z = 185 mm at an axial distance of 215 mm from the top surface for four casting speeds and for an inlet superheats of 32°C, an open-top delivery system with a filter having a width of 865 mm.

Quantity	Values of casting speed (u_s) in mm/min

	60	100	140	180
Local surface heat flux (kW/m^2)	3077.36	31.1 % more as compared with 60 mm/min	49.5 % more as compared with 60 mm/min	61.0 % more as compared with 60 mm/min

(c) Velocity and Temperature Fields for $\Delta T = 64^oC$

The 3-D surface plots of the predicted temperature and velocity fields for four casting speeds, and for a melt superheat of 64°C, are shown in Figures 7.9(i-iv). The velocity field in the right hand panel and the temperature field in the left hand panel, at three longitudinal cross-sections (z = 0, z = 62.5 mm, and z = 312.5 mm) at an inlet superheat of 64°C, for the aforementioned casting speeds are shown in Figures 7.10(a,b,c) through 7.13(a,b,c). The temperature fields, at different transverse cross-sections (y-z plane) parallel to the slab-free surface, are illustrated for four casting speeds in Figs. 7.14(a-d). In Figs. 7.14(a-d), the shapes of the solid and liquid isotherms have been depicted for an interval of 100 mm distance in the axial direction from the top of the ingot, at seven y-z planes.

Figures 7.9(b,d,f,h) illustrate the 3-D velocity vector fields. Except for the inlet superheat, all conditions were identical to the predicted velocity fields of Figs. 7.3(b,d,f,h). Flow patterns which are depicted in Figures 7.9(b,d,f,h), closely resemble to those observed for $\Delta T = 32^oC$ in Figures 7.3(b,d,f,h). Due to the increased melt superheat, the influence of thermal convection on bulk fluid motion is also increased, which is evident by the magnitude of the velocity vector inside the ingot. The magnitude of the maximum velocity is enhanced for each casting speed compared to the previous case of inlet superheat of 32^oC.

The flow patterns of the right hand panels of Figures 7.10(a,b,c) through 7.13(a,b,c) for $\Delta T = 64^oC$ are similar to those in the right hand panels of Figures 7.4(a,b,c) through 7.7(a,b,c) at three longitudinal cross sections for four casting speeds, with minor exceptions. The strength of the flow increases with increasing inlet melt superheat. The vertical jet near the narrow face is impacting the solidification front with

a higher momentum compared to the earlier cases for the correspondingly same casting speeds.

Figures 7.9(a,c,e,g) illustrate the 3-D temperature distributions. The most noteworthy influence of increasing melt pouring temperature is the reduction in growth of the solid phase. The influence of increasing melt temperature on solidification can be found by comparing the results with those of Figs. 7.3(a,c,e,g) for $\Delta T = 32^oC$. The patterns of the isotherms in both the solid and liquid regions of Figs. 7.9(a,c,e,g) are closely similar to those of Figs. 7.3(a,c,e,g), with minor differences in the local positions of the isotherms. All the isotherms of Figs. 7.9(a,c,e,g) have slightly moved axially downward compared to those of Figs. 7.3(a,c,e,g). This observation is confirmed by the left hand panels of Figures 7.10(a) through 7.13(a) at the wide symmetry plane, which reveals a significant delay in the solidification rate compared to the previous case at $\Delta T = 32^oC$. The solidification front irregularities around the middle of the wide symmetry plane also persist for this case. A comparison of the left hand panels of Figures 7.10(b,c) through 7.13(b,c) at z = 62.5 mm, and z = 312.5 mm, with the corresponding figures for $\Delta T = 32^oC$, shows the relative delay of the solidification process inside the ingot and also in the vicinity of the wide symmetry plane.

The growth of the solid and mushy regions presented in Figures 7.14(a-d) for $\Delta T = 64^oC$ are similar in trend to those for $\Delta T = 32^oC$ (Figs. 7.8(a-d)). The similarities in trends of these figures with the previous results are attributable to the same descriptions used to describe the latter figures.

(d) Quantitative Analysis for $\Delta T = 64^oC$

(i) Sump Depth and Mushy Layer Thickness

The predicted sump depth and the mushy zone thickness at the ingot center for various casting speeds at an initial superheat, $\Delta T = 64^oC$ are listed in Table 7.6. From this table it is evident that with the increase of casting speed, the above mentioned quantities are enhanced sharply due to the increase of thermal convection, except for the mushy

thickness at casting speed of 100 mm/min, which shows the smallest value compared to the other three casting speeds.

For $\Delta T = 64^oC$, at a casting speed of 60 mm/min, the sump depth is 332 mm, whereas at the higher casting speeds of 100, 140, and 180 mm/min, the sump depth is about 45 %, 120 %, 195 % , respectively , higher in comparison to the lower casting speed of 60 mm/min, due to the decreased residence time.

The sump depth and liquid pool depth at the ingot center at each casting speed for $\Delta T = 64^oC$ (Table 7.6) differ slightly from those predicted for $\Delta T = 32^oC$ (refer to Table 7.3). The comparison between these two inlet superheats reveals that, the sump depth at casting speeds of 60, 100, 140, and 180 mm/min for $\Delta T = 64^oC$, is only 0.9 %, 0 %, 2.8%, and 0.3%, respectively larger, whereas the liquid pool depth at the slab center is only 0.4 %, 0.5%, 0.9%, and 1.4%, respectively higher compared to those found for $\Delta T = 32^oC$. Relatively very small differences are observed in both the locations of the liquidus and solidus isotherms at the ingot center at each casting speed for two melt superheats. The liquidus and the solidus positions both are shifted little bit downward as inlet superheat is increased. The primary cause of the increment in the axial distance of the above isotherms is due to the increase in heat content of the liquid region.

Table-7.6: Sump depth and mushy thickness in mm at the center of the ingot for an open-top delivery system with a filter having a width of 865 mm at four casting speeds and a superheat of 64^oC.

Quantity	Values of casting speed (u_s) in mm/min			
	60	100	140	180
Sump depth (mm)	332	44.6 % higher than u_s = 60 mm/min	119.8 % higher than u_s = 60 mm/min	194.6 % higher than u_s = 60 mm/min
Mushy thickness (mm)	55	31.0 % lower than u_s = 60 mm/min	181.8 % higher than u_s = 60 mm/min	369.1 % higher than u_s = 60 mm/min

(ii) Formation of Solidified Shell

The solidified layer thickness for an inlet superheat of 64^{o}C is given graphically in Figs. 7.15(b) and numerically predicted values are listed in Table 7.7 for four casting speeds. Here, the thickness of the solid shell from the narrow slab face at the wide symmetry plane (z = 0) at an axial distance of 160 mm from the slab top surface is taken into consideration. An increase in the casting speed leads in delaying the development of solid shell. In this particular case, one can see from the table that, at a casting speed of 60 mm/min, the solid shell thickness is 51 mm, whereas at the higher casting speeds of 100, 140, and 180 mm/min, the thickness of the solidifying shell is about 57 %, 80 %, 94 %, respectively lower in comparison to the lower casting speed of 60 mm/min.

With increasing melt superheat (ΔT), the existence of additional heat in the liquid bath always shows relatively smaller shell formation and is consistent with the observed results (Figs. 7.15(a), and Table 7.4 for $\Delta T = 32^{o}$C; Figs. 7.15(b) and Table 7.7 for $\Delta T = 64^{o}$C). The relative difference of solidified layer thickness at casting speeds of 60, 100, 140, and 180 mm/min for $\Delta T = 64^{o}$C, is about 7.3 %, 8.3%, 23.1%, and 66.7%, respectively lower in comparison to $\Delta T = 32^{o}$C. The impact of increasing melt superheat is weaker for lower casting speed cases in contrast to the higher casting speed cases.

Table-7.7: The thickness of the solidifying shell (mm) at wide symmetry plane from the narrow slab face at an axial distance of 160 mm from the top surface inside the mold for four casting speeds and inlet superheat of 64°C for an open-top delivery system with a filter having a width of 865 mm.

Quantity	Values of casting speed (u_s) in mm/min			
	60	100	140	180
Thickness of the solidifying shell (mm)	51	56.9 % lower than u_s = 60 mm/min	80.4 % lower than u_s = 60 mm/min	94.1 % lower than u_s = 60 mm/min

(iii) Local Surface Heat Flux

The local surface heat flux on the narrow face at z = 185 mm and on the wide face at y = 857.5 mm along the axial direction of the caster for $\Delta T = 64^oC$ (Figs. 7.17(a,b)) are similar in tend to those observed in Figs 7.16(a,b) for $\Delta T = 32^oC$. With the increase in casting speeds, the local surface heat flux increases at each axial grid point, as can be seen in Figs.7.17(a,b). Moreover, from Table-7.8, it is observed that, the surface heat flux at a casting speed of 60 mm/min at z = 185 mm, x = 215 mm, is 3120.32 kW/m^2, which is only about 33 %, 49 %, and 62 % higher for the higher casting speeds of 100, 140, and 180mm/min, respectively in comparison to lower casting speed of 60 mm/min.

The local surface heat flux increases with the increase of melt superheat at each casting speed and the corresponding enhancement is driven by the additional heat content in the liquid-mushy regions. From Table-7.5, and Table 7.8, it is evident that, at z = 185 mm, and x = 215 mm, for $\Delta T = 64^oC$, only 1.4 %, 2.6 % , 0.79 %, and 2.0 % more local surface heat flux is obtained at casting speed of 60, 100, 140, and 180 mm/min, respectively compared to those predicted for $\Delta T = 32^oC$.

Table-7.8: The local heat flux in kW/m^2 at z = 185 mm at an axial distance of 215 mm from the top surface for four casting speeds and for an inlet superheats of 64°C, an open-top delivery system with a filter having a width of 865 mm.

Quantity	Values of casting speed (u_s) in mm/min			
	60	100	140	180
Local surface heat flux (kW/m^2)	3120.32	32.6 % more as compared with 60 mm/min	48.6 % more as compared with 60 mm/min	61.9 % more as compared with 60 mm/min

7.4.2 Half-Filtered Case

(a) Velocity and Temperature Fields for $\Delta T = 32^oC$, and $\Delta T = 64^oC$

The 3-D surface plots of the velocity fields along with the corresponding temperature distributions for two inlet superheats of 32^oC, and 64^oC, are shown in Figs. 7.18(i,ii,iii,vi) and 7.24(i,ii,iii,vi), respectively for four casting speeds for an open top with a porous filter having a width of 433 mm. Figs.7.19(a,b,c) – 7.22(a,b,c) and Figs. 7.25(a,b,c) – 7.28(a,b,c) illustrate 2-D temperature and velocity profiles for an inlet superheats of 32^oC, and 64^oC, respectively at the wide symmetry plane (z = 0) and parallel to the wide symmetry plane at z = 62.5 mm, and z = 312.5 mm for the aforementioned casting speeds. Each plot is magnified, which extends up to two-third of the domain from the top. Figures 7.23(a-d) and 7.29(a-d) present temperature contours for transverse cross-sections (y-z plane) parallel to the slab-free surface at an inlet superheats of 32^oC, and 64^oC, respectively, which illustrate how the shape and growth of the solid shell and mushy region are developing along the ingot casting direction. In the above figures, only a vertical portion of about 700 mm of the ingot are portrayed and magnified.

In this melt feeding system, melt is delivered into the hot-top through a 433 mm horizontal porous filter placed at the center and as a result there is a horizontal opening of 432 mm between the narrow face and the end of the porous filter. Due to this 433 mm filter, a large portion of the downward flow coming from the top rotates 90 deg clockwise at and around the central region of the ingot. The above horizontal flow is obstructed near the exit of the filter by the downward vertical flow, and then passing through the 432 mm horizontal opening. The strength of the latter flow is weakened because of this interaction. A much smaller portion of the melt is passing through the filter. This can be seen in Figures 7.18(b,d,f,h) and Figures 7.24(b,d,f,h) for $\Delta T = 32^oC$ and for $\Delta T = 64^oC$, respectively. The strength of the downstream melt passing through the gap between the filter and the ingot narrow face can be identified by observing the velocity vectors in the right hand panels of the two-dimensional velocity fields in Figs. 7.19(a,b,c) through 7.22(a,b,c) and Figs. 7.25(a,b,c) through 7.28(a,b,c) for $\Delta T = 32^oC$ and $\Delta T = 64^oC$, respectively for four casting speeds.

Unlike the full-filtered case, for the half-filtered case and for the same operating conditions, there are greater convection currents for the latter case, which are represented by the maximum resultant velocity values for four casting speeds and two inlet superheats. The magnitudes of the maximum resultant velocities are listed in Table-7.9, which are obtained from three-dimensional velocity vector plots.

Table 7.9: Comparison of maximum resultant velocities (mm/min) between the full-filtered and half-filtered case.

Geometry	Inlet superheat (ΔT)	Values of casting speed (u_s) in mm/min			
		60	100	140	180
Full-filtered domain	32^oC	101.4	152.4	201.0	257.4
	64^oC	121.8	184.8	204.0	295.2
Half filtered domain	32^oC	102.0	154.8	203.4	259.2
	64^oC	121.8	186.0	205.2	297.0

From Table 7.9, it is seen that, the value of the maximum resultant velocity increases with the increase in melt superheat from $\Delta T = 32^oC$ to $\Delta T = 64^oC$ at each casting speed for half-filtered case, and for a fixed superheat, the maximum resultant velocity increases with increase in the casting speed, similar to those seen for the full-filtered case. While the change in the maximum resultant velocity with increase in casting speed is significant but for the increase of the superheat the corresponding change is insignificant.

The isotherms shown in Figs 7.18(a,c,e,g), and Figs 7.24(a,c,e,g) for $\Delta T = 32^oC$ and $\Delta T = 64^oC$, respectively are for four casting speeds. The delay in the local solidification process is due to increase in thermal convection resulting from the increase of the melt superheat, which can be seen by inspecting these figures. With the increase in the casting speed from 60 to 180 mm/min, a similar behavior has been observed by investigating the cases for $\Delta T = 32^oC$ and $\Delta T = 64^oC$, from the above figures, this is due

to the additional enthalpy of the incoming melt. In comparison to the increase in melt superheat, the increase in casting speed has caused the isotherms to move sharply downward.

Locations and shapes of the discussed isotherms at three longitudinal cross-sections (z = 0, z = 62.5 mm, and z = 312.5 mm) are depicted in the left hand panels of Figs. 7.19(a,b,c) through 7.22(a,b,c), and Figs. 7.25(a,b,c) through 7.28(a,b,c) for corresponding two selected inlet superheats of 32^{o}C and 64^{o}C, respectively and for four casting speeds support the patterns found in the 3-D plots. The comparison among these three cross-sections reveals that, as one proceeds along the narrow face from symmetry to the rolling face, one can see that the isotherms move upward, which is due to the enhancement in heat extraction rate. The progress of the formation of solid shell along the axial direction is plotted in Figs. 7.23(a-d) and 7.29(a-d), for $\Delta T = 32^{o}$C and $\Delta T = 64^{o}$C, respectively at four casting speeds. These figures confirm that with increasing casting speeds relatively thinner solid shells are observed in the corresponding y-z plane presented by the blue color and a similar behavior is observed for the increase in melt superheat.

(b) Quantitative Analysis for $\Delta T = 32^{o}$C and $\Delta T = 64^{o}$C

(i) Sump Depth and Mushy Layer Thickness

The numerically predicted sump depth and mushy thickness at the ingot center for all four casing speeds and two melt superheats of 32^{o}C and 64^{o}C are tabulated in Tables 7.10 and 7.11. These tables show that, the sump depth is getting deeper considerably with increasing casting speed and it enhances at a much slower rate with increasing inlet superheat. These observations are consistent with previous full-filtered case studies. The mushy thickness increases at the ingot center for all casting speeds and two melt superheats, except for the casting speed of 100 mm/min, where it is found to decrease for both melt superheats, and this exception was also observed in the full-filtered case.

The comparison between the two inlet superheats reveals that, the depth of the solidification front at the center at casting speeds of 60, 100, 140, and 180 mm/min for

$\Delta T = 64^oC$, is only 0.6%, 0 %, 0.6%, and 0.2%, respectively deeper, whereas the liquid pool depth at the slab center is only 0.4 %, 0.5%, 0.9%, and 1.4%, respectively higher compared to those numerically predicted for $\Delta T = 32^oC$.

From the above comparative study, one can see, a dramatic decline in solidification rate occurs which accompany with increasing casting speed, and this is due to the higher rate of melt flow into the mold. With increasing melt superheat, the locations of the liquidus and solidus isotherms at the ingot center shift downward. These observations closely resemble with full-filtered case, with minor exception. The exception is, at an initial superheat of 32^oC, the sump depth at casting speeds of 60, 100, 140, and 180 mm/min for half-filtered case, is only 1.8%, 1.1%, 2.5%, and 0.3%, respectively more, compared to those predicted for full-filtered case (refer to Table 7.3). At an inlet superheat of 64^oC, the sump depth at casting speeds of 60, 100, 140, and 180 mm/min for half-filtered case, is only 1.5%, 1.1%, 0.3%, and 0.2%, respectively greater, compared to those predicted for full-filtered case (refer to Table 7.6). The most noteworthy influence of the half-filtered delivery system is the enhancement in the depth of the sump due to the less obstructed area for melt feeding.

Table-7.10: Sump depth and mushy thickness in mm at the center of the ingot for an open-top delivery system with a filter having a width of 433 mm at four casting speeds and a superheat of 32^oC.

Quantity	Values of casting speed (u_s) in mm/min			
	60	100	140	180
Sump depth (mm)	335	44.8 % higher than u_s = 60 mm/min	117.3 % higher than u_s = 60 mm/min	192.0 % higher than u_s = 60 mm/min
Mushy thickness (mm)	55	36.4 % lower than u_s = 60 mm/min	169.1 % higher than u_s = 60 mm/min	378.2 % higher than u_s = 60 mm/min

Table-7.11: Sump depth and mushy thickness in mm at the center of the ingot for an open-top delivery system with a filter having a width of 433 mm at four casting speeds and a superheat of 64^{o}C.

Quantity	Values of casting speed (u_s) in mm/min			
	60	100	140	180
Sump depth (mm)	337	44.0 % higher than u_s = 60 mm/min	117.2 % higher than u_s = 60 mm/min	191.0 % higher than u_s = 60 mm/min
Mushy thickness (mm)	56	41.1 % lower than u_s = 60 mm/min	162.5 % higher than u_s = 60 mm/min	355.4 % higher than u_s = 60 mm/min

(ii) Formation of Solidified Shell

The solidified layer thickness at an inlet superheat of 32^{o}C and 64^{o}C is given graphically in Figs. 7.30(a, b) and the predicted values are listed in Table 7.12 for four casting speeds. Here, the growth of the solidified shell at the wide symmetry plane (z = 0) at an axial distance of x = 160 mm measured from the narrow slab face from the slab top surface is taken into consideration. Both the figures and table illustrate that the increased casting speed and increasing melt superheat are both leading to the decrease in the growth of the solid shell.

For ΔT = 32^{o}C, and ΔT = 64^{o}C, at a casting speed of 60 mm/min, the solid shell thickness is 55, and 46 mm, respectively, whereas at the higher casting speeds of 100, 140, and 180 mm/min, the thickness of the solidifying shell is about 60 %, 80 %, 86 %, respectively, and about 57 %, 83 %, 94 %, respectively lower in comparison to the lower casting speed of 60 mm/min. At higher casting speeds the thermal convective effects become strong, which inhibits the growth rate of solid shell.

A comparison between the two inlet superheats reveals that, the shell thickness at casting speeds of 60, 100, 140, and 180 mm/min for ΔT = 64^{o}C, is about 16 %, 9 %, 27 %, and 63 %, respectively lower compared to those predicted for ΔT = 32^{o}C. This lower

value is obtained due to the additional heat of the incoming hot melt at each casting speed that is required to be removed before solidification can take place.

For full-filtered case, at $\Delta T = 32^oC$ (refer to Table 7.4), and $\Delta T = 64^oC$ (refer to Table 7.7), the shell thickness at casting speeds of 60, 100, 140, and 180 mm/min, is about 0 %, 9 %, 18 %, and 13 %, respectively, and is about 11 %, 10 %, 25 %, and 0 %, respectively, thicker compared to those predicted for half-filtered case due to the weaker convective flow in the melt for the full-filtered case.

Table-7.12: The thickness of the solidifying shell (mm) at wide symmetry plane from the narrow slab face at an axial distance of 160 mm from the top surface inside the mold for four casting speeds and inlet superheats of 32°C, and 64°C for an open-top delivery system with a filter having a width of 433 mm.

Quantity	Values of casting speed (u_s) in mm/min			
	60	100	140	180
Solid shell thickness for $\Delta T = 32^oC$ (mm)	55	60.0 % lower than u_s = 60 mm/min	80.0 % lower than u_s = 60 mm/min	85.5 % lower than u_s = 60 mm/min
Solid shell thickness for $\Delta T = 64^oC$ (mm)	46	56.5 % lower than u_s = 60 mm/min	82.6 % lower than u_s = 60 mm/min	93.5 % lower than u_s = 60 mm/min
Percentage enhancement with respect to $\Delta T = 32^oC$	16.4	9.1	27.3	62.5

(iii) Local Surface Heat Flux

The local surface heat flux on the narrow face at z = 185 mm and on the wide face at y = 857.5 mm along the axial direction of the caster for $\Delta T = 32^oC$ is shown in Figs. 7.31(a,b), respectively, and $\Delta T = 64^oC$ is shown in Figs. 7.32(a,b), respectively. The

trend of these graphs are very much similar to those observed for full-filtered case for the four casting speeds and two melt superheats (refer to Figs 7.16(a,b) and Figs 7.17(a,b)).

With the increase in the casting speed, and melt superheat, the local surface heat flux increases which is consistent with the physics of the phenomena. For $\Delta T = 32^oC$, and $\Delta T = 64^oC$, at a casting speed of 60 mm/min, the local surface heat flux at z = 185 mm, x = 215 mm, is 3078.09, and 3137.06 kW/m^2, respectively, whereas at the higher casting speeds of 100, 140, and 180 mm/min, the local surface heat flux is about 31 %, 50 %, 61 % , respectively , and is about 32 %, 48 %, 63 % , respectively higher in comparison to the lower casting speed of 60 mm/min, as shown in Table 7.13.

A comparison between the two inlet superheats reveals that, the local surface heat flux at z = 185 mm, x = 215 mm, at casting speeds of 60, 100, 140, and 180 mm/min for $\Delta T = 64^oC$, is only about 2 %, 2.5 %, 0.7 %, and 3 %, respectively greater compared to those predicted for $\Delta T = 32^oC$, as shown in Table 7.13.

For half-filtered case, at $\Delta T = 32^oC$ and $\Delta T = 64^oC$, the heat flux at z = 185 mm, x = 215 mm at each casting speed is slightly higher compared to those predicted for full-filtered case (refer to Tables 7.5 and 7.8) due to the more convection effect because of the less restricted flow area at the inlet.

Table-7.13: The local heat flux (kW/m^2) at z = 185 mm at an axial distance of 215 mm from the top surface for four casting speeds and for two inlet superheats of 32°C and 64°C, for an open-top delivery system with a filter having a width of 433 mm.

Quantity	Values of casting speed (u_s) in mm/min			
	60	100	140	180
Local surface heat flux for $\Delta T = 32^oC$ (kW/m^2)	3078.09	31.4 % more as compared with 60 mm/min	50.0 % more as compared with 60 mm/min	61.0 % more as compared with 60 mm/min
Local surface heat flux for $\Delta T = 64^oC$ (kW/m^2)	3137.06	32.2 % more as compared with 60 mm/min	47.9 % more as compared with 60 mm/min	62.8 % more as compared with 60 mm/min

Percentage of enhancement with respect to $\Delta T = 32^oC$	1.9 %	2.5%	0.66 %	3.1%

7.5 Conclusions

The numerically predicted results show that the sump depth, the mushy region thickness, the thickness of the solid shell, and the local surface heat flux of the two melt feeding configurations differ considerably. As expected, the sump depth, and the local surface heat flux increase with increasing casting speed and increasing inlet melt superheat for both feeding systems. This is consistent with the fact that a higher casting speed induces stronger convection, and reduces the residence time of the melt inside the mold, both of these are leading to the prolongation of the solidification process. Increasing the melt inlet temperature introduces more heat into the system and thus enhancing the thermal convective effects. For the same regions, at higher casting speeds and higher melt inlet temperatures, the thickness of the solid shell inside the mold decreases. The thickness of the mushy zone at the center of the ingot (not all) shows irregular characteristics for both feeding systems. Between the two melt feeding configurations, the full-filtered case gives more favorable results compared to the half-filtered case for this complex solidification problem.

From the above discussion it is evident that the increase in melt superheat produces a relatively insignificant effect on the solidification process compared to the increase in casting speed. So, the influence of casting speed is more pronounced in terms of quality and productivity of the ingot. The parametric study on casting speed seems to be necessary in designing the inlet melt delivery system compared to inlet melt superheat. Therefore, in the next two chapters only the effect of casting speed on the turbulent flow and solidification process for various other melt feeding systems will be studied.

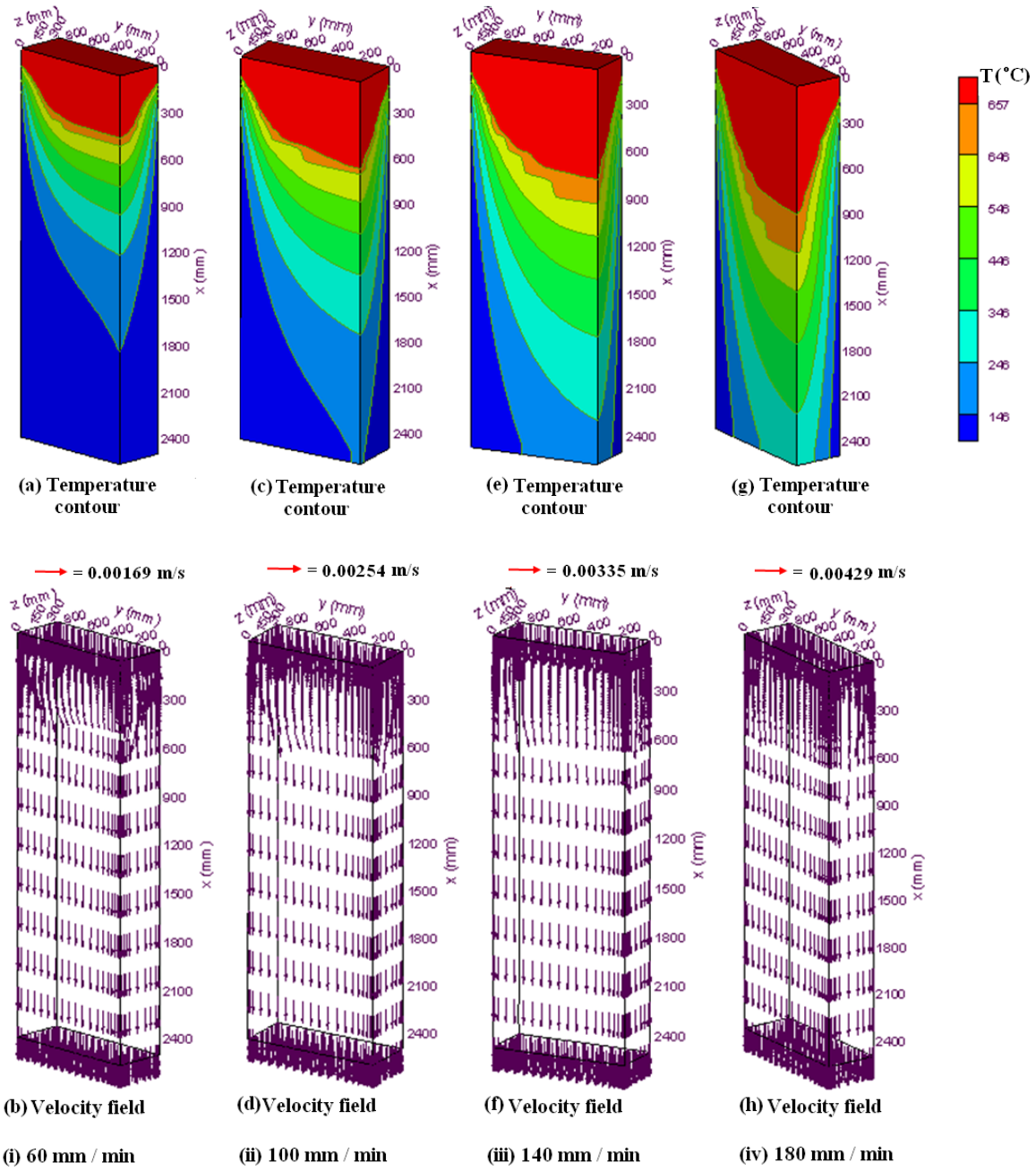

Figure 7.3: 3-D surface plots for the complete solution domain for four casting speeds and 32^0C superheat using the open top delivery system with a porous filter having a width of 865 mm for porosity, $\phi = 0.4$ and Darcy value 0f 1.0×10^{-4}: (i) temperature contours (a) and velocity field (b) for a casting speed of 60 mm/min; (ii) temperature contours (c) and velocity field (d) for a casting speed of 100 mm/min; (iii) temperature contours (e) and velocity field (f) for a casting speed of 140 mm/min; (iv) temperature contours (g) and velocity field (h) for a casting speed of 180 mm/min.

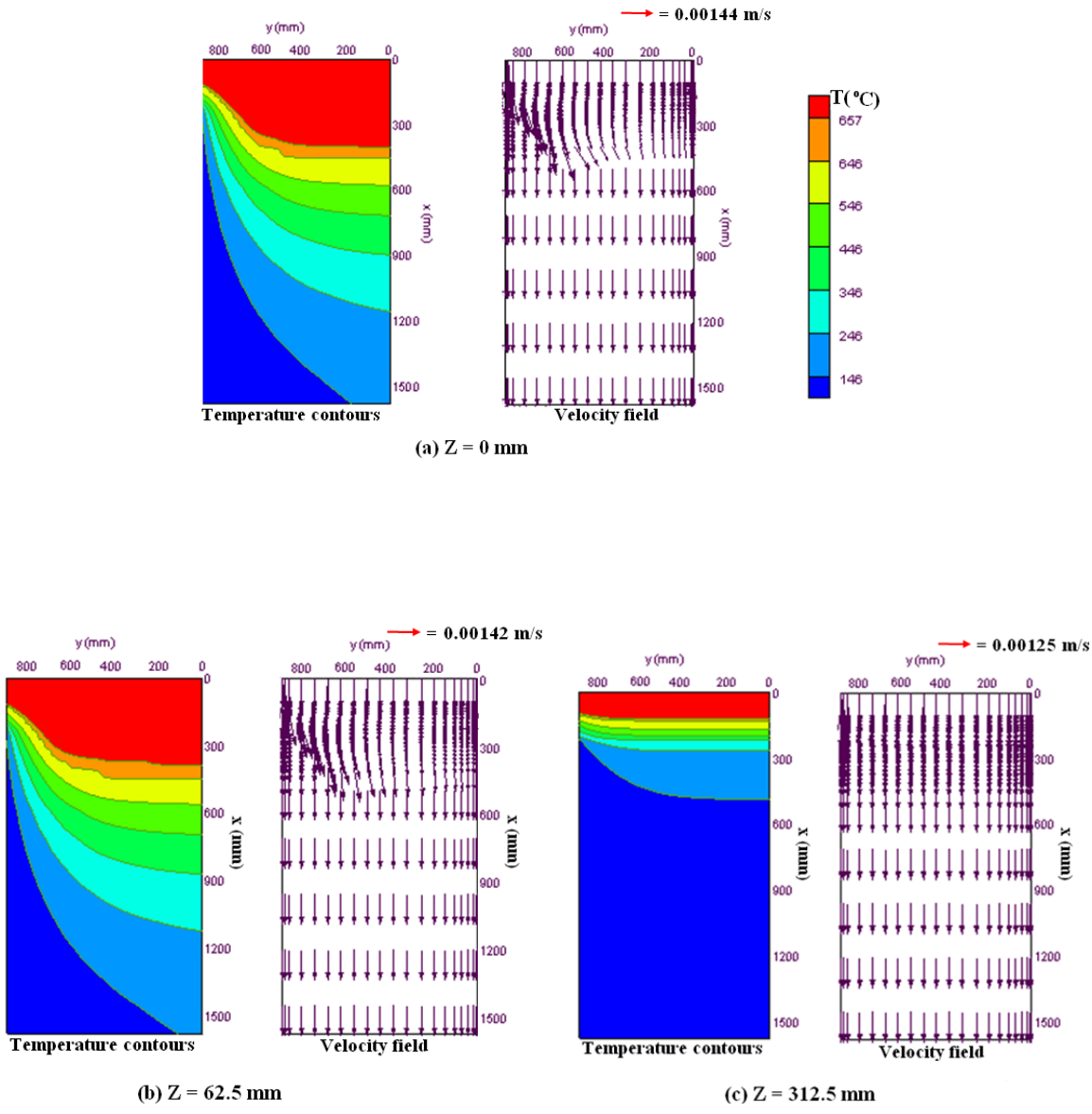

Figure 7.4: Enlarged 2-D view of temperature contours and velocity vectors of the top domain using the open top delivery system with a porous filter having a width of 865 mm for porosity, $\phi = 0.4$ and Darcy value 0f 1.0×10^{-4} for a casting speed of 60 mm/min and 32°C superheat at: (a) wide symmetry plane at z = 0 mm, (b) vertical plane parallel to the wide face at z = 62.5 mm, (c) vertical plane parallel to the wide face at z = 312.5 mm.

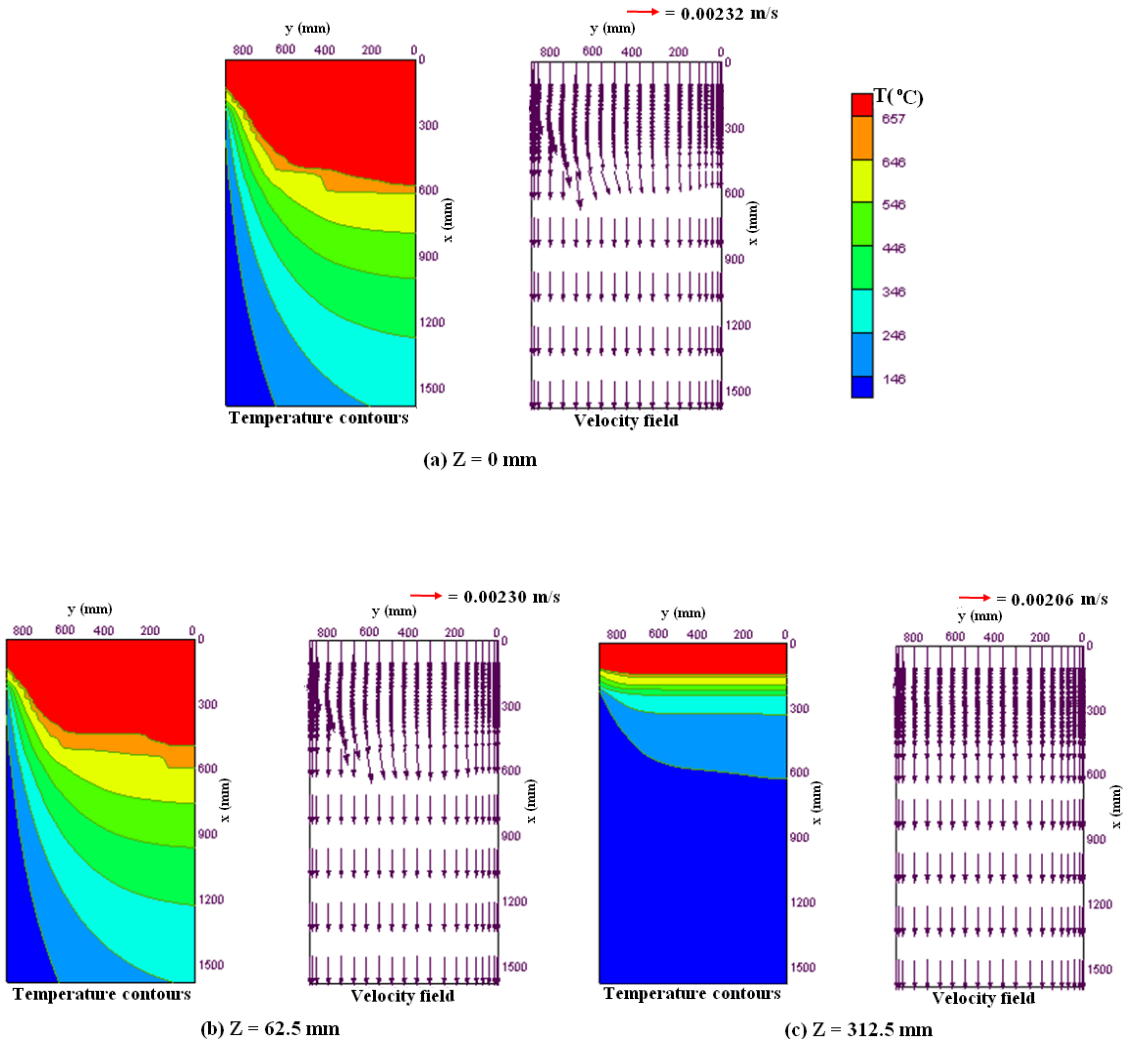

Figure 7.5: Enlarged 2-D view of temperature contours and velocity vectors of the top domain using the open top delivery system with a porous filter having a width of 865 mm for porosity, $\phi = 0.4$ and Darcy value 0f 1.0×10^{-4} for a casting speed of 100 mm/min and 32°C superheat at: (a) wide symmetry plane at z = 0 mm, (b) vertical plane parallel to the wide face at z = 62.5 mm, (c) vertical plane parallel to the wide face at z = 312.5 mm.

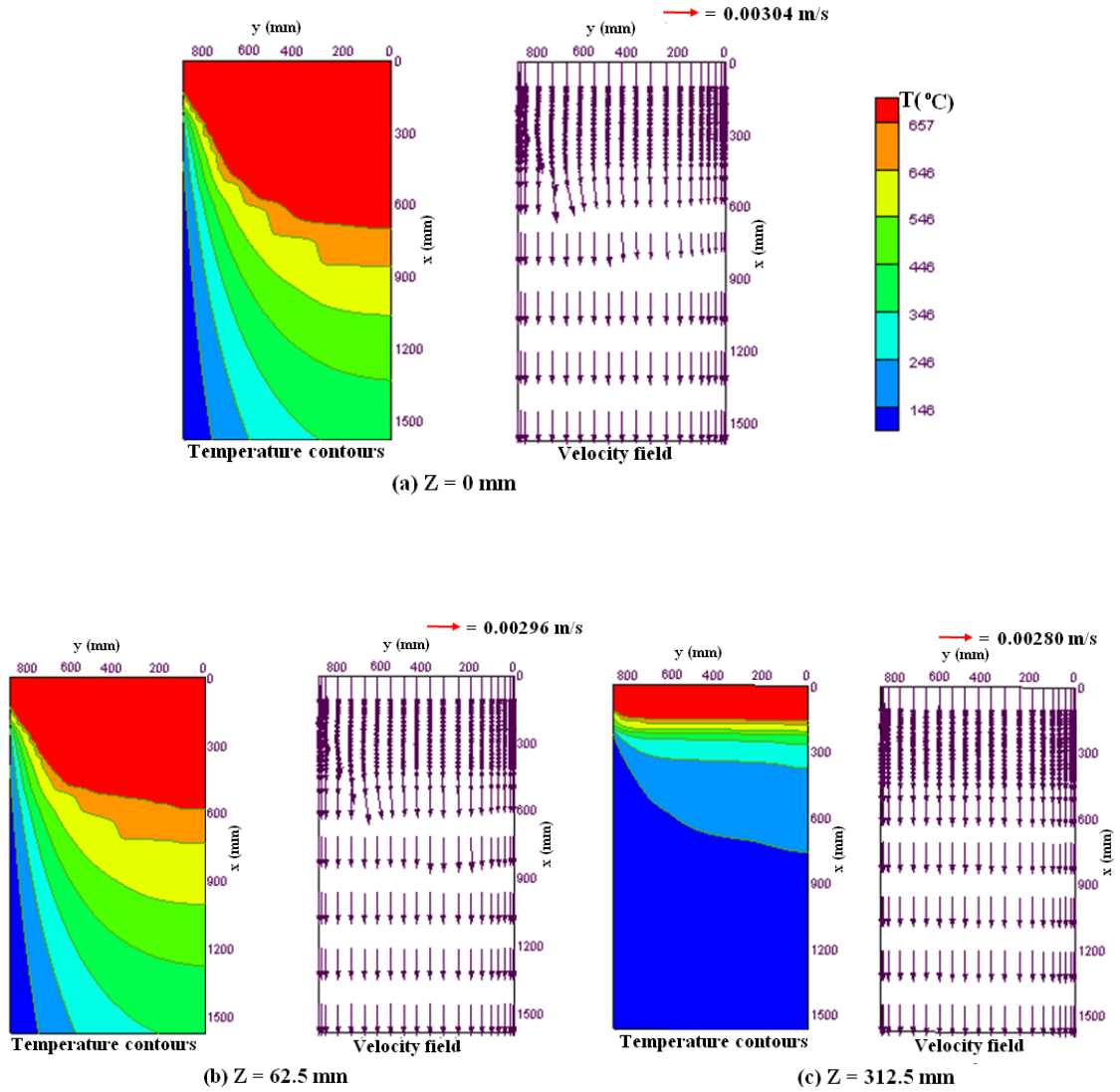

Figure 7.6: Enlarged 2-D view of temperature contours and velocity vectors of the top domain using the open top delivery system with a porous filter having a width of 865 mm for porosity, $\phi = 0.4$ and Darcy value 0f 1.0×10^{-4} for a casting speed of 140 mm/min and 32°C superheat at: (a) wide symmetry plane at z = 0 mm, (b) vertical plane parallel to the wide face at z = 62.5 mm, (c) vertical plane parallel to the wide face at z = 312.5 mm.

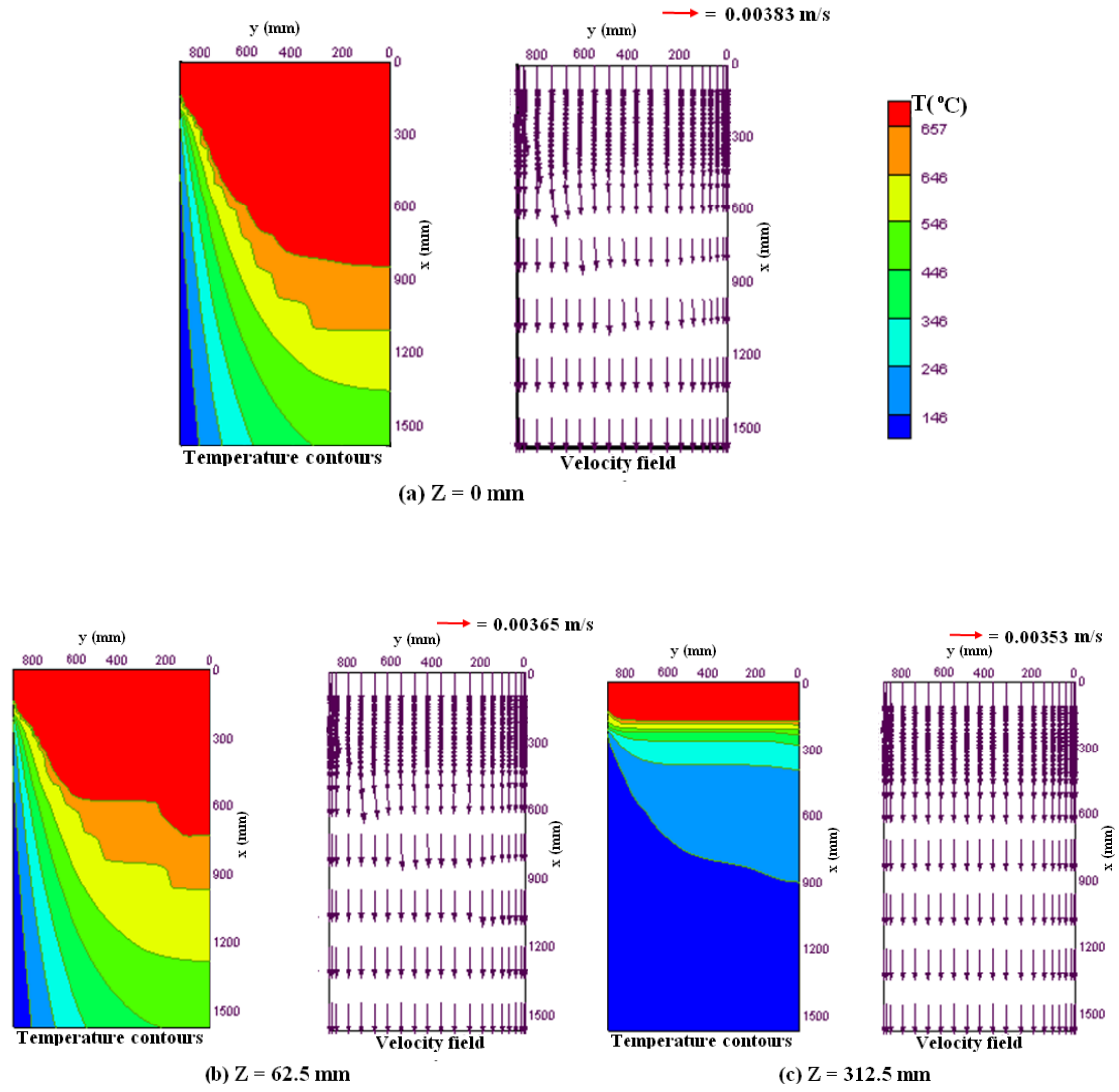

Figure 7.7: Enlarged 2-D view of temperature contours and velocity vectors of the top domain using the open top delivery system with a porous filter having a width of 865 mm for porosity, $\phi = 0.4$ and Darcy value 0f 1.0×10^{-4} for a casting speed of 180 mm/min and 32°C superheat at: (a) wide symmetry plane at z = 0 mm, (b) vertical plane parallel to the wide face at z = 62.5 mm, (c) vertical plane parallel to the wide face at z = 312.5 mm.

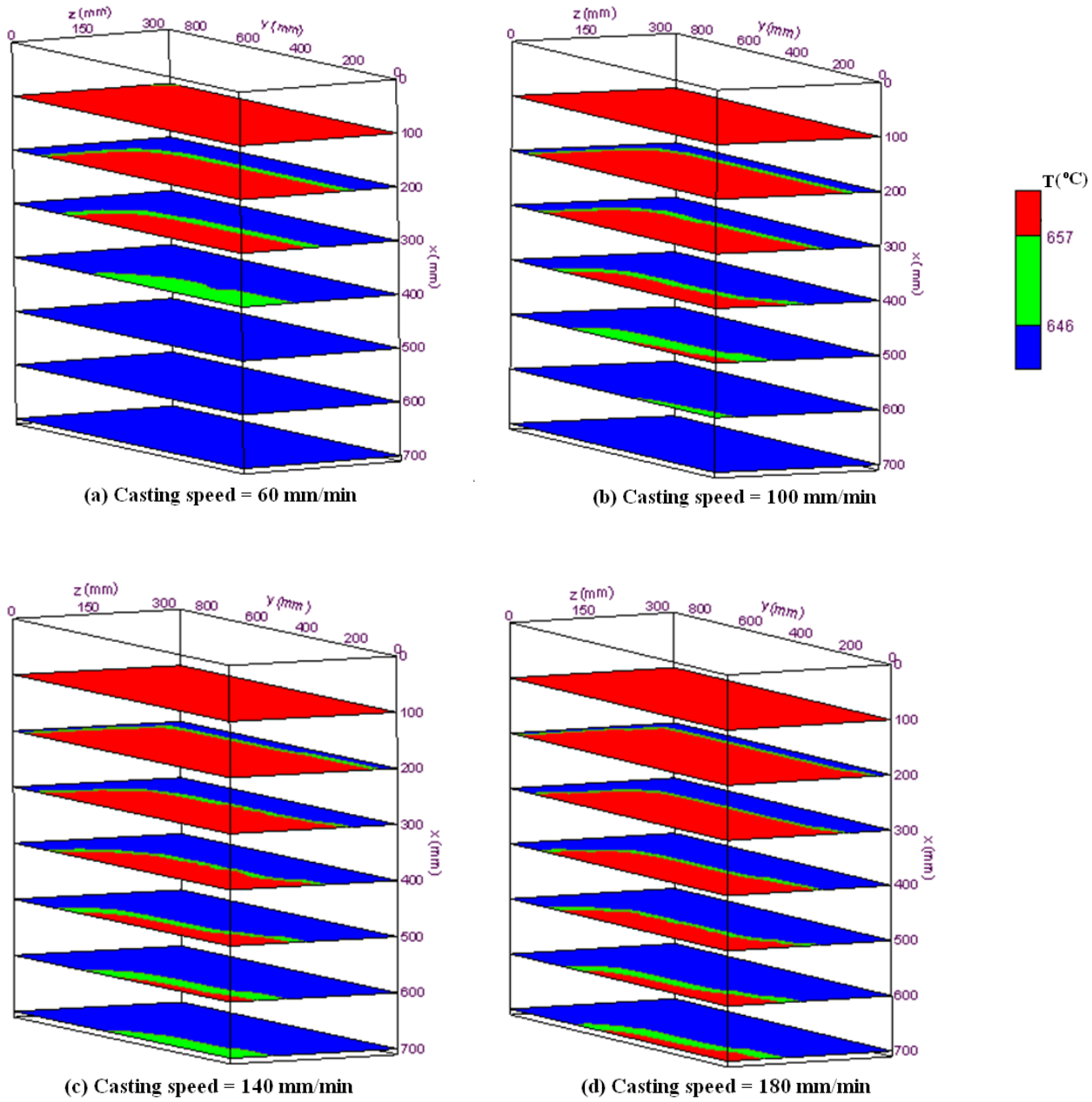

Figure 7.8: Contours of solidus and liquidus temperatures at various transverse cross-sectional planes (y-z planes) of the top part of the ingot using the open top delivery system with a porous filter having a width of 865 mm for porosity, $\phi = 0.4$ and Darcy value 0f 1.0×10^{-4} for a superheat of 32°C and casting speeds of (a) 60 mm min^{-1} (b) 100 mm min^{-1} (c) 140 mm min^{-1} (d) 180 mm min^{-1}.

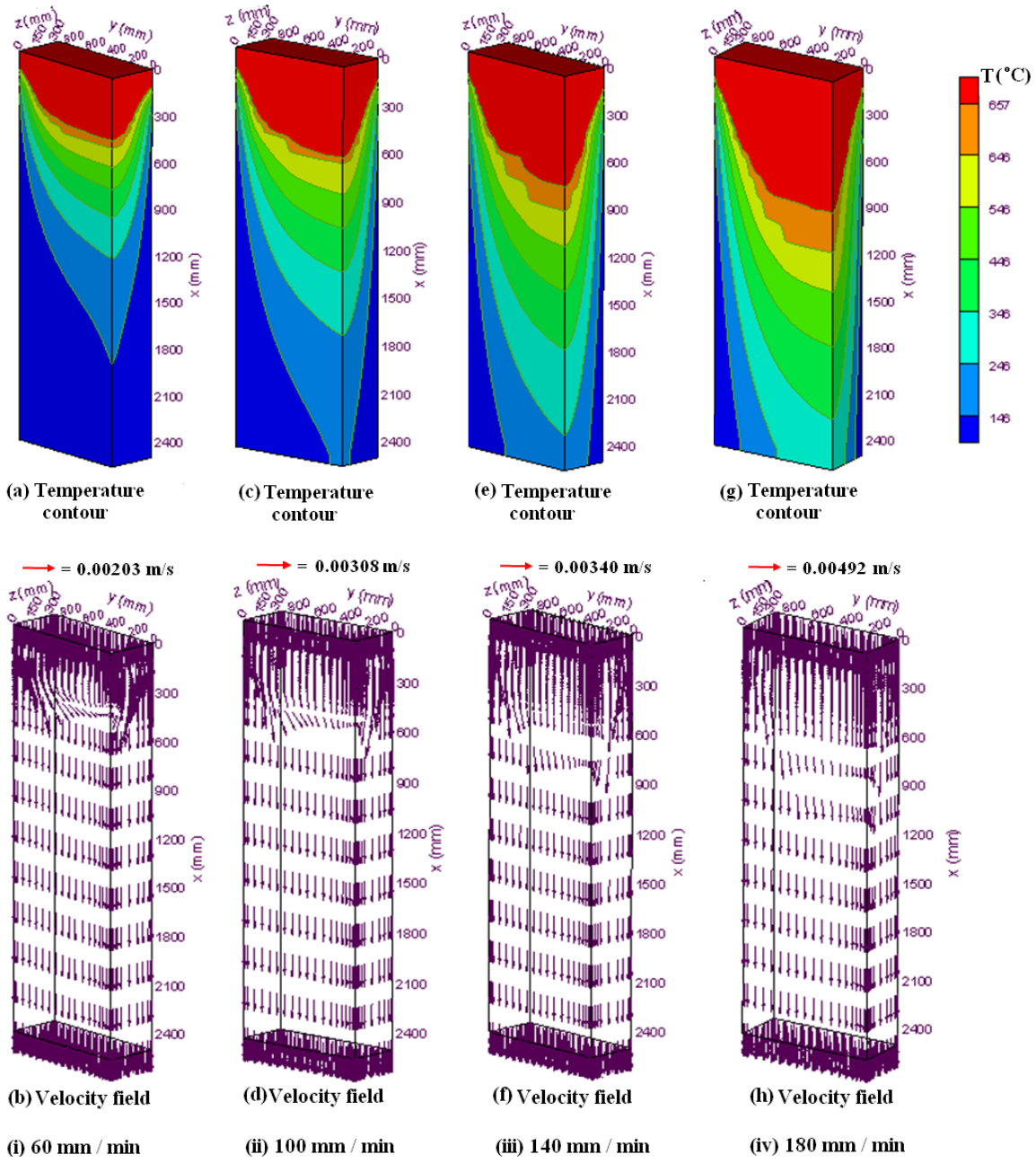

Figure 7.9: 3-D surface plots for the complete solution domain for four casting speeds and 64^{0}C superheat using the open top delivery system with a porous filter having a width of 865 mm for porosity, ϕ = 0.4 and Darcy value 0f 1.0 × 10^{-4}: (i) temperature contours (a) and velocity field (b) for a casting speed of 60 mm/min; (ii) temperature contours (c) and velocity field (d) for a casting speed of 100 mm/min; (iii) temperature contours (e) and velocity field (f) for a casting speed of 140 mm/min; (iv) temperature contours (g) and velocity field (h) for a casting speed of 180 mm/min.

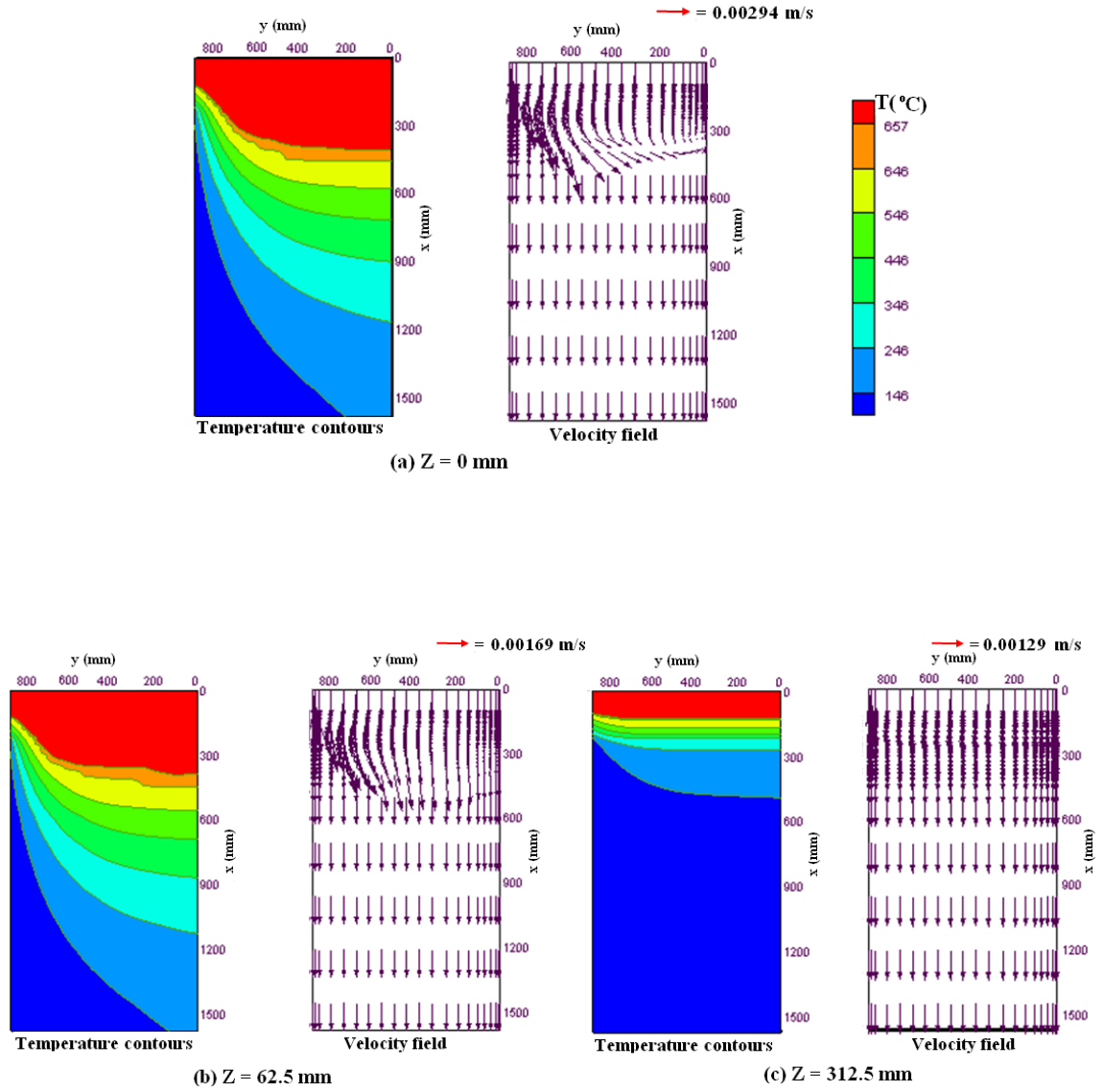

Figure 7.10: Enlarged 2-D view of temperature contours and velocity vectors of the top domain using the open top delivery system with a porous filter having a width of 865 mm for porosity, $\phi = 0.4$ and Darcy value 0f 1.0×10^{-4} for a casting speed of 60 mm/min and 64°C superheat at: (a) wide symmetry plane at z = 0 mm, (b) vertical plane parallel to the wide face at z = 62.5 mm, (c) vertical plane parallel to the wide face at z = 312.5 mm.

.

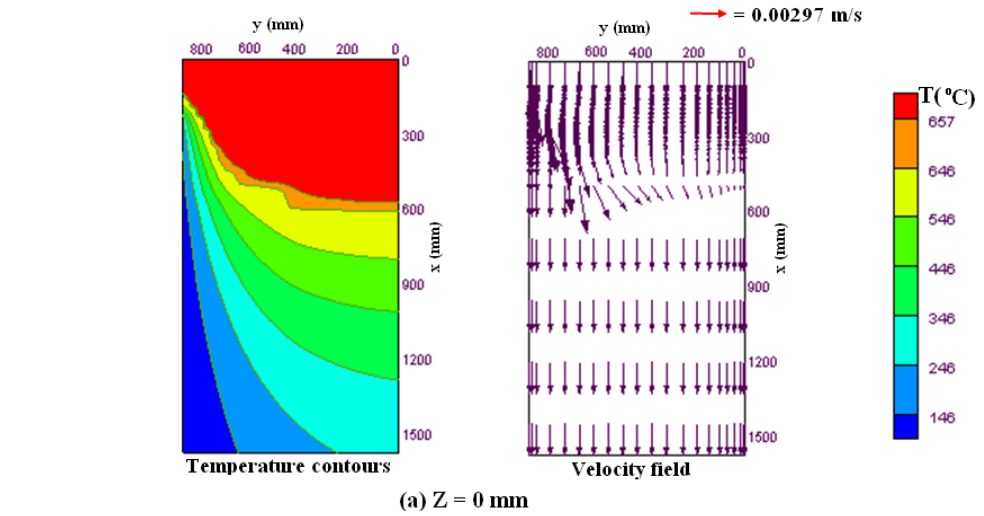

Figure 7.11: Enlarged 2-D view of temperature contours and velocity vectors of the top domain using the open top delivery system with a porous filter having a width of 865 mm for porosity, $\phi = 0.4$ and Darcy value 0f 1.0×10^{-4} for a casting speed of 100 mm/min and 64°C superheat at: (a) wide symmetry plane at z = 0 mm, (b) vertical plane parallel to the wide face at z = 62.5 mm, (c) vertical plane parallel to the wide face at z = 312.5 mm.

.

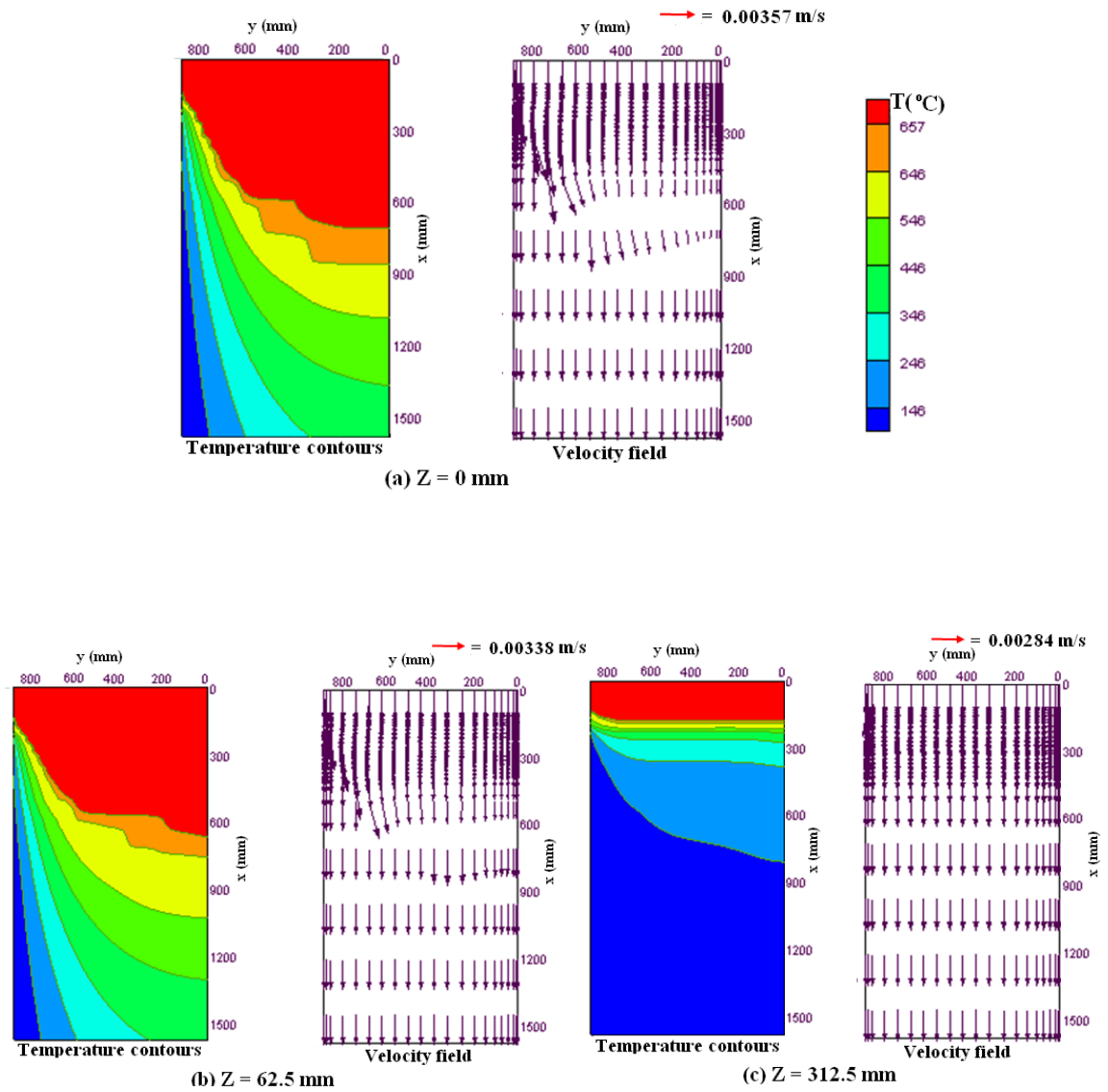

Figure 7.12: Enlarged 2-D view of temperature contours and velocity vectors of the top domain using the open top delivery system with a porous filter having a width of 865 mm for porosity, $\phi = 0.4$ and Darcy value 0f 1.0×10^{-4} for a casting speed of 140 mm/min and 64°C superheat at: (a) wide symmetry plane at z = 0 mm, (b) vertical plane parallel to the wide face at z = 62.5 mm, (c) vertical plane parallel to the wide face at z = 312.5 mm.

.

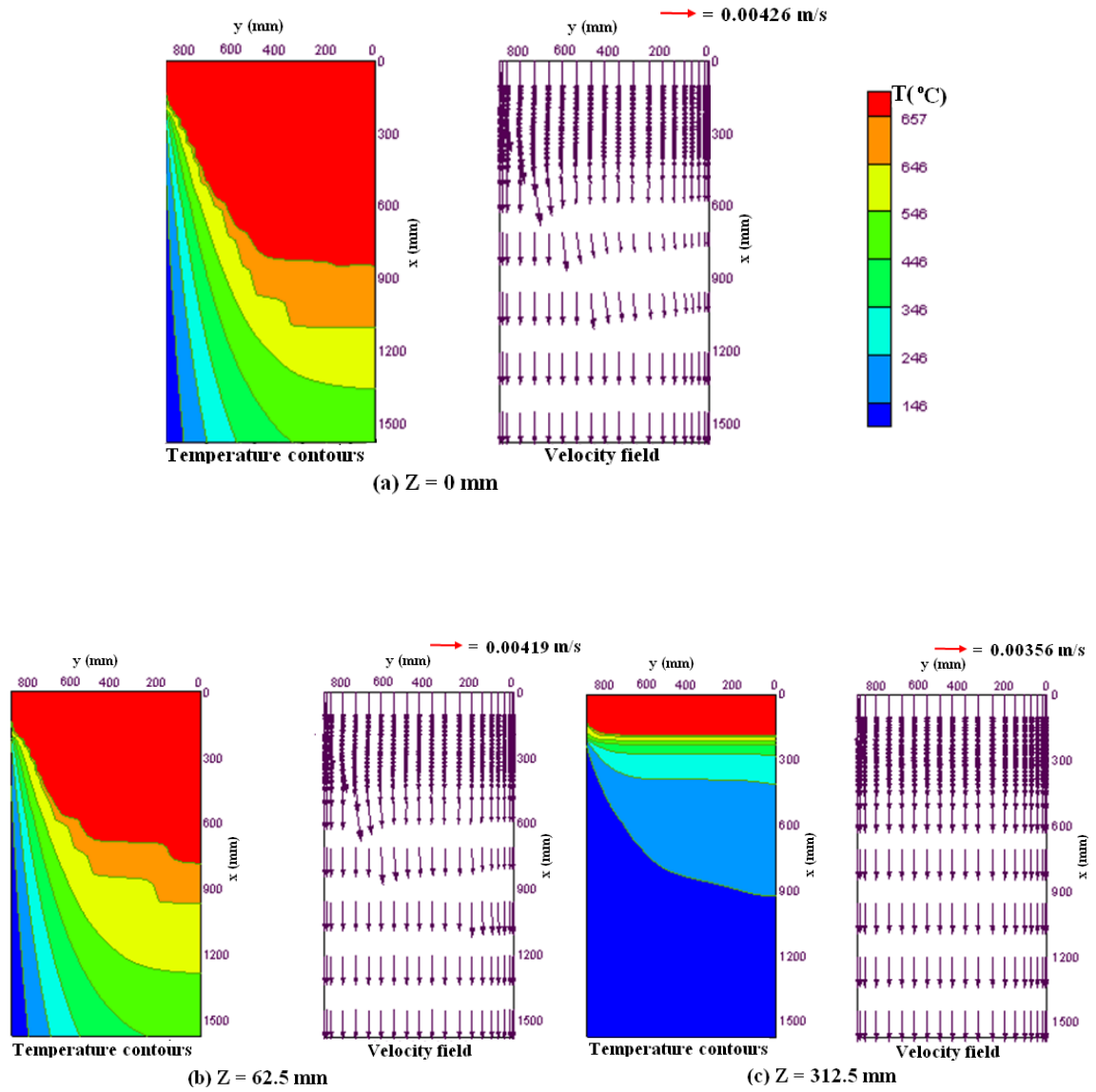

Figure 7.13: Enlarged 2-D view of temperature contours and velocity vectors of the top domain using the open top delivery system with a porous filter having a width of 865 mm for porosity, $\phi = 0.4$ and Darcy value 0f 1.0×10^{-4} for a casting speed of 180 mm/min and 64°C superheat at: (a) wide symmetry plane at z = 0 mm, (b) vertical plane parallel to the wide face at z = 62.5 mm, (c) vertical plane parallel to the wide face at z = 312.5 mm.

.

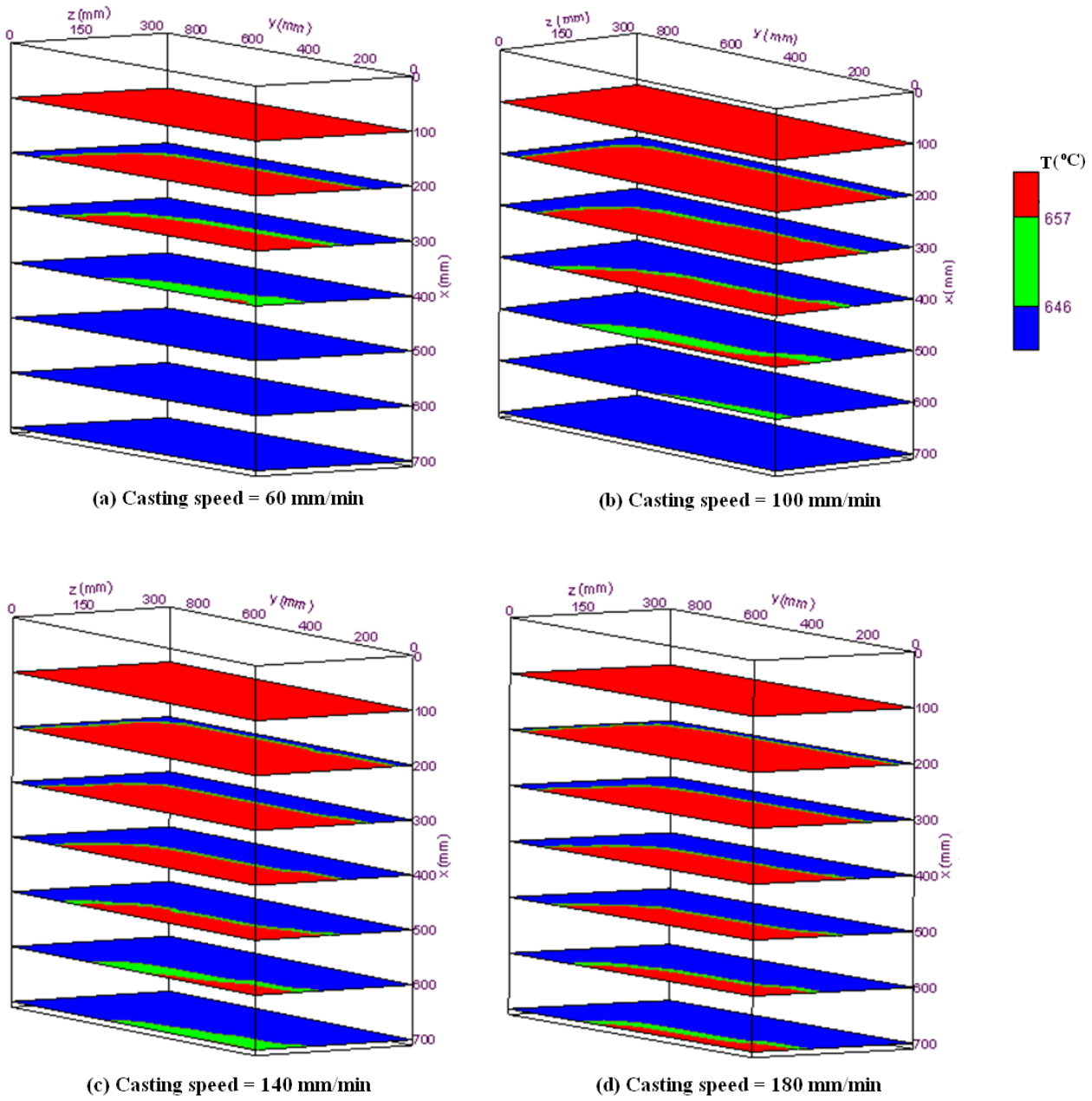

Figure 7.14: Contours of solidus and liquidus temperatures at various transverse cross-sectional planes (y-z planes) of the top part of the ingot using the open top delivery system with a porous filter having a width of 865 mm for porosity, $\phi = 0.4$ and Darcy value 0f 1.0×10^{-4} for a superheat of 64°C and casting speeds of (a) 60 mm min^{-1} (b) 100 mm min^{-1} (c) 140 mm min^{-1} (d) 180 mm min^{-1}.

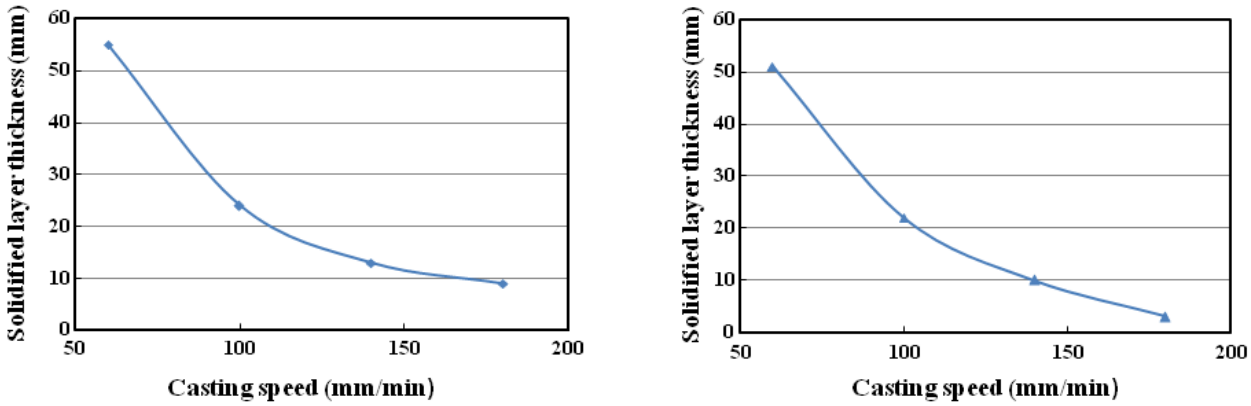

Figure 7.15: Solidified layer thickness from the narrow slab face at an axial distance of x = 160 mm from the top free surface at the wide symmetry plane versus casting speed using the open top delivery system with a porous filter having a width of 865 mm for porosity, $\phi = 0.4$ and Darcy value 0f 1.0×10^{-4} for: (a) inlet superheat of 32^{o}C, (b) inlet superheat of 64^{o}C.

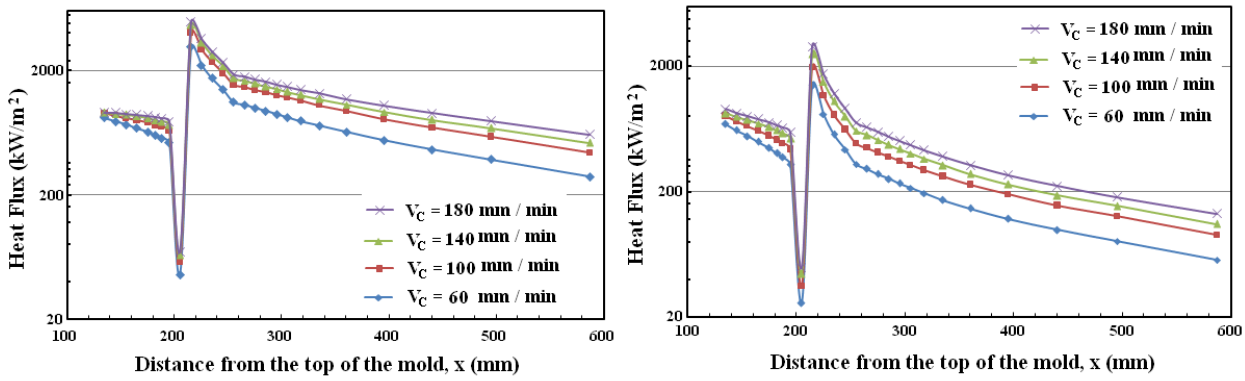

(a) Narrow slab face = 185 mm

(b) Wide slab face = 857.5 mm

(i) Inlet superheat = 32 °C

Figure 7.16: Variations of local surface heat fluxes for various casting speeds during solidification at 32°C superheat along the axial direction of the strand wall at: (a) z = 185 mm (b) y = 857.5 mm, using the open top delivery system with a porous filter having a width of 865 mm for porosity, ϕ = 0.4 and Darcy value 0f 1.0×10^{-4}.

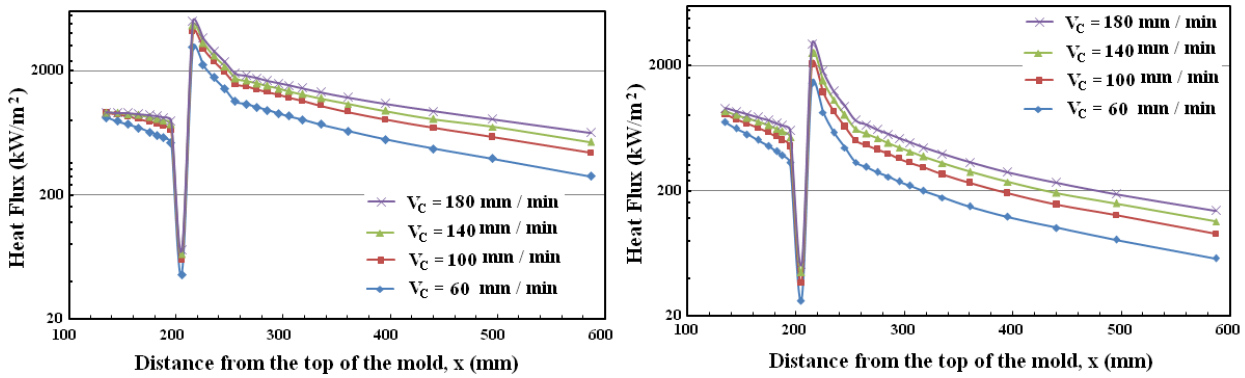

(a) Narrow slab face = 185 mm

(b) Wide slab face = 857.5 mm

(ii) Inlet superheat = 64°C

Figure 7.17: Variations of local surface heat fluxes for various casting speeds during solidification at 64°C superheat along the axial direction of the strand wall at: (a) z = 185 mm (b) y = 857.5 mm, using the open top delivery system with a porous filter having a width of 865 mm for porosity, ϕ = 0.4 and Darcy value 0f 1.0×10^{-4}.

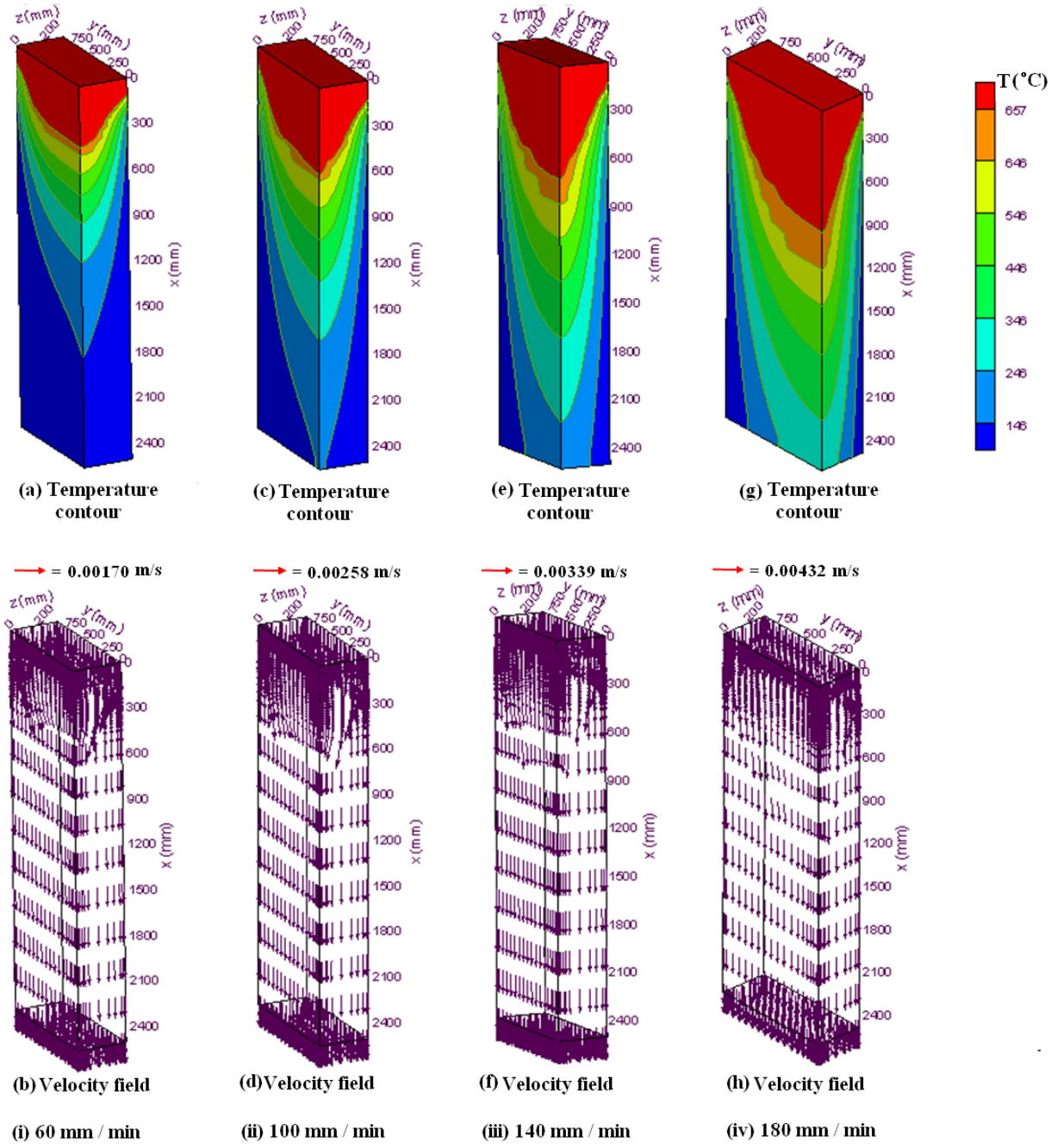

Figure 7.18:3-D surface plots for the complete solution domain for four casting speeds and 32^0C superheat using the open top delivery system with a porous filter having a width of 433 mm for porosity, $\phi = 0.4$ and Darcy value 0f 1.0×10^{-4}: (i) temperature contours (a) and velocity field (b) for a casting speed of 60 mm/min; (ii) temperature contours (c) and velocity field (d) for a casting speed of 100 mm/min; (iii) temperature contours (e) and velocity field (f) for a casting speed of 140 mm/min; (iv) temperature contours (g) and velocity field (h) for a casting speed of 180 mm/min.

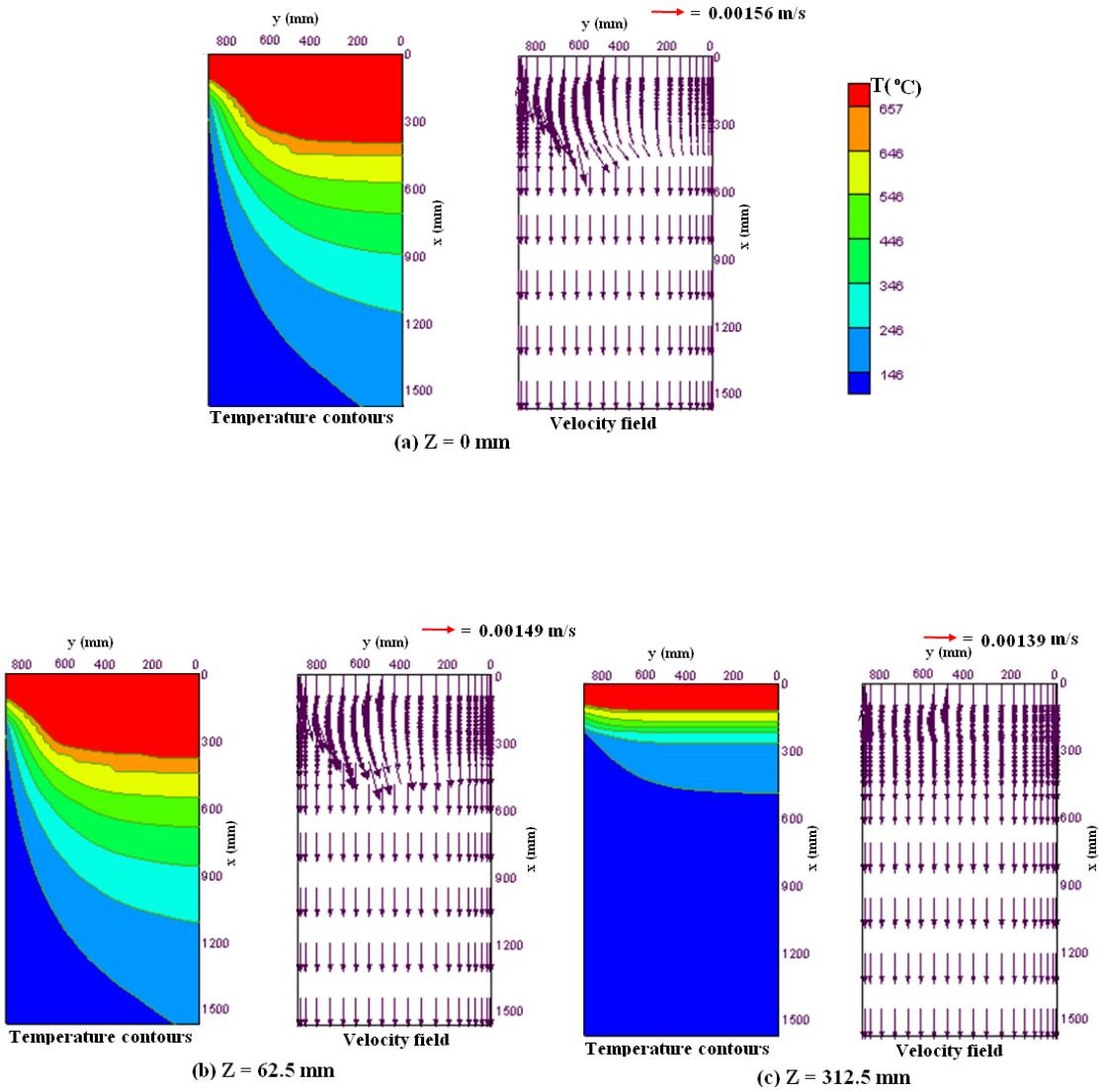

Figure 7.19: Enlarged 2-D view of temperature contours and velocity vectors of the top domain using the open top delivery system with a porous filter having a width of 433 mm for porosity, $\phi = 0.4$ and Darcy value 0f 1.0×10^{-4} for a casting speed of 60 mm/min and 32°C superheat at: (a) wide symmetry plane at z = 0 mm, (b) vertical plane parallel to the wide face at z = 62.5 mm, (c) vertical plane parallel to the wide face at z = 312.5 mm.

.

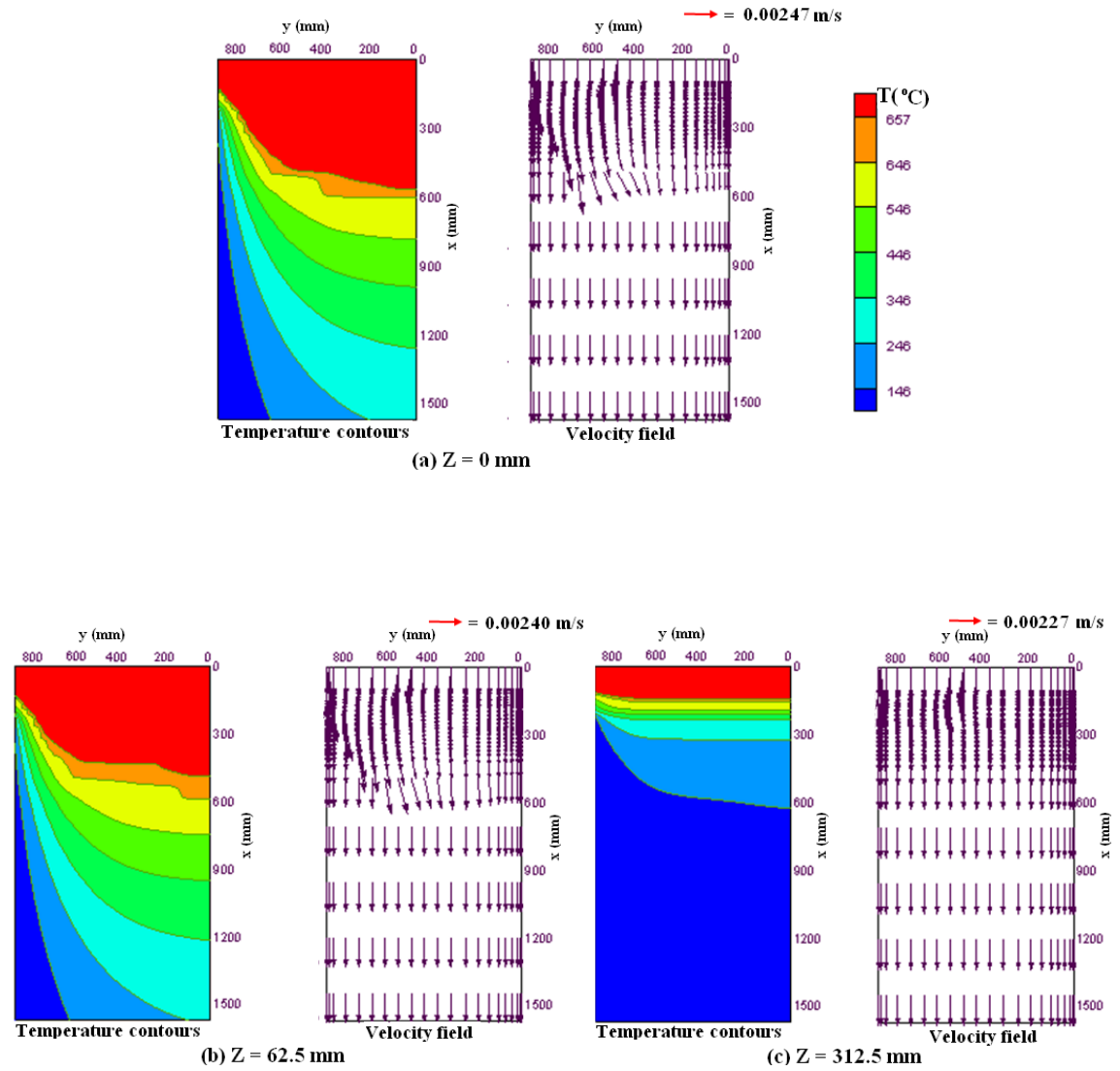

Figure 7.20: Enlarged 2-D view of temperature contours and velocity vectors of the top domain using the open top delivery system with a porous filter having a width of 433 mm for porosity, $\phi = 0.4$ and Darcy value 0f 1.0×10^{-4} for a casting speed of 100 mm/min and 32°C superheat at: (a) wide symmetry plane at z = 0 mm, (b) vertical plane parallel to the wide face at z = 62.5 mm, (c) vertical plane parallel to the wide face at z = 312.5 mm.

.

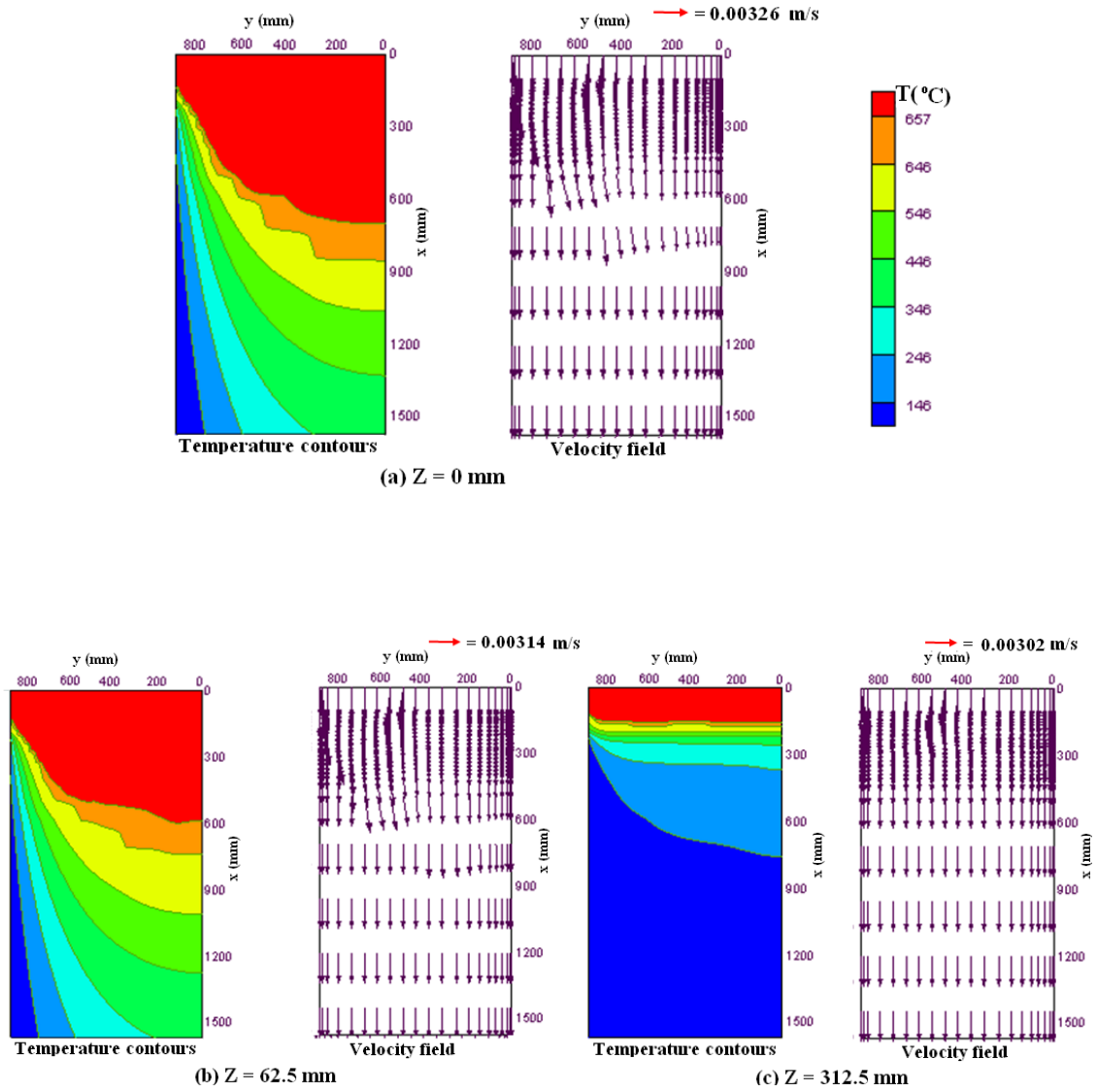

Figure 7.21: Enlarged 2-D view of temperature contours and velocity vectors of the top domain using the open top delivery system with a porous filter having a width of 433 mm for porosity, $\phi = 0.4$ and Darcy value 0f 1.0×10^{-4} for a casting speed of 140 mm/min and 32°C superheat at: (a) wide symmetry plane at z = 0 mm, (b) vertical plane parallel to the wide face at z = 62.5 mm, (c) vertical plane parallel to the wide face at z = 312.5 mm.

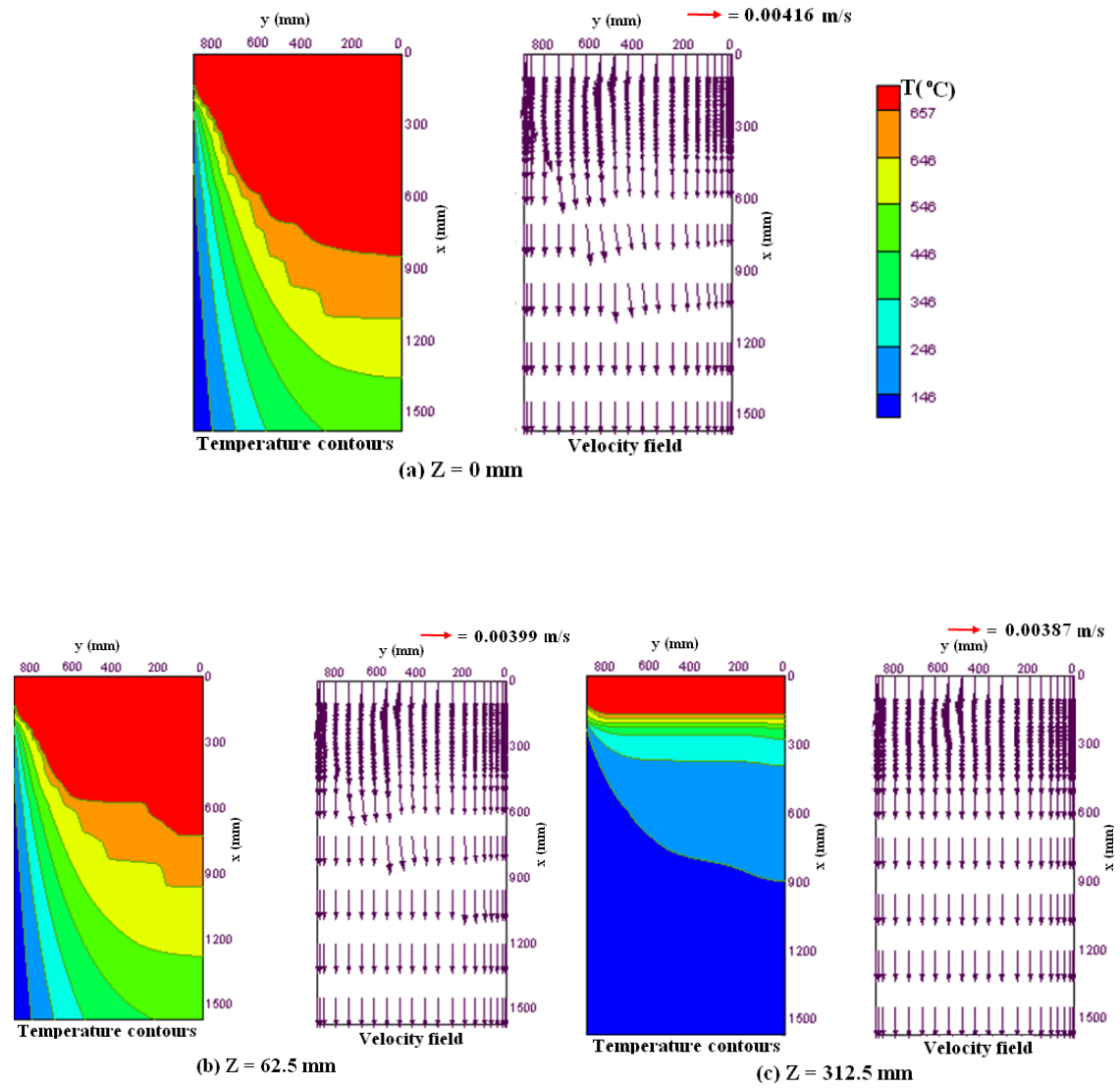

Figure 7.22: Enlarged 2-D view of temperature contours and velocity vectors of the top domain using the open top delivery system with a porous filter having a width of 433 mm for porosity, $\phi = 0.4$ and Darcy value 0f 1.0×10^{-4} for a casting speed of 180 mm/min and 32°C superheat at: (a) wide symmetry plane at z = 0 mm, (b) vertical plane parallel to the wide face at z = 62.5 mm, (c) vertical plane parallel to the wide face at z = 312.5 mm.

.

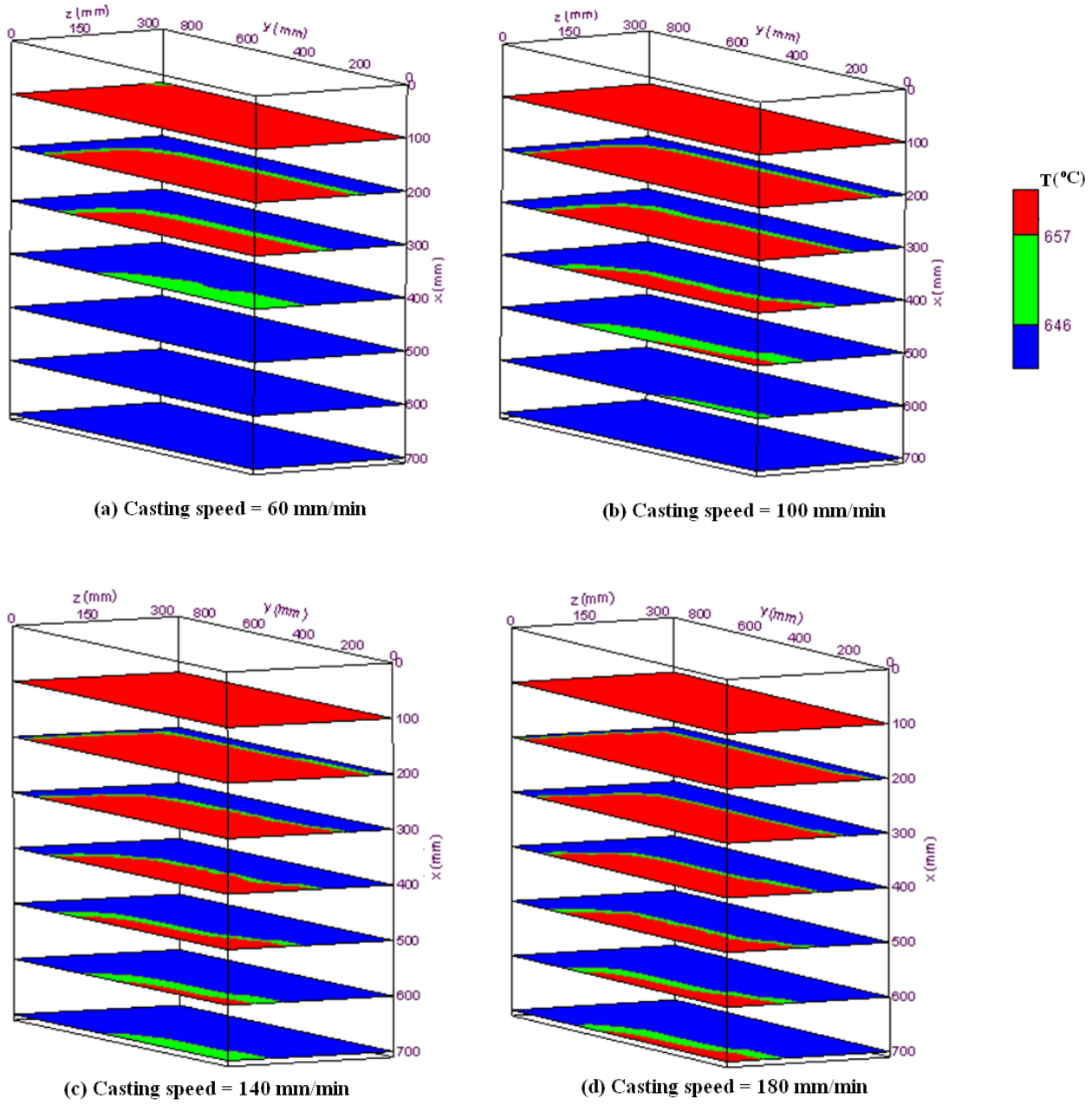

Figure 7.23: Contours of solidus and liquidus temperatures at various transverse cross-sectional planes (y-z planes) of the top part of the ingot using the open top delivery system with a porous filter having a width of 433 mm for porosity, $\phi = 0.4$ and Darcy value 0f 1.0×10^{-4} for a superheat of 32°C and casting speeds of (a) 60 mm min^{-1} (b) 100 mm min^{-1} (c) 140 mm min^{-1} (d) 180 mm min^{-1}.

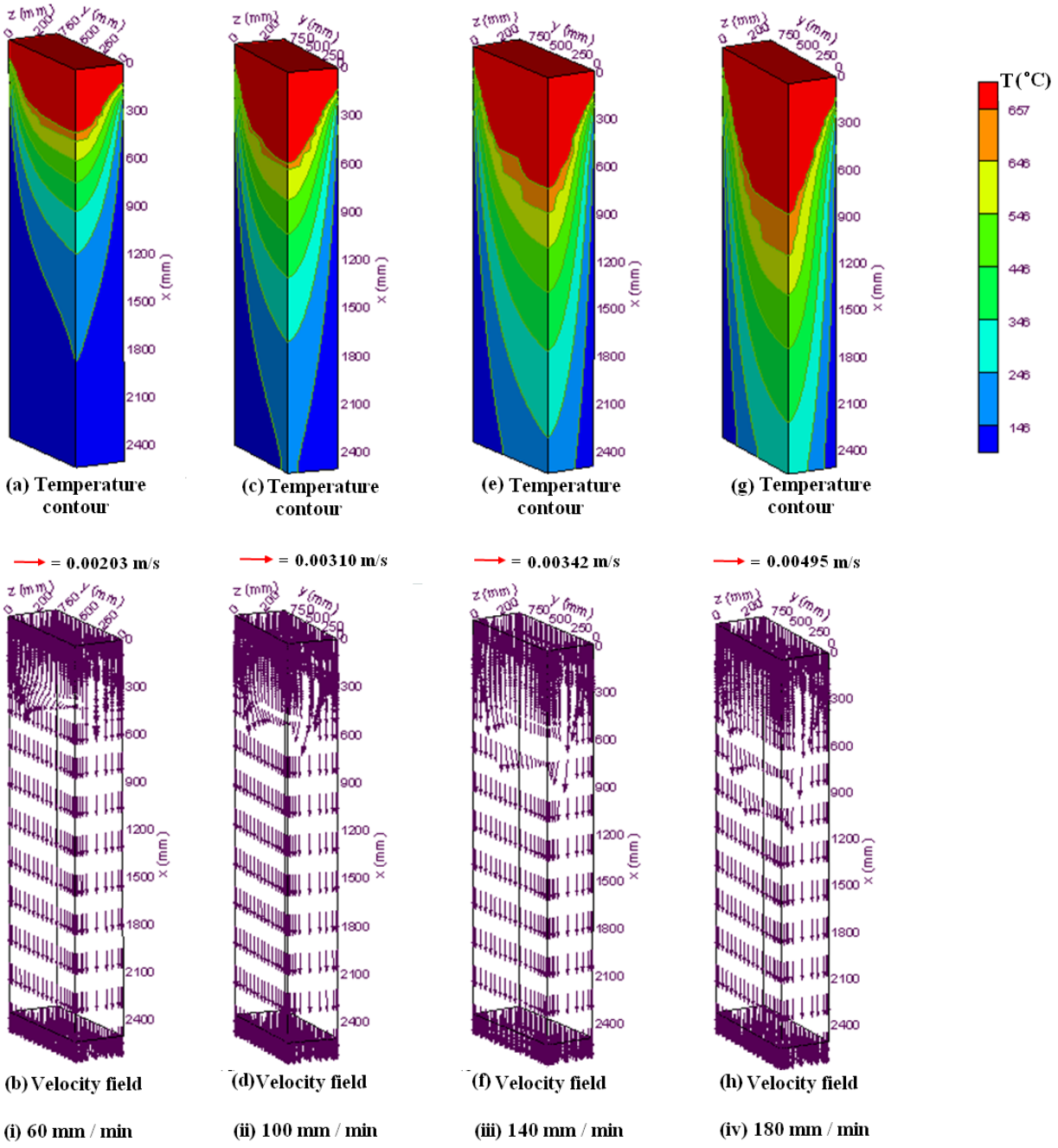

Figure 7.24:3-D surface plots for the complete solution domain for four casting speeds and 64^0C superheat using the open top delivery system with a porous filter having a width of 433 mm for porosity, $\phi = 0.4$ and Darcy value 0f 1.0×10^{-4}: (i) temperature contours (a) and velocity field (b) for a casting speed of 60 mm/min; (ii) temperature contours (c) and velocity field (d) for a casting speed of 100 mm/min; (iii) temperature contours (e) and velocity field (f) for a casting speed of 140 mm/min; (iv) temperature contours (g) and velocity field (h) for a casting speed of 180 mm/min.

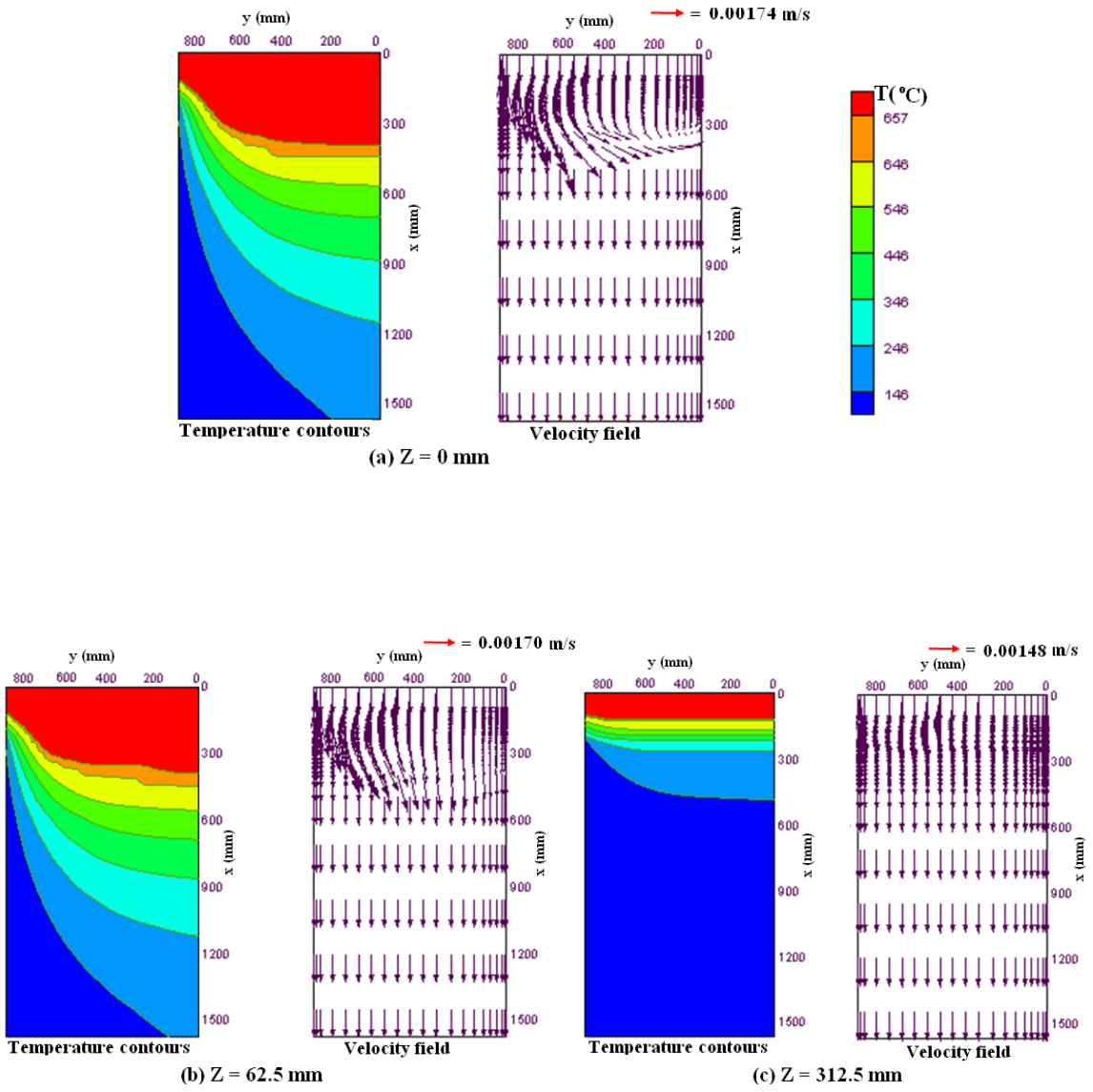

Figure 7.25: Enlarged 2-D view of temperature contours and velocity vectors of the top domain using the open top delivery system with a porous filter having a width of 433 mm for porosity, $\phi = 0.4$ and Darcy value 0f 1.0×10^{-4} for a casting speed of 60 mm/min and 64°C superheat at: (a) wide symmetry plane at z = 0 mm, (b) vertical plane parallel to the wide face at z = 62.5 mm, (c) vertical plane parallel to the wide face at z = 312.5 mm.

.

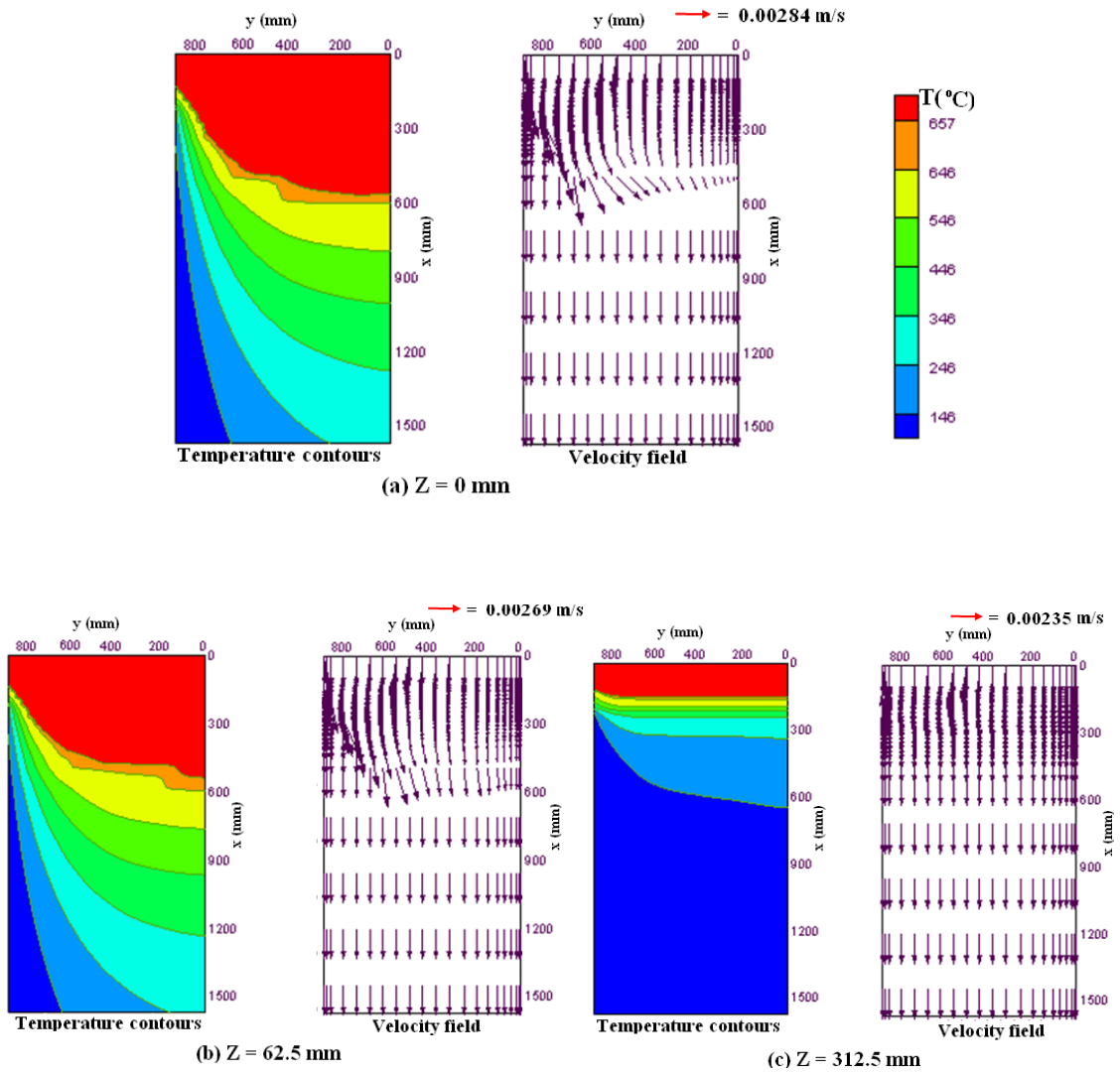

Figure 7.26: Enlarged 2-D view of temperature contours and velocity vectors of the top domain using the open top delivery system with a porous filter having a width of 433 mm for porosity, $\phi = 0.4$ and Darcy value 0f 1.0×10^{-4} for a casting speed of 100 mm/min and 64°C superheat at: (a) wide symmetry plane at z = 0 mm, (b) vertical plane parallel to the wide face at z = 62.5 mm, (c) vertical plane parallel to the wide face at z = 312.5 mm.

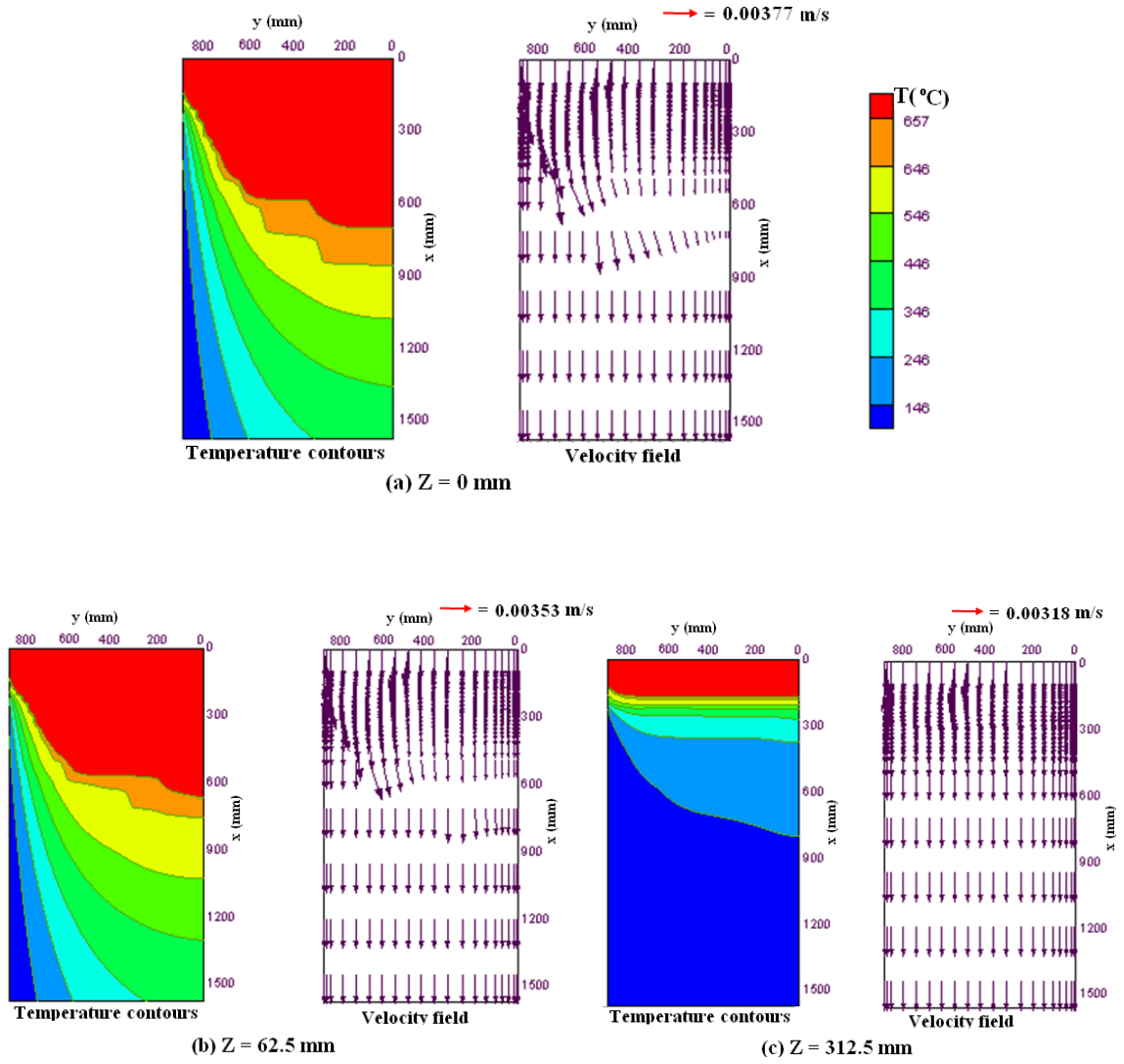

Figure 7.27: Enlarged 2-D view of temperature contours and velocity vectors of the top domain using the open top delivery system with a porous filter having a width of 433 mm for porosity, $\phi = 0.4$ and Darcy value 0f 1.0×10^{-4} for a casting speed of 140 mm/min and 64°C superheat at: (a) wide symmetry plane at z = 0 mm, (b) vertical plane parallel to the wide face at z = 62.5 mm, (c) vertical plane parallel to the wide face at z = 312.5 mm.

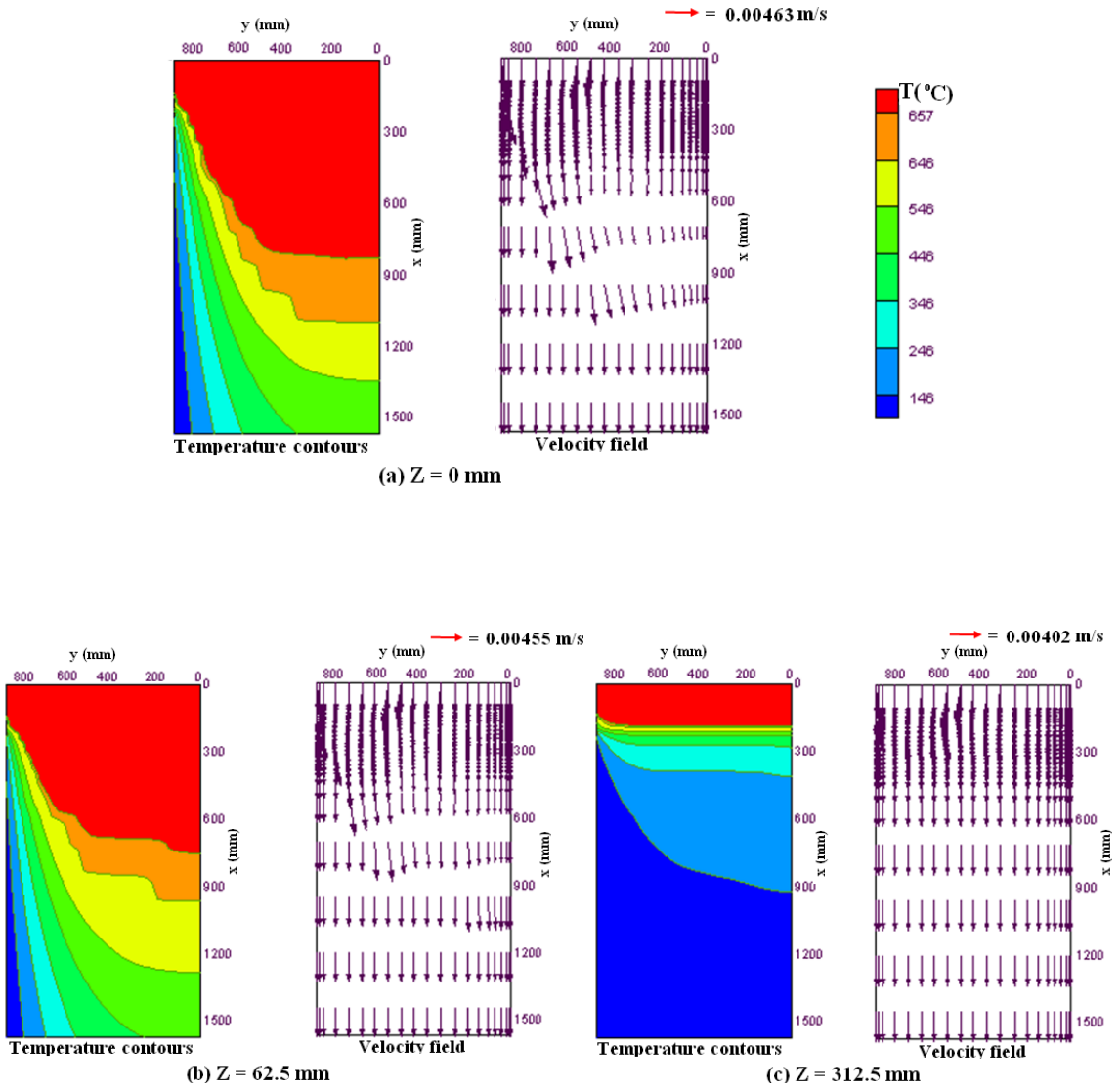

Figure 7.28: Enlarged 2-D view of temperature contours and velocity vectors of the top domain using the open top delivery system with a porous filter having a width of 433 mm for porosity, $\phi = 0.4$ and Darcy value 0f 1.0×10^{-4} for a casting speed of 180 mm/min and 64°C superheat at: (a) wide symmetry plane at z = 0 mm, (b) vertical plane parallel to the wide face at z = 62.5 mm, (c) vertical plane parallel to the wide face at z = 312.5 mm.

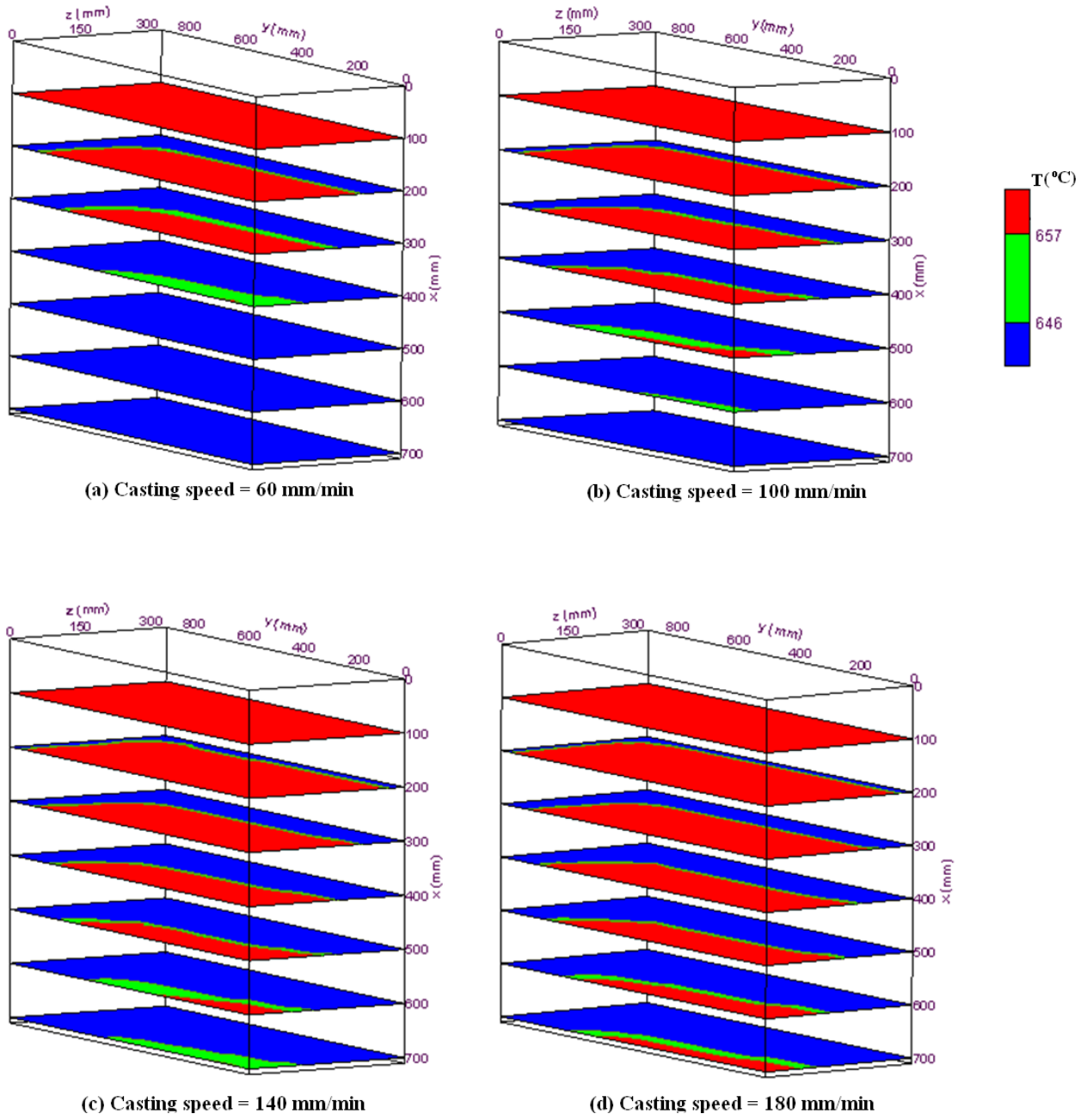

Figure 7.29: Contours of solidus and liquidus temperatures at various transverse cross-sectional planes (y-z planes) of the top part of the ingot using the open top delivery system with a porous filter having a width of 433 mm for porosity, $\phi = 0.4$ and Darcy value 0f 1.0×10^{-4} for a superheat of 64°C and casting speeds of (a) 60 mm min^{-1} (b) 100 mm min^{-1} (c) 140 mm min^{-1} (d) 180 mm min^{-1}.

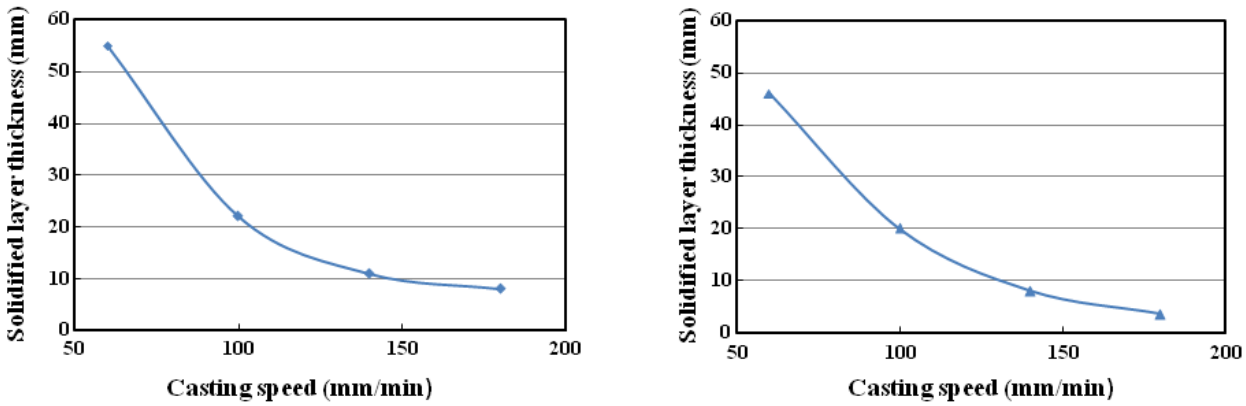

Figure 7.30: Solidified layer thickness from the narrow slab face at an axial distance of x = 160 mm from the top free surface at the wide symmetry plane versus casting speed using the open top delivery system with a porous filter having a width of 433 mm for porosity, $\phi = 0.4$ and Darcy value 0f 1.0×10^{-4} for: (a) inlet superheat of 32^{o}C, (b) inlet superheat of 64^{o}C.

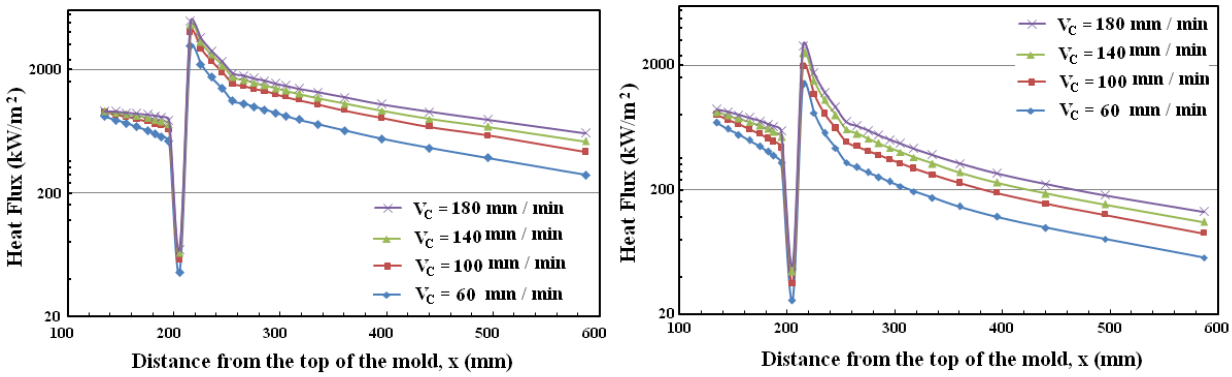

(a) Narrow slab face = 185 mm

(b) Wide slab face = 857.5 mm

(i) Inlet superheat = 32 °C

Figure 7.31: Variations of local surface heat fluxes for various casting speeds during solidification at 32°C superheat along the axial direction of the strand wall at: (a) z = 185 mm (b) y = 857.5 mm, using the open top delivery system with a porous filter having a width of 433 mm for porosity, ϕ = 0.4 and Darcy value 0f 1.0 × 10^{-4}.

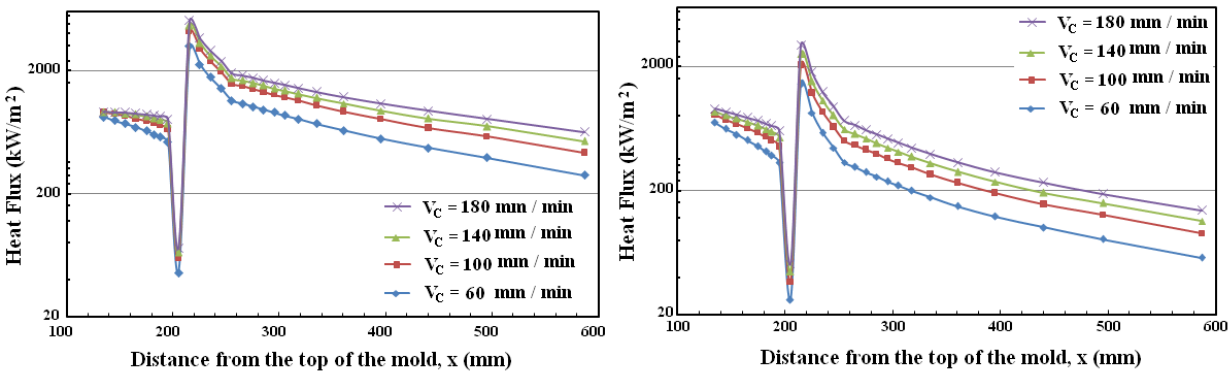

(a) Narrow slab face = 185 mm

(b) Wide slab face = 857.5 mm

(ii) Inlet superheat = 64°C

Figure 7.32: Variations of local surface heat fluxes for various casting speeds during solidification at 64°C superheat along the axial direction of the strand wall at: (a) z = 185 mm (b) y = 857.5 mm, using the open top delivery system with a porous filter having a width of 433 mm for porosity, ϕ = 0.4 and Darcy value 0f 1.0 × 10^{-4}.

CHAPTER 8

SUBMERGED NOZZLE WITH CHANNEL AND COMBO-BAG

8.1 Introduction

The aim of the current study is to come up with general suggestions for the studied parameters which would produce good slab characteristics. In order to identify the optimum distribution system for a particular VDC caster, the designer has to make sure that the general objectives, beside the special ones, are fulfilled by the employed melt distribution system. One of the prime objectives of a distribution system is to feed metal to all parts of the mold while minimizing the temperature gradient between the hottest and coldest areas. The areas identified as being of significant importance with regard to the metal feeding system include, the corners, short sides and the center of the rolling face. Another condition that has to be accomplished is that the distribution system has to deliver the required amount of metal with minimum oxide contamination. Increased turbulence level, especially at the melt free surface, was found to be the principle reason behind the generation of oxide inclusions [125].

In DC casting industries, usually one of the two, either the combo bag or the channel bag metal feeding system is widely used particularly for vertical direct chill (VDC) casters [122,124]. In order to increase the productivity there are serious on-going efforts in this industry to cast slab of high aspect ratios (width/thickness), specially slabs having aspect ratios greater than 3.0. The channel bag distribution system is usually used in casters which produce aluminum slabs of large aspect ratios. The aspect ratio of the current modeled slab was 2.62. This section is devoted to analyzing the effect on solidification for using the channel and combo bag distribution systems under a steady state condition. The channel bag is simply a channel which is sealed from all sides except the sides facing the narrow sides of the cast, as shown in Figure 8.2. The newly proposed

combo bag is similar to the channel bag except that the bottom part of the bag is porous, as shown in Figure 8.3. Two different values of porosity (void volume) for the porous bottom plate were modeled. In one case, it was assumed that the bottom plate acted as a filter medium having a porosity of 0.4. In another case, the bottom plate was assumed to act as foam having a porosity of 0.9. The permeability of the porous medium was assumed constant and was considered to be 9.0×10^{-8} m^2. This value of the permeability is of the same order that has been experimentally obtained for aluminum foams having porosities in the range of 0.9 to 0.97 [11]. The dimensions of the bag were 35 mm (h) × 400 mm (l) × 180 mm (w) in the x, y, and z directions, respectively, for both channel and combo bag distribution systems. It is assumed that the porous plate was made of stainless steel having open-celled structure through which the liquid melt could pass. In addition, a local thermal equilibrium between the solid structure of the porous plate and the liquid contained there was assumed. The latter assumption simplified the energy equation, and as a result only one energy equation for the solid structure and liquid region was solved. To account for the variable thermal conductivities, variable specific heats and density variations of the solid and liquid regions, the effective values of these variables were used, and listed in Table-7.1. The melt was delivered into the bag from an overhead trough through a square-shaped nozzle having a cross-sectional area of 900 mm^2. The nozzle walls, the walls of the distributor bag, and the porous bottom plate were all assumed to have a constant thickness of 5 mm. The nozzle was immersed in the liquid metal pool to a depth of 20 mm and placed at the center of the distributor bag, and the whole nozzle-distribution bag assembly was placed at the geometrical center of the caster, as schematically shown in Fig. 8.1. For each of the two melt distribution systems, namely, the channel and combo bags, a total of four casting speeds, viz, 40, 60, 80, and 100 mm/min were simulated. The modeled ingot was an industrial-sized slab having dimensions of 2500 mm × 1730 mm × 660 mm in the x, y and z directions, respectively. Due to symmetry reasons, only a quarter of the whole domain was considered as the calculation domain (refer to Figure 8.1). The modeled alloy was AA-1050. The thermo-physical properties of AA-1050 alloy were summarized in Table 3.1 of Chapter-3. The boundary conditions used were the same as those given in details in Chapter-3.

It is to be noted here that due to non-dimensionalization of the thermal boundary conditions, a parameter appeared which was the Biot number ($Bi = \frac{\gamma D}{K}$). Where, h is the effective heat transfer coefficient, D is the characteristic length, and K is the conductivity of the solid. The values of *Bi* differed from the open-top melt feeding scheme due to different value of the characteristic length 'D' (refer to Chapter-5, Section-5.2). In the present delivery system, at the metal-mold contact regions of the mold, the *Bi* was kept fixed at about 0.2 while at the air gap region within the mold it took a very low value of 0.02. At the water impingement point (x = 215 mm) *Bi* was about 2.6 and it decreased linearly with the axial distance up to a length of 40 mm from the impingement point and achieved a value of 1.3. For the rest of the length of the caster beyond 255 mm the value of *Bi* was fixed at the latter value.

In simulating such systems, while increasing the casting speed, one need to pay attention to two very important out comes. In order to avoid breakouts, the first objective is to make sure that the ingot has developed sufficiently thick solid shell around all four sides such that the cast is capable of holding the molten metal before exiting the mold. The second objective is to make sure that the vertical recirculation does not reach to the slab free surface so that the oxide inclusions prevailing there do not mix with the melt underneath.

In addition to the above factors, the strong convective currents created by the side opening in such systems should be carefully controlled since they develop a vertical recirculation zone, which is found to be a major cause of negative segregation at the ingot center [52]. This solute-lean region is formed by solute-lean grains that are carried by the convective currents along the mushy interface of the sump to the center of the ingot. These grains then settle out of molten sump and become entrained by the advancing solidification front. The rejection of solute from the grains, which is called micro-segregation, formed by nucleation or dendrite shearing is taking place at the lower portion of the molten sump. Settling of the solute-lean grains at the bottom of the sump and the displacement of solute rich liquid, results in a negative segregation at the center of the ingot. The displaced solute-rich liquid is then carried by convection upward and outward toward the surface of the ingot. It then re-circulates with the incoming melt,

floods the rigid portion of the mushy zone, and results in a positive segregation region near the slab surface. Therefore, reduction of these convective currents will reduce the macro-segregation problems [28]. It is well established that with the increase of the casting speed, the extent of macro-segregation increases.

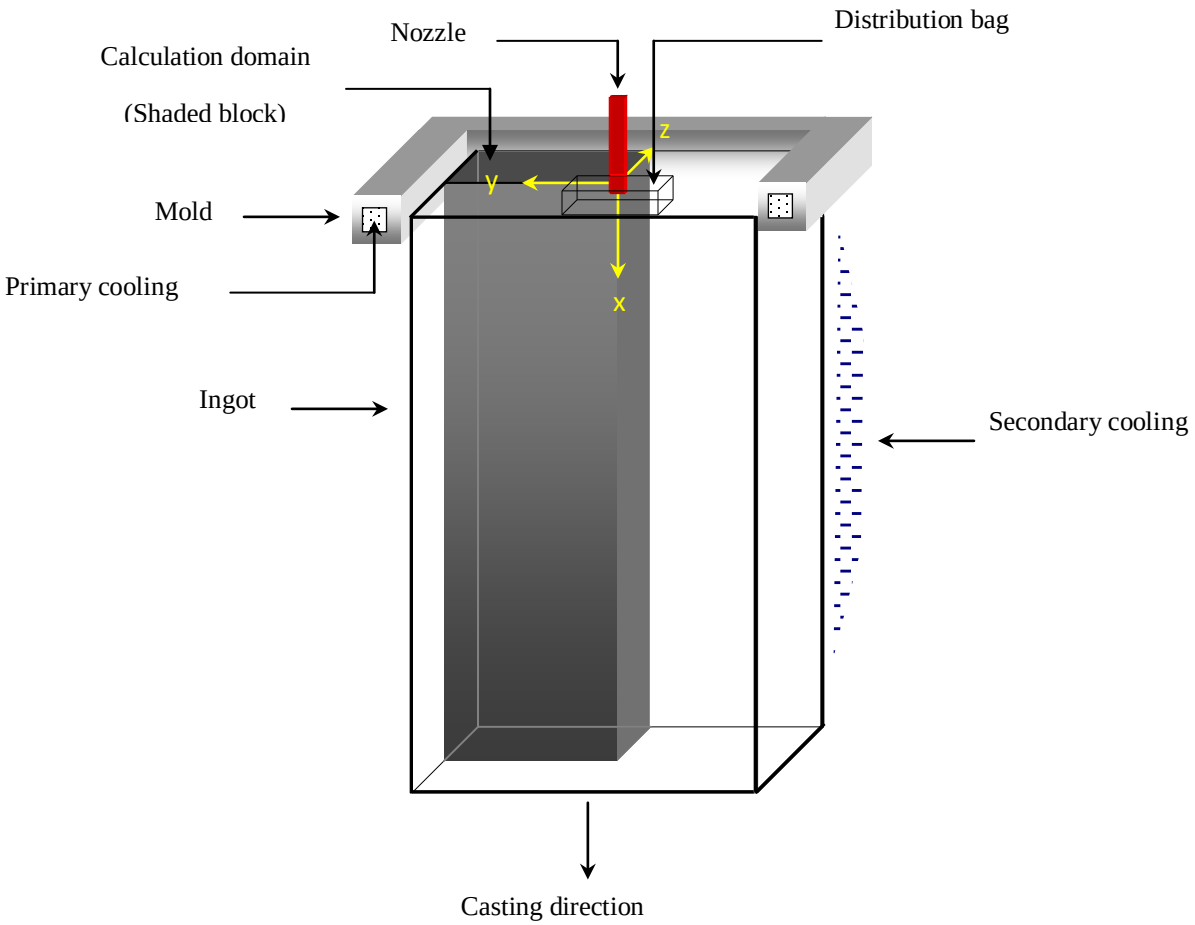

Figure 8.1: Schematic of a vertical DC caster with the calculation domain represented by ash color for a submerged nozzle with a distributor plate.

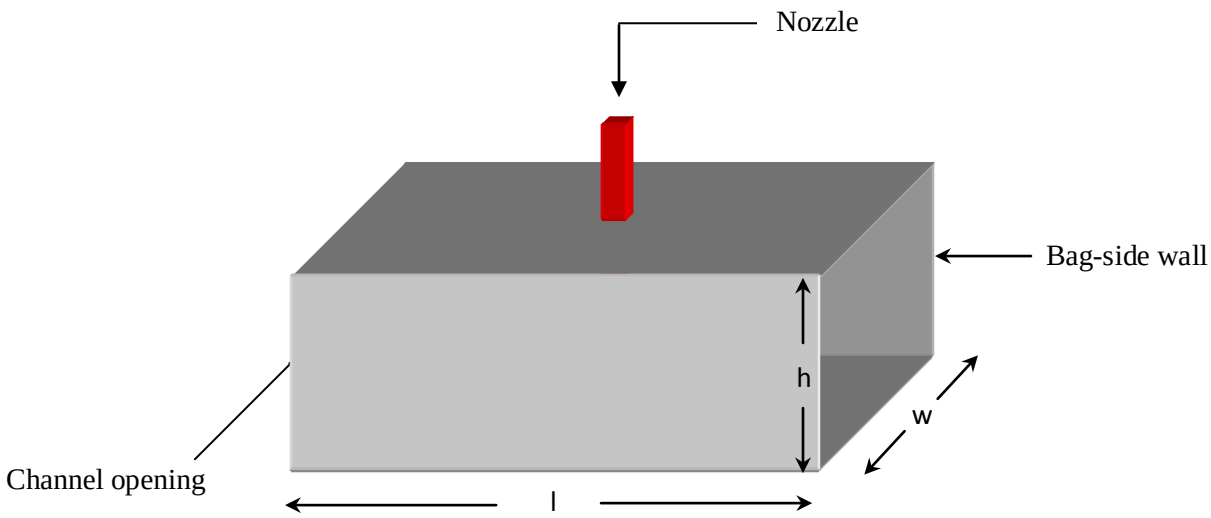

(a) Channel bag

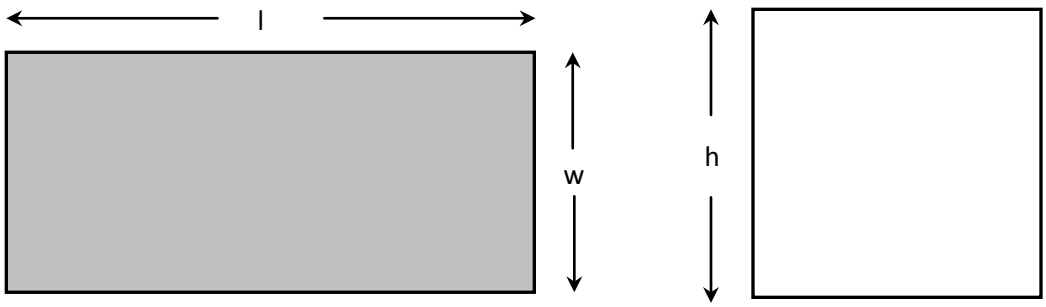

(b) Bottom view

(c) Side window

Figure 8.2: Schematic of a channel bag

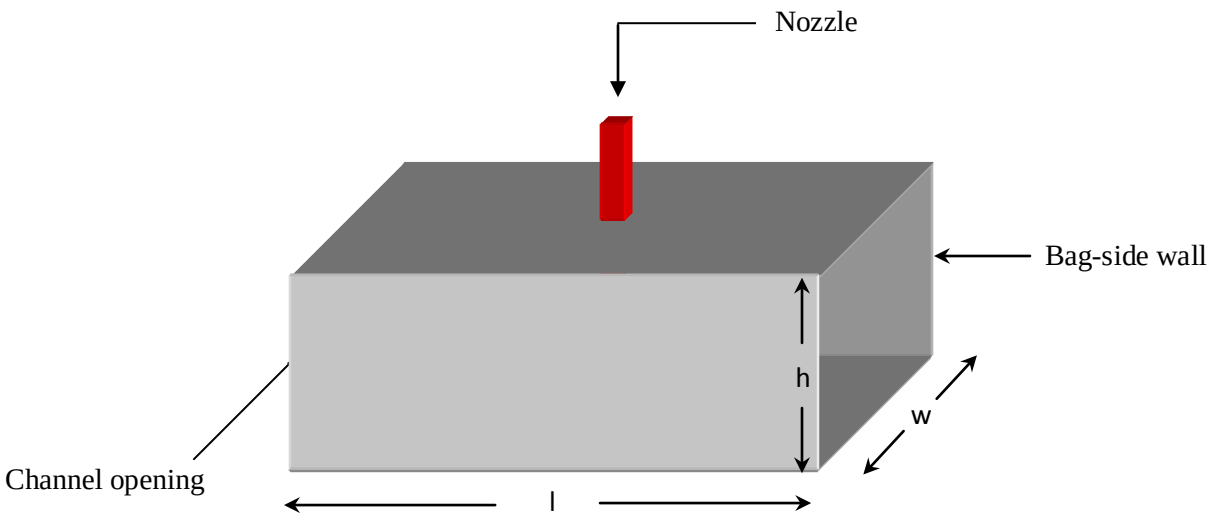

(a) Combo bag

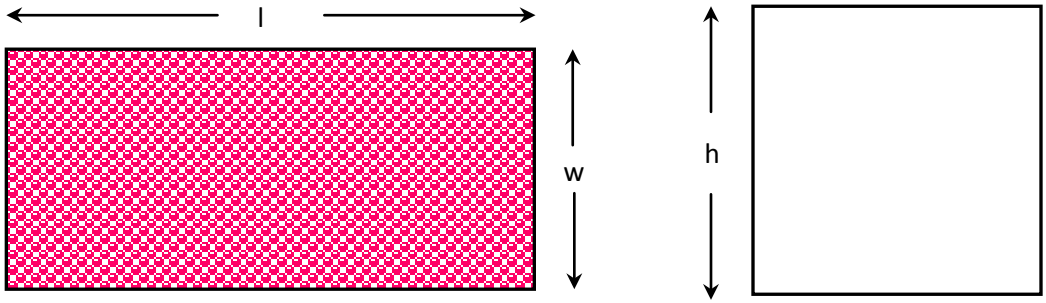

(b) Bottom view

(c) Side window

Figure 8.3: Schematic of a combo bag
having a bottom porous plate

8.2 Results and Discussion

This section is divided into three subsections. In section one the results obtained for a submerged nozzle distributing melt into a channel bag having a solid bottom plate are discussed. In the second section, the numerical results obtained for a submerged nozzle distributing melt into a combo-bag having a porous bottom plate with a porosity of 0.4 are discussed. Here, the porous plate is acting as a filter media. In the third section, the predicted results obtained for a submerged nozzle distributing melt into a combo-bag having a porous bottom plate with a porosity of 0.9 are discussed. The highly porous plate is acting as foam. While discussing the results the above three cases will be referred to as geometry-1, geometry-2, and geometry-3, respectively. In order to avoid confusion, the discussion of the velocity and temperature fields will be followed by a discussion of other relevant quantities, namely, sump depth and thickness of the mushy layer developed at the ingot center. The latter discussion will be followed by the solid layer thickness and the local surface heat flux at two specific regions (see Fig. 3.3). Finally, an overall conclusion is drawn. To facilitate the discussion a summary of the relevant parameters is given in Table 8.1.

Table 8.1: Values of the parameter used in three melt delivery arrangements.

Case	Casting speed, u_s [mm/min]	Inlet Raynolds number, (Re_L)	Inlet Peclet number, ($Pe = Re_L \times Pr$)
1	40	42,367.20	267.41
2	60	63,550.80	401.11
3	80	84,734.40	534.82
4	100	105,918.0	668.52

8.2.1 Geometry-1

a. Velocity and Temperature Fields

Figures 8.4(i-iv) show a 3-D surface plot of the computed temperature and velocity fields for four casting speeds, namely, 40, 60, 80, and 100 mm/min, respectively,

and all for a fixed melt superheat of 32°C. Each figure shows the calculation domain, which consists of two symmetry planes [wide (x-y plane) and narrow (x-z plane)] as well as the top surface of the ingot. Figures 8.4(b,d,f,h) show the corresponding 3-D velocity vector fields. These figures indicate the molten metal coming out of the nozzle is directed horizontally toward the narrow side of the mold by the distribution bag. After reaching the narrow side of the slab, the horizontal flow of hot melt is split into two streams. One stream is forming a counter clockwise vortex at the wide symmetry plane, hence forth, will be called the lower recirculation zone. Another part of the steam moves upward and then it travels along narrow and wide faces and finally reaches at the corner of the wide face and narrow symmetry plane where it divides into two streams. One stream forms a clockwise recirculation zone at the top free surface, which is referred to as upper recirculation zone, while the other stream moves in an inclined manner, termed as angle flow, and meets underneath the channel bag with a part of the upwardly directed flow of the lower recirculation zone. This angle flow can clearly be seen from the velocity vector fields at the narrow symmetry plane (x-z plane) of the same figures. These two turbulent recirculation zones lead to the enhancements of the mass, momentum, and energy transport in the upward region of the caster. The upper recirculation zone may promote the oxide contamination from the top surface. A comparison of Figs. 8.4(b,d,f,h), clearly show that with the increase of the casting speed the strength and extent of the lower and upper recirculation zones are increased. This can be observed by comparing the indicated maximum resultant velocities reported in the above four figures. This is mainly due to the additional incoming melt for the higher casting speeds.

Figures 8.4(a,c,e,g) show the temperature contours along with the solidification front and the liquidus isotherm. The effect of casting speed on temperature fields can be seen by studying the above figures. Isotherm plots in these figures indicate that increasing the casting speed increases liquid melt region inside the domain which is represented by the red color. The dark yellow color region in Figures 8.4(a,c,e,g) represent the mushy region. This region is confined by the solidus (646°C) and liquidus (657°C) temperature of the alloy. The solid part along with the mushy region of the ingot, according to the model assumptions, is traveling axially downward with the casting speed. The same figures reveal that the solidification front is becoming steeper and moving downward

with the increase of the casting speed. Compared to the solidification front, one can see in each of the above figures that the liquidus isotherm is completely non-uniform and forms a 'cliff' at around the middle of the wide symmetry plane (of the computational domain) and close to the side window of the bag. This has caused an increase in the thickness of the mushy layer there compared to the other regions of the cast. This marked-lift of the liquidus isotherm is due to enhanced thermal convection currents resulting from the merging of the angle flow with the upwardly directed flow of the lower recirculation zone. With the increase of the casting speed this cliff-shaped region is seen moving upward and expanding due to the stronger thermal convection. A similar cliff-shaped region is also recently reported by Zhang et al. [2012] in their 2-D modeling of an AA7050 round billet caster for a vertical melt feeding system through a delivery nozzle.

Figs. 8.5(a,b,c) - 8.8(a,b,c) illustrate explicitly 2-D temperature contours and vector fields at the wide symmetry plane(z = 0) and parallel to the wide symmetry plane at z = 62.5 mm, and z = 312.5 mm for various casting speeds for a fixed inlet superheat of 32^{o}C. These figures are magnified for clear understanding.

The left hand panels of Figures 8.5(a), 8.6(a), 8.7(a), 8.8(a) show temperature contours while the right hand panels of these figures portray the velocity vectors for wide symmetry plane (z = 0). Since the top surface of the distribution bag is sealed therefore there is no flow in that region, which can be seen from the velocity fields. The velocity vector plot of each of these figures illustrates the strong stream of hot melt is exiting from the distribution-channel-side opening. This stream is heading towards the narrow side of the cast and a strong recirculating flow is formed at the wide symmetry plane, as explained earlier. The left panel of each of the same figures shows that at the top region in the middle of the symmetry plane, a markedly lifted liquidus isotherm is formed with an increasingly high peak with increase in casting speed.

The left hand panels of Figures 8.5(b), 8.6(b), 8.7(b), 8.8(b) show temperature contours while the right hand panels of these figures portray the velocity vectors for a plane parallel to the wide symmetry plane at z = 62.5 mm. A close look of the velocity vector field in each panel shows the vertical eddy is still active there. The temperature isotherms in each panel are seen to have lifted upward in comparison to the isotherms presented in the wide symmetry plane. The upward movements of these isotherms, is

mainly due to the weak convection within the melt itself, and also due to the comparatively nearer location with respect to the wide face where greater heat transfer takes place.

Similar to the earlier figures, the left hand panels of Figures 8.5 (c), 8.6 (c), 8.7 (c), 8.8(c) show temperature contours while the right hand panels of these figures portray the velocity vectors for a plane parallel to the wide symmetry plane at z = 312.5 mm, which is close to the wide face. The velocity field shows the melt is moving horizontally from the narrow face toward the slab center in the hot top region and the magnitude of the maximum resultant velocity is much lower compared to the corresponding values in other two longitudinal planes. From the temperature contours it is evident that most of the melt is solidified there, with only a narrow and uniform horizontal mushy region is left to be solidified. Since these panels are very close to wide face, as a result, the solidification is almost complete there. A comparison of the isotherms among the four panels shows that with the increase of the casting speed isotherms move rapidly downward.

Figures 8.9(a-h) give numerical results for transverse cross-sections (y-z planes) parallel to the slab-free surface for a fixed inlet superheat, $\Delta T = 32^{o}C$ and for four different casting speeds. The left hand panels of these figures show the liquid, mushy, and solid regions along the ingot cross-sections presented by red, green, and blue colors, respectively, while the right hand panels of these figures portray the flow patterns. In these figures, the first slice is taken near the end of the adiabatic section of the hot top at an axial distance, x = 100 mm. The second cross-section is taken near the end of the mold at x = 200 mm. Another five transverse cross-sections are located at 300, 400, 500, 600, and 700 mm from the slab top surface. These latter five sections are located in the secondary cooling region. Examinations of the figures in the left hand panels show how the solidification proceeds along the wide and narrow faces of the ingot. At x = 100 mm, only liquid melt exist, therefore the vector field covers the whole section as shown in the right hand panels of these figures. Near the end of the mold, a thicker solidified layer is formed along the ingot rolling face compared to the ingot narrow face. The slow moving melt along the rolling section allows more heat to be extracted by the primary coolant of the mold. Whereas, the high momentum melt stream delivered to the narrow side of the mold through the side opening of the distribution bag has delayed the formation of the

solidified layer in that part. The mushy layer is separated between the center of the ingot and near the narrow slab face, and becomes thinner there. From previous discussion on various longitudinal cross-sectional views, it is evident that a counter-clockwise vortex is formed right after the channel opening. The angle flow, coming from the narrow symmetry plane, is merging with the upwardly directed flow of the lower recirculation zone and is leading to a wider transition region. At the merging zone, these two streams restrict the advancement of liquidus isotherm, which is reflected on the mushy layer formation. Because of intense cooling in the secondary cooling region, the growth of solid layer becomes greater which is demonstrated in the left hand panels of these figures. Considering the effect of casting speed, one can find that the solidification growth rate along the wide and narrow faces is decreased due to the increase in the casting speed. With increasing casting speed, the mushy layer is seen to exist at a higher depth.

In an actual DC casting process it is well known that the heat transfer rate not only varies axially but also varies peripherally, that is along the y and z axes. This change in the heat transfer along the transverse directions has not been implemented in the current mathematical model due to the lack of values in the literature of the proper heat transfer coefficient functions that describe this change. Therefore, it is expected, once appropriate heat transfer coefficient functions are implemented along the transverse directions, more correctly predicted solidified layer thickness will be achieved along the entire slab surface. This goal, once achieved, might compare well with the experimental results.

b. Quantitative Analysis

(i) Sump Depth and Mushy Layer Thickness

The quantitative predictions of the sump depth and the mushy zone thickness at the ingot center for various casting speeds are illustrated in Table 8.2. The results demonstrate that a higher sump depth is obtained at a higher casting speed. At a given casting speed of 40 mm/min, the sump depth is approximately 220 mm from the top of the mold. The relative difference of sump depth at casting speeds of 60, 80, and 100

mm/min, is about respectively 52 %, 79 %, and 121 % higher, in comparison to the lowest casting speed of 40 mm/min, which can be seen in Table 8.2. In the same table, the results show that the thickness of the mushy layer at the center is getting thinner with the increase of the casting speed. An approximately 103 mm thick mushy layer is seen at a casting speed of 40 mm/min, which is about 43 %, 77 %, and 61 % thicker compared to the mushy layer thickness obtained at casting speeds of 60, 80, and 100 mm/min, respectively. In this melt delivery arrangement, the streams exiting from the distributor-side-openings control both the depth of the sump at the slab center and the thickness of the mushy layer. As discussed earlier, the upward component of the lower re-circulating vortex is reinforced by the angle flow at the center. With the increase of the casting speed, both the angle flow and the upward component of the lower re-circulating vortex are increased, and hence, there is a greater convective heat transfer, which is leading to the decreasing in the growth of the mushy layer.

Table-8.2: Sump depth and mushy thickness in mm at the center of the ingot for geometry-1 for four casting speeds and a superheat of 32^{o}C.

Quantity	Values of casting speed (u_s) in mm/min			
	40	60	80	100
Sump depth (mm)	220	52.0 % higher than u_s = 40 mm/min	79.1 % higher than u_s = 40 mm/min	120.5 % higher than u_s = 40 mm/min
Mushy thickness (mm)	103	42.7 % lower than u_s = 40 mm/min	76.7 % lower than u_s = 40 mm/min	61.2 % lower than u_s = 40 mm/min

(ii) Formation of Solidified Shell

In Figure 8.10, the profile of shell thickness shows the effect of casting speed on the formation of shell at the wide symmetry plane for geometry 1. The thickness of solidified shell is predicted from the narrow slab face at an axial distance of 160 mm

below the slab top surface. This position is located at around the middle of the mold. In Table 8.3, the quantitative values of the shell thickness for the same location are listed for four specified casting speeds. From both, Fig. 8.10 and Table 8.3, it is observed that with the increase in the casting speed the shell thickness decreases very slowly and almost linearly. At a casting speed of 40 mm/min, a shell thickness of approximately 15 mm is obtained from the narrow face. The relative difference in shell thickness at casting speeds of 60, 80, and 100 mm/min, is respectively about 13 %, 27 %, and 33 % lower in comparison to the lowest casting speed of 40 mm/min, which can be seen in Table 8.3. This is caused by the strong and heated horizontal jet which is emerging from the side window of the bag that has been observed at this location. The strength and the heat content of the jet increases with the increase of the casting speed, and thereby resulting in thinner shell thickness.

Table-8.3: The thickness of the solidifying shell (mm) at wide symmetry plane from the narrow slab face at an axial distance of 160 mm from the top free surface inside the mold for four casting speeds and inlet superheat of 32°C for geometry-1.

Quantity	Values of casting speed (u_s) in mm/min			
	40	60	80	100
Thickness of the solidifying shell (mm)	15	13.3 % lower than 40 mm/min	26.7 % lower than 40 mm/min	33.3 % lower than 40 mm/min

(iii) Local Surface Heat Flux

Figures 8.11(a) and (b) show the local surface heat flux with the axial distance taken from x =135 mm to x = 587 mm down from the top surface on the narrow (at z = 185 mm) and wide faces (at y = 857.5 mm) for various casting speeds.

The local heat flux versus axial distance plotted in Figs. 8.11(a) and (b) shows that, initially, there is an almost linear decrease of heat flux within the mold, which is the metal-mold contact region. The local heat flux then rapidly decreases due to the formation of air gap within a cast length of 10 mm inside the mold. At the pre-impingement zone, which is the axial distance from the bottom of the mold to the impingement point, the predicted local heat flux increases very sharply up to the impingement point and then there is a steep decrease up to the axial distance of 255 mm. After that, there is a monotonic decrease of the heat flux along the rest of the cast surface. The distribution of local heat flux is seen to be similar in trend for each casting speed at both the locations as illustrated in the two figures. The abrupt decrease or increase in the local heat flux on the cast surface is particularly troublesome because it encourages differential thermal contraction/expansion in the solidifying shell and promotes the generation of high thermal stress and strain. This can ultimately lead to internal and surface defects which can severely compromise the quality of the cast product. It is also worth noting that with respect to the local heat flux, with the increase of the casting speed, the extent of the rapid fall in the air-gap decreases (heat flux increases) while extent of the rapid rise at the impingement point increases. The higher casting speed shows the higher local heat flux at each grid point. Actually, at a higher casting speed, the melt flow rate increases, and the residence time of the melt inside the mold decreases. These result in the surface temperature to increase due to increased convection currents. It should be mentioned that, for the same thermal boundary conditions at the wide and narrow slab faces, there is a difference in the axial distributions of the local heat flux. A higher value of the local heat flux is achieved along the cast at z = 185 mm compared to the value obtained for the same axial location but at y = 857.5 mm. This is for the same reasons as explained earlier. The observed high strength flow patterns near the narrow face cause surface temperature enhancement, thereby generating high local heat fluxes on the narrow face. On the contrary, near the rolling face, a slow moving metal flow generates lower thermal convective flow and resulted in the reduction of the surface temperature and local heat flux at this location.

To understand clearly the role played by the casting speed during the solidification process, quantitative values of the surface heat flux are listed in Table 8.4

for four casting speeds at z = 185 mm, x = 215 mm, which represents the water jet impingement point where the highest heat transfer coefficient has been imposed. The predicted value of the heat flux at this location is quite high and is the highest along the cast surface, and it increases with the increase of the casting speed.

Table-8.4: The local heat flux in kW/m^2 at z = 185 mm at an axial distance of 215 mm from the top free surface for four casting speeds and inlet superheats of 32°C for geometry-1.

Quantity	Values of casting speed (u_s) in mm/min			
	40	60	80	100
Surface heat flux (kW/m^2)	2988.0	24.6 % more as compared with 40 mm/min	30.4 % more as compared with 40 mm/min	35.8 % more as compared with 40 mm/min

8.2.2 Geometry-2

(a) Velocity and Temperature Fields

Figures 8.12 (i-iv) show a 3-D surface plot of the predicted temperature and velocity fields for four casting speeds, namely, 40, 60, 80, and 100 mm/min, respectively, all for a fixed melt superheat of 32°C using the standard combo bag with a bottom porous plate having a porosity of 0.4 and an assigned Darcy number of 10^{-4}. Figs. 8.13(a,b,c) - 8.16(a,b,c) illustrate 2-D temperature and velocity profiles at the wide symmetry plane (z = 0) and parallel to the wide symmetry plane at z = 62.5 mm, and z = 312.5 mm for the aforementioned casting speeds. In presenting the results, only about two-third portion of the ingot is taken and magnified for the purpose of clarifying the results. The left hand panels of these figures show temperature contours while the right hand panels of these figures illustrate the velocity vectors at three longitudinal cross-sectional planes. Figures 8.17(a-h) present results for transverse cross-sections (y-z plane) parallel to the slab-free surface which illustrate how the growth of the solid shell and mushy region and the

corresponding velocity field are progressed along the ingot axial direction. Here, only the parts showing the extent of the sump are presented and magnified. To convey the results, seven cross-sections of the ingot are taken, which are at an axial distance of 100, 200, 300, 400, 500, 600, and 700 mm from the top ingot surface.

In the ingot cast with geometry-2 feeding, the flow patterns are partially different compared to those obtained using geometry-1 feeding system (refer to Figs. 8.4(b,d,f,h)), as shown in Figures 8.12(b,d,f,h). The melt flow presenting in these figures shows that there are two streams of hot melt coming out from the distributor bag at each casting speed, which is contrary to geometry-1. One jet is coming out from the side window, which is named earlier as the horizontal jet, and another stream is emerging through the bottom porous plate of the distributor bag, the latter stream is referred to as the downward vertical jet. The strength of the horizontal jet is reduced because a portion of the incoming melt from the nozzle is exiting from the bottom porous plate. It is to be recognized here that the porous plate is very active just beneath the nozzle area where the jet momentum is high. Since the porosity is 0.4, the porous plate offers a significant hydrodynamic resistance to the flow. This can be observed from the flow field above the plate. As the melt travels along the plate towards the exit window, there is very little flow normal to the porous plate.

The above figures demonstrate that there are three vortex cores, two vortices are formed at the wide symmetry plane and one vortex is formed at the top surface. Similar to geometry-1 feeding scheme, the two vortices, which are referred earlier as the lower recirculation and upper recirculation zones, and the angle flow, have also been generated here. The reasons behind the generations of the above flow behavior are explained in details in the previous section of geometry-1. These recirculation zones can clearly be seen at the wide symmetry plane and at the slab free surface, and the angle flow can be found at the narrow-symmetry plane (x-z plane) in Figures 8.12 (b,d,f,h).

The third vortex which forms at the wide symmetry plane near the central area rotates in the counter-clockwise direction, which is referred to as the vertical recirculation zone. This strong vertical recirculation zone is a result of the melt flow through a part of the porous bottom plate at the center. The angle flow which is coming from the narrow symmetry plane and the downward vertical jets issuing from the bottom porous plate

collide close to the center. The flow then creates an anticlockwise vortex at this position and is lifted upward and merges with the horizontal part of the flow of the lower recirculation zone, similar to geometry-1. Hence, near the center, the flow intensity is reduced.

The two vortices along the wide symmetry plane formed by the lower and vertical recirculation zones can be clearly seen in the 2-D velocity plots of the right hand panels of Figures 8.13 (a), 8.14 (a), 8.15 (a), 8.16(a). Though the flow out of the side window is similar in pattern to those shown in the right hand panels of Figures 8.5(a), 8.6(a), 8.7(a), 8.8(a), but the strong downward vertical jet in this geometry is believed to have reduced the strength of the lower and upper vortices. The strength of the vertical recirculation zone increases with the increase of the casting speed. The strength of the flow is represented by the magnitude of the maximum resultant velocity. The maximum resultant velocity increases with increasing casting speed, as expected. The trend of the melt flow at z = 62.5 mm and z = 312.5 mm for four casting speeds appear similar in nature as those presented in the case of geometry-1. As one moves towards the rolling face one can see that, in the longitudinal plane at z = 62.5 mm, the vertical recirculation vortex has completely disappeared. It for the first time that the current mathematical model results show the critical role played by the downward stream of melt issued from the bottom porous plate of the combo bag in shaping the solidification front profile which will be explained later.

The temperature distributions for four casting speeds predicted for geometry-2 feeding scheme are presented in Figs 8.12(a,c,e,g). For the purpose of comparison, the isotherms have been chosen for the same values as in geometry-1. The shape of the liquidus and solidus isotherms are seen to be quite different in geometry-2 compared to geometry-1. In geometry-2, the solidification profile is more horizontally-uniform along the wide and narrow symmetry planes at the slab center, which may be, due to the enhanced conductive mode of heat transfer in those locations. For a given casting speed of 40 mm/min, the horizontally-flat part of the solidification front is approximately 143 mm measured from the central axis towards the narrow slab face, whereas, this horizontal distance for casting speeds of 60, 80, and 100 mm/min is increased approximately to 342, 380, and 420 mm, respectively, from the slab center, as illustrated in the 2-D temperature

contours of the left hand panels of Figs. 8.13(a), 8.14(a), 8.15(a), 8.16(a), The increased uniformity of the solidification front with the increase in the casting speed is a very desirable metallurgical characteristic in DC casting for the following reasons.

First, increasing the casting speed implies the increase in the production rate of aluminum slabs. Second, an increase in the flat part of the solidification front implies that uniform heat transfer is taking place over the increased surface area of the solidification front. The latter would allow the slab to have better homogeneous metallurgical characteristics. The increase in length of the almost-horizontally-flattened solidification front is attributed mainly due to the collision between the angle flow and the downward vertical jet issued from the bottom porous plate of the distributor bag. The two collided jets form a single jet which is moving upward into a limited area, thus locally producing a uniform solid front. The vertical recirculation is pushed toward the solidification front by the action of the vertical jet. An increase in the casting speed causes the speed of the vertical jet to be increased. Consequently, the strength of the collision is also increased which squeezes the vertical recirculation near the central area with the increase in casting speed. Additionally, the reduction of the buoyancy-induced flow exiting from the porous bottom plate causes the solidification front in the central portion of the ingot to be more uniform.

An extended cliff-shaped mushy zone is observed at each casting speed near the exit of the side window at the wide symmetry plane for geometry-2 compared to geometry-1 feeding scheme (refer to Figs 8.4(a,c,e,g)), as can be seen in Figs 8.12(a,c,e,g) and in the 2-D temperature contour figures at z = 0, and at z = 62.5 mm. The reasons for the extended cliff-shaped mushy zone are due to the difference in the flow behaviors for the two geometries. The flow field and the isotherms in the longitudinal cross-section at z = 312.5 mm, presented in Figs 8.13(c) - 8.16(c), appear similar in trends as geometry 1.

A close observation of the flow patterns and shape of the liquidus and solidus isotherms along the various transverse cross-sections (y-z planes) parallel to the slab-free surface presented in Figs. 8.17(a-h) for four casting speeds exhibit similar trends, as are seen in the corresponding plots of velocity vectors and temperature contours for geometry-1 feeding system (refer to Figs. 8.9(a-h)). While discussing the results in the

subsection of geometry-1, the Figs. 8.9(a-h) are discussed in detail, and hence it is not necessary to explain Figs. 8.17(a-h) here again.

(b) Quantitative Analysis

(i) Sump Depth and Mushy Thickness

The predicted sump depth and the thickness of the mushy zone at the slab center for four casting speeds are presented in Table 8.5. The values of the above quantities are listed in terms of the relative differences, in percentage from, in comparison to the lowest casting speed. The sump depth and the mushy layer thickness are both observed to increase with the increase of the casting speed, as expected.

A comparison of the results generated by geometry-1 (refer to Table 8.2) and geometry-2, reveals that for geometry-2, the sump depth is nearly 2.21, 1.48, 1.29, and 1.07 times at casting speed of 40, 60, 80, and 100 mm/min, respectively, with respect to geometry-1. Thus, as seen, in geometry-2 feeding system, a strong vertical recirculation zone is formed near the ingot center, leading to a strong thermal convection there, which acts as a dominant factor for the enhancement of the sump depth. For the same reason, the mushy thickness at the center for geometry-2 feeding system decreases considerably compared with geometry-1. One can see in Table 8.5, the mushy layer becomes thicker as casting speed is increased. This happens due to the higher thermal convective effect in the mushy layer offered by the downward vertical jet at the center.

Table 8.5: Sump depth and mushy thickness in mm at the ingot center for geometry-2 for four casting speeds and a superheat of 32^{o}C.

Quantity	Values of casting speed (u_s) in mm/min			
	40	60	80	100
Sump depth (mm)	486	1.7 % higher than u_s = 40 mm/min	4.3 % higher than u_s = 40 mm/min	6.6 % higher than u_s = 40 mm/min
Mushy	7	71.4 % higher than	114.3 % higher	171.4 % higher

thickness (mm)		u_s = 40 mm/min	than u_s = 40 mm/min	than u_s = 40 mm/min

(ii) Formation of Solidified Shell

Figure 8.18 and Table 8.6 show graphically and quantitatively the growth of the solid shell from the narrow slab face at around the middle of the mold (x = 160 mm) at the wide symmetry plane (z = 0) for various casting speeds. It is clear from the figure and the table that with an increase in the casting speed, the solidified-layer thickness decreases almost linearly, due to the greater amount of hotter melt directed against the narrow wall. At a casting speed of 40 mm/min, the shell thickness is found to be approximately 24 mm from the narrow face. The relative difference in shell thickness at casting speeds of 60, 80, and 100 mm/min, is respectively about 25 %, 33 %, and 50 % lower in comparison to the lowest casting speed of 40 mm/min, which can be seen in Table 8.6.

Comparing the Tables 8.3 and 8.6, it can be seen that, for all four casting speeds, the shell thickness for the geometry-2 feeding is nearly 1.2 to 1.6 times more than those for the geometry-1 feeding scheme. The thicker shell thickness is predicted in each casting speed for geometry-2, because here the downward vertical flow immerging from the bottom porous plate follows the center of the ingot downward and, then it turns horizontally towards the narrow faces, and is engulfed by the lower recirculation, thereby decelerating the thermal convection near the narrow face.

Table-8.6: The thickness of the solidifying shell (mm) at wide symmetry plane from the narrow slab face at an axial distance of 160 mm from the top free surface inside the mold for four casting speeds and inlet superheat of 32°C for geometry-2.

Quantity	Values of casting speed (u_s) in mm/min			
	40	60	80	100

Thickness of the solidifying shell (mm)	24	25 % lower than 40 mm/min	33.3 % lower than 40 mm/min	50 % lower than 40 mm/min

(iii) Local Surface Heat Flux

Figures 8.19 (a) and (b) show the effect of the casting speed on the predicted local surface heat flux along the axial direction of the cast for two faces. The location of the two faces, narrow and wide, is discussed while discussing geometry-1. An investigation of the local heat flux in these two figures reveals that the local heat flux first decreases linearly a little inside the mold and then decreases sharply in the air gap region. In the impingement zone of the ingot, the highest heat flux is predicted and then it decreases almost linearly in the downstream of the cast. For such an uneven cooling, the local heat flux or the surface temperature varies quite significantly in different sections of the ingot. The higher the casting speed, the greater the local heat flux on the ingot surface, which is also observed for the previous geometry. A comparison between geometry-1 and geometry-2 shows that the local heat flux decreases axially at each grid point for all the four casting speeds at both locations (z = 185 mm, and y = 857.5 mm) for geometry-2 compared to geometry-1. For example, for geometry-1, the local surface heat flux takes a value of approximately 1.1 times than that is obtained for geometry-2 for a casting speed of 40 mm/min at z = 185 mm, x = 215 mm, which can be seen in Tables 8.4 and 8.7. In geometry-2, the momentum and the heat content of the horizontal jet issuing from the side window is believed to be have reduced due to the strong downward vertical jet exiting from the bottom porous plate, which indicates that the thermal convection near the walls is not as strong as in the case of geometry-1. A higher value of the local heat flux is achieved along the cast at z = 185 mm compared to the value obtained for the same axial location but at y = 857.5 mm, because of the greater thermal convective effects near the narrow wall. The same pattern is also seen in geometry-1 for the same locations.

Table-8.7: The local heat flux in kW/m^2 at z = 185 mm at an axial distance of 215 mm from the top free surface for four casting speeds and inlet superheats of 32°C for geometry-2.

Quantity	Values of casting speed (u_s) in mm/min			
	40	60	80	100
Surface heat flux (kW/m^2)	2741.58	30.6 % more as compared with 40 mm/min	37.2 % more as compared with 40 mm/min	42.0 % more as compared with 40 mm/min

8.2.3 Geometry-3

(a) Velocity and Temperature Fields

The 3-D surface plots of the predicted temperature and velocity fields are presented in Figures 8.20 (i-iv) for four casting speeds, namely, 40, 60, 80, and 100 mm/min, respectively, and for a fixed melt superheat of 32°C using the standard combo bag with a bottom porous plate having a porosity of 0.9 and an assigned Darcy number of 10^{-4}. Figs. 8.21(a,b,c) - 8.24(a,b,c) illustrate 2-D temperature and velocity profiles at the wide symmetry plane (z = 0) and parallel to the wide symmetry plane at z = 62.5 mm, and z = 312.5 mm for the aforementioned casting speeds. For the clarification of the results, about two-third portion of the ingot is taken again and magnified. Identical to the earlier two geometries, the left hand panels of these figures show temperature contours while the right hand panels of these figures illustrate the velocity vectors at three longitudinal cross-sectional planes. Figures 8.25(a-h) present results for transverse cross-sections (y-z plane) parallel to the slab-free surface which illustrate how the shape and growth of the solid shell and mushy region, and the corresponding velocity field are developing along the ingot axial direction. In the above figures, only a vertical portion of about 700 mm of the ingot are portrayed and magnified. Similar to the earlier two

geometries, seven cross-sections of the ingot are taken, which are at an axial distance of 100, 200, 300, 400, 500, 600, and 700 mm from the top ingot surface.

Inspections of the velocity fields in Figures 8.20(b,d,f,h) depict that there is an insignificant variation of the velocity field obtained in geometry-3 compared to geometry-2 (refer to Figs. 8.12(b,d,f,h)). In geometry-3, after the melt exits from the submerged nozzle, the flow is divided in to two jets similar to the latter case. Two jets are clearly visible exiting from the bag, which have formed three vortices. The clockwise recirculation zone that has developed at the top of the ingot is consistent with the previous discussion. In general, the flow always tends to follow the path of the least hydraulic resistance. Because of high porosity (ϕ = 0.9), there is a larger void space in geometry-3, and as a result a larger amount of melt is delivered through the central part of the porous plate compared to the porous filter used in geometry-2. This resulted in a lesser amount of melt coming out from the side window. In this case, the momentum of the downward jet is lower, and as a consequence the thermal convection is reduced in the central area compared to geometry-2.

The right hand panels of Figures 8.21(a,b,c) - 8.24(a,b,c) show the 2-D velocity plots at z = 0, z = 62.5 mm, and z = 312.5 mm for four casting speeds for geometry-3. The flow patterns are similar to those predicted for geometry-2. This is consistent with the 'lower recirculation and vertical recirculation' zones at z = 0 described for geometry-2. The strength of the recirculation increases with increasing casting speed, as expected. Similar to geometry-2, in the longitudinal plane at z = 62.5 mm, the vertical recirculation vortex is seen to have completely disappeared.

The 3-D surface plots of the isotherms for four casting speeds predicted for geometry-3 feeding scheme are presented in Figs 8.20(a,c,e,g). In contrast to geometry-2, in geometry-3 the lower momentum vertical jet exiting the highly porous bottom plate collides with the angle flow coming from the narrow symmetry plane and forms relatively weaker flow. This flow then moves horizontally and strengthens the lower recirculation zone near the exit of the side window. A region of cliff-shaped mushy layer forms there, the dimensions of which are lower compared to geometry-2. In addition, the vertical recirculation in the central region created a stagnant zone, which has led to the formation of an almost horizontal solidification front at and around the center. For the

casting speed of 40 mm/min, the horizontally-flat part of the solidification front is approximately 58 mm, measured from the center towards the narrow slab face, whereas, this horizontal distance for casting speeds of 60, 80, and 100 mm/min is increased to approximately 140, 152, and 165 mm, respectively, from the slab center, as illustrated in the 2-D temperature contours of the left hand panels of Figs. 8.21 (a), 8.22 (a), 8.23 (a), 8.24(a). The combined effect of the lower recirculation vortex and weaker strength of the downward vertical jet for increased porosity and fixed permeability, is leading to the formation of a shorter horizontal solidification front at the slab center for geometry-3 compared to geometry-2 for all four casting speeds.

The left hand panels of Figures 8.21(a,b,c) - 8.24(a,b,c) show the isotherms, and Figs.8.25(a-h) show flow patterns and shapes of the liquidus and solidus isotherms, which are similar to those discussed for geometry-2 and thus will not be further discussed here.

(b) Quantitative Analysis

(i) Sump Depth and Mushy Thickness

The predicted sump depth and the thickness of the mushy zone at the slab center for four casting speeds are presented in Table 8.8. The values of the above quantities are listed in terms of the relative differences (in terms of percentage), in comparison to the lowest casting speed. The sump depth and the mushy layer thickness are both observed to increase with the increase of the casting speed, as expected. A comparison of the results generated by geometry-2 (refer to Table 8.5) and geometry-3 (Table 8.8), reveals that for geometry-2, the sump depth is nearly 1.03 times greater at each casting speed, with respect to geometry-3. This is due to the lower thermal convection in the latter geometry. The mushy thickness at the center for geometry-3 feeding system remains virtually unchanged compared to geometry-2. One can see in Table 8.8, the mushy layer becomes thicker as casting speed is increased.

A shallower sump depth and a thicker mushy layer at the ingot center are found to form in case of geometry-1 compared to geometry-3 for all four casting speeds. As seen

from the plots of velocity field for geometry-3 feeding system, a high momentum downward vertical jet is exiting at the ingot center under the identical operating conditions which is not there in geometry-1.

The sump depth is 473 mm at casting speed of 40 mm/min for geometry-3, which in comparison to geometry-1 and geometry-2, is 53.5 % higher and 2.75% lower, respectively. This is an indication of the progressive increase in the intensity of melt turbulence created at the center of the melt pool by the melt feeding scheme presented in geometry-1, geometry-3 and geometry-2. The melt feeding through the channel bag shows a relatively shallower sump, which is one of the desirable characteristics of a good quality cast.

Table-8.8: Sump depth and mushy thickness in mm at wide symmetry plane (z = 0) for geometry-3 for four casting speeds and the superheat of 32^{o}C.

Quantity	Values of casting speed (u_s) in mm/min			
	40	60	80	100
Sump depth (mm)	473	3.0 % higher than u_s = 40 mm/min	3.4 % higher than u_s = 40 mm/min	6.1 % higher than u_s = 40 mm/min
Mushy thickness (mm)	7	57.2 % higher than u_s = 40 mm/min	42.9 % higher than u_s = 40 mm/min	142.9 % higher than u_s = 40 mm/min

(ii) Formation of Solidified Shell

Figure 8.26 and Table 8.9 show graphically and quantitatively the growth of the solid shell from the narrow slab face at around the middle of the mold (x = 160 mm) at the wide symmetry plane (z = 0) for various casting speeds. From the figure and the table, it can be seen that the solidified-layer thickness decreases linearly with an increase in the casting speed. From Table 8.9 it evident that an approximately 16 mm shell thickness from the narrow face has developed at a casting speed of 40 mm/min. The relative differences in the shell thickness at casting speeds of 60, 80, and 100 mm/min, is

respectively about 13 %, 25 %, and 31 % lower in comparison to the lowest casting speed of 40 mm/min.

Upon a comparison of the Tables 8.6 and 8.9, it can be seen that, for all four casting speeds, the shell thickness for geometry-2 feeding is nearly 1.1 to 1.5 times greater than that for geometry-3 feeding scheme. A thinner shell thickness is predicted in each casting speed for geometry-3 because of the fact the bottom porous plate having a greater porosity and has caused a decrease in the momentum of the downward vertical jet which is issuing from the bottom porous plate at the central region. This jet then turns upward and combines with the horizontal flow underneath and parallel to the distributor plate, and as a result there is an enhancement of the momentum of the horizontal flow, which can be seen from the contours of the isotherms (refer to Figs.8.25(a-h)).

Upon a comparison of the Tables 8.3 and 8.9, it can be seen that, for all four casting speeds, the shell thickness for geometry-3 feeding is nearly 1.1 times greater than that for geometry-1 feeding scheme. A thinner shell thickness is predicted in each casting speed for geometry-1 because of the fact that here all of the liquid streams are issuing only through the side window.

Table-8.9: The thickness of the solidifying shell in mm at wide symmetry plane from the narrow slab face at an axial distance of 160 mm from the top free surface inside the mold for four casting speeds and inlet superheat of 32°C for geometry-3.

Quantity	Values of casting speed (u_s) in mm/min			
	40	60	80	100
Thickness of the solidifying shell (mm)	16	12.5 % lower than 40 mm/min	25 % lower than 40 mm/min	31.3 % lower than 40 mm/min

(iii) Local Surface Heat Flux

The local surface heat flux versus axial distance along the cast for various casting speeds at the narrow and wide faces is shown in Figures 8.27(a) and (b), respectively for geometry-3. It is observed that the pattern of the local heat flux at both locations is not modified for geometry-3 feeding scheme in comparison to the local heat flux profiles obtained for geometry-1 and geometry-2, but the magnitude of the local heat flux decreases and increases at each grid point for four casting speeds compared to geometry-1 and geometry-2, respectively. It is also seen that the local heat flux increases with the increase of casting speed and the difference in the local heat flux is substantial when casting speed is in the range of 40-100 mm/min, as can be seen in Table 8.10.

A comparison of the local surface heat flux among the three melt feeding schemes at z = 185 mm, x = 215 mm (refer to Tables 8.4, 8.7, and 8.10) shows that the local surface heat flux is 2842.2 kW/m^2 at a casting speed of 40 mm/min for geometry-3, which in comparison to the geometry 1 and geometry 2, is approximately 5.1 % lower, and 3.54 % higher, respectively. A quantitative comparison of the local heat flux is probably an appropriate way to understand about the differences in the heat extraction rate from the cast.

Table-8.10: The local heat flux in kW/m^2 at z = 185 mm at an axial distance of 215 mm from the top free surface for four casting speeds and inlet superheats of 32°C for geometry-3.

Quantity	Values of casting speed (u_s) in mm/min			
	40	60	80	100
Surface heat flux (kW/m^2)	2842.18	29.3 % more as compared with 40 mm/min	33.4 % more as compared with 40 mm/min	37.5 % more as compared with 40 mm/min

8.4 Concluding Remarks

The effects of melt feeding scheme and casting speed on sump depth, mushy layer thickness, solid shell thickness and local surface heat flux have been investigated and some conclusions are drawn, which are stated as follows:

(a) An increase in the casting speed results in a deeper sump, a thinner shell and a higher local surface heat flux for all the three melt feeding schemes due to the increased intensity of thermal convection.

(b) A cliff-shaped mushy region is observed right after the exit of the side window of the bag in each melt delivery system. The most wider and extended mushy region is obtained in combo bag having a porosity of 0.4, and the narrowest cliff-shaped region is formed for the channel bag.

(c) The trend in the thickening/narrowing of the mushy region at the ingot center with the increase of the casting speed is different between the channel and the combo bag. In a channel bag melt feeding scheme, the mushy thickness decreases as casting speed is increased, whereas in the combo-bag feeding system a completely opposite trend has been found. This anomalous development of the mushy thickness may be due to the complex interactions of the superimposed velocities in that region.

(d) The maximum growth of the solid shell and the minimum local surface heat flux are obtained for a combo bag of porosity 0.4 in comparison to the other two geometries. The channel bag distribution has provided the minimum growth of the solid shell and resulted in the maximum local surface heat flux.

(e) In the channel bag melt feeding system, the sump depth is the shallowest while in the combo bag with a porosity of 0.4 the sump depth is the deepest.

In summary, it is difficult to identify which one of the three melt feeding systems will result in a cast with the most desirable metallurgical characteristics for the studied aluminum alloy.

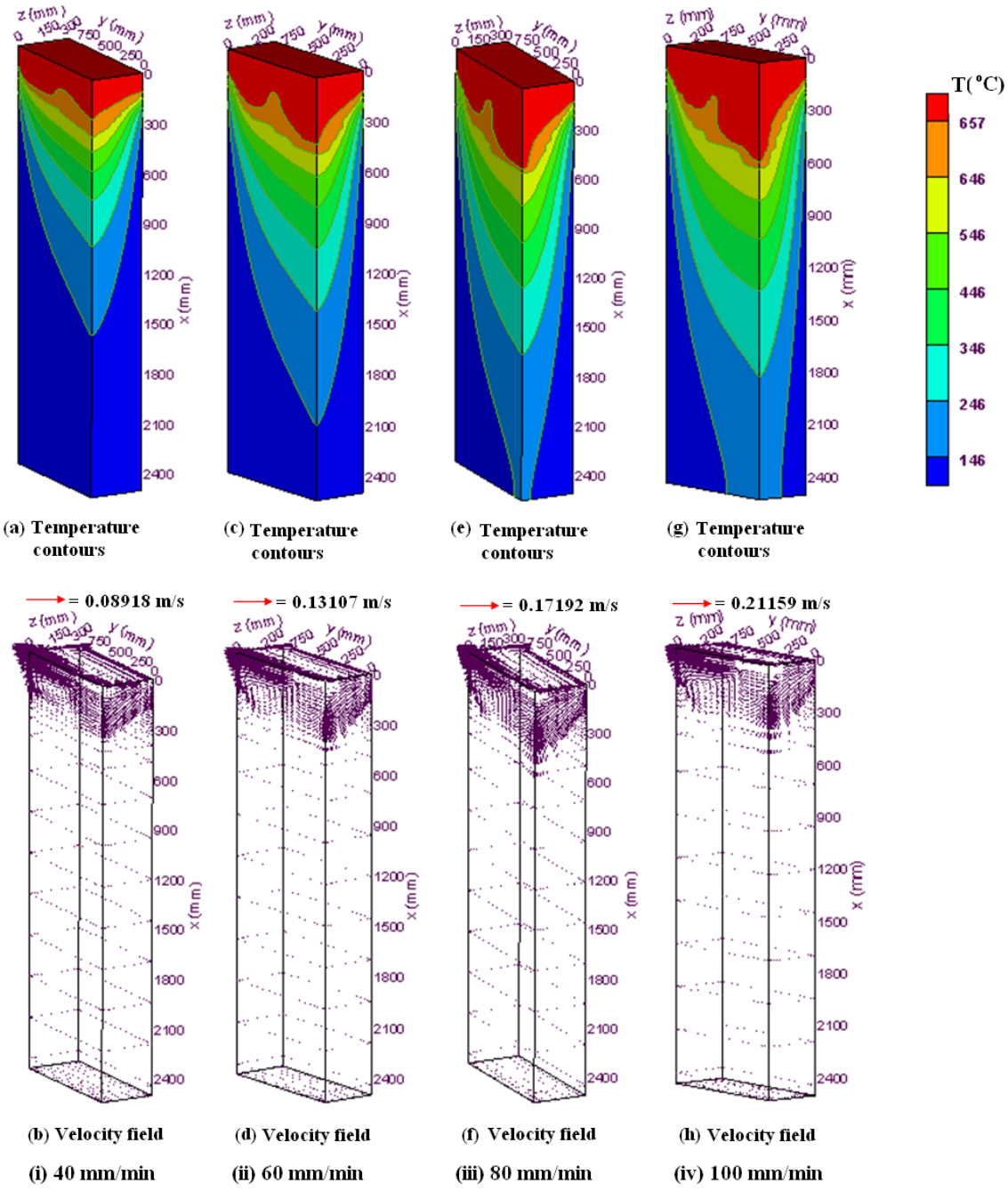

Figure 8.4: 3-D surface plots for the complete solution domain for four casting speeds and 32^0C superheat using the submerged nozzle with a distributor plate melt feeding scheme: (i) temperature contours (a) and velocity field (b) for a casting speed of 40 mm/min; (ii) temperature contours (c) and velocity field (d) for a casting speed of 60 mm/min; (iii) temperature contours (e) and velocity field (f) for a casting speed of 80 mm/min; (iv) temperature contours (g) and velocity field (h) for a casting speed of 100 mm/min.

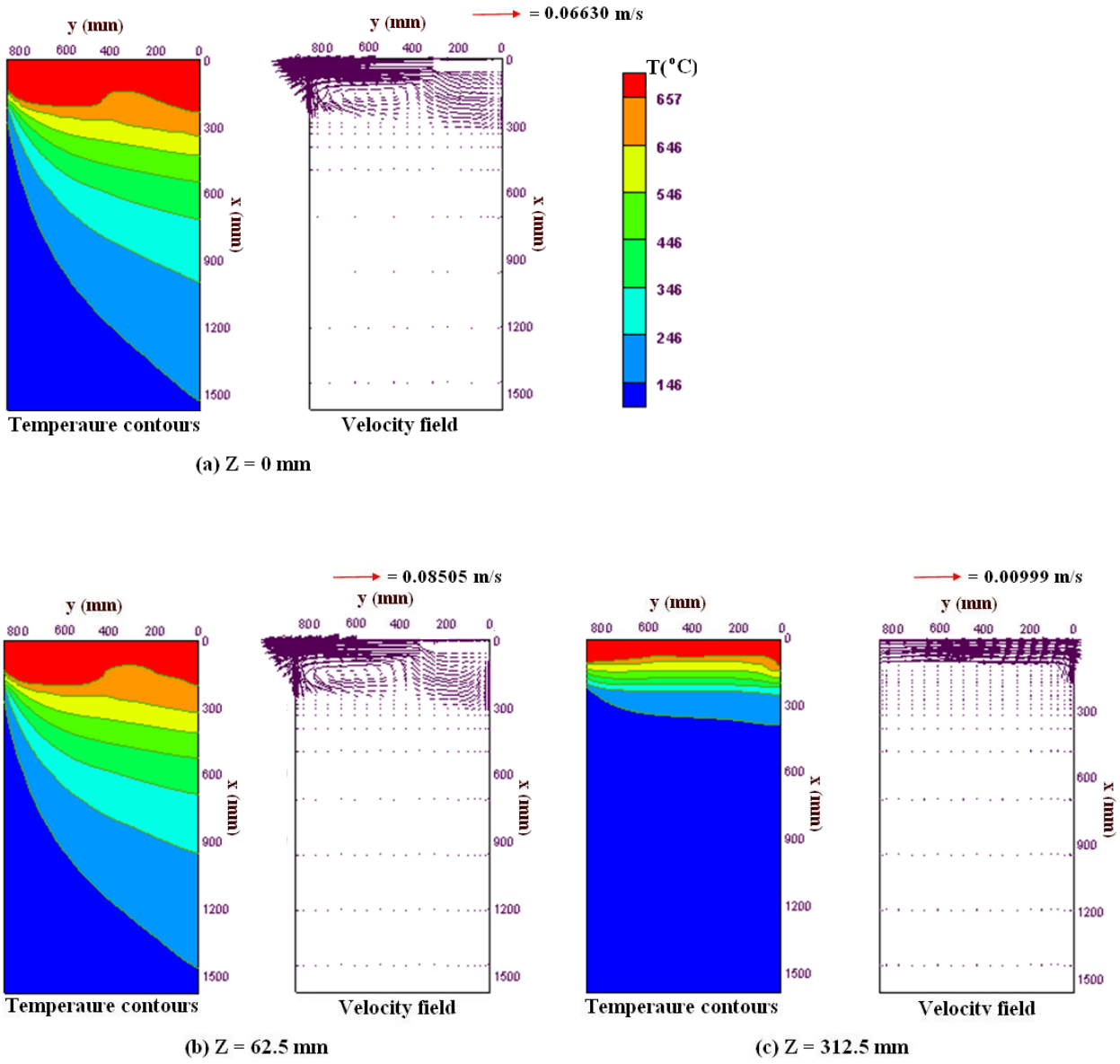

Figure 8.5: Enlarged 2-D view of temperature contours and velocity vectors of the top domain using the submerged nozzle with a distributor plate melt feeding scheme for a casting speed of 40 mm/min and 32°C superheat at: (a) wide symmetry plane at z = 0 mm, (b) vertical plane parallel to the wide face at z = 62.5 mm, (c) vertical plane parallel to the wide face at z = 312.5 mm.

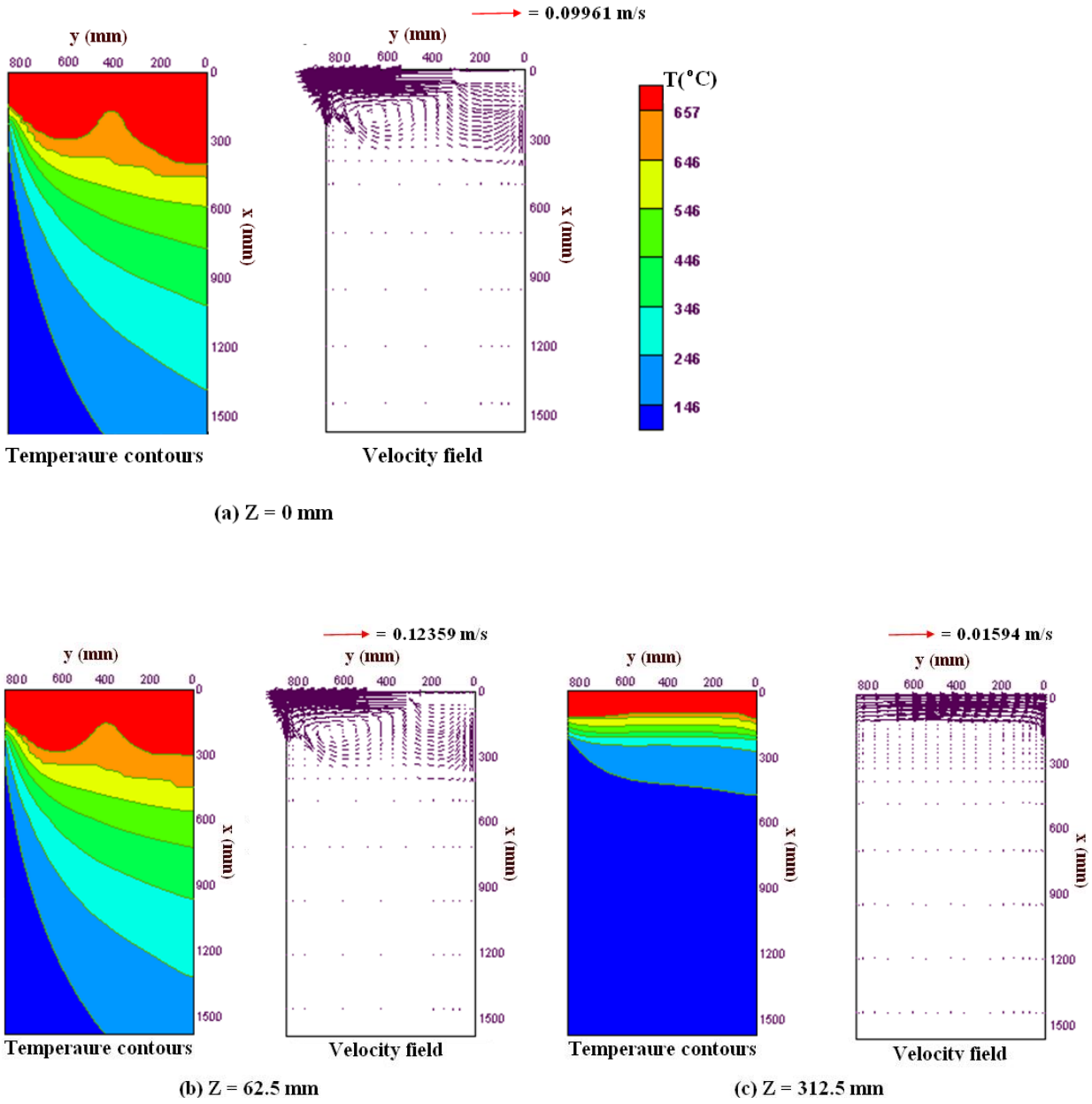

Figure 8.6: Enlarged 2-D view of temperature contours and velocity vectors of the top domain using the submerged nozzle with a distributor plate melt feeding scheme for a casting speed of 60 mm/min and 32°C superheat at: (a) wide symmetry plane at z = 0 mm, (b) vertical plane parallel to the wide face at z = 62.5 mm, (c) vertical plane parallel to the wide face at z = 312.5 mm.

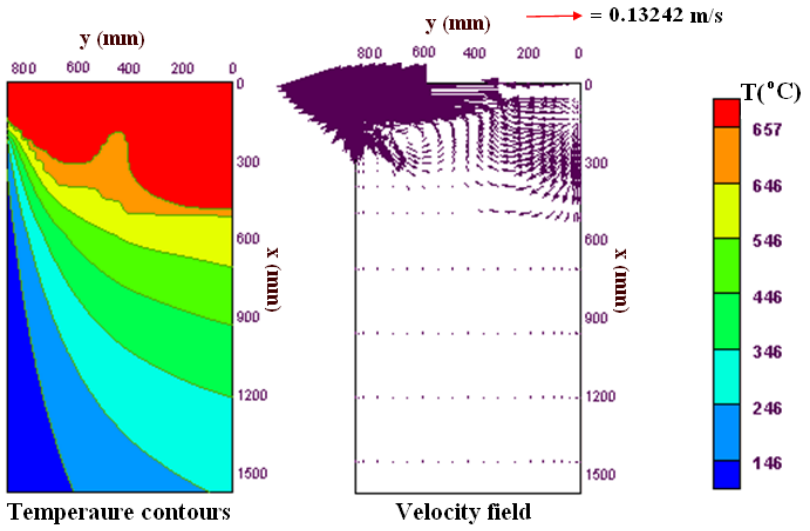

(a) Z = 0 mm

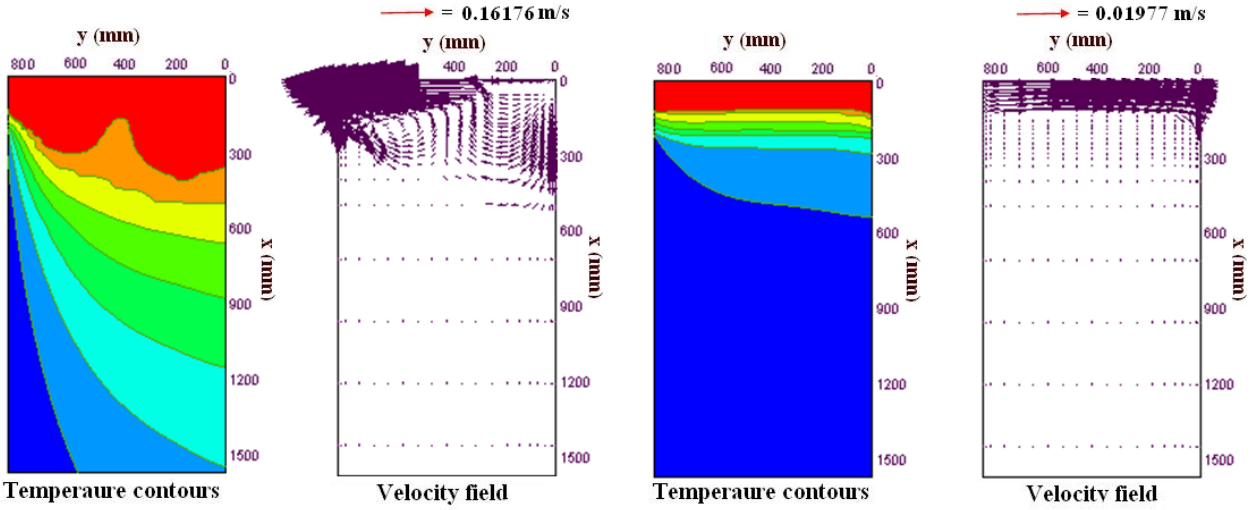

(b) Z = 62.5 mm

(c) Z = 312.5 mm

Figure 8.7: Enlarged 2-D view of temperature contours and velocity vectors of the top domain using the submerged nozzle with a distributor plate melt feeding scheme for a casting speed of 80 mm/min and 32°C superheat at: (a) wide symmetry plane at z = 0 mm, (b) vertical plane parallel to the wide face at z = 62.5 mm, (c) vertical plane parallel to the wide face at z = 312.5 mm.

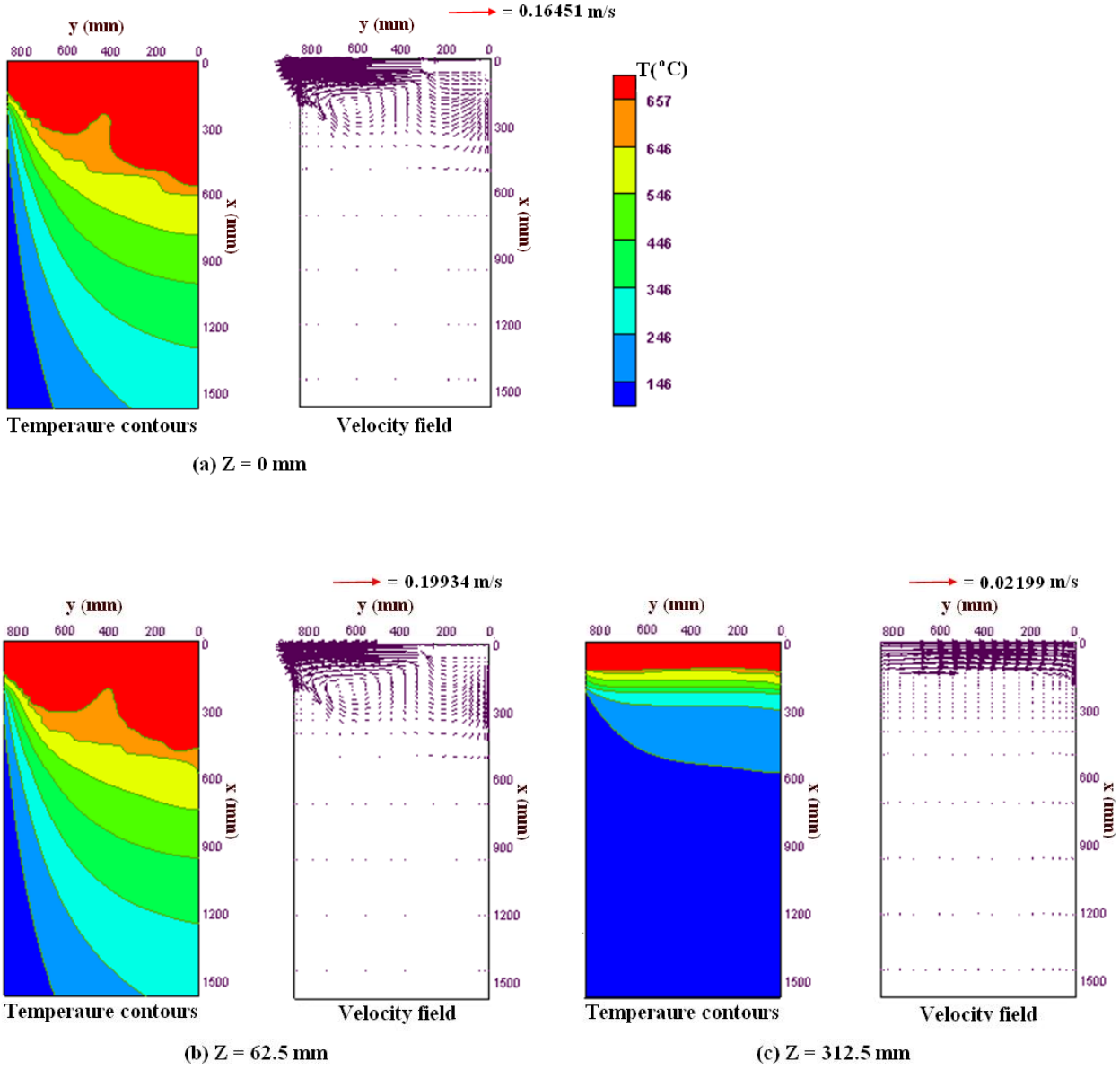

Figure 8.8: Enlarged 2-D view of temperature contours and velocity vectors of the top domain using the submerged nozzle with a distributor plate melt feeding scheme for a casting speed of 100 mm/min and 32°C superheat at: (a) wide symmetry plane at z = 0 mm, (b) vertical plane parallel to the wide face at z = 62.5 mm, (c) vertical plane parallel to the wide face at z = 312.5 mm.

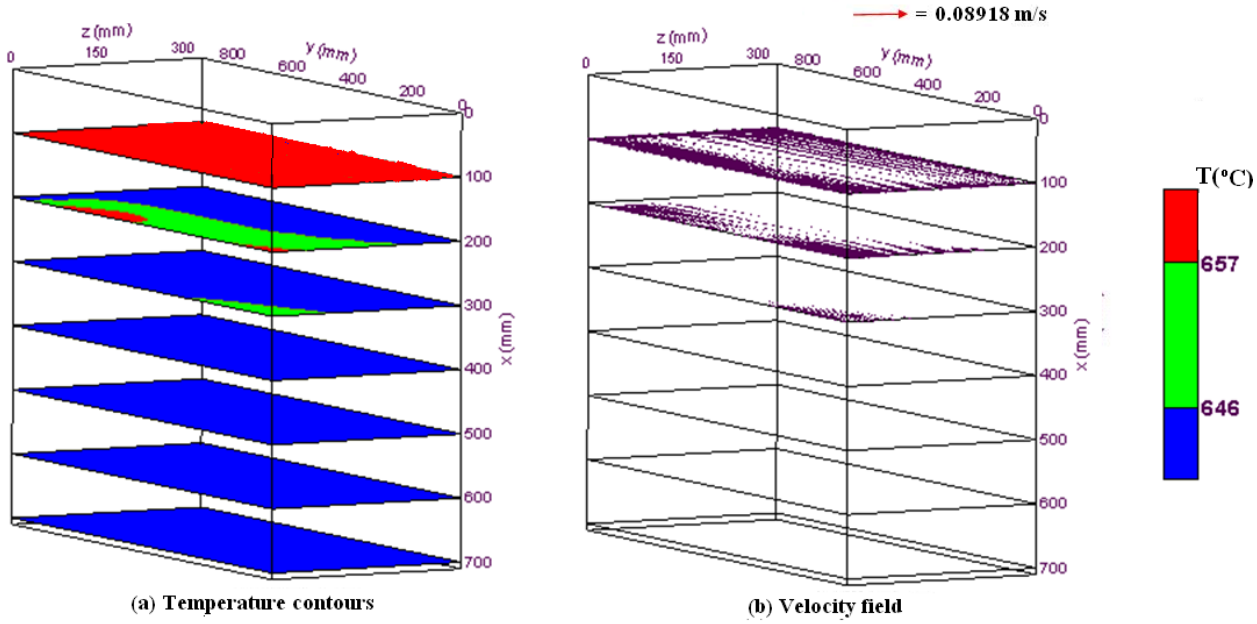

(a) Temperature contours (b) Velocity field

(i) Casting speed = 40 mm/min

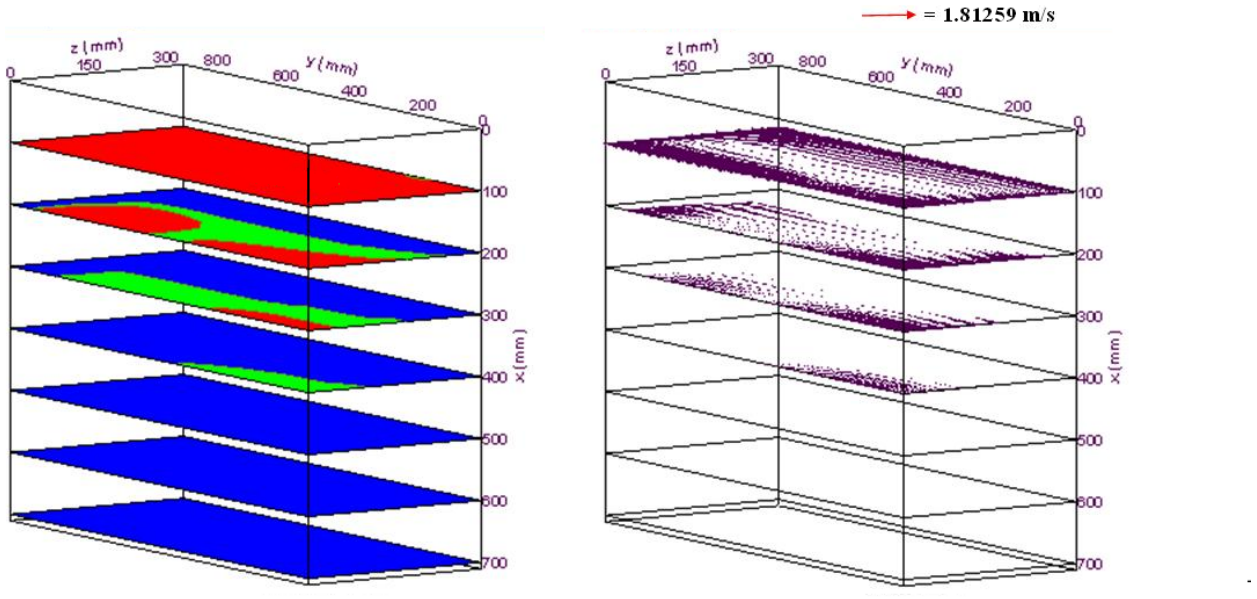

(c) Temperature contours (d) Velocity field

(ii) Casting speed = 60 mm/min

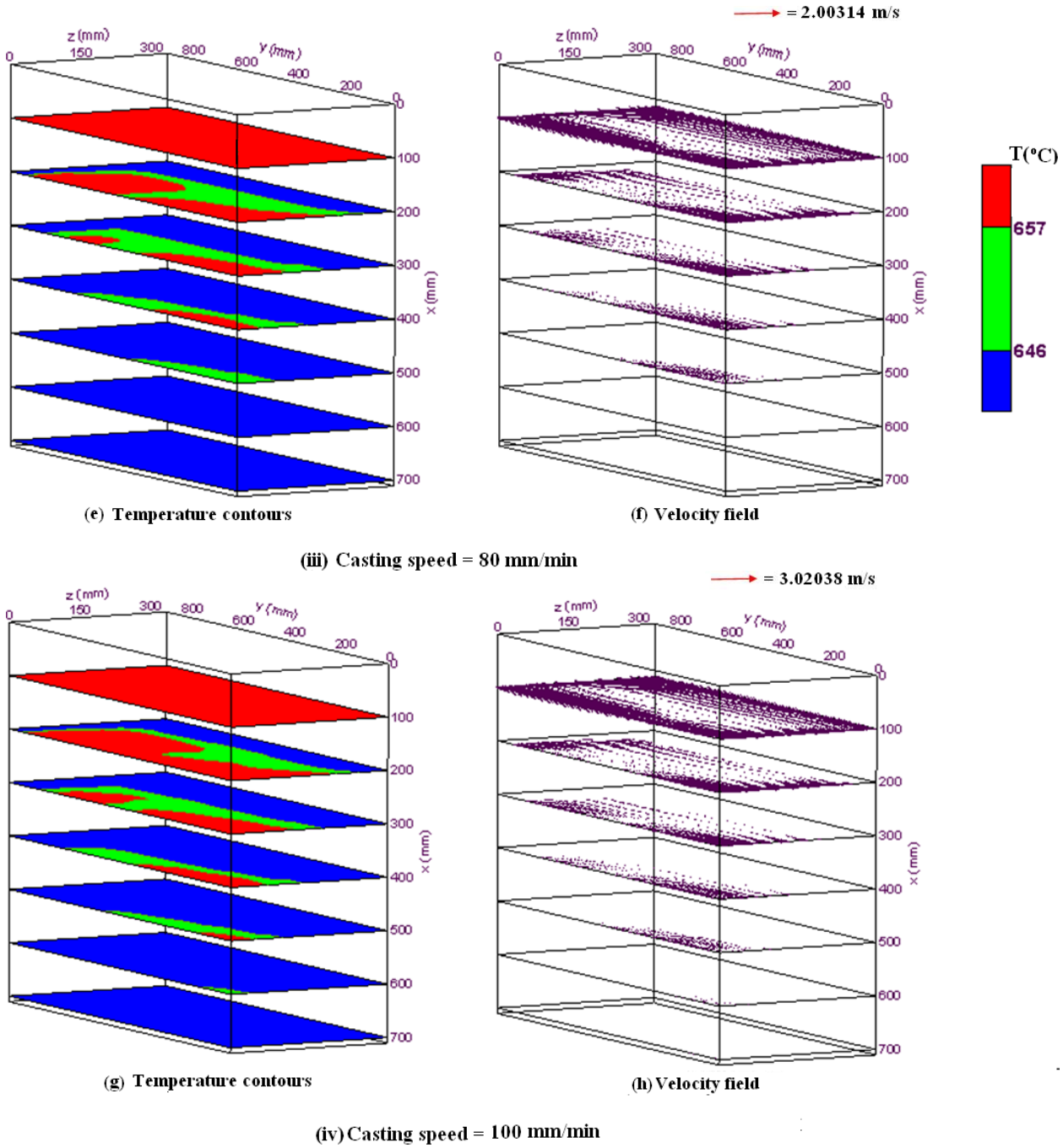

Figure 8.9: Contours of solidus and liquidus temperatures and velocity fields at various transverse cross-sectional planes (y-z planes) of the top part of the ingot using the submerged nozzle with a distributor plate melt feeding scheme for a superheat of 32°C and casting speeds of: (i) 40 mm min^{-1} (ii) 60 mm min^{-1} (iii) 80 mm min^{-1} (iv) 100 mm min^{-1}.

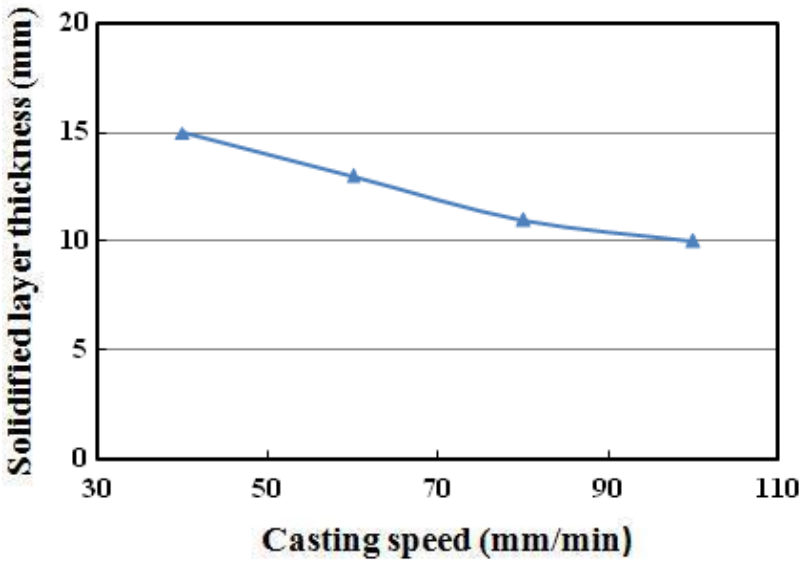

Figure 8.10: Solid shell thickness from the narrow slab face at an axial distance of x = 160 mm from the top free surface at the wide symmetry plane versus casting speed at an inlet superheat of 32°C using the submerged nozzle with a distributor plate melt feeding scheme.

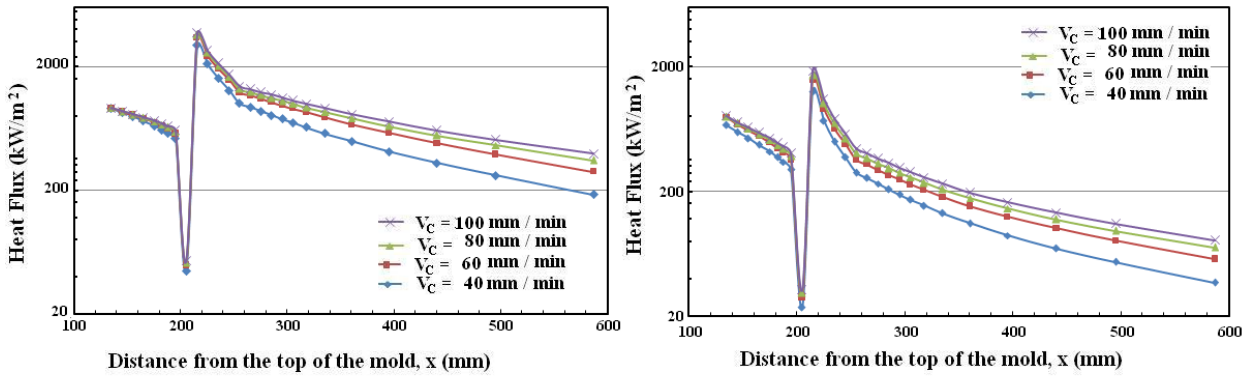

Figure 8.11: Variations of local surface heat fluxes for various casting speeds during solidification at 32°C superheat along the axial direction of the strand wall at: (a) z = 185 mm (b) y = 857.5 mm, using the submerged nozzle with a distributor plate melt feeding scheme

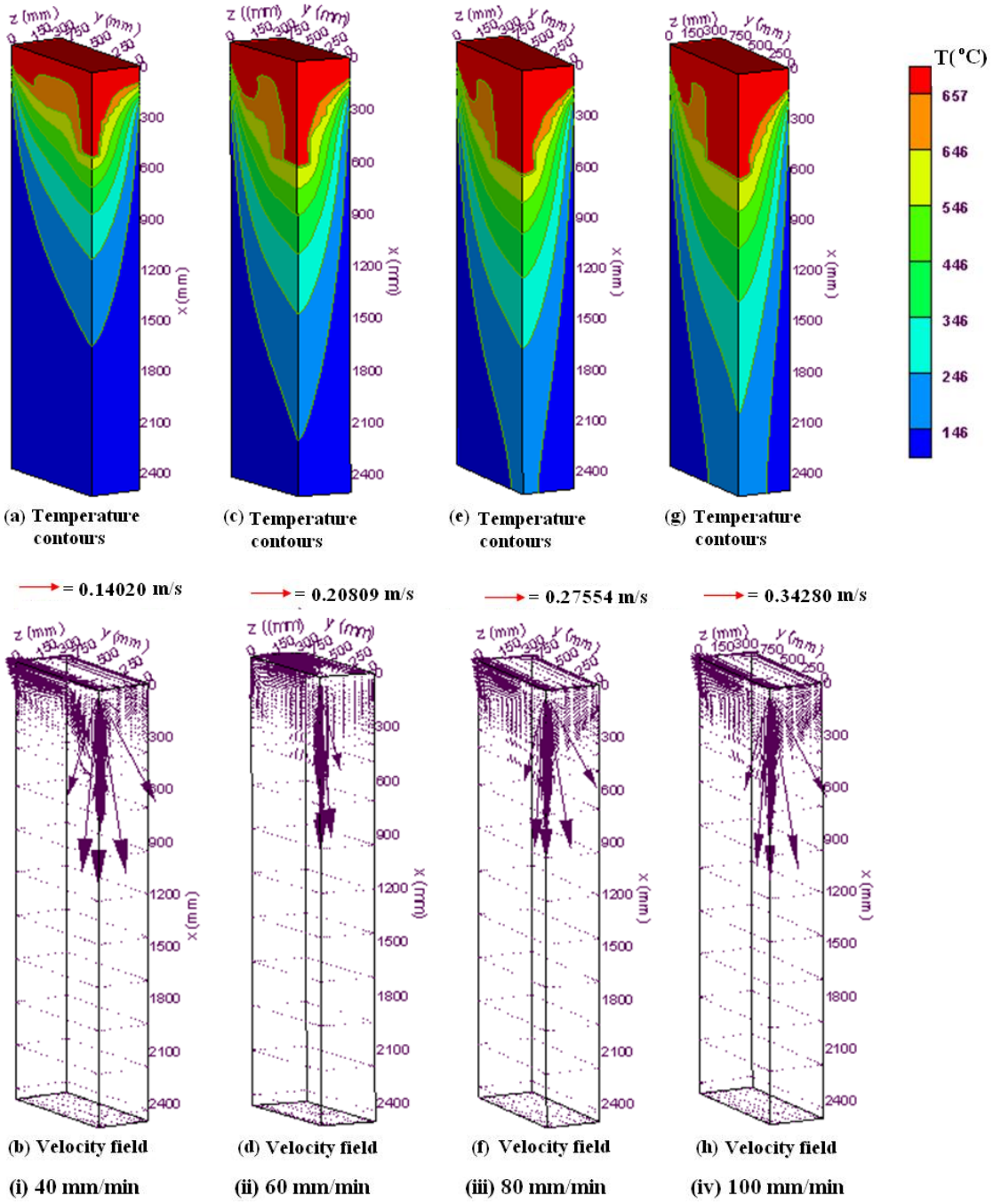

Figure 8.12: 3-D surface plots for the complete solution domain for four casting speeds and 32^0C superheat using the submerged nozzle with a porous bottom plate distributor bag melt feeding scheme for porosity, $\phi = 0.4$ and Darcy value 0f 1.0 x 10^{-4}: (i) temperature contours (a) and velocity field (b) for a casting speed of 40 mm/min; (ii) temperature contours (c) and velocity field (d) for a casting speed of 60 mm/min; (iii) temperature contours (e) and velocity field (f) for a casting speed of 80 mm/min; (iv) temperature contours (g) and velocity field (h) for a casting speed of 100 mm/min.

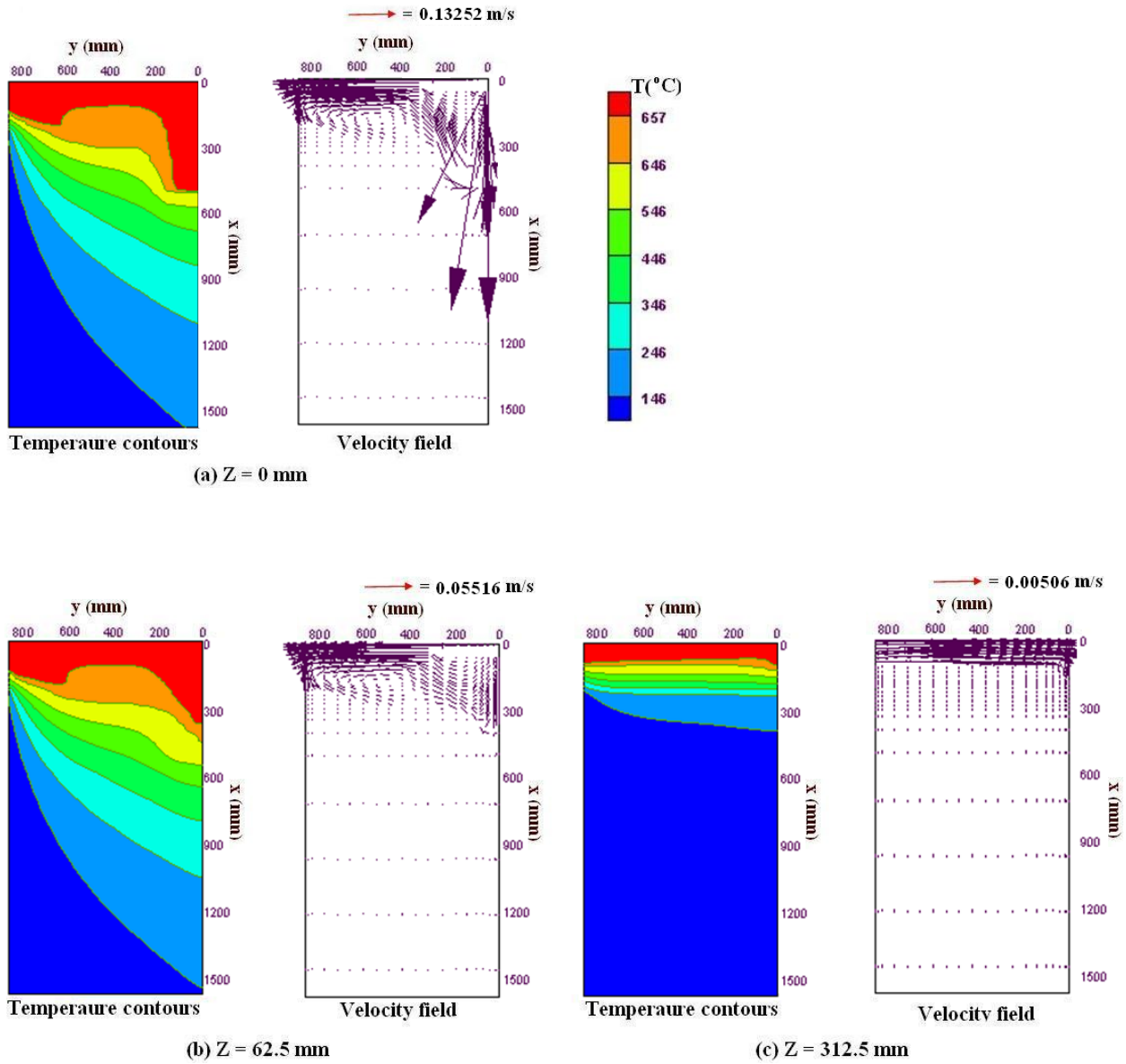

Figure 8.13: Enlarged 2-D view of temperature contours and velocity vectors of the top domain using the submerged nozzle with a porous bottom plate distributor bag melt feeding scheme at porosity, $\phi = 0.4$ and Darcy value 0f 1.0 x 10^{-4} for a casting speed of 40 mm/min and 32°C superheat at: (a) wide symmetry plane at z = 0 mm, (b) vertical plane parallel to the wide face at z = 62.5 mm, (c) vertical plane parallel to the wide face at z = 312.5 mm.

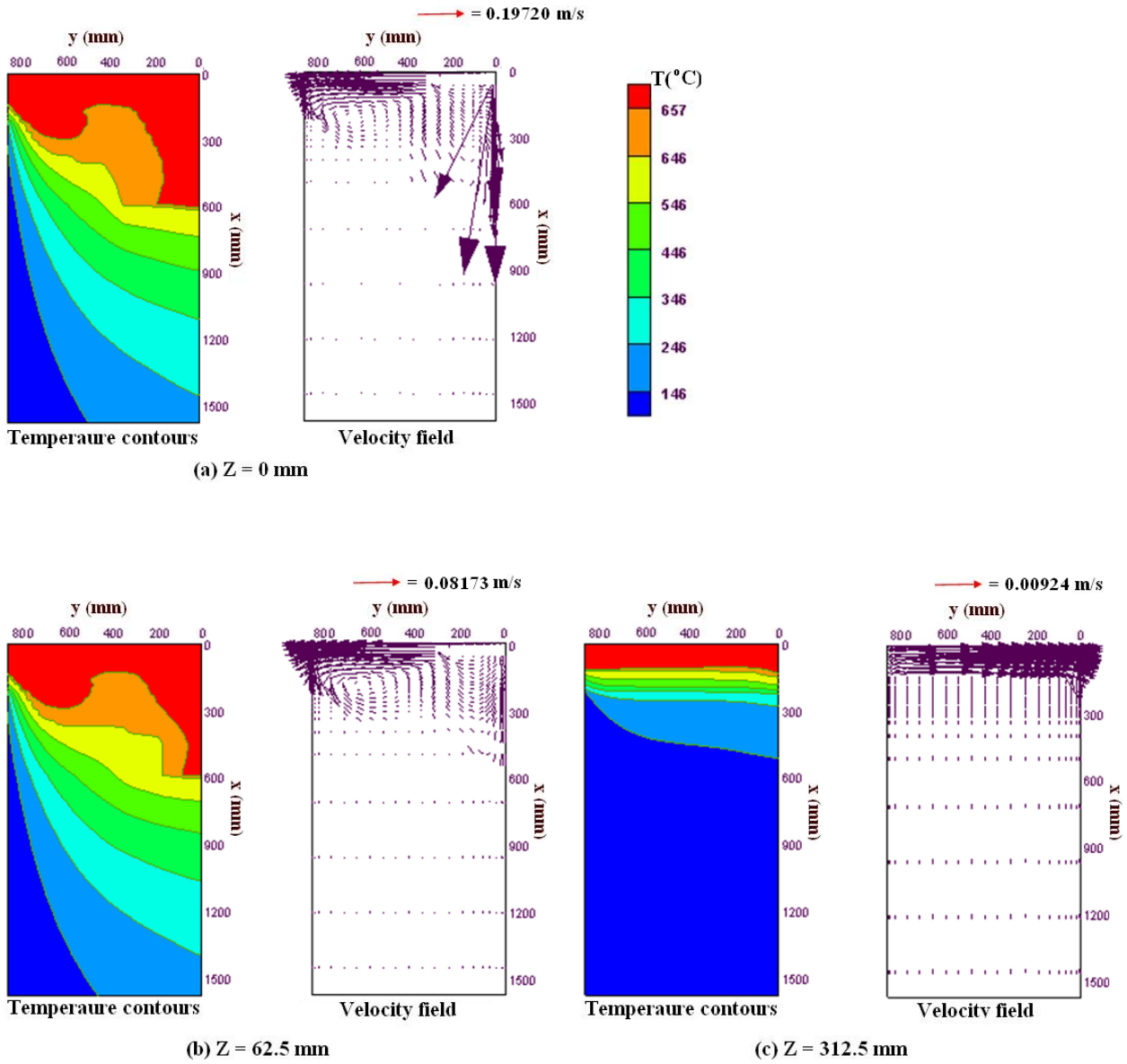

Figure 8.14: Enlarged 2-D view of temperature contours and velocity vectors of the top domain using the submerged nozzle with a porous bottom plate distributor bag melt feeding scheme at porosity, ϕ = 0.4 and Darcy value 0f 1.0 x 10^{-4} for a casting speed of 60 mm/min and 32°C superheat at: (a) wide symmetry plane at z = 0 mm, (b) vertical plane parallel to the wide face at z = 62.5 mm, (c) vertical plane parallel to the wide face at z = 312.5 mm.

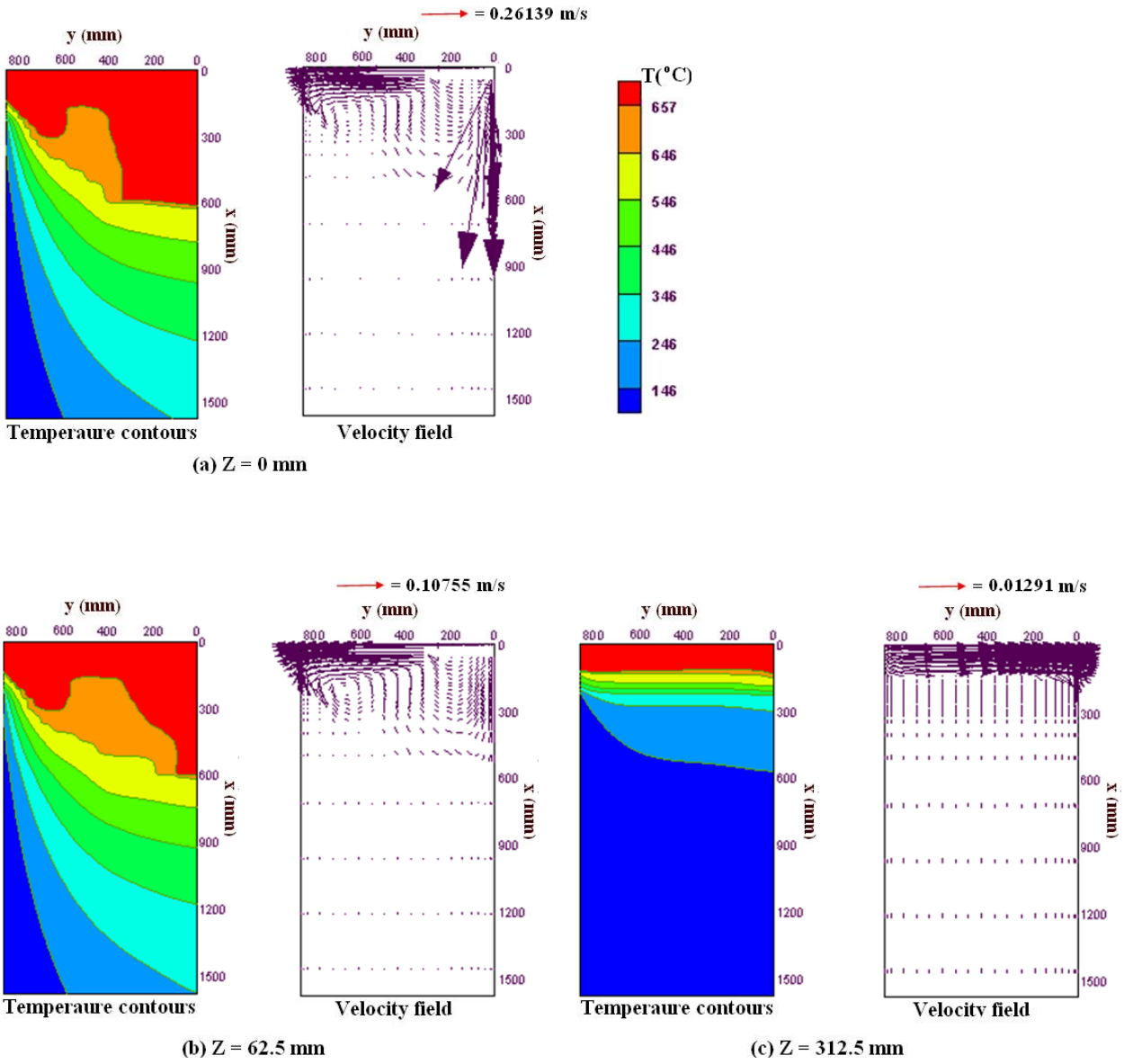

Figure 8.15: Enlarged 2-D view of temperature contours and velocity vectors of the top domain using the submerged nozzle with a porous bottom plate distributor bag melt feeding scheme at porosity, $\phi = 0.4$ and Darcy value 0f 1.0×10^{-4} for a casting speed of 80 mm/min and 32°C superheat at: (a) wide symmetry plane at z = 0 mm, (b) vertical plane parallel to the wide face at z = 62.5 mm, (c) vertical plane parallel to the wide face at z = 312.5 mm.

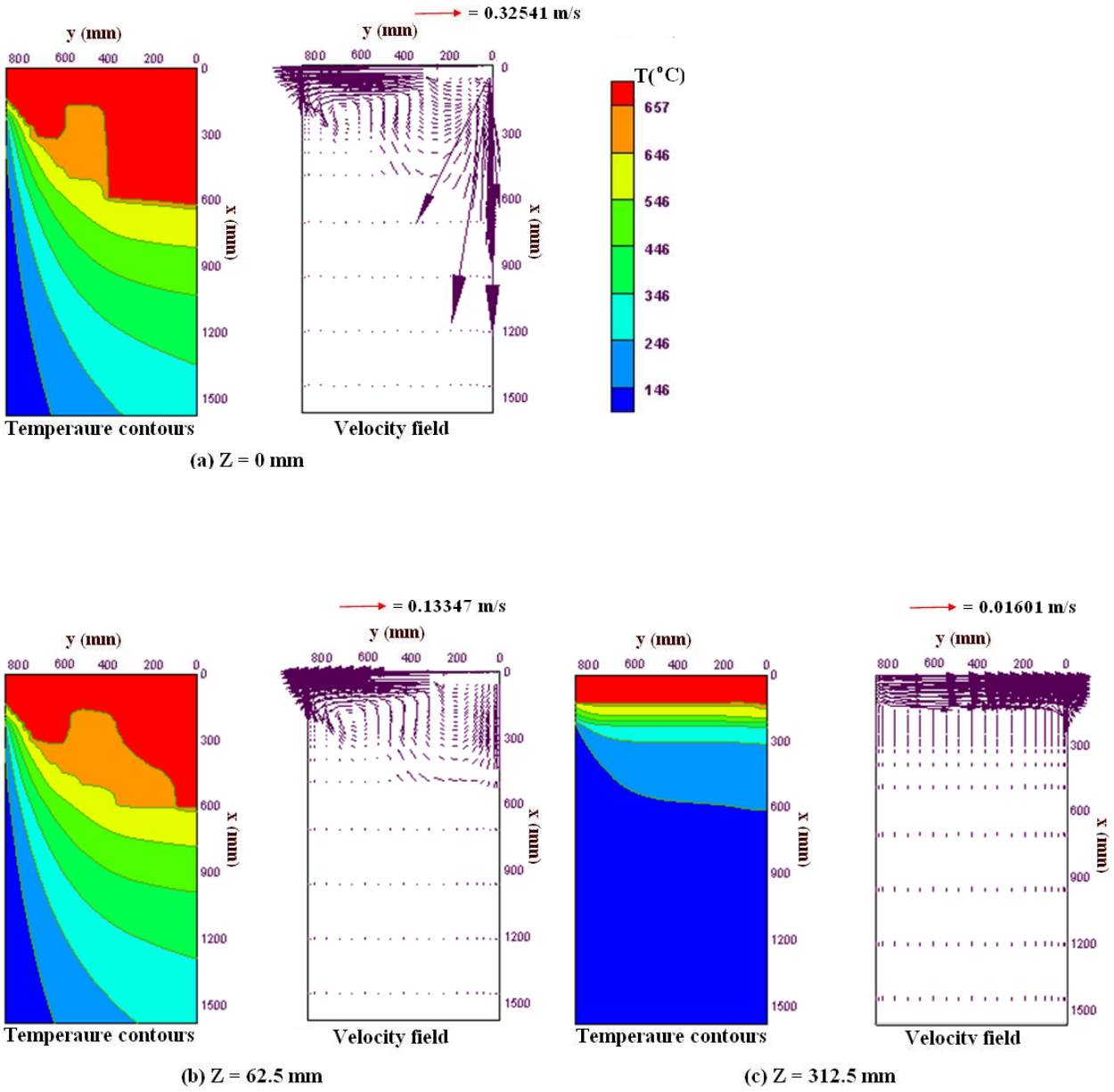

Figure 8.16: Enlarged 2-D view of temperature contours and velocity vectors of the top domain using the submerged nozzle with a porous bottom plate distributor bag melt feeding scheme at porosity, $\phi = 0.4$ and Darcy value 0f 1.0 x 10^{-4} for a casting speed of 100 mm/min and 32°C superheat at: (a) wide symmetry plane at z = 0 mm, (b) vertical plane parallel to the wide face at z = 62.5 mm, (c) vertical plane parallel to the wide face at z = 312.5 mm.

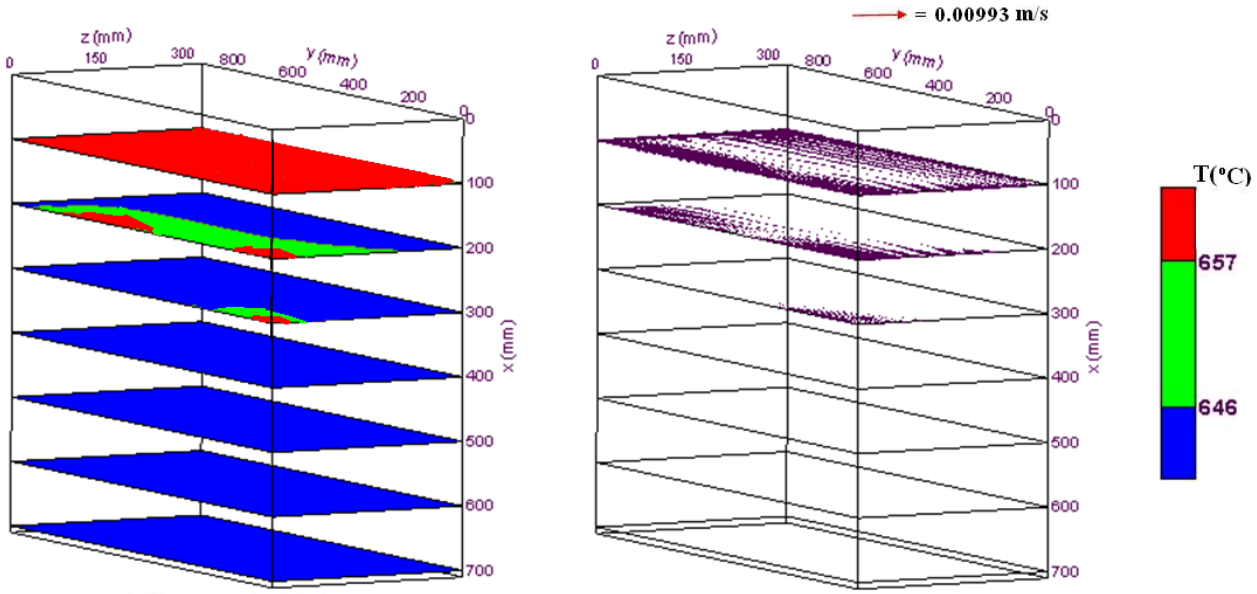

(a) Temperature contours (b) Velocity field

(i) Casting speed = 40 mm/min

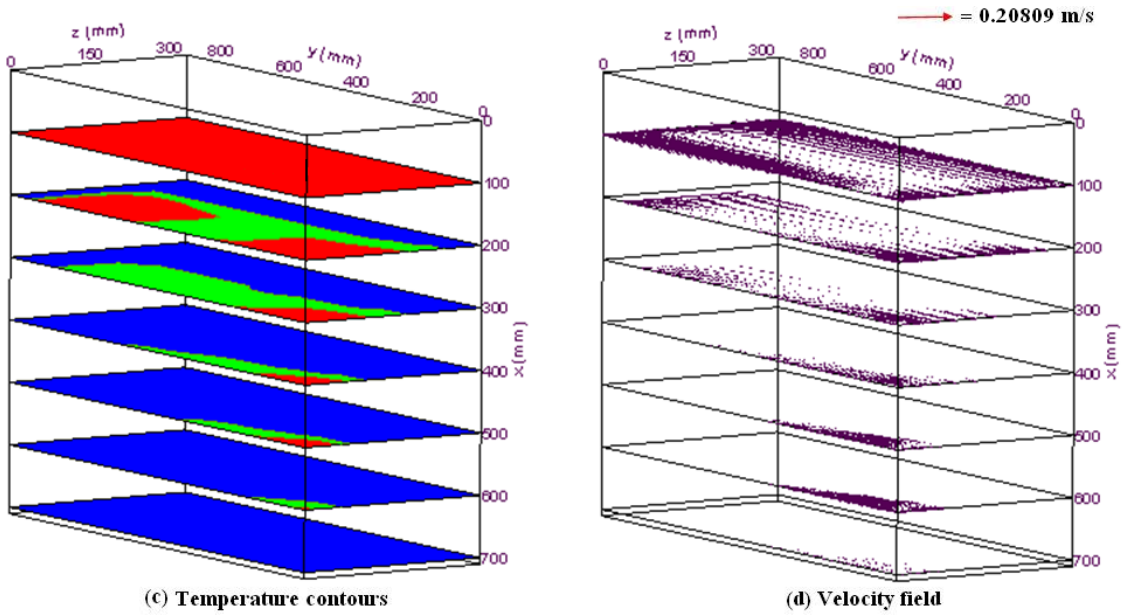

(c) Temperature contours (d) Velocity field

(ii) Casting speed = 60 mm/min

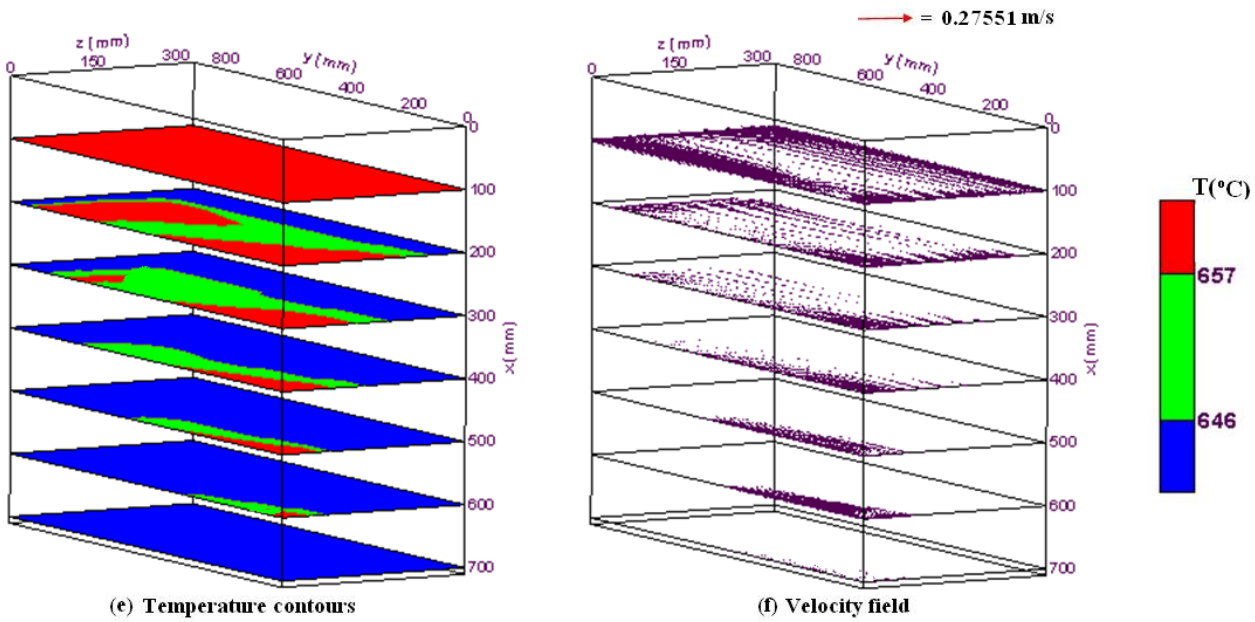

(e) Temperature contours (f) Velocity field

(iii) Casting speed = 80 mm/min

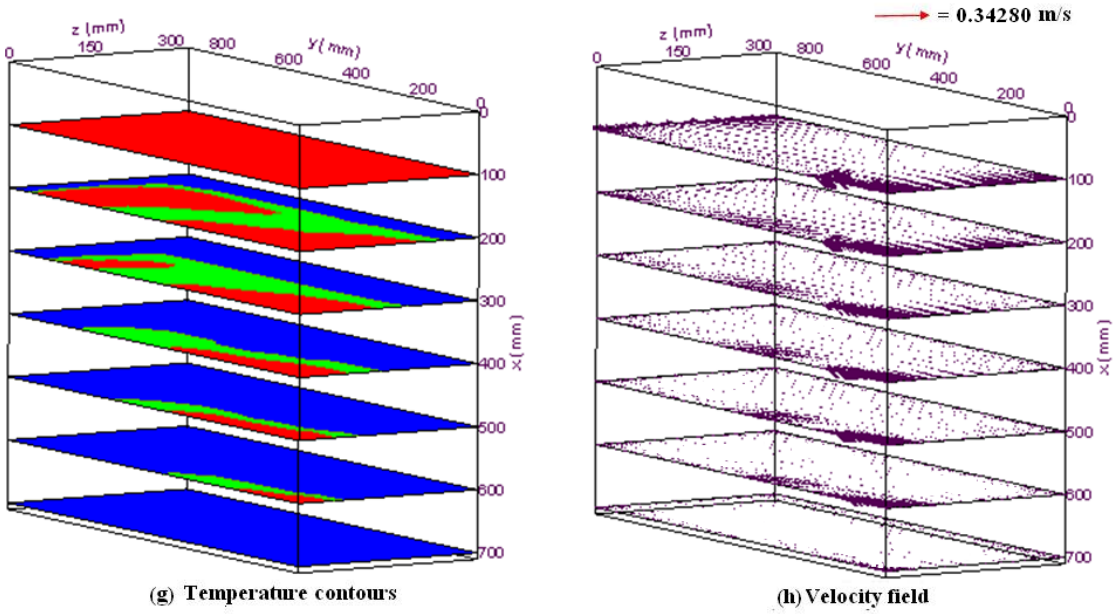

(g) Temperature contours (h) Velocity field

(iv) Casting speed = 100 mm/min

Figure 8.17: Contours of solidus and liquidus temperatures and velocity fields at various transverse cross-sectional planes (y-z planes) of the top part of the ingot using the submerged nozzle with a porous bottom plate distributor bag melt feeding scheme at porosity, $\phi = 0.4$ and a Darcy value 0f 1.0 x 10^{-4} for a superheat of 32°C and casting speeds of: (i) 40 mm min^{-1} (ii) 60 mm min^{-1} (iii) 80 mm min^{-1} (iv) 100 mm min^{-1}.

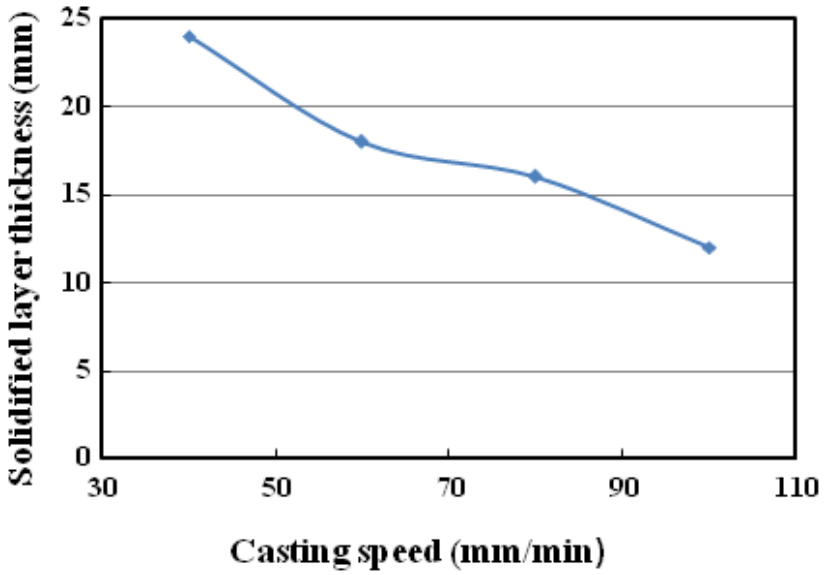

Figure 8.18: Solid shell thickness from the narrow slab face at an axial distance of x = 160 mm from the top free surface at the wide symmetry plane versus casting speed at an inlet superheat of 32°C using the submerged nozzle with a porous bottom plate distributor bag melt feeding scheme at porosity, $\phi = 0.4$ and Darcy value 0f 1.0 x 10^{-4}.

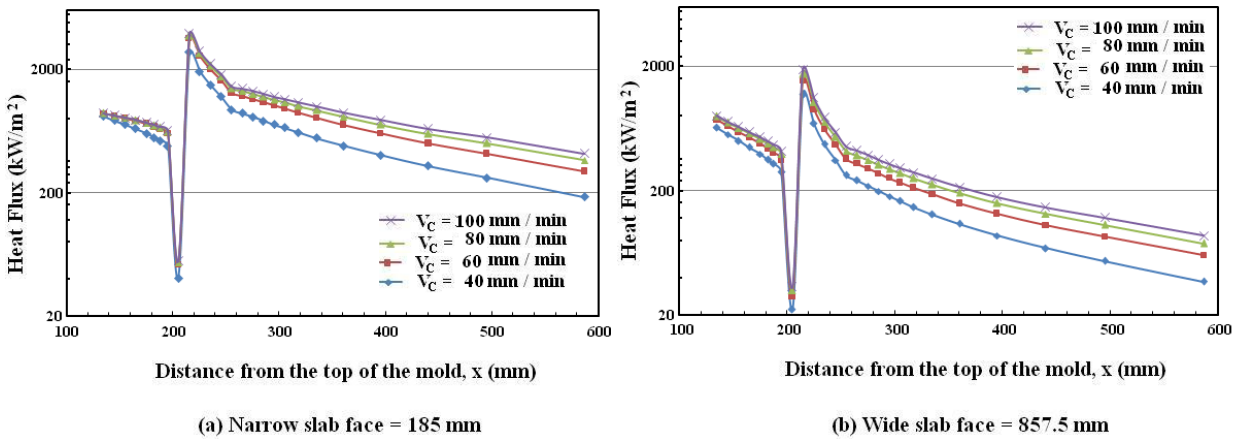

Figure 8.19: Variations of local surface heat fluxes with various casting speeds during solidification at 32°C superheat along the axial direction of the strand wall at: (a) z = 185 mm (b) y = 857.5 mm, using the submerged nozzle with a porous bottom plate distributor bag melt feeding scheme at porosity, $\phi = 0.4$ and Darcy value 0f 1.0 x 10^{-4}.

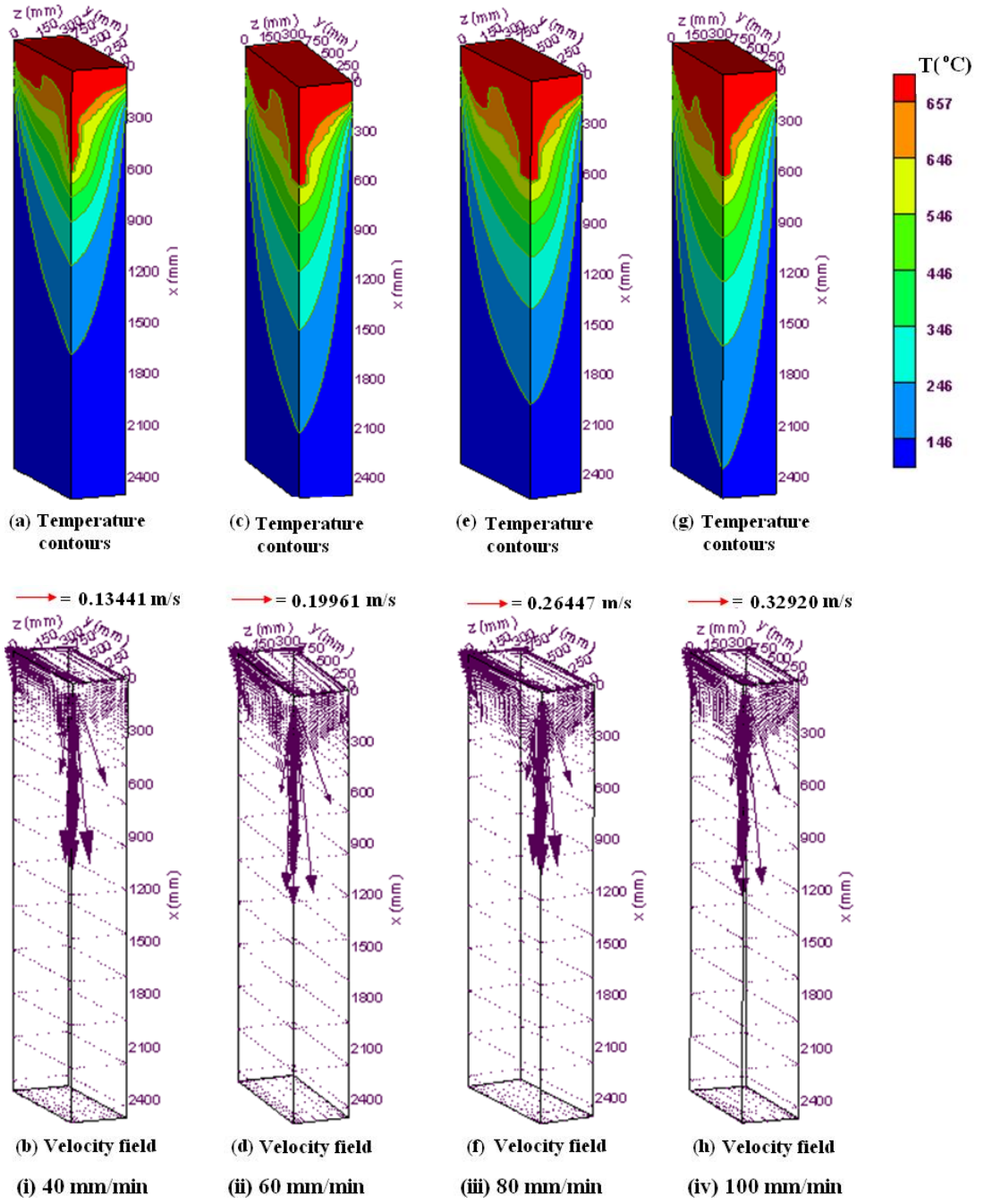

Figure 8.20: 3-D surface plots for the complete solution domain for four casting speeds and 32^0C superheat using the submerged nozzle with a porous bottom plate distributor bag melt feeding scheme for porosity, $\phi = 0.9$ and Darcy value 0f 1.0×10^{-4}: (i) temperature contours (a) and velocity field (b) for a casting speed of 40 mm/min; (ii) temperature contours (c) and velocity field (d) for a casting speed of 60 mm/min; (iii) temperature contours (e) and velocity field (f) for a casting speed of 80 mm/min; (iv) temperature contours (g) and velocity field (h) for a casting speed of 100 mm/min.

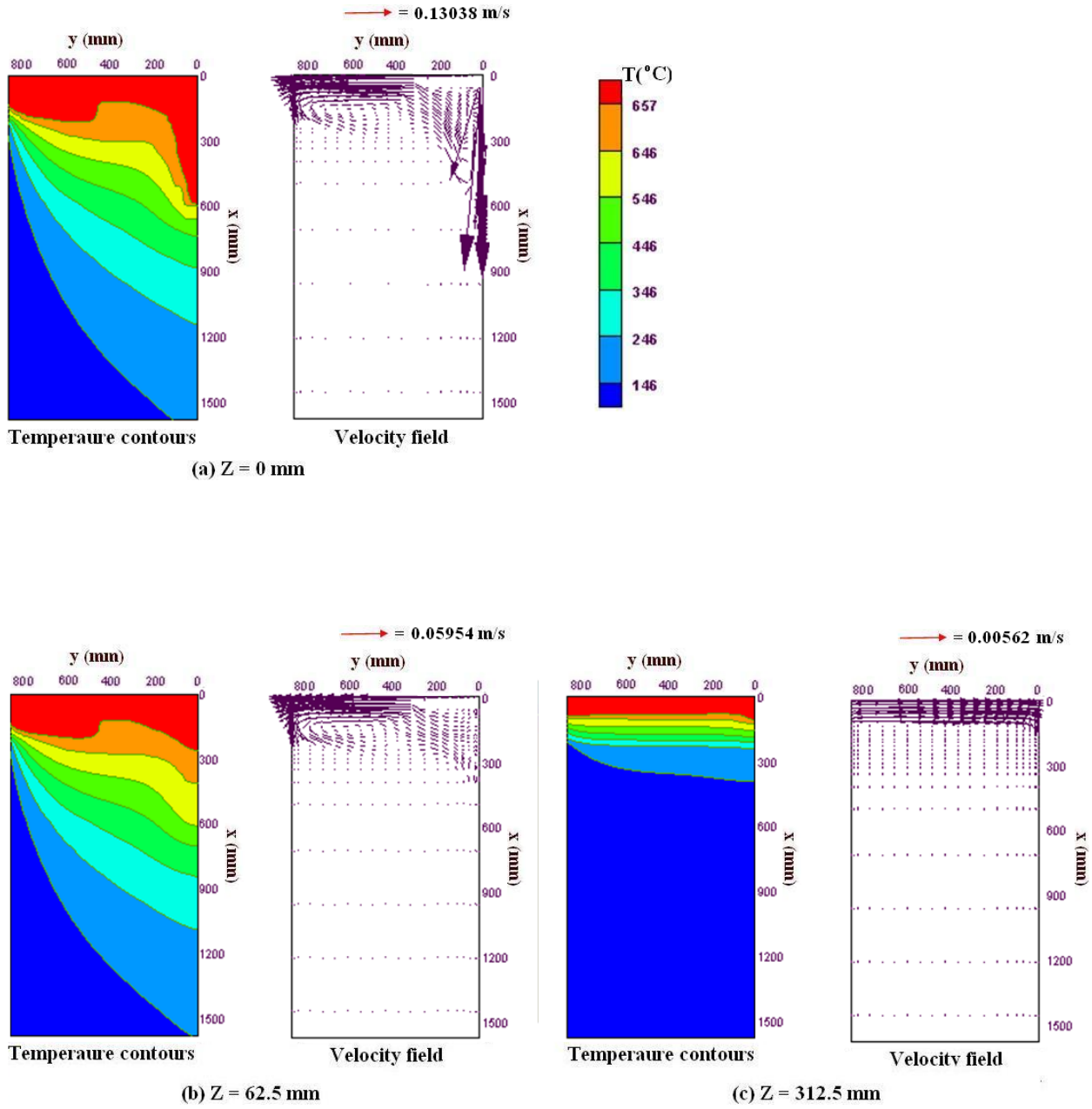

Figure 8.21: Enlarged 2-D view of temperature contours and velocity vectors of the top domain using the submerged nozzle with a porous bottom plate distributor bag melt feeding scheme at porosity, ϕ = 0.9 and Darcy value 0f 1.0 x 10^{-4} for a casting speed of 40 mm/min and 32°C superheat at: (a) wide symmetry plane at z = 0 mm, (b) vertical plane parallel to the wide face at z = 62.5 mm, (c) vertical plane parallel to the wide face at z = 312.5 mm.

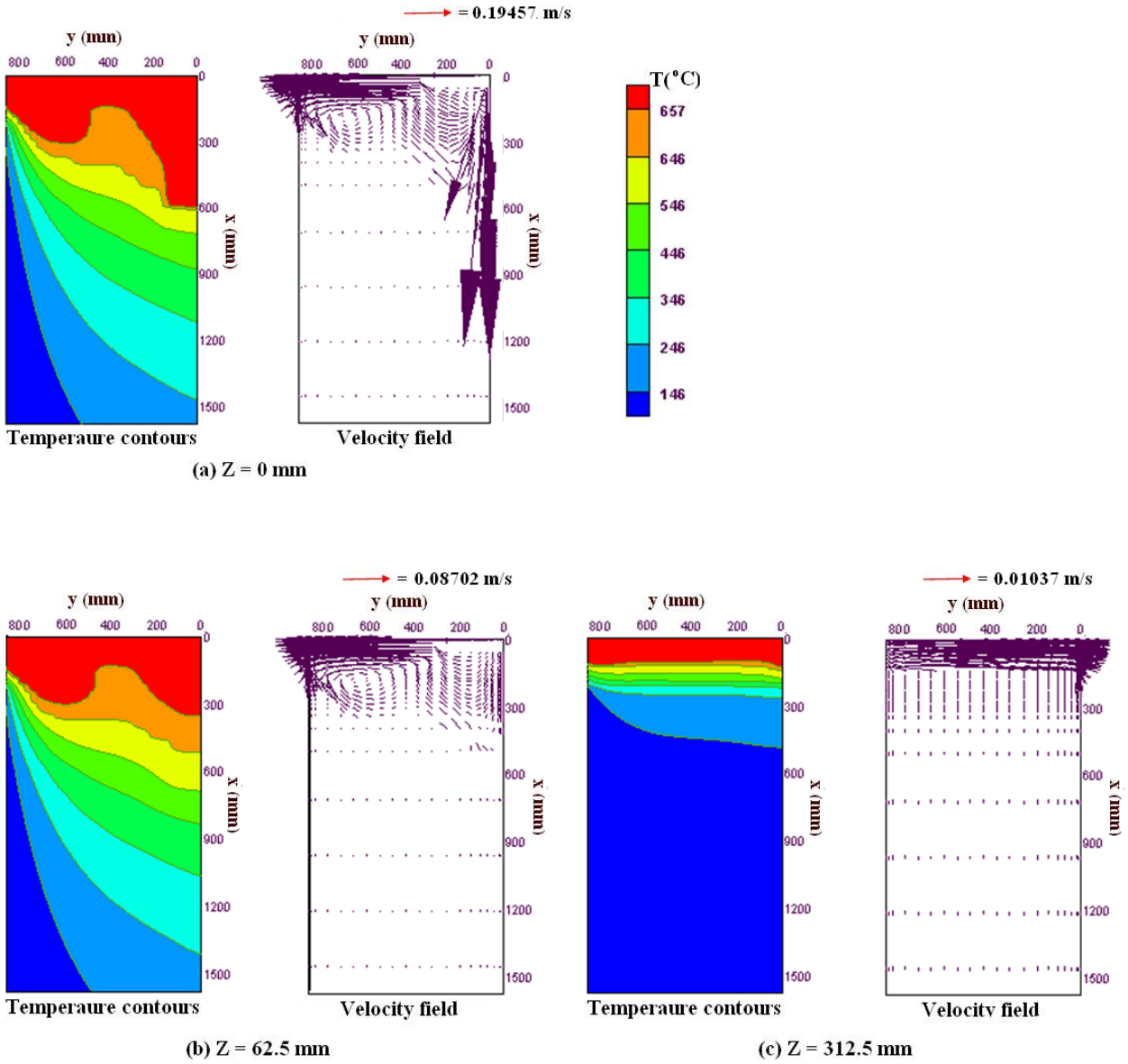

Figure 8.22: Enlarged 2-D view of temperature contours and velocity vectors of the top domain using the submerged nozzle with a porous bottom plate distributor bag melt feeding scheme at porosity, ϕ = 0.9 and Darcy value 0f 1.0 x 10^{-4} for a casting speed of 60 mm/min and 32°C superheat at: (a) wide symmetry plane at z = 0 mm, (b) vertical plane parallel to the wide face at z = 62.5 mm, (c) vertical plane parallel to the wide face at z = 312.5 mm.

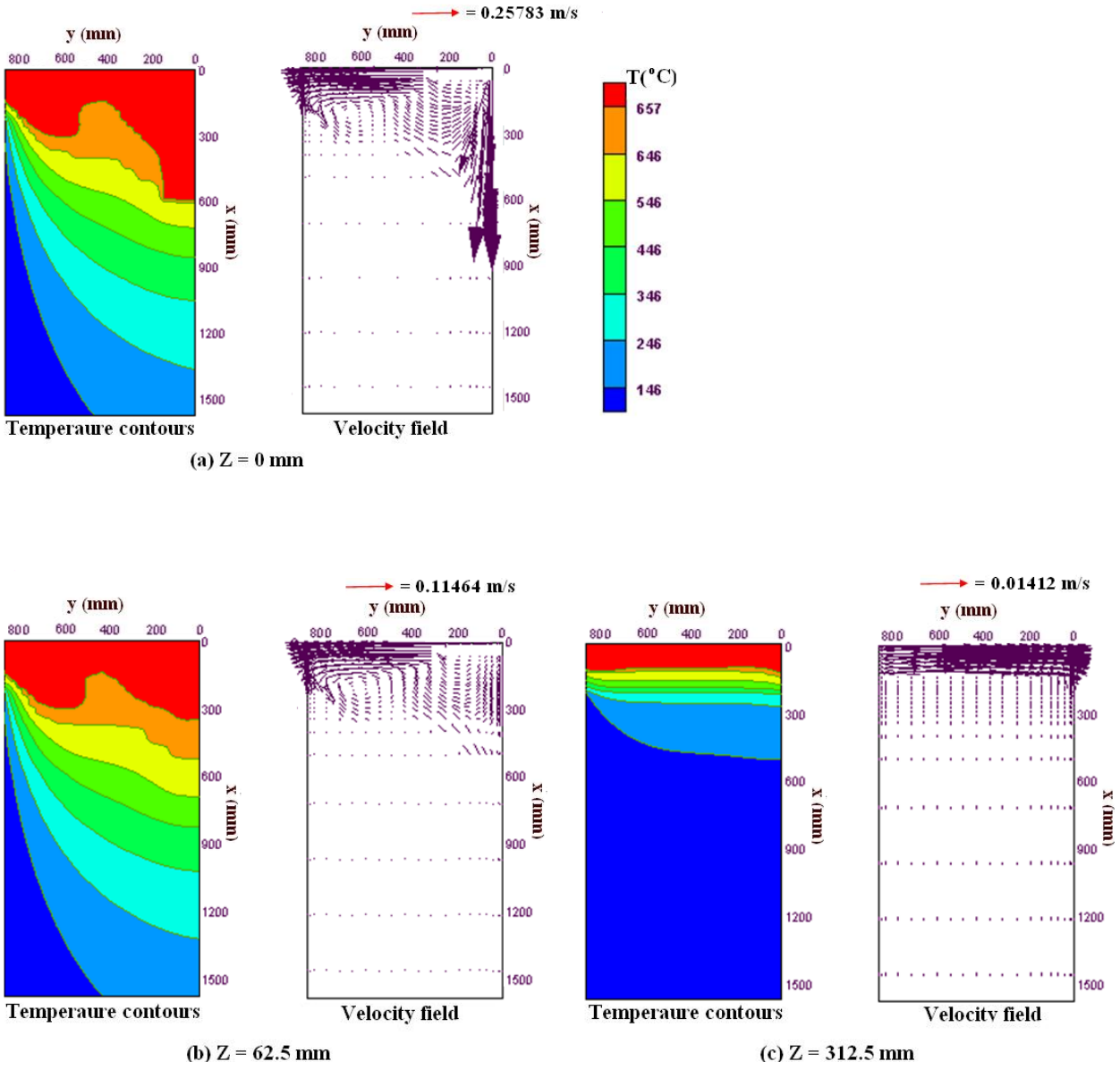

Figure 8.23: Enlarged 2-D view of temperature contours and velocity vectors of the top domain using the submerged nozzle with a porous bottom plate distributor bag melt feeding scheme at porosity, $\phi = 0.9$ and Darcy value 0f 1.0 x 10^{-4} for a casting speed of 80 mm/min and 32°C superheat at: (a) wide symmetry plane at z = 0 mm, (b) vertical plane parallel to the wide face at z = 62.5 mm, (c) vertical plane parallel to the wide face at z = 312.5 mm.

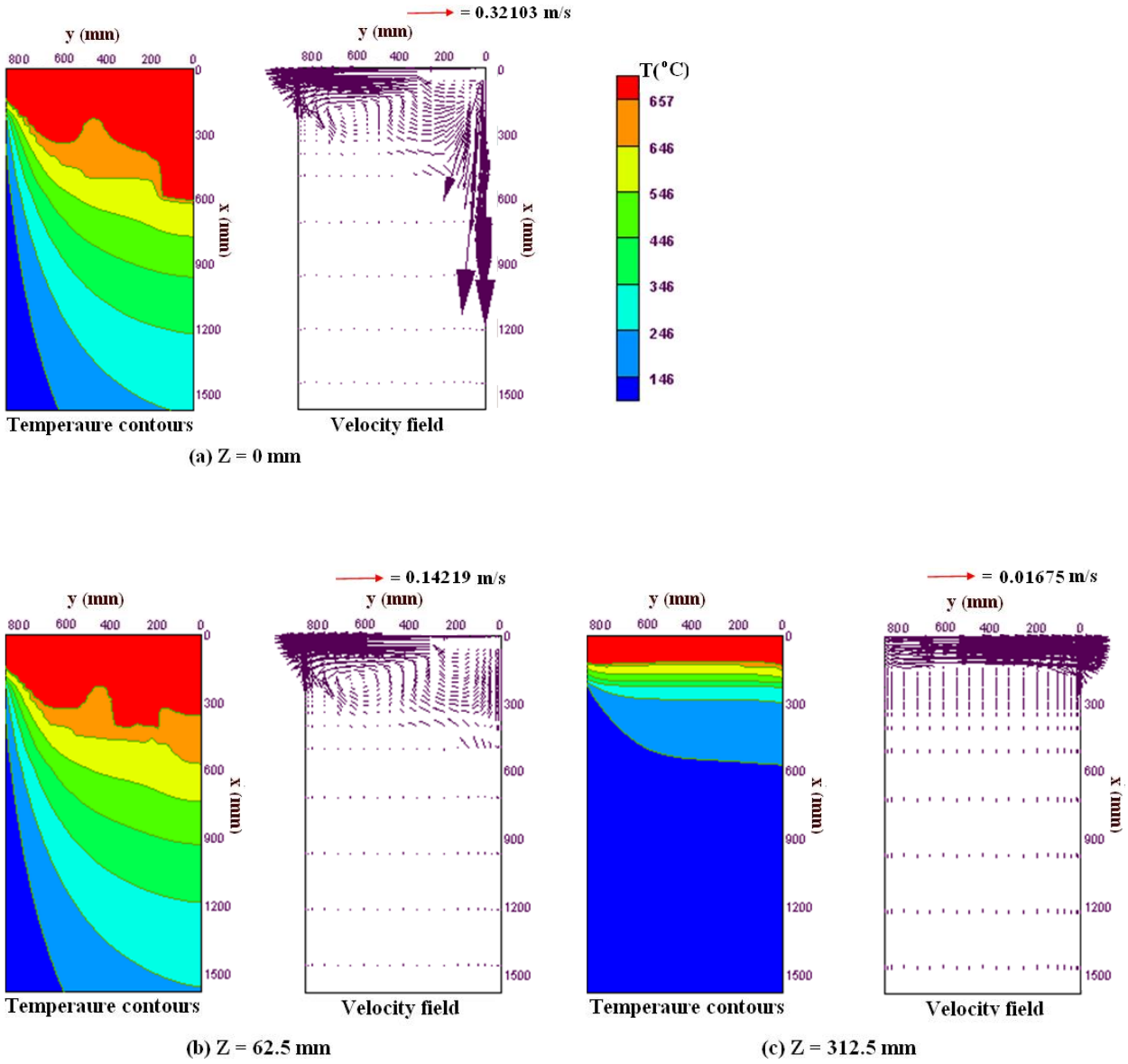

Figure 8.24: Enlarged 2-D view of temperature contours and velocity vectors of the top domain using the submerged nozzle with a porous bottom plate distributor bag melt feeding scheme at porosity, $\phi = 0.9$ and Darcy value 0f 1.0 x 10^{-4} for a casting speed of 100 mm/min and 32°C superheat at: (a) wide symmetry plane at z = 0 mm, (b) vertical plane parallel to the wide face at z = 62.5 mm, (c) vertical plane parallel to the wide face at z = 312.5 mm.

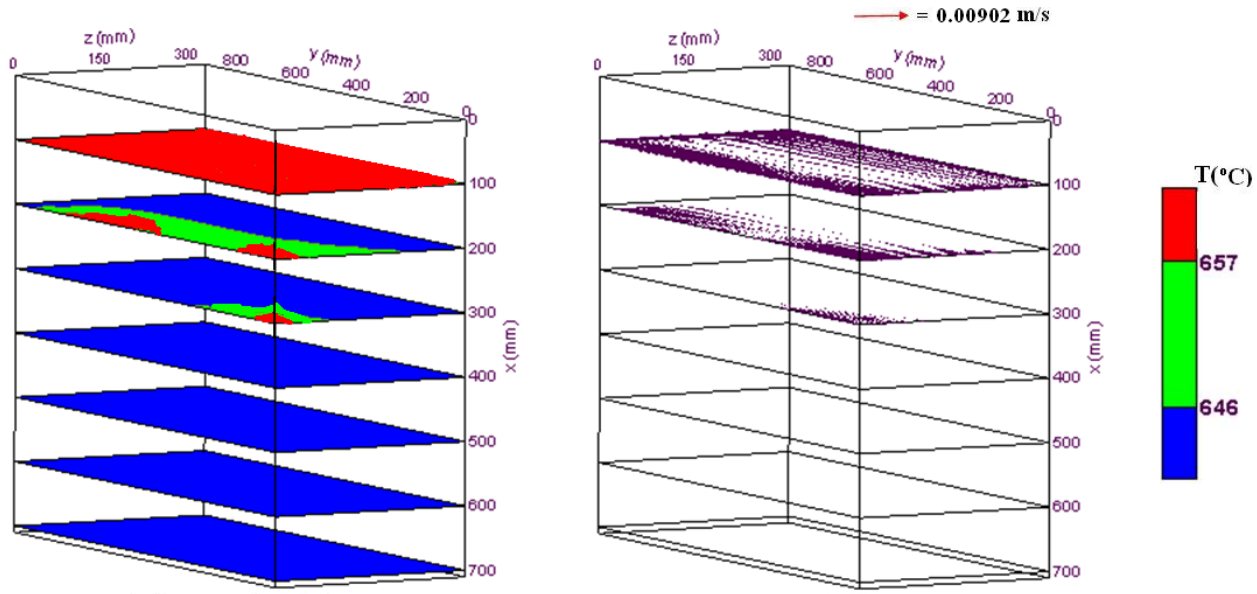

(a) Temperature contours (b) Velocity field

(i) Casting speed = 40 mm/min

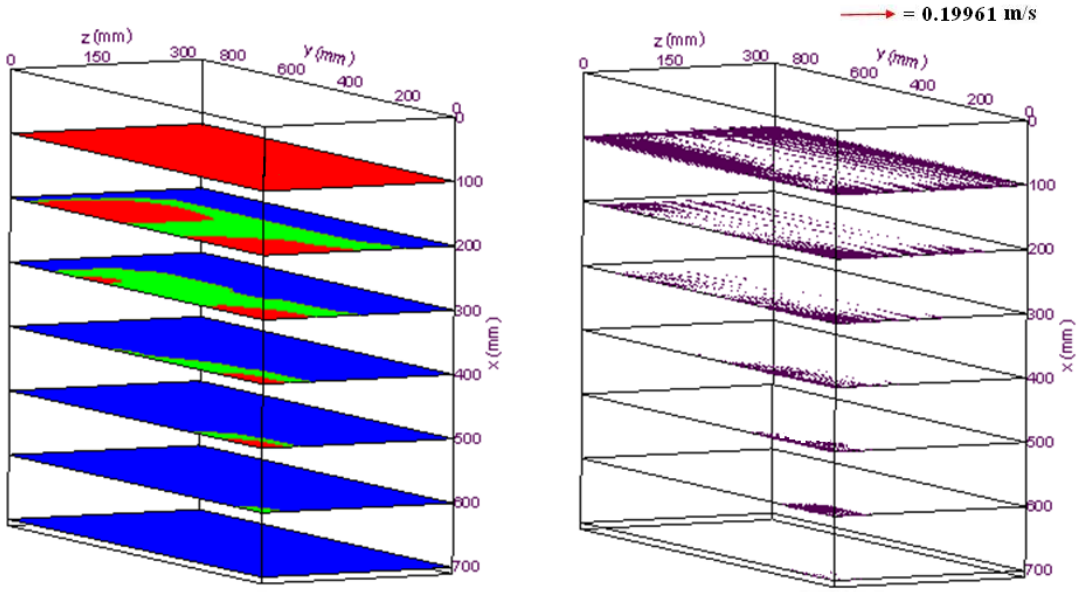

(c) Temperature contours (d) Velocity field

(ii) Casting speed = 60 mm/min

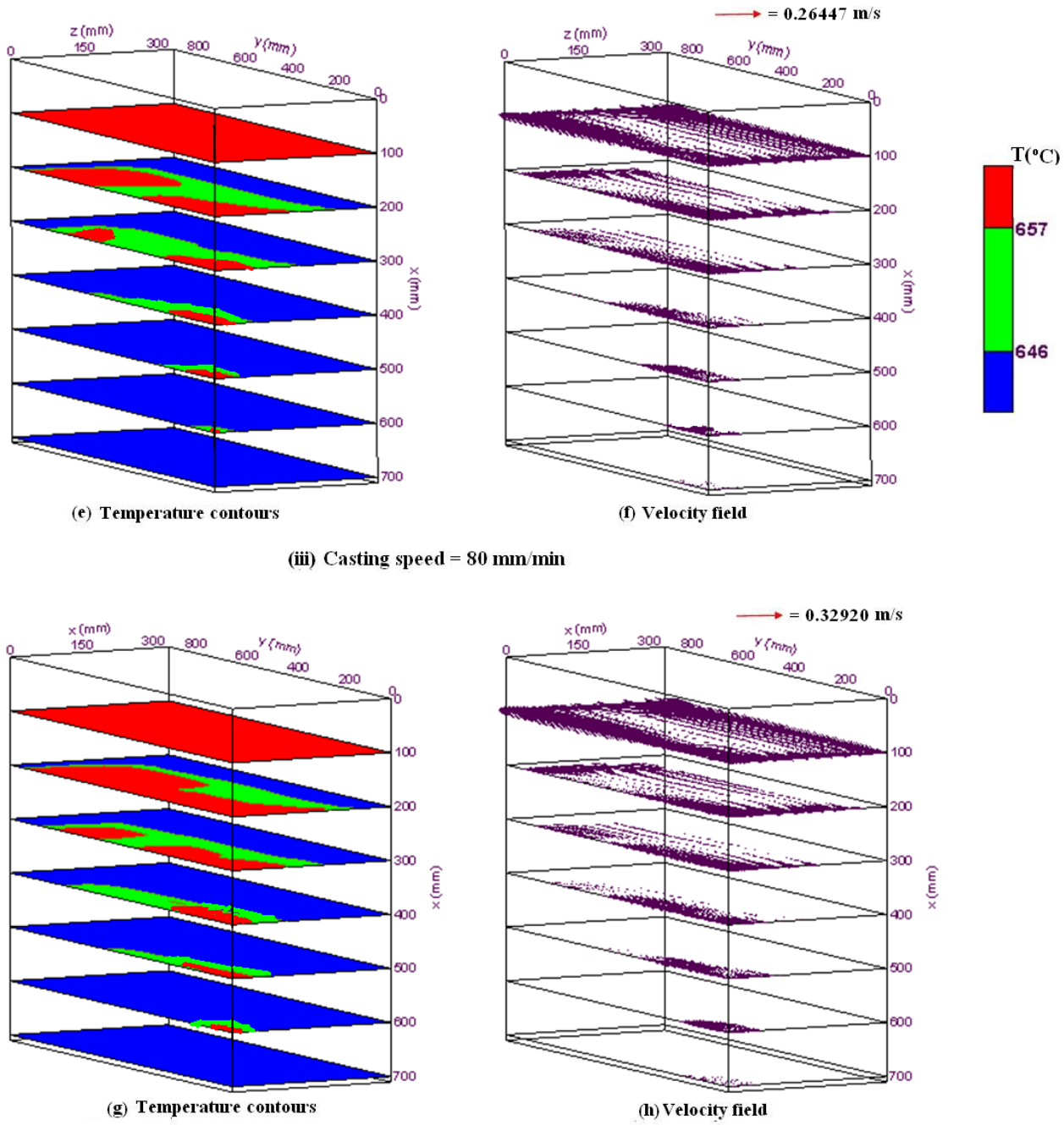

Figure 8.25: Contours of solidus and liquidus temperatures and velocity fields at various transverse cross-sectional planes (y-z planes) of the top part of the ingot using the submerged nozzle with a porous bottom plate distributor bag melt feeding scheme at porosity, $\phi = 0.9$ and a Darcy value 0f 1.0 x 10^{-4} for a superheat of 32°C and casting speeds of: (i) 40 mm min^{-1} (ii) 60 mm min^{-1} (iii) 80 mm min^{-1} (iv) 100 mm min^{-1}.

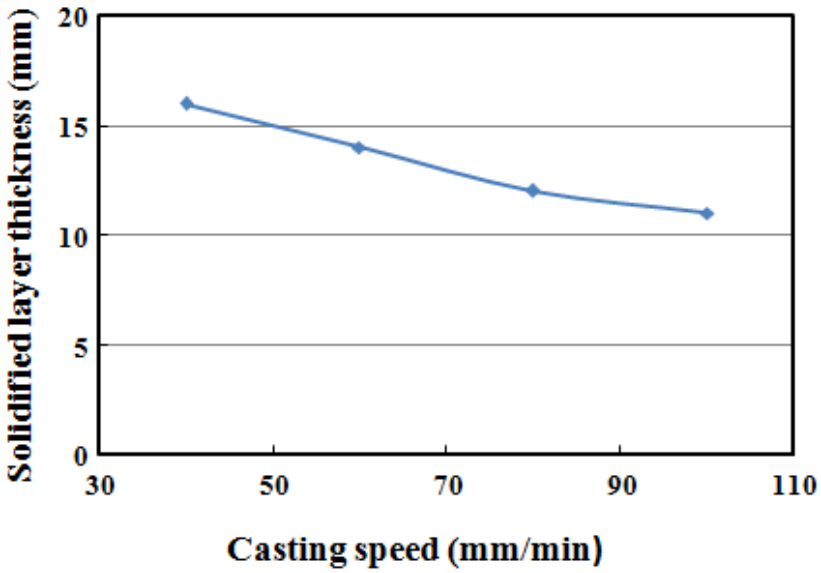

Figure 8.26: Solid-shell thickness from the narrow slab face at an axial distance of x = 160 mm from the top free surface at the wide symmetry plane versus casting speed at an inlet superheat of 32°C using the submerged nozzle with a porous bottom plate distributor bag melt feeding scheme at porosity, $\phi = 0.9$ and Darcy value 0f 1.0 x 10^{-4}.

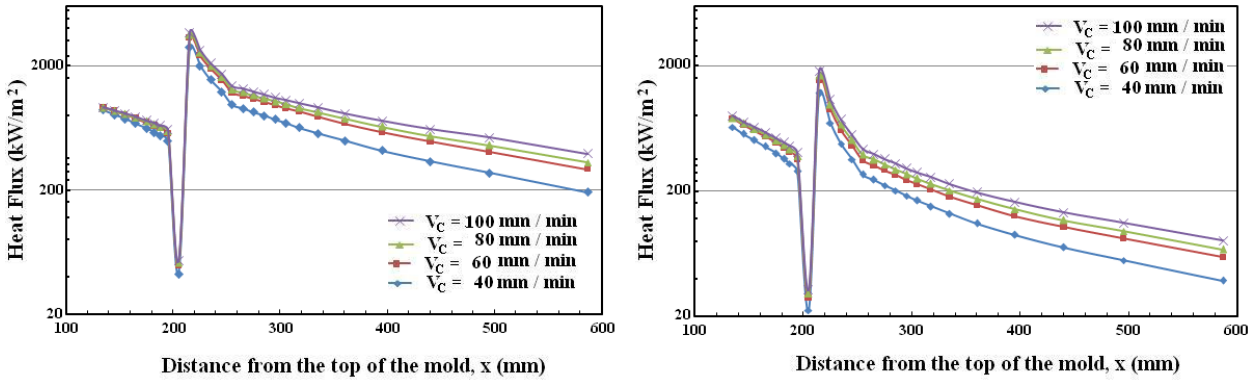

Figure 8.27:Variations of local surface heat fluxes for various casting speeds during solidification at 32°C superheat along the axial direction of the strand wall at: (a) z = 185 mm (b) y = 857.5 mm, using the submerged nozzle with a porous bottom plate distributor bag melt feeding scheme at porosity, $\phi = 0.9$ and Darcy value 0f 1.0 x 10^{-4}.

CHAPTER 9

DELIVERY SYSTEM WITH A SUBMERGED NOZZLE AND A POROUS FILTER

9.1 Introduction

In the previous chapter, the importance of employing a porous filter inside the domain for the homogeneous distributions of the melt during solidification was discussed. In practice, a fiberglass permeable cloth distributor system is used which essentially acts as a porous filter. Designs of this distributor system vary enormously from plant to plant and optimum distributor design for rolling slab casting is the subject of ongoing research [Tremblay and Lapointe, 2002; Arsenault et al., 2008; Hasan and Ragel, 2009]. Often in industry to increase the productivity, the design parameters of the casters are changed. The impact of these changes on the metal distribution system in the liquid pool is usually ignored. Since, the distributor system is the first entry point of the melt from the launder/trough to the mold, a careful delivery of the melt flow is required for minimizing the occurrence of various defects in the cast.

In a typical set-up during DC casting, the melt is distributed along the ingot top surface from the overlying trough through multiple nozzles arranged in a regular manner. In many other cases, the melt is distributed from the trough through a single submerged nozzle. In the present study, the latter system is modeled except that underneath the submerged nozzle there is a porous filter occupying the total horizontal cross-section of the VDC caster. Usually, in industry where the fiberglass distributor is used, it is placed only in the central region where the melt enters through a submerged nozzle.

In this study a different but new melt delivery system is proposed. A schematic diagram for the proposed set-up is shown in Figure 9.1. A square-shaped submerged nozzle was placed at the center which was distributing the melt. The nozzle and the

porous filter were assumed to be made of stainless steel, so that it could withstand the heat and impact of the incoming melt.

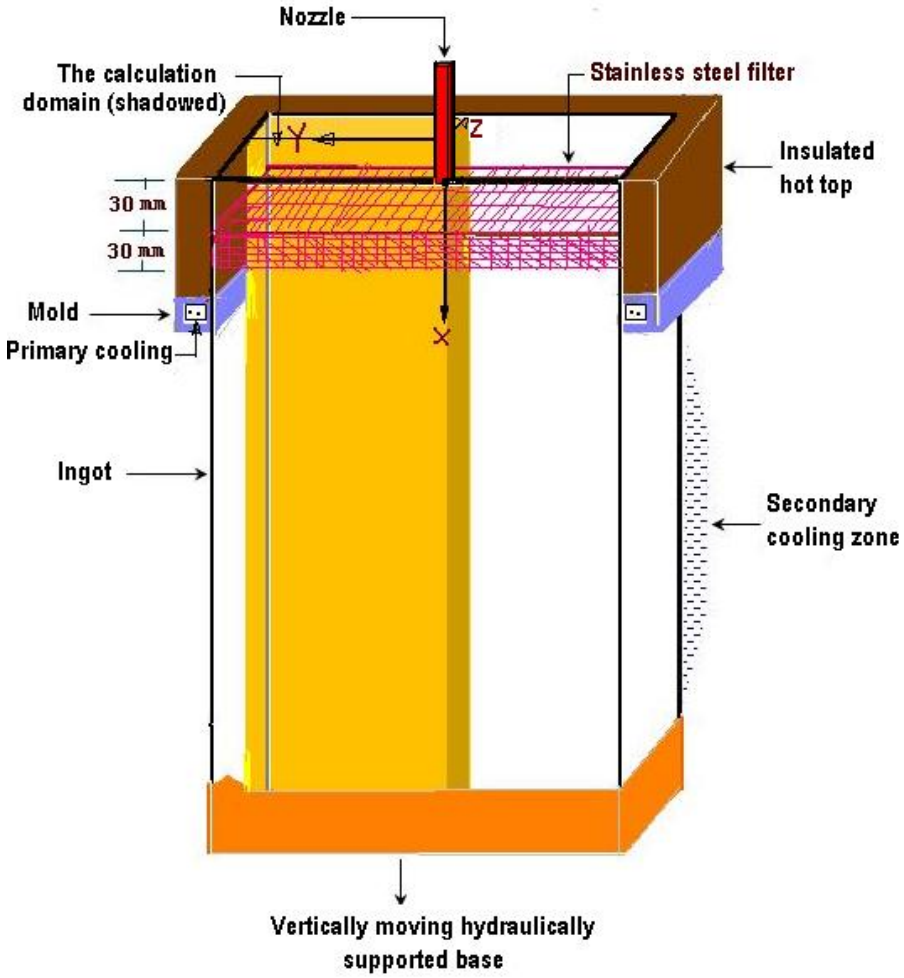

Figure 9.1: Schematic of a vertical DC caster with the calculation domain represented by yellow color for a submerged nozzle and a porous filter.

The dimensions of the computational domain and the thermo-physical properties of the AA-1050 are given in Section-3.2(a), and Table-3.1 of Chapter-3. In addition, the thermo-physical properties of stainless-steel used in the present simulation are given in Table-7.1 of Chaper-7. The nozzle walls were assumed to have a constant thickness of 5

mm [123]. The submerged nozzle had a depth of 5 mm and had a cross-sectional area of 900 mm^2. The filter dimensions inside the rectangular domain were arbitrarily set to Δx = 30 mm (height) $\times$ Δy = 1730 mm (width) $\times$ Δz = 660 mm (thickness). The filter was located at a distance of 30 mm from the top free surface (25 mm from the nozzle exit plane). It was assumed that the porous filter had a porosity (φ) of 0.4 and permeability of 9.0×10^{-8} m^2. For this geometry the latter corresponds to a Darcy number (Da) of 1.0×10^{-4}. The parameter Da (K/D^2) appeared in the non-dimensionalized transport equations. In this study, the effect of natural convection in the liquid pool was incorporated through the Grashof number (Gr) which aroused in the non-dimensionalized momentum equations. A fixed value of 10^9 for Gr was used here for all the studied cases. The boundary conditions used here for the transport equations are the same as those given in details in Chapter-3.

9.2 Results and Discussion

A summary of the relevant parameters used in modeling the present system is given in Table 9.1.

Table-9.1: Description of the parameters used for melt delivered through a nozzle with a porous filter.

Case	Casting speed, u_s [mm/min]	Porosity, ϕ	Darcy number, $Da = K/D^2$	Inlet Raynolds number, (Re_L)	Inlet Peclet number, ($Pe = Re_L \times Pr$)
1	40	0.4	1.0×10^{-4}	42,367.20	267.41
2	60	0.4	1.0×10^{-4}	63,550.80	401.11
3	80	0.4	1.0×10^{-4}	84,734.40	534.82
4	100	0.4	1.0×10^{-4}	105,918.0	668.52

It is to be noted from Table 9.1 that the melt superheat of 32^0C, porosity of 0.4 and Da of 1.0×10^{-4} were all kept fixed, while only the casting speed was varied from 40-100 mm/min. Another feature of importance is that because of the nozzle entry the inlet

Raynolds number was quite high for this delivery scheme and was found to vary from 4.2×10^4 to 10.5×10^4.

a. Velocity and Temperature Fields

Figures 9.2 (i-iv) show a 3-D surface plot of the predicted temperature and velocity fields for four casting speeds, namely, 40, 60, 80, and 100 mm/min, respectively, and for a fixed melt superheat of 32°C with a porous plate having a porosity of 0.4 and Darcy number of 10^{-4}. The flow fields presenting in Figs. 9.2(b,d,f,h) show that the strong jet of melt coming from the nozzle is striking the top surface of the filter at and around the ingot center. A smaller portion of the jet stream is passing through the filter and a bigger portion of the jet is spreading horizontally along the top surface and is also passing vertically through the filter. The filter is offering high hydraulic resistance thereby dampening the turbulence and is leading to an almost uniform vertical flow underneath the filter. Unlike the cases of the nozzle with a distributor plate, no re-circulation zone or vortices are seen to form in this case. This uniformity of the flow from the distributor system which is entering the mold is expected to produce a homogeneous cast. The filter will also prevent the generation and release of oxide films and patches and it will also arrest upstream inclusions which might come from the launder/trough or are generated in the nozzle. The above figures illustrate that the convection (indicated by maximum resultant velocity) increases with increasing casting speed, which is consistent with the physics of the problem.

The temperature contours along with the solidification front and the liquidus isotherm are depicted in Figures 9.2(a,c,e,g) for four casting speeds. The effect of casting speed on the solidification process can be clearly visualized by inspecting these figures. Making changes to the casting speed implies a change in the liquid metal flow rate feeding inside the ingot. As the convective heat transfer boundary conditions at the ingot surfaces do not change, as a result the solidification process is prolonged for higher casting speeds. For a higher casting speed, an increase in the inlet velocity and with the resultant decrease in the residence time in the mold, there is a delay in the casting

process. This delay in solidification can be seen by inspecting and comparing the solidus isotherms in Figures 9.2(a,c,e,g). From these figures further it can be seen that the solidus (646°C) and liquidus (657°C) are becoming steeper as well as they shifted downward with the increase in casting speed. The mushy layer is also extending because of the increase in the vertical separation distance between the liquidus and solidus with casting speed.

Figs. 9.3(a,b,c) – 9.6(a,b,c) illustrate a 2-D temperature contours and vector fields, in a magnified form for the upper two-third of the simulated length of the caster, at the wide symmetry plane (z = 0) and parallel to the wide symmetry planes at z = 62.5 mm, and z = 312.5 mm for various casting speeds for a fixed inlet superheat of 32^{o}C. The left hand panels of Figures 9.3(a), 9.4(a), 9.5(a), 9.6(a) show temperature contours while the right hand panels of these figures portray the velocity vectors for wide symmetry plane (z = 0). Since, the temperature and velocity fields at the wide symmetry plane are already visible in 3-D surface plot, the Figs 9.3(a) through 9.6(a) have been plotted for clear understanding and visualization of the results. Hence these figures will not be discussed any further.

The right hand panels of Figures 9.3(b), 9.4(b), 9.5(b), 9.6(b) show velocity vectors for a plane parallel to the wide symmetry plane at z = 62.5 mm. From the velocity vector fields it is apparent that the nozzle jet is hitting the top surface of the porous filter facing the nozzle and a portion of the melt is spreading out all over the cross-section with a high momentum.

The velocity vectors at z = 312.5 mm are illustrated in Figs. 9.3(c) through 9.6(c), which show that the melt is flowing parallel to the rolling face towards the end face from the narrow symmetry plane. This is due to the low porosity filter which is offering significant resistance for the downward movement of the flow. From Table 9.2, it is clear that for a fixed casting speed, as one move from wide symmetry plane towards the rolling face, the maximum resultant velocity is decreasing, while it is increasing with the casting speed for a fixed longitudinal cross-section.

Table-9.2: Maximum values of the resultant velocity in mm/min at inlet superheat of 32^{o}C.

Location in x-y plane	Values of casting speed (u_s) in mm/min			
	40	60	80	100
At z = 0 mm	39418.2	59153.4	78996.6	98630.4
At z = 62,5 mm	24970.8	37410.6	49891.2	62273.4
At z = 312,5 mm	1631.4	2268.6	3005.4	3335.4

The left hand panels of Figures 9.3(a) through 9.6(a), 9.3(b) through 9.6(b), and 9.3(c) through 9.6(c), show the temperature contours at z = 0, z = 62.5 mm, and z = 312.5 mm, respectively for four casting speeds. From these figures, it is apparent that for a fixed casting speed, as one move from wide symmetry plane towards the rolling face, the isotherms move progressively upward, while they are moving rapidly downward with the casting speed for a fixed longitudinal cross-section.

The temperature and velocity fields, at different transverse cross-sections (y-z plane) parallel to the slab top free surface, are illustrated for four casting speeds in Figs. 9.7(a-h). In Figs. 9.7(a-h), seven y-z planes are considered with an interval distance of 100 mm between the planes in the cast direction from the top of the ingot. Examinations of these figures in the left hand panels show how the solidification proceeds along the wide and narrow faces of the ingot, while in the right hand panels show the corresponding velocity fields. With the increase in the axial distance, as more heat is being extracted from the ingot through the mold and by the chilled water jets in the post mold region, the thickness of the solid layer from the wide and narrow sides, presented by the blue color, is progressively increasing in a uniform manner as can be seen from these figures at each casting speed. The apparent uniformity in the thickness of the solid shell on the narrow and wide faces signifies that a uniform rate of heat extraction has taken place from both of these sides at each cross-section. This types of solidification fronts usually develop in a 2-D horizontal geometry for an unsteady conduction dominated phase change problems. Around the corner an almost round-shaped solid layer

and mushy zone are observed. This is due to the fact the heat is extracted by the two sides at the corner, resulting there in a higher rate of heat extraction. The dramatic reduction of the solid region (represented by blue color) and corresponding increase of in the liquid region (represented by red color) along the cast direction with the increase in the casting speed can be easily visualized from the above figures. The reason for this shift has already been explained in earlier paragraph.

b. Quantitative Analysis

(i) Predicted Sump Depth and Mushy Layer Thickness

Table 9.3 provides sump depth and mushy layer thickness at the ingot center for four casting speeds. The sump depth is deepening and the mushy zone is extending with the increase in the casting speed, as expected. This increase in sump depth is caused by the higher rate of melt flow into the liquid sump and is consistent with the previous melt feeding studies.

The sump depth is found to be approximately 252 mm from the top of the mold for a withdrawal speed of 40 mm/min. Compared to the lowest simulated casting speed of 40 mm/min, the relative difference in sump depth for higher casting speeds of 60, 80, and 100 mm/min, is about 54 %, 55 %, and 150 % higher. At the center, for a casting speed of 40 mm/min the mushy thickness is about 10 mm, whereas, for casting speeds of 60, 80, and 100, the thickness increases by 300 %, 170 %, and 310%, respectively compared to the casting speed of 40 mm/min.

Table-9.3: Sump depth and mushy thickness (mm) at wide symmetry plane (z = 0) for melt delivered through a nozzle and a filter for four casting speeds and a superheat of 32^{o}C.

Quantity	Values of casting speed (u_s) in mm/min			
	40	60	80	100
Sump depth (mm)	252	54.0 % higher than u_s = 40 mm/min	55.0 % higher than u_s = 40 mm/min	150.0 % higher than u_s = 40

				mm/min
Mushy thickness (mm)	10	300.0 % higher than u_s = 40 mm/min	170.0 % higher than u_s = 40 mm/min	310.0 % higher than u_s = 40 mm/min

(ii) Formation of Solidified Shell

The shell thickness is predicted from the narrow face at the wide symmetry plane at an axial distance of 160 mm (the selected location is about the middle of the mold) from the top free surface and is plotted as a function of casting speed in Figure 9.8. A sharp decrease of the shell thickness is seen to occur for a change of casting speed from 40 to 60 mm/min and from 80 to 100 mm/min. while a gradual decrease of shell thickness is observed for a change of casting speed from 60 to 80 mm/min. The reason for this inconsistent behavior could be due to the interaction of the mushy layer and the surrounding flow.

For ease of understanding, the magnitudes of the shell thickness for four casting speeds are listed in Table 9.4. This table is self explanatory so far the casting speed is concerned.

Table-9.4: The thickness of the solidifying shell (mm) at wide symmetry plane from the narrow slab face at an axial distance of 160 mm from the top free surface inside the mold for four casting speeds and inlet superheat of 32°C for a submerged nozzle and a filter.

Quantity	Values of casting speed (u_s) in mm/min			
	40	60	80	100
Thickness of the solidifying shell (mm)	123	45.5 % lower than 40 mm/min	49.6 % lower than 40 mm/min	77.2 % lower than 40 mm/min

(iii) Local Surface Heat Flux

The effect of casting speed on the local surface heat flux distributions on the narrow face at z = 185 mm along the axial distance of the caster (from x = 135 mm to x = 587 mm) is illustrated in Figure 9.9(a) and the values for four casting speed at the water impingement point (x = 215 mm) are listed in Table-9.5. Figure 9.9(b) is a similar plot as Fig. 9.9(a) except that the local surface heat flux values are at y = 857.5 mm on the wide face. The values used for the imposed effective convective heat transfer coefficients (HTC) on the ingot surfaces were discussed in detail in Section 3.2.6 of Chapter-3. The trends are similar in nature to those predicted for five different melt feeding schemes, which are presented in the previous chapters.

From Fig. 9.9(a) it can be seen that for a casting speed of 40 mm/min and at z = 185 mm, a local heat flux of about 709 kW/m^2 is predicted near the top of the mold, and then it drops gradually inside the mold and it takes a minimum value of about 409 kW/m^2. In the air gap region, a sharp reduction in the local surface heat flux is observed taking a value of about 35 kW/m^2. At the water impingement point, the local surface heat flux is the highest, which is about 2359 kW/m^2. A sharp decrease of the local heat flux is found in the secondary cooling region dropping from a value of 2359 to 831 kW/m^2 within an axial distance of 40 mm. This region represents the nucleate boiling regime. After that, the heat flux decreases to a value of about 182 kW/m^2, which is the film boiling regime. From the above results presented in Figure 9.9(a) one sees that in the air gap, the surface temperature is oscillatory, which may lead to various surface and internal defects in the cast. With the increase in the casting speed, the local surface heat flux increases at each axial position, as can be seen in Figs. 9.9(a) and (b), which is consistent with the previous heat flux analyses discussed in Chapter-5 through Chapter-8. From Table-9.5, it is observed that, at a fixed location of z = 185 mm, x = 215 mm, the surface heat flux at a casting speed of 40 mm/min, is about 2359 kW/m^2, while it is about 26 %, 34 %, and 70 % higher for the higher casting speeds of 60, 80, and 100 mm/min, respectively in comparison to the lower casting speed of 40 mm/min.

For the identical effective convective heat transfer boundary condition, at the wide and narrow faces, it is observed that, there is a wide variation in the local heat flux

for the same axial position. The local heat flux at z = 185 mm is much higher compared to the value obtained at y = 857.5 mm (4001 kW/m^2 versus 1952 kW/m^2, at x= 215 mm and u_s = 100 mm/min). The reason is due to the proximity of the wide slab face from the symmetry axis compared to the narrow side, which was also stated in the earlier chapter.

Table-9.5: The local heat flux (kW/m^2) at z = 185 mm at an axial distance of 215 mm from the top free surface for four casting speeds and inlet superheats of 32°C, for a submerged nozzle and a filter.

Quantity	Values of casting speed (u_s) in mm/min			
	40	60	80	100
Local surface heat flux (kW/m^2)	2359.32	26.1 % more as compared with 40 mm/min	34.1 % more as compared with 40 mm/min	69.6 % more as compared with 40 mm/min

9.3 Conclusions

In this chapter, a short submerged nozzle with an underneath porous filter melt feeding system is presented for the VDC casting of a rectangular ingot. The use of this melt feeding scheme has led to the following observations:

1. Due to the low porosity porous filter, the velocity field depicts an almost uniform flow in the mold and post mold regions, which eventually shows a promising result with regard to the casting of an ingot.
2. This melt feeding scheme proved to be reasonably more efficient with regard to the growth of the solid-shell near the mold walls in comparison to other five melt feeding systems. This is especially true for lower casting speeds, viz., 40, 60, and 80 mm/min. The shell thickness decreases with increasing casting speed, as usual.

3. In this melt feeding scheme, a shallower sump is generated compared to other melt feeding schemes due to the weak convective flow underneath the filter at lower casting speeds of 40, 60, and 80 mm/min. The sump depth increases with increase in casting speed, as expected.
4. With the increase in the casting speed, there is an enhanced convection in the liquid pool and in the mushy zone which has resulted the mushy thickness to increase but rather in an irregular manner.
5. The local surface heat flux increases with increase in casting speed.

It is to be noted here that apart from the modeling study of the newly proposed design of the melt distribution system, there exists no prior work in the literature which has modeled a 3-D turbulent liquid metal flow in the presence of a porous medium for any system, let alone a coupled 3-D turbulent flow and solidification study in the presence of a porous medium.

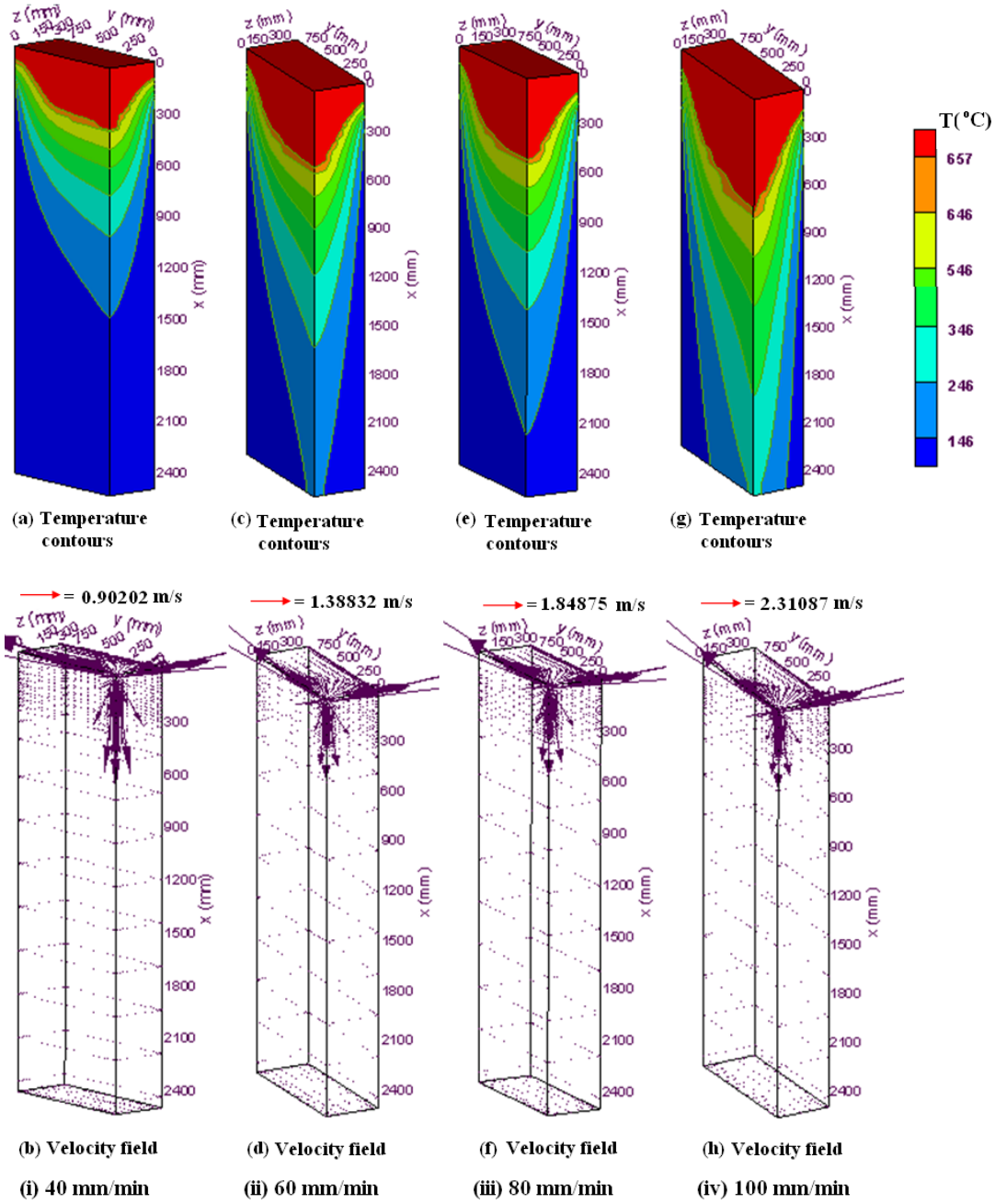

Figure 9.2: 3-D surface plots for the complete solution domain for four casting speeds and 32^0C temperature superheat using the submerged nozzle and a porous filter feeding scheme for porosity, $\phi = 0.4$ and Darcy value 0f 1.0 x 10^{-4}: (i) temperature contours (a) and velocity field (b) for a casting speed of 40 mm/min; (ii) temperature contours (c) and velocity field (d) for a casting speed of 60 mm/min; (iii) temperature contours (e) and velocity field (f) for a casting speed of 80 mm/min; (i) temperature contours (g) and velocity field (h) for a casting speed of 100 mm/min.

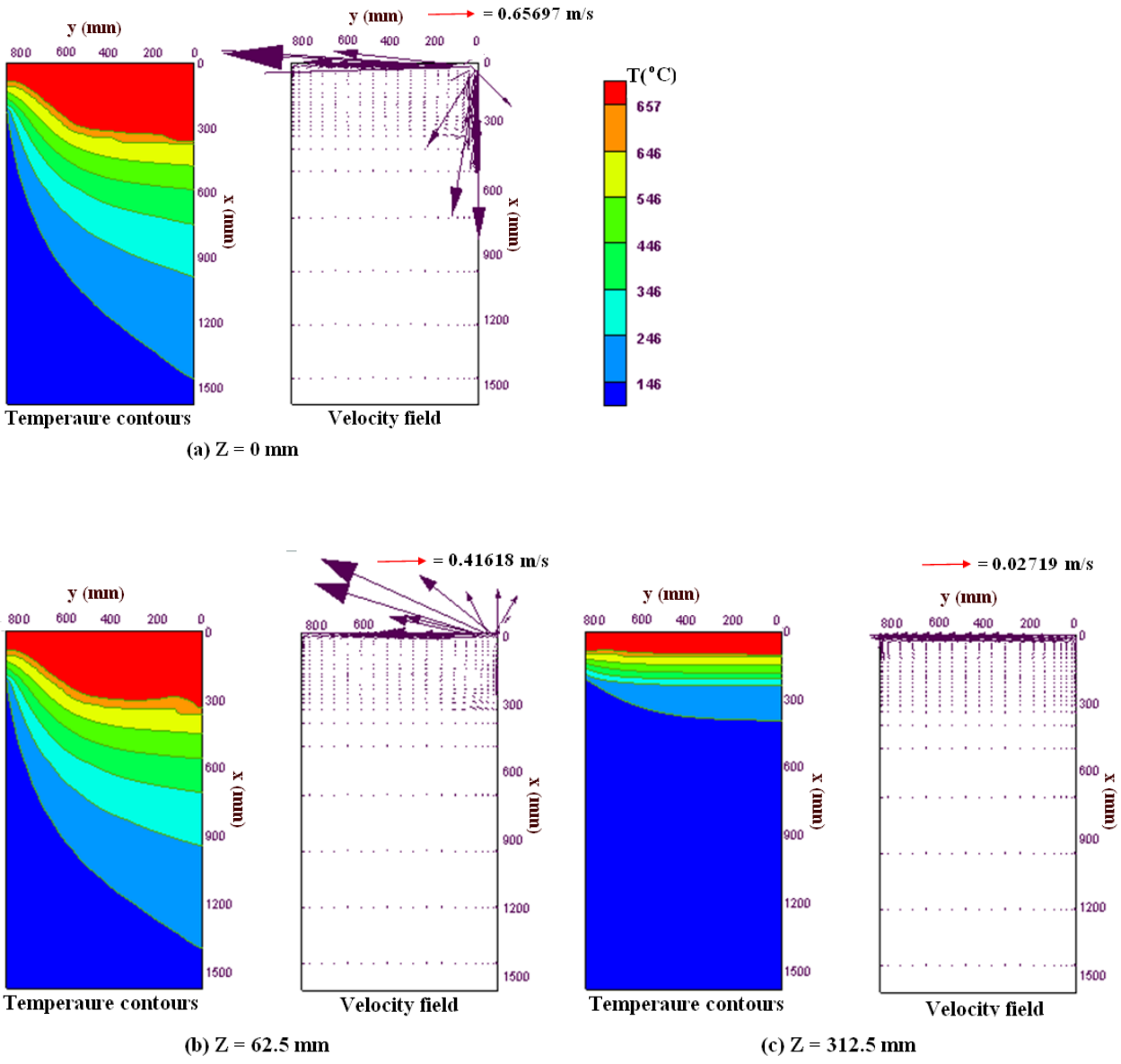

Figure 9.3: Enlarged 2-D view of temperature contours and velocity vectors field using the submerged nozzle and a porous filter feeding scheme for porosity, ϕ = 0.4 and Darcy value 0f 1.0 x 10^{-4} for a casting speed of 40 mm/min and 32°C superheat at: (a) wide symmetry plane at z = 0 mm, (b) vertical plane parallel to the wide face at z = 62.5 mm, (c) vertical plane parallel to the wide face at z = 312.5 mm.

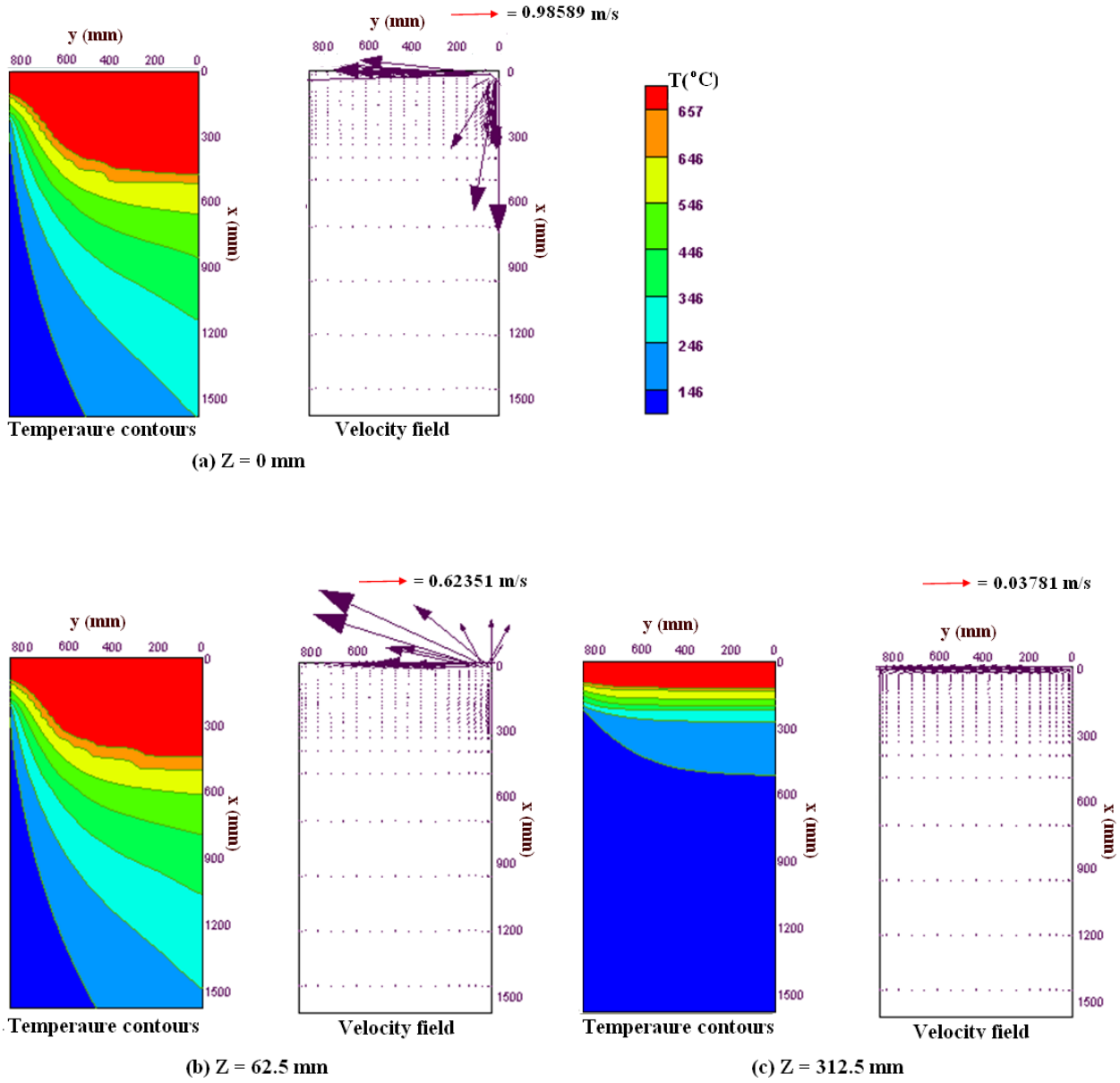

Figure 9.4: Enlarged 2-D view of temperature contours and velocity vectors field using the submerged nozzle and a porous filter feeding scheme for porosity, ϕ = 0.4 and Darcy value 0f 1.0 x 10^{-4} for a casting speed of 60 mm/min and 32°C superheat at: (a) wide symmetry plane at z = 0 mm, (b) vertical plane parallel to the wide face at z = 62.5 mm, (c) vertical plane parallel to the wide face at z = 312.5 mm.

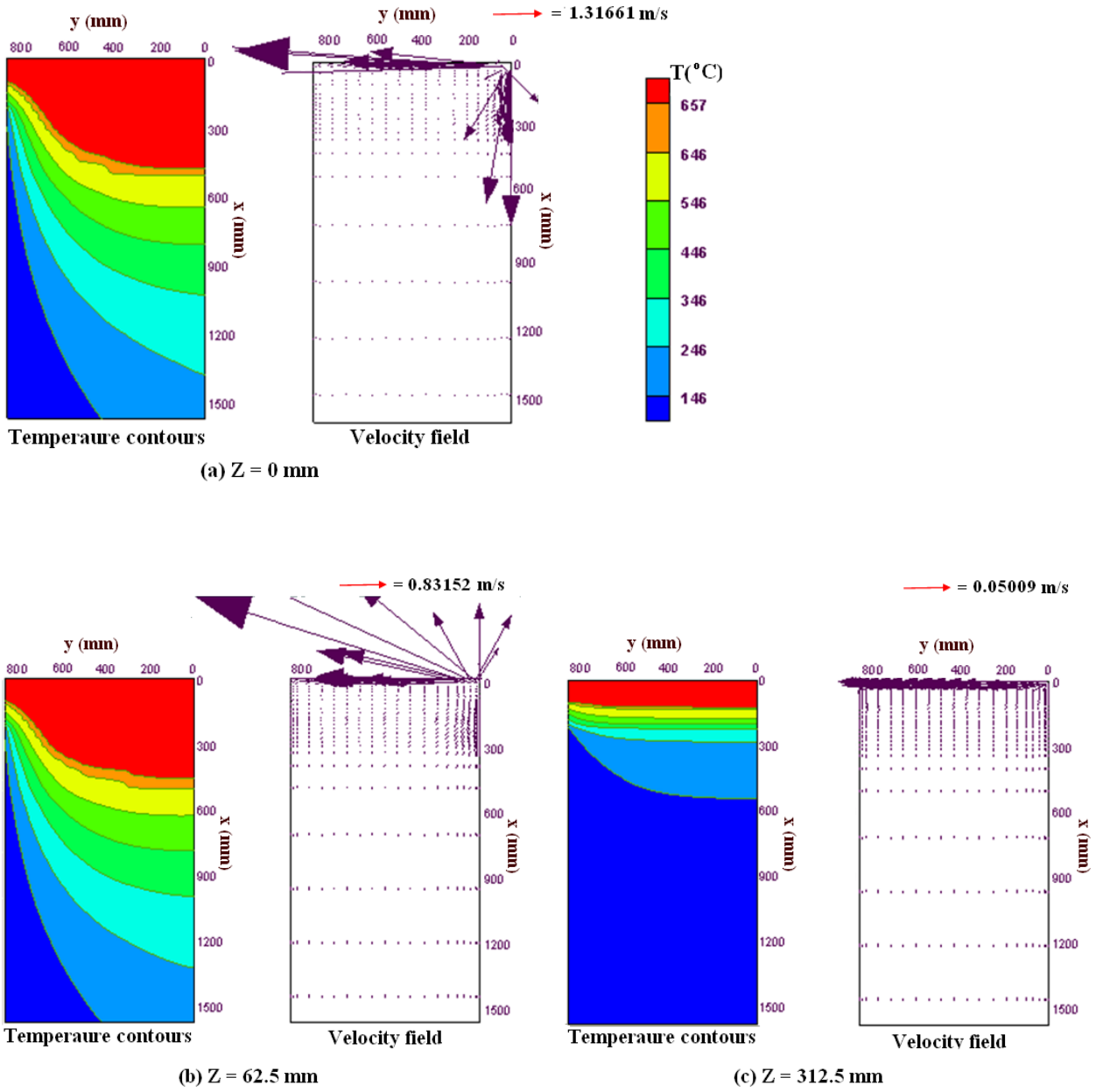

Figure 9.5: Enlarged 2-D view of temperature contours and velocity vectors field using the submerged nozzle and a porous filter feeding scheme for porosity, ϕ = 0.4 and Darcy value 0f 1.0 x 10^{-4} for a casting speed of 80 mm/min and 32°C superheat at: (a) wide symmetry plane at z = 0 mm, (b) vertical plane parallel to the wide face at z = 62.5 mm, (c) vertical plane parallel to the wide face at z = 312.5 mm.

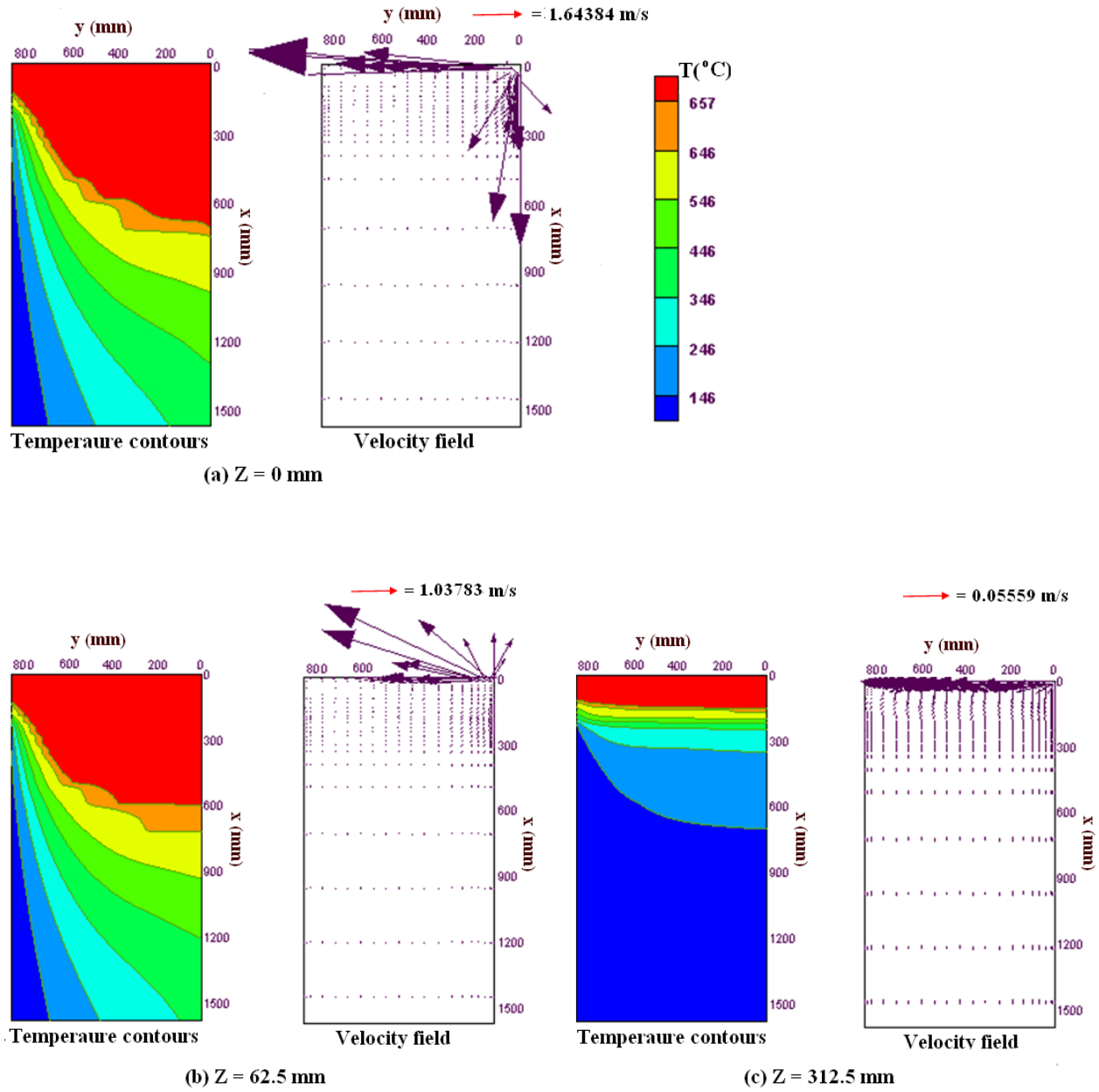

Figure 9.6: Enlarged 2-D view of temperature contours and velocity vectors field using the submerged nozzle and a porous filter feeding scheme for porosity, ϕ = 0.4 and Darcy value 0f 1.0 x 10^{-4} for a casting speed of 100 mm/min and 32°C superheat at: (a) wide symmetry plane at z = 0 mm, (b) vertical plane parallel to the wide face at z = 62.5 mm, (c) vertical plane parallel to the wide face at z = 312.5 mm.

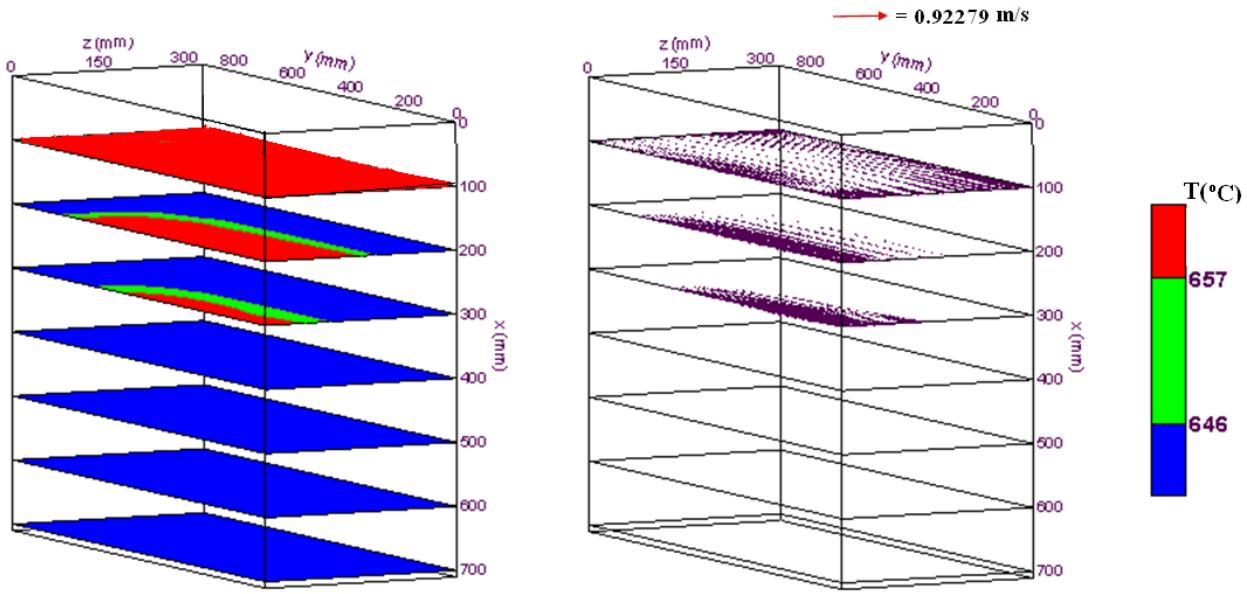

(a) Temperature contours (b) Velocity field

(i) Casting speed = 40 mm/min

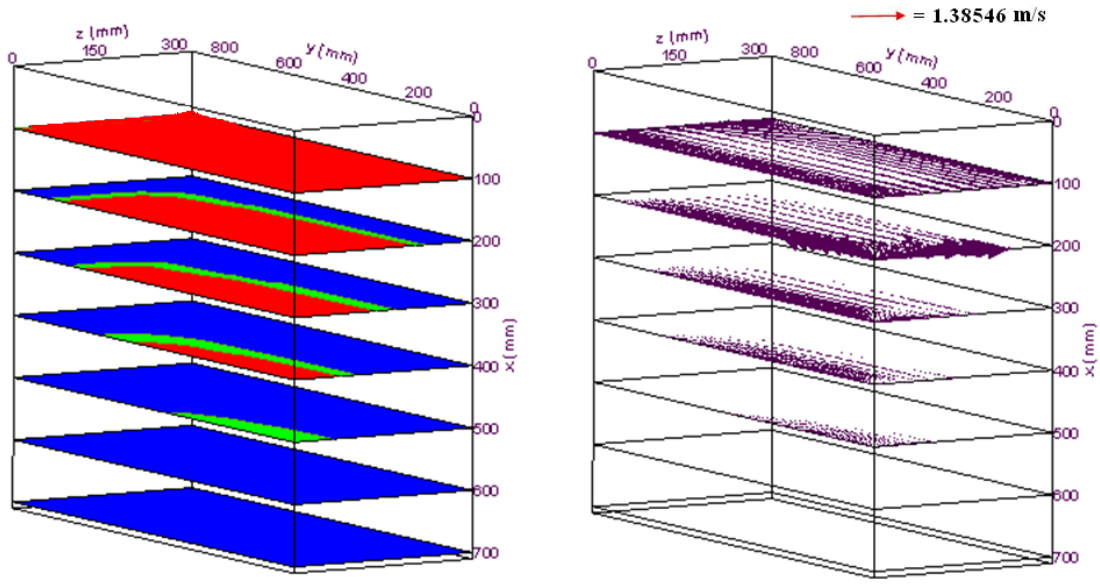

(c) Temperature contours (d) Velocity field

(ii) Casting speed = 60 mm/min

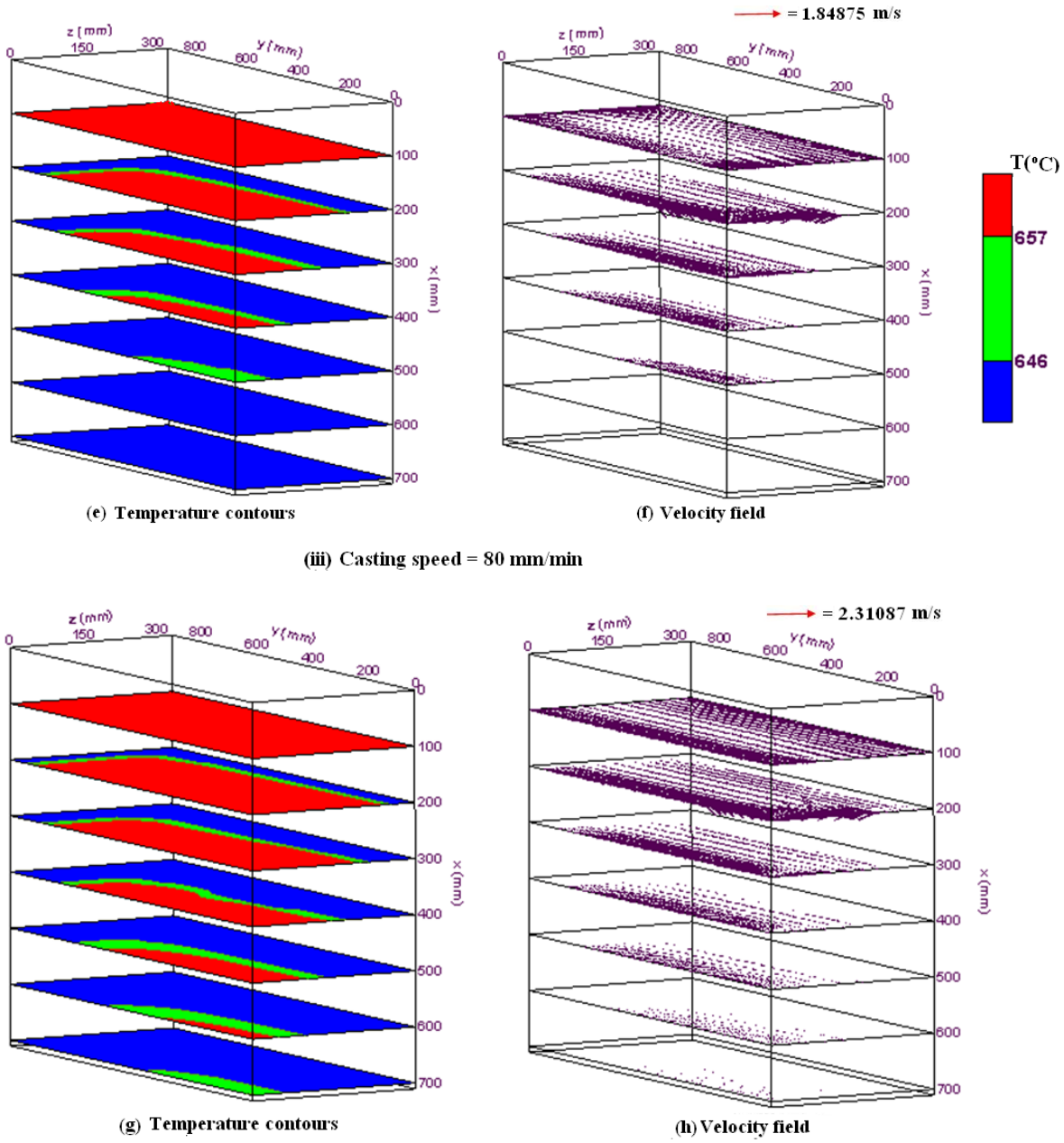

Figure 9.7: Contours of solidus and liquidus temperatures and velocity fields at various transverse cross-sectional planes (y-z planes) of the top part of the ingot using the submerged nozzle and a porous filter feeding scheme for porosity, ϕ = 0.4 and Darcy value 0f 1.0 x 10^{-4} melt feeding scheme for a superheat of 32°C and casting speeds of: (i) 40 mm min^{-1} (ii) 60 mm min^{-1} (iii) 80 mm min^{-1} (iv) 100 mm min^{-1}.

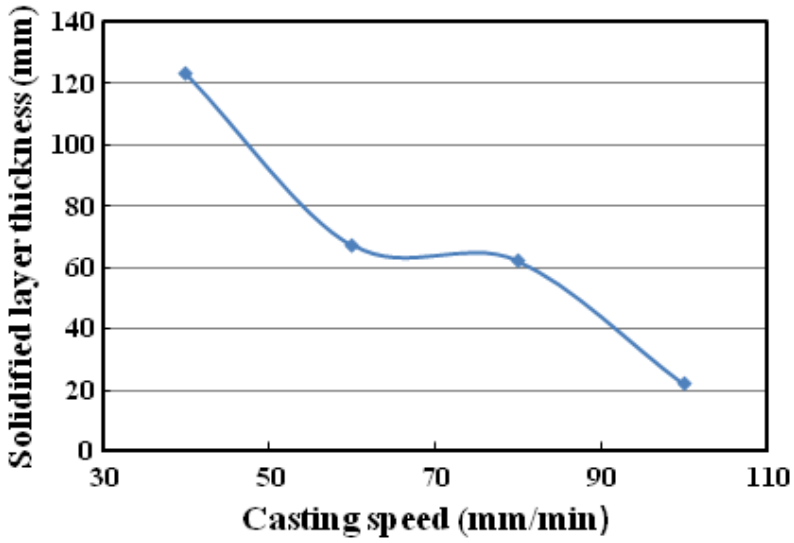

Figure 9.8: Solidified layer thickness from the narrow slab face at an axial distance of x = 160 mm from the top free surface at the wide symmetry plane versus casting speed at an inlet superheat of 32°C using the submerged nozzle and a porous filter feeding scheme for porosity, ϕ = 0.4 and Darcy value 0f 1.0 x 10^{-4}.

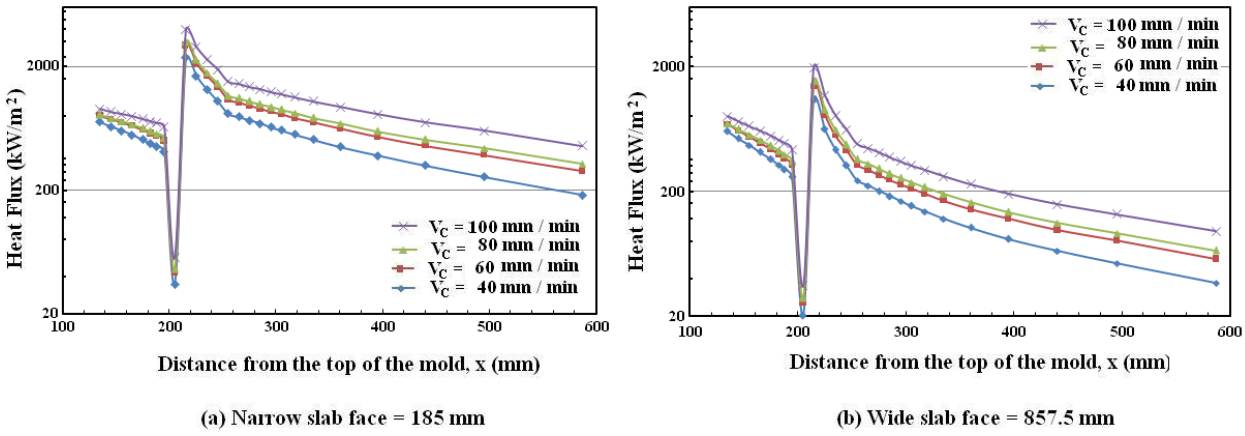

Figure 9.9: Variations of surface heat fluxes for various casting speeds during solidification at 32°C superheat along the axial direction of the strand wall at: (a) z = 185 mm (b) y = 857.5 mm, using the submerged nozzle and a porous filter feeding scheme for porosity, ϕ = 0.4 and Darcy value 0f 1.0 x 10^{-4}.

CHAPTER 10

SUMMARY

10.1 Overall Concluding Remarks

In this study, a three-dimensional, coupled turbulent flow, heat transfer and macroscopic solidification model was developed which simulated the steady state part of the vertical DC casting of an industrial-sized slab caster of an aluminum-alloy (AA-1050). The modeled equations were the time-averaged 3-D turbulent Navier-Stokes and energy equations. The two-equation k-ϵ model of Launder and Sharma [78] was included in the model to account for the turbulent aspect of the flow. The buoyancy force was introduced in the model through the Boussinesq approximation. The mushy region, which developed during the solidification process of the alloy, was taken care through the modification of the momentum equations using the usual Darcy-type source term which was dependent on the liquid fraction. The so-called 'enthalpy-porosity' approach was used to couple the energy equation with the momentum equations. The effective heat transfer coefficients employed in the primary and the secondary cooling zones on the slab surface were taken from the relevant literature. The governing transport equations with the associated boundary conditions were suitably non-diensionalized to generalize the solutions obtained. An in-house developed 3-D CFD code (DCCAST) was used to solve the dimensionless form of the modeled equations and boundary conditions. The code is based on the control-volume based finite-difference technique and uses the well-known SIMPLE algorithm to resolve the velocity-pressure coupling in the momentum equations. The convective terms of the transport equations were discretized using the hybrid difference scheme. Numerical accuracy of the model was tested by comparing the predicted sump profile with the only known experimentally measured sump profile of a slab caster. Considering the unknown factors such as thermal boundary conditions in the experiment, the comparison showed a reasonably good agreement. The discrepancy

between the predicted and measured sump profile could have been minimized if the experimental heat transfer boundary conditions in both the primary and secondary cooling zones could have been known. Before going for the production runs, grid independency tests were performed. The used grid system of $60\times42\times24$ in the x, y, z directions, respectively was a compromise in terms of numerical accuracy and computational cost.

Upon verification of the model, it was later used in carrying out an extensive parametric study for the said caster for six different melt distribution systems, namely, the open-top, open-top with a full porous filter, open-top with a half porous filter, channel bag, two types of combo bags, and submerged nozzle and a porous filter. For first three metal feeding schemes, the studied parameters were the four different casting speeds, namely 60 mm/min (0.001 m/s), 100 mm/min (0.00167 m/s), 140 mm/min (0.00233 m/s) and 180 mm/min (0.003 m/s), and two inlet melt superheats, viz., 32^{o}C and 64^{o}C. For the rest three metal feeding schemes a total of four different casting conditions, namely 40 mm/min (0.00067 m/s), 60 mm/min, 80 mm/min (0.00133 m/s), and 100 mm/min are selected, all for a fixed delivered superheat of 32^{o}C. By varying the above mentioned parameters, the model was then used to predict the sump depth, the shell thickness, the growth rate of the mushy region in the center of the ingot, the local heat flux on the ingot surface, as well as the velocity, the temperature, and the turbulent kinetic energy fields in the liquid, mushy, and solid regions as were appropriate within the caster. The studied parameter demonstrated the ability of the developed model as an efficient tool that could be used in order to cast slabs with different aspect ratios and of different alloys. The model can also be used in analyzing the effects of possible scenarios that may occur after some period the caster is in operation. Since much computational effort is needed in predicting the 3-D solidification phenomenon in the presence of circulating fluid flow in the liquid sump, a simple thermal model was developed and applied to solve solidification heat transfer for the open top delivery system. To ensure consistency between the thermal model and the corresponding CFD model, the boundary conditions were kept identical in the mold and sub-mold regions for both the models. In the thermal model, the convection was considered by assuming a slug flow in the liquid sump.

In this chapter, a brief conclusion of the numerical results predicted by the thermal model will be given first, which will be followed by a comparison with the predicted results obtained from a CFD model. Finally, the simulation results obtained and described in Chapters 6-9 for different delivery systems will be summarized.

The following conclusions are drawn from the study of the thermal model for open-top melt feeding configuration:

1. The 3-D thermal model is an approximate model by using which the temperature profiles were predicted by assuming slug flow (equal to the casting speed) in the liquid. The model was able to quantify the effects of the casting speed and the melt superheat on the sump depth, the mushy thickness at the center of the ingot, the shell thickness, the local surface heat flux, the ingot surface temperature, etc. in a relatively very short time.
2. An increase in the casting speed caused the sump depth and the mushy thickness at the ingot center to increase, while the solidified-layer thickness was seen to decrease by a significant amount. This would benefit the cast engineer in specifying the upper and lower limits of the casting speed in the design of a new D.C. semi-continuous casting machine.
3. It was found that the local heat flux near the corner of rolling face and at the middle of the narrow face of the ingot in the downstream direction was increasing with the increase in the casting speed. Therefore, an increase in the casting speed will result in the increase of the surface temperature.
4. The effects of delivered superheat on the sump depth and shell thickness were found to be insensitive up to a casting speed of 100 mm/min. The reason for this insensitivity is due to the insignificant effect of thermal convection on to the growing solid. The casting speed above 100 mm/min shows that, an increase in the melt superheat increases the sump depth slightly but decreases the shell thickness significantly. An increase in the inlet melt temperature does not have much effect on the sump depth, but widens the mushy region by moving the liquidus and solidus isotherms vertically downward.

5. The temperature profiles obtained from the thermal model can be fed into a thermal stress model to calculate quickly the approximate stresses that develop in the DC casting slab. This model can also be used to develop a real-time automatic control system for such a process and to determine the optimum mold depth for preventing the reheating of the thin shell within the mold so that a catastrophic break-out condition does not arise.

After analyzing the results from the thermal model, it was felt that the turbulent aspect of the flow was not appropriately considered. Hence, the CFD model was developed, which can offer a significant benefit in solving the macro-segregation and the hot tearing problems associated with DC semi-continuous casting process. Besides the above statement a consideration of the flow field is important since during the mushy region solidification process the dendritic tips and arms may be broken off and swept downward into the bottom of the pool which will affect significantly on the ultimate cast structure. The variations in the predicted results generated by the thermal and CFD models under the same operating conditions are summarized below:

1. A comparison between the two models revealed that, the shell thickness predicted by the thermal model was approximately 1.0, 1.35, 1.50, and 1.57 times higher for a fixed $\Delta T = 32^{o}C$, and for a fixed $\Delta T = 64^{o}C$ it was 1.38, 1.42, 1.86, and 1.17 times greater, at casting speeds of 60, 100, 140, and 180 mm/min, respectively compared to those predicted by the CFD model. In contrast to the thermal model, in the CFD model the 3-D velocity fields were solved which had accurately considered the effect of thermal convection on the retardation of growth of the solidified shell in the transverse plane (y-z plane).
2. A comparison of the sump depth predicted by the thermal and CFD models showed that there was an insignificant increment obtained by the thermal model for a fixed $\Delta T = 32^{o}C$. At a higher melt superheat of $64^{o}C$, thermal model showed a little-bit deeper sump than that was found in CFD model at a casting speed of 140 mm/min and above and the difference in sump depth increased as the casting speed increased beyond that value.

3. For neglecting the interaction of fluid flow, if one can determine the relative errors introduced into the final solution using a thermal model in that case a thermal model could be useful.

The above comparative study clearly signifies the importance and need for a three-dimensional, conjugate turbulent flow, heat transfer and solidification modeling study for a DC semi-continuous slab casting process. As a result the turbulent aspect of the flow was studied. In addition, in the present study an attempt was also made to develop an optimized metal feeding scheme. To fulfill this objective, a total of six melt feeding systems for the said caster was analyzed separately and described in Chapter-6 through Chapter-9. A conclusion was drawn for each melt feeding scheme, which was provided in each concerned chapter. Here an overall conclusion is presented form the previously discussed findings, these being:

1. A higher casting speed is always desirable for increasing productivity which is correlated to the corresponding increase in the cooling rate. It is to be noted that a higher casting speed will increase the productivity while an increase in the cooling rate will increase the operational cost. For a fixed water flow rate, a higher casting speed produces a deeper sump profile, which is more noticeable in the central part of the ingot than at the periphery. A higher casting speed will always lead to the increase in the volume flow rate of melt inside the domain. More melt enables the enhancement of the convective current and this phenomenon frequently results with the deeper sump and favors higher temperature gradients, which in turn enhances thermal convection [89]. This known observation is consistent with the present simulations results. For an identical operating condition, the predicted sump depth increased with the increasing casting speed for each melt delivery system.
2. An increase in melt temperature will deepen the sump due to the increase in total heat that needs to be removed via heat transfer through the slab surface, and will cause to raise the temperature gradients in the liquid pool [34]. For the increase in melt superheat the current simulated results also showed a slight increment in the

sump depth and liquid pool depth at the ingot center at each casting speed for the studied three melt feeding schemes, these were the open-top metal feeding, open-top with a full-filtered melt feeding, and open-top with a half-filtered melt feeding ingot. Which mean, the shapes of the liquidus and solidus isotherms were slightly affected by the higher melt temperature for the above mentioned feeding configurations.

3. The thickness of the mushy zone at the ingot center usually tends to increase with increase in casting speed by shifting both the liquidus and solidus isotherms downward. This trend was observed for each melt feeding scheme except for the channel bag distribution system. In the latter system, a slight decrease in mushy thickness was found as casting speed increases. This evidently is due to the recirculation of the melt which created a large vortex that penetrated a longer axial distance at the central area.
4. The predicted solidified shell thickness at the wide symmetry plane and in the middle of the mold showed that it decreased with increasing casting speed and melt superheat. This was true for each melt feeding scheme. The reason is the large metallostatic pressure and stronger thermal convection at higher casting speeds.
5. The local heat flux on the cast surface increased with increasing casting speed and melt superheat in each melt feeding scheme for the above mentioned reasons.
6. Between the two casting parameters, namely, casting speed and melt superheat, it was found that the casting speed exerts the maximum and direct effect on the growth of the solidified shell thickness, on the local surface heat flux, on the sump depth, and on the thickness of the mushy layer. The inlet melt temperature does not have much effect on the above mentioned quantities. At higher casting speeds, the shell thickness at the mold exit tended to decrease with increasing melt superheat. Hence, the combination of the said two parameters must be such that a bleed-out condition does not arise during casting.
7. On the basis of the above observed facts, while modeling three additional melt feeding systems, namely, the channel bag, two types of combo bags, and nozzle with a full filter, only the effect of casting speed was studied.

8. The nozzle with a small submergence depth with a porous filter was seen to enhance the level of turbulence in the liquid region. This is due to the higher velocity gradients resulting from the filter placed in the entire cross-section at the hot-top.
9. Simulated results clearly showed that casting speed and melt feeding scheme are important factors affecting the sump depth, shell thickness, mushy thickness in DC casting of Al-alloy ingots.
10. Considering the effect of three melt feeding systems on the solid layer thickness, and on the local surface heat flux, the combo-bag with a porosity of 0.4 was found to be more beneficial than the combo-bag with a porosity of 0.9 and channel bag. The minimum sump depth was observed in the channel bag melt feeding scheme. By considering the above mentioned quantities it is difficult to suggest which one is the best design among the three melt feeding schemes.
11. Among the six melt feeding schemes, the nozzle with a porous filter predicted the thickest solid shell at the wide symmetry plane inside the mould for each casting speed. This is due to the effect of the fine pores of the filter which diverted a major portion of the melt flow from the vertical to the horizontal direction around the entire cross section in the hot-top. This resulted in the decrease of thermal convection intensity dramatically underneath the filter and near the mould walls.
12. A comparison of the six feeding schemes showed that for lower casting speeds ($\leq$ 60 mm/min) the nozzle with a full porous filter feeding system is the best delivery system. But for a higher casting speed this observation is not true. For example, at a fixed casting speed of 100 mm/min and delivered superheat of 32^{o}C, the open-top with a full-filtered feeding system predicted the shallowest sump depth which was 480 mm, while the nozzle with a full porous filter feeding system gave the thickest shell which was 28 mm. Therefore, for a higher casting speed greater than 60 mm/min, if sump depth is of major concern then one should select the open-top with a full filter feeding ingot. On the contrary, if the shell thickness is the choosing criteria then one should employ the nozzle with a full porous filter feeding ingot.

13. In this study, the effect of mold heat transfer coefficient (HTC) on the growth of the solid-shell was investigated. The solid-shell thickness at the exit of the mold from the narrow face at the wide symmetry plane for various effective values of HTC ranging from 225 to 3000 W/(m^2-K) was predicted and compared for the casting of AA1050 alloy at a speed of 100 mm/min and an inlet melt superheat of 32^{o}C using the open-top melt feeding scheme. The comparison showed the value of the primary HTC had direct influence on the solidification process. Therefore, an appropriate mold HTC should be judiciously implemented to improve the as-cast quality.

It is expected that an optimum design of the melt flow distributor system can reduce the segregation significantly through a stable and turbulent free filling. In a real VDC caster, the flow characteristics in the sump are mainly determined by the forced and thermo-solutal (natural) convection. The thermo-solutal (natural) convection is initiated due to the temperature and concentration gradients. Though, in the present CFD model, the solutal (natural) convection is not considered, but the flow patterns which have been obtained using the present model show a clear picture of the flow patterns in the liquid sump which resulted from the contributions of various parameters. By visualizing the flow patterns one will be able to predict the susceptibility of macrosegregation and hot tear which are directly linked with flow patterns.

10.2 Statement of Originality

The following aspects of the present numerical modeling study concerning a vertical DC semi-continuous casting of a slab can be considered new:

1. The development of a three-dimensional numerical code for studying turbulent flow with coupled solidification and heat transfer for a vertical DC casting process fitted with various metal feeding schemes is a novel undertaking.

2. The associated code is applicable for the analysis of semi-continuous casting practices for square and rectangular ingots with any geometrical dimensions and for any alloy system for which detailed physical properties are known.

3. A 3-D thermal model is developed to predict the temperature distributions in the liquid, mushy and solid regions to facilitate the development of an automatic control system for a DC slab caster.

4. The 3-D thermal and CFD models' results are compared in order to investigate the impact of the melt flow on the solidification process. A comparison between the two models, on the basis of shell thickness and sump depth, is new and has never been reported in the literature.

5. The effect of open top melt feeding scheme has resulted in the minimization of the overall turbulence in the system. Such a study for the DC casting process is not reported earlier.

6. A newly designed combo distributor bag with a porous bottom plate acting as a filter/foam is proposed and detail results are presented for the first time. A comparison between the channel and combo bags is also reported.

7. For controlling the incoming oxides and inclusions into the mold, a porous filter is fitted into the hot top and its effect on the uniformity of flow and temperature fields is studied in detail. In case of DC casting, the application of a porous filer on the hot-top is a new and non-tested concept. In the literature, the transport equations governing the turbulent flow in a porous media, is a serious controversial issue until today. The turbulent transport in the porous filter is considered by first time averaging the equations and then by volume averaging the obtained equations.

8. The variations of the important DC casting process variables, such as, casting speed and melt superheat for the proposed melt feeding schemes are studied and compared. A similar study does not exist in the literature.

9. A sensitivity analysis of the effective convective heat transfer boundary condition for the mold is studied and the predicted shell thickness on the narrow face at the mold exit is compared to ascertain the possible breakout condition. To the best of the author's knowledge such studies are yet to appear in the DC casting literature for a slab caster.

10. From the studied melt feeding systems, a proposal is made for the most effective delivery system. Such a system could be easily retrofitted in existing vertical DC casting processes with a minimum cost and effort not only for aluminum alloys but also for other non-ferrous alloys, such as magnesium, copper, etc.

10.3 Suggestions for Future Work

1. In a DC casting process various types of cracks are believed to develop from stresses resulting from the highly non-uniform cooling of the ingot passing through the primary and secondary cooling regions. A thermo-mechanical analysis is suggested in order to study the developments of various stresses that prevail within the cast. Such a study should be able to suggest how to minimize the developments of non-uniform stresses by applying appropriate thermal boundary conditions in the mold and post mold regions.

2. Macrosegregation is a common quality problem in DC casting processes. It is due to the chemical non-homogeneity of the alloying elements in the cast. The present model should be extended in such a way that the model can also predict macrosegregation that develops during solidification in a DC cast for using various alloying elements.

3. It is now well established that in a DC casting process, the proper controlling of heat transfer and withdrawal speed of the dummy block during the start-up phase are necessary to minimize the surface cracks, butt curl and other surface related defects. Therefore, a transient free-surface flow analysis along with solidification

heat transfer during filling of the mold cavity in the presence of a dummy block should be carried out to take into account the start-up phase of the DC casting process.

4. To simplify 3-D modeling of the DC casting problem, it is assumed in this study that the thermo-physical properties of the solid and liquid are same and are invariant with temperature. In reality, the thermo-physical properties of the solid and liquid phases differ and are dependent on temperature. Hence, it is suggested that the model should be modified to account for these changes in thermo-physical properties.

5. In this study, simulations are carried out for Al 1050 alloy, which is a short solidification range alloy having a difference of only $11^0 C$ between the liquidus and solidus. In order to confirm the general applicability of the present 3-D turbulent flow and coupled-solidification model, it is suggested here that simulations should also be carried out for an alloy having a long solidification range, for example, Al 2040 which has a solidification range of $138^0 C$.

6. Further sensitivity analysis concerning the effective heat transfer coefficient for the mold and post mold regions should be carried out for different alloys. It would be interesting to find out, for a fixed casting speed, what should be the minimum effective heat transfer coefficient in the mold region that will prevent the breakout condition to develop This will allow the operator to correctly control the water flow-rate and chilling water temperature circulating in the outside mold walls.

7. Simulations should be carried out for higher aspect ratio casters than the one modeled in this research. To increase the productivity, the modern DC casting industries are using or are planning to use casters having high aspect ratios than the one modeled here.

8. The porosity as well as the permeability of the filter/foam should be varied in order to ascertain their influences on the solid-shell thickness and on the sump depth. By varying these two properties, a suitable filter/foam may be suggested for a particular system. In the model, the position and thickness of the filter/foam should be varied in order to assess the implications of these changes in minimizing and dampening the turbulence in the melt entering the mold.

9. In the studied model, the solid network- structure of the porous filter/foam was assumed to be in local thermal equilibrium with the surrounding melt. This is justified by the fact that the thermal diffusivity of the steel filter/foam used in this study is quite high and as a result it will reach local thermal equilibrium with the melt rather quickly. The ceramic (alumina) filter/foam is usually used by the DC casting industry for filtering aluminum alloy melts, Since ceramic has a very low thermal diffusivity, the local thermal equilibrium assumption in that case may not be applicable and thus may require the implementation of the more complex local non-equilibrium thermal model between the melt and the porous filter/foam.

10. Besides Launder and Sharma's low Reynolds number $k-\varepsilon$ model, there are many other low Reynolds number k-e models which have been proposed and successfully used in the literature for solving various single phase turbulent flow, heat and mass transfer problems. One can implement these models to resolve turbulent melt flow in the DC caster and see if the other $k-\varepsilon$ models do predict consistent and reliable results similar to those obtained in this research. Also, one can try to use higher order turbulence models, like Large Eddy Simulation (LES) model, Reynolds stress model, etc to ascertain their influences, if any, on the predicted results.

REFERENCES

[1] Alcan Primary Metal British Columbia Website, Alcan Corporate Affairs, B.C. Operations, http://www.sno.net/alcan/,2002.

[2] Amin, M. R. and Greif, D. Conjugate heat transfer during two-phase solidification process in a continuously moving metal using average heat capacity method, Int. J. Heat Mass Transfer, Vol. 42, pp. 2883-2895, 1999.

[3] Amin, M. R., Thermal analysis during continuous casting process using effective heat capacity method, J Thermophysics & Heat Transfer, Vol. 14, No. 2, pp. 170-176, 2000.

[4] Amin, M. R. and Mahajan, A. Modeling of turbulent heat transfer during the solidification process of continuous castings, J. Materials Processing Tech., Vol. 174, pp. 155-166, 2006.

[5] Argyropoulos, S. A. and Carletti, H. Comparisons of the effects of air and helium on heat transfer at the metal-mold interface, Metallurgical and Materials Transactions B, Vol. 39B, pp. 457-468, 2008.

[6] Arsenault, A., Larouche, D., Tremblay, S. P. and Dube, J. P. DC cast thermal and fluid flow simulation using a semi-permeable model of TF combo bag, Light Metals (Ed. DeYoung D. H.), TMS, pp.781-785, 2008.

[7] Aubrey, L. S., Cummings, M. A. and Oliver, C. L. et al. The development and performance evaluation of a dual stage ceramic foam filtration system, Light Metals, pp. 845- 855, 1996.

[8] Baserinia, A. R., Ng, H., Weckman, D. C., Wells, M. A., Barker, S. and Gallerneault, M. A simple model of the mold boundary condition in Direct-Chill (DC) casting of aluminum alloys, Metallurgical and Materials Transactions B, Vol. 43B, pp. 887- 901, 2012.

[9] Beattie, D. D., Davies, G. J., and Tizard, A. H., Proc. Conf. modeling and simulation for applied control system, Inst. Measurement and Control, pp. 57-65, University of Bath (1973).

[10] Beckermann. C., Ramadhyani, S. and Viskanta, R. Natural convection flow and heat transfer between a fluid layer and a porous layer inside a rectangular

enclosure, J. of Heat Transfer- Transactions of the ASME, Vol. 109, No. 2, pp. 363-370, 1987.

[11] Beckermann. C., Viskanta, R. and Ramadhyani, S. A numerical study of non-Darcian natural convection in a vertical enclosure filled with a porous medium, Numerical Heat Transfer, Vol. 10, No. 6, pp. 557-570, 1986.

[12] Brochu, C., Dault, R., Dery, J., et al. Liquid metal filtration and distribution using fiberglass fabric, Light Metals, TMS, Warrendale, PA, USA, pp.839-844, 1996.

[13] Caretto, L. S., Curr, R. M., and Spalding, D. B. Two numerical methods for three-dimensional boundary layers, *Comp. Methods in Appl. Mech. Eng.*, Vol. 1, pp. 39-48, 1972.

[14] Caron, Y., Bernard, D. and LeBlanc, G. A new advanced mould technology for sheet ingot casting, Light Metals, pp. 991-998, 1994.

[15] Chien, K.-Y. Predictions of channel and boundary-layer flows with a Low-Reynolds-Number turbulence model," AIAA Journal, pp. 33-38, 1982.

[16] Chu M. G., Jacoby J. E. Macrosegregation characteristics of commercial size aluminum alloy ingot cast by the direct chill method, Light Metals (Ed. Bickert C.M.), TMS, Warrendale, Pennsylvania, USA, pp. 925–930, 1990.

[17] Coates, B. and Argyropoulos, S. A. The effects of surface roughness and metal temperature on the heat-transfer coefficient at the metal mold interface, Metallurgical and Materials Transactions B, Vol. 38B, pp. 243-255, 2007.

[18] Das, S. K. Modeling and optimization of direct chill casting to reduce ingot cracking, Final Technical Report, ORNL/TM-2006/56, 61- pages, 2006.

[19] Das, S. K. Thermal modeling of DC continuous casting including submould boiling heat transfer, Applied Thermal Engineering, Vol. 19, pp. 897-916, 1999.

[20] Das. S. K. and Sarkar, A. Computational modeling of thermal transport phenomena in continuous casting process based on non-orthogonal control volume approach, Communications in Numerical Methods in Engineering, Vol.12, pp. 657-671, 1996.

[21] Davidson, P. A. and Flood, S. C. Natural Convection in Aluminum Ingot, Metallurgical and Materials Transactions B, Vol. 25B, pp. 293- 302, 1994.

[22] Devadas, C. and Grandfield, J. F. Experiences with modeling D.C. casting of aluminum, Light Metals (Ed. Rooy E.L.), The Minerals, Metals and Materials Society, Warrendale, Pennsylvania, USA, pp. 883-892, 1991.

[23] Dickhaus, C. H., Ohm, L. and Engler, S. Models to reflect the mechanical-properties of solidifying shells during continuous casting, Metall. , Vol. 46, No. 6, pp. 581-584, 1992.

[24] Dobatkin, V. I. Continuous casting and casting properties of alloys, Moscow: Oborongiz, 1948.

[25] Dorward, R. C. and Beerntsen, D. J. Effects of casting practice on macro-segregation and microstructure of 2024 alloy billet, Light Metals (Ed. Bickert C.M.), TMS, Warrendale, PA, USA, pp. 919-24, 1990.

[26] Droste, W. and Schneider, W. Laboratory Investigations about the influence of starting conditions on butt curl and swell of D.C. cast sheet ingots, Light Metals (Ed. Rooy E.L.), The Minerals, Metals & Materials Society, Warrendale, USA, pp. 945-951, 1991.

[27] Du, J., Kang, B. S. J., Chang, K. M. and Harries, J. Computational modeling of DC casting of aluminum alloy using finite element method, Light Metals (Ed. Welch B.), TMS, pp.1025-1030, 1998.

[28] Du, Q., Eskin, D. G. and Katgerman, L. Modeling macrosegregation during direct chill casting of multi component aluminum alloys, Metallurgical and Materials Transactions A – Physical Metallurgy and Materials, Vol. 38A, No. 1, pp. 180-189, 2007.

[29] El-Demerdash, M. F. Modeling of temperature distribution during DC casting of aluminum alloys, Light Metals (Ed. Subodh K. D.), pp. 949-954, 1993.

[30] El-Raghy, T. S., El-Demerdash, M. F., Ahmed, H. A. and El-Sheikh, A. M. Modeling of the transient and steady state periods during aluminum DC casting, Light Metals (Ed. Evans, J.), pp. 925-929, 1995.

[31] Emley, E.F. Continuous casting of aluminum, International Metals Reviews, Vol. 21. pp. 75–115, 1976.

[32] Eskin D. G. Physical metallurgy of direct chill casting of aluminum alloys, Advances in Metallic Alloys, CRC Press, 2008.

[33] Eskin, D. G. and Katgerman, L. Solidification Phenomena related to direct chill casting of aluminum alloys: Fundamental studies and future challenges, Materials Technology: Advanced Performance Materials, Vol.24, No. 3, pp.152–156, 2009.

[34] Eskin, D. G., Savran, V. I. and Katgerman, L. Effects of melt temperature and casting speed on structure and defect formation during direct chill casting of an Al-Cu alloy, Metallurgical and Materials Transactions A– Physical Metallurgy and Materials, Vol.31, No. 7, pp.1965–1976, 2005.

[35] Eskin, D. G., Suyitno and Katgerman, L. Mechanical properties in the semi-solid state and hot tearing of aluminum alloys, Progress in Materials Science, Vol. 49, No. 5, pp. 629-711, 2004.

[36] Eskin, D. G., Zuidema, J., Savran, V. I. and Katgerman, L. Structure formation and macrosegregation under different process conditions during DC casting, Materials Science and Engineering A– Structural Materials Properties Microstructure and Processing, Vol. 384 Nos. 1-2, pp.232–244, 2004.

[37] Etienne, J. F. R. C., Baserinia, A. R., Ng, H., Wells, M. A. and Weckman D. C. Heat-transfer measurements in the primary cooling phase of the direct-chill casting process, Metallurgical and Materials Transactions B, Vol. 43B, pp.1202-1213, 2012.

[38] Evans, J. W. and Jones Jr, W. K. Mathematical modeling in aluminum casting and molten metal treatment, Light Metals (Ed Schneider, W.), TMS (Warrendale, PA: The Minerals Metals and Materials Society), pp. 669-678, 2002.

[39] Flemings, M.C., “Solidification processing”, McGraw-Hill, New York, 1974.

[40] Flood, S. C., Katgerman, L., Langille, A. H., Rogers, S. C. and Read, M. Modelling of fluid flow and stress phenomena during DC casting of aluminum alloys, in: P.G. Campbell (Ed.), Light Metals, pp. 943-947, 1989.

[41] Flood, S. C., Davidson, P. A., Rogers, S., et al. A scaling analysis for the heat flow, solidification and convection in continuous casting of aluminum,

Modeling of Casting, Welding and Advanced Solidification Processes VII (London, England) pp. 801-808, 1995.

[42] Fortier, M., Larouche, A., Chen, X. G. and Caron, Y. The effect of process parameters on the metal distribution for DC sheet ingot casting, Light Metals (Ed. Kvande, H.), TMS, pp.1019-1024, 2005.

[43] Gariepy B, Caron Y. Investigation in the effects of casting parameters on the extent of centerline macrosegregation in DC cast sheet ingots, Light metals (Ed. Rooy, E.L.), New Orleans, LA, USA, Minerals, Metals and Materials Society (TMS), pp. 961–971, 1991.

[44] Grandfield, J. F. and McGlade P. T. DC casting of aluminum: Process behavior and technology, Materials Forum Vol. 20. pp. 29–51, 1996.

[45] Grandfield, J. F. DC casting of aluminum: A short review of process development, Proceedings of 5th Australasian – Asian Pacific Conference on Aluminum Cast House Technology, pp. 231–243, 1997.

[46] Grandfield, J. F., Nguyen, V., et al. Ingot caster productivity improvement through examination of mould heat flow and deformation, Proceedings of the Australasian Conference and Exhibition – Aluminum Cast House Technology, Sydney, pp. 147-154, 2007.

[47] Grealy, G. P., Davis, J. L., Jensen, E. K. and Moritz, P. A. T. J. Advances for DC Ingot Casting: Part 1- Introduction and Metal Distribution, Light Metals (Anjier, J. L.), pp. 805-811, 2001.

[48] Grealy, G. P., J. L., Jensen, Jensen, E. K. and Moritz, P. A. T. J. Advances for DC Ingot Casting: Part 2- Heat Transfer and Casting Results, J Light Metals (Anjier, J.L.), pp. 813-821, 2001.

[49] Grijn, G. U., Schneider, W., Ray, S. and Marthinusen, J. O. Recent improvements in ceramic foam filter bowl design by coupled heat and fluid flow modelling, Light Metals, The Minerals, Metals & Materials Society, pp.1041-1047, 1999.

[50] Gruen, G. U., Buchholz, A. and Mortensen, D. 3-D modeling of fluid flow and heat transfer during the DC casting process- Influence of flow modeling approach, Light Metals (ED. Peterson, R.D.), Proceedings of Sessions, TMS,

Annual Meeting (Warrendale, Pennsylvania), Nashville, TN, pp. 573- 578, 2000.

[51] Gruen, G. U. and Vogelsang E. D. Optimum design of a distribution pan for level pour casting, Light Metals (Ed. Evans, J.), TMS, pp. 1061-1069, 1995.

[52] Gruen, G. U., Eick, I. and Vogelsang, D. 3-D modeling of fluid flow and heat transfer for DC casting of rolling ingots, Light Metals (Ed. Mannweiler, U.), pp. 863-869, 1994.

[53] Guthrie, R.I.L. and Nilmani, M. Impurity sources and control - general principles of melt treatment, Aluminum Cast House Technology; Theory & Practice, Melbourne University, pp. 85-104, 1993.

[54] Hakonsen, A. M. Dimensionless diagram for the temperature distribution in direct-chill continuous casting, Cast Metals, Vol. 8, No. 3, pp. 147-157, 1995.

[55] Hao, H., Maijer, D. M., Wells, M. A., Cockcroft, S. L., Sediako, D. and Hibbins, S. Development and validation of a thermal model of the direct chill casting of AZ31 Magnesium billets, Metallurgical And Materials Transactions A, Vol.35A, pp.3843-3854, 2004.

[56] Hasan, M. and Ragel, K. R. Advanced CFD modeling of DC casting of aluminum alloys, TMS Annual Meeting, Light Metals, pp. 805-810, 2009.

[57] Hawkins, G, Chatterjee, S., Ahmed, R. A., Jacobs, M. S., Charlie, S. and Freytes, C. Bottom control pouring system of Alba's DC 6 slab caster, Materials and Manufacturing Processes, Vol. 22, pp. 939-946, 2007.

[58] Hollworth, B. R. and Berry, R. D. Heat transfer from arrays of impinging jets with large jet-to-jet spacing, ASME paper No. 78, GT-117, 1978.

[59] Hong, J. T., Tien, C. L. and Kaviany, M. Non-Darcian effects on vertical plate natural convection in porous media with high porosities, Int. J. Heat Mass Transfer, Vol. 28, No. 11, pp. 2140-2157, 1985.

[60] Hu, W., Le, Q., Zhang, Z., Bao, L. and Cui, J. Numerical simulation of DC casting of AZ31 magnesium slab at different casting speeds, J. Magnesium Alloys, Vol.1, pp. 88-93, 2013.

[61] Ilinca, F., Hetu, J. F., Arsenault, A., Larouche, D. and Tremblay, S. P. 3-D modeling of the flow and heat transfer during DC casting with a combo bag, Light Metals (Ed. Bearne, G.), TMS, pp.799-804, 2009.

[62] Improving performance: Billet Casting, Pyrotek Supplement, http://www.pyrotec.info/documents/brochure/873_billet_casting_insert_web.pdf.

[63] Improving performance: Slab Casting, Pyrotek Supplement, http://www.pyrotec.info/documents/brochure/849%20Slab%20Casting%20Insert_Web.pdf.

[64] Instone, S., Badowski, M. and Schneider, W. Development of molten metal filtration technology for aluminum, Light Metals, TMS, San Francisco, CA, pp.933-938, 2005.

[65] Jacoby, J. Direct chill casting defects, Aluminum cast house technology, 5th Australian Asian Pacific Conference, 1995.

[66] Jaradeh, M. M. and Carlberg, T. Analysis of distribution of nonmetallic inclusions in aluminum DC-cast billets and slabs, Metallurgical and Materials Transactions B, Vol. 43B, pp. 82-91, 2012.

[67] Jensen, E .K. and Schneider, W. Investigations about starting cracks in DC-Casting of 6063-Type billets, II. Modeling results, Light Metals, The Minerals, Metals and Materials Society, pp. 937-943, 1990.

[68] Jensen, E .K. Mathematical model calculations in lever pour DC casting of aluminum extrusion ingots, Light Metals, TMS-AIME, pp.631-642, 1980.

[69] Jones Jr, W. K. and Evans, J. W. Physical modeling of the effects of non-symmetric placement of flow control bags used in semi-continuous casting of aluminum, Light Metals, Minerals, Metals and Materials Society/AIME, pp. 1051- 1057, 1998.

[70] Jones Jr, W. K., Xu, D., Evans, J., Williams, W. E. and Cook, D. P. Effects of combo-bag geometry on the thermal history and sump profile of a 3104 DC cast ingot, Light Metals, pp. 841-845, 1999.

[71] Katgerman, L. Developments in continuous casting of aluminum alloys, Cast Metals, Vol. 4, No. 3, pp. 133-139, 1991.

[72] Katgerman, L., Flood, S. C. and Langille, A. H. Modelling of DC casting of aluminum alloys, Production, Refining, Fabrication and Recycling of Light Metals (Eds. Bouchard, M. and Tremblay, P.) Pergamon Press, New York, pp. 96-110, 1990.

[73] Kieft, R., Oord, J. V., Frinking, F., Bal, D. and Schoonevelt, H. van. Detailed modeling of a metal distributor by means of a combined numerical and physical approach, Light Metals (Ed. Crepeau, P. N.), TMS, pp.821-827, 2003.

[74] Korti, A. I. N. and Khadraoui, Y. A numerical simulation of the DC continuous casting using average heat capacity, Scandinavian Journal of Metallurgy, Vol. 33, pp. 347-354, 2004.

[75] Kroeger, P.G. and Ostrach, S. The solution of a two-dimensional freezing problem including convection effects in the liquid region, International Journal of Heat and Mass Transfer, Vol. 17, pp.1191- 1207, 1974.

[76] Lam, C. G. K. and Bremhorst, K. A modified form of the k-ε model for predicting wall turbulence, Transactions of ASME, Vol. 103, pp. 456-460, 1981.

[77] Large, J. L. The fundamental theory of flow through permeable media from Darcy to turbulence, in Transport Phenomena in Porous Media, D. B. Ingham and I. Pop, eds., Elsevier Science, ISBN: 0-08-042843-6, pp. 446, 1998.

[78] Launder, B. E. and Sharma, B. I. Application of the energy dissipation model of turbulence to the calculation of the flow near a spinning disk, Letters in Heat and Mass Transfer, Vol. 1, pp. 131-138, 1974.

[79] Lewis, D. M., Savage, J. The principles of continuous casting of metals, Metallurgical Reviews, The Institute of Metals; London, Vol. 1. pp. 65–116, 1956.

[80] Long, Z., Han, Q., Viswanathan, S., et al. Integrated 3D model to simulate solidification and predict hot cracking during DC casting of aluminum alloys, Light Metals (Ed. Kvande, H.), TMS (The Minerals Metals and Materials Society), pp. 1057-1062, 2005.

[81] Masuoka, T. and Takatsu, Y. Turbulence model for flow through porous media. Int. J. Heat mass Transfer, Vol. 39, No. 13, pp. 2803 -2809, 1996.

[82] Minakawa, S., Samarasekera, I. V. and Weinberg, F. Centerline porosity in plate castings, Metall. Trans., Vol. 16B, pp. 245-255, 1987.

[83] Mo, A., Rusten, T., Thevik, H. J. et al. Modeling of surface segregation development during DC casting of rolling slab ingots, Light Metals, Proceedings of Sessions, TMS Annual Meeting(Warrendale, Pennsylvania), Orlando, FL, USA, Minerals, Metals & Materials Soc.(TMS), pp. 667-674, 1997.

[84] Mortensen, D. A mathematical model of the heat and fluid flows in Direct-Chill casting of aluminum sheet ingots and billets, Metallurgical & Materials Transactions B, Vol. 30B, pp. 119-133, 1999.

[85] Mortensen, D., Henriksen, B. R., M'Hamidi, M. et al**.** Coupled modeling of air-gap formation and surface exudation during extrusion ingot DC- casting, TMS Light Metals, New Orleans, LA, pp.773-779, 2008.

[86] Muojekwu, C. A., Samarasekera, I. V. and Brimacombe, J. K. Heat transfer and microstructure during the early stages of metal solidification, Metallurgical and Materials Transactions B- Process Metallurgy & Materials Processing Science, Vol. 26, No. 2, pp. 361-382, 1995.

[87] Nadella R, Eskin D. G. and Katgerman L. Effect of grain refining on defect formation in DC cast Al-Zn-Mg-Cu alloy billet, TMS Light Metals (Ed. Sørlie M.), Orlando, FL, pp. 727-732, 2007.

[88] Nadella, R. K., Eskin, D. G. and Katgerman, L. Continuous Casting of Non-Ferrous Metals, Ed. Mu¨ ller HR., Neu-Ulm, Germany, Wiley-VCH Verlag GmbH&Co., pp. 277–82, 2005.

[89] Nadella, R., Eskin, D. G., Du,. Q. and Katgerman, L. Macrosegregation in direct-chill casting of aluminium alloys, Progress in Materials Science, Vol.53, pp.421-480, 2008.

[90] Nadella, R., Eskin, D. G. and Katgerman, L. Role of grain refining in macrosegregation upon direct chill casting of AA 2024 round billet, Materials Science Forum, Vancouver, 519–521:1841–1846, 2006.

[91] Nagano, Y. and Hishida, M. Improved form of the k-ε model for wall turbulent shear flows, Transactions of ASME, Vol. 109, pp. 156-160, 1987.

[92] Nallathambi, A. K., Specht, E. and Bertram A. Computational aspects of temperature-based finite element technique for the phase-change heat conduction problem, Computational Materials Science, Vol. 47, pp. 332-341, 2009.

[93] Netto, P.G.Q. and Guthrie, R.I.L. Modeling of a novel configuration for single belt caster: The influence of empirical parameters on the solidification profile, ISIJ International, Vol. 40, No. 5, pp. 460-468, 2000a.

[94] Netto, P.G.Q. and Guthrie, R.I.L. The importance of turbulence modeling in the design of a novel delivery system for a single belt steel casting process, Int. J. Heat Mass Transfer, Vol. 43, No. 1, pp. 21-37, 2000b.

[95] Nofal, A. A. Surface defect formation in the D.C.-Cast aluminum products, Advances in Continuous Casting: Research and Technology, Abington Hall, Abington, Cambridge, Woodhead, pp. 205-218, 1992.

[96] Patankar, S. V. Numerical heat transfer and fluid flow, Hemisphere Publishing Corporation, 1980.

[97] Patankar, S. V. Numerical prediction of three-dimensional flows, in B. E. Launder (ed.) Studies in Convection: Theory, Measurment and Applications, Vol. 1, Academic, New York, 1975.

[98] Patel, V. C. and Scheuerer, G. Turbulence models for near-wall and Low-Reynolds number flows: A review, AIAA Journal, Vol. 23, No. 9, pp. 1308-1319, 1985.

[99] Patnkar, S. V. and Spalding, D. B. A calculation procedure for heat, mass and momentum transfer, Int. J. Heat and Mass Transfer, Vol. 15, pp. 1787-1806, 1972.

[100] Pedras, M. H. J. and de Lemos, M. J. S. On the definition of turbulent kinetic energy for flow in porous media, Int. Comm. in Heat & Mass Transfer, Vol. 27, No. 2, pp. 211 -220, 2000.

[101] Pedras, M. H. J. and de Lemos, M. J. S. Macroscopic turbulence modeling for incompressible flow through undeformable porous media, International Journal of Heat and Mass Transfer, Vol. 44, pp. 1081-1093, 2001a.

[102] Pedras, M. H. J. and de Lemos, M. J. S. On the mathematical description and simulation of turbulent flow in a porous medium formed by an array of elliptic rods, Journal of Fluids Engineering, Vol. 123, pp. 941-947, 2001b.

[103] Pedras, M. H. J. and de Lemos, M. J. S. Computation of turbulent flow in porous media using a low-Reynolds k-ε model and an infinite array of transversally displaced elliptic rods, Numerical Heat Transfer, Part A, Vol. 43, pp. 585-602, 2003.

[104] Peel, D. A., and Pengelly, A. E., Mathematical models in metallurgical process development, Iron and Steel Institute Publication 123, London, Vol. 2, pp. 186-196, 1970.

[105] Prasad, A. and Bainbridge, I. Experimental determination of heat transfer across the metal/mold gap in a Direct-Chill (DC) casting mold-Part-I: Effect of gap size and mold gas type, Metallurgical and Materials Transactions A, Vol. 44A, pp. 456-468, 2013.

[106] Prillhofer, B., Bottcher, H. and Antrekowitsch, H. Strategies to reduce inclusion input during liquid metal transportation and melt distribution during DC casting of Al alloys, Light Metals (Ed. Johnson J. A.), TMS, pp.785-790, 2010.

[107] Q. Du, Eskin, D. G. and Katgerman, L. Modeling macrosegregation during Direct-Chill casting of multicomponent aluminum alloys, Metallurgical and Materials Transactions A, Vol.38A, pp.180-189, 2007.

[108] Raffourt, C., Fautrelle, Y., Meyer, J. L. and Hannart, B. Liquid metal distribution in a slab DC casting: Experiments and modeling approach, Light Metals, New Orleans, LA, USA, Publ. by Minerals, Metals & Materials Soc. (TMS), pp. 877-882, 1990.

[109] Reese, J. M. Characterization of the flow in the molten metal sump during direct chill aluminum casting, Metallurgical and Materials Transactions B,

Process Metallurgy and Materials Processing Science, Vol. 28B, pp. 491-499, 1997.

[110] Sanders, R. E. Continuous casting for aluminum sheet: A product perspective, JOM, Vol. 6, No. 2, pp. 291-301, 2012.

[111] Schneider, W. and Jensen, E .K. Investigations about starting cracks in DC-Casting of 6063-Type billets, Part-I: Experimental results, Light Metals, Anaheim, CA, USA, Minerals, Metals and Materials Soc.(TMS), pp. 931-936, 1990.

[112] Schneider, W. DC casting of aluminum alloys-past present and future, Light Metals, Proceedings of Sessions, TMS Annual Meetings (Warrendale, Pennsylvania), Seattle, WA, pp. 953-960, 2002.

[113] Sengupta, J., Cockcroft, S. L., Maijer, D. M., Wells, M. A. and Larouche, A. On the development of a three-dimensional transient thermal model to predict ingot cooling behavior during the start-up phase of the direct chill-casting process for an AA5182 aluminum alloy ingot, Metallurgical and Materials Transactions B, Vol. 35A, pp. 523-540, 2004.

[114] Sengupta, J., Cockcroft, S. L., Maijer, D. M., Wells, M. A. and Larouche, A. The effect of water ejection and water incursion on the evolution of thermal field during the start-up phase of the direct chill casting process, Journal of Light Metals, Vol. 2, pp. 137-148, 2002.

[115] Sengupta, J., Thomas, B. G. and Wells, M. A. The use of water cooling during the continuous casting of steel and aluminum alloys, Metallurgical and Materials Transactions A, Vol.36A, pp.187-204, 2005.

[116] Sengutpa, J. Mathematical modeling of the evolution of thermal field during start-up phase of the direct-chill casting process for AA5182 sheet ingots, Ph. D. Thesis, Dept. of Metals and Materials Engineering, University of British Columbia, Vancouver, Canada, 2002.

[117] Shuyan, S., Hai, H., Xingguo, Z., Canfeng, F., Shan, Y. and Junze J. A 3-D mathematical model of thermal field evolution in the direct chill casting of superlight magnesium alloy slabs, Rear Metal Materials and Engineering, Vol. 38, No. 2, pp. 203-207, 2009.

[118] Somerton, C. V., Mcdonouch, J. M. and Catton, I. Natural convection in a volumetrically heated porous layer, J. of Heat Transfer- Transactions of the ASME, Vol. 106, No. 1, pp. 241-244, 1984.

[119] Takatsu, Y. and Masuoka, T. Turbulent phenomena in flow through porous Media, J. Porous Media, Vol. 3, pp. 243 -251, 1998.

[120] Tarapore, E. D. Thermal modeling of D.C. continuous billet casting, Light Metals (Ed. Campbell P.G.), TMS, pp. 875-880, 1989.

[121] Tilak, R. Improved extrudability of aluminum alloys with LARS refinement. metalword, http://www.metalword.co.in/cover12.pdf,2005.

[122] Tremblay, S. P. and Lapointe, M. The manufacturing, design and use of a new reusable molten metal distributor for sheet ingot casting, Light Metals, Proceedings of Sessions, TMS Annual Meeting (Warrendale, Pennsylvania), Seattle, WA, pp. 961-965, 2002.

[123] Tremblay, S. P. and Vincent, M. Development and use of a new composite material for aluminium contact applications, Light Metals (Ed. Kvande, H), TMS (The Minerals, Metals and Materials Society), pp. 1007-1012, 2005.

[124] Tremblay, S. P. and Ruel, M. The manufacture, use and plant test results of TF combo bags for DC sheet ingot casting, TMS, 2003 Annual Meeting, San Diego, CA, USA, Light Metals, pp.2-8, 2003.

[125] Tsunekawa, M., Tani, S., Okazaki, H. and Hayashi, N. Mechanisms of oxide generation anti mixing into aluminum ingot in cast start phase, Light Metal Technical Reports, pp. 831-37, 2001.

[126] Vafai, K. and Tien, C. L. Boundary and inertia effects on flow and heat transfer in porous media, Int. J. Heat Mass Transfer, Vol. 24, pp. 195 -203, 1981.

[127] Vafai, K., Alkire, R. L. and Tien, C. L. An experimental investigation of heat transfer in variable porosity media, J. of Heat Transfer- Transactions of the ASME, Vol. 107, No. 3, pp. 642-647, 1985.

[128] Van Driest, E. R. On turbulent flow near a wall, Journal of the Aeronautical Sciences, Vol. 23, pp. 1007-1011, 1956.

[129] Versteeg, H. K. and Malalasekera, W. An introduction to computational fluid dynamics, The Finite Volume Method, Harlow: Pearson/Prentice Hall 2007.

[130] Voller, V. R. and Prakash, C. A fixed grid numerical modeling methodology for convection-diffusion mushy region phase-change problems, Int. J. Heat Mass Transfer, Vol. 30, pp. 1709-1719, 1987.

[131] Vreeman, C. J. and Incropera, F. P. The effect of free-floating dendrites and convection on macrosegregation in direct chill cast aluminum alloys Part II: predictions for Al-Cu and Al-Mg alloys, International Journal of Heat and Mass Transfer, Vol. 43, pp. 687-704, 2000.

[132] Wagstaff, F. E., Wagstaff, R. B., Bowles, K. D. and Ekenes, J. M. An improved DC casting technology, Light Metals, pp. 709-714, 1993.

[133] Weckman, D. C. Horizontal continuous casting of non-ferrous alloy rods and surface quality, Ph. D. Thesis, Dept. of Mechanical Engineering, University of Waterloo, Ontario, Canada, 2002.

[134] Weckmann, D. C. and Niessen, P. A numerical simulation of the D.C. continuous casting process including nucleate boiling heat transfer, Metallurgical and Materials Transactions B, Vol. 13B, pp. 593- 602, 1982.

[135] Weckman, D. C. and Niessen, P. Mathematical models of the DC continuous casting process, Canadian Metallurgical Quarterly, Vol. 23, No. 2, pp. 209-216, 1984.

[136] Williams, A. J., Croft, T. N. and Cross, M. Modeling of ingot development during the start-up phase of direct chill casting, Metallurgical and Materials Transactions B, Vol. 38B, pp. 727- 734, 2003.

[137] Wiskel, J. B. and Cockcroft, S. L. Heat-flow-based analysis of surface crack formation during the start-up of the direct chill casting process: Part I. Development of the inverse heat-transfer model, Metallurgical and Materials Transactions B, Vol. 27B, pp. 119-127, 1996.

[138] Wiskel, J. B. and Cockcroft, S. L. Heat-flow-based analysis of surface crack formation during the start-up of the direct chill casting process: Part II. Experimental study of an AA5182 rolling ingot, Metallurgical and Materials Transactions B, Vol. 27B, pp. 129-137, 1996.

[139] Wiskel, J. B., Thermal analysis of the Start-up Phase for D.C. casting of an AA5182 aluminum ingot, Ph. D. Thesis, Dept. of Metals and Materials Engineering, University of British Columbia, Vancouver, Canada, 1996.

[140] Xu, D. and Evans, J. W. Physical modeling (by Particle Image Velocimetry) and mathematical modeling of metal delivery devices for EM and DC casting of aluminum, Light Metals, pp. 1051-1058, 1997.

[141] Xu, D., Jones Jr, W. K. and Evans, J. W. The use of Particle Image Velocimetry in the physical modeling of flow in electromagnetic or Direct-Chill casting of aluminum Part I. development of the physical model, Metallurgical and Materials Transactions B, Process Metallurgy and Materials Processing Science, Vol. 29B, No. 6, pp. 1281- 1288, 1998.

[142] Xu, D., Jones Jr, W. K. and Evans, J. W. The use of Particle Image Velocimetry in the physical modeling of flow in electromagnetic or Direct-Chill casting of aluminum Part II. Results of the physical model, including bag geometry, blockage, and nozzle placement, Metallurgical and Materials Transactions B, Process Metallurgy and Materials Processing Science, Vol. 29B, No. 6, pp. 1289- 1295, 1998.

[143] Xu, Y., Wang, J. C., Guo, S. J., Li, X. T. and Xue, G. X. Effects of water-restricted panel on the casting process of high strength aluminum alloy ingots, J. Mater. Process. Technol., Vol. 211, pp. 78-83, 2011.

[144] Yang, Y. T. and Hwang, M. L. Numerical simulation of turbulent fluid flow and heat transfer characteristics in a rectangular porous channel with periodically spaced heated blocks, Numerical Heat Transfer, Part A, Vol. 54, pp. 819- 836, 2008.

[145] Zhang, L., Eskin, D.G., Miroux, A., Subroto, T. and Katgeran, L. Influence of melt feeding scheme and casting parameters during direct-chill casting on microstructure of an AA7050 billets, Metallurgical and Materials Transactions B, Vol. 43B, pp. 1565- 1573, 2012.

[146] Zuidema jr, J., Katgerman, L., Opstelten, I. J. and Rabenberg, J. M. Secondary cooling in DC casting: Modeling and experimental results, Light Metals (Ed.

Anjier, J.L.), TMS (The Minerals, Metals & Materials Society), NM, USA, pp. 873-878, 2001.